MANY-BODY ENTANGLED DYNAMICS OF CLOSED AND OPEN SYSTEMS FOR QUANTUM SIMULATORS

by

Daniel Jaschke

A thesis submitted to the Faculty and the Board of Trustees of the Colorado School of Mines in partial fulfillment of the requirements for the degree of Doctor of Philosophy (Applied Physics).

Golden, Colorado

Date _____

Signed: _____
Daniel Jaschke

Signed: _____
Dr. Lincoln D. Carr
Thesis Advisor

Golden, Colorado

Date _____

Signed: _____
Dr. Uwe Greife
Professor and Head
Department of Physics

ABSTRACT

When *D-wave* was founded in 1999, quantum computing was still an ambitious vision. In the past five years, quantum computing has moved from this vision to a very reachable goal with major companies such as *Google*, *IBM*, *Intel*, and *Microsoft* investigating quantum computation investing in this technology. Together with a vivid start-up scene including companies such as *1QBit*, *ionQ*, *Q-CTRL*, *QuantumCircuits*, and *Rigetti*, they aim to develop hardware and software for a new generation of computers which can tackle problems intractable on classical computers. This thesis revolves around the simulation of such quantum systems and, thus, it has some direct connections to this intriguing new wave of technology. Our focus is shifted toward the side of quantum simulators, which use quantum systems to investigate a specific research question, e.g., predicting the properties of new materials. The results of such simulations can be thought of as an analog measurement outcome of the final state of the quantum simulator. Quantum annealing is one prominent example where the final state encodes the solution to an optimization problem. In contrast, quantum computers work in the spirit of a classical computer calculating in terms of zeros and ones while allowing superpositions and entanglement to reach a quantum advantage. They favor a formulation in terms of quantum gates, which are adapted from the logical gates used in classical computers.

We establish a common understanding of the terminology and questions arising in this area of research in the first part of the thesis. We consider the dynamics of closed quantum systems, which has direct connections to the quantum annealing architectures. We analyze how long-range interactions in the quantum Ising model modify the quantum phase diagram. The quantum critical point for the ferromagnetic model shifts to higher external fields to break up the order in comparison to the nearest neighbor model. In contrast, the antiferromagnetic order breaks at lower external fields when including long-range interactions. In

the dynamics, we quench through the quantum critical points evaluated for different values for the long-range interactions and analyze the Kibble-Zurek hypothesis via the defects generated in the ferro- and antiferromagnetic limits. These simulations reveal how the number of defects depends on the quench rate and the strength of the long-range interactions, where we find that the defect density decreases toward the nearest-neighbor limit in the ferromagnetic model. Such results are valuable when considering the balance between long-range interactions and quench rates in adiabatic quantum computing.

We then move on to open quantum systems. Closed systems are an incomplete description of a quantum system when it is disturbed from an environment or measurement devices not included in the description of the closed system; such effects lead to decoherence of the system. We focus on large reservoirs described by the Lindblad master equation. The research questions revolve around the thermalization of a many-body quantum system. This study treating open quantum systems can be seen as the analog of the eigenstate thermalization hypothesis vs. generalized Gibbs ensemble handling closed quantum systems with regards to the question of whether or not thermalization occurs. The choice of the operator in the interaction Hamiltonian between the system and the reservoir governs which limit of the phase diagram cannot thermalize by definition in the global multi-channel approach. Furthermore, we find regions in the phase diagram of a small quantum Ising chain protected from thermalization and decoherence. Evidently, other regions are favorable to reach thermalization as quick as possible, which is essential to dissipative state preparation. In addition to the global multi-channel model, we analyze the concept of neighborhood single-channel Lindblad operators, which allows one to install non-trivial long-range order; this is a task where single-site single-channel Lindblad operators fail.

The next part treats the numerical methods used in the first chapters of this thesis. We describe the exact diagonalization and tensor network algorithms; both are available in our open source package *Open Source Matrix Product States*. The algorithms contain a selection of state-of-the-art methods for closed and open quantum system, e.g., matrix product den-

sity operators as tensor network type and the time-dependent variational principle as time evolution method. We aim for an upgrade from a stand-alone package to the integration into a science gateway. Science gateways serve as a cloud resource for research software. The results from the research on tensor network methods during this thesis will significantly contribute to an efficient science gateway using the algorithms with optimal scaling and versatile features such as meaningful error bars. The equations to estimate error bars for many observables depend on easily accessible parameters such as the system size, the energy gap to the first excited state, and the variance of the energy. The error bounds of the bond entropy in the quantum Ising model are at the level of 10^{-2}, where most other observables such as spin measurements have a tighter error bound of around 10^{-3} for 256 sites. The choice of the most efficient algorithm plays a key role in many-body mixed states as we simulate the density matrix instead of a pure state. Providing all three major methods for mixed states within our library, we have the option to pick locally purified tensor networks to calculate thermal states and matrix product density operators for the dynamics governed by the Lindblad equation. Both choices are based on the examples in this thesis. Quantum trajectories are favorable for systems generating a large amount of entanglement and simulations parallelized across a large number of CPU cores, which is on the order of magnitude of the number of trajectories.

We close the thesis with a discussion of the results in the context of the present research and highlight how the work presented raises even more intriguing questions. This collection of open questions is considered in the second part of the conclusion. These projects can be divided loosely into additions to the numerical methods enabling novel modeling of quantum systems and simulations predicting the actual behavior of physical systems, where most of them can be solved with the present software.

TABLE OF CONTENTS

LIST OF FIGURES

LIST OF TABLES

LIST OF SOURCE CODES

LIST OF SYMBOLS

Identity matrix . . . . . $\mathbb{I}$

Dimension of the local Hilbert space of one site . . . . . d

Dimension of the local Hilbert space of one site (Sec. 6) . . . . . d_{loc}

Dimension of Hilbert space of the complete system (Sec. 8) . . . . . D

Dimension of Hilbert space of the complete system in a symmetry sector (Sec. 8) . . D_S

Trace distance . . . . . $\mathcal{D}$

Time step in discretized time evolution . . . . . dt

Energy . . . . . E

Fidelity of quantum states . . . . . $\mathcal{F}$

Critical external field in the quantum Ising model (Sec. 4) . . . . . h_c

External field in the quantum Ising model (Sec. 4) . . . . . h

Reduced Plack constant . . . . . $\hbar$

Hamiltonian of a quantum system . . . . . H

Imaginary unit i

Spin interaction strength (Sec. 4) . . . . . J

Boltzmann constant . . . . . k_B

System size (except Sec. 6) / Lindblad operator L

Liouville operator from Lindblad master equation in Liouville space . . . . . $\mathcal{L}$

System size (Sec. 6) . . . . . N

Global number operator (except Sec. 6) . . . . . N

Real part of a complex number . . . . . $\Re$

von Neumann entropy, bond entropy . . . . . S

Operator in the interaction Hamiltonian acting on the system's site k (Sec. 6 and 7) . . S_k

Trace or partial trace if subscript present . . . . . Tr

Power-law decay of the long-range interactions (Sec. 4) . . . . . α

Thermodynamic beta $1/(k_B T)$ with temperature T . . . . . β

Singular values of the Schmidt decomposition . . . . . λ

Eigenvalues of the Liouville operator containing the thermalization rate (Sec. 6) . . . . Λ_j

Density matrix / defect density . . . . . ρ

Thermal density matrix . . . . . ρ_{th}

Density matrix in its vector representation for Liouville space . . . . . $|\rho\rangle\rangle$

Pauli spin matrices . . . . . σ^x, σ^y, and σ^z

Total time of a quench . . . . . τ

Tuning parameter across the quantum Ising phase diagram (Sec. 6) . . . . . ϕ

Bond dimension between sites in a tensor network . . . . . χ

The list of symbols represents their most common use in the thesis. Due to the different publications included in this work, symbols might be used occassionally with a different meaning.

LIST OF ABBREVIATIONS

Basic linear algebra subprograms . . . . . BLAS

Bose-Einstein condensate . . . . . BEC

Central processing unit . . . . . CPU

Commutator free Magnus expansion . . . . . CFME

Completely positive trace-preserving (map) . . . . . CPT

Decomposition into orthogonal matrix Q and upper triangular matrix R . . . QR or RQ

Density Matrix Renormalization Group . . . . . DMRG

Double well . . . . . DW

Exact diagonalization . . . . . ED

Finite size scaling . . . . . FSS

General Public License . . . . . GPL

Greenberger-Horne-Zeilinger (state) . . . . . GHZ

Kibble-Zurek mechanism . . . . . KZM

Linear algebra Package . . . . . LAPACK

Local Runge-Kutta (time evolution) . . . . . LRK

Locally purified tensor networks . . . . . LPTN

Long-range quantum Ising (model) . . . . . LRQI

Matrix product density operator . . . . . MPDO

Matrix product operator . . . . . MPO

Matrix product state . . . . . MPS

Message Passing Interface . . . . . MPI

Minimally entangled typical thermal states . . . . . METTS

Multiscale entanglement renormalization ansatz . . . . . MERA

Nearest-neighbor . . . . . NN

Nitrogen vacancy (center) . . . . . NV

Open Source Matrix Product States . . . . . OSMPS

Projected entangled pair states . . . . . PEPS

Quantum Ising . . . . . QI

Quantum elementary cellular automata . . . . . QECA

Quantum trajectories . . . . . QTs

Random-access memory . . . . . RAM

Singular Value Decomposition . . . . . SVD

Tensor network . . . . . TN

Time-dependent variational principle . . . . . TDVP

Time-evolving block decimation . . . . . TEBD

Tree tensor network . . . . . TTN

infinite Matrix Product States . . . . . iMPS

open Multi Processing . . . . . openMP

ACKNOWLEDGMENTS

I want to thank the members of my committee, Mahadevan Ganesh, Mark T. Lusk, and Jeramy Zimmerman for their useful feedback on a rather long thesis. I am especially grateful to Inés de Vega for joining the committee and for always providing encouraging advice throughout our collaboration on open quantum systems. Moreover, I want to thank all the other collaborators I was fortunate to work with, foremost M. L. Wall for his feedback on two joint articles and useful insights on his perspective of the Open Source Matrix Product States code. Further collaborators include A. Dhar, K. Maeda, S. Montangero, G. Shchedrin, M. A. Valdez, D. L. Vargas, and J. Whalen. I also was lucky to have many fruitful discussion with other members of the Carr Theoretical Physics Research Group, i.e., D. Alcala, M. Alotaibi, J. Anderson, A. Gladkina, L. Hillberry, M. Jones, C. Benett, M. McLain, H. North, N. Smith, and S. Strong. I thank the Science Gateways Community Institute for helping the Carr Theoretical Physics Research Group to get started with the science gateway for the Open Source Matrix Product States including the possibility to participate in the Incubator Bootcamp in October 2017. This work would not have been possible without the support from the HPC group at Colorado School of Mines, foremost Torey Battelle, Tim Kaiser, and Michael Robbert. Finally, I want to thank my advisor Lincoln D. Carr for all the freedom he gave me during my Ph.D. research. I will always remember the time I had during these four years in his research group.

CHAPTER 1

QUANTUM TECHNOLOGY WITH STRONGLY CORRELATED SYSTEMS

Quantum mechanics has been in the focus of research since the early 20^{th} century, but recent experimental advances suggest a wave of technological innovations. These new technologies including quantum simulators and quantum computers use quantum mechanics' most fascinating attributes, such as entanglement and superpositions of states, down to the level of single atoms. The European *quantum manifesto* [1–3] emphasizes the importance of these upcoming technologies and names, beyond quantum simulators and quantum computers, new quantum measurement devices, quantum links and the quantum internet. Another example of a large-scale effort is the Chinese program [4, 5]. This revolution in the applications of quantum mechanics impacts many different aspects of technologies such as high-precision measurements, encryption and computation. For this reason, we outline the introduction; it is separated into a discussion of old technologies vs. the principles of their quantum analog. Then, we describe the very rich variety of experimental platforms used for today's research. We briefly discuss the impact of theoretical and numerical quantum physics for these technologies. Finally, we introduce the concepts of open quantum systems and tensor network methods representing the main tool for numerical simulations. As these two topics constitute the main goal of this thesis, each topic has a dedicated, detailed introduction in Sections 2 and 3.

Two of the technologies of the European quantum manifesto are already in discussion outside the physics community today and underline the importance of quantum mechanics. First, quantum encryption allows us to communicate with secure algorithms beyond classical encryption such as the RSA method using large prime numbers. It is named after Ron Rivest, Adi Shamir, and Leonard Adleman. It exploits the fact that two large prime numbers can be multiplied with each other quickly, but the decomposition of the product in its prime numbers

is NP-hard (non-deterministic polynomial time) on a classical computer. A quantum internet infrastructure would extend or replace the current internet and use quantum encryption for online banking and other applications. Point-to-point encryption is already available from companies such as ID Quantique [6]. A Chinese effort has successfully demonstrated a quantum link over 1200km using a satellite for distribution [7]. The generation of such pairs of entangled qubits is, moreover, useful to test the laws of quantum physics. The Bell inequality can prove the difference between quantum mechanics and local, hidden variable theories. One of these tests has been implemented with Nitrogen-Vacancy (NV) centers [8].

Second, the general quantum computer is a well-discussed topic promising major speedup compared to classical computers. These speedups allow quantum algorithms to break classical encryption through the factorization of prime numbers. This algorithm is known as Shor's algorithm [9]. Another application to be mentioned is Grover's approach to search databases leading to a speedup of the quantum algorithm over its classical counterpart [10]. In detail, algorithms are divided into different classes according to their scaling of resources. The two most important classes are the polynomial time class, i.e., P class, and the NP time class. For the latter class, a solution can be verified fast, but the actual algorithm, which finds the solution, does not scale polynomially. These computational complexity classes are formulated for classical computation and have been extended since then for quantum computation. The time scaling on a classical computer for integer factorization is sub-exponential, while the quantum version is polynomial. Moreover, quantum computers would likely ensure Moore's law, where classical computers are predicted to fail soon or do not fulfill the expected improvement at present [11]. The balance between the increasing speed of the processors and the substantial heat production with increasing clock-speeds is the crucial problem. The computer chips for classical computers have reached sizes small enough such that quantum effects are unavoidable when reducing their size even more. The current development at major chip manufacturers is on 7 nm and 5 nm chips, where classical computation can already be affected by quantum effects. Thus, quantum mechanics helps either way to

improve the current computational architecture. For example, a hybrid quantum device may use photons, possibly entangled, to communicate between machines at different locations or diffent parts within a single quantum computer, while the actual computation is executed with trapped ions. The storage of quantum states on a long time-scale can be carried out by a third technology with large coherence times, e.g., NV centers. Quantum simulators are an initial step toward a quantum computer, although their value cannot be underestimated; they address a specific question or task. For example, they can improve the development of new materials by mapping their characteristics to the quantum simulator and allow us to predict the material's behavior beforehand.

The experimental platforms are as diverse as the possible applications of quantum simulators and quantum computers. The list of promising architectures includes ultracold atoms and molecules, trapped ions, color/nitrogen-vacancy centers, Josephson-junction-based superconducting quantum circuits, Rydberg systems, and integrated quantum optics. This set of different technologies might be the key to build an efficient quantum device combining the advantaged of each approach into one device. Initially, these differences might be addressability of the quantum states for computation and their lifetime for storing intermediate results for long computations.

The ultracold atom experiments have had a huge impact since the first experimental observation of the Bose-Einstein condensate (BEC) in 1995 [12]. Since then, the field has expanded to many different types of ultracold atoms and molecules [13]. One of next important steps is the observation of the superfluid-Mott quantum phase transition [14], which can be modeled with the Bose-Hubbard model. The underlying optical lattice generated by counter-propagating laser fields allows for a much easier formulation of quantum simulator approaches. Furthermore, the atoms can be individually imaged [15] and addressed [16] in the optical lattice. Recent advances in experimental techniques allow for the creation of BEC without evaporative cooling, using only Doppler cooling and sideband cooling [17]. The benefit of this new approach is the faster generation of BECs. The original preparation included

a two-step cooling process with a laser cooling [18] and evaporative cooling [19]. The laser cooling uses counter-propagating laser beams below a transition energy of the atoms to be cooled. Atoms moving faster have a higher probability of absorbing the photons due to the Doppler shift. The following emission of the photon going back to the ground state is in a random direction. Therefore, the atoms lose momentum after a series of absorptions and emissions. This technique alone is not sufficient for the generation of a BEC. The subsequent step of evaporative cooling takes advantage of the statistics, where the fastest atoms escape from the trap and the atoms left in the trap have a lower temperature until the BEC phase transition is reached.

Ultracold molecules follow the path of ultracold atoms [20]. Their higher degrees of freedom and internal level structure comes at the price of more challenges for the generation of the BEC. These additional degrees of freedom are the ro-vibrational states of the molecule, i.e., rotational and vibrational degrees of freedom between the atoms in the molecule and the different spin states, including nuclear hyperfine and internal angular momentum states. A recent experiment using $^{23}Na^{40}K$ molecules measures coherence times in the order of one second [21], which is an improvement by order of magnitudes to previous coherence times. This improvement becomes valuable when trying to apply a sequence of gates towards quantum computing applications. The cooling technique for ultracold molecules is based on Feshbach resonances [22] and the Stimulated Adiabatic Raman Passage (STIRAP) [23]. The Feshbach resonances allow experiments to transfer a fraction of their atoms into a molecule, i.e., a bound state, by tuning the magnetic field. STIRAP can then be used to transfer these molecules into their ro-vibrational ground states, which is necessary to achieve BECs of ultracold molecules.

Trapped ions are a possible candidate for the efficient application of quantum gates for over twenty years [24]. Recent experiments trap between 53 in a one-dimensional system [25] to 300 ultracold ions in two dimensions [26]. The first uses a Paul trap and has access to the measurement of single qubits in the chain. The latter uses a Penning trap. Both types

of traps benefit from the repulsion of ions due to their charge; thus, they arrange in a lattice type structure. An example of such an arrangement in a one-dimensional structure can be found in the review [27]. An example of the two-dimensional structure in a Penning trap is in [26]. The qubit in a one-dimensional trapped ion experiment is encoded into spin states; motional degrees of freedom have to be cooled to the ground state.

Nitrogen-vacancy centers (NV centers) [28, 29] are another platform for highly tunable quantum systems. The name *color centers* refers to the same type of architecture. The defect in the diamond lattice, i.e., the nitrogen and the vacancy, are not affected by the energy band structure of the diamond. One of their unique features among other structures is their accessibility at room temperature. Their coherence time at low temperatures has recently improved by orders of magnitude to the order of milliseconds [30]. In addition, experiments can use the fine structure levels at low temperatures. The natural ratio of ^{12}C and ^{13}C in the diamond leads to a few nuclear spins in the neighborhood of the NV center. Protocols using the NV center and the nuclear spins can be designed. One disadvantage of NV centers is their random location within diamond and the random location of nuclear spins of the ^{13}C atoms. Thus, regular lattices of NV centers are not available. The applications of the NV centers go well beyond the aforementioned measurement of the Bell inequality [8]. The nuclear spin of the ^{13}C atom can serve as a quantum memory, which can store information on the order of seconds [31]. The NV centers can serve as sensors for measuring magnetic fields [32] or current flow in graphene [33]. Moreover, a variety of protocols to implement quantum gates have been implemented in experiments. The fidelity of such gates has reached 0.9 already more than ten years ago [34]. The system also has application to open quantum systems. The decoherence of the qubit represented by the NV center is due to the interaction with the nuclear spins of the surrounding ^{13}C, as described in detail in [35]. Protocols for a dissipative state preparation of two NV center qubits have been proposed in [36].

Superconducting qubits are today one of the most commonly used platforms for early industry quantum computers. Although suggestions tend towards hybrid systems of the different types of superconducting qubits combining the strengths of each [37], it is worth listing the different types first. There are flux qubits, phase qubits, and charge qubits. All types have in common that they use superconducting circuits to protect from dissipation and thus quantum decoherence. A second necessary feature for superconducting qubits is a nonlinearity in the energy spectrum; this characteristic is achieved with the Josephson junction. An accessible review is presented in [38]. The nonlinearity guarantees that the transition between ground state and first excited state is not driven at the same time as the transition between the first and second excited state. This nonlinearity is required in all technologies using qubits. The fabrication techniques from classical semiconductor-based transistors come with pros and cons. On the one hand, these techniques have a clear path to scaling up the number of qubits, which can be difficult to foresee in other technologies. On the other hand, qubits are not equal as in atomic transitions. If we look at the current platforms designed by Google, D-Wave, and IBM, the advantages of this technology seem to outweigh the disadvantages.

The current state-of-the-art quantum simulator using Rydberg atoms is a quantum simulator with 51 atoms [39]. The features of a Rydberg system are excellent for many applications in quantum technologies. While generating the Rydberg atom, i.e., an atom with a highly excited electron, other atoms around this Rydberg atom cannot become a Rydberg atom due to a blockade. This blockade, allowing one to have only one Rydberg atom in a certain radius, leads to lattice-like structures as demonstrated in an experiment using ^{87}Rb atoms [40]. Rydberg systems can be used to mediate the interactions between photons as demonstrated in [41]. The study of transient dynamics to equilibrium states [42] moves the platform toward the application to quantum simulators. Rydberg systems have large dipole-dipole interactions and are one important example for long-range interactions. With the highly excited electron, the system looks similar to the electron in the hydrogen atom. The

quantum number of this excited electron characterizes many features such as the blockade radius. The quantum number is also the reason for the name *Rydberg atom*; Johannes Rydberg presented the equation connecting the quantum number and the frequencies in spectral lines dating as far back as 1889 [43].

We keep these experimental realizations in mind, and they are a meaningful basis and context for the later work of this thesis. For example, during the exploration of long-range models, it is important to keep in mind which systems exhibit stronger or weaker long-range effects. While neutral cold atoms exhibit only $1/r^6$ decay over distance in their van der Waals interactions and are therefore short range, exploring $1/r^3$ decay is meaningful for dipole-dipole interactions as present in Rydberg systems; $1/r$ occurs for Coulomb interactions in trapped ions, where in some systems the power law can even be tuned to $1/r^\alpha$ with α ranging from 0, i.e., infinite range, to about 4. Even the inverse cube power law for the dipole-dipole case can be seen as a rule of thumb, as transverse effects from an optical lattice can tune the power law [44].

Based on the experimental platforms, we may take two different paths to derive many-body models based on the interactions. The first approach is to start in the continuum limit, e.g., with a Bose-Einstein condensate for more than 10^6 atoms. The state of the BEC can be described in terms of the Bloch functions, which are plane waves. For the purpose of the following discussion, we assume that the system has some underlying periodical lattice. Counter-propagating laser fields create such a standing wave. The basis function of plane waves, i.e., momentum states, is not the preferred basis most of the time. A basis describing the position of the particle is convenient. The Wannier functions are such a set of orthogonal basis functions localized around a certain position [45]. Using the periodicity of the lattice, we can construct these Wannier functions from integrating over the entire Bloch function in one Brillouin zone. During the process of this transformation, certain approximations are usually made. For example, any population in the second band of the Bloch function is neglected in the most simplistic approach.

The second possibility for the derivation of many-body models is the consideration of the actual particles. In the BEC scenario, the atoms are free to move; in contrast, nitrogen vacancy centers, or more generally color vacancy centers, in diamonds are localized and do not have a momentum themselves. Likewise, Rydberg systems with a lattice structure or experiments with hundreds of trapped ions are better suited for this type of scenario.

Quantum computers and simulators are closely connected to the field of open quantum systems. Briefly, an open quantum system can be any interacting composite system, where the actual interest for measuring observables is only in one part of the composite system. This description applies to quantum simulators and computers being linked to measurement devices, exposed to background radiation, or coupled to thermal reservoirs. Moreover, an open quantum system can describe the effects from one computational unit to the other, e.g., two neighboring quasi one-dimensional systems in an optical lattice. The approaches to tackle open quantum systems vary depending basically on the size of the environment. A consideration of the full system and environment dynamics is feasible for small environments as the neighboring one-dimensional systems in the optical lattice; the environment has approximately the same size as the system itself. The opposite limit of a large reservoir coupled weakly to the system has a convenient treatment with the Lindblad master equation. [46–49]. The most challenging regime is in between, where the environment is too large to be included in the simulation and the approximations for the Lindblad master equation break down.

All of the above mentioned experimental platforms benefit hugely from the interplay with analytical and numerical techniques in quantum physics. The latter aspect is the focus of this thesis. The analytically solvable models and approaches are very few. Among them is the solution to the quantum Ising model with periodic boundary condition via the Jordan-Wigner transformation. Analytical techniques are mean-field approaches, dynamical mean field theory and perturbation theory, both for statics and dynamics. Furthermore, there exists a number of computational solutions to handle quantum systems. These options in-

clude density functional theory (DFT) and time-dependent density functional theory, which are numerical methods available. Quantum Monte Carlo methods and phase space representations are further options which are also not treated within this work, but belong to a complete list of possible techniques. Detailed insights can be gained in literature, e.g., in [50]. We concentrate on exact diagonalization methods and tensor network algorithms, where the tensor networks are introduced in detailed in a separate introduction in Sec. 3.

Throughout the work, we use a very wide definition of exact diagonalization methods for our numerical simuations, which includes any approach acting on the quantum state without truncating parts of the state. In contrast, a narrow definition of exact diagonalization relies purely on the eigendecomposition of the Hamiltonian leading to the eigenenergies and the energy-eigenstates. These approximations to the time evolution can be converged similarly to the errors introduced by discretizing a time-dependent Hamiltonian at different time steps; errors are well-controlled as a function of the time step. This approach allows us to extract ground and excited states of systems and, therefore, thermal states. The propagators for a time-evolution are based on the exponential of the Hamiltonian, and we also calculate them via eigendecomposition. Our usage of the term exact diagonalization includes approximations to the propagator in terms of a Trotter decomposition or approximations of the propagated state, i.e., a Krylov method. Both approximations overcome the unfavorable scaling of the eigendecomposition with the number of qubits in the system. The matrix size of the Hamiltonian scales exponentially with the number of qubits; in addition, the eigendecomposition scales cubically with the matrix dimension. This improvement does not allow us to simulate systems up to or beyond forty-five qubits as done in the smallest quantum circuits simulations [51]. In contrast to our effort optimized for a large set of different Hamiltonians and applications even on desktop computers, these simulations are highly optimized for answering a single question with a parallelized algorithm, here simulating quantum advantage circuits.

We may point out one important theme raised by this overview to exact diagonalization methods and discussed in many chapters of this thesis: convergence and resolution of numerical methods. Analytical results either yield exact results or allow one to specify the error directly in terms of a small parameter, e.g., for perturbation theory. Numerically simulations require a convergence study for each of the parameters used. This task becomes especially challenging with an increasing number of parameters in complicated algorithms. Moreover, numerical methods have to sample over parameter space, e.g., to find the critical point of a phase transition within the resolution of the sampling, where analytical approaches would yield the value of the critical point on one shot. The value of numerically tools, despite all the obstacles just mentioned, is underlined in the vast amount of these methods available and their ability to push physics beyond the limits of analytically solvable problems while keeping the possibility to check the results against analytical limits. We find these examples of checking numerical results against theoretical limits and evaluating errors throughout this work.

The limits of exact diagonalization are the major motivation for the development of tensor network methods. In summary, the tensor network methods use approximated quantum states; we truncate parts of the entanglement. The approximate time evolution methods, i.e., the Trotter decomposition and Krylov method, have their formulation in terms of tensor networks, too. Again, we refer to Sec. 3 for a detailed introduction.

The numerical methods have a wide range of applications beyond the support of current experimental architectures. They can provide the phase diagrams for novel Hamiltonians. We can explore phenomena such as the Kibble-Zurek mechanism predicting the generation of defects when changing external parameters leading to a crossing of the quantum critical point obtained in the phase diagrams. This question is closely connected to adiabatic quantum computing as the solution to a problem is obtained via a quench, and the rate of the quench determines the density of defects.

Finally, we give an outline of this work. We complete the introduction in the following two chapters with a detailed look into open quantum systems, i.e., Chapter 2, and Chapter 3 leads to tensor network methods for many-body quantum systems. The study of the Kibble-Zurek hypothesis in the long-range quantum Ising model in Chapter 4 gives an impression of the many-body simulations applied to closed quantum systems. Then, we turn to open quantum systems. Chapter 5 contains a problem set intended to introduce advanced undergraduate students or graduate students entering the field to open quantum systems. We continue with the problem of thermalizing a quantum system coupled to a reservoir in Chapter 6, where we choose the Lindblad master equations to govern the dynamics. We explain the corresponding derivation of the Lindblad master equation in Chapter 7. The next part of this thesis describes the numerics to simulate the quantum systems, i.e., exact diagonalization methods in Chapter 8, tensor network methods for closed systems as present in the second release of our Open Source Matrix Product States simulation platform [52] in Chapter 9, and tensor networks methods for open quantum systems, see Chapter 10. This trio of numerical recipes to simulate quantum physics is completed with Chapter 11, which treats coding, software issues, and simulation platform questions related to the past and future releases of our software. We provide a discussion of our results and conclusions in Chapter 12. Additional material accompanying chapters is featured in the appendices.

This thesis contains the following publications and manuscripts under review:

- Chapter 4. *Critical Phenomena and Kibble-Zurek Scaling in the Long-Range Quantum Ising Chain*, D. Jaschke, K. Maeda, J. D. Whalen, M. L. Wall, and L. D. Carr, New Journal of Physics 19, 033032 (2017). `http://doi.org/10.1088/1367-2630/aa65bc`. Permission is provided by the *Creative Commons Attribution 3.0 Unported license* (CC-BY) [53] used by New Journal of Physics [54].

- Chapter 6. *Thermalization in the quantum Ising model − Approximations, Limits, and beyond* , D. Jaschke, I. de Vega, and L. D. Carr, submitted to Quantum Science

and Technology. https://arxiv.org/abs/1805.04934. Permission is provided by the *Non-exclusive license to distribute* used for this arXiv submission [55].

- Chapter 8. *Open source Matrix Product States: Exact diagonalization and other entanglement-accurate methods revisited in quantum systems*, D. Jaschke and L. D. Carr, submitted to Journal of Physics A: Mathematical and Theoretical. http://arxiv.org/abs/1802.10052. Permission is provided by the *Non-exclusive license to distribute* used for this arXiv submission [55].

- Chapter 9. *Open source Matrix Product States: Opening ways to simulate entangled many-body quantum systems in one dimension*, D. Jaschke, M. L. Wall, and L. D. Carr, Computer Physics Communications 225, 59 (2018). https://doi.org/10.1016/j.cpc.2017.12.015. Permission is provided by the *non-commercial Creative Commons user license* (CC-BY-NC-ND) [56] used by Computer Physics Communications [57].

- Chapter 10. *OSMPS: Many-body entangled open quantum systems*, D. Jaschke, S. Montangero, and L. .D. Carr, submitted to Quantum Science and Technology. https://arxiv.org/abs/1804.09796. Permission is provided by the *Non-exclusive license to distribute* used for this arXiv submission [55].

CHAPTER 2

OPEN QUANTUM SYSTEMS

Open quantum systems have the power to advance quantum physics in areas such as quantum error correction, state preparation, or decoherence effects. The current research will help unify the comprehension of open quantum systems and their notations. The applications of quantum systems have already contributed to new technologies such as lasers, and the advancement of open quantum systems has potential to contribute to refined applications and enable new technologies, for example, the ones discussed in the quantum manifesto [1–3] and pursued in the Chinese efforts [4, 5].

The aim of an open quantum system is simply the description of some system A coupled to another system B, where we are solely interested in measuring subsystem A. We are not interested in the measurements of subsystem B or observables acting on A and B at the same time. Figure 2.1 represents a sketch of this configuration. Reservoir, bath, and environment are common names for the subsystem B.

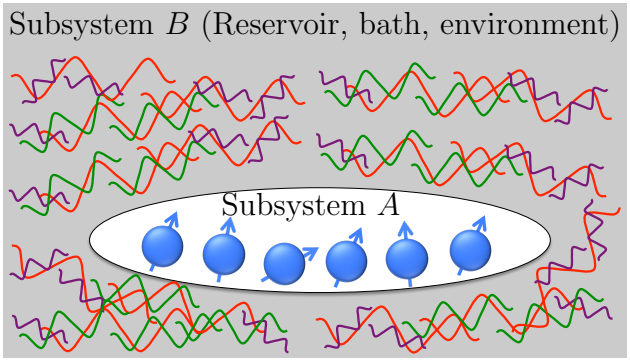

Figure 2.1: *Schematic of an open quantum system.* The subsystem A interacts with subsystem B, but the measurement on subsystem B is not of interest. Open quantum systems look for the best technique to predict the state of the subsystem A. The best technique is a balance between the necessary approximations and the feasibility of the approach with regards to the analytical or numerical effort. We show a set of spins as the system and a set of harmonic oscillators of different frequencies represented by the different colored waves. This choice is one possible example which we revisit in Chapter 6.

Open systems often rely on the formulation of the quantum system in terms of the density matrix ρ, in contrast to the state vector for a pure, closed system. The main characteristics of the density matrix are its positivity, or semi-positivity to be exact, and the trace equal to one. Both trace and positivity are connected and can be explained via thermal states. In a thermal state, we expect that each energy has a probability according to the Bose-Einstein statistics or Fermi-Dirac statistics. The Gibbs distribution is one example for such a thermal state, i.e.,

$$\rho \;=\; \frac{\exp(-\beta H)}{Z}\,, \qquad Z = \mathrm{Tr}\left[\exp(-\beta H)\right]\,, \tag{2.1}$$

where H is the Hamiltonian of the system, Z the partition function, and $\beta = 1/(k_{\mathrm{B}}T)$. The trace of a matrix is written as Tr. Thus, the state depends on the temperature T and k_{B} is the Boltzmann constant. The description of such thermal states in open quantum systems is of interest as we, in general, expect a system to thermalize if it is in contact with a large reservoir at a certain temperature. This assumption has to be verified for each quantum system as discrete spectra might prevent thermalization or multiple steady states might exist. This question is a complete field of research for closed quantum system as discussed in the eigenstate thermalization hypothesis vs. the generalized Gibbs ensemble [58]. The integrability of the system plays the key role to prevent a closed system from thermalizing [59, 60]. We can motivate the positivity and trace normalization of the density matrix in the specific case of the thermal state when rewriting the Hamiltonian and, then, the exponential in terms of the eigenstates $H = \sum_k E_k \mid k\rangle\langle k \mid$. We define the probability $p_k = \exp(-\beta E_k)/Z$. The positivity and normalization of ρ follow from the characteristics of the probability distribution represented by the p_k's; they are maintained throughout any mixed state. From the positivity, we can derive the Hermitian characteristics of the density matrix, because only Hermitian matrices are guaranteed to have real eigenvalues.

Open quantum systems have different paths to describe the evolution of the subsystem of interest. The choice depends on the feasibility of analytical or numerical approaches

and the choice of approximations made. We describe in the following different approaches, i.e., the Lindblad master equation, decay operators in the Schrödinger equation, the Kraus operators, and alternative techniques. We point out our view on feasibility and restrictions due to approximations in each corresponding section.

(i) The approximations in the *Lindblad master equation* [46–49] only hold for systems coupled weakly to large reservoirs. Despite this restrictive approximation, it is one of the most common formulations of an open quantum system. Its appeal is the conservation of the properties of the density matrix such as the trace and the positivity. The Lindblad master equation can be simulated with the complete density matrix or via quantum trajectories (QTs) [61] sampling over pure states, which is close to a measurement in an experiment randomly observing one state out of the mixed state. Each quantum trajectory represents one possible state in the probabilistic ensemble of the complete density matrix. Random numbers generated for the choice of each trajectory ensure that any possible trajectory contributes according to its weight in the limit of an infinite number of QTs. Only for rare cases, more than 10,000 QTs are necessary; a couple of hundred are often sufficient. Thus, the computational feasibility to simulate the Lindblad equation is acceptable for the complete density matrix and via QTs. But we point out the conditions to use the Lindblad master equation: (1) The environment has no memory and is big enough to stay in its state without being disturbed by the quantum system considered. Thus, the timescale of the environment is short in comparison with other time scales. (2) There is no correlation or entanglement between the system and the environment at any time. This condition includes the initial state. (3) The relaxation time of the system is long in comparison to the time step considered. The corresponding approximations are the Born-Markov approximation followed by the secular approximation. We present details on the approximations in Chapter 7 while deriving the Lindblad equation for the case of the quantum Ising model. Examples which clearly violate these assumptions are two small interacting spin chains with one acting as the reservoir, and an NV center coupled to the few surrounding ^{13}C nuclear spins. The evolution

of the density matrix of the system is governed via

$$\dot{\rho} \;=\; \underbrace{\frac{-\mathrm{i}}{\hbar}\left[H,\rho\right]}_{(I)} + \underbrace{\sum_{\nu} \gamma_\nu L_\nu \rho L_\nu^\dagger - \frac{\gamma_\nu}{2}\left\{L_\nu^\dagger L_\nu, \rho\right\}}_{(II)} \,. \tag{2.2}$$

The Hamiltonian H contains the system Hamiltonian of the closed system and possible corrections of hermitian terms from the system-environment interaction. The Lindblad operators L_ν are solely from the system-environment interaction. Thus, we may change the perspective and consider the terms of (II) as the dissipative part of the evolution. The terms in (I) are the unitary part of the evolution. Note that (I) corresponds to the von-Neumann equation for the unitary time evolution of a density matrix in the Schrödinger picture. The Heisenberg equation for operators, i.e., observables, differs from the von-Neumann equation by a minus sign.

A careful derivation for a single multi-level quantum system and its reservoir is accessible. The implications for many-body quantum systems are in contrast non-trivial. Often, energy eigenstates are not diagonal in the basis we choose to represent the system. Thus, the operators yielded from the derivation leak a convenient representation in these basis states. We have to overcome this obstacle to treat many-body systems beyond ten qubits carefully; Chapter 6 develops an intuition for the many-body case. Every interacting system build from a set of multi-level system can distinguish the single-channel and multi-channel Lindblad approach. Briefly, the single-channel approach chooses a Lindblad operator acting on a local neighborhood of the system, e.g., the spontaneous decay from an excited state to the ground state. This approach does not necessarily match the energy landscape of the interacting many-body system. Thus, the multi-channel approach includes the spectrum of the full system Hamiltonian in its derivation.

(ii) In contrast to the Lindblad master equation, one can add terms representing the decay directly to the Hamiltonian of a system and evolve according to the Schrödinger equation [62]. Because such additional terms destroy the hermicity of the Hamiltonian, the quantum

state does not preserve its norm under the time evolution and requires normalization. Furthermore, we emphasize that this approach to the evolution remains a pure state and does not reflect the statistical mixture usually associated with open quantum systems.

(iii) Another method conserving the properties of the density matrix is a set of *Kraus operators*, which can be connected to the Lindblad equation, although it is more general than the Lindblad equation. The Kraus operators can be seen as an open system analog to a gate or quantum circuit. The matrix representation of a quantum circuit propagates a quantum state for some time interval without solving the corresponding differential equation as we do in the Lindblad master equation. The governing equation is

$$\rho(t+dt) \;=\; \sum_{\nu} K_\nu \rho(t) K_\nu^\dagger \,. \tag{2.3}$$

Here, K_ν are the different Kraus operators and ν is the index to iterate over the Kraus operators. Reference [63] describes Kraus operators used for a non-Markovian evolution, emphasizing the statement that they are more general than the Lindblad master equation. The case of a single Kraus operator describes a unitary time evolution and the operators can be considered as a quantum gate applied to the state. The Kraus operators are also known as CPT maps, i.e., complete positive trace-preserving maps. While positive maps only guarantee to get a positive density matrix, the CPT maps also ensure positivity for every possible subsystem after a partial trace.

(iv) Apart from these techniques, Redfield master equations drop the characteristic of positivity. Hierarchical equations of motions can treat open quantum systems correlated to their environments. Ferialdi is presenting a technique based on Bloch vectors [64]. The availability of multiple approaches makes it possible to test each existing and new method in the corresponding limits to another technique. A review of methods for non-Markovian systems can be found in [65].

The early applications of open quantum systems were directed at single-body physics. The older formulations of the Lindblad equations were based on two-level systems. Electro-

magnetically-induced transparency can be explained via a master equation for a three-level Λ-system [66]. Making the transition to the many-body open quantum system, we encounter various questions: (i) does the system have a unique steady state; and (ii) is the thermal state the unique steady state? Resolving these two questions solely in the Lindblad equation requires a huge effort due to the pure dimension of the Hilbert space in a many-body system. Although these questions might seem philosophical, they have a physical impact once extended to a rate approaching the steady state. For example, a slow rate would leave more time to realize experiments before the quantum system is affected by thermalization. Next, (iii) can one target steady states with specific properties? The question of dissipative state preparation is discussed in [67, 68], where the authors address the issue of open systems leading to decoherence and the corresponding steady state. On the other hand, they point out the possibility of generating steady states with characteristics such as entanglement using a proper engineering of the reservoir. Preparing the states as steady states of an open system would make them less vulnerable; after a perturbation they would return to the steady state. This feature is also known in classical attractors. The effects of the environment on the system's dynamics can be extended to the limit of purely dissipative systems [69]. (iv) Furthermore, can one simulate the transport of heat, current, or particles when coupling a quantum system to two reservoirs at different temperatures or with different chemical potentials? Can coherent and incoherent transport be simulated with open quantum systems? The transport problems for nano systems coupled to two separate reservoirs in the case of electronic transport can go beyond the simulations for mesoscopic systems: tensor network methods allow us to decrease the size of the system further. In contrast, mesoscopic systems are based on tight-binding Hamiltonians and the scattering of the wave function [70]. Leaving behind implementations based on semiconductors, field-effect transistors based on single molecules [71], e.g., benzene rings, represent a possibility for future transistor technologies in addition to other approaches such as carbon nanotubes. These composite systems of molecules connected to the source and drain can be represented as

open systems. (v) Finally, do we have to reformulate theorems for closed systems under the influence of an environment? For example, does the Lieb-Robinson bound for information propagation speed still hold? Is the Kibble-Zurek mechanism for crossing a quantum critical point still valid? Is there an equivalent to the area law bounding entanglement for ground states for steady states of open systems? The Lieb-Robinson bound may be enhanced through information transport in the reservoir over and above the information transport in the system itself, if one global reservoir is coupled to the system. In contrast, the decoherence introduced by the environment may slow down the speed of information transport. The Kibble-Zurek mechanism generates excitations when crossing a quantum critical point in a dynamical quench and is often characterized by the closing gap between the ground state and the first excited state in the system. But if the energy spectrum of the system influences the process of thermalization, a coupling during the quench might affect the physics of the mechanism. The equivalent of an area law in open systems would be a great benefit for simulation techniques in one dimension.

Knowing all these limitations of the different approaches to open quantum systems, we have to keep in mind to study the convergence and outcomes carefully. We recall that quantum phase transitions happen in the strict definition only in the thermodynamic limit and at zero temperature, but nonetheless, they have been observed in experiments. Thus, it is important to think if despite imposed conditions methods are useful close to these limits. For example, the error induced from approximations might be lower than the experimental uncertainty and becomes only relevant as experiments can improve the precision.

It is vital that future experiments with quantum simulators, quantum computers, and quantum encryption algorithms consider all these aspects of open quantum systems. Understanding such systems as an open quantum system will have the benefit of mitigating decoherence and improving quantum error correction tools. The various questions, e.g., thermalization and transport problems, may be explored best with different formulations of open quantum systems or different limiting cases. For example, thermalization profits from a

global picture and the Lindblad equation can be sufficient. In contrast, transport is suitable for local operators on the boundary. Therefore, we see these approaches not as competing techniques, but as complementary.

CHAPTER 3

TENSOR NETWORK METHODS

For our research, we use the approach of tensor networks and the Density Matrix Renormalization Group (DMRG) [72–74]. The DMRG algorithm is designed to find the ground state of either an infinite system or a finite system. The common restriction is to one-dimensional systems, while higher dimensional systems are subject to research. The tensor network algorithms using Matrix Product States (MPSs)[75, 76] were always close to the DMRG algorithms, but recent work has been highlighting the connection or equivalency between the two formulations [77]. The area law for entanglement [78] plays an important role for the motivation of MPS algorithms. MPSs, and any other tensor network method, truncate entanglement in the system. Thus, the scaling of entanglement is of great interest to tensor networks. The entanglement increases for higher dimensional systems and, thus, the focus of many tensor networks is towards one-dimensional systems. Other approaches are Tree Tensor Networks (TTN) [79] and, for open quantum systems and mixed states, Matrix Product Density Operators (MPDOs) [80, 81] and the Locally Purified Tensor Network (LPTN) [82]. Further approaches are the Multiscale Entanglement Renormalization Ansatz (MERA) [83], and Projected Entangled Pair States (PEPS) [84]. The latter is the most common approach to two-dimensional systems. As a large part of this work is about tensor networks, we take the opportunity to introduce them properly in the following as a part of the introduction. We start with the basic idea of a tensor network decoupled from the application in quantum physics. Then, we turn to the usage within quantum physics and matrix product states and discuss the possibilities of symmetries. We end with a summary of the requirements underlying our numerical platform, which are reflected in the development of the *Open Source Matrix Product State* package [52]. Throughout this introduction and the later chapters on tensors network methods, one should keep in mind that we break

down the problem in terms of different indices. The qubit, or the generalization of the qudit as a multi-level quantum system is the smallest building block of any quantum many-body system. One index is referring to the different quantum states in the single qubit or qudit, which we call the local index. Its dimension is the local dimension and equal to the number of levels within one site. The next necessary index is an index to address the different qubits in the many-body systems, for instance indexing the site in a spin chain. The last index appearing in tensor networks is the least accessible; its physical meaning is associated with the entanglement, and each index represents one possible superposition of the entangled system, where each of the superpositions can have a different weight. We dub this the entanglement index. The concept of local, site, and entanglement indices will appear throughout this thesis.

Mathematically, a tensor is the generalization of a vector or a matrix to an object with an arbitrary number of indices. Thus, any vector is a rank-1 tensor, and any matrix is a rank-2 tensor. In physics, the tensor notation is very useful and used in many different contexts reaching from the Levi-Civitas symbol, a rank-2 or rank-3 tensor, to the stress tensors in mechanics. The pictorial representation of such tensors is shown in Figure 3.1(a).

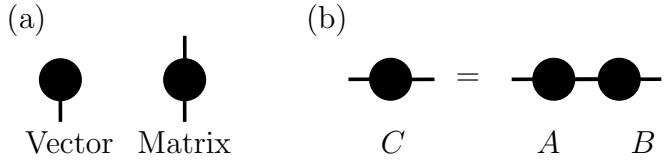

Figure 3.1: *Tensors and tensor networks.* (a) Representation of a vector and matrix in the pictorial tensor network notation. Each index, i.e., dimension, is represented as a link in the tensor. The node itself represents the tensor. (b) The tensor network diagram for the multiplication of two matrices, e.g., $C = AB$. The index notation is $C_{ik} = \sum_j A_{ij} B_{jk}$. The contracted index j is the index connecting the tensors A and B in the diagram notation.

A tensor network describes the relation between the tensors. The matrix-matrix multiplication of two matrices A and B to a matrix C is one example:

$$C \;=\; AB \quad \Leftrightarrow \quad C_{ik} = \sum_j A_{ij} B_{jk} \,. \tag{3.1}$$

Here, we can see the difference between the indices. j is part of the summation and the other two indices, i and k are part of the final matrix C. Figure 3.1(b) is the tensor network diagram of this matrix-matrix multiplication. We remark that we have a certain degree of freedom choosing the matrices A and B if only the final matrix C is of interest. We can introduce a unitary square matrix U. This unitary matrix fulfills by definition $U^\dagger U = \mathbb{I}$ and we modify Eq. (3.1) as follows

$$C \;=\; AB = \underbrace{AU^\dagger}_{A'} \underbrace{UB}_{B'} = A'B' \,. \tag{3.2}$$

The possibility to exploit such freedoms is an essential part of tensor network methods.

The next step is to translate these concepts of tensors to quantum physics. For simplicity we restrict ourselves to qubits, i.e., two-level systems, in this part of the discussion; the generalization to qudits, i.e., d-level system, requires no additional steps. We label the two quantum states in the qubits with $|\,0\rangle$ and $|\,1\rangle$. The state of a single qubit $|\,\psi\rangle$ is written as a rank-1 tensor, i.e., vector

$$|\,\psi\rangle \;=\; c_0\,|\,0\rangle + c_1\,|\,1\rangle = \sum_j c_j\,|\,j\rangle = \begin{pmatrix} c_0 \\ c_1 \end{pmatrix} . \tag{3.3}$$

The scalars hold the normalization constraint of the wave function $c_0 c_0^* + c_1 c_1^*$. If we describe two qubits, the complete Hilbert space $\mathcal{H}$ describing both qubits is an outer product of the local Hilbert spaces $\mathcal{H} = \mathcal{H}_1 \otimes \mathcal{H}_2$. The state of two qubits can be represented as a rank-2 tensor. The super-script indices refer to the 1st and 2nd qubit:

$$\begin{aligned} |\,\psi^{[1,2]}\rangle \;&=\; c_{00}\,|\,0^{[1]}\rangle\,|\,0^{[2]}\rangle + c_{10}\,|\,1^{[1]}\rangle\,|\,0^{[2]}\rangle + c_{01}\,|\,0^{[1]}\rangle\,|\,1^{[2]}\rangle + c_{11}\,|\,1^{[1]}\rangle\,|\,1^{[2]}\rangle \\ &=\; \sum_{j_1=0}^{1}\sum_{j_2=0}^{1} c_{j_1 j_2}\,|\,j_1^{[1]}\rangle\,|\,j_2^{[2]}\rangle = \begin{pmatrix} c_{00} \\ c_{10} \\ c_{01} \\ c_{11} \end{pmatrix} . \end{aligned} \tag{3.4}$$

The status of two qubits is stored in a tensor with four, possibly complex, entries. In contrast, the state of two classical bits can be saved in two booleans storing if the bit is in the state 0 or 1. While the superposition of states and the entanglement between qubits is considered a resource for any quantum computation [85], it turns out to be the major limitation when simulating a quantum system on a classical computer. If we represent L qubits, the corresponding rank-L tensor has 2^L entries. To understand how tensor networks are able to represent such states, we take a look at the Schmidt decomposition. It decomposes the state of the two qubits $|\psi^{[1,2]}\rangle$ into a sum of local states

$$|\psi^{[1,2]}\rangle = \sum_{\mu=1}^{2} \lambda_\mu \, |\psi_\mu^{[1]}\rangle \, |\psi_\mu^{[2]}\rangle \, . \tag{3.5}$$

The outer product for the two qubits is implied. The λ_μ are the weights for each product and hold $\sum_\mu \lambda_\mu^2 = 1$. The entanglement measure defined on the Schmidt decomposition is the Schmidt number counting the number of non-zero values λ_μ. The Schmidt number for two qubits is either 1 or 2, where Schmidt number 1 always signals that there is no entanglement between the systems decomposed. The local state vectors form a unitary basis; thus, the decomposition corresponds to a singular value decomposition. The idea of tensor networks is to keep only a limited amount of singular values, i.e., the biggest singular values and truncating the smallest singular values. We can immediately calculate the overlap of the true wave function of the qubits with the truncated wave function $|\,\phi^{[1,2]}\rangle = |\,\psi_1^{[1]}\rangle \;|\,\psi_1^{[2]}\rangle$ keeping only λ_1 with $\lambda_1 \geq \lambda_2$.

$$\left\langle \psi^{[1,2]} \middle| \phi^{[1,2]} \right\rangle \;=\; \left(\sum_{\mu=1}^{2} \lambda_\mu \langle \psi_\mu^{[1]}| \, \langle \psi_\mu^{[2]}| \right) \left(|\,\psi_1^{[1]}\rangle \, |\,\psi_1^{[2]}\rangle \right) = \lambda_1 \, . \tag{3.6}$$

We see that in the limit $\lambda_2 \to 0$, the approximation becomes exact. As the number of qubits in the Schmidt decomposition increases, the approximation becomes more gradual and does not switch between no entanglement or entanglement. Independent of the number of singular values taken in Eq. (3.6), we achieved a representation of our 2-qubit quantum state either

as one rank-2 tensor or two rank-2 tensors. The singular values can be stored as a diagonal matrix and can be multiplied into either of the tensors. Figure 3.2(a) follows through these steps in terms of tensor network diagrams. The Schmidt decomposition for two qubits is equivalent to two qubits written as an MPS. Section 9 continues with a detailed derivation of MPS based on this motivation. We remark that the singular value decomposition is not unique to quantum physics, but is widely used, e.g., for data compression. Figure 3.2(b) shows the data compression of an image based on the singular values kept.

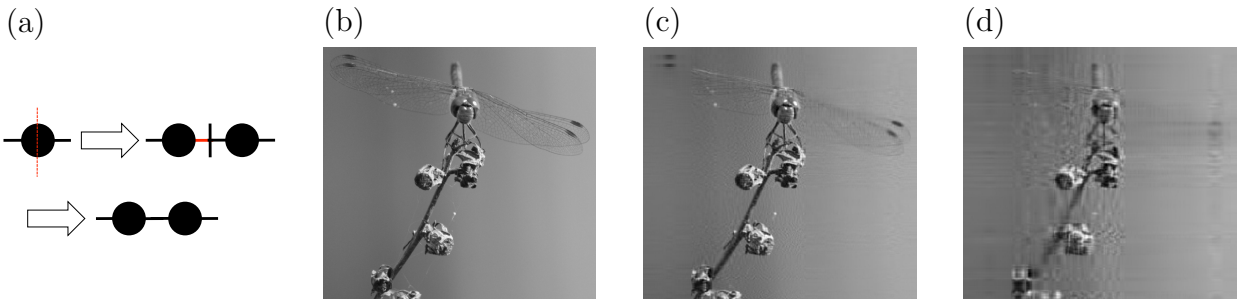

Figure 3.2: *Compression with singular value decomposition.*(a) The tensor network diagrams for the Schmidt decomposition of two qubits represented as a single tensor. The row and column indices of the matrix for the SVD are separated by a red dotted line. In the first step after the SVD $M = USV$, we obtain the two tensors with the unitary rows and columns and the diagonal matrix S containing the singular values λ_μ. The diagonal matrix is represented by a vertical line. We can choose to contract the singular values to the left tensor over the index highlighted in red. We obtain the two tensors representing the two local Hilbert spaces. (b)-(d) The singular values decomposition can be used for data compression, e.g., in the case of images. (b) is the image with all 1549 singular values, where (c) and (d) keep only the biggest 50 and 15 singular values, respectively [86].

The basic motivation for tensor networks as a representation for quantum states has been presented in the last paragraph with a two-qubit example. We now generalize to more qubits. The goal is to define one tensor for each qubit, or, in the generalization, for each local Hilbert space. The global Hilbert space is defined as $\mathcal{H} = \bigotimes_{k=1}^{L} \mathcal{H}_k$ with L being the number of qubits and k being the site index. Figure 3.3 shows a variety of possible tensor networks. We have (a) a general tensor network, (b) a general loopless tensor network, (c) the representation of a one-dimensional system with open boundary conditions, (d) the

one-dimensional tensor network with periodic boundary conditions, (e) a tree tensor network, and (f) the PEPS network. We point out that one-dimensional systems with periodic boundary conditions can be mapped to a tensor network with open boundary conditions if the interactions between the sites are limited in the distance. The relevance for periodic boundary conditions to simulate experimental systems with one-dimensional quantum is small, e.g., consider ions confined in an ion trap or the quasi one-dimensional systems created in optical lattices. Superconducting qubit architectures have a two-dimensional layout imprinted on the underlying wafer or substrate, but obey open boundaries condition. The relevance for periodic boundary conditions originates in the simulation of the thermodynamic limit where all sites are now equal, and theoretical approaches which simplify with periodic boundary conditions, e.g., the energy spectrum of the quantum Ising model can be calculated analytically with a Jordan-Wigner transformation and Majorana fermions in such a case. The major distinction between tensor networks with loops and without loops is that the latter one can install a gauge based on the freedom introduced in Eq. (3.2) [87], i.e., we can use the knowledge that specific contractions result in identities without actually calculating them. Our work concentrates on the loopless one-dimensional tensor networks as in Figure 3.3(c). This restriction is by choice as there are many different applications for such types of network.

The introduction to tensor networks shows that certain parts are vital to any tensor network package, including the one underlying our open source simulation platform entitled Open Source Matrix Product States (OSMPS) [52]. An exhaustive description of the setup for a tensor network algorithm library is reference [87]. We define the layers in terms of the modules for OSMPS and suggest: (i) linear algebra routines containing matrix-matrix contractions, singular value decomposition (SVD), QR decompositions into a unitary matrix and an upper triangular matrix, and eigendecomposition. (ii) The next layer consists of basic operations on tensors. (iii) Based on the two precedent modules, tensors with symmetry can be defined. (iv) By choice, more advanced tensor operations such as contractions and

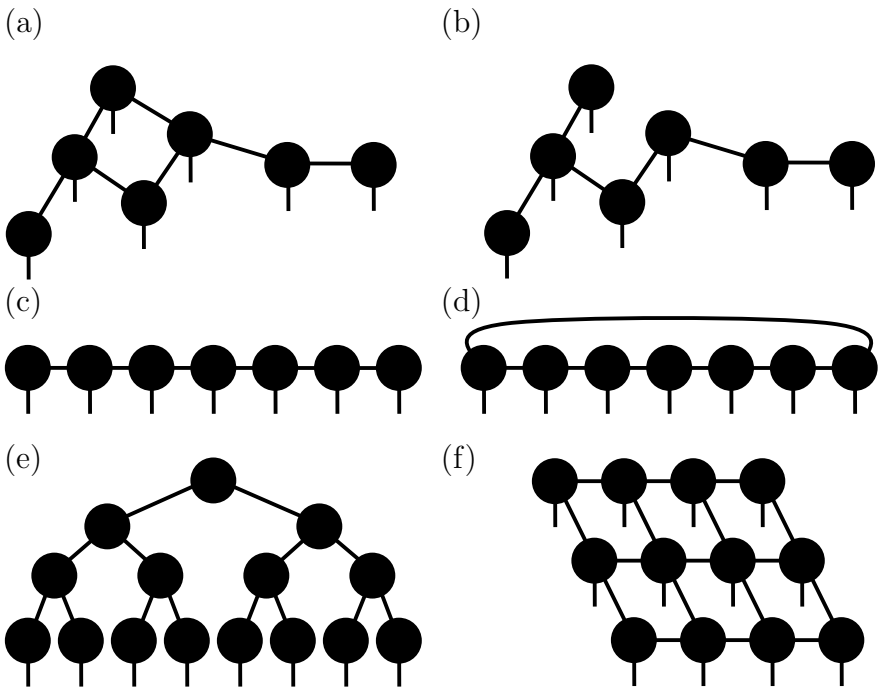

Figure 3.3: *Tensor networks.* There are a variety of tensor networks which can encode quantum states representing each local Hilbert space as a tensor. (a) A general network with loops. (b) A general network without loops. (c) A one-dimensional tensor network with open boundary conditions, i.e., a Matrix Product State. (d) The Matrix Product State representation with periodic boundary conditions. (e) A tree tensor network for eight qubits: the local Hilbert spaces are represented by the tensor in the bottom layer; other layers represent auxiliary tensors. (f) Projected Entangled Pair States encode a two-dimensional system as a tensor network.

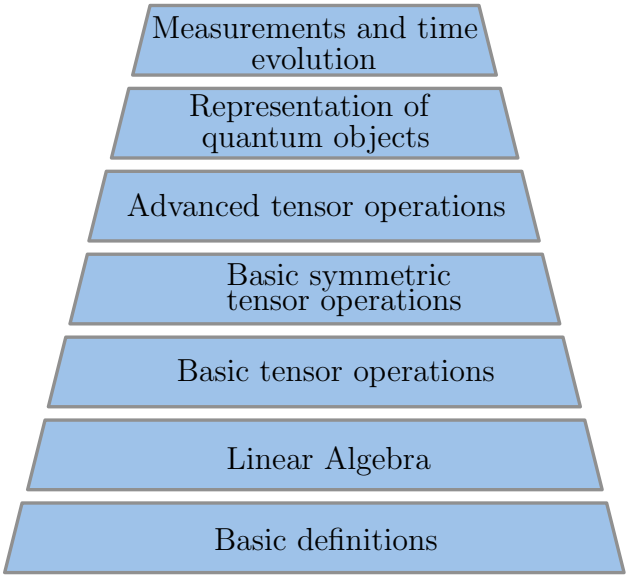

Figure 3.4: *OSMPS package structure.* The modules of the Open Source Matrix Product States package reach from basic linear algebra operations to time evolution methods.

decompositions form the next layer; they represent multi-tensor operations. (v) The next step is the definition of the tensor networks for the different objects such as the quantum state and the Hamiltonian, represented as a Matrix Product Operator (MPO). (vi) The top layer is formed by measurement subroutines and different time evolution methods. We sketch this structure in Figure 3.4.

Overall, the popularity of tensor network methods is clearly visible by the amount of research groups developing tensor network methods for quantum many-body systems. The incomplete list of open source codes includes already fifteen packages [88–102], without even counting software not published under an open source license.

CHAPTER 4

CRITICAL PHENOMENA AND KIBBLE-ZUREK SCALING IN THE LONG-RANGE QUANTUM ISING CHAIN

Published previously in *New Journal of Physics*[1]

D. Jaschke,[2] K. Maeda,[3] J. D. Whalen,[4] M. L. Wall,[5] and L. D. Carr[6]

Abstract

We investigate an extension of the quantum Ising model in one spatial dimension including long-range $1/r^{\alpha}$ interactions in its statics and dynamics with possible applications from heteronuclear polar molecules in optical lattices to trapped ions described by two-state spin systems. We introduce the statics of the system via both numerical techniques with finite size and infinite size matrix product states and a theoretical approaches using a truncated Jordan-Wigner transformation for the ferromagnetic and antiferromagnetic case and show that finite size effects have a crucial role shifting the quantum critical point of the external field by fifteen percent between thirty-two and around five-hundred spins. We numerically study the Kibble-Zurek hypothesis in the long-range quantum Ising model with Matrix Product States. A linear quench of the external field through the quantum critical point yields a power-law scaling of the defect density as a function of the total quench time. For example,

[1] "Critical Phenomena and Kibble-Zurek Scaling in the Long-Range Quantum Ising Chain", D. Jaschke, K. Maeda, J. D. Whalen, M. L. Wall, and L. D. Carr, New J. Phys. 19, 033032 (2017). `http://doi.org/10.1088/1367-2630/aa65bc`. Use in agreement with CC-BY license [53].

[2] primary researcher and author responsible for the manuscript.

[3] contribution of theoretical approximation including writing of Sec. 4.3; post-doctoral researcher in the group of L. D. Carr during parts of the paper.

[4] initial draft during his senior design project at Colorado School of Mines including the draft of phase diagram with iMPS for ferromagnetic and antiferromagnetic case and the initial study of Kibble-Zurek scaling for ferromagnet for nearest-neighbor and one long-range case without the $\mathbb{Z}_2$ symmetry; currently graduate student at Rice University.

[5] advising J. D. Whalen as part of his post-doctoral work within L. D. Carr's group; the MPS methods used were developed during his Ph.D. thesis; extensive feedback on the final versions of the draft; currently at Johns Hopkins University, Applied Physics Laboratory.

[6] principal investigator and advisor.

the increase of the defect density is slower for longer-range models and the critical exponent changes by twenty-five percent. Our study emphasizes the importance of such long-range interactions in statics and dynamics that could point to similar phenomena in a different setup of dynamical systems or for other models.

4.1 Introduction

Common quantum many-body models, such as the quantum Ising model or Hubbard models, include only a nearest-neighbor interaction, while e.g. the Coulomb forces or the dipole-dipole interactions have power law tails of the form $1/r^{\alpha}$. This leads to the core question: "to what extent does the physics of these models changes when including decaying long-range interactions?" Physical models with tunable long-range interactions have been successfully realized in recent experiments due to advances in atomic and molecular physics. This especially includes experiments in heteronuclear polar molecules in optical lattices [20, 103] and trapped ions [104]. Further examples for the realization of a long-range Ising model are the cold ion experiment in [26] realizing a two dimensional lattice and ultracold molecules with long-range dipole interactions, which have been successfully realized in recent experiments [105, 106]. Furthermore, realizations in Rydberg atoms through long-range van der Waals interactions [107, 108] or solid state physics, e.g. based on $LiHoF_4$ [109], exist and provide a large number of spins, e.g. in comparison to ultracold ion experiments at the current stage. In addition, magnetic dipoles can lead to the same long-range interactions which have been realized in recent experiments in terms of Chromium [110], Erbium [111], and Dysprosium [112], and further setups with long-range interactions tuned by optical cavities have been made [113], too. The list of experiments can be further extended with nitrogen vacancies in diamonds with a ferromagnetic long-range Ising interaction [114]. Recent advances in quantum annealing have fostered the mapping of problems onto a generalized quantum Ising model [115], which is a more general Hamiltonian than the long-range interaction. This is as well the case for quantum spin glasses [116]. These systems have in common that they can be described by two-state spin models with $1/r^{\alpha}$ interactions coupled

to external transverse fields, including the long-range quantum Ising (LRQI) model. While the experimental systems range from implementations in one to three dimensions, we study a one-dimensional system, because our numerical techniques are best suited to this case. The recent work of several groups discussed new emerging phases due to long-range interactions [117] and different regimes that hold or violate the Lieb-Robinson bounds, limiting the speed of transferring information depending on the initial state [118].

For numerical studies of many-body systems, tensor network methods offer a variety of algorithms which can be tailored to certain problems [75]. The infinite Matrix Product States (iMPS) [119] on infinite translationally invariant lattices and the Matrix Product States (MPS) for finite systems are well suited for the ground state calculations of quantum systems. Dynamics can be simulated with the Time-Dependent Variational Principle (TDVP) [120], where other methods as Krylov or local Runge-Kutta were explored for comparison [121, 122]. The quantum Ising model is not only fundamental because of the various experimental implementations mentioned, but also since it has a similar classical model in the Ising model, originally introduced in 1925 [123] with analytic solutions in one and two dimensions. Moreover, the quantum model in d dimensions can be mapped onto the classical Ising model in $d+1$ dimensions; the solution for the classical model in two dimensions is linked to our one dimensional quantum chain. Therefore, it is an ideal starting ground to explore long-range interactions before including them into other models and has always been the toy model to explore a huge variety of methods before using them on other models since it is the description for a vast majority of physical problems. This includes methods such as the exact spectrum, perturbation theory, or the mapping of the ferromagnetic case to the corresponding classical Ising model in higher dimensions without using numerical methods. It is applicable to many problems that can be mapped into two-level systems and therefore accessible for researchers from fields as different as solid state physics and atomic, molecular, optical physics just mentioned before.

While the experimental systems can be in higher dimension, we consider one dimensional spin chains with long-range interactions subjected to the external magnetic field in its transverse direction. From there, we lay out the discussions of static and dynamic simulations via tensor network methods for models with long-range interactions. Numerical algorithms based on tensor networks perform optimally in one dimension and have limitations in higher dimension, although they have been proposed for two dimensional systems [84]. However, the Kibble-Zurek mechanism yields a fascinating topic for the long-range quantum Ising model in real time evolution; for example, quenching across the critical point could be used for state preparation whenever it is easier to prepare the ground state in one phase.

As for the usual quantum Ising (QI) chain, that is integrable, both static properties such as the phase diagram, critical exponents or correlation lengths, and dynamic properties have been studied at length. The latter includes the Kibble-Zurek mechanism (KZM) being applied to show that the density of defects in the ferromagnetic chain follows a scaling law for linear quenches [124–126], i.e. the density of defects increases for faster quenches across the quantum critical point. Those properties of the Ising model have always paved the road to study other models. Then, there appears a natural question: how do these long-range interactions affect the well-known results in the quantum Ising model? These answers are relevant to ultracold molecules with characteristic long-range dipole-dipole interactions or Rydberg atoms with long-range interactions. Therefore, we present the reader new results on the Kibble-Zurek scaling with the comparison of the static results using three different approaches. Our analytical approach uses an approximation which truncates phase terms of the Jordan-Wigner transformation and the two numerical algorithms cover infinite and finite systems. With those comparisons we see finite size effects as the lower critical external fields for decreasing system sizes; dynamic simulations are based on these results. We introduce the dynamics with experimentally measurable observables such as the local magnetization in Figure 4.1 and compare the scaling of defects with the Kibble-Zurek hypothesis. The Kibble-Zurek mechanism posits that for decreasing quench times, the defect density increases

less for the ferromagnetic case in regard to the nearest-neighbor quantum Ising model. In contrast, the number of defects stays at the same rate for the antiferromagnetic model for faster quenches in comparison to the quantum Ising model. With the exponent of the Kibble-Zurek mechanism changing about 25% in the ferromagnetic case, this should be an observable effect. Apart from the prediction of defects when quenching across the quantum critical point for preparing states it might even allow for characterization of long-range effects according to the critical exponent.

Throughout the paper we concentrate on both the antiferromagnetic and ferromagnetic case. Moreover, we address the challenges with those studies, e.g. simulations breaking down in certain regimes of the long-range quantum Ising. We use the Open Source Matrix Product States package (OSMPS) [121] freely available from [52]. As a secondary goal, we provide with those practical calculations and discussions on the numerical results a basis for future researchers to interpret their results on statics and dynamics gained with OSMPS or any other tensor network method library. The models suitable for further studies range from more advanced spin models of XYZ-type to all kind of Hubbard models.

While static aspects such as the phase diagram of the long-range quantum Ising model have been studied in the past [127], the antiferromagnetic case has been investigated recently by Koffel [128] and extended in [129] to the correlations. We add to these works the aspects of infinite size MPS algorithms. A study in the thermodynamic limit with Linked Cluster Expansions for both the ferromagnetic and antiferromagnetic case has been presented in [130]. The dynamics of the long-range quantum Ising chain has lately attracted a huge interest. The entanglement growth of a bipartition during a quench was described in [131]. The speed of information spreading and the building of correlations was studied in [118, 132–135] and the equilibration time of long-range quantum spin models in [136]. We not only extend the picture of dynamics in the long-range interaction in the Ising model to the Kibble-Zurek hypothesis, but provide a detailed path how such aspects can be studied numerically keeping a side-by-side view of the antiferromagnetic and ferromagnetic cases.

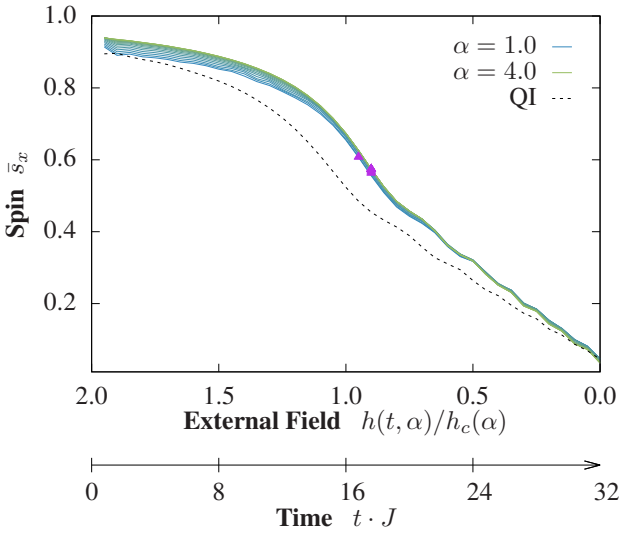

Figure 4.1: *Quench of the Long-Range Quantum Ising Model.* The mean local x-magnetization as average over the sites of the measurement of σ_i^x, i.e., $(1/L)\sum_1^L \sigma_i^x$, is a typical observable for spin models and realizable in cold ion experiments. The measurement during the quench from the paramagnetic phase to the to the ferromagnetic phase for different interaction strength governed by power law $1/|j-i|^\alpha$ displayed for α in steps of 0.2 is compared to the nearest-neighbor quantum Ising (QI, dashed curve). The triangles mark spots with first maximum of the gradient disregarding numerical fluctuations. The magnetization in x-direction is vanishing equally for all α, since the quench is starting at $h(t=32,\alpha) = 2h_c(\alpha)$ and ending at $h(t=\tau,\alpha) = 0$. h_c is the value of the quantum critical point which differs for each α. We emphasize the unified dynamics of the quench independent of α for the symmetric setup around the critical point.

The structure of the paper is as follows: after introducing the Hamiltonian of the long-range quantum Ising model in Sec. 4.2, Sec. 4.3 presents the theoretical approximation for the phase boundary. The actual results are then discussed in Sec. 4.4 containing the phase boundaries for all different methods used, the observables during the dynamics, and the Kibble-Zurek scaling for the long-range quantum Ising model. We finish with the discussion of our results in the conclusion. The description of the numerical methods follows in the 4.8 and consists of the numerical algorithms used and the studies on their convergence. Further aspects on the convergence can be found in 4.9.

4.2 Modeling Long-Range Interactions in the Quantum Ising Model

The system is modeled by the long-range quantum Ising Hamiltonian,

$$H_{\mathrm{LRQI}} \;=\; -J\sum_{i<j}\frac{\sigma_i^z\sigma_j^z}{|i-j|^\alpha} - |J|h\sum_i \sigma_i^x \;, \tag{4.1}$$

where i, j are 1D lattice coordinates, J and the unitless h represent the strengths of the interaction and transverse field, respectively, and α takes some positive value parameterizing the long-range interactions. Examples for well-known models are Coulombic interactions with $\alpha = 1$, dipole-dipole interactions decreasing with $\alpha = 3$, and $\alpha = 6$ for van der Waals models and the tail of the Lennard-Jones potential. In the following, we investigate phase diagrams both for the ferromagnetic ($J > 0$) and antiferromagnetic ($J < 0$) cases in Eq. (4.1). The long-range quantum Ising model in Eq. (4.1) reduces to the usual quantum Ising Hamiltonian in the limit of $\alpha \to \infty$,

$$H_{\mathrm{QI}} \;=\; -J\sum_i \sigma_i^z\sigma_{i+1}^z - |J|h\sum_i \sigma_i^x \;, \tag{4.2}$$

which exhibits a quantum phase transition at $h = 1$ both in ferro- and antiferromagnetic cases. For $h > 1$ we have in both cases the paramagnetic phase where spins align with the external field in the limit $h \to \infty$. The ferromagnetic phase appears for $h < 1$ where the ground state is described for $h = 0$ by a $\mathbb{Z}_2$ symmetric ground state $\left(|\Uparrow \ldots \uparrow\rangle \pm |\Downarrow \ldots \downarrow\rangle\right)/\sqrt{2}$ subject

to spontaneous symmetry breaking. The antiferromagnetic ground state has a staggered order in z-direction $\left(|\Uparrow\downarrow\uparrow\downarrow\ldots\rangle \pm |\Downarrow\uparrow\downarrow\uparrow\ldots\rangle\right)/\sqrt{2}$ referred to as Néel order. The Hamiltonian of the long-range quantum Ising in Eq. (4.1) builds the foundation of the following work and the standard quantum Ising from Eq. (4.2) is used frequently to check limits.

A common approach to quantum many-body systems are critical exponents. These universal scaling laws are independent of the system size and describe quantities as a function of the distance to the quantum critical point [137]. One typical example for such a quantity is the correlation length in the system. We relate to the critical exponents in the analysis of the Kibble-Zurek scaling, where [60] gives a review of the link between the critical exponents and the crossing of a quantum critical point in a quench. This setup is described by the critical exponent ν and the dynamical critical exponent z. The more detailed description is included in 4.8.2.

4.3 Theoretical Boundary via a Truncated Jordan-Wigner Transformation

Having a general overview of the long-range quantum Ising model, we now derive a well-controlled analytic approximation to rely on. This is important to have a comparison to the numerical results introduced later. In general, the long-range quantum Ising problem is not exactly solvable like the nearest-neighbor case, but a truncation of the phase terms in the Jordan-Wigner transformation regains a long-range fermion model along the Kitaev model, which allows us to approximate the critical transverse field for quantum phase transitions, h_c. We show the derivation of the critical transverse fields with the use of the Jordan-Wigner transformation [137, 138] and a truncation approximation. The derivation can be divided into two steps. First, we use the Jordan-Wigner transformation to map our spin Hamiltonian onto fermions. The Jordan-Wigner transformation is a non-local mapping from spins onto fermions, and fermions onto spins, where the non-locality of the transformation is necessary to obey the corresponding commutation relations. In the case of a nearest-neighbor spin Hamiltonian, the result of the Jordan-Wigner transformation is a nearest-neighbor fermion Hamiltonian where the non-local terms of the transformation cancel each other. In contrast,

long-range spin Hamiltonians are mapped into long-range fermion Hamiltonians with k-body interactions of arbitrarily large k. After the truncation in the second step, we obtain a Kitaev-type Hamiltonian with long-range two-body interactions, which has been solved exactly in [139]. The Kitaev Hamiltonian is itself important as it describes spinless fermions with p-wave pairing interactions and displays topological states [140]. For a complete picture we show both steps to derive the theoretical boundary. In the following, we rewrite the long-range quantum Ising Hamiltonian in one dimension from Eq. (4.1) with a general site dependent coupling $V(i,j)$:

$$H = \sum_{i<j} V(i,j)\,\sigma_i^z\sigma_j^z - |J|h\sum_i \sigma_i^x \ , \tag{4.3}$$

and keep a constant in front of the external field in order to have a unitless h. This general equation describes a variety of different models starting from a quantum spin glass with random $V(i,j)$ originally proposed as classical model [141], over the completely connected case with $V(i,j)=1$ for all i,j which is equivalent to a special case of the Lipkin-Meshkov-Glick model [142, 143] ranging to *chimera* setup in the d-wave quantum annealing computers [144] with a limited number of interaction to other qubits. This Hamiltonian reduces to our long-range quantum Ising model with $V(i,j) = -J/|i-j|^\alpha$, while to the usual quantum Ising model with $V(i,j) = -J\delta_{j-i,1}$. In order to use the Jordan-Wigner transformation, we have to rotate our coordinate system around the y-axis mapping $\sigma^x \to \sigma^z$ and $\sigma^z \to -\sigma^x$ following the approach used in [137]. We obtain

$$H_{\rm rot} = \sum_{i<j} V(i,j)\,\sigma_i^x\sigma_i^x - |J|h\sum_i \sigma_i^z \ , \tag{4.4}$$

where the minus sign of the transformation cancels out appearing as a pair in the interaction term. The Jordan-Wigner transformation, which is exact for the usual quantum Ising model, is given by

$$\sigma_i^x = \left\{\prod_{j<i}(1-2c_j^\dagger c_j)\right\}(c_i + c_i^\dagger) \ , \tag{4.5}$$

$$\sigma_i^y = -\mathrm{i}\left\{\prod_{j<i}(1-2c_j^\dagger c_j)\right\}(c_i - c_i^\dagger) \ , \tag{4.6}$$

$$\sigma_i^z = 1 - 2c_i^\dagger c_i \ , \tag{4.7}$$

where c_i, $c_i^\dagger$ are annihilation and creation operators for spinless fermions satisfying the anticommutation relations. Applying the Jordan-Wigner transformation, we can rewrite the Hamiltonian Eq. (4.4) with the fermionic operators,

$$\begin{aligned} H &= \sum_{i<j} V(i,j)(c_i^\dagger - c_i)\left\{\prod_{m=i+1}^{j-1}(1-2c_m^\dagger c_m)\right\}(c_j + c_j^\dagger) \\ &\quad -|J|h\sum_i (1-2c_i^\dagger c_i) \ . \end{aligned} \tag{4.8}$$

Note that for the nearest-neighbor potentials, like in the usual quantum Ising model, there are no operator products in terms of the index m, thus the Hamiltonian becomes quadratic in the fermionic operators, reducing to the well-known Jordan-Wigner transformed quantum Ising model. The approximation step replaces the operator products $\prod_m(1-2c_i^\dagger c_i)$ in the interaction term of the Hamiltonian running over the index m with an identity. This is equivalent with truncating fermionic operators up to quadratic order to obtain an analytically solvable form and the reason behind calling it a truncated Jordan-Wigner approach. We continue with

$$\begin{aligned} H &\approx \sum_{i<j} V(i,j)(c_i^\dagger c_j + c_j^\dagger c_i + c_i^\dagger c_j^\dagger + c_j c_i) \\ &\quad -|J|h\sum_i (1-2c_i^\dagger c_i) \ . \end{aligned} \tag{4.9}$$

This Hamiltonian corresponds to the long-range Kitaev model exactly solved in [139]. Our truncation approximation becomes exact only for the nearest-neighbor potentials. In general,

it becomes better for ferromagnetic states, since they satisfy $\langle \sigma_i^z \rangle = \langle 1 - 2c_i^\dagger c_i \rangle \approx 1$, where σ_i^z refers to the rotated Hamiltonian in Eq. (4.4).

We perform a standard Fourier transform and Bogoliubov transform [137], which completes the diagonalization of Eq. (4.9) with the result,

$$H = \sum_q \epsilon_q \left(\gamma_q^\dagger \gamma_q - \frac{1}{2} \right) , \tag{4.10}$$

where the excitation spectrum ϵ_q is given by

$$\epsilon_q = 2\sqrt{(\mathcal{S}_q)^2 + (\mathcal{C}_q)^2 + 2h\mathcal{C}_q + |J|h^2} , \tag{4.11}$$

with cosine and sine transforms of the potential where we replaced (i, j) with the distance $r = j - i$ valid for the long-range quantum Ising model

$$\mathcal{C}_q = \sum_{r=1}^{\infty} V(r) \cos(qr) , \tag{4.12}$$

$$\mathcal{S}_q = \sum_{r=1}^{\infty} V(r) \sin(qr) , \tag{4.13}$$

respectively. The excitation spectrum Eq. (4.11) could have a gapless Γ-point ($q = 0$) at the critical field

$$h_c^\Gamma = -\frac{1}{|J|} \sum_{r=1}^{\infty} V(r) , \tag{4.14}$$

and a gapless K-point ($q = \pm\pi$) at

$$h_c^K = -\frac{1}{|J|} \sum_{r=1}^{\infty} (-1)^r V(r) , \tag{4.15}$$

though it depends on details of the potentials as to whether or not the spectrum exhibits the gapless points. For ferromagnetic long-range interaction, $V(r) = -J/r^\alpha$ with $\alpha > 1$, we have a gapless Γ-point at

$$h_c^{\Gamma} \;=\; \sum_{r=1}^{\infty} \frac{1}{r^{\alpha}} \;=\; \zeta(\alpha)\ , \tag{4.16}$$

where $\zeta(\alpha)$ is the Riemann Zeta function. In contrast, for antiferromagnetic long-range interaction, $V(r) = |J|/r^{\alpha}$, we have a gapless K-point at

$$h_c^{K} \;=\; \sum_{r=1}^{\infty} \frac{(-1)^{r+1}}{r^{\alpha}} \;=\; \left(1 - \frac{1}{2^{\alpha-1}}\right)\zeta(\alpha)\ . \tag{4.17}$$

We remark that for the usual quantum Ising model with $V(i,j) = -J\delta_{j-i,1}$, we expect a gapless Γ-point at $h_c^{\Gamma} = 1$ in the ferromagnetic case, and a gapless K-point at $h_c^{\Gamma} = 1$ in the antiferromagnetic case.

4.4 Phase Diagram of the Long-Range Quantum Ising Chain

Our first result for the phase boundary is obtained analytically. In Sec. 4.3 we used the Jordan-Wigner transformation, which solves the nearest-neighbor quantum Ising chain exactly, for the long-range quantum Ising leading to an infinite series of fermionic operators. We truncate such series to obtain analytic estimates for the critical magnetic fields and recall the results from Eqs. (4.16) and (4.17)

$$h_c^{\mathrm{FM}}(\alpha) = \zeta(\alpha)\ , \qquad h_c^{\mathrm{AFM}}(\alpha) = \left(1 - \frac{1}{2^{\alpha-1}}\right)\zeta(\alpha)\ , \tag{4.18}$$

for the ferromagnetic and antiferromagnetic cases, respectively. We compare this to the numerical values of the critical field h_c discussed thoroughly in 4.8.1. In Figure 4.2 we show the phase boundaries for the different methods, where the results of the Kitaev model from Sec. 4.3 corresponds to the solid blue curves. We observe as a first trend that in the ferromagnetic long-range quantum Ising chain, as α decreases, that is, as the potential becomes more strongly long-range, the ferromagnetic phase becomes more favorable: the negative energy contribution from the ferromagnetic ordering increases in its absolute value. On the other hand, in the antiferromagnetic long-range quantum Ising chain, the antiferromagnetic phase

becomes less favorable for smaller values of α because the long-range potential induces more frustration in the staggered ordering. Next, we perform numerical simulations to estimate the critical lines more accurately.

During the numerical simulations we follow two different paths. First we use the infinite Matrix Product State algorithm [119, 121] to search for a translationally invariant ground state for a unit cell of q sites. We search for this kind of ground state for $q = 2$, although the Hamiltonian in Eq. (4.1) fulfills translational invariance in the thermodynamic limit for any q. The energy is minimized via variational methods and the strong finite size effects at the boundaries due to the long-range interactions are avoided. Second, we consider finite size systems with a number of sites $L \in \{32, 64, 128, 256, 512\}$ and approximate the critical point in the thermodynamic limit $L \to \infty$ via finite size scaling. On the one hand this is an appropriate check on the results. On the other hand, we use finite size systems for the dynamics later on and provide a prediction for finite size effects commonly present in quantum simulators. To identify the critical point we keep α and J fixed and iterate over the transverse field h. The von Neumann entropy as a function of the external field has a maximum located at the critical value of the external field h_c. For the nearest-neighbor model the critical point can be found based that the area law for entanglement is violated for gapless states [78], where the entanglement is measured with the von Neumann entropy. Although long-range models may in general violate this area law away from the critical point, we take the same approach knowing that the ground state obeys the area law for the two limiting cases $h \to 0$ and $h \to \infty$. The Ising model has a closing gap around the critical point and therefore the von Neumann entropy S can be used as indicator for the quantum critical point

$$S(h) = -\sum_{i=1}^{\chi} \lambda_i \log(\lambda_i) \ , \tag{4.19}$$

where λ_i are the singular values squared of the Schmidt decomposition of the system and χ is the maximum bond dimension controlling the truncation of the Hilbert space. In the

finite size systems, the eigenvalues of the reduced density matrices correspond to λ_i when splitting into a bipartition. The entropy and the entanglement have a unique extremum at the phase transition which must coincident with the closing gap and can therefore be used to identify the critical point. An alternative approach would be to use the correlation length of the system or the maximal gradient in the magnetization, both with respect to the external field. We explore the critical behavior of the infinite chain (triangles) and the finite size scaling results (diamonds) in Figure 4.2.

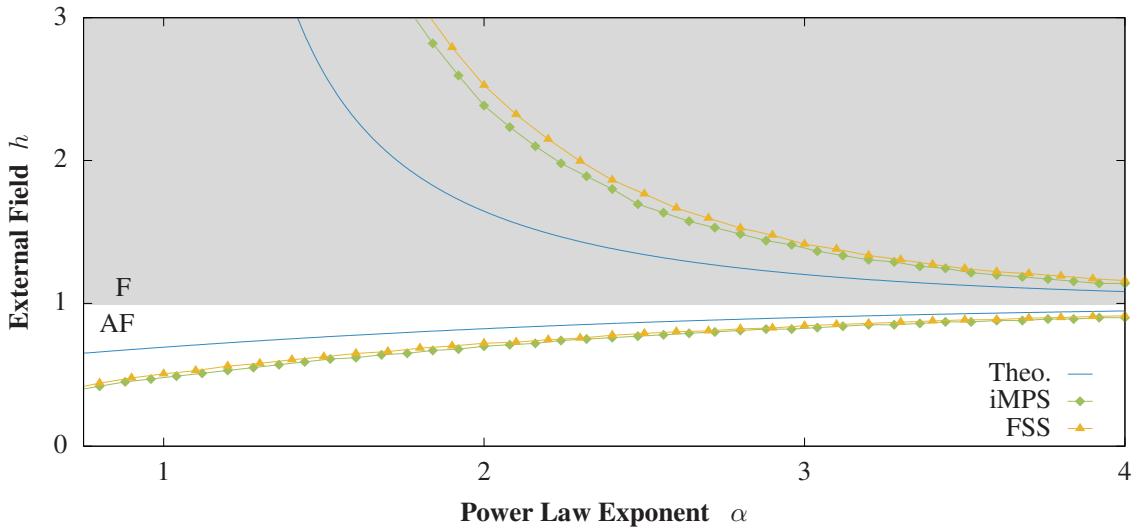

Figure 4.2: *Phase Boundary.* Critical behavior of the long-range quantum Ising model in the ferromagnetic and antiferromagnetic case as a function of the power law exponent α. We compare the theoretical approximation (Theo.) based on a truncated Jordan Wigner transformation, the infinite MPS results (iMPS), and the finite size scaling (FSS) of the MPS results. The boundary between the gray and white shading is the critical point in the limit $\alpha \to \infty$ corresponding to the nearest-neighbor quantum Ising model. We observe that both cases react differently when increasing the long-range interactions. In the ferromagnetic case the paramagnetic phase decreases at cost of the ferromagnet, while the antiferromagnetic phase becomes smaller in the other case due to the concurrency in the staggered order. All three different methods show these trends, although they show in the regime α significant relative differences above 0.1.

In conclusion, the relative difference between the iMPS and the theoretical estimate is bound by 0.37 (0.17) for the ferromagnetic (antiferromagnetic) model considering $\alpha \geq 2$. The relative difference for two arbitrary values x and x' is defined as $(x - x')/((x + x')/2)$.

The actual trend with the difference between iMPS and the theory curve vanishing in the limit $\alpha \to \infty$ reflects the analysis in Sec. 4.3. Further we state that the relative difference between iMPS and finite size scaling results are below 0.11 (0.04). The details on the finite size scaling are described in 4.8.1.

4.5 Scaling of Defect Density for the Kibble-Zurek Hypothesis under a Quantum Quench

We now turn our focus to the dynamics of the long-range quantum Ising model. We analyze the quench through the quantum critical point by means of finite systems. We first analyze measurable observables during the quench and then determine the Kibble-Zurek scaling according to the final state, that is a power-law describing the generation of defects as a function of the quench time and a critical exponent. The linear quench for a time dependent external field is defined as

$$h(t) = h_i + (h_f - h_i)\frac{t}{\tau}\,, \tag{4.20}$$

and replaces the coupling h in Eq. (4.1). τ is the total time of the quench. We quench from $h_i = h(t = 0) = 2h_c$ to $h_f = h(t = \tau) = 0$. When considering our observables during the quench, we stay close to experimentally realizable measurements. In Figure 4.1 we presented the average magnetization $\bar{s}_x$

$$\bar{s}_x = \frac{1}{L}\sum_{k=1}^{L}\langle\sigma_k^x\rangle\,. \tag{4.21}$$

This is e.g. measurable in cold ion experiments [26]. We choose to plot the magnetization in the x-direction which is measurable in the ferromagnetic and antiferromagnetic case, and can not average out in the simulations due to superpositions, e.g. the ferromagnetic ground state $\alpha \to \infty$, and $h = 0$: $(|\uparrow \ldots \uparrow\rangle \pm |\downarrow \ldots \downarrow\rangle)/\sqrt{2}$ has no net magnetization for a local measurement of σ^z. We note in Figure 4.1 for $\alpha \approx 4$ the steep gradient around $t/\tau \approx 0.5$, which corresponds to the critical value for the transverse field in the ferromagnetic case

treated here. Therefore, we extract the first maximum of the gradient disregarding all minor fluctuations and plot them over α in Figure 4.3. We see a similarity to the critical value of the transverse field from the static calculations for big τ, while for faster quenches the deviation from the static result increases. We present the analogous analysis for the antiferromagnetic case as well in Figure 4.3. For faster quenches the maximal gradient is again below the static result leading to the assumption that this effect is due to a delay during which the system takes time to react. The antiferromagnetic case shows an additional effect as a function of α: longer-range interactions exhibit an extra delay in their maximum gradient. If we consider the antiferromagnetic quench for $\tau = 128$ in Figure 4.3 (a), the maximum of the gradient moves from $h = h_c$ for $\alpha = 4$ to values of $h \leq 0.75 h_c$ for $\alpha < 2$. One suggestion to explain this is the concurrent spin configuration in the staggered order in the antiferromagnet which grows for smaller α and might cause this extra delay to establish an antiferromagnetic state. The results on this analysis vary if the quench scheme is not symmetric around the critical point h_c.

Next, we present results for a non-global spin measurement. Such a measurement of a single spin in an optical lattice is technically possible [145] and can be realized in cold ion experiments, too. In Figure 4.4 we show the nearest-neighbor spin-spin correlation in the z-direction for the antiferromagnetic case as a function of time and site in the system. As mentioned above, local measurements of σ^z average out due to symmetry apart from numerical fluctuations. Correlations grow during the quench, and finite system boundary effects are visible at both ends of the chain. The total quench time is $\tau = 32$, the system size $L = 128$, and $\alpha = 3$ in this example, corresponding to dipole-dipole interactions.

Now we turn to the Kibble-Zurek hypothesis in the quenches already discussed above. The Kibble-Zurek mechanism [60, 124, 146] predicts a scaling of the defects in the quantum system as a function of the quench time τ. We recall that the scaling for the nearest-neighbor Ising model is [147]:

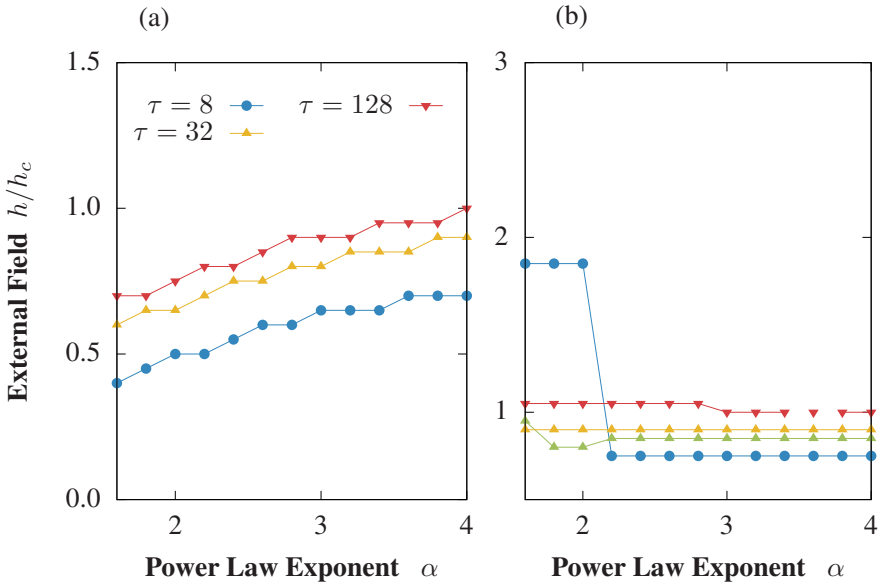

Figure 4.3: *Dynamics and Phase Boundaries.* Around the critical value of the transverse field h_c, the gradient of the magnetization in the x-direction has its maximum. The system needs time to react to the change and therefore fast quenches with a low quench time τ reach the maximum in the gradient at later times. (a) The first maximum during the quench for the antiferromagnetic model. Instead of the time we show the corresponding transverse field $h(t)$ divided through the corresponding critical field. The small plateaus arise from the discretized measurements. (Remark: Small maxima (0.5 times max gradient) in the gradient are neglected.) (b) Analogous to (a) for the ferromagnetic case (same legend as (a)). The analysis failed for the data point with $\tau = 128$ and $\alpha = 3.6$, which was filled with the unconnected point from the simulation with $\chi = 95$. (Jump for fast quenches and small α appears for both bond dimensions).

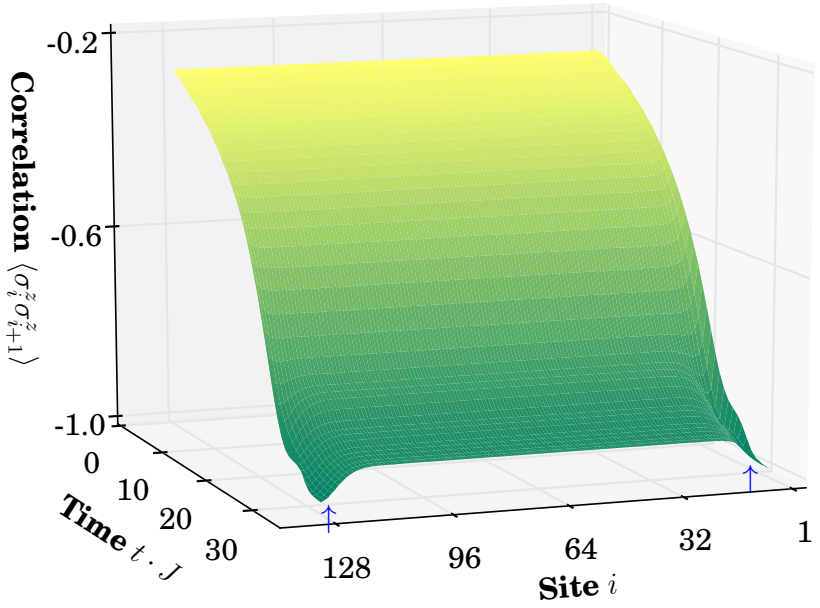

Figure 4.4: *Nearest-Neighbor Correlation in Dynamics.* Space-time evolution of the z spin-spin correlation during the quench into the antiferromagnetic phase where the correlation between sites i and $i+1$ builds up as the external field vanishes. As expected for staggered order in an antiferromagnetic state the correlation is negative. Further we point out more strongly negative correlation due to boundary effects at the end of the quench, where the affected region is indicated with arrows (↑).

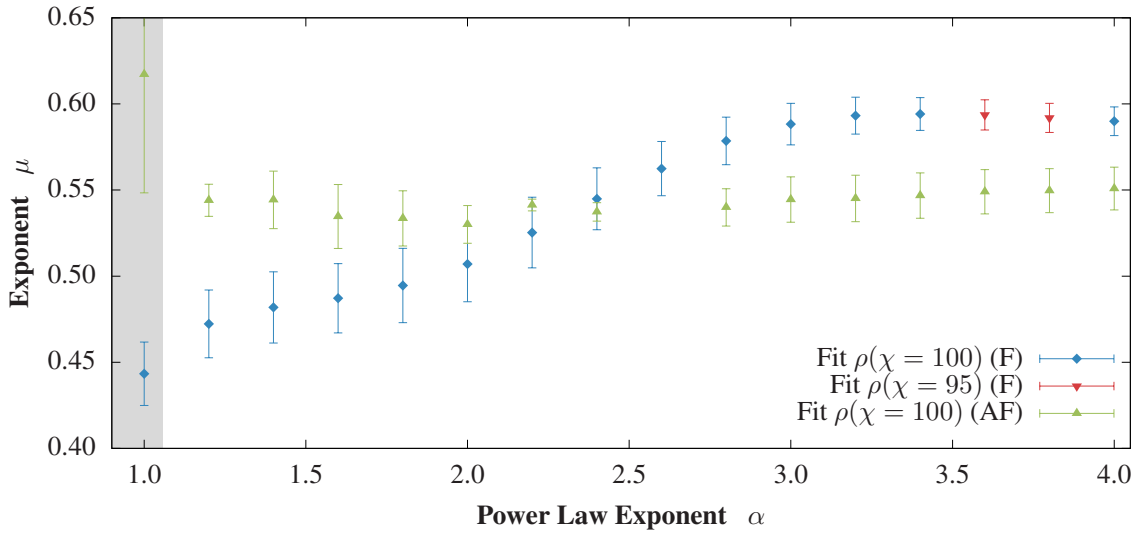

Figure 4.5: *Kibble-Zurek Scaling for the Long-Range Quantum Ising Model.* The exponent μ relates the quench time to the defect density ρ for the power law exponent α as in Eq. (4.23). The ferromagnetic model has smaller μ's for longer-range interactions. The defect density grows slower for longer-range interactions for faster quenches regardless of their original density. Two outliers in the data with large errors bars ($\alpha = 3.6$ and 3.8) have failed to converge and are replaced with simulations with lower bond dimension showing that there is no singularity. In contrast, for the antiferromagnetic model μ stays constant within the error bars and the defects increase at the same rate independent of long-range interactions, but do not necessarily have the same number of defects at the beginning. One non-converging point is not displayed ($\alpha = 2.6$). The error bars for both cases show the standard deviation from the fit of the critical exponent for the different quench times and do not contain truncation errors of the time evolution.

$$\rho \propto |\tau|^{-\frac{\nu}{z\nu+1}} , \tag{4.22}$$

where we use ρ for the defect density, and ν and z for the critical exponents. We have already considered a one-dimensional system in Eq. (4.22). Furthermore, Eq. (4.22) and the following analysis applies only to linear quenches defined over $\partial h/\partial t = \text{const.}$, but extensions for the Kibble-Zurek scaling to non-linear quenches are possible [148]. Plugging in the critical exponents for the nearest-neighbor quantum Ising model with $\nu = 1$ and $z = 1$ we obtain $\rho \propto \tau^{-0.5}$. The exponent $1/2$ is a checkpoint for the calculations in the nearest-neighbor limit $\alpha \to \infty$. The match between theory and experiment does depend on the experimental realization, but yields all over a power law for the defects according to the review in [60].

We are interested in how much the exponent changes when tuning α for the long-range interactions and how it deviates from the $1/2$ in the nearest-neighbor case. We estimate the exponent μ in the proceeding analysis which is defined as

$$\rho \propto \tau^{-\mu} . \tag{4.23}$$

Although the scaling can be used in more general cases, we restrict ourselves to the linear quenches crossing the quantum phase transition located at the critical value h_c analyzed in the previous Section 4.4. This quench scheme starting at twice the critical value was discussed in Eq. (4.20). The quench starts in the paramagnetic phase and ends in the ferromagnetic/antiferromagnetic phase. When we are considering the ferromagnetic ground state, the number of defects corresponds to the number of kinks, respectively domain walls, and we use the defect density ρ defined as the number of kinks per unit length and introduced in detail in 4.8, Eq. (4.29). Expressing ρ in terms of the kinks is constrained to the final point of the quench $h = 0 = h_f$, where the measure is best defined, as the defects are clearly identifiable in terms of the kinks. The data in Figure 4.5, is obtained from simulations based on systems with $L = 128$ and evolution with the time-dependent variational principle

[120] at $\chi = 95, 100$. We expect that the critical exponent μ approaches 0.5 in the limits $\alpha \to \infty$ and $L \to \infty$ resulting in the ferromagnetic nearest-neighbor quantum Ising model in the thermodynamic limit. We provide a brief overview of the finite size effects in nearest-neighbor model in 4.11 to support this statement. The error bars are the standard deviation for μ of the fit for the different values of τ. Examples for the fit are shown in Figure 4.9 in 4.8.2. It does not contain the truncation or methodical error of the time evolution method. From the two curves with the different bond dimensions we deduce that certain simulations fail, resulting in a large standard deviation in the fitting procedure. We consider those points with large standard deviation as a failure of convergence since another set of simulations with a slightly different bond dimension fit into the trend of converged points and have an equally small standard deviation. The critical exponent grows for increasing values of α, meaning if we double the quench velocity for two systems with different long-range interactions, the number of defects increases more slowly in the system governed by longer-range interactions. But as we show in 4.8.2, longer-range systems have initially a higher defect density as shown in Figure 4.9.

However, these results just discussed for the ferromagnetic case are not true for the antiferromagnetic model. The critical exponent stays constant independent of the long-range interaction. The deviation from the nearest-neighbor case $\mu = 0.5$ should be due to finite size effects. But we know from Figure 4.9 that the density of defects is again higher for longer range interactions. The defect density of the antiferromagnetic model is defined analogously to the ferromagnetic model: a missing kink in the staggered order is one defect.

4.6 Conclusion and Open Questions

In this study we have established that the introduction of long-range interactions changes the physics of one-dimensional quantum spin systems non-trivially as observed in various aspects of the statics and the defect density and therefore merits further attention. This is not limited to the quantum Ising model, e.g. the Bose-Hubbard and many other models could be discussed under the influence of the long-range interactions such as dipole-dipole

interactions. First we summarize the results from our study of the long-range quantum Ising model and then raise open problems associated with long-range quantum physics.

We have presented multiple aspects of long-range quantum Ising model, e.g. the Kibble-Zurek scaling, which lead to a better understanding of physical systems with long-range interactions, e.g. the scaling of generated defects during the quench through a quantum critical point. For the ferromagnetic case we find a slower increasing defect density in comparison to the nearest-neighbor limit when increasing the quench velocity. The defect density is higher in comparison to the nearest-neighbor model for the same quench time. Our simulations give a detailed picture of the critical value of the transverse field in the thermodynamic limit using infinite Matrix Product States along with a practical guidance how to resolve issues introduced by degeneracy in those systems. We also presented an alternative to the infinite size algorithm using finite size scaling methods to obtain the value of the critical external field in the thermodynamic limit. This uncovers the finite-size effects, which will certainly be present in experiments with small system sizes. The relative difference for the value of the critical point between $L = 32$ and $L = 512$ is approximately 15% for the antiferromagnetic case for $\alpha = 3$. The same comparison for the ferromagnetic yields a relative difference of around 20%. The iMPS and finite size scaling phase boundaries are supported by an approximate analytical result using a truncated Jordan-Wigner transformation approach in combination with the Kitaev model. We introduced the dynamics of the long-range quantum Ising model through local and global observables during a quench from the paramagnetic phase into the ferromagnetic and antiferromagnetic phases crossing the critical point. We related those measurements to the actual quantum critical point through the maximum of the gradient of average global magnetization in the x-direction and analyzed how this is affected by the total time of the quench. Finally, we evaluated the scaling of defects in the Kibble-Zurek scenario leading to the result of a slowly increasing (constant) defect density at the end for increasing quench velocity in comparison to the nearest-neighbor limit of the ferromagnetic (antiferromagnetic) long-range quantum Ising model. This is reflected in the

exponent of the Kibble-Zurek scaling, e.g. in the ferromagnetic case we observe exponents in the range from $\mu = 0.45$ to $\mu = 0.6$ for power law exponents $\alpha > 1.5$, where $\mu = 0.5$ is the limit of the nearest-neighbor quantum Ising model in the thermodynamic limit.

Having concluded our study, we point out open problems that can be addressed in future research. As indicated by the list of the recent studies concerning the dynamics of the long-range quantum Ising model [118, 131, 133, 134], static physics has been well explored [127–129], but near-equilibrium dynamics such as the Kibble-Zurek hypothesis remain largely unknown, let alone far-from-equilibrium dynamics. One aspect which could be explored in statics and dynamics is the extension to two or higher dimensional systems which we have excluded due to the limitation of MPS algorithms to one spatial dimension for studies of this kind. Two-dimensional setups allow more options for quantum computation to apply gates [144]. In the case of the antiferromagnetic case triangular lattices can lead to the similar concurrence of the staggered order than for long-range interactions in the one-dimensional case. While two-dimensional systems might be accessible through simulations with tensor network methods such as Projected Entangled Pair States (PEPS) [84], this route seems to be more accessible for experiments for any of the models mentioned before. Discrete Truncated Wigner methods are another tool to approach two-dimensional systems with numerical simulations [149]. A further path starting from here is the investigation of dynamical phase diagrams. Where recent studies treat e.g. binary pulses in regards to interaction and transverse field of the quantum Ising model [150], further possibilities considering time-dependent periodic long-range interactions arise. One study obtaining a dynamical phase diagram for the long-range quantum Ising chain in the infinite limit using iMPS is [151]. So called completely interacting models at $\alpha = 0$ form another topic for research.

We have shown that the long-range quantum Ising model is a good starting point for any kind of long-range study. Other models may show new behaviors when including long-range interactions. We think here of the generalization of the quantum Ising in terms of the XY-model with a realization in Rydberg systems [152] or the XYZ-model as realized in

polyatomic molecules [153]. Furthermore, this includes Hubbard models such as the Bose-Hubbard model, Fermi-Hubbard model as they appear e.g. for molecules. For macroscopic quantum tunneling in the Bose-Hubbard model [154] results might change if the distance of the long-range interaction is larger than the width of the barrier. Other problems suitable for extension to long-range interactions include the quantum rotor model and the bilinear biquadratic spin-one Hamiltonian [155].

4.7 Acknowledgments

We acknowledge useful discussions with Jad C. Halimeh, Gavriil Shchedrin, and David L. Vargas. This work has been supported by the National Science Foundation under grant numbers PHY-120881 and PHY-1520915 and the AFOSR grant FA9550-14-1-0287. The calculations were carried out using the high performance computing resources provided by the Golden Energy Computing Organization at the Colorado School of Mines.

4.8 Numerical Methods for Long-Range Statics and Dynamics

In this section we describe the numerical algorithms used, which can be skipped by readers not interested in the computational aspects of this work. The motivation for using tensor network methods for the simulation of our systems is their versatile applications for finite and infinite size statics and finite systems dynamics. Since the invention of the finite size version of MPS [76], various tensor network methods have been proposed. These types of tensor networks include for pure states Tree Tensor Networks (TTNs) [79], Multiscale Entanglement Renormalization Ansatz (MERA) [83], and Projected Entangled Pair States (PEPS) [156]. All approaches are based on a parameterization of states in the Hilbert space in order to capture many-body physics which is well beyond the reach of exact diagonalization. For an overview we refer to [75]. We divide our description of the specific methods used into three parts. First, we discuss the convergence of the iMPS algorithm used to determine the phase boundary in terms of the critical external field h_c as a function of the interaction decay α. This algorithm is based on variational methods to find the ground state of a translationally

invariant unit cell. Second, we treat the path to finite size simulations via MPS returning the ground state of a system of size L. Iterating over different system sizes L, we discuss how to obtain the critical value of the external field h_c in the limit $L \to \infty$ via finite size scaling. Third, we complete the section with a discussion of the dynamic results obtained with the time-dependent variational principle [120] which is able to intrinsically capture long-range interactions and is therefore preferable over a Suzuki-Trotter decomposition as used in many implementations of MPS/TEBD libraries.

4.8.1 Static Simulations: Infinite Systems and the Finite Size Scaling Approach

We explain the numerical methods behind the simulation data shown in Figure 4.2. The iMPS algorithm is designed to find the ground state of an infinite system without boundary effects, returning the translationally invariant unit cell of size L. New sites are inserted in the middle of the existing system and variationally optimized in order to converge to the ground state. The previous iteration is included as the *environment*, where environment is understood in the sense that it exchanges quantum numbers with the system, and not in an system-bath open quantum system context. In the first step of the algorithm, the unit cell is optimized without any environment; in the second step the solution of the first step is considered as the environment. From that point on the environment grows subsequently with each step. The algorithm terminates if the newly introduced sites fulfill the orthogonality fidelity condition:

$$\mathcal{F}\left(\rho_{n-1}, \rho_n^R\right) \;=\; \mathrm{Tr}\sqrt{\sqrt{\rho_n^R}\rho_{n-1}\sqrt{\rho_n^R}}\,, \tag{4.24}$$

where n indicates the iteration step and R is the right part of the system excluding the site introduces in the most recent step. Therefore, the density matrices ρ_{n-1} and ρ_n^R represent the same part of the system and the latter one has one more update included. When the overlap is sufficiently big, the update did not change the result any more. We refer to [119, 121] for a detailed description. The phase boundary for the infinite MPS simulation is obtained for

each value of α evaluating the maximum of the bond entropy iterating over the external field h. The bond entropy is defined by the von Neumann entropy introduced in Eq. (4.19). We obtain the singular values squared λ when splitting the unit cell of the infinite MPS into the bipartition. The bond entropy is one of a variety of possible entanglement measures [85, 157], and it is based on the Schmidt decomposition separating a quantum system into bipartitions. The entanglement can be measured via the number of singular values, the Schmidt number, or the entropy of the singular values according to Eq. (4.19). For example, a Bell state has Schmidt number 2 and von Neumann entropy $-2 \cdot (\frac{1}{2}\log(\frac{1}{2}))$, while an unentangled product state has Schmidt number 1 with von Neumann entropy 0. The maximum of the bond entropy is found using a grid of 21 points ranging from $h^{[1]}_{\text{min}} = 0.9$ ($h^{[1]}_{\text{min}} = 0.0$) to $h^{[1]}_{\text{max}} = 3.9$ ($h^{[1]}_{\text{max}} = 2.0$) in the ferromagnetic (antiferromagnetic) long-range Ising model. We run this evaluation for 51 different values of α ranging from $\alpha = 0$ to $\alpha = 4$. The critical value $h_c^{[1]}$ is the grid point with the maximal bond entropy. Based on this result, we refine the search on the next grid defined as

$$h_c^{[i]} \Longrightarrow h^{[i+1]}_{\text{low}} = h_c^{[i]} - dh^{[i]}\,, h^{[i+1]}_{\text{up}} = h_c^{[i]} + dh^{[i]}\,, \tag{4.25}$$

where $dh^{[i-1]}$ is the step size on the grid. The results presented in Sec. 4.4 and in the following convergence studies are for $h_c^{[2]}$, that is the external field at the quantum critical point between the paramagnetic and ferromagnetic, or antiferromagnetic phase. The superscript denotes the iteration refining the grid for the search and has no physical meaning past an indication for the precision of h_c.

We now discuss convergence of the iMPS results. We take the default convergence parameters of the OSMPS library [52] with the modification of an iterative bond dimension of $\chi = 10, 20, 40$. In Figure 4.7 (a) we show the difference in bond entropy $|S(\chi = 40, h_c) - S(\chi = 20, h_c)|$, $|S(\chi = 40, h_c) - S(\chi = 10, h_c)|$, and $|S(\chi = 20, h_c) - S(\chi = 10, h_c)|$. These results call for a technical discussion of this behavior due to the large difference for many points with $\alpha \gtrsim 2$, here in the antiferromagnetic case. This behavior is related to

symmetry breaking. The degenerate ground state in the limit $h \to 0$ is the GHZ state

$$|\psi_0\rangle = |\psi_{\mathrm{GHZ}}\rangle \;=\; \frac{\Uparrow \cdots \uparrow\rangle \pm \Downarrow \cdots \downarrow\rangle}{\sqrt{2}}\,, \tag{4.26}$$

but without enforcing $\mathbb{Z}_2$ any superposition of $\Uparrow \cdots \uparrow\rangle$ and $\Downarrow \cdots \downarrow\rangle$ minimizes the energy of the system. Therefore, the bond entropy can be between the bond entropy $S = 0$ of a product state and $S = \log(2) \approx 0.69$ of the GHZ ground state. We discuss the origins of this problem related to the numerical algorithm of iMPS. Tracking the singular values, we find either a distribution of pairs in the states with high entropy corresponding to the two different signs as pointed out in the limit $h \to 0$ for the GHZ state in Eq. (4.26). The low entropy states have decaying non-degenerate singular values. The iMPS algorithm selects one of the degenerate states at non-predictable points due to the randomized initial state at the very beginning of the algorithm, as well as the entanglement truncation step, which can randomly pick a particular parity sector for the environment. This is related to the dominant eigenvector of the transfer matrix (see [119]). Note that, once one of the broken symmetry states $|\uparrow \cdots \uparrow\rangle$ or $|\downarrow \cdots \downarrow\rangle$ becomes more dominant, this dominance is "stored" for all subsequent iterations in the environment in the iMPS algorithm. Hence, symmetry breaking by random random numerical noise cannot be removed by running more iterations. The higher bond dimension and the number of iterations in the algorithm lead to smaller differences in the pairs of degenerate singular values until one of the dominant eigenvectors of the transfer matrix is kept and the other truncated. For $\chi = 10$, the difference in the leading singular values is ≈ 0.15 decreasing to ≈ 0.05 for $\chi = 20$. Therefore, the singular values double in magnitude since an equal counterpart was neglected. In summary we can state the following: (1) For $\alpha \lesssim 1.3$ symmetry breaking is not resolved. The result converges, as expected, better for faster decaying long-range interaction up to 10^{-3} between the results for $\chi = 20$ and $\chi = 40$. (2) For $a \gtrsim 2$ we truncate one of the symmetry broken states for $\chi = 40$ meaning that the difference in entropy is large for any comparison to $\chi = 40$. The results with bond dimension 20 have an error between 10^{-1} and 10^{-2} with regard to

$\chi = 10$. The singular values for $\chi = 40$ are close enough to be resolved as degeneracy leading to the conclusion that the state is also well converged. (3) The region in between the algorithm alternates between resolving the symmetry broken ground state or not, leading to convergence up to 10^{-4}. The same trend can be stated in the ferromagnetic case shown in Figure 4.7 (b). A corresponding example for the degeneracy evolving in the singular values can be seen in Figure 4.6. We emphasize that this analysis is relevant if searching for the maximal entropy on a very coarse grid or when trying to show convergence across bond dimensions. For a single bond dimension we may use the final value of the orthogonality fidelity described in Eq. (4.24). The convergence in terms of the orthogonality fidelity is discussed in 4.10.

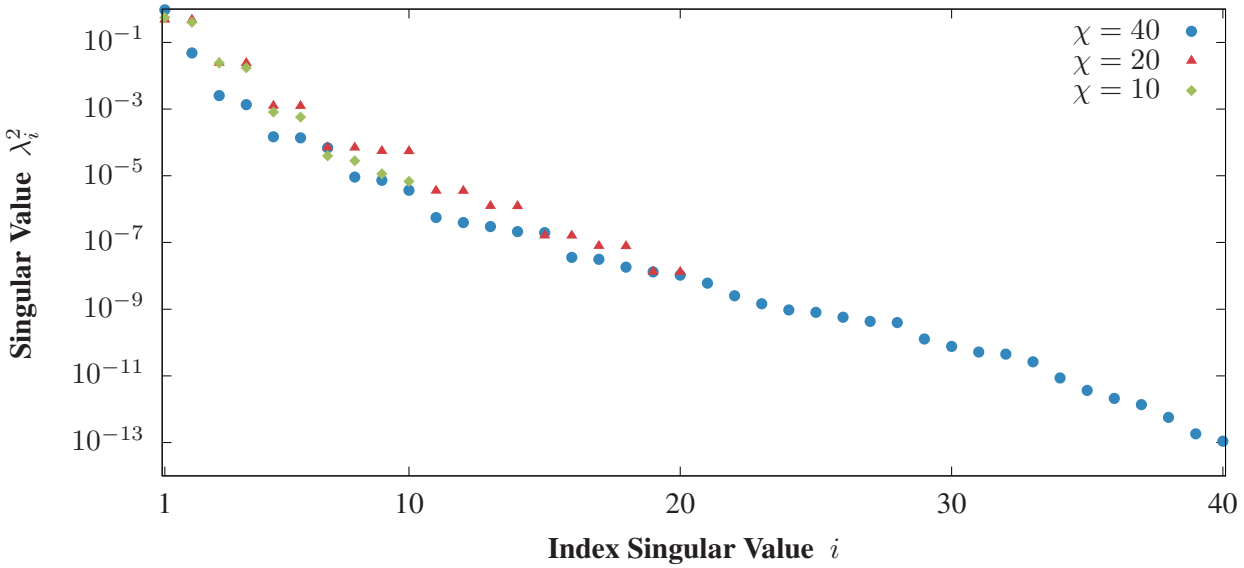

Figure 4.6: *Degenerate Singular Values in iMPS.* The key for understanding the convergence of the bond entropy is Λ, the singular values squared, shown for different bond dimensions χ. The difference in entropy is here related to the symmetry breaking appearing for $\chi = 40$. In contrast the singular values for $\chi = 10$ and $\chi = 20$ appear in pairs. Considering the convergence with regards to χ by means of the bond entropy fails for this reason. This example represents a simulation for $\alpha = 4$ and $h = 1.14$ in the ferromagnetic model.

The finite size simulations have a two-fold purpose. On the one hand, finite size scaling provides an alternate route to obtain the thermodynamic limit of the system and is therefore a check against the iMPS results. While iMPS simulations are only limited by the bond

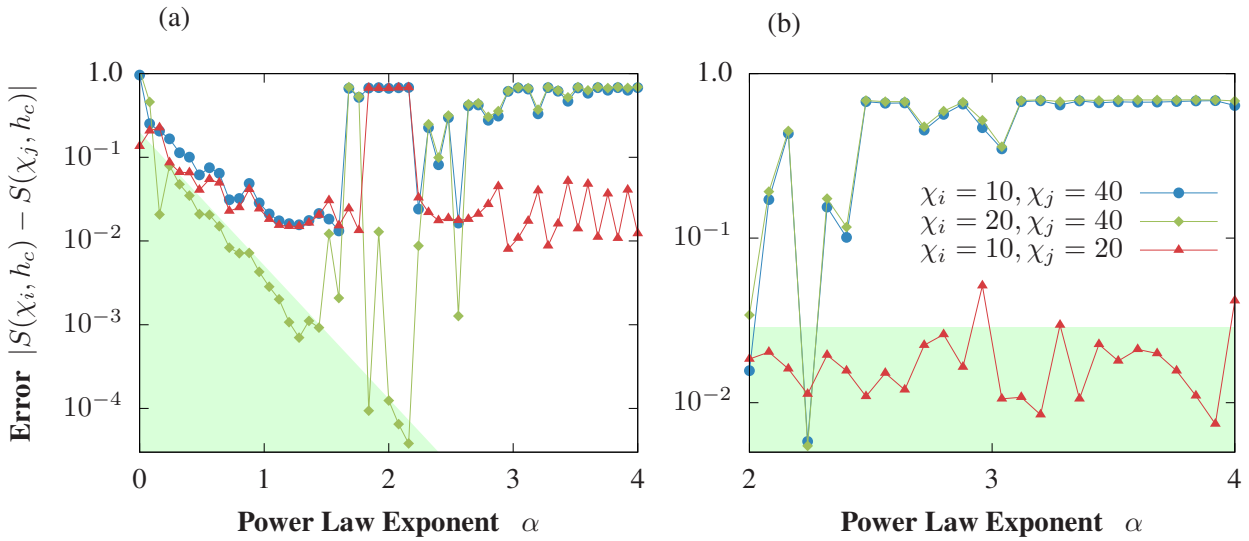

Figure 4.7: *Convergence of iMPS.* (a) in the antiferromagnetic model on the left part of the plot we see the expected behavior that the error is increasing for longer-range interactions. This is indicated by the shaded green triangle, where values within the triangle have broken the symmetry or not for both bond dimensions $\chi = 20$ and $\chi = 40$. In contrast on the right part of the plot we have one simulation with conserved symmetry and one with broken symmetry for the comparison between $\chi = 20$ and $\chi = 40$. (b) In the range shown in the plot for the ferromagnetic case, the degeneracy is never kept up to $\chi = 40$ so that the error $|S(\chi = 40) - S(\chi = 20)|$ is not a reasonable basis on which to judge convergence. But the simulations comparing $\chi = 10$ and $\chi = 20$ in the shaded green rectangle are a meaningful error with regards to the iMPS symmetry breaking issue. Legend applies to both (a) and (b).

dimension used, finite size simulations enforce the $\mathbb{Z}_2$ symmetry and avoid for this reason the symmetry-breaking effects discussed in the previous section. On the other hand, we see the finite size effects affect the system, which is important as the dynamic simulations are for finite systems. For the finite size scaling we use the same grid method as for iMPS before with the initial grid boundaries $h^{[1]}_{\text{min}} = 0.8$ ($h^{[1]}_{\text{min}} = 0.0$) and $h^{[1]}_{\text{max}} = 9.8$ ($h^{[1]}_{\text{max}} = 2.0$) with nine (seven) grid points for each α and L in the ferromagnetic (antiferromagnetic) case. We refine the grid four times after the initial run ending with the bond dimensions $\chi = (256, 512)$ for the iteration over the OSMPS convergence parameters. The final distance between points is for both cases $dh^{[5]} \approx 0.004$. For the refinement we find $h_c^{[i]}(\alpha, L)$ with the bond entropy at the middle of the system and construct the next, refined, grid $i + 1$ in the interval $h_c^{[i]}(\alpha, L) \pm dh^{[i]}$. The maximum number of sweeps are $(4, 6)$ for the corresponding iterations in bond dimension $\chi = (256, 512)$. The other convergence parameters, which stay constant for each set of convergence parameters iterated over, are a variance tolerance of 10^{-10} and a local tolerance of 10^{-10}. For power law exponents of $\alpha > 1.5$, we actually reach a variance superior to 10^{-7} where simulations converge better away from the critical value for the ferromagnetic Hamiltonian. In the antiferromagnetic case, longer-range interactions show worse convergence independent of the critical value of the external field. We discuss the details in 4.9. The critical values are evaluated for system sizes 32, 64, 128, 256, and 512. By using finite size scaling, we obtain the critical value h_c of an infinite system. From Cardy [158] we know that for a finite system the distance of the critical point $h_c(L)$ to the critical point in the thermodynamic limit h_c can be described by

$$|h_c(L) - h_c| \propto L^{-\frac{1}{\nu}} . \tag{4.27}$$

Knowing that the values of h_c are increasing in the ferromagnetic and antiferromagnetic case according to Figure 4.8, we can use

$$h_c(L) = h_c - cL^{-\frac{1}{\nu}} , \tag{4.28}$$

and fit the unknown parameters h_c, ν, and c via [159]. Due to the logarithmic choice of the system size, small system sizes are overrepresented in the fit. We account for this by assigning an uncertainty proportional to $1/L$ at each data point. The results for different system sizes and the data from the finite size scaling can be seen in Figure 4.8. In the antiferromagnetic case (a), the points show the expected behavior with smaller spacing between bigger system sizes; thus the simulations are converging to the thermodynamic limit. When the interactions are not decaying for $\alpha \to 0$, the finite size scaling breaks down due to poorly-converging simulations. The black curve represents the $L \to \infty$ limit achieved through the finite size scaling fit. Figure 4.8 (b) shows the same behavior for the ferromagnetic case. We point out that the weights for each data point are necessary in this case to avoid an intersection of the curve for $L \to \infty$ with the finite size solution $L = 512$ for longer-range interactions.

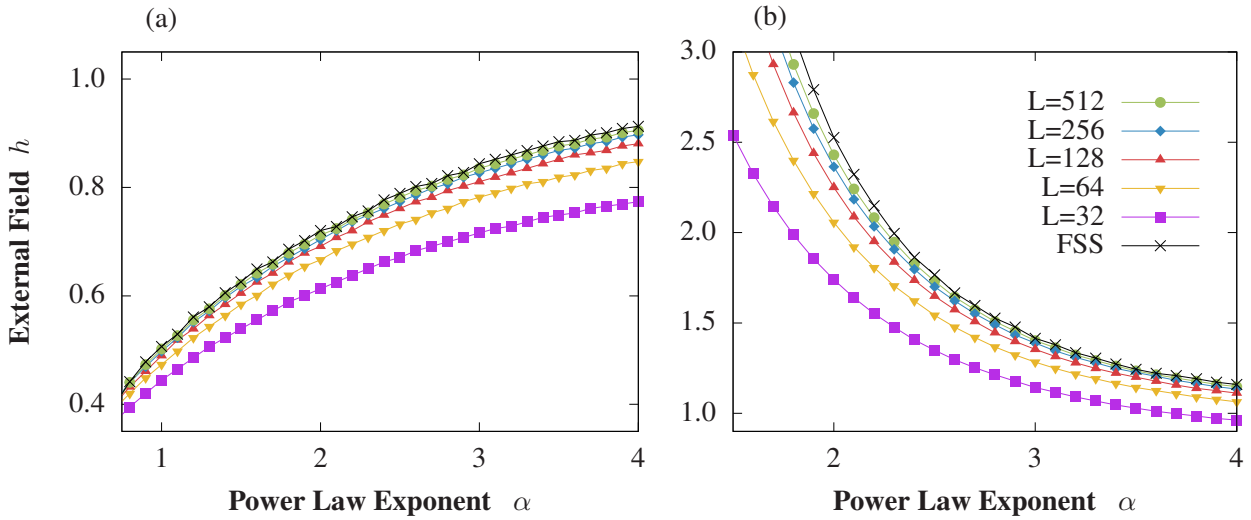

Figure 4.8: *Finite Size Scaling for the Long-Range Quantum Ising Model.* Finite-size effects lead to a decrease of the critical value of the external field h_c for smaller system sizes. Furthermore we achieve the thermodynamic limit for infinite system size via finite size scaling (FSS). (a) antiferromagnetic case; (b) ferromagnetic case. Legend applies to (a) and (b) both. We point out that for the limit $\alpha \to 0$ and $h \to 0$ the ground state for the ferromagnetic case is always the GHZ state, while the antiferromagnetic case has an exponential degeneracy. The latter might contribute to convergence problems when α is approaching zero. The limits $\alpha \to \infty$ is equal to the nearest-neighbor case and all limits $h \to \infty$ have a ground state aligned with the external field.

4.8.2 Dynamic Simulations with MPS

In this section we analyze the scaling of the numerical simulation with regards to the Kibble-Zurek hypothesis. The Kibble-Zurek mechanism describes the scaling of the defect density when driving a quantum system through a quantum phase transition and was originally formulated in terms of cosmology [160], and later brought to quantum systems such as helium [161] or the nearest-neighbor quantum Ising model [124]. There, the external field is changed in order to cross the quantum critical point at $h_c = 1$ in the nearest-neighbor quantum Ising model. In our analysis the quantum critical point h_c depends on the actual value of the power law exponent α as presented in Sec. 4.2.

In order to analyze the Kibble-Zurek hypothesis in the present of long-range interactions, we first define the defect density for the ferromagnetic model. The defect density was defined in [162] using nearest-neighbor correlations, and we divide by $(L-1)$ instead of L to account for the open boundary condition:

$$\rho \;=\; \frac{1}{2(L-1)} \sum_{i=1}^{L-1} \left(1 - \langle \sigma_i^z \sigma_{i+1}^z \rangle\right) . \tag{4.29}$$

We now shortly outline why this works in the ferromagnetic case for the nearest-neighbor model. We recall that at the end of the quench the external field $h = 0$ and therefore the ground states $|\psi_0^{\mathrm{F}}\rangle$ are defined through

$$|\psi_0^{\mathrm{F}}\rangle = \frac{1}{\sqrt{2}} \left(|\Uparrow \ldots \uparrow\rangle \pm |\Downarrow \ldots \downarrow\rangle\right) . \tag{4.30}$$

This is equivalent to the GHZ state and we recall that this is the ground state before $\mathbb{Z}_2$ symmetry breaking. The first excited state has $2(L-1)$ degeneracies and is described by a single kink in the system, e.g. $|\ldots \uparrow\uparrow\downarrow\downarrow \ldots\rangle$. The number of kinks is equal to the number of excitations. If we consider first a state with a product state of only spins up or down, one is easily convinced that Eq. (4.29) describes the defect density. For every domain wall the nearest-neighbor correlation inside the sum contributes, while for spin inside the domain

wall the term is cancelled. Moreover, it is a reasonable measurement even when the spins are changing slowly. Let us verify this point with an example of three spins changing from up to down, $|\phi\rangle = \Uparrow\rangle\ \Uparrow\rangle_x\ \Downarrow\rangle$. The subscript reflects the basis if it differs from z. The measurement of the correlation yields zero in both cases:

$$\begin{aligned} \langle\Uparrow\langle\Uparrow|_x\,\sigma_1^z\sigma_2^z\,\Uparrow\rangle\Uparrow\rangle_x = 0 \qquad \langle\Uparrow|_x\langle\Uparrow|\,\sigma_2^z\sigma_3^z\,\Uparrow\rangle_x\Uparrow\rangle = 0 \\ \Longrightarrow \rho = \frac{1}{2L}\left((1-0)+(1-0)\right) = \frac{1}{L}\times 1\,. \end{aligned} \tag{4.31}$$

The measurement in Eq. (4.29) yields one defect, as expected, with the spins flipping once over the chain. We emphasize that this cannot be used in any region with $h \neq 0$, except as an approximation for $h < h_c$. Let us turn to the defects of the ferromagnetic long-range quantum Ising model. The defects are local kinks, but the states with one kink are not all degenerate. In fact, the energy gap to the ground state is smaller for kinks closer to the boundaries. This is a manifestation of the boundary effects. Counting all kinks equally, we make an error growing in the limit $\alpha \to 0$. The defect density of the antiferromagnetic case in the nearest-neighbor model is defined as

$$\rho_{\mathrm{AF}} \;=\; \frac{1}{2(L-1)}\sum_{i=1}^{L-1}\left(1+\langle\sigma_i^z\sigma_{i+1}^z\rangle\right)\,. \tag{4.32}$$

We again point out that the single defects have a different excitation energy depending on their position in the bulk.

In order to retrieve the critical exponent scaling in the form of Eq. (4.23), we simulate the quenches for $L = 128$ for the set of τ's containing $\{4, 8, 16, 32, 64, 128\}$. For each α we fit the coefficient c and the critical exponent μ via [159]. In order to estimate if any non-converged simulations are included in the data, the standard deviation σ_μ is calculated through the covariance matrix given by the fitting function. In Figure 4.9 we show one example in the ferromagnetic model for $\alpha = 1, 2, 3$, and 4. The error of the fit can be seen as an indicator for the validity of the dynamic results. Running simulations with different χ helps us to identify

failing simulations versus singularities. For weaker long-range interactions with big α the fits reproduce the results while for longer-range interaction the procedure fails ($\alpha = 1$). The initial state is based on the same convergence parameters as the statics discussed in 4.8.1, except for the bond dimension which is lowered to $\chi = 95$ or 100. For the dynamics we keep the corresponding maximal bond dimension and use the default TDVP convergence parameters in OSMPS [52] for all other parameters.

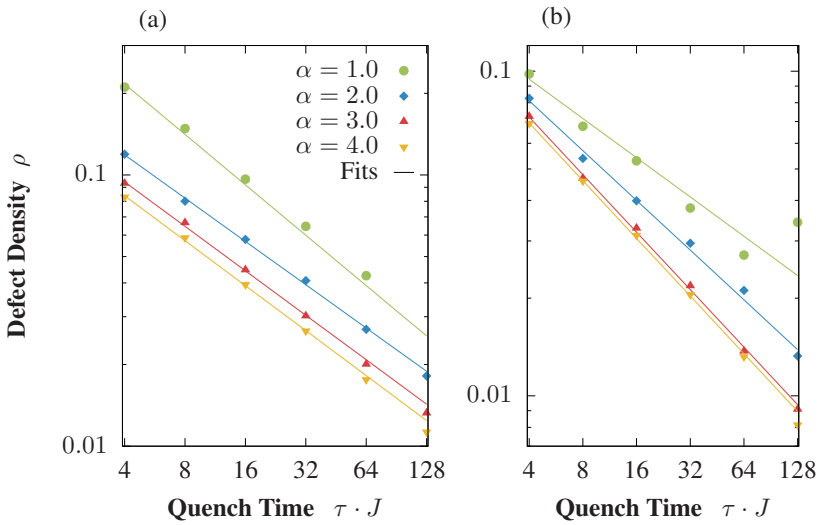

Figure 4.9: *Fitting the Exponent for the Defect Density in the Kibble-Zurek Hypothesis.* (a) Examples for the defect density at the end of the quench for the antiferromagnetic long-range quantum Ising model plotted over the quench time τ for different power law exponents α shows the decrease in defect density for slower quenches. The power law in the scaling leads ideally to a line in the log-log plot which is here slightly affected by failing simulations. This is especially evident for small α, e.g. in the antiferromagnetic case for $\alpha = 1.0$ and $\tau = 128$. (b) Corresponding data for the ferromagnetic model.

4.9 Convergence of Finite-Size Statics

In the appendix we briefly address the convergence of the finite size statics. We already discussed the convergence of iMPS in 4.8 and therefore it is known that the convergence can be studied in different fashions. In OSMPS, the variance of H is considered for statics of finite size systems. The user chooses a value, we take 10^{-10}, and OSMPS iterates through the different bond dimension χ. We consider $\chi = 256$ and $\chi = 512$ of the last grid. This

fifth grid has a discretization of $dh \approx 0.0044$ (ferro) and $dh \approx 0.0042$ (antiferro) around the critical point of the fourth grid. The output contains the flag if the simulation converged according to the value for each χ; in addition the actual value of the variance is saved as well.

We start to look if the simulation converged with a variance of $L \cdot 10^{-10}$. This information is contained in the left part of Figure 4.10 for the ferromagnetic model. The coloring is as follows: green for convergence at the first convergence parameter with $\chi = 256$, red for convergence the second convergence parameter at $\chi = 512$, and blue if not converged at either of the previous bond dimensions. In order to estimate the variance of the blue region, we plot the actual value for the critical value h_c as a function of α and system size in the right part of Figure 4.10. For the analysis used in the main part of the paper we achieve a variance less than 10^{-7}.

We follow the similar scheme to study the convergence in the antiferromagnetic long-range quantum Ising Hamiltonian, presented in Figure 4.11. The convergence becomes in general more difficult in the longer-range interacting region with $\alpha \to 0$, still reaching a variance of 10^{-6} or better for the shorter-range region with $\alpha > 1.5$.

4.10 Convergence of Infinite-Size Statics

We discussed at length that it is difficult to study convergence as a function of the bond dimension in terms of the bond entropy in 4.8.1. But we give in the following a brief overview of the convergence of the iMPS in terms of the orthogonality fidelity defined in Eq. (4.24). In order to show convergence it is convenient to switch from the orthogonality fidelity to the actual error, the infidelity

$$\mathcal{I} = 1 - \mathcal{F} \,. \tag{4.33}$$

Figure 4.12 shows the convergence for the antiferromagnetic and the ferromagnetic model for the highest bond dimension $\chi = 40$ of our convergence parameters and the second grid.

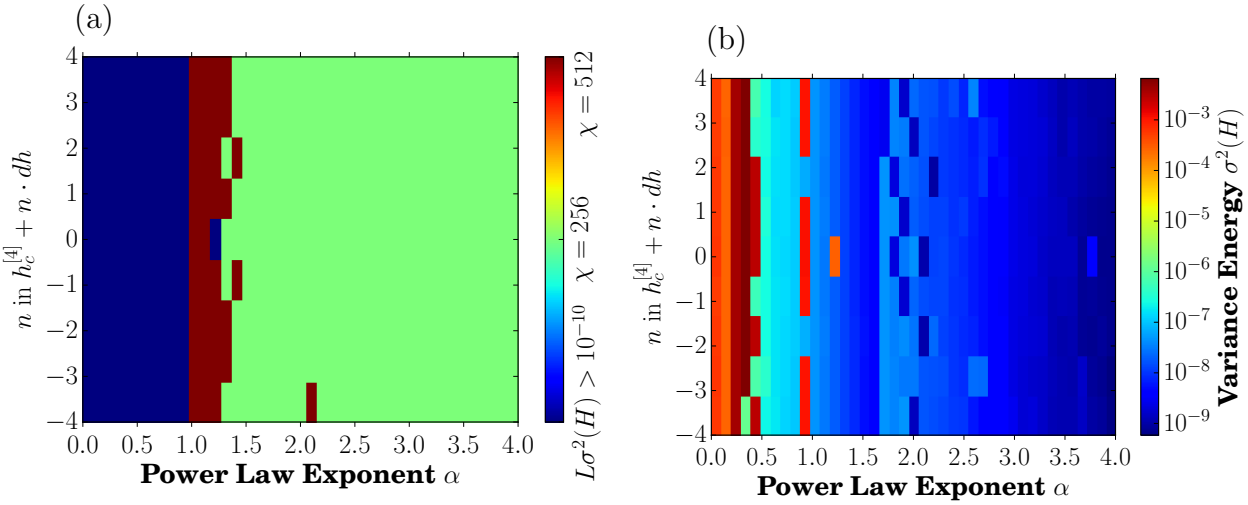

Figure 4.10: *Convergence of Finite Size MPS Ground States:* built-in convergence check of OSMPS using the variance of H for the last grid and $L = 512$ in the ferromagnetic case. (a) The critical region causes most problems to converge up to variance $L \cdot 10^{-10}$ (green converged with $\chi = 256$, red converged with $\chi = 512$, blue not converged). (b) The actual variance of H of the fifth grid for the results used in the main section is at least converged around 10^{-6}.

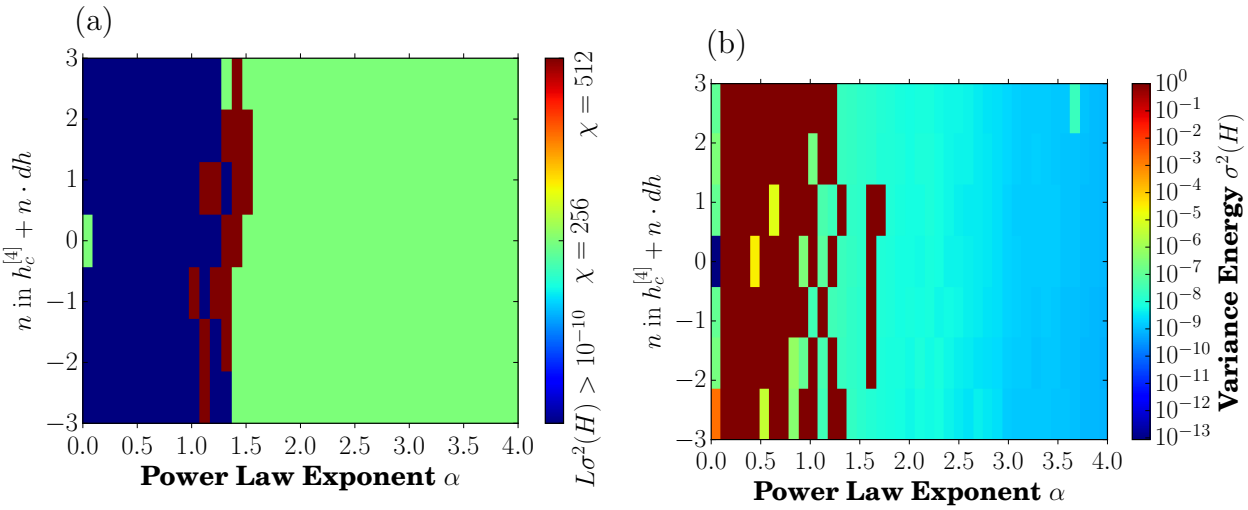

Figure 4.11: *Convergence of Finite Size MPS Ground States:* built-in convergence check of OSMPS using the variance of H for the coarse grid and $L = 512$ in the antiferromagnetic case. (a) The longer-range interaction region causes most problems to converge up to variance $L \cdot 10^{-10}$ (green converged with $\chi = 256$, red converged with $\chi = 512$, blue not converged). (b) The actual variance of H of the fifth grid is shown on the right. Some antiferromagnetic simulations did not finish in the allotted time.

In terms of the orthogonality fidelity the simulations are well converged at an error $\mathcal{I}$ of 10^{-8} or better for $\alpha > 1$. Convergence close to the critical point is in general worse. For $\alpha < 1$ interaction become too long-range to converge at the same level for these convergence settings. We remind the reader that the search interval for the ferromagnetic case shown in Figure 4.12 (b) does not contain the critical value for very small α with an upper bound of $h_{\text{upper}} = 3.9$.

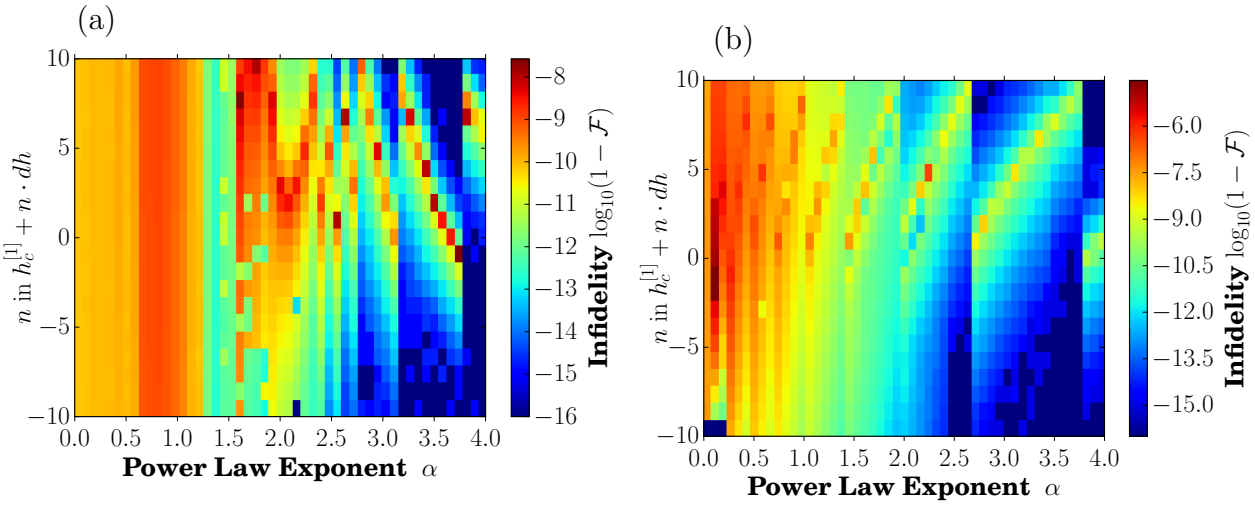

Figure 4.12: *Convergence of the iMPS.* We consider the infidelity of the orthogonality fidelity plotted as logarithm of base 10. Both the ferromagnetic case (a) and the antiferromagnetic case (b) convergence for $\alpha > 1$ mostly to an infidelity of 10^{-8} or better. Non-converging points are typically around the critical point of the model moving downwards for the antiferromagnetic case and upwards for the ferromagnetic case. The vertical stripes originate in the fact that each simulation might have a different critical value from the first grid, where h_c is identical within one strip.

4.11 Finite Size Effects in the Kibble-Zurek Scaling

Section 4.8.2 raised the question of how finite size effects influence the value of the critical exponent μ in the dynamics. We consider the quench times $\tau = 4, 8, 16, 32, 64, 128$ and different system sizes $L = 32, 64, 128, 256$ to show these finite size effects in the nearest-neighbor limit. This limit corresponds to $\alpha \to \infty$. Table 4.1 presents the data. The error is solely from the fit and does not contain truncation error or methological errors from the time

Table 4.1: *Finite Size Effects in the Kibble-Zurek Scaling for the Quantum Ising Model.* The finite size effects lead to a growing critical exponent for smaller system sizes. In the thermodynamic limit the critical exponent of 0.5 is reached.

System size	$L = 32$	$L = 64$	$L = 128$	$L = 256$	$L \to \infty$
Anitferro	0.810±0.060	0.614±0.026	0.532±0.016	0.502±0.017	0.48
Ferro	0.810±0.060	0.614±0.026	0.532±0.016	0.500±0.017	0.48

evolution. The thermodynamic limit is obtained via finite size scaling using the following approach:

$$|\mu_\infty - \mu_L| \propto L^{-c_2} \Longrightarrow \mu(L) = \mu_\infty + c_1 L^{-c_2} \,. \tag{4.34}$$

The value μ_∞ is shown in the last column of Table 4.1. As in the finite size scalings previous discussed, we weight the data points for large system sizes more since we have less data points in the corresponding interval. We do not show the error here, because of the limited number of data points with regards to the degrees of freedom. In conclusion, the data supports the assumption that the finite size effects are relevant and the thermodynamic limit in the nearest-neighbor model approaches $\mu = 0.5$ in both the ferromagnetic and antiferromagnetic case.

CHAPTER 5

OPEN QUANTUM SYSTEMS PEDAGOGY

The following problem sets aims to introduce advanced undergraduate and graduate students to open quantum systems. We concentrate on the numerical techniques centered on the Lindblad master equation. Therefore, we first recap closed quantum systems and basic methods for density matrices and entanglement. The open quantum system exercises treat the single-channel Lindblad equation for a two-level system and introduce the Liouville space. We thank H. North and N. C. Smith for their feedback while solving the problem set.

5.1 Problem set: qubit on the Bloch sphere

A qubit is the quantum analog to a classical bit. The classical bit can have only values of either 0 or 1, which could be described with a two-component vector where the upper entry contains the probability for 1 and the lower for 0. One can think of 0 and 1 as a placeholder for other classical measurement outcomes, e.g., head or tail of a coin flip, drawing a black or white sphere from a box, or having a spin pointing up or down. Due to the "or" we have exactly two possible vectors:

$$\text{State 0}: \quad \begin{pmatrix} 1 \\ 0 \end{pmatrix}, \qquad \text{State 1}: \quad \begin{pmatrix} 0 \\ 1 \end{pmatrix}. \tag{5.1}$$

In contrast, the state of a qubit − in the bra-ket notation written as $|\,\psi\rangle$ − can have any combination of probabilities, called superposition of states,

$$|\,\psi\rangle = c_0 \begin{pmatrix} 1 \\ 0 \end{pmatrix} + c_1 \begin{pmatrix} 0 \\ 1 \end{pmatrix} = \begin{pmatrix} c_0 \\ c_1 \end{pmatrix}. \tag{5.2}$$

The middle part of the equation expresses the probability for each state 0/1 together with their basis of the corresponding vector, while the far right part implies that you know which state, 0 or 1, belongs to the upper and lower entry in the vector. Moreover, the entries have

to fulfill the normalization condition $c_0 c_0^* + c_1 c_1^* = 1$. That corresponds to a total probability of 1. c_0 and c_1 are complex numbers and c^* is the complex conjugate of c.

For the visualization of the quantum state for a qubit $|\psi\rangle$, we may use the Bloch sphere, which is a unit sphere. The north and south pole, lying on the z-axis of the unit sphere, represent the classical state 1 and 0. Any other point on the Bloch sphere is a quantum mechanical superposition of those two classical states. The other directions are referred to as x and y. This is shown in Figure 5.1. We emphasize that the vector $|\psi\rangle$ has two entries c_0 and c_1, but the visualization in the Cartesian coordination system has three basis vectors in the x, y, and z direction. Therefore, we emphasize that we have the space for the vector $|\psi\rangle$, the *Hilbert space*, as one description. The Hilbert space is defined over the basis vectors − in our case the vectors for the state 0 and 1 − and its dimensions d is the number of those basis vectors, here 2. In contrast, the Bloch sphere and its three dimension are inherited from a measurement approach, e.g. in the Stern-Gerlach experiment you measure the qubit in a lab, which is best described in a three dimensional Cartesian coordinate system for the possibilities to arrange your measurement apparatus.

1. Find the coefficients for the six vectors pointing in and opposite to the axis of the coordinate system of the Bloch sphere, which are in the $\pm x$-direction, $\pm y$-direction, and $\pm z$-direction.

2. Describe the part of the Bloch sphere for real valued vectors $|\psi\rangle$ and explain why two entries in the complex valued vector are sufficient to describe measurement outcomes in the x, y, and z direction.

Below, we suggest two paths to solve these exercises.

Suggested path for numerical solution: Our open source library *openMPS* for the simulation of many-body quantum systems has an extension to plot the Bloch sphere, which is located in the module *Qubit*. In order to use these plots, save the package *MPSPyLib* and the modules *Qubit.py* and *blochsphere.py* in the same folder. Go to this folder and open the

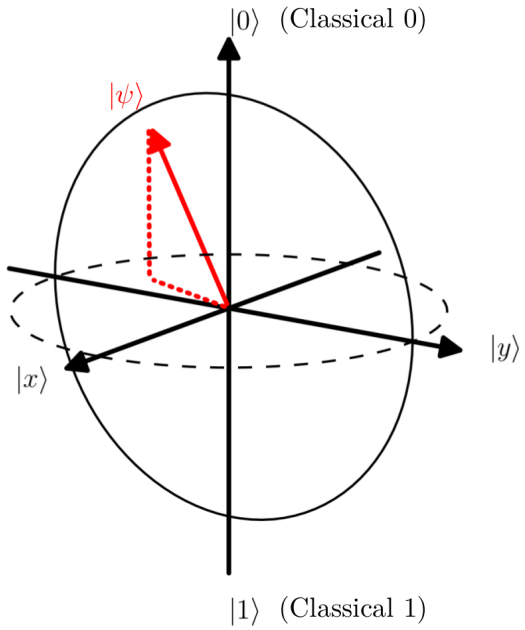

Figure 5.1: *Bloch sphere*: the random state of the qubit with $c_0 = 0.73 + 0.59\mathrm{i}$ and $c_1 = 0.11 - 0.33\mathrm{i}$ is displayed as unit vector in red. The corresponding points of a classical bit on the Bloch sphere are on the top, at the point $(0, 0, 1)$, and at the bottom of the sphere with coordinates $(0, 0, -1)$.

python command line mode (type `python` on the bash command line). Make sure you have the necessary libraries by typing

```
import numpy as np

import scipy as sc

import matplotlib.pyplot as plt
```

If those libraries are available on your system, then the following two lines plot a vector on the Bloch sphere.

```
from Qubit import bloch_sphere

bloch_sphere([c0, c1])
```

where you replace `c0` and `c1` with the actual values (or define them before). This can help you to find the vector in the directions of the coordinate system or the subspace of real valued vectors.

Suggested path for analytical solution: Measurements of a qubit, and quantum states in general, are a vector-matrix-vector multiplication of an operator $\hat{O}$ represented by a matrix:

$$\langle \hat{O} \rangle \;=\; \langle \psi | \hat{O} | \psi \rangle = \begin{pmatrix} c_0^* & c_1^* \end{pmatrix} \begin{pmatrix} O_{11} & O_{12} \\ O_{21} & O_{22} \end{pmatrix} \begin{pmatrix} c_0 \\ c_1 \end{pmatrix} . \tag{5.3}$$

The vector on the Bloch sphere has three components, where each of them is obtained through a measurement of one Pauli matrix σ^α with $\alpha \in \{x, y, z\}$:

$$\vec{r} = \begin{pmatrix} \langle \sigma^x \rangle \\ \langle \sigma^y \rangle \\ \langle \sigma^z \rangle \end{pmatrix} , \qquad \sigma^x = \begin{pmatrix} 0 & 1 \\ 1 & 0 \end{pmatrix} , \qquad \sigma^y = \begin{pmatrix} 0 & -\mathrm{i} \\ \mathrm{i} & 0 \end{pmatrix} , \qquad \sigma^z = \begin{pmatrix} 1 & 0 \\ 0 & -1 \end{pmatrix} . \tag{5.4}$$

Thus, the vector on the Bloch sphere corresponds to

$$\vec{r} = \begin{pmatrix} c_0^* c_1 + c_0 c_1^* \\ -\mathrm{i} c_0^* c_1 + \mathrm{i} c_0 c_1^* \\ c_0^* c_0 - c_1 c_1^* \end{pmatrix} . \tag{5.5}$$

Use equations (5.3) to (5.5) as help to solve the exercise analytically.

5.2 Problem set: qubit on the Bloch sphere II

In the next step, we explore the time evolution of a qubit on the Bloch sphere. The time evolution of a qubit can be described with a pulse. This pulse can be an external field applied over a certain time for a magnetic spin. In an atomic two level system, described by a qubit, the pulse would be applied through a laser field. The state of the qubit describes a path on the Bloch sphere illustrated with Figure 5.2. Those pulses are essential in experiments such as the spin echo or quantum computing. The spin echo experiment uses such pulses to refocus the total spin of multiple qubits after they spread out due to precession at different frequencies in the $x - y$ plane of the Bloch sphere. For quantum computers, we have to rebuild the quantum analog of the classical gates, e.g. `NOT` or `AND` gates for a single qubit or two qubits, respectively. These gates are represented by a pulse which can be used to built circuits for algorithms.

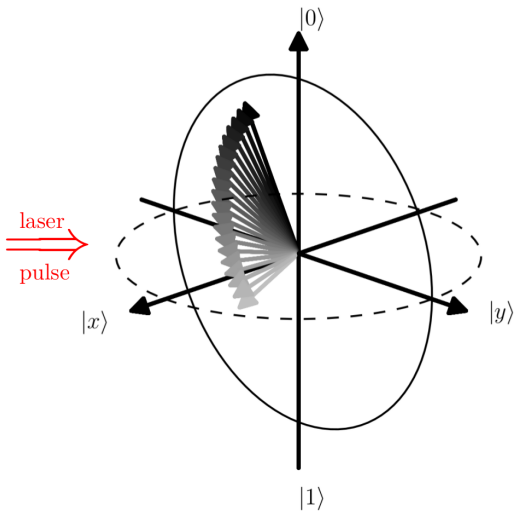

Figure 5.2: *Pulse on the Bloch sphere*: We apply a $\frac{\pi}{2}$ pulse, e.g via a laser, to the random quantum state defined over the coefficients $c_0 = 0.73+0.59\text{i}$ and $c_1 = 0.11-0.33\text{i}$ in Figure 5.1. The color of the Bloch vectors is turning into grey over the time evolution.

We now explore some of the possible pulses. From the six states you found in Exercise 1, choose three pairs of initial and final state. Find a corresponding pulse sequence to get from the initial state to the final state for all of your three pairs. Describe what each of the pulses is doing.

Suggested path for numerical solution: In the module Qubit, we have as well the capability to carry out time evolutions of a qubit according to the Schrödinger equation. Therefore, you can import the following module and function in the same or a new session of the python command line

```
import numpy as np
from Qubit import Qubits
```

`numpy` is a powerful **num**erical library for **py**thon. `Qubits` is the class able to simulate time evolutions for one to a few qubits with predefined pulses. You can generate a qubit with a specific initial state with

```
Q = Qubits(state0=np.array([c0, c1]))
```

In contrast to before, the initial vector `state0` has now to be a numpy array. You can add a pulse to the time evolution, e.g. with

```
Q.add_free()
```

The following pulses are predefined:

- `add_free`
- `add_pi2` (Figure 5.2 is an example of this pulse.)
- `add_pi`
- `add_pi2y`
- `add_piy`

After adding one or more terms, the animation of the Bloch sphere is shown with a call to

```
Q.animate()
```

If you want to display the path as in Figure 5.2, you can use the optional argument `path=True`, then call the function with `Q.animate(path=True)`.

Suggested path for analytical solution: The evolution of a quantum state according to the Schrödinger equation is described via a matrix exponential

$$|\,\psi(t)\rangle = \mathrm{e}^{-\frac{\mathrm{i}}{\hbar}\hat{H}t}\,|\,\psi(t=0)\rangle\,, \tag{5.6}$$

where $\hat{H}$ is the Hamiltonian of the system defined with operators. $\hbar$ is set to one for numerical simulations. If $\hat{H}$ is written in terms of the Pauli matrices σ^α, there is a solution to the exponential

$$\mathrm{e}^{\mathrm{i}a\vec{n}\cdot\vec{\sigma}} \;=\; \mathbb{I}\cos(a) + \mathrm{i}\vec{n}\cdot\vec{\sigma}\sin(a)\,, \qquad \vec{\sigma} = \begin{pmatrix}\sigma^x\\ \sigma^y\\ \sigma^z\end{pmatrix}\,, \qquad \|n\| = 1\,. \tag{5.7}$$

$\vec{n}$ is a unit vector weighting the Pauli matrices accordingly and a is a scalar constant containing an overall weight. $\mathbb{I}$ is the identity matrix. We consider the following pulses for a time unit set to $t = 1$

- Unperturbed evolution with $\hat{H} = \mathbb{I}$:

$$\vec{n} = \begin{pmatrix} 1 \\ 0 \\ 0 \end{pmatrix}, \quad a = 0 \quad \Longrightarrow \quad \mathrm{e}^{-\mathrm{i}Ht} = \mathbb{I} = \begin{pmatrix} 1 & 0 \\ 0 & 1 \end{pmatrix}. \tag{5.8}$$

- $\frac{\pi}{2}$ pulse with $\hat{H} = \frac{\pi}{4}\sigma^x$:

$$\vec{n} = \begin{pmatrix} 1 \\ 0 \\ 0 \end{pmatrix}, \quad a = -\frac{\pi}{4} \quad \Longrightarrow \quad \mathrm{e}^{-\mathrm{i}Ht} = \mathbb{I}\cos(a) + \mathrm{i}\sigma^x \sin(a) = \frac{1}{\sqrt{2}} \begin{pmatrix} 1 & -\mathrm{i} \\ -\mathrm{i} & 1 \end{pmatrix}. \tag{5.9}$$

- π pulse with $\hat{H} = \frac{\pi}{2}\sigma^x$:

$$\vec{n} = \begin{pmatrix} 1 \\ 0 \\ 0 \end{pmatrix}, \quad a = -\frac{\pi}{2} \quad \Longrightarrow \quad \mathrm{e}^{-\mathrm{i}Ht} = \mathrm{i}\sigma^x \sin(a) = \begin{pmatrix} 0 & -\mathrm{i} \\ -\mathrm{i} & 0 \end{pmatrix}. \tag{5.10}$$

- $\frac{\pi}{2}$ y-pulse with $\hat{H} = \frac{\pi}{4}\sigma^y$:

$$\vec{n} = \begin{pmatrix} 0 \\ 1 \\ 0 \end{pmatrix}, \quad a = -\frac{\pi}{2} \quad \Longrightarrow \quad \mathrm{e}^{-\mathrm{i}Ht} = \mathbb{I}\cos(a) + \mathrm{i}\sigma^y \sin(a) = \frac{1}{\sqrt{2}} \begin{pmatrix} 1 & -1 \\ 1 & 1 \end{pmatrix}. \tag{5.11}$$

- π y-pulse with $\hat{H} = \frac{\pi}{2}\sigma^y$:

$$\vec{n} = \begin{pmatrix} 0 \\ 1 \\ 0 \end{pmatrix}, \quad a = -\frac{\pi}{2} \quad \Longrightarrow \quad \mathrm{e}^{-\mathrm{i}Ht} = \mathrm{i}\sigma^y \sin(a) = \begin{pmatrix} 0 & -1 \\ 1 & 0 \end{pmatrix}. \tag{5.12}$$

Multiplying the resulting matrices with the state vectors $|\psi\rangle$ allows you to find a pulse sequence leading from one state to another.

5.3 Problem set: Density matrix and partial trace

The third problem set introduces the density matrix to represent mixed states and the partial trace over subsystems.

5.3.1 Density matrices

The quantum state $|\psi\rangle$ is not the only way to represent a quantum system. In fact, density matrices are a more general description and are extremely useful for open systems. The partial trace yields a density matrix ρ as result, and therefore we introduce it beforehand to familiarize you with this approach. To calculate the density matrix ρ of a single qubit state $|\psi\rangle$, the outer product[1] is used as defined in the following:

$$|\psi\rangle = \begin{pmatrix} c_0 \\ c_1 \end{pmatrix} \qquad \Longrightarrow \qquad \rho = |\psi\rangle\langle\psi| = \begin{pmatrix} c_0 \\ c_1 \end{pmatrix} \otimes \begin{pmatrix} c_0^* & c_1^* \end{pmatrix} = \begin{pmatrix} c_0 c_0^* & c_0 c_1^* \\ c_1 c_0^* & c_1 c_1^* \end{pmatrix} . \tag{5.13}$$

Check that the trace of the density matrix fulfills normalization to 1, where the trace of a matrix is defined as sum over the diagonal entries. Here is an example for a 2×2 matrix:

$$\mathrm{Tr}\,[\rho] = \mathrm{Tr}\left[\begin{pmatrix} \rho_{11} & \rho_{12} \\ \rho_{21} & \rho_{22} \end{pmatrix} \right] = \rho_{11} + \rho_{22} \, . \tag{5.14}$$

Suggested path for analytical solution: Recall the normalization constraint for a quantum state defined in Section 5.1 to prove that the trace of a density matrix equals 1.

Suggested path for numerical solution: The *openMPS* package comes with a class for density matrices. To initialize an instance of the class from a state vector the following lines help:

```
import numpy as np

from MPSPyLib.EDLib import DensityMatrix

Rho = DensityMatrix(np.array([c0, c1]), 2, 1, None)
```

This class is actually designed for many body systems. Therefore, you pass next to the state vector, which contains c_0 and c_1, the local dimension of the state vector − which is 2

[1] Tensor product or Kronecker product are alternative names for the outer product.

for qubits − and the number of qubits, i.e. 1. Finally `None` specifies that we do not have symmetries in the system. The trace of `Rho` can be taken as

```
Rho.trace()
```

5.3.2 Partial trace for two qubits

We introduce in this exercise the partial trace over one qubit in a pair of qubits. Therefore, we have to describe the state $|\psi\rangle_{AB}$ expressing the quantum state of both qubits A and B:

$$|\psi\rangle_{AB} = c_{00} \underbrace{\begin{pmatrix}1\\0\\0\\0\end{pmatrix}}_{=|0\rangle_A|0\rangle_B} + c_{01} \underbrace{\begin{pmatrix}0\\1\\0\\0\end{pmatrix}}_{=|0\rangle_A|1\rangle_B} + c_{10} \underbrace{\begin{pmatrix}0\\0\\1\\0\end{pmatrix}}_{=|1\rangle_A|0\rangle_B} + c_{11} \underbrace{\begin{pmatrix}0\\0\\0\\1\end{pmatrix}}_{=|1\rangle_A|1\rangle_B} = \begin{pmatrix}c_{00}\\c_{01}\\c_{10}\\c_{11}\end{pmatrix} . \quad (5.15)$$

For simplification the state $|i\rangle_A\,|j\rangle_B$ can be written as $|i\rangle\,|j\rangle$ or $|ij\rangle$ when it is known that the left part refers to qubit A and the right part to qubit B. The bra-states have the same order $\langle i|_A\,\langle j|_B$. We continue in the following with the notation

$$|\psi\rangle_{AB} = c_{00}\,|0\rangle\,|0\rangle + c_{01}\,|0\rangle\,|1\rangle + c_{10}\,|1\rangle\,|0\rangle + c_{11}\,|1\rangle\,|1\rangle\,. \quad (5.16)$$

Assuming we are interested in the first qubit A, we trace out over the second qubit, that is summing over all the basis states of the second qubit. These basis states are referred to with the index j in the following. The partial trace acts on the density matrix $\rho_{AB} = |\psi\rangle_{AB}\langle\psi|_{AB}$, and we obtain the density matrix for the qubit A:

$$\begin{aligned}\rho_A &= \mathrm{Tr}_B\left[\rho_{AB}\right] = \sum_{j=0}^{1}\langle j|_B|\psi\rangle_{AB}\langle\psi|_{AB}|j\rangle_B \\ &= \sum_{j=0}^{1}\langle j|_B\left(c_{00}\,|0\rangle\,|0\rangle + c_{01}\,|0\rangle\,|1\rangle + c_{10}\,|1\rangle\,|0\rangle + c_{11}\,|1\rangle\,|1\rangle\right)\times \\ &\qquad \left(c_{00}^*\langle 0|\,\langle 0| + c_{01}^*\langle 0|\,\langle 1| + c_{10}^*\langle 1|\,\langle 0| + c_{11}^*\langle 1|\,\langle 1|\right)|j\rangle_B\,. \end{aligned} \quad (5.17)$$

The basis states of each qubit form an orthogonal basis, that means $\langle i|j\rangle = \delta_{ij}$, where δ_{ij} is the Kronecker delta defined as

$$\delta_{ij} = \begin{cases} 1 & \text{if } i = j \\ 0 & \text{if } i \neq j \, . \end{cases} \tag{5.18}$$

1. Use the orthogonality of the basis states to get an expression for ρ_A after taking the partial trace and check it with numerical methods. Choose two or more examples of your choice.

Suggested path for analytical solution: We write the sum in Eq. (5.17) explicitly and move the term $\langle j\,|_B$ to the corresponding next ket $|\rangle$ of the second qubit B to the right. This leads to

$$\begin{aligned} \rho_A &= (c_{00}\,|0\rangle\langle 0\,|_B|0\rangle + c_{01}\,|0\rangle\cancel{\langle 0|_B|1\rangle} + c_{10}\,|1\rangle\langle 0\,|_B|0\rangle + c_{11}\,|1\rangle\cancel{\langle 0|_B|1\rangle}) \times \\ &\quad (c_{00}^*\langle 0|\,\langle 0| + c_{01}^*\langle 0|\,\langle 1| + c_{10}^*\langle 1|\,\langle 0| + c_{11}^*\langle 1|\,\langle 1|)\,|0\rangle_B \\ &\quad + (c_{00}\,|0\rangle\cancel{\langle 1|_B|0\rangle} + c_{01}\,|0\rangle\langle 1\,|_B|1\rangle + c_{10}\,|1\rangle\cancel{\langle 1|_B|0\rangle} + c_{11}\,|1\rangle\langle 1\,|_B|1\rangle) \times \\ &\quad (c_{00}^*\langle 0|\,\langle 0| + c_{01}^*\langle 0|\,\langle 1| + c_{10}^*\langle 1|\,\langle 0| + c_{11}^*\langle 1|\,\langle 1|)\,|1\rangle_B \\ &= (c_{00}\,|0\rangle + c_{10}\,|1\rangle) \cdot (c_{00}^*\langle 0|\,\langle 0| + c_{01}^*\langle 0|\,\langle 1| + c_{10}^*\langle 1|\,\langle 0| + c_{11}^*\langle 1|\,\langle 1|)\,|0\rangle_B \\ &\quad + (c_{01}\,|0\rangle + c_{11}\,|1\rangle) \cdot (c_{00}^*\langle 0|\,\langle 0| + c_{01}^*\langle 0|\,\langle 1| + c_{10}^*\langle 1|\,\langle 0| + c_{11}^*\langle 1|\,\langle 1|)\,|1\rangle_B \end{aligned} \tag{5.19}$$

Make the corresponding step for $|\,j\rangle_B$, merging it with the next bra-vector $\langle\,|$ for the qubit B and apply the Kronecker deltas. What remains are scalars for the matrix entries $|\,i\rangle\langle\,j\,|$. The constants go to the following positions in the density matrix depending on values of the basis vectors $|\,i\rangle\langle\,j\,|$:

$$\rho \leftrightarrow \begin{pmatrix} |0\rangle\langle 0| & |0\rangle\langle 1| \\ |1\rangle\langle 0| & |1\rangle\langle 1| \end{pmatrix} \tag{5.20}$$

Suggested path for numerical solution: In the first part of this exercise, you have learned how to create a density matrix in *OpenMPS*. There is another class representing quantum states. You can create a two qubit state with an analogous syntax

```
import numpy as np
from MPSPyLib.EDLib import PureState
Psi = PureState(np.array([c00, c01, c10, c11]), 2, 2, None)
```

You get the reduced density matrix for qubit A and print it with the following calls:

```
rhoa = Psi.traceout([1])
print(rhoa.rho)
```

Notice that the function `traceout` takes a list of site indices to be traced out. The index in python starts at zero, therefore `[1]` is tracing out the second site. Moreover, it returns an instance of the class `DensityMatrix`, where the actual matrix is saved in the field `rho` of the class `DensityMatrix`.

5.4 Problem set: Bell state via Hadamard and CNOT gates

We generate a maximally entangled state on two qubits, i.e., a Bell state, in the following.

5.4.1 Entanglement of two qubits - Bell states via gates

We discussed before the encryption and secure data transfer. Entanglement is key for this, and many other, applications. While the superposition of states can be used on a single qubit, we need at least two qubits to explore entanglement. For secure data transfer with quantum encryption, Alice and Bob would have each one qubit of the entangled pair of qubits[2]. The state, called a Bell state, is defined as

$$|\psi\rangle_{AB} = \frac{|00\rangle + |11\rangle}{\sqrt{2}}, \tag{5.21}$$

where commonly there are three other Bell states listed:

$$|\psi\rangle_{AB} = \frac{|00\rangle - |11\rangle}{\sqrt{2}}, \qquad |\psi\rangle_{AB} = \frac{|01\rangle + |10\rangle}{\sqrt{2}}, \qquad |\psi\rangle_{AB} = \frac{|01\rangle - |10\rangle}{\sqrt{2}}. \tag{5.22}$$

We explore in the following how to create the Bell state in Eq. (5.21) and visualize the entanglement on the Bloch sphere. Assuming we are able to prepare an initial state $|\psi_0\rangle = |00\rangle$, we apply the Hadamard gate G_H to qubit A and then the CNOT gate G_{CN} on the qubits A and B:

[2]These kind of pairs are used in the EPR protocol, see Nielsen & Chuang [85] for a detailed description.

$$G_H = \frac{1}{\sqrt{2}}\begin{pmatrix}1 & 1\\ 1 & -1\end{pmatrix}, \qquad G_{\mathrm{CN}} = \begin{pmatrix}1 & 0 & 0 & 0\\ 0 & 1 & 0 & 0\\ 0 & 0 & 0 & 1\\ 0 & 0 & 1 & 0\end{pmatrix}. \tag{5.23}$$

1. Verify that the gates applied to the initial state, that is $G_{\mathrm{CN}} \cdot G_H(A) \cdot |\,00\rangle$, result in the Bell state $(|\,00\rangle + |\,11\rangle)/\sqrt{2}$. $G_H(A)$ implies that we apply the Hadamard gate to qubit A. Therefore, start with a sketch on paper of the initial state, i.e., the north pole of the Bloch sphere, and the final state.

2. Describe where the name *controlled not gate* comes from looking at the action of the gate.

3. Which initial state $|\,\psi_0\rangle$ would you choose to arrive at the Bell state

$$|\,\psi\rangle_{AB} = \frac{|\,01\rangle + |\,10\rangle}{\sqrt{2}}\ ? \tag{5.24}$$

   Or which additional pulse could you apply to $|\,\psi_0\rangle = |\,00\rangle$ at the beginning of the pulse sequence in order to prepare your initial state for this Bell state in Eq. (5.24)?

Suggested path for solution: The answer to the solution is a matrix-matrix multiplication and small enough for pen and paper. You should first define the single qubit Hadamard gate on a Hilbert space for two qubits. This is done via the tensor product. If the Hadamard gate is acting on the first qubit A, we wrote the gate on the complete system as $G_H(A)$. In contrast, the action of the Hadamard gate on qubit B is $G_H(B)$. To construct a gate modifying the complete system while acting only on a single qubit, we use the tensor product and identities, i.e.,

$$G_H(A) = G_H \otimes \mathbb{I}, \qquad \mathbb{I} = \begin{pmatrix}1 & 0\\ 0 & 1\end{pmatrix}, \tag{5.25}$$

where the identity after the tensor product indicates that there is no action on qubit B. The tensor product in case of two 2×2 matrices is defined as follows:

$$
\begin{aligned}
A \otimes B &= \begin{pmatrix} A_{11} & A_{12} \\ A_{21} & A_{22} \end{pmatrix} \otimes \begin{pmatrix} B_{11} & B_{12} \\ B_{21} & B_{22} \end{pmatrix} = \begin{pmatrix} A_{11}B & A_{12}B \\ A_{21}B & A_{22}B \end{pmatrix} \\
&= \begin{pmatrix} A_{11}B_{11} & A_{11}B_{12} & A_{12}B_{11} & A_{12}B_{12} \\ A_{11}B_{21} & A_{11}B_{22} & A_{12}B_{21} & A_{12}B_{22} \\ A_{21}B_{11} & A_{21}B_{12} & A_{22}B_{11} & A_{22}B_{12} \\ A_{21}B_{21} & A_{21}B_{22} & A_{22}B_{21} & A_{22}B_{22} \end{pmatrix}
\end{aligned} \tag{5.26}
$$

Double check your solution with python, utilizing `import numpy as np` and using numpy's matrix multiplication `np.dot(Gate, StateVector)` to multiply the matrix for the gate with the state vector. The tensor product of two matrices is defined over `np.kron(A, B)` .

5.4.2 Bell state - Hamiltonian for Hadamard

In order to create a Bell state via a simulation of the Schrödinger equation, we have to find the Hamiltonian for the gates that we applied in the previous part of the exercise. And we only have to find the gate up to a phase ϕ, that means we can always exclude a complex number of norm 1, i.e. for the Hadamard gate:

$$
\tilde{G}_H = \mathrm{e}^{\mathrm{i}\phi} G_H \,. \tag{5.27}
$$

The reason for this is that we consider for measurement always the state vector $|\psi\rangle$ and its complex conjugated $\langle\psi|$. For the Hadamard gate $G_H^\dagger = G_H$ holds.[3] If $|\psi'\rangle$ is the state vector after the application of the gate $\tilde{G}_H$ and we use some arbitrary measurement operator $\hat{O}$, we summarize:

$$
\langle\psi'|\,\hat{O}\,|\psi'\rangle = \langle\psi|\,\tilde{G}_H^\dagger \hat{O} \tilde{G}_H\,|\psi\rangle = \langle\psi|\,\mathrm{e}^{-\mathrm{i}\phi} G_H^\dagger \hat{O} \mathrm{e}^{\mathrm{i}\phi} G_H\,|\psi\rangle = \langle\psi|\,G_H^\dagger \hat{O} \underbrace{\mathrm{e}^{-\mathrm{i}\phi}\mathrm{e}^{\mathrm{i}\phi}}_{=1} G_H\,|\psi\rangle \tag{5.28}
$$

1. Find the Hamiltonian for the Hadamard gate up to a phase ϕ, e.g. you can find a Hamiltonian for $\phi = \pi/4$.

[3] The symbol † is the complex conjugate transposed of a matrix; If used on a scalar, it reduces to the complex conjugate.

2. Suggest any other pulse you could use to arrive at the same outcome as the Hadamard gate, knowing that your initial state is $|0\rangle$. To do so, first sketch the initial state $|0\rangle$ and the final state after the application of the Hadamard gate on the Bloch sphere.

Suggested path for analytical solution: Recall the general solution for the matrix exponential in terms of Pauli operators

$$e^{ia\vec{n}\cdot\vec{\sigma}} = \mathbb{I}\cos(a) + i\vec{n}\cdot\vec{\sigma}\sin(a)\,, \tag{5.29}$$

which helps you to build a solution.

Suggested path for numerical solution: There is no distinguished path to obtain a numerical solution for this. You can at least check your solution with python:

```
import numpy as np
import scipy.linalg as sla
H = np.array([[c00, c01], [c10, c11]])#Defines your Hamiltonian
U = sla.expm(-1j * H)#U is the propagator, and in this case gate
```

Note that functions such as numpy's `np.exp` take the element-wise exponential, but not the matrix exponential.

5.4.3 Bell state - Completing the pulse series

The Hamiltonian for the CNOT gate acts on two gates and is therefore more complicated to derive. It can be written as

$$H_{\mathrm{CN}} = \frac{\pi}{2}\begin{pmatrix} 0 & 0 & 0 & 0 \\ 0 & 0 & 0 & 0 \\ 0 & 0 & -1 & 1 \\ 0 & 0 & 1 & -1 \end{pmatrix}, \tag{5.30}$$

and completes the required terms for creating a Bell state with a pair of qubits.

1. Show that the Hamiltonian for the CNOT gate, H_{CN} actually leads to the CNOT gate. The time period considered is the $t = 1$.

2. Make a sketch on paper of the first qubit in the Bell state and after the application of each gate. Check your intuition while visualizing the same states − and possibly its evolution over time − during the application of the two gates via the Bloch sphere.

3. If you (visually) track the evolution of its length of the vector on the Bloch sphere over time, can you try to describe how the length is linked to entanglement. Note that a Bell state is a maximally entangled state.

Suggested path for analytical solution: The exponential of the Hamiltonian can be taken analytical using the block diagonal structure of H_{CN}. Instead of taking the exponential of a 4×4 matrix, we can solve the following two 2×2 matrices on the diagonal:

$$\begin{pmatrix} 0 & 0 \\ 0 & 0 \end{pmatrix}, \qquad \begin{pmatrix} -1 & 1 \\ 1 & -1 \end{pmatrix}. \tag{5.31}$$

In order to visualize the first qubit on the Bloch sphere, you might use the partial trace and then carry out the measurements[4]. For different point in times, you would need to solve the matrix exponential for different times or retain its general dependence on t, which is optional for the analytic path. Measurements of a single qubit density matrix, e.g. for σ^x, are defined via the trace

$$\mathrm{Tr}\left[\sigma^x \rho_A\right]. \tag{5.32}$$

Suggested path for numerical solution: Matrix exponentials of this size can be easily checked with python, in detail with its linear algebra package. Assume you define the Hamiltonian as `H`, the following packages and commands help you to calculate any matrix exponentials:

```
import numpy as np #to define the Hamiltonian

import scipy.linalg as sla

H = ...

U = sla.expm(-1j * H)#U is the propagator, and in this case gate
```

[4]The other option is to use the full state and define the local observable as well on the full space. In order to practice the use of the partial trace, we do not pursue this path.

The Qubit module embedded in *openMPS* helps you to visualize the first qubit on the Bloch sphere during the whole time evolution. You have learned in the previous exercises how to define a two qubit state, see Section 5.3.2, and how to visualize a time evolution on the Bloch sphere, see Section 5.2. By default, always the first qubit is plotted. To solve the Bell state problem, we introduce another two pulses named after the corresponding gates:

- `add_hadamard` for the Hadamard gate. By default, the pulse is applied to all sites. You can specify the site, e.g. `sites=[0]` for the first site.
- `add_cnot` for a controlled not gate. The gate is applied to the first two sites by default.

5.5 Problem set: the interplay of entropy and entanglement

The following two problem consider a pure state and how the entropy of a subsystem is connected to the entanglement of the subsystem and other parts of the complete state.

5.5.1 Entanglement in terms of entropy from density matrix

We are already able to detect entanglement of a pure state via the plot of a single qubit on the Bloch sphere. We exploit now a second method, the von Neumann entropy. It is defined as follows:

$$S = -\sum_{i=1} \Lambda_i \log(\Lambda_i) \; . \tag{5.33}$$

Λ_i are in general probabilities which are normalized to 1. We consider the case of two qubits and are interested in the entanglement between the first and the second qubit. In *Exercise 3.2* we introduced the partial trace. If we trace out over the second site, we get the density matrix ρ_1. The eigenvalues of this density matrix can be analyzed with the von Neumann entropy from Eq. (5.33).

1. Calculate the von Neumann entropy S for one selected Bell state. Calculate it for ρ_1 and ρ_2 tracing out over site 2 or respectively 1.

2. Calculate the von Neumann entropy for product states of the form

$$|\psi_{1,2}\rangle \;=\; |\psi_1\rangle \otimes |\psi_2\rangle = \begin{pmatrix} c_0 \\ c_1 \end{pmatrix} \otimes \begin{pmatrix} c_0' \\ c_1' \end{pmatrix} = \begin{pmatrix} c_0 c_0' \\ c_0 c_1' \\ c_1 c_0' \\ c_1 c_1' \end{pmatrix} . \tag{5.34}$$

   Again, compare the von Neumann entropy for the first site $S(\rho_1)$ with $S(\rho_2)$.

3. Generate random quantum states for two qubits and calculate the von Neumann entropy for both reduced density matrices ρ_1 and ρ_2.

4. What is your conclusion with regards to the entropies of the two density matrices ρ_1 and ρ_2? What does the von Neumann entropy of two qubits tell you about the entanglement?

Suggested path for analytical solution: (1) Take one Bell state as an example to trace out and calculate the eigendecomposition by hand to check your numerical result. (2) You can either do at least two examples or prove a general equation for arbitrary coefficients c_0, c_1, c_0', and c_1'. There is no analytical path for questions (3) and (4).

Suggested path for numerical solution: First, you need to create the quantum state and get the reduced density matrix. We recall that this can be done with

```
import numpy as np
import numpy.linalg as la
from MPSPyLib.EDLib import PureState
Psi = PureState(np.array([c00, c01, c10, c11], 2, 2, None))
rhoii = Psi.traceout([ii])
```

The eigenvalue decomposition is implemented in the linear algebra package of numpy:

```
vals, vecs = la.eigh(rhoii.rho)
```

It remains to calculate the von Neumann entropy in python.

5.5.2 Entanglement in terms of Schmidt decomposition

The results of the previous section indicate that there is a connection between the von Neumann entropy of the first and second qubit. We discover now this connection: the Schmidt decomposition. The Schmidt decomposition calculates the entanglement between a bipartition of two subsystems which is in our case the first and second qubit. In order to understand the Schmidt decomposition, we briefly review the singular value decomposition (SVD) of a matrix A into

$$A = U\lambda V^\dagger\,, \tag{5.35}$$

where U and V are unitary matrices and λ is a diagonal matrix containing the singular values λ_i. The orthogonal vectors of U and V are contained in the columns of U and V, respectively. Numerical libaries such as numpy return $V^\dagger$ and not V; thus, the orthogonal vectors are stored along the rows of the matrix returned by numpy. The maximal number of non-zero singular values is the minimum of the number of rows and columns. In order to use the singular value decomposition on a quantum state, we have to point out a way to construct the matrix A. We take the index notation from the state in Eq. (5.34) and reshape the four entries into a 2×2 matrix. The indices of the first qubit increase over the rows of the matrix and the indices of the second qubit increase over the columns:

$$|\,\psi_{1,2}\rangle = \begin{pmatrix} c_0c_0' \\ c_0c_1' \\ c_1c_0' \\ c_1c_1' \end{pmatrix} \;\rightarrow\; \begin{pmatrix} c_0c_0' & c_0c_1' \\ c_1c_0' & c_1c_1' \end{pmatrix}\,. \tag{5.36}$$

This can be generalized to more qubits, e.g. for three qubits the rows of the matrix may iterate over the first two qubits, while the columns iterate over the third qubit resulting in a 4×2 matrix. The actual representation of the Schmidt decomposition for our two qubits is then

$$|\psi_{1,2}\rangle = \sum_{i=1}^{2} \lambda_i \, |\phi_1^{[i]}\rangle \, |\phi_2^{[i]}\rangle \, . \tag{5.37}$$

The i$^{\text{th}}$ column of the matrix U contains $|\phi_1^{[i]}\rangle$ and the i$^{\text{th}}$ row of V represents $|\phi_2^{[i]}\rangle$. If we normalize the singular values λ_i, we can use them in the von Neumann entropy from Eq. (5.33).

1. Derive analytically the connection between the singular values λ_i and the eigenvalues of the reduced density matrix Λ_i using the partial trace.

2. Calculate the SVD for one Bell state, one product state, and one random state from Section 5.5.1. Use the relation between singular values and eigenvalues to determine the von Neumann entropy. (If you don't have the relation from (1) yet, you can normalize the singular values to 1 instead.)

3. The number of non-zero singular values is another entanglement measure, the Schmidt number. What does the Schmidt number tell you about the entanglement of two qubits? Would you prefer it over the von Neumann entropy if you wanted to have a statement about the entanglement of two qubits?

Suggested path for analytical solution of (1.): Start with the pure state in the Schmidt decomposition in Eq. (5.37) and use this representation to build the density matrix according to $\rho = |\psi\rangle\langle\psi|$. Use the partial trace over site 1 to obtain the reduced density matrix for site 2, and then trace out site 2 to obtain the reduced density matrix for site 1. This partial trace was solved basically in Section 5.3.2 excepting the summation over the singular values i. In the last step recall the unitary property of the SVD.

Once you have clarified the connection between singular values and eigenvalues, you can use the result to obtain the Schmidt number and the von Neumann entropy from you calculations in Section 5.5.1.

Suggested path for numerical solution (2.): First you define your state vector for the two qubits as a numpy array:

```
psi = np.array([c00, c01, c10, c11])
```

In the next step you reshape it to a matrix.

```
Apsi = np.reshape(psi, [2, 2])
```

The second argument is the new dimensions of the array. You could have written the matrix directly, but reshaping can be generalized easily when dealing with more qubits. The SVD is defined in the linear algebra package

```
U, lamb, V = la.svd(Apsi)
```

From here you can calculate the von Neumann entropy with the singular values in `lamb`. (note: `lambda` is a keyword in python reserved for the definition of lambda functions, thus we use `lamb` instead.)

5.6 Problem set: spontaneous emission of a two level system

We introduce in this exercise the Lindblad master equation, which can be applied to a quantum system coupled to a very large reservoir under certain conditions, such as the Born-Markov approximation and the secular approximation. Both of the are beyond this problem set.[5] The system we consider is a single two-level system, initially in the excited state $|e\rangle$. It has no Hamiltonian, i.e. $H = 0$, and therefore we can see that it would stay in the excited state and not evolve to the ground state $|g\rangle$:

$$\mathrm{i}\hbar\frac{\partial}{\partial t}|\psi\rangle = H|\psi\rangle = 0|\psi\rangle = 0 \tag{5.38}$$

While this equation is true for the closed system, we couple the two-level system now to a large vacuum. The excited state can decay to the ground state emitting a photon. It is unlikely that the same photon would ever excite the system again. Therefore, we model the system S plus the vacuum $|V\rangle = |0\rangle$ with a single process creating an excitation in the

[5]The derivation of Chapter 7 contains these derivations.

vacuum when the transition from the excited to the ground state happens:

$$a_S a_V^\dagger \,|e\rangle_S \,|0\rangle_V = |g\rangle_S \,|1\rangle_V \,. \tag{5.39}$$

a is the operator annihilating an excitation, and $a^\dagger$ is creating an excitation. The subscripts for the operators refer to the system (S) and the vacuum (V). Our system is a two level system; thus, the two operations are $a_S \,|e\rangle_S = |g\rangle_S$ and $a_S^\dagger \,|g\rangle_S = |e\rangle_S$. We could act with multiple creation operators on the vacuum state, i.e., $\left(a_V^\dagger\right)^n \,|0\rangle_V = |n\rangle_V$, but recall we only have one excitation in our system. Moreover, one of the assumptions during the Lindblad equation is that the environment stays in its state as the perturbation due to the system is small. The system always sees the vacuum; in other words, the vacuum has no memory if it already absorbed an excitation. This assumption is in contradiction to Eq. (5.39), but a good approximation made for the Lindblad equation for a large reservoir. The Lindblad master equation models for this example is the following equation where we plug in $H = 0$ in the second step.

$$\frac{\partial}{\partial t}\rho \;=\; \frac{-\mathrm{i}}{\hbar}\left[H, \rho\right] + \gamma a \rho a^\dagger - \frac{\gamma}{2}\left\{a^\dagger a, \rho\right\} = \gamma a \rho a^\dagger - \frac{\gamma}{2}\left\{a^\dagger a, \rho\right\} \,. \tag{5.40}$$

This equation only considers the density matrix of the qubit, and all operators a and $a^\dagger$ act now on the system S without using the subscript. γ is the coupling between the system and the vacuum.

Derive the analytical expression for the evolution of the density matrix assuming that the two level system is in the excited state at time $t = 0$.

Suggested path for analytical solution: Start with a general density matrix with scalars a, b, c and d of form

$$\rho = \begin{pmatrix} a & b \\ c & d \end{pmatrix} \,. \tag{5.41}$$

Then calculate all the matrix multiplications on the right hand side of Eq. (5.40) leading to a form similar to

$$\frac{\partial \rho}{\partial t} = \gamma \begin{pmatrix} a' & b' \\ c' & d' \end{pmatrix}, \tag{5.42}$$

where a', b', c', and d' depend on a, b, c, d and γ. This expression can be rewritten as a system of differential equations and be solved.

Suggested path for numerical solution: Following the suggested path for the numerical solution will introduce you to some of the syntax within OSMPS. We start by importing the necessary libraries

Source Code 5.1: Import external modules.

```
5.1 import MPSPyLib as mps
5.2 import MPSPyLib.EDLib as ed
5.3 import sys
5.4 import numpy as np
5.5 import matplotlib.pyplot as plt
```

Then we let OSMPS generate a default set of operators. We decide to use the spin operators in this example:

Source Code 5.2: Operators.

```
5.20     Ops = mps.BuildSpinOperators(0.5)
```

With these operators we can build the Lindblad equation from Eq. (5.40).

Source Code 5.3: System definition.

```
5.23     Liou = mps.MPO(Ops)
5.24     Liou.AddMPOTerm('lind1', 'sminus', hparam='gamma')
```

We specify the kind of term we add to our system. `lind1` is a local Lindblad operator. The second argument is the string label of the actual Lindblad operator, where

$$\text{sminus} = \begin{pmatrix} 0 & 0 \\ 1 & 0 \end{pmatrix} . \tag{5.43}$$

This operator σ^- is a pre-defined operator from OSMPS and represents our annihilation operator a. Finally, `'gamma'` is the coupling between the two level system and the vacuum where we define the actual strength later. Next we define the measurements and the corresponding operators, because they are not within the default operators in `Ops`. Defining new operators works like a dictionary

Source Code 5.4: Additional operators.

```
5.27    Ops['ne'] = np.array([[1., 0], [0, 0]])
5.28    Ops['ng'] = ... # Fill
```

`ne` measures the population in the excited state and `ng` should be defined such that it measures the population in the ground state. The measurements are a class themselves, which is created as follows. We immediately add the measurements of the populations

Source Code 5.5: Measurements.

```
5.30    Obs = mps.Observables(Ops)
5.31    Obs.AddObservable('site', 'ne', '<ne>')
5.32    Obs.AddObservable(...) # Fill in population of the
          ground state
```

The arguments are the type of the observable (`'site'` for measuring on a single site), the name of the observable (`'ne'`), and an identifier to address the result in the post processing. In addition we need a description of how the coupling of our system changes over time. Since it does not change, we define it with empty lists `[]`:

Source Code 5.6: Time evolution.

```
5.35    Quench = mps.QuenchList(Liou)
5.36    T = ... # Fill
5.37    ndt = ... # Fill
5.38    dt = float(T) / ndt
5.39    Quench.AddQuench([], T, dt, [])
```

The variables `T` and `ndt` have to be set with the total evolution time and the number of time steps. Together they define the time step `dt`. We now define a list of simulation. We start with one simulation, so the list contains one dictionary:

Source Code 5.7: Simulation dictionary.

```
5.41    params = [{
5.42        'simtype' : 'Finite',
5.43        'job_ID' : 'TwoLevel_SpontaneousEmission',
5.44        'Write_Directory' : 'TMP/',
5.45        'Output_Directory' : 'OUTPUTS/',
5.46        # System size and Hamiltonian parameters
5.47        'L' : 1,
5.48        'gamma' : 0.05,
5.49        # Setting time evolution and observables
5.50        'Quenches' : Quench,
5.51        'DynamicsObservables' : Obs,
5.52        # Setting that there is an initial state
5.53        'MPS' : False,
5.54        'timeevo_mps_initial' : 'TMP/excited.mps'
```

Source Code 5.7 Continued

```
5.55        }]
```

We highlight some entries in the dictionary besides the filenames and other settings which can be neglected at this point. We set the system size `'L'` to one site. Moreover, we can now pass along the coupling between our two level system and the vacuum with `'gamma'` which has to be set with a value. The setup for the quenches and observables defined previously are now used in the dictionary. The initial state specified at the end has to be written out in the following.

We always call the function `WriteFiles`, and in case we are actually running the simulation we define the initial state and call the exact diagonalization module.

Source Code 5.8: Runing simulation.

```
5.58    main_files = mps.WriteFiles(params, Ops, Liou,
            PostProcess=PostProcess)
5.59    if(not PostProcess):
5.60        psi = np.array([1., 0])
5.61        np.save('TMP/excited.mps.npy', psi)
5.62        ed.runED(params, Ops, Liou)
```

In order to read the data, we call the corresponding function and create an empty numpy array.

Source Code 5.9: Reading data.

```
5.67    DynOutputs = mps.ReadDynamicObservables(params)
5.68    neg = np.zeros((ndt, 2))
```

The outputs are stored in a list, where each entry corresponds to the simulation defined in `params`. We address element `0` for the first (and only) simulation. This object is again a

list, where each entry corresponds to a measurement during the time evolution. We write the population for the excited state in the first column, and the populations of the ground state to the second column:

Source Code 5.10: Reading populations.

```
5.70    for ii in range(ndt):
5.71        neg[ii, 0] = DynOutputs[0][ii]['<ne>']
5.72        neg[ii, 1] = ... # Fill
```

We leave the actual plotting to you. There is no need to copy or retype the code snippets. The corresponding file with those lines of code is available along with the exercises.

5.7 Problem set: The Liouville space applied to a two level system

In this problem set, we introduce the Liouville space, which is a common technique to simulate the Lindblad master equation numerically.

5.7.1 The Liouville space

We recall the general formulation of the Lindblad master equation

$$\frac{\partial}{\partial t}\rho \;=\; \frac{-\mathrm{i}}{\hbar}\left[H,\rho\right] + \sum_{\mu=1}^{N} \gamma_\mu L_\mu \rho L_\mu^\dagger - \frac{\gamma_\mu}{2}\left\{L_\mu^\dagger L_\mu, \rho\right\}\,, \tag{5.44}$$

which is in not very practical to solve numerically. Actually, we would prefer an equation of the type

$$\frac{\partial}{\partial t}\rho \;=\; A\rho\,. \tag{5.45}$$

This looks similar to the Schrödinger equation and could be solved for small time steps taking the matrix exponential of the matrix A. Such a representation exists and can be constructed in the Liouville space. The transformation is

$$A\rho B = A \otimes B^T \left|\rho\right\rangle\!\rangle \,, \tag{5.46}$$

where the tensor product $\otimes$ was introduced in the suggestions for *Exercise 4.1.* The superscript T indicates that the corresponding matrix is transposed. $|\rho\rangle\!\rangle$ is the density matrix ρ rewritten as a vector as follows in the example of a 2×2 matrix

$$\rho = \begin{pmatrix} c_{0,0} & c_{0,1} \\ c_{1,0} & c_{1,1} \end{pmatrix} \qquad \Longrightarrow \qquad \left|\rho\right\rangle\!\rangle = \begin{pmatrix} c_{0,0} \\ c_{0,1} \\ c_{1,0} \\ c_{1,1} \end{pmatrix} . \tag{5.47}$$

It can be described reading the elements row-by-row and putting the corresponding entries into the vector $|\rho\rangle\!\rangle \in \mathbb{C}^{D^2}$ if $\rho \in \mathbb{C}^{D\times D}$. The corresponding operator has therefore the dimension $A \otimes B^T \in \mathbb{C}^{D^2\times D^2}$ where each operator holds $A, B \in \mathbb{C}^{D\times D}$.

Prove analytically that the transformation is correct, yielding the same result for each entry of ρ in both definitions.

Suggested path for analytical solution: It is useful to rewrite the matrix multiplication in a summation over an index starting with the left hand side expression of Eq. (5.46). For a matrix-matrix multiplication that is for a single entry i, j in the final matrix

$$[A \times B]_{ij} = \sum_k A_{ik} B_{kj} \,. \tag{5.48}$$

The following transformation holds to obtain a tensor product of matrices:

$$A_{ij} B_{kl} = (A \otimes B)_{(ik),(kl)} \,, \tag{5.49}$$

where (i, k) can be considered as new index of two combined indices.

5.7.2 Your own two-level system with spontaneous emission

Apply the transformation to the two-level system with spontaneous emission from Section 5.6 and simulate the system numerically with your own code. Plot the population of the

excited and/or ground state. Evaluate if your implementation is correct with the analytic expression you have obtained in Section 5.6.

Suggested path for numerical solution: Consider the three different terms in Eq. (5.40)

$$\mathcal{L}_1 \quad \text{is Liouville transformation of} \quad \gamma a \rho a^\dagger \,, \tag{5.50}$$

$$\mathcal{L}_2 \quad \text{is Liouville transformation of} \quad -\frac{\gamma}{2} a^\dagger a \rho \,, \tag{5.51}$$

$$\mathcal{L}_3 \quad \text{is Liouville transformation of} \quad -\frac{\gamma}{2} \rho a^\dagger a \,, \tag{5.52}$$

$$\mathcal{L} \;=\; \mathcal{L}_1 + \mathcal{L}_2 + \mathcal{L}_3 \tag{5.53}$$

and calculate the Liouville transformation for $\mathcal{L}_1$, $\mathcal{L}_2$, and $\mathcal{L}_3$ according to Eq. (5.46). You can bring the second and the third term in the form of Eq. (5.46) by introducing an identity matrix on the left or right side. Further you choose an initial state for your system and write down the corresponding density matrix as ρ and $|\rho\rangle\rangle$. Choose a time step dt and you can propagate your density matrix represented as $|\rho\rangle\rangle$ with

$$|\rho(t+dt)\rangle\rangle = \mathrm{e}^{\mathcal{L}dt} \, |\rho(t)\rangle\rangle \,. \tag{5.54}$$

Recall that numpy has the corresponding function `numpy.linalg.expm` to calculate the exponential of a matrix.

5.8 Problem set: Simulating Rabi oscillations in an open quantum system

We combine the Rabi oscillations with the Lindblad equation to study two examples of coherence measures.

5.8.1 Rabi Hamiltonian, rotating wave approximation, and interaction picture

This exercise introduces the Rabi problem, which is fundamental to any driven two level system. The two levels are separated by an energy gap $\omega = \omega_e - \omega_g$, the Rabi frequency. We can drive the transition between the two levels with a frequency ν and an amplitude Ω_R, e.g., with a laser at this frequency, which leads us to the detuning defined as $\Delta = \omega - \nu$. The

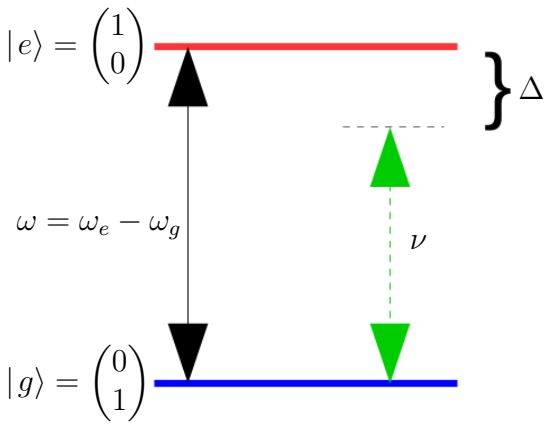

Figure 5.3: *Scheme for Energy Levels in the Rabi Problem.* The energy difference between the two states is defined as ω. The detuning Δ is the difference between the laser frequency ν and ω.

Rabi oscillation is a fundamental phenomena occuring while driving an atomic or molecular system between two energy levels with a laser. Figure 5.3 sketches the energy structure. The Hamiltonian describing the system after the rotating wave approximation is

$$H_R(\Omega_R, \Delta) \;=\; \begin{pmatrix} \frac{\Delta}{2} & \frac{\Omega_R}{2} \\ \frac{\Omega_R}{2} & -\frac{\Delta}{2} \end{pmatrix} . \tag{5.55}$$

This system is the focus of interest. If we drive the system on resonance ($\Delta = 0$), you observe the Rabi oscillation of a period $2\pi\Omega_R$ as shown in Figure 5.4. Derive analytically the Hamiltonian H_R, which is in the interaction picture. The Hamiltonian of the two level system and the driving in the Schrödinger picture are defined as

$$H \;=\; \begin{pmatrix} \omega_e & 0 \\ 0 & \omega_g \end{pmatrix} + \Omega_R \cos(\nu t)\sigma^x \, . \tag{5.56}$$

Here, σ^x is the Pauli operator coupling the ground state and excited state of the system. The time is denoted with t.

Suggested path for analytical solution: Derive first the Hamiltonian in the interaction picture by separating the Hamiltonian in the Schrödinger picture into the two parts H_0 and H_1. Recall that the transformation into the interaction picture is defined as

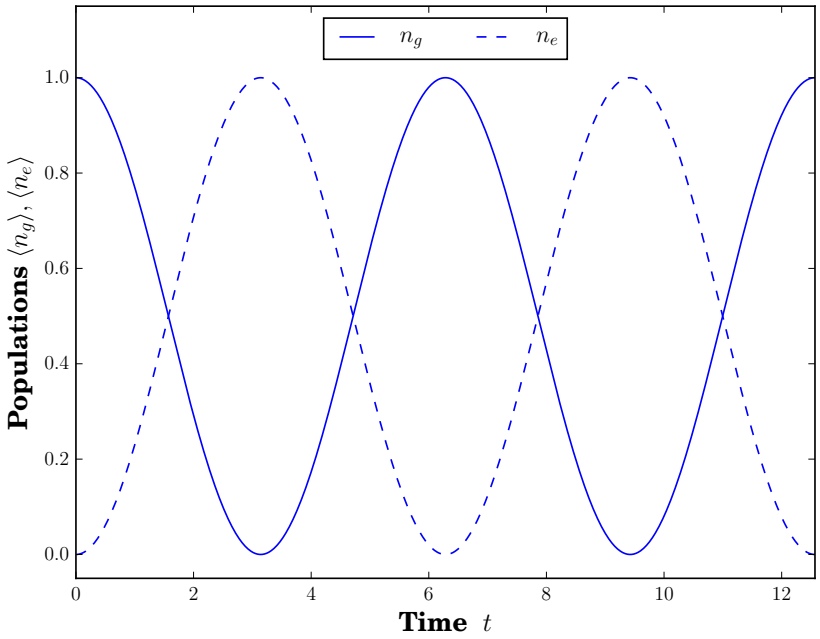

Figure 5.4: *Rabi Oscillations without Detuning.*

$$H^{[I]} = \mathrm{e}^{\mathrm{i}H_0 t} H_1 \mathrm{e}^{-\mathrm{i}H_0 t} \,. \tag{5.57}$$

Once you have the expression in the interaction picture, you can use the rotating wave approximation. This approximation discards all high frequencies. You can assume $\omega - \nu \ll \omega + \nu$. In the third step you assume that your state in the interaction picture can be written as

$$|\psi(t)\rangle = \begin{pmatrix} \mathrm{e}^{\mathrm{i}\frac{\Delta}{2}t} c_a(t) \\ \mathrm{e}^{-\mathrm{i}\frac{\Delta}{2}t} c_b(t) \end{pmatrix} \,, \tag{5.58}$$

This transformation leads to an equation for c_a and c_b with the Hamiltonian in Eq. (5.55).

5.8.2 Coherence in the closed system Rabi problem

We start with simulations for the closed system for one qubit and advance to two qubits in an open system with the Lindblad master equation. We expect that the coupling of our Rabi system, that is our qubit, to the environment will lead to decoherence. Therefore, we use the

closed single qubit problem to familiarize you with coherence or decoherence measures. We suggest two coherence measures, one being the l_1 norm of coherence as introduced in [163][6]:

$$C_{l_1}(\rho) \;=\; \sum_i \sum_{j \neq i} |\rho_{i,j}| \,, \tag{5.59}$$

where ρ is the density matrix of the system. The second coherence measure is defined in the same work as relative entropy of coherence

$$S_C(\rho) = S(\rho_{\text{diag}}) - S(\rho) \,, \tag{5.60}$$

and $S(\,\cdot\,)$ is the entropy as previously defined (see Eq. (5.33)). The matrix ρ_{diag} is the original density matrix ρ with all off-diagonal elements set to zero. The maximally coherent state is defined in this context for the qubit as

$$|\,\phi\rangle = \frac{1}{\sqrt{2}} \begin{pmatrix} 1 \\ 1 \end{pmatrix} \;. \tag{5.61}$$

1. Calculate the coherence (analytically) for the maximally coherent state $|\,\phi\rangle$ and the ground state $|\,\psi\rangle = |\,g\rangle$ for both measures. Are there more maximally coherent states and can you generalize Eq. (5.61)?

2. Set up numerical simulations with the initial state $|\,\psi(t=0)\rangle = |\,g\rangle$ for the closed system Rabi problem and measure population in the ground state and the excited state as well as the coherence measures C_{l_1} and $S_C(\rho)$. How do positive and negative detunings Δ change the frequency of the Rabi oscillations with regards to zero detuning $\Delta = 0$?

3. Now choose the maximally coherent state as an initial state for the simulation. What do you observe for different detunings? What do you observe for the coherence measures? Which initial state and parameters for the Hamiltonian would you choose for an open

[6]Both measures have in common that they allow one to treat coherence as resource. Separating actions on the system into coherent and incoherent operations, these two measures guarantee monoticity under incoherent operations. We do not derive which kind of operations we have for our Rabi system.

system to study coherence independent of effects from the Hamiltonian of the closed system?

Suggested path for analytical solution: (1) (No hints).

Suggested path for numerical solution: (2), (3) You already have a basic script for the simulation of a two level system. We extend this script for the purpose of the adapting it to the Rabi problem. Write down your Hamiltonian in terms of the spin operators.[7] The spin matrix S^z is pre-built and you should verify it with

```
import MPSPyLib as mps
Ops = mps.BuildSpinOperators(0.5)
print(Ops['sz'])
```

Moreover, the spin raising operator S^+ (`Ops['splus']`) and the spin lowering operator S^- (`Ops['sminus']`) are pre-built. With these two operators you can build S^x:

```
Ops['sx'] = ...
```

We have used the local Lindblad operator before, see Section 5.6, and the implementation of the operator `'sminus'` defined in Eq. (5.43). Now you need another term, a local operator for the Hamiltonian. You can add such a term as follows:

```
Ham = mps.MPO(Ops)
Ham.AddMPOTerm('site', 'name_of_operator', hparam='key_for_coupling')
```

You certainly want to loop over different parameters. So instead of creating a list for `params` with exactly one element as in the *TwoLevel_SpontaneousEmission.py*, you might prefer to create an empty list and add the actual entries in a loop. If we take the example from the purely dissipative two level system and would like to simulate different decay rates, we would use:

Source Code 5.11: Looping over decay parameters.

```
5.1     params = []
```

[7] The spin operator $S^\alpha = \frac{1}{2}\sigma^\alpha$, where σ^α are the Pauli matrices we used before.

Source Code 5.11 Continued

```
5.2
5.3     for jj in range(3):
5.4         params.append({
5.5         'simtype' : 'Finite',
5.6         'job_ID' : 'TwoLevel_SpontaneousEmission',
5.7         'Write_Directory' : 'TMP/',
5.8         'Output_Directory' : 'OUTPUTS/',
5.9         # System size and Hamiltonian parameters
5.10        'L' : 1,
5.11        'gamma' : 0.05 * (jj + 1),
5.12        # Setting time evolution and observables
5.13        'Quenches' : Quench,
5.14        'DynamicsObservables' : Obs,
5.15        # Setting that there is an initial state
5.16        'MPS' : False,
5.17        'timeevo_mps_initial' : 'TMP/excited.mps'
5.18        })
```

If we would like to print the population for the excited state, we have now an additional loop over the different simulations:

Source Code 5.12: Reading all decay parameters.

```
5.21    for jj in range(3):
5.22        print('Coupling gamma=' + str(0.05 * (jj + 1)))
5.23        for ii in range(ndt):
5.24            ne = DynOutputs[jj][ii]['<ne>']
5.25            print('Time step', ii, 'Population excited
                    state', ne)
```

Source Code 5.12 Continued

You can define the single site density matrix as observable adding it two you observable class

```
Obs.AddObservable('DensityMatrix_i', [])
```

You cannot define a string key to access them, but all reduced density matrices are stored under the key `['rho']` as a dictionary. You can access the density matrix of the first site therefore as `['rho']['1']`.

5.8.3 Coherence in the open system Rabi problem

We now introduce the open system to the qubit having gained a basic understanding of the closed Rabi system. We consider two scenarios. First, we recall our open two level system with spontaneous emission. We introduce this approach now in our Rabi system using the Hamiltonian from Eq. (5.55):

$$\dot{\rho} \;=\; -\mathrm{i}\,[H_R, \rho] + \gamma L \rho L^\dagger - \frac{\gamma}{2}\left\{L^\dagger L, \rho\right\} \;, \quad L = \sigma^- \,. \tag{5.62}$$

We recall that σ^- is the operator for the transition from the excited state to the ground state, here used to model the spontaneous emission. In contrast to the previous system, we cannot expect an exponential decay of the excitations anymore, since we drive the transition (ground state $\rightarrow$ excited state) at the same time. We refer to this case as spontaneous emission.

In addition, we take a second approach with the following Lindblad equation:

$$\dot{\rho} \;=\; -\mathrm{i}\,[H_R, \rho] + \gamma L \rho L^\dagger - \frac{\gamma}{2}\left\{L^\dagger L, \rho\right\} \;, \quad L = n_e \,. \tag{5.63}$$

This Lindblad operator, the number operator for the excited state n_e, does not change the state, but adds a phase to the population in the excited state. We call this scenario the dephasing case. Of course, we can combine both types of interaction in one Lindblad master equation:

$$\dot{\rho} \;=\; -\mathrm{i}\,[H_R,\rho] + \sum_{\mu=1}^{2} \gamma_\mu L_\mu \rho L_\mu^\dagger - \frac{\gamma_\mu}{2}\left\{L_\mu^\dagger L_\mu, \rho\right\} \;, \quad L_1 = n_e \;,\; L_2 = \sigma^- \;. \tag{5.64}$$

We have introduced a subscript μ to label the two different Lindblad L_μ operators and their corresponding coupling γ_μ. There are two different Lindblad operators n_e and σ^- included; thus, the sum over μ runs from 1 to 2.

1. Set up a simulation in the spontaneous emission case according to Eq. (5.62). Choose an initial state and detuning such that you can track decoherence without an influence from the closed system. Iterate over different couplings to the environment and fit the decoherence rate with and appropriate decaying function. We would like to have an expression for one of the coherence measures (Eqs (5.59) and (5.60)) for the complete case in Eq. (5.64).

2. Set up a simulation in the dephasing case according to Eq. (5.63). Choose an initial state and detuning such that you can track decoherence. Iterate over different couplings to the environment and fit the decoherence rate.

3. Combine both scenarios (Eq. (5.64)) and make a prediction via fitting the combined rate of decoherence. It is sufficient to choose one of the two coherence measures. (Document which rates you are using for the fit.)

4. Set up a simulation with the initial state equal to the ground state tracking the Rabi oscillations for the ground and excited state. How would you measure the decoherence in this scenario? Define the corresponding function for the decoherence rate for Eq. (5.64).

5.8.4 From the single Rabi system to the two qubit problem

We extend our problem now to two Rabi oscillators coupled to each other. We introduce an additional index to iterate over the two Rabi oscillators, i.e., i. We write the Hamiltonian

of our two qubit problem as

$$H_{2R} \;=\; \sum_{i=1}^{3} H_R^{[i]}(\Omega_R^{[i]}, \Delta^{[i]}) - J(\sigma_1^+\sigma_2^- + \sigma_1^-\sigma_2^+)\;, \tag{5.65}$$

where $H_R^{[i]}(\Omega_R^{[i]}, \Delta^{[i]})$ is the Rabi Hamiltonian acting on site i, and it takes as arguments the Rabi frequency $\Omega_R^{[i]}$ and the detuning $\Delta^{[i]}$ on the corresponding site i indicated in the superscript brackets. This notation allows one to describe non-identical systems on site 1 and 2. The coupling term (coupling J) allows one to exchange an excitation between the two sites; it creates the excitation with σ^+ on one site while destroying it on the other with σ^-. We recall that the subscripts on the operators $\sigma^\pm$ specify the site where the operators act on. The Lindblad equation has to be extended for Lindblad operators on each site:

$$\dot{\rho} \;=\; -\mathrm{i}\,[H_{2R}, \rho] + \sum_{\mu=1}^{2}\sum_{i=1}^{2} \gamma_{\mu i} L_{\mu i}\rho L_{\mu i}^\dagger - \frac{\gamma_{\mu i}}{2}\left\{L_{\mu i}^\dagger L_{\mu i}, \rho\right\}\;, \tag{5.66}$$

which is a quite general case allowing for site dependent coupling of each Lindblad operator. The two sums now iterate over the two sites in our system, i.e., index i, and the two different Lindblad operators, see μ.

1. Calculate the coherence measures for the maximally coherent state.

2. Simulate the closed system to find a case where coherence is conserved during the time evolution. List cases when coherence is not conserved.

3. Simulate the open system for two qubits and check if the prediction for coherence still holds. Assume equal coupling for the Lindblad operators in the master equation modeling the probabilistic jumps with the coupling strengths $\gamma_{\mu,1} = \gamma_{\mu,2}$.

Suggested path for analytical solution: (1) (No hints).

Suggested path for numerical solution: You need to define a bond term for the interaction $\sigma_1^+\sigma_2^-$. It can be added via

```
Ham.AddMPOTerm('bond', ['splus', 'sminus'], hparam='J', weight=-1.0)
```

The Hermitian conjugate is considered automatically if the operators are not Hermitian. Site-dependent couplings are defined as an array instead of a scalar.

You can define the two site density matrix as an observable, adding it to your observable class

```
Obs.AddObservable('DensityMatrix_ij', [])
```

The results are stored as well under the dictionary accessed with the key `['rho']`. You can access the density matrix of the first two sites as `['rho']['1_2']`.

CHAPTER 6

THERMALIZATION IN THE QUANTUM ISING MODEL – APPROXIMATIONS, LIMITS, AND BEYOND

Submitted to *Quantum Science and Technology*[1]

D. Jaschke,[2] L. D. Carr,[3] and I. de Vega[4]

Abstract

We simulate the thermalization of qubits forming a quantum Ising spin chain when coupled to a thermal reservoir or environment. We consider different schemes in the system-reservoir coupling: the system qubits coupled to a common reservoir, and an independent local reservoir for each qubit, and a single reservoir coupled only to the first site of the system. Our simulations show the presence of favorable scenarios for enhancing or preventing thermalization of the spins. First, all independent local reservoirs enable more rapid thermalization in the comparison to a common reservoir. Second, the thermalization timescale changes depending on the position in the phase diagram of the quantum Ising model, which stops thermalizing in the paramagnetic limit for our choice of the model. Further, growing system sizes show a slow down in the thermalization process for a common reservoir. These results use the Lindblad master equation with multi-channel Lindblad operators. Moreover, we explore if these Lindblad operators which are non-local can be approximated with Lindblad operators acting on a small neighborhood of spins. We find that this approach is most successful in the extreme ferromagnetic and paramagnetic limits. Throughout our analysis, we use exact diagonalization methods.

[1] "Thermalization in the Quantum Ising Model – Approximations, Limits, and Beyond", D. Jaschke, L. D. Carr, and I. de Vega (2018). `https://arxiv.org/abs/1805.04934`. Use in agreement with arXiv license [55].

[2] primary researcher and author responsible for the manuscript.

[3] principal investigator and advisor at Colorado School of Mines.

[4] outline for theoretical side of work including interpretations within the field of open quantum systems; detailed feedback and suggestions on the draft; minor editing of passages within the draft; currently post-doctoral researcher at the Ludwigs-Maximilians-Universität München.

6.1 Introduction

According to statistical mechanics, a many-body quantum system coupled to a thermal bath will thermalize independently of the initial state. However, the conditions for thermalization need to be questioned for each specific setting. For example, the presence of gaps in the environment density of states of the environment[164], the existence of system symmetries [165] or the emergence of dynamical phase transitions in the thermodynamic limit may affect the thermalization process. Understanding dissipation and thermalization is fundamental for the development of quantum technologies, including the engineering of environments for state preparation, and the dynamics associated with decoherence. While setting up a comprehensive study, multiple aspects and concepts are necessary to understand the problem, including selecting the model for the system and the environment, choosing the approximations to describe the dynamics and thus the governing equation, and eventually proposing experiments to observe these dynamics.

The most convenient simplification to describe the evolution of a quantum system coupled to a thermal reservoir is the Lindblad master equation [46–48, 166], which preserves mathematical properties of the open system density matrix such as positivity and norm. With this framework the description of a single-body system is accessible, but many-body open quantum systems still impose challenges and imply from our perspective an extension to the standard numerical methods. The main numerical challenge is that the Lindblad equation contains as many terms or *decaying channels* as transitions between the system energy levels. A common simplification is to consider single-channel Lindblad equations, which depend on Lindblad operators that act locally on each element of the open system. This approach is accurate for situations where the environment produces a single relevant transition, for instance in weakly interacting qubits. It has been used to analyze transport in spin problems, where a one-dimensional many-body open system couples to reservoirs via both the first and last site [167, 168] or to study decoherence in strongly correlated systems [61, 169–171]. However, as shown in [172–175] for single open systems, the single-channel

approach may not be sufficiently accurate to describe thermalization. A qualitative reason is that a many-body, or even a multi-level, open system only relaxes to its thermal equilibrium state when the environment can redistribute the occupation probabilities of all its energy levels according to a Gibbs distribution. Naturally, this process can only occur when the Lindblad equation produces transitions among all system energy levels.

In this work, we consider an environment composed of a continuous set of independent harmonic oscillators that are weakly coupled to our system. To justify our use of the Lindblad equation, a Born-Markov approximation is considered, in which we take the relaxation timescale of the environment to be very short in comparison to the relaxation timescale of the system. This approximation implies that the reservoir state only suffers small fluctuations around its thermal initial state, such that only short-time system-environment correlations are considered. Moreover, to derive the Lindblad equation it is necessary to consider the secular approximation, which truncates fast frequencies, i.e., large differences between energy transitions, and which is based on a similar argument as used for the rotating wave approximation.

We further consider the quantum Ising model [123] as our system in the system-reservoir setting. From a theoretical perspective, the quantum Ising model is appealing due to the broad toolset available to treat its static solutions. For instance, the Jordan-Wigner transformation allows us to solve an infinite one-dimensional chain analytically and provides many insights for other questions such as the energy spectrum. The equilibrium and dynamics of a closed system have been analyzed to a great extent including generalizations of the quantum Ising model with, e.g., long-range interactions [127–129, 176]. On the one hand, equilibrium properties of the thermal many-body state can be analyzed via imaginary time evolution of matrix product density operators [80, 81] or locally purified tensor networks [82] and minimally entangled typical thermal states [177]. On the other hand, the dynamics of the closed system produced when quenching a part of it gives rise to the convergence to a local equilibrium as described by the eigenstate thermalization hypothesis [58]. However, a

complete framework to analyze the Ising model as an open many-body system coupled to a thermal environment has not been explored to our knowledge. Although we could have considered other Hamiltonians such as the Bose-Hubbard model, we choose the quantum Ising model due to the overlap most researchers have with this model in at least one aspect of their work. In addition, the quantum Ising model can also be motivated with regards to experiments; it is one option to describe quantum simulator experiments among other spin systems such as the XYZ model, as well as Bose- and Fermi-Hubbard models.

Quantum simulator platforms mimicking the quantum Ising model include ultracold atoms and molecules [20], trapped ions [26], and Rydberg systems [108]. The choice of environments coupled to these architectures is subtle, especially if the corresponding interaction is to be described with a Lindblad master equation. For simplicity, we consider an environment consisting of a three-dimensional electromagnetic field present in AMO-based (atomic molecular optical) quantum simulator platforms, which couples to the spins of our system via dipole interactions. The black-body radiation of the surrounding experiment can serve as motivation to choose such a field. In addition, trapped ions [178], Rydberg atoms [179] and ultracold atoms [180] can be confined in an optical cavity considered in the *bad cavity* limit, where the electromagnetic field has a broad-band density of states and therefore produces the desired Markovian interaction [181]. Although we use the electromagnetic field as a basis throughout the paper, a set of interacting spins coupled to a continuous bosonic environment can be mimicked via other models. One possibility is to consider ultracold atoms coupled to the bosonic field formed by the excitations of a Bose-Einstein condensate (BEC) as proposed in [182] and extended in [183] for the Ising model. A very close alternative is to consider atoms with two internal levels, a first one that is trapped by an optical lattice and that implements the open system dynamics and a second one that is untrapped and plays the role of an environment [184, 185]. Similarly, recent progress enabled the coupling of qubits to acoustic phonons in superconducting qubits [186], although the long coherence times between qubit and phonon modes cannot be accurately described with our approach based on

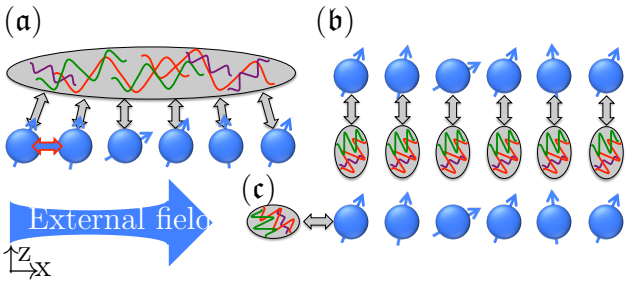

Figure 6.1: *Spins in the quantum Ising model coupled to a reservoir.* The thermalization of the quantum Ising model when coupled to a thermal reservoir raises many intriguing questions: Will the systems thermalize for the ferromagnetic and paramagnetic regime? If so, at what rate? Are there any suitable approximations to model the process in the many-body limit? The system Hamiltonian consists of an external field in the x-direction indicated by the big blue arrow trying to align the spin 1/2 (blue spheres with arrow) in the x-direction in the ground state. The nearest-neighbor interaction in the z-direction, highlighted only for the first two sites in (a), competes with the external field in the ground state trying to align neighboring spins. The reservoirs correspond to a three-dimensional electromagnetic field represented by grey ovals with a dense and wide mode spectrum. The grey arrows indicate the interaction with each of the system spins. We consider: (a) a common reservoir coupled to all sites, (b) independent local reservoirs for each site, and (c) a single site coupled to a local reservoir. Multi-channel Lindblad operators can simulate all of the three scenarios; neighborhood single-channel Lindblad operators are enabled for scenarios (b) and (c).

the Born-Markov approximations. However, both BEC excitations at low momenta [187] and acoustic phonons have a linear dispersion, analogous to photons in the electromagnetic field. This analogy draws the similarity to the model here studied and further underlines the experimental applicability of our work.

The dynamics of an open Ising model has been studied by considering independent baths coupled to both ends of the chain with mathematically constructed Lindblad operators [167] and by considering a thermal reservoir coupled to just two spins together with periodic boundary conditions [188]. However, a general description of an Ising chain coupled to a thermal bath in different configurations and without periodic conditions has not been done up to now to our knowledge. In this work, we build such a description and extend previous studies in two ways. (i) We analyze three distinct scenarios of coupling a reservoir to our system as presented in Figure 6.1 and analyze its decay with a multi-channel approach. In detail, we consider three basic scenarios, namely the case of (a) a common reservoir coupled

to all sites, thus producing atom-atom interactions, (𝔟) independent local reservoirs coupled to each site, and (𝔠) a single reservoir coupled only to the first site in the spin chain. We analyze the resulting timescale for thermalization and discuss how to resolve the symmetry present in the quantum Ising model, which might prevent thermalization. (ii) We raise the question of whether neighborhood single-channel Lindblad operators are sufficient to describe thermalization due to the aforementioned limitations of single-site single-channel Lindblad operators. In contrast, the neighborhood single-channel operators act on up to three sites and allow us to control the interaction better and generate long-range order. In detail, one qubit will be changed while the other two nearest-neighbor qubits act as a control leading to the full three-site neighborhood; a two-site neighborhood is sufficient for the boundaries in this scenario with open boundary conditions. The single site operator captures the paramagnetic limit where the energy contribution is defined by the local magnetization and not the interaction between nearest-neighbor spins. Such control scenarios can also be explored explicitly and quantitatively in the future in universal quantum computers utilizing appropriate quantum gates; the CNOT (controlled-not) gate is an example of an analogous idea in a closed system with unitary time evolution, where an operation on one qubit is based on the state of another qubit.

We obtain our results with an exact diagonalization implementation [189] from the OSMPS package [52]. The choice of exact diagonalization limits us to a few qubits, and the multi-channel method is also bounded to few qubits since the number of transitions to be considered grows exponentially with system size. This limit is because the number of transitions or channels and the dimension of the density matrix grow exponentially in the number of spins, N, i.e., as 2^N without considering symmetries. Moreover, we analyze the spectrum of the Liouville propagator and study steady states and timescales characterized by the gap in the Liouville propagator. In detail, the gap between the first and the second eigenvalue of the Liouville operator determines the slowest possible timescale in the system, while the time evolution of different initial states may be governed by decaying timescales from

larger eigenvalues. Such spectrum analysis requires diagonalizing a matrix of dimension 2^{2N}, which is even more limiting. Hence, calculations beyond six qubits are unfeasible without parallelization, and each additional qubit in the open systems increases the computational resources used by a factor of 64 due to the cubically scaling eigenvalue decomposition. Our results from these simulations show the following:

(i) The multi-channel Lindblad operators cannot be replaced with our suggested simpler approach apart from the extreme limits of the phase diagram.

(ii) Moreover, the multi-channel Lindblad operators show significant differences if used with configurations ($\mathfrak{a}$), ($\mathfrak{b}$), or ($\mathfrak{c}$). These configurations give rise to completely different thermalization rates, which are faster for the system coupled to independent reservoirs, ($\mathfrak{b}$) and ($\mathfrak{c}$), in comparison to the coupling to a common environment ($\mathfrak{a}$). Within the independent-local reservoirs, all sites coupled to their own reservoir thermalizes faster than coupling just the first site to its reservoir. We disregard the neighborhood single-channel approach for this analysis.

(iii) The thermalization rate also depends on the Ising phase. In general, the closer to the ferromagnetic phase the faster the thermalization, while in the paramagnetic limit the system does not thermalize at all.

(iv) Finally, we have seen that the larger the number of spins in the Ising chain, the slower the thermalization.

The outline of our work is as follows. We introduce the closed and the open quantum system in the next two Secs. 6.2 and 6.3. We continue with a detailed look at our approach of neighborhood single-channel Lindblad operators in Sec. 6.4. Then, we evaluate the thermalization timescales for different scenarios in Sec. 6.5. Finally, we conclude our results in Sec. 6.6. The appendices add further aspects of this study, i.e., the odd symmetry sector in App. 6.7, the choice of a different operator in the interaction Hamiltonian in App. 6.8, and details on the standard derivation of the multi-channel operators including their coupling, see App. 6.9.

6.2 Transverse quantum Ising model in a closed system

We focus on the transverse quantum Ising model in one dimension with a Hamiltonian given as

$$H_{\mathrm{QI}} = -\sum_{k=1}^{N-1} \cos(\phi)\sigma_k^z\sigma_{k+1}^z - \sum_{k=1}^{N} \sin(\phi)\sigma_k^x\,, \tag{6.1}$$

where the formulation of the coupling in terms of sine and cosine simplifies addressing the ferromagnetic ($\phi = 0$) and paramagnetic ($\phi = \pi/2$) limit. The system size or the number of qubits in the quantum Ising chain is N. The Pauli spin operators σ_k^x and σ_k^z are acting on site k, $\cos(\phi) \equiv J/\sqrt{J^2+g^2} > 0$ is the unitless interaction energy, and $\sin(\phi) \equiv g/\sqrt{J^2+g^2}$ is the unitless coupling to the external field. The critical point of the quantum Ising model is at $\phi_c = \pi/4$ for the thermodynamic limit $N \to \infty$, i.e., $J_c = g_c = 1/\sqrt{2}$. We treat systems below ten qubits and the position of the minimum of the gap ϕ_c, i.e., an indicator of the quantum critical points, shifts to values $\phi_c < \pi/4$ due to finite-size effects. Note that in this formulation the Hamiltonian H_{QI} is expressed in terms of the $\sqrt{J^2+g^2}$, and all quantities are therefore unitless.

The quantum Ising model has a $\mathbb{Z}_2$ symmetry, which is very useful when treating the closed quantum system. The two sectors of the symmetry, e.g., manifesting in the block-diagonal structure of the Hamiltonian, are the even and odd sector of the $\mathbb{Z}_2$ symmetry. This symmetry can be used for the open system if the full Hamiltonian of the system and the bath commutes with the generator of the symmetry $\left(\oplus_{k=1}^{N} n_k^x\right) \bmod 2$. Here, $n_k^x = \sigma_x^- \sigma_x^+$. The open system evolution as described with the Lindblad master equation does not break the symmetry. Thus, any state $|\,\phi\rangle = S_k\,|\,\psi\rangle$ with $S_k = \sigma_k^x$ is in the same symmetry sector, and the remaining steps of the derivation of the Lindblad master equation are carried out solely in that symmetry sector. We remark that the choice $S_k = \sigma_k^z$ does not conserve the symmetry. Reference [190] presents a more detailed discussion of symmetries in the Lindblad master equation.

6.3 System-reservoir couplings and Lindblad equation for our system

In this section, we introduce the different system-environment configurations as well as the models of Lindblad master equation we will consider. Section 6.3.1 discusses the configurations ($\mathfrak{a}$), ($\mathfrak{b}$), and ($\mathfrak{c}$) from Figure 6.1 to the corresponding Hamiltonians. Then, we explain the two different formulations of the Lindblad operators in the master equation in Sec. 6.3.2. Section 6.3.3 reminds the reader of properties of the Lindblad master equations, which we use later on for our analysis.

6.3.1 System-reservoir configurations

We now explore the quantum Ising system coupled to a dissipative environment for the following three different configurations.

6.3.1.1 Global environment

First, we consider the case in which all spins are coupled to a common bath of harmonic oscillators, as described in Figure 6.1($\mathfrak{a}$), such that the total Hamiltonian of the system (S) and the reservoir (R) can be written as

$$H_{S+R}^{(\mathfrak{a})} \;=\; H_{\mathrm{QI}} + \sum_{k=1}^{N}\sum_{q} S_k(g_{kq}b_q + g_{kq}^{*}b_q^{\dagger}) + \sum_{q}\omega_q n_q\,, \tag{6.2}$$

where $b_q^{\dagger}$ (b_q) is the creation (annihilation) operator of the environment with a frequency ω_q, and $n_q = b_q^{\dagger}b_q$ is the number operator. The sums over q are not specified as the set of harmonic oscillators is large, and the exact number of them does not have any significance. The second term of Eq. (6.2) describes the interaction between the system and the bath, which is modulated by the coupling strength g_{kq}. In this work, we consider that the environment is a three-dimensional electromagnetic field, such that the coupling strengths correspond to a dipole coupling of the type presented in [191], i.e.,

$$g_{kq} \;\sim\; -\mathrm{i}\sqrt{\hbar\omega_q/(\nu\epsilon_0)}\;(\vec{r}_k\cdot\vec{d}_{\mathrm{dip}})/r_k\exp(-\mathrm{i}\vec{r}_k\cdot\vec{q}) \tag{6.3}$$

where ν is the quantization volume. We consider the Planck constant $\hbar$ and the electric permitivity ϵ_0 as unit constants. Thus, the coupling g_{kq} contains the dipole interaction via $(\vec{r}_k\vec{d}_{\rm dip})/r_k$ and the phase relation inside the reservoir for each frequency as $\exp(-{\rm i}\vec{r}_k\vec{q})$. The position of the $k^{\rm th}$ spin in the quantum Ising chain is $\vec{r}_k$ and $\vec{d}_{\rm dip}$ the dipole moment of the spin coupling to the electromagnetic field; we assume that all spins have equal dipole moments and $\vec{d}_{\rm dip}$ is independent of k. The interaction Hamiltonian also depends on the system coupling operators S_k, which we choose as $S_k = \sigma_k^x$. We point out that the limit $\phi = \pi/2$ corresponds to a non-interacting model coupled via a common reservoir. This case has been discussed in a generalized fashion in [192].

6.3.1.2 Local environments

As a second configuration, we consider that each spin is coupled to its independent local reservoir, as described in Figure 6.1($\mathfrak{b}$). The total Hamiltonian is

$$H_{S+R}^{(\mathfrak{b})} \;=\; H_{\rm QI} + \sum_{k=1}^{N}\sum_{q} S_k(g_{kq}b_{kq} + g_{kq}^{*}b_{kq}^{\dagger}) + \sum_{k=1}^{N}\sum_{q}\omega_q n_{kq}\,, \tag{6.4}$$

where now there is a set of harmonic oscillators $b_{kq}^{\dagger}$ corresponding to the bath attached to each spin k. We note that the same physics described with Eq. (6.4) can be obtained with the Hamiltonian in Eq. (6.2), i.e., with a single environment, under particular conditions. In detail, one should consider the spins separated at a minimal spatial distance L such that $q_0 a_{\rm lat} N \gg 1$, where q_0 is the largest resonant wave vector of the field and $a_{\rm lat}$ is the distance between the spins in the chain. Such resonant wave vectors correspond to those bath modes that interact resonantly with the system frequencies, ω, i.e., such that $\omega(q_0) = \omega$. If this condition is fulfilled, we can assure that there are no bath-mediated dipole-dipole interactions between the spins, and therefore these spins evolve as though each of them was coupled to their independent reservoir. This limit is essential as one can hardly imagine implementing independent reservoirs in experiments for very close quantum spins.

6.3.1.3 Coupling to a single site

Finally, the configuration in Figure 6.1(𝔠) corresponds to the case described in Eq. (6.2) with $g_{kq} = 0$ for every $k \neq 1$. The Hamiltonian of system and reservoir on the first site (R1) is then reduced to

$$H^{(\mathfrak{c})}_{S+R1} \;=\; H_{\mathrm{QI}} + \sum_q S_1(g_{1q}b_{1q} + g^*_{1q}b^\dagger_{1q}) + \sum_q \omega_q n_{1q}\,. \tag{6.5}$$

6.3.2 Choice of Lindblad operators

Apart from the scenarios detailing how the quantum Ising chain can be coupled to the reservoir, we briefly point out the difference between the global multi-channel approach and neighborhood single-channel approach. We use the same Lindblad master equation for both approaches, which we define as

$$\dot\rho \;=\; -\frac{\mathrm{i}}{\hbar}\,[H,\rho] + \sum_{abcd} \mathcal{C}_{abcd}\left(L_{ab}\rho L^\dagger_{cd} - \frac{1}{2}\left\{L^\dagger_{cd}L_{ab},\rho\right\}\right) \quad\Longleftrightarrow\quad \frac{\partial}{\partial t}\,|\rho\rangle\!\rangle = \mathcal{L}\,|\rho\rangle\!\rangle\,, \tag{6.6}$$

where the formulation with the density matrix ρ (left hand side) or with the super-ket $|\rho\rangle\!\rangle$ in Liouville space (right hand side) are equivalent. Equation (6.6) evolves the density matrix ρ of a shape $D \times D$, where D is the dimension of the Hilbert space of the quantum Ising chain. In contrast, the vector representation $|\rho\rangle\!\rangle$ of the density matrix has D^2 entries while the matrix $\mathcal{L}$ acting on $|\rho\rangle\!\rangle$ from the left-hand side is of dimension $D^2 \times D^2$ due to the outer product or Kronecker product, e.g., $H \otimes I$ and I an identity matrix of size $D \times D$. The Liouville operator is defined as

$$\mathcal{L} \;=\; -\frac{\mathrm{i}}{\hbar}\left(H\otimes\mathbb{I} - \mathbb{I}\otimes H^T\right) + \sum_{abcd}\frac{\mathcal{C}_{abcd}}{2}\left(2L_{ab}\otimes L^*_{cd} - L^\dagger_{cd}L_{ab}\otimes\mathbb{I} - \mathbb{I}\otimes L^T_{ab}L^*_{cd}\right)\,, \tag{6.7}$$

In the Lindblad equation, the Hamiltonian H corresponds to the Hamiltonian of the system and possible corrections from the system-reservoir interaction. L_{ab} are the Lindblad operators encoding the dissipative part of the dynamics via a transition from state $|\,b\rangle$ to $|\,a\rangle$ with a

coupling $\mathcal{C}_{abcd}$. Thus, the sum over a, b, c, and d iterates over a set of states. The superscripts T and $*$ are the transposed and complex conjugate of an operator, respectively. Throughout the work, we choose our units such that $d_{\text{dip}} = 1$, the lattice spacing $a_{\text{lat}} = 1$ between sites, the speed of light $C = 1$, the Boltzmann constant $k_B = 1$, and no chemical potential, $\mu = 0$, for the Bose-Einstein statistics. Moreover, we set $\hbar = 1$. Thus, the temperature T is implicitly in units of $\sqrt{J^2 + g^2}$ and times are given implicitly in units of $1/\sqrt{J^2 + g^2}$. The choice of the Lindblad operators and decay rates depend on the particular case considered. We shall consider two different cases, a multi-channel Lindblad equation as derived from Markov and secular approximations [49], and a single-channel equation with neighborhood single-channel Lindblad operators. These are detailed in the following.

6.3.2.1 Multi-channel Lindblad equation

For the first approach, i.e., the multi-channel Lindblad operators via the energy eigenstates, we follow the steps of the Born-Markov approximation [49] and resolve the secular approximation in the interaction picture via introducing the energy eigenstates of the Hamiltonian

$$H_S \;=\; \sum_a E_a \,|\, a\rangle\langle a\,|\;. \tag{6.8}$$

The sum over a contains d_{loc}^N eigenstates without $\mathbb{Z}_2$ symmetry, and d_{loc}^{N-1} eigenstates within a symmetry sector. This step of formulating the problem in its eigenstates leads finally to the Lindblad operators defined in terms of the eigenstates. According to this derivation, the Lindblad operators are defined as

$$L_{ab} \;=\; |\, a\rangle\langle b\,|\,, \tag{6.9}$$

that is, induce a transition from energy eigenstate $|\, b\rangle$ to $|\, a\rangle$. These energy eigenstates can be entangled in the computational basis, i.e., the Fock basis corresponding to the qubits; thus, the state of any spin k' can have different values in the eigenstates $|\, a\rangle$ and $|\, b\rangle$ and

change during the action of L_{ab}, although the operator in the interaction Hamiltonian acts on site k via $S_k, k \neq k'$. This property contributes to their being named as global Lindblad operators. Therefore, the number of Lindblad operators is d_{loc}^{2N} where the local dimension is $d_{\text{loc}} = 2$ in our case.[5]

The decay rates $\mathcal{C}_{abcd}$ describe the dissipative action of the reservoir, i.e., the electromagnetic field, on our system. These coupling strengths fulfill the detailed balance condition for the Lindblad operators L_{ab} and L_{ba} via the underlying Bose-Einstein statistics. Further explanations for the detailed balance can be found in Eqs. (6.29) and (6.30) in the appendix. Moreover, $\mathcal{C}_{abcd}$ contains the overlap of the eigenstates with the operator from the interaction Hamiltonian of the type $\langle a| \, S_k \, |b\rangle$. In our case, the system Hamiltonian $H = H_{\text{QI}}$ presented in Eq. (6.1); we do not use the principle value part which occurs due to a pole in the integration over the spatial and time integral to reach the coupling constant. The principal value part is a imaginary contribution and adds a correction to the Hamiltonian part of the Lindblad equation, but does not alter the Lindblad operators in the dissipative part of the Eq. (6.6). A detailed explanation of these steps and the rates used for the simulations follows in App. 6.9.

6.3.2.2 Neighborhood single-channel Lindblad equation

The neighborhood single-channel Lindblad operators allow us to express the action of the environment in terms of the number of decaying channels which grows with the number of qubits only. This advantage, together with the fact that they act only on a neighborhood, make them computationally more feasible. Our design of the neighborhood single-channel Lindblad operators is inspired by the spectral decomposition described in Sec. 6.3.2.1, but does not strictly follow the spectral decomposition. In detail, we can write the eigenstate $|a\rangle$ as a tensor product between the state $|a\rangle_k$ on site k and the state $|a\rangle_{\bar{k}}$, where $\bar{k}$ is the set of all other sites k' with $k' \neq k$. This formulation allows us to execute the following reduction:

[5]This upper bound could, in theory, be reduced to $d_{\text{loc}}^{2N} - 1$, but is not of interest for numerical implementation.

$$|\,a\rangle\langle a\,|\,S_k\,|\,b\rangle\langle b\,| \;\;=\;\; |\,a\rangle_k\langle a\,|_k\,S_k\,|\,b\rangle_k\langle b\,|_k \otimes \mathbb{I}_{\bar{k}}\,, \tag{6.10}$$

where $\mathbb{I}_{\bar{k}}$ is the identity operator acting on the specified Hilbert spaces. Thus, these local operators induce the transition between the eigenstates $|\,a\rangle$ of the Hamiltonian H_S in the paramagnetic limit. We resolve the ferromagnetic limit with neighborhood operators acting on up to three sites, where the neighborhood operator is in our eyes the price to pay to resolve the energy contributions from the interaction Hamiltonian depending on the state of two neighboring spins in the system. This approach reduces the number of decaying channels to one, i.e., a pair of Hermitian conjugate operators with the corresponding rates, in the paramagnetic limit. We obtain two decaying channels, i.e., two pairs of Hermitian conjugate Lindblad operators, in the ferromagnetic limit.

More details about the neighborhood single-channel Lindblad operators are given in Sec. 6.4. We note that to observe thermalization in the paramagnetic limit, we have to choose a coupling operator which is not diagonal to the paramagnetic Hamiltonian, for instance, $S_k = \sigma_k^z$. A complete numerical analysis of the system dynamics for such a case is presented in App. 6.8.

6.3.3 Properties of the Lindblad equation

It can be analytically shown that when the dissipative rates and Lindblad operators of the Lindblad equations obey the detailed balance conditions, as happens in the derivation of Sec. 6.3.2.1, its steady state or fixed point is a thermal state of the system [49]. We define the thermal state of the quantum system for the temperature T as

$$\rho_{\text{th}} \;\;=\;\; \exp\left(-\beta H_S\right)/Z\,, \tag{6.11}$$

with $\beta = 1/(k_B T)$ and the partition function $Z = \text{Tr}\left[\exp\left(-\beta H_S\right)\right]$, where H_S is the Ising model in our case. However, even if the multi-channel Lindblad equation of Sec. 6.3.2.1 governs the evolution, the system may not relax to the thermal state. To analyze this

as well as the decay rates of the system, it is convenient to consider the formulation of the Lindblad equation in its vector form Eq. (6.6), with the Liouville operator defined in Eq. (6.7). Since the Liouville operator is not Hermitian, its diagonalization gives rise to left and right eigenvectors. The right eigenvectors, denoted as $|v_j\rangle\rangle$, fulfill the condition $\mathcal{L}\,|v_j\rangle\rangle = \Lambda_j\,|v_j\rangle\rangle$, where Λ_j are the corresponding eigenvalues of the Liouville operator $\mathcal{L}$. Thus, the eigenvectors $|v_j\rangle\rangle$ form a complete basis and we can express any initial density matrix as a linear combination of the basis vectors with some complex weight c_j, i.e., $|\rho(0)\rangle\rangle = \sum_j c_j\,|v_j\rangle\rangle$. The time-evolved state can then be written as

$$|\rho(t)\rangle\rangle \;=\; \sum_j c_j \mathrm{e}^{\Lambda_j t}\,|v_j\rangle\rangle\,, \tag{6.12}$$

where $c_j = \langle\langle v_j|\rho(0)\rangle\rangle$. Hence, the weights of the eigenvectors with eigenvalues Λ_j having zero real part do not change over time and, therefore, they correspond to steady states. However, the eigenvectors with a negative real part will decay to a steady state, with a decaying time scale given by $|\Re(\Lambda_j)|$, where $\Re$ refers to the real part. Eigenvalues with a positive real part cannot exist for physically meaningful states as the norm would grow over time. If the steady state is unique, there is a single eigenstate with zero real part eigenvalue. If we sort the eigenvalues as $|\Re(\Lambda_j)| \leq |\Re(\Lambda_{j+1})|$, the first one denoted as Λ_0 corresponds to the zero real part, while the second eigenvalue $|\Re(\Lambda_1)|$ defines the gap of the Liouville operator and defines the longest possible timescale for decaying to the steady state. Further details have been discussed in literature [190, 193, 194].

Therefore, the eigenvalues Λ_j with zero real part do not change over time, and their eigenvectors are steady states, given they have the characteristics of a density matrix. Eigenvectors of $\mathcal{L}$ with negative real part eigenvalues will decay to a steady state, where the timescale of the decay depends on $|\Re(\Lambda_j)|$. Eigenvalues with a positive real-part cannot exist for physically meaningful states as the norm would grow over time. If the steady state is unique, the thermal state is the steady state and, thus, $|\Re(\Lambda_j)|$ characterizes the timescale for the thermalization. The second eigenvalue $|\Re(\Lambda_1)|$ of $\mathcal{L}$ is dubbed the gap of the Liouville op-

erator as it defines the longest possible timescale for decaying to the steady state; the first eigenvalue is Λ_0. Detailed aspects can be found in [190, 193–195].

6.3.4 Symmetries

As mentioned in Sec. 6.2 the Ising model has a $\mathbb{Z}_2$ symmetry that is preserved by the dissipation, i.e., the Hilbert space is divided into two symmetry sectors. For simplicity our analysis of thermalization will be within the even sector. Thus, instead of analyzing thermalization to the total state defined in Eq. (6.11), we will analyze the system thermalization to

$$\rho_{\mathrm{th}}^{\mathrm{e}} \;=\; \frac{\exp\left(-\beta H_S^{\mathrm{e}}\right)}{Z}\,, \tag{6.13}$$

with H_S^{e} the Ising Hamiltonian in the even sector. We briefly visit the odd symmetry section in App. 6.8. The use of the symmetry has three advantages:

Firstly, if we do not use the symmetry and do not break it with an additional symmetry breaking field, we have at minimum two steady states, i.e., one for each symmetry sector. Eigenvectors of degenerate eigenvalues can be rotated in the degenerate subspace, which makes it difficult to identify the steady state for each symmetry sector. If we obtain for instance a third degenerate state, we have to identify which sector has actually two steady states, while the remaining eigenvector must be the unique steady state of the other sector. In our study, for instance, we find up to four degenerate states within a single symmetry sector for just two qubits. Resolving and separating the symmetry sectors from the beginning simplifies the analysis.

Secondly, the symmetry improves the computational scaling. For our spin system, the size of the Liouville operator decreases from $2^{2N} \times 2^{2N}$ to $2^{2(N-1)} \times 2^{2(N-1)}$ which simplifies computational operations such as the eigenvalue decomposition. Therefore, we also have only two sets of $2^{2(N-1)}$ eigenvalues and eigenstates instead of 2^{2N}.

Finally, since the Lindblad operator also conserves the symmetry, the probability between the two symmetry sectors does not change during a time evolution. However, to thermalize to the global thermal state defined in Eq. (6.11) the probability of each sector should also change as a function of the temperature. Thus, if we start in the ground state being one hundred percent in one symmetry sector, we cannot thermalize to Eq. (6.11) as we cannot dynamically move some probability into the other sector. However, the system will thermalize to Eq. (6.13). Thus, the inclusion of symmetries has benefits regarding multiple aspects.

6.4 Thermalization in the paramagnetic and ferromagnetic limits

We introduce in this section the neighborhood single-channel Lindblad operators. For this approach, we take the lessons learned from the spectral decomposition of the multi-channel approach. The idea is to mimic the spectral decomposition obtained for independent local reservoirs by introducing simpler local or neighborhood single-channel Lindblad operators, corresponding to the paramagnetic and ferromagnetic limits, respectively. With a simpler structure, they serve as an approximation for multi-channel Lindblad operators. Therefore, the neighborhood single-channel Lindblad operators are very useful to describe dissipation in many-body systems without considering the complete energy spectrum, but while still transitioning between energy eigenstates.

6.4.1 Neighborhood single-channel operators in the paramagnetic limit

To derive simpler Lindblad operators which in the paramagnetic limit give rise to thermalization, we consider solely for this subsection to $S_k = \sigma_k^z$. We concentrate on the action of the operator S_k in $|\,a\rangle\langle a|\, S_k\, |\,b\rangle\langle b|$ on site k, and aim to isolate the site k when accounting for this step. The Schmidt decomposition [85] allows us to rewrite the eigenstates $|\,a\rangle$ and $|\,b\rangle$ in terms of a bipartition between the site k and all others sites $\bar{k}$, i.e., all k' with $k' \neq k$. This decomposition depends on the site k and is written as

$$|\,a\rangle = \sum_i \lambda_{ika}\,|\,a_k^i\rangle\,|\,a_{\bar{k}^i}\rangle\,, \qquad |\,b\rangle = \sum_j \lambda'_{jkb}\,|\,b_k^j\rangle\,|\,b_{\bar{k}^j}\rangle\,. \tag{6.14}$$

The Schmidt decomposition characterizes the entanglement between two subsystems of a pure quantum state and generates two orthonormal sets of basis states for each of the bipartition. The Schmidt decomposition uses a singular values decomposition, i.e., a generalized eigenvalue decomposition applicable to rectangular matrices; therefore, the basis depends on the actual state. The weight of each basis state within the decomposition is set via the singular values λ_{ika}, which are larger than or equal to zero by definition. So far, the new formulation is generally applicable, and we obtain

$$\begin{aligned} |\,a\rangle\langle a|\,S_k\,|\,b\rangle\langle b| &= \sum_{ij'} {}^{ij'}\mathcal{C}_{ab}^{[k]}\,|\,a_k^i\rangle\langle b_k^{j'}|\otimes|\,a_{\bar{k}}^i\rangle\langle b_{\bar{k}}^{j'}|\,, \\ {}^{ij'}\mathcal{C}_{ab}^{[k]} &= \lambda_{ika}\lambda'_{j'kb}\left(\sum_{i'j}\lambda_{i'ka}\lambda'_{jkb}\langle a_k^{i'}|\,S_k\,|\,b_k^j\rangle\cdot\left\langle a_{\bar{k}}^{i'}\middle|b_{\bar{k}}^j\right\rangle\right)\,. \end{aligned} \tag{6.15}$$

The coupling ${}^{ij'}\mathcal{C}_{ab}^{[k]}$ is defined with a similar notation as used for the rates of the multi-channel case in Eq. (6.26); a and b are eigenstates of the system Hamiltonian H_{QI}. Subscripts (superscripts) for the eigenstate label the subsystem (basis state) for the Schmidt decomposition. To distinguish the basis state of the Schmidt decomposition in the weight $\mathcal{C}$, the orthonormal basis states of the Schmidt decomposition are a superscript in front of the symbol. The upper and lower limit for the indices running over the basis states of the Schmidt decomposition depends on the system size and amount of entanglement and is therefore not specified.

We know that the eigenstates are product states of local eigenstates of the Pauli matrices for the paramagnetic limit, i.e., product states of spins aligned and anti-aligned with the external field. The Schmidt decomposition of a product state has exactly one non-zero singular value, e.g., $\lambda_{1ka} = 1$. Thus, Eq. (6.15) reduces drastically, and we obtain

$${}^{ij'}\mathcal{C}_{ab}^{[k]} = \underbrace{\langle a_k^{i'=1}|\,S_k\,|\,b_k^{j=1}\rangle}_{(I)}\,\underbrace{\left\langle a_{\bar{k}}^{i'=1}\middle|b_{\bar{k}}^{j=1}\right\rangle}_{(II)}, \lambda_1 = \lambda'_1 = 1\,, \tag{6.16}$$

while all other Schmidt values being zero. We interpret the two terms (I) and (II) in Eq. (6.16) as conditions when there are non-zero contribution to the coupling ${}^{ij'}\mathcal{C}_{ab}^{[k]}$; we use an orthogonal set of basis vectors for k and $\bar{k}$ and thus each of the terms is either 0 or 1. These equations can be used directly to construct the Lindblad operators for the paramagnetic limit considering the conditions (I) and (II). The condition (I) marked in Eq. (6.16) is fulfilled if $\langle a_k^{i'=1}|$ and $|b_k^{j=1}\rangle$ are anti-aligned as S_k flips the spin. Condition (II) from Eq. (6.16) is equal to one if the sites $k' \neq k$ do not change their state. Thus, we obtain that the Lindblad operator for each site, producing cooling of the system is

$$L^{[k]} \;=\; |\Uparrow_x\rangle_k\langle\downarrow_x|_k\,, \tag{6.17}$$

while $(L^{[k]})^\dagger$ produces cooling respectively. The state on site k aligned with the external field in the x-direction is $|\Uparrow_x\rangle_k$, while the state anti-aligned is $|\Downarrow_x\rangle_k$. Therefore, the Lindblad operator in Eq. (6.17) aligns the spin k with the external field and brings this spin to the ground state of the paramagnetic limit. Further details are presented in App. 6.8.

6.4.2 Neighborhood single-channel operators in the ferromagnetic limit

For the ferromagnetic limit, we return to $S_k = \sigma_k^x$ and start over at Eq. (6.15). For simplicity in the derivation, we do not consider the $\mathbb{Z}_2$ symmetry here. Therefore, we have two degenerated ground states, $|\Uparrow\cdots\uparrow\rangle$ and $|\Downarrow\cdots\downarrow\rangle$. Arrows without a subscript indicate implicitly basis states in the z-direction. Considering a similar argument as in the paramagnetic limit we could be tempted to chose the Lindblad operators acting solely on each site k as $|\Uparrow\rangle_k\langle\Downarrow|_k$ and its conjugate $|\Downarrow\rangle_k\langle\Uparrow|_k$. However, due to the energy contribution from the nearest-neighbor interactions, it is not clear whether these operators increase the system energy, leave it equal, or decrease it, which is essential for them to fulfill the detailed balance condition and thus produce thermalization.

To solve this problem, we propose Lindblad operators defined on a neighborhood of up to three sites. The operators acting on the additional spins help to identify how the energy

changes depending on the state of the nearest-neighbors. Thus, we call them control-spins that decide upon the flip of the middle spin during the process.

We associate the complete three-site operators with heating (cooling) depending on whether they increase (decrease) the energy when driving the system toward a thermal equilibrium as they fulfill the detailed balance between different energy levels of the system Hamiltonian H_{QI}. Operators which do not change the energy are not taken into account. In this way, we can distinguish between a thermalization and randomization of the system. In detail, we define the states $|\,m\rangle_k = |\Uparrow\uparrow\uparrow\rangle_k$, $|\,o\rangle_k = |\Uparrow\downarrow\uparrow\rangle_k$, $|\,r\rangle_k = |\Downarrow\uparrow\downarrow\rangle_k$, and $|\,t\rangle_k = |\Downarrow\downarrow\downarrow\rangle_k$ on the three neighboring sites $k-1, k, k+1$. In addition, we define the two site states $|\,u\rangle_k = |\Uparrow\uparrow\rangle_k$, $|\,v\rangle_k = |\Downarrow\uparrow\rangle_k$, $|\,w\rangle_k = |\Uparrow\downarrow\rangle_k$, and $|\,x\rangle = |\Downarrow\downarrow\rangle_k$ for the sites k and $k+1$. We can now define a generic Lindblad operator $L_{ab}^{[k]} = |\,a\rangle_k\langle b\,|_k$ acting on the bulk of the system on a three-site neighborhood. Then, the heating operators have the form

$$L_{rt}^{[k]} \;=\; |\,r\rangle_k\langle t\,|_k\,,\; L_{om}^{[k]} = |\,o\rangle_k\langle m\,|_k\,, k = 2, \ldots, N-1\,, \tag{6.18}$$

and give rise to an increase in energy. Further, we define the Lindblad operators $L_{wx}^{[1]}$, $L_{vu}^{[1]}$, $L_{vx}^{[N-1]}$, and $L_{wu}^{[N-1]}$ for the boundary sites. Each of these Lindblad operators can be interpreted as a spin flip with one or two control-spins. Similarly, we define the operators for cooling the bulk of the system as their Hermitian conjugates, i.e.,

$$L_{tr}^{[k]} \;=\; |\,t\rangle_k\langle r\,|_k\,,\; L_{mo}^{[k]} = |\,m\rangle_k\langle o\,|_k\,, k = 2, \ldots, N-1\,, \tag{6.19}$$

and $L_{xw}^{[1]}$, $L_{uv}^{[1]}$, $L_{xv}^{[N-1]}$, and $L_{uw}^{[N-1]}$ for the boundary sites. Each of these processes in the bulk of the system introduces an energy difference of $\Delta = \pm 4J$. The boundaries Lindblad operators have an energy difference of $\Delta = \pm 2J$.

6.4.3 Neighborhood single-channel operators in between the limits

We explored as well the possibility of using the neighborhood single-channel Lindblad operators from both limits to capture the region between the limits with $0 < \phi < \pi/2$, where the neighborhood single-channel operators for the paramagnetic limit are explained in Appendix 6.8. An optimization over the ratio of the two coupling strengths, i.e., the coupling strength for the neighborhood single-channel Lindblad operators from the ferromagnetic limit and the local single-channel Lindblad operators for the paramagnetic limit, did not lead to trace distances close to the steady state. For example, the trace distances for values of $\phi \approx \pi/4$ do not drop below 0.1. This result indicates that the multi-channel approach is required to picture thermalization in interacting many-body systems unless non-trivial approximations can simplify dynamics to neighborhood single-channel Lindblad operators.

6.5 Thermalization timescales

We have introduced three different possibilities for coupling the spins of the quantum Ising model to reservoirs, as described in Sec. 6.3.1 and Figure 6.1. In the following, we analyze both time evolution of the system and the spectrum of the Liouville operators $\mathcal{L}$. We execute this analysis for the different scenarios of a system-environment coupling sketched in Figure 6.1 and presented in Eqs. (6.2) to (6.5). Firstly, we find the timescale for the thermalization of the system for the multi-channel Lindblad operators.

We compare data from the Liouville operator $\mathcal{L}$ and the time evolution in selected figures throughout the paper. We explore two different conditions for the thermalization time, T_{th} based on the macroscopic observable of the averaged magnetization $\bar{\sigma}^x$ in the x-direction, and $T_{\text{th}\mathcal{D}}$ based on the trace distance $\mathcal{D}$:

$$T_{\text{th}} = \min_t \left(|\bar{\sigma}^x(t) - \bar{\sigma}^x_{\text{th}}| < 10^{-10} \right) , \tag{6.20}$$

$$T_{\text{th}\mathcal{D}} = \min_t \left(\mathcal{D}(\rho(t), \rho_{\text{th}}) < 10^{-10} \right) , \tag{6.21}$$

$$\bar{\sigma}^x = \frac{1}{N} \sum_{k=1}^{N} \langle \sigma_k^x \rangle , \quad \mathcal{D}(\rho, \rho') = \frac{1}{2} \|\rho - \rho'\| . \tag{6.22}$$

The density matrix of the thermal state is ρ_{th}, and the corresponding expectation value of the average magnetization is $\bar{\sigma}^x_{\text{th}}$. We use these measures for both initial states, i.e., the ground state and a random state, throughout our analysis.

We may use a quick analogy system to motivate our choice to extract the timescale. Assume we have a three-level V-system and we want to extract the timescale for the spontaneous emission into the ground state when there is no driving of the transitions. (i) We can fit a double-exponential, e.g., $A_1 \exp(\lambda_1 t) + A_2 \exp(\lambda_2 t)$, to capture both timescales at once, which is preferable if we know the number of timescales involved and there is no decay possible between the two excited states in the V-system. (ii) We can fit one exponential knowing that it is not the ideal fit. (iii) We can wait until the ground state has a certain probability close to one and this time is dominated by the longest timescale. When this probability is reached, we can extract the timescale without being biased by the multiple timescales of the dynamics on a short timescale.

However, the number of timescales in the Liouville operator grows with the number of sites in our many-body system and, their contribution will depend on the initial state. The timescales involved in the decay can be far more complicated than a V-system in our case. Thus, we will use option (i) for the two-qubit system knowing the number of timescales is 2 and switch to option (iii) for the remaining analysis avoiding the problems identified with (i) and (ii). We point out that even in the two-qubit case in Figure 6.2, the double-exponential fit cannot resolve the two timescales over the full range of ϕ failing for small ϕ. Choosing a relatively tight threshold of 10^{-10} ensures capturing the longest timescales while being definitely above the machine precision of 10^{-14}. Based on these considerations, we can extract the slowest rate from the expected exponential decay as

$$\Re(\Lambda_j) \quad = \quad \frac{-\log\left(\mathcal{D}(\rho(dt), \rho_{\text{th}})/\mathcal{D}(\rho(T_{\text{th}\mathcal{D}}), \rho_{\text{th}})\right)}{T_{\text{th}\mathcal{D}} - dt}\,, \tag{6.23}$$

where we would replace the distance with the difference to the steady state values for macroscopic observables as the magnetization. The first measurement is after one time step, i.e.,

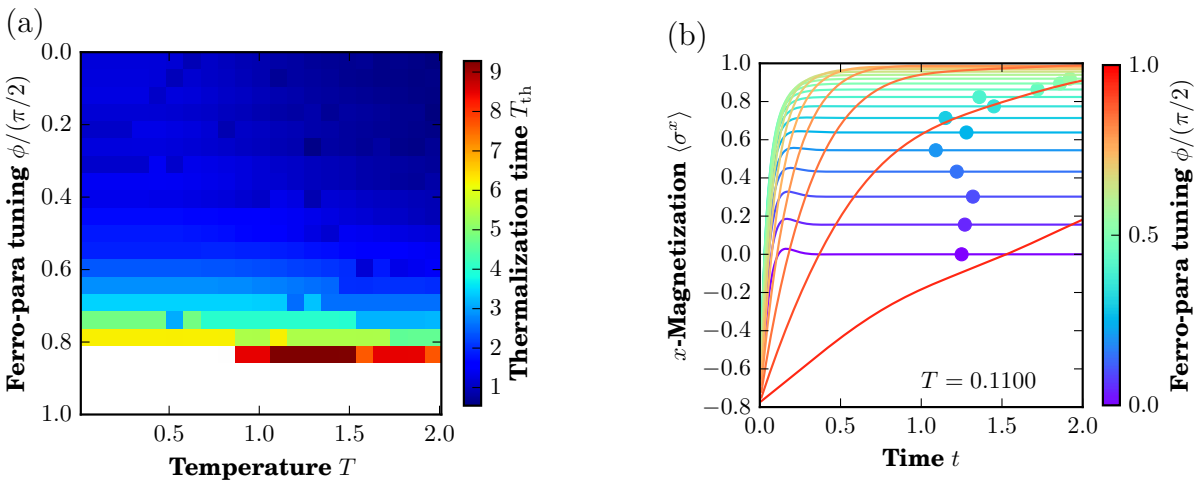

Figure 6.2: *Thermalization timescales for the multi-channel Lindblad operators with a common reservoir.* We consider two different criteria for the thermalization timescale for $N = 2$ qubits in the even sector of the $\mathbb{Z}_2$ symmetry and the operator σ^x in the interaction Hamiltonian starting from a random pure state. We use the scenario ($\mathfrak{a}$) with a common reservoir, i.e., the multi-channel Lindblad equation. (a) The thermalization time necessary to approach the steady state value of the magnetization up to a tolerance. We observe thermalization times for this macroscopic measure larger than our evolution time $\tau = 10$ and indicate the corresponding region in white color. These long timescales appear towards the paramagnetic limit. (b) The local magnetization plotted over time describes the transient behavior to the steady state value, which slows down towards the paramagnetic limit $\phi = \pi/2$, see red colored curves. Circles indicate the time where the magnetization is first within tolerance to the steady state value.

dt, and the value of j depends on the initial state and which timescales it follows. The equation can be derived taking the logarithm of the ratio at two points in time while assuming and exponential decay, i.e., $\mathcal{D}((\rho(dt), \rho_{\rm th})/\mathcal{D}(\rho(T_{{\rm th}\mathcal{D}}), \rho_{\rm th}) = \exp(\Re(\Lambda_j)(dt - t))$. We choose the thermalization time $T_{{\rm th}\mathcal{D}}$ and the first measurement after one time step in the evolution dt to cover a long interval. Later on, we observe in our examples that different initial states pick up either the first non-zero eigenvalues of the Liouville operator $\mathcal{L}$ with $j = 1$ or the second, that is $j = 2$.

6.5.0.1 Two site systems

Figure 6.2(a) shows an increasing thermalization time before the thermalization time is beyond the total time of the evolution $\tau = 10$ for $\phi \gtrsim 0.9\frac{\pi}{2}$, where ϕ can tune between the

ferromagnetic and paramagnetic phase of the quantum Ising model, as previously defined in Eq. (6.1). These simulations are for a random, pure initial state. We point out that both measures yield different thermalization times $T_{\rm th}$ and $T_{{\rm th}\mathcal{D}}$. The maximal difference between the two definitions for all data points with a thermalization time smaller than τ is 3.75. While the magnetization, e.g., $\bar{\sigma}^x$ in the x-direction from Eq. (6.22), is more useful with regards to experiments, we use for further calculations the trace distance $\mathcal{D}$. Orthogonal states can yield the same magnetization or energy. This problem becomes more exposed as we are dealing with an ensemble of pure states. The actual convergence of the x-magnetization at a temperature $T = 0.11$ over time shows the same trend in Figure 6.2(b).

We now analyze in Figure 6.3 the Liouville spectrum corresponding to the Lindblad master equation Eq. (6.6). The figure shows that the Liouville operator has a unique steady state apart from the limit $\phi = \pi/2$. There is another unique steady state for the odd sector of the $\mathbb{Z}_2$ symmetry. The gap, i.e., $|\Re(\Lambda_1)|$, defines the timescale for thermalization. We recall that this gap is in the Liouville operator and not to be mistaken for an energy gap in the Hamiltonian. Larger eigenvalues $|\Re(\Lambda_1)|$ corresponding to a larger gap decay faster. Thus, a particular decay scale Λ_j shall only be relevant if there is no projection of the initial state on the eigenstates $|v_{j'}\rangle\rangle$ with $0 < j' < j$. Treating a first order differential equation, we expect the solution to be an exponential. Thus, we calculate an exponential decay λ for the trace distance between the time-evolved state $\rho(t)$ and the thermal state $\rho_{\rm th}$:

$$\mathcal{D}_{\rm fit} \;=\; \mathcal{D}(\rho(t=0), \rho_{\rm th}) \exp(-\lambda t)\,. \tag{6.24}$$

This decay parameter λ, extracted from Eq. (6.23), captures the importance of the gap in the Liouville spectrum as it matches the value of the gap, see Figure 6.3. To point out the important role of the initial state we compare a system initialized in the ground state $|\,\psi_0\rangle$ with a random pure state $|\,\psi_R\rangle$, and find out that the ground state thermalizes much faster since it does not depend on the slower timescale present in the spectrum of $\mathcal{L}$. In contrast, the random initial state follows the long timescale.

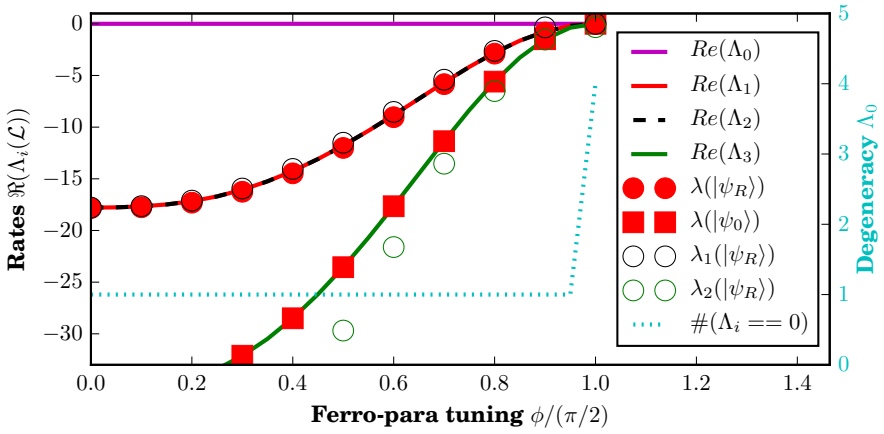

Figure 6.3: *Spectrum of the Liouville operator for the global multi-channel Lindblad operators with a common reservoir.* The spectrum of the Liouville operator, here of case ($\mathfrak{a}$), defines the thermalization timescale and we show the four eigenvalues of the two-spin problem in the even sector as curves. Λ_0 is the steady-state which has to have an eigenvalue with zero real part. The rates emerge from the eigenvalues $\Lambda_j, j > 0$ of the Liouville operator and diminish towards the paramagnetic limit, which leads to increasing thermalization timescales. The empty circles show the results from fitting two exponentials $A_1 \exp(\lambda_1 t) + A_2 \exp(\lambda_2 t)$ for a random initial state $|\psi_R\rangle$ in the time evolution. The filled circles (squares) show the timescale extracted from the trace distance dropping below 10^{-10} for the initial state $|\psi_R\rangle$ ($|\psi_0\rangle$, i.e., the ground state). The four times degenerate eigenvalues Λ_0 in the paramagnetic limit lead to an infinite timescale for $\phi = \pi/2$ and is not an artifact. We point out the different timescales for the different initial states $|\psi_0\rangle$ and $|\psi_R\rangle$.

Finally, Figure 6.3 also shows the failure of thermalization far in the paramagnetic regime. The gap in the Liouville operator closes towards the paramagnetic limit $\phi \to \pi/2$ and reaches degeneracy with four real parts of the overall four eigenvalues being zero within machine precision for $\phi = \pi/2$ preventing any thermalization. This property originates in the fact that the eigenstates of the Hamiltonian are also eigenstates of the operator σ^x in the interaction Hamiltonian building the full spectrum. Thus, they induce no transition but represent a dephasing with respect to the two states of each site k.

6.5.0.2 Beyond two site systems

We now go beyond the two-site system and consider system sizes up to five sites in the even symmetry sector. We investigate how the system size affects the thermalization timescale, how does the coupling scheme affect the thermalization, and question the accuracy

of considering neighborhood single-channels Lindblad operators. Along with this analysis, we consider the multi-channel approach.

Figure 6.4(a) shows the spectra of the common reservoir for different system size $N \in \{2, 3, 4, 5\}$ for the multi-channel approach. We observe that the gap of the Liouville operator is decreasing for increasing system size leading to slower thermalization timescales. Interestingly, although this observation is not shown here, this trend also occurs when considering other decay rates different than the ones given by Eq. (6.29) which are here considered.

The different system-environment coupling schemes are analyzed in Figure 6.4(b). The three thermalization timescales grow for the three cases as one gets closer to the paramagnetic limit, where the thermalization time goes to infinity. Towards the ferromagnetic limit, the thermalization time gets in general shorter. Moreover, the two configurations corresponding to independent local reservoirs thermalizes faster than the one corresponding to a single common reservoir. Indeed, the single common reservoir introduces spin-spin interactions mediated by the field which apparently hinder the thermalization process. Moreover, the configuration corresponding to all spins coupled to their independent reservoirs thermalizes faster than the one where a single spin is coupled. The fact that the gap corresponding to ($\mathfrak{a}$) is in general much smaller than in ($\mathfrak{b}$) can be exploited in two possible directions. On the one hand, a common environment ($\mathfrak{a}$) will slow down dissipation and decoherence processes when they are not desired, like in certain quantum information schemes. On the other hand, independent local reservoirs can be used in situations where a thermal state should be reached as fast as possible. Figure 6.4(c) and (d) corresponding to the common and the independent local reservoirs respectively, show that the qualitative behavior of the thermalization rate with ϕ is the same for all temperatures T. In both cases, we observe a faster thermalization towards the ferromagnetic limit, but the common reservoir case shows additionally the presence of a second gap minimum around $\phi = 0.3(\pi/2)$ for high temperatures starting around $T \geq 0.51$.

We follow the finite-size scaling approach to extrapolate the value of the gap $\Re(\Lambda_1)$ from the spectrum of the Liouville operator $\mathcal{L}$ for the thermodynamic limit $N \to \infty$. We choose the function

$$|\Re(\Lambda_{1\infty}) - \Re(\Lambda_{1N})| \;=\; \alpha_1 N^{\alpha_2} \quad \Longleftrightarrow \quad \Re(\Lambda_{1N}) = \Re(\Lambda_{1\infty}) - \alpha_1 N^{\alpha_2}\,, \tag{6.25}$$

where the system size N is the function argument, the absolute value is resolved by the trend observed in Figure 6.4, and we fit the values $\Re(\Lambda_{1\infty})$, α_1, and α_2. We consider all three scenarios ($\mathfrak{a}$), ($\mathfrak{b}$), and ($\mathfrak{c}$) for the finite-size scaling and do not obtain consistent values throughout our analysis, i.e., some rates for $N = \infty$ become positive including the effects from the errors bar indicated by the fit. Thus, the question of the thermalization rate for larger systems and the thermodynamic limit remains an intriguing question for quantum simulator experiments.

To analyze the feasibility of using neighborhood single-channels to simulate thermalization, we focus on the independent-local reservoir configuration ($\mathfrak{b}$). Figure 6.5 considers the neighborhood single-channel Lindblad operators mimicking the transition between the eigenstates presented in Sec. 6.4; strictly, these Lindblad operators represent the energy transition between eigenstates only in the ferromagnetic and paramagnetic limits, respectively. As previously discussed, these Lindblad operators produce spin flips. In the paramagnetic limit flips spins locally independent of the state on neighboring sites and are described by Eq. (6.17). In contrast, the spin flip is controlled by the nearest-neighbor sites in the ferromagnetic limit, as described by Eqs. (6.18) and (6.19).

We consider the ferromagnetic single-channel Lindblad operators in our simulations to evolve a random initial state until a time $\tau = 10$ and plot its trace distance to the thermal state in Figure 6.5(a). The system size for the data is $N = 4$. We set the minimal trace distance to 10^{-3} for a meaningful coloring away from the ferromagnetic limit $\phi = 0$. As expected, the simple single-channel approach makes the system converge to the thermal state in the ferromagnetic limit, and it does so down to a trace distance of 10^{-14}. We observe that

we reach relatively small trace distances to the thermal state of 10^{-2} for small perturbations of $\phi \lesssim 0.032\frac{\pi}{2}$ around the ferromagnetic limit. However, the neighborhood single-channel approach will not be valid away from the limiting case. Moreover, we observe that apparently, at temperatures $T \leq 0.8$ the system has not thermalized even in the ferromagnetic limit.

The reason for this is that the trace distance has been calculated at a time $\tau = 10$ in which the system might not have thermalized yet. Indeed, as observed in Figure 6.5(b) the gap of the corresponding Liouville operator $\Re(\Lambda_1)$ is decreasing for smaller temperatures, which confirms that a time $\tau = 10$ is not enough to reach the thermal state in (a) for low temperatures. However, we should stress that the same argument does imply that, away from the small region around $\phi = 0$, the system would thermalizing when considering longer times. Indeed, the rate $\Re(\Lambda_1)$ indicates a fast convergence to a steady state, but nevertheless this state does not correspond to the thermal one, which marks the failure of the neighborhood single-channel Lindblad operators beyond the extreme ferromagnetic limit. We discuss the neighborhood single-channel Lindblad operators for the paramagnetic limit in App. 6.8.

6.6 Conclusions

We studied thermalization of the quantum Ising model, concentrating on two different approaches: (i) We consider a multi-channel approach, which considers Lindblad operators producing transitions between the system eigenstates and is valid in any region of the phase diagram. However, it is a problematic approach for larger systems as the number of energy eigenstates increases exponentially with system size. The numerical challenge becomes visible when trying to simulate an open system composed of six qubits, which corresponds to twelve qubits in a closed system from the perspective of taking a matrix exponential or diagonalizing the operator. The careful construction for six qubits has to iterate over 4096 possible Lindblad operators and possibly construct their representation in Liouville space, i.e., a matrix of size 4096×4096. (ii) We introduce neighborhood single-channel operators mimicking the transitions between energy eigenstates in the ferromagnetic and paramagnetic limits. This approach can be generalized to many-body quantum systems but, on the

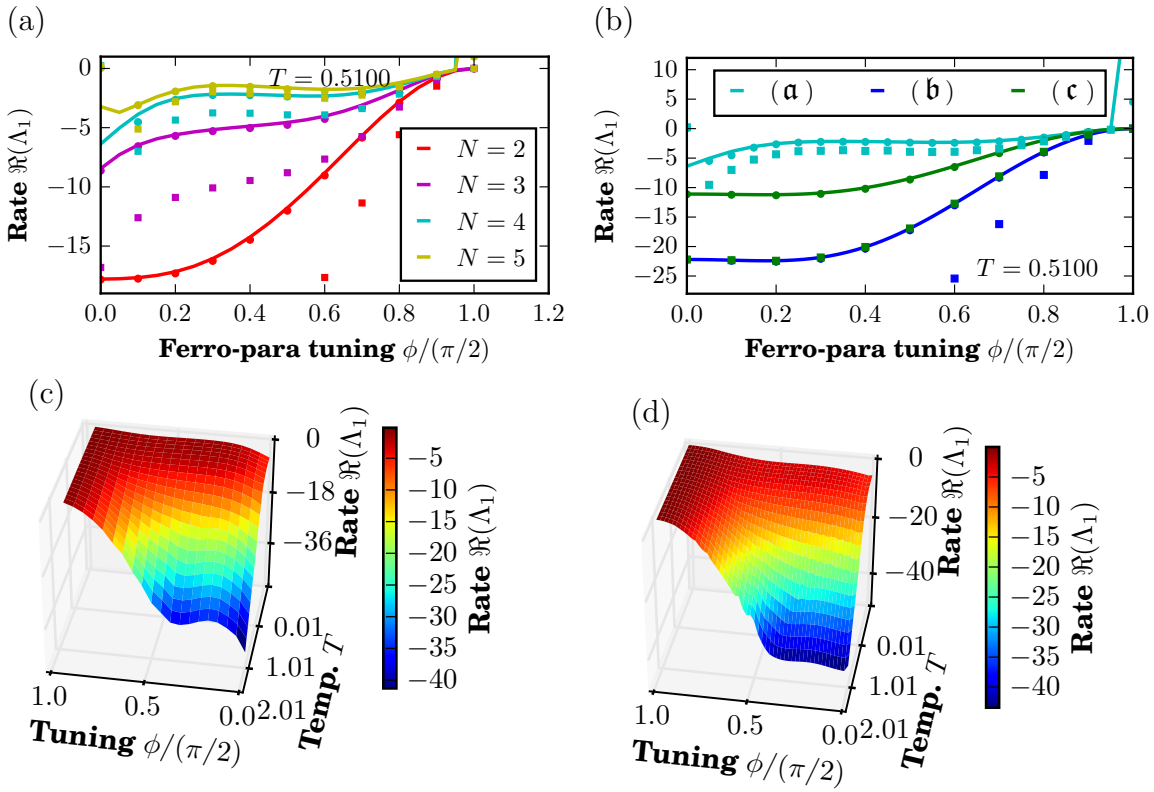

Figure 6.4: *Thermalization rates for different systems with multi-channel Lindblad operators.* We use independent local reservoirs according to scenarios (𝔟) and (𝔠) with a multi-channel Lindblad equation. (a) The rates for (𝔞) extracted from the eigenvalue of the Liouville operator Λ_1 show that the thermalization slows down for an increasing number of qubits, here shown as curves for $N = 2$ to $N = 5$. Circles (squares) represent the rate extracted from the trace distance to the thermal state starting from a random state (the ground state) in a time evolution. (b) The rate for different system-reservoir coupling schemes (𝔞), (𝔟), and (𝔠) from Figure 6.1 for $N = 4$. Curves, circles, and squares as in (a). Independent-local reservoirs have faster thermalization rates; fastest in the case of all sites coupled to their independent-local reservoir. (c) The rates for thermalization for $N = 4$ across different temperatures T and values for ϕ for the common reservoir remain qualitatively the same for temperatures T different to the one chosen in (a). (d) The rates for thermalization for $N = 4$ across different temperatures T and values for ϕ are qualitatively similar for all T for scenario (𝔟).

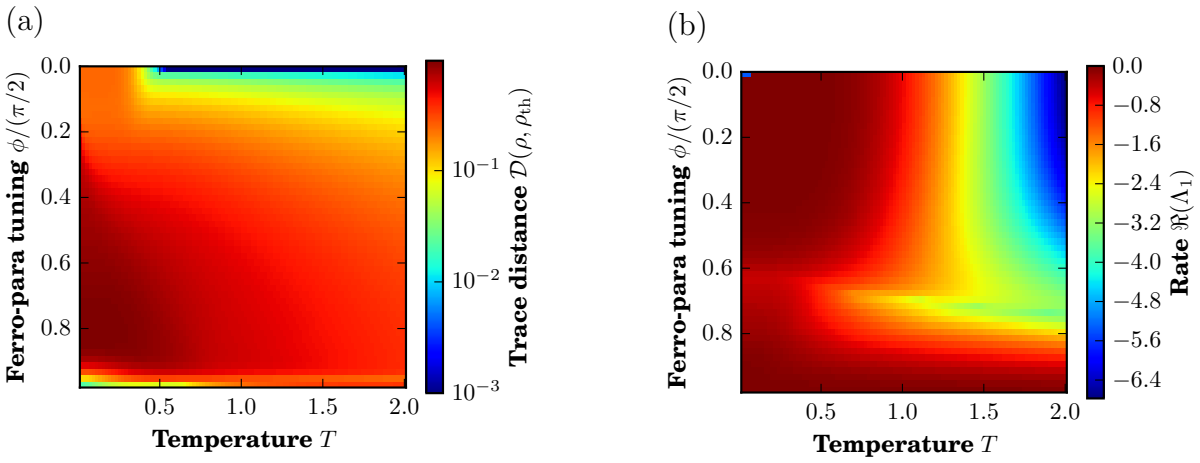

Figure 6.5: *Neighborhood single-channel Lindblad operators.* Three-site Lindblad operators designed for the ferromagnetic limit thermalize in scenario (𝔟) only in a very small region around the ferromagnetic limit, and the multi-channel Lindblad operators are the only way to thermalize the system in the complete range of the phase diagram. (a) The trace distance between the time-evolved quantum state and the thermal state at the end of the time evolution with $\tau = 10$ shows thermalization around the limit $\phi = 0$. (b) The rate given by the eigenvalues of the Liouville operator answers the question if the time-evolved state in (a) does not approach the thermal state at $\tau = 10$ due to long timescales or due to the failure of the neighborhood single-channel approach.

downside, it is only exact in these two limits.

We have studied the thermalization timescales as a function of the type of system reservoir configuration, the number of qubits in our system, and the effectiveness of neighborhood single-channel Lindblad operators. The knowledge of regions with fast or slow timescale allows one to enhance thermalization or to protect at least certain states from decoherence. One could even design protocols to quench the system into a region protected from decoherence and reverse the quench to regain the state when needed. The errors introduced due to non-adiabatic quenches might be less critical than the errors from decoherence while storing the state for a long time. In detail, we found the following.

a) The timescale for thermalization increases toward the paramagnetic limit for all three of our system-reservoir coupling scenarios and the multi-channel Lindblad operators, i.e., the common reservoir, independent local reservoirs for each site, and one local reservoir for the first site. This trend is related to the choice of σ^x in the interaction Hamiltonian between system and reservoir. The common reservoir has the slowest thermalization time among these three cases. Independent local reservoirs thermalize faster if all sites are coupled to a reservoir instead of only one site. This result is supported by data from the spectrum of the Liouville operator and the time evolution of the Lindblad equation. Thus, we suggest the independent-local reservoir scenario to enhance thermalization or the common reservoir to suppress it and extend coherence times.

b) The thermalization time slows down for the common reservoir with increasing system size between two and five qubits. A further aspect is a second local minimum for the gap in the Liouville operator spectrum for five qubits and temperatures above $T \geq 0.51$. Although the minimum is not very distinguished, it might be used as a "sweet spot" with the slowest thermalization timescale around $0.3(\pi/2)$ if the region with $\phi > 0.7(\pi/2)$ and an equivalent timescale is not an option.

c) Our approximation using neighborhood single-channel Lindblad operators, designed for the ferromagnetic and paramagnetic limits, mimic thermalization only in a very narrow region around the extreme limits.

The approach presented leaves open a variety of parameters to be studied in more detail. One may explore all possible angles between the direction of the dipoles and the spin chain, or even think about different dipole directions for each spin. The distance between the spins could also be changed to a non-equidistant spacing to reproduces what happens, for example, in one-dimensional ion traps. There are other questions which can be addressed within this framework, such as the coupling to reservoirs at different temperatures and the resulting

equilibrium temperature and possible temperature gradients. Another possible extension to this research is the increase of precision. If we have such a well-defined description of the system-reservoir interaction being able to express interactions of distant spins mediated by the reservoir, we may include the long-range interactions intrinsic to the system's Hamiltonian in a next step. These long-range interactions occur in various experimental platforms and change the statics and dynamics of a closed system [176].

We also suggest revisiting the secular approximation towards many-body systems; the large number of possible transitions will increase the possibility of smaller differences between two transition frequencies for an increasing number of spins. Moreover, it remains an open question if the conclusions are altered when going beyond the Markov and weak coupling approximations. This question evolves toward the thermalization of non-Markovian open quantum systems [65, 196, 197].

Relaxing these approximations can open the way to consider further experimental setups which are not covered by the approximations of the Lindblad equation. An example is a sympathetic cooling in ultracold atomic and molecular experiments [198]. Ultracold molecules have been considered in the context of collisions leading to decoherence of the system [199, 200], which can be described with the Lindblad master equation. However, considering the environment as a quantum gas may allow one to explore Fermi vs. Bose statistics, by selecting the corresponding isotopes, or choosing a coupling which ranges from weakly to strongly interacting. Further, some open systems cannot be described with a Markov approximation such as ladder-type structures where the system is of the same size as the reservoir [201]; one rail represents the system, the other the environment. Another example is the few nuclear spins of ^{13}C atoms surrounding a color center [202]. Future research may focus on local or neighborhood single-channel operators leading to the thermalization of the system, for and beyond the quantum Ising model. Such a step would help to move beyond five spins and towards the thermodynamic limit.

Acknowledgments – We gratefully appreciate discussions with K. Maeda, S. Montangero, G. Shchedrin, and N. C. Smith. This work was performed in part at the Aspen Center for Physics, which is supported by National Science Foundation grant PHY-1607611. This work was performed with partial support of the NSF under grants PHY-1520915 and OAC-1740130, and the AFOSR under grant FA9550-14-1-0287. We acknowledge support of the U.K. Engineering and Physical Sciences Research Council (EPSRC) through the "Quantum Science with Ultracold Molecules" Programme (Grant No. EP/P01058X/1). I.D.V. was financially supported by the Nanosystems Initiative Munich (NIM) under project No. 862050-2 and the DFG-grant GZ: VE 993/1-1.

6.7 Thermalization for odd symmetry sector and $S_k = \sigma_k^z$

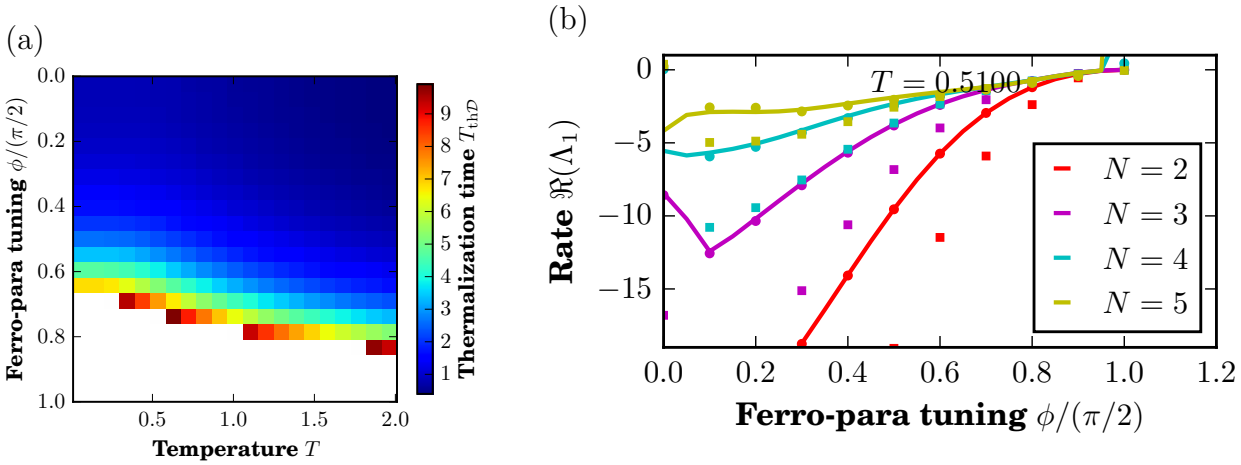

Figure 6.6: *Summary for the odd symmetry sector.* (a) Thermalization timescale for the odd symmetry sector via the trace distance. We observe the same trend as in the even sector, i.e., the timescale becomes longer toward the paramagnetic limit. Time evolution for $\tau = 10$; white regions do not meet criterion within this time. (b) Rate and timescales for different system sizes for the global multi-channel approach and initial states. The curves represent the closing rate toward the paramagnetic limit and for growing system size. A random initial state (circles) matches this rate of the Liouville operator $\mathcal{L}$; the ground state (squares) as initial state thermalizes faster.

The article picked so far the choice of the even symmetry sector of the $\mathbb{Z}_2$ symmetry. We summarize the odd sector in this brief appendix. We expect similar behavior. The thermalization time $T_{\mathrm{th}\mathcal{D}}$ is slowing down toward the paramagnetic limit, see Figure 6.6(a)

for multi-channel Lindblad operators in scenario ($\mathfrak{a}$). If we consider increasing system size N within the same setup, we note that the gap is closing for an increasing number of qubits. The initial state has an equal effect on the timescale as in the even sector: the ground state (squares) has a shorter thermalization time than the random initial state (circles); the latter match the gap $\Re(\Lambda_1)$ in the spectrum of the Liouville operator $\mathcal{L}$. We conclude from these two examples, that the feature presented in our work are not unique to the choice of the symmetry sector.

6.8 Thermalization for $S_k = \sigma_k^z$

Up to now, all the numerical calculations in the paper have considered the system coupling operator as $S_k = \sigma_k^x$. However, in this appendix, we analyze the case $S_k = \sigma_k^z$. We have some obvious changes associated with this choice. (i) The paramagnetic limit can now thermalize as the eigenstates of the paramagnetic limit do not correspond to the eigenstates of S_k. In contrast, thermalization in the ferromagnetic limit suffers from this effect where the Lindblad operators induce a dephasing, but no transitions. (ii) The $\mathbb{Z}_2$ symmetry is broken by the Lindblad operator, and there is no distinction between the odd and the even sector for this choice $S_k = \sigma_k^z$. Figure 6.7(a) shows the thermalization timescale $T_{\text{th}\mathcal{D}}$ for the multi-channel approach, as defined in Eq. (6.22). We observe the opposite behavior than before, as expected: the ferromagnetic limit now has a slow timescale indicated by the white regions where the criterion is not met within $\tau = 10$. We study the gap as a function of the system size in Figure 6.7(b), where the gap of the Liouville operator decreases for larger system sizes comparing $N = 2, 3$ and 4. Analogously to Figure 6.4(a), the data represents scenario ($\mathfrak{a}$) with the multi-channel Lindblad operators. Thus, the thermalization timescale also gets slower for larger systems in this case.

We now consider the single channel Lindblad operators derived in Sec. 6.4 for the paramagnetic limit, which are given by Eq. (6.17) for cooling the system, while its Hermitian conjugate heats it. To rephrase the operators in terms of the transition between states according to Eq. (6.6), we would define the states $|\,y\rangle = |\Uparrow\rangle_k$ and $|\,z\rangle = |\Downarrow\rangle_k$ and the corresponding

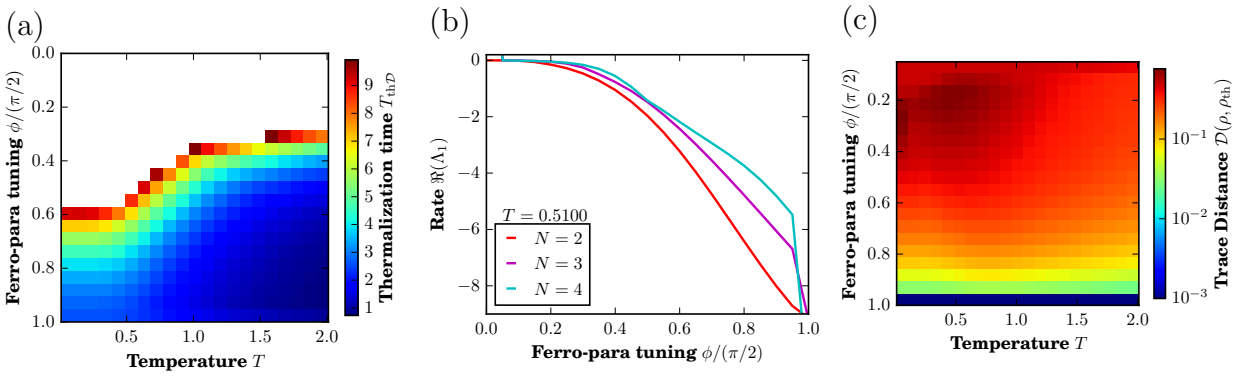

Figure 6.7: *Summary for operator $S_k = \sigma_k^z$ in the interaction Hamiltonian.* (a) The thermalization time $T_{\text{th}\mathcal{D}}$ determined via the trace distance show longer timescales towards the ferromagnetic limit. White areas indicate thermalization times beyond $\tau = 10$. (b) The rate of the Liouville operator for the multi-channel approach with a common reservoir with growing system size. The rate decreases toward the ferromagnetic limit and decreases for increasing system sizes. (c) We choose the neighborhood single-channel Lindblad operators designed for the paramagnetic limit on a system of $L = 4$. We observe that the system only thermalizes in the limit $\phi = \pi/2$ and these operators cannot be used apart from $\phi = \pi/2$. Here, we consider the final state of the time evolution with $\tau = 10$ starting from a random initial state. The rate has non-zero values around $\phi \approx \pi/2$ and does not prevent thermalization.

Lindblad operators $L_{yz}^{[k]}$ and $L_{zy}^{[k]}$. The corresponding energy difference used to calculate the rates is $\Delta = \pm 2g$. These Lindblad operators correspond to spin raising and lowering operators in the x-direction, and therefore they are similar to the single-channel approaches usually considered in the literature [61, 169–171]. Figure 6.7(c) shows that indeed the chosen single-channel operators thermalize the system in the paramagnetic limit. The distance to the thermal state in the limit $\phi = \pi/2$ is below 10^{-12}, but we set the minimal trace distance artificially to 10^{-3} for better visualization of the gradient around the limit.

6.9 Full Spectrum with local and global reservoirs

We turn to a more detailed description of the full spectrum approach. We consider the spins of the quantum Ising model coupled to an electromagnetic field in three dimensions, based on references [191]. The electromagnetic fields serve as an example to settle relations such as the dispersion relation. We provide the major steps to allow readers to follow

the approach. The derivation includes the introduction of the energy eigenstates in the interaction picture to resolve the secular approximation correctly. We obtain the Lindblad equation presented in Eq. (6.6), where we specify the coupling as

$$\mathcal{C}^{[jk]}_{abcd} \;=\; \delta_{b-a,d-c}\gamma^{[jk]}_{abcd}\,, \qquad \mathcal{C}_{abcd} = \sum_{j=1}^{N}\sum_{k=1}^{N}\mathcal{C}^{[jk]}_{abcd}\,. \tag{6.26}$$

The secular approximation introduces the Kronecker delta and forces both Lindblad operators to correspond to the same transition frequency. The coupling $\gamma^{[jk]}_{b-a}$ encodes the dependence on the reservoir and the spatial distance between the sites j and k. To simplify the indices for the coupling $\mathcal{C}$, we put indices running over the complete set of eigenvectors of the system Hamiltonian H_{QI} in the subscript, i.e., a, b, c, and d. The superscript contains in brackets the corresponding sites where the operators S_k from the interaction Hamiltonian is acting on. This operator, in our examples chosen as $S_k = \sigma^x_k$, enters as the overlap of the eigenstates with σ^x_k acting on the eigenstate:

$$\gamma^{[jk]}_{abcd} \;=\; \langle a|\, S_j\, |b\rangle\langle d|\, S_k\, |c\rangle\gamma(b-a,|j-k|)\,. \tag{6.27}$$

The remaining function $\gamma(b-a,|j-k|)$ calculates the coupling for the given reservoir for a specific energy transition and spatial distance. The dependence on the temperature T is implicit. We consider an electromagnetic field in three dimensions in the following as our reservoir for the quantum Ising model. The interaction between the spins in our chain and the reservoir is governed by the dipole interaction with the field. We assume that the dipoles are aligned with the spin chain leading to $\xi \equiv (\vec{d}_{\mathrm{dip}}\cdot\vec{r}_{jk})/(d_{\mathrm{dip}}r_{jk}) = 0$. The last step assumes that the spin chain is orthogonal to the dipole moments of the spins, i.e., the distance $\vec{r}_{jk} = \vec{r}_j - \vec{r}_k$ is orthogonal to the dipole moment of the spins, which are all in equal as previously assumed. The transition frequency is $\omega = b - a$. We use for the zero spatial distance case $j = k$

$$\gamma(\omega,0) = \tilde{n}(\omega)\underbrace{\frac{4\omega^3 d_{\text{dip}}^2}{3C^3}}_{=\Gamma_0} = \tilde{n}(\omega)\Gamma_0\,. \tag{6.28}$$

Here, C is the speed of light and $\tilde{n}(\omega)$ is the Bose-Einstein statistic. The coupling γ for the non-zero spatial distance is

$$\gamma(\omega, r_{jk}) \;=\; \tilde{n}(\omega)\Gamma_0\left((1-\xi^2)\frac{-\mathrm{i}\mathrm{e}^{\mathrm{i}\omega r_{jk}}}{\omega r_{jk}} + (1-3\xi^2)\left(\frac{\mathrm{e}^{\mathrm{i}\omega r_{jk}}}{(\omega r_{jk})^2} + \frac{\mathrm{i}\mathrm{e}^{\mathrm{i}\omega r_{jk}}}{(\omega r_{jk})^3}\right)\right). \tag{6.29}$$

We point out the role of the angle between the direction of the spin chain and the dipoles of the spins, where the dipole of each spin is pointing in the same direction. If the are parallel and $\xi = 1$, the first term in Eq. (6.29) is canceling and the second and third order term in $1/r_{jk}$ survive. In contrast, for $\xi = 1/\sqrt{3}$, the second and third order terms in $1/r_{jk}$ is set to zero, while the first order term remains with a pre-factor of $2/3$. This case is apart from the pre-factors such as Γ_0 the case of the spins coupled to BEC and shows the versatility at which this system can be tuned. We ran simulations similar to Figure 6.4(a) for selected values of ξ and observe the same behavior, i.e., the thermalization timescale slows down for more qubits.

The last missing piece is the Bose-Einstein statistics $\tilde{n}(\omega)$ carrying the dependency on the temperature of the environment. The Bose-Einstein statistics are encoded as

$$\tilde{n}(\omega) \;=\; \begin{cases} n(\omega)\,, & \forall\omega > 0\,, \\ 1 + n(-\omega)\,, & \forall\omega < 0\,. \end{cases} \tag{6.30}$$

This approach leads to an enormous number of multi-channel Lindblad operators. The number of energy levels is d_{loc}^N with a local dimension of $d_{\text{loc}} = 2$ in the quantum Ising model. The possible transitions are then d_{loc}^{2N}. We finally have $d_{\text{loc}}^{2N} N(N+1)/2$ possible couplings iterating over the N sites in the system where the environment could interact. We suggest a reduction of the number of terms in three steps to decrease the number of multi-channel Lindblad operators for future studies. (1) Truncate high energy levels in the quantum system

according to the temperature of the environment. Thus, we assume that the system will thermalize at the same temperature. This approach is restricted to simulations starting in the ground state. If the initial state has a projection onto an excited state which was truncated, there is no possibility to decay to an energetically lower state. Therefore, we do not employ this truncation. (2) Truncate transitions between the energy levels based on the weight $\langle a \mid S_k \mid b \rangle$. For zero overlap, the operator in the interaction Hamiltonian S_k cannot induce the transition between the eigenstates $\mid a \rangle$ and $\mid b \rangle$ and, therefore, the Lindblad operator L_{ab} does not contribute. For small overlaps in comparison to other Lindblad operators, the operator L_{ab} has only an insignificant contribution. (3) Truncate transitions based on the probability of the transition induced by the bath. Overall, these truncations will allow one in future to reduce the number of multi-channel Lindblad operators significantly for a multi-channel approach.

CHAPTER 7

DERIVATION OF THE LINDBLAD EQUATION FOR THE QUANTUM ISING CHAIN

In this chapter, we present a complete derivation of the Lindblad master equation in the case of the quantum Ising chain. Similar derivations can be found in textbooks, e.g., reference [49], but details of the many-body scenario are worth being explicitly discussed. This derivation is used for Chapter 6 and many ideas to elegantly solve the many-body derivation go back to Inés de Vega and various discussions. We start with the definition of the reservoir in Section 7.1 to have this Chapter accessible independent of the other chapters. Then, we move to the interaction picture for the given Hamiltonian. The last pre-calculating discusses the thermal state and its partial trace in Section 7.5. The next steps are dedicated to deriving the Lindblad form in the interaction picture starting with the Born-Markov approximation, the partial trace over the reservoir, the secular approximation, and the conversion to Lindblad form from Sections 7.5 to 7.7. The last two chapters discuss the transformation back to the Schrödinger picture in Section 7.8, and additional aspects on the coupling between system and reservoir.

7.1 Hamiltonian for system and reservoir

We use for our derivation the following Hamiltonians of the system (S) and the reservoir (R), which are

$$H_S = -J\sum_{k=1}^{L-1}\sigma_k^z\sigma_{k+1}^z - g\sum_{k=1}^{L}\sigma_k^x\,, \tag{7.1}$$

$$H_R = \sum_q \omega_q n_q\,. \tag{7.2}$$

Thus, the system is the standard quantum Ising chain for L sites with open boundary conditions, where the Pauli operators σ_k^x and σ_k^z acting on site k. The interaction strength is J, and the coupling to the external field is g. For instance, we represent the reservoir as

a large set of harmonic oscillators with different frequencies, where the summation over q is not specified due to the large number. The number operator n_q measures the occupation of a specific mode q. The complete Hamiltonian (S+R) also includes the interaction Hamiltonian H_I between the two systems

$$H_I = \sum_{k'=1}^{L} \sum_{q'} g_{k'q'} \sigma_{k'}^x b_{q'} + g_{k'q'}^* \sigma_{k'}^x b_{q'}^\dagger \,, \tag{7.3}$$

$$H_{S+R} = H_S + H_R + H_I \,. \tag{7.4}$$

The operator b_q ($b_q^\dagger$) is the annihilation (creation) operator for the mode q within the harmonic oscillators in the reservoir. We use primed indices to distinguish them from the indices use in Eqs (7.1) and (7.2), but the iterate over the same sites and set of harmonic oscillators. The choice of the system operator σ_k^x can be easily replaced with other types of interaction. The coupling constant $g_{k'q'}$ is kept general and depends on the site and frequency of the harmonic oscillator; it fulfills Hermiticity via its complex conjugate $g_{k'q'}^*$; we dedicate one section at the end to explain the coupling and how to handle it, i.e., Section 7.9. We remark that the following commutation relation holds

$$[H_S, H_R] = 0 \,, \tag{7.5}$$

which becomes important in a few steps.

7.2 Interaction picture for system-reservoir scenario

We move to the interaction picture for the derivation of the Lindblad master equation, which we define and derive here. The interaction Hamiltonian is evidently the perturbation $H_1 = H_I$ from Eq. (7.3); the Hamiltonians of the system H_S and reservoir H_R, i.e., $H_0 = H_S + H_R$. The Hamiltonian in the interaction picture is indicated with a superscript I in brackets

$$H^{[I]} = \mathrm{e}^{\mathrm{i}H_0 t} H_1 \mathrm{e}^{-\mathrm{i}H_0 t} \,, \tag{7.6}$$

where the time is t. We set $\hbar = 1$ to avoid a too convoluted notation. We plug in the actual terms for H_0 and H_1 and obtain while using the commutator from Eq. (7.5) to separate the two Hamiltonians in the exponential

$$\begin{aligned} H^{[I]} &= \mathrm{e}^{\mathrm{i}(H_S+H_R)t}\left(\sum_{k'=1}^{L}\sum_{q'} g_{k'q'}\sigma_{k'}^{x}b_{q'} + g_{k'q'}^{*}\sigma_{k'}^{x}b_{q'}^{\dagger}\right)\mathrm{e}^{-\mathrm{i}(H_S+H_R)t} \\ &= \sum_{k'=1}^{L}\sum_{q'}\left(g_{k'q'}\mathrm{e}^{\mathrm{i}H_S t}\sigma_{k'}^{x}\mathrm{e}^{-\mathrm{i}H_S t}\mathrm{e}^{\mathrm{i}H_R t}b_{q'}\mathrm{e}^{-\mathrm{i}H_R t} + g_{k'q'}^{*}\mathrm{e}^{\mathrm{i}H_S t}\sigma_{k'}^{x}\mathrm{e}^{-\mathrm{i}H_S t}\mathrm{e}^{\mathrm{i}H_R t}b_{q'}^{\dagger}\mathrm{e}^{-\mathrm{i}H_R t}\right) \\ &= \sum_{k'=1}^{L}\sum_{q}\left(g_{k'q}\mathrm{e}^{\mathrm{i}H_S t}\sigma_{k'}^{x}\mathrm{e}^{-\mathrm{i}H_S t}b_{q}\mathrm{e}^{-\mathrm{i}-\omega_q t} + g_{k'q}^{*}\mathrm{e}^{\mathrm{i}H_S t}\sigma_{k'}^{x}\mathrm{e}^{-\mathrm{i}H_S t}b_{q}^{\dagger}\mathrm{e}^{\mathrm{i}\omega_q t}\right). \end{aligned} \tag{7.7}$$

In the last step, we used the relations $\mathrm{e}^{\mathrm{i}\omega_q n_q t}b_q\mathrm{e}^{-\mathrm{i}\omega_q n_q t} = b_q\mathrm{e}^{-\mathrm{i}\omega_q t}$ and $\mathrm{e}^{\mathrm{i}\omega_q n_q t}b_q^{\dagger}\mathrm{e}^{-\mathrm{i}\omega_q n_q t} = b_q^{\dagger}\mathrm{e}^{\mathrm{i}\omega_q t}$. These relations also lead to $q = q'$ as number, creation, and annihilation operator acting on different harmonic oscillators $q \neq q'$ commute. These relations are yielded from the Baker-Campell-Hausdorff equation $\exp(X)Y\exp(-X) = Y + [X,Y] + \frac{1}{2!}[X,[X,Y]] + \frac{1}{3!}[X,[X,[X,Y]]] + \ldots$ with X and Y matrices and the commutation relations $\left[b_q^{\dagger}b_q, b_q\right] = b_q^{\dagger}b_q b_q - b_q b_q^{\dagger}b_q = \left[b_q^{\dagger}, b_q\right]b_q = -b_q$ as well as $\left[b_q^{\dagger}b_q, b_q^{\dagger}\right] = b_q^{\dagger}b_q b_q^{\dagger} - b_q^{\dagger}b_q^{\dagger}b_q = b_q^{\dagger}\left[b_q, b_q^{\dagger}\right] = b_q^{\dagger}$ in the following equation. We recall that $n_q = b_q^{\dagger}b_q$.

$$\begin{aligned} \mathrm{e}^{\mathrm{i}\omega n_q t}b_q\mathrm{e}^{-\mathrm{i}\omega n_q t} &= b_q + (\mathrm{i}\omega t)\left[b_q^{\dagger}b_q, b_q\right] + \frac{(\mathrm{i}\omega t)^2}{2!}\left[b_q^{\dagger}b_q, \left[b_q^{\dagger}b_q, b_q\right]\right] + \ldots \\ &= b_q + (\mathrm{i}\omega t)(-b_q) + \frac{(\mathrm{i}\omega t)^2}{2!}\left[b_q^{\dagger}b_q, -b_q\right] + \frac{(\mathrm{i}\omega t)^3}{3!}\left[b_q^{\dagger}b_q, \left[b_q^{\dagger}b_q, -b_q\right]\right] + \ldots \\ &= b_q\left(1 + (-\mathrm{i}\omega t) + \frac{(-\mathrm{i}\omega t)^2}{2!} + \frac{(-\mathrm{i}\omega t)^3}{3!} + \ldots\right) \\ &= b_q\mathrm{e}^{-\mathrm{i}\omega t} \end{aligned} \tag{7.8}$$

The steps for the relation for $b_q^{\dagger}$ are similar, and we leave them to the reader. If we look back at Eq. (7.7), we have successfully resolved the interaction picture for the reservoir, but the exponential of the system Hamiltonian is still present. We use the eigendecomposition of the Hamiltonian to resolve this piece, where the eigendecomposition of H_S is

$$H_S \;=\; \sum_a a\,|\,a\rangle\langle a\,|\,, \tag{7.9}$$

where a is looping over all eigenenergies a and their corresponding eigenvectors $|\,a\rangle$. Shortly, we use the letters b, c, and d to iterate over the same set of eigenstates. The summation limits are not specified to avoid convoluted notations, but the number of eigenstates in the quantum Ising models scales with the system size L as 2^L. The eigenstates form an orthonormal basis, and the identity matrix can be written as

$$\mathbb{I} \;=\; \sum_a |\,a\rangle\langle a\,|\;. \tag{7.10}$$

To resolve the exponentials of the system Hamiltonian in the interaction picture, we concentrate on one term

$$\begin{aligned}
\mathrm{e}^{\mathrm{i}H_S t}\sigma^x_{k'}\mathrm{e}^{-\mathrm{i}H_S t} &= \mathrm{e}^{\mathrm{i}H_S t}\sum_a |\,a\rangle\langle a\,|\,\sigma^x_{k'}\sum_b |\,b\rangle\langle b\,|\,\mathrm{e}^{-\mathrm{i}H_S t}\\
&= \sum_a \mathrm{e}^{\mathrm{i}at}\,|\,a\rangle\langle\epsilon\,|\,\sigma^x_{k'}\sum_b |\,b\rangle\langle b\,|\,\mathrm{e}^{-\mathrm{i}bt}\\
&= \sum_{ab}\mathrm{e}^{\mathrm{i}(a-b)t}\langle a\,|\,\sigma^x_{k'}\,|\,b\rangle\,|\,a\rangle\langle b\,|\\
&= \sum_{ab}\mathrm{e}^{\mathrm{i}\omega_{ab}t}S_{k'}(\omega_{ab})\,,
\end{aligned} \tag{7.11}$$

where we introduce the shortcut for the difference of two eigenenergies $\omega_{ab} \equiv a-b$ and define the operator $S_{k'}(\omega_{ab}) \equiv \langle a\,|\,\sigma^x_{k'}\,|\,b\rangle\,\times|\,a\rangle\langle b\,|$. Thus, we obtain the interaction Hamiltonian

$$H^{[I]} \;=\; \sum_{k'=1}^{L}\sum_{abq}\left(g_{k'q}\mathrm{e}^{\mathrm{i}(\omega_{ab}-\omega_q)t}S_{k'}(\omega_{ab})b_q + g^*_{k'q}\mathrm{e}^{\mathrm{i}(\omega_{ab}+\omega_q)t}S_{k'}(\omega_{ab})b^\dagger_q\right)\;. \tag{7.12}$$

We remind the reader that we loop over four indices, i.e., the site index k' addressing each spin in the chain, a and b loop over the eigenstates of the system Hamiltonian H_S, and the index q refers to the different harmonic oscillators in the reservoir. Furthermore, the following relation holds for the new operator $S_{k'}(\omega_{ab})$

$$S^\dagger_{k'}(\omega_{ab}) \;=\; (\langle a|\,\sigma^x_{k'}\,|b\rangle\,|a\rangle\langle b|)^\dagger = \langle b|\,\sigma^x_{k'}\,|a\rangle\,|b\rangle\langle a| = S_{k'}(\omega_{ba}) = S_{k'}(-\omega_{ab})\,. \quad (7.13)$$

7.3 Implications of tracing thermal states

We study the thermalization and assume that our reservoir is in a thermal state at a temperature T to be specified. This state is defined as

$$\rho_{R\mathrm{th}} \;=\; \frac{\mathrm{e}^{-\beta H_R}}{Z}\,, \quad (7.14)$$

where $\beta = 1/(k_B T)$, $Z = \mathrm{Tr}\left[\exp(-\beta H_R)\right]$ is the partition function, and Tr takes the trace of a matrix. Our reservoir is a set of harmonic oscillators and, thus, diagonal in terms of the harmonic oscillator states. This property leads to the fact that traces over the complete reservoir under the action of annihilation and creation operators never contribute for an odd number of operators; here, the first orders

$$\begin{aligned}
\mathrm{Tr}\left[\rho_R\right] &= 1\,, & (7.15)\\
\mathrm{Tr}\left[b_q\rho_R\right] &= 0\,, \qquad \mathrm{Tr}\left[b^\dagger_q\rho_R\right] = 0\,, & (7.16)\\
\mathrm{Tr}\left[b^\dagger_q b_{q'}\rho_R\right] &= \delta_{qq'}n_q\,, \qquad \mathrm{Tr}\left[b^\dagger_q b^\dagger_{q'}\rho_R\right] = 0\,, \qquad \mathrm{Tr}\left[b_q b_{q'}\rho_R\right] = 0\,, & (7.17)\\
\mathrm{Tr}\left[O_q O_{q'} O_{q''}\rho_R\right] &= 0\,, O_q \in \{b_q, b^\dagger_q\}\,. & (7.18)
\end{aligned}$$

These relations become relevant when taking the partial trace over the reservoir under the action of operators b_q and $b^\dagger_q$.

7.4 Dyson series to Born-Markov approximation

So far, we have collected a lot of mathematical relations; we can now start with the actual derivation of the Lindblad equation. We write down the Dyson series for the density matrix of system and reservoir for all even orders up to the second order

$$\rho_{S+R}(t) \;=\; \rho_{S+R}(t_0) - \int_{t_0}^{t}\mathrm{d}t_1\int_{t_0}^{t_1}\mathrm{d}t_2\left[H^{[I]}(t_1),\left[H^{[I]}(t_2),\rho_{S+R}(t_2)\right]\right]\,. \quad (7.19)$$

We emphasize that this density matrix ρ is in the interaction picture. The argument to exclude the odd orders of the expansion is based on the thermal state and Eqs. (7.16) and (7.18). Later, we take the partial trace over the reservoir being in the thermal state. The interaction Hamiltonian contains only first-order terms acting on the reservoir. Thus, odd orders in the Dyson expansion have odd orders of operators acting on the reservoir and vanish when taking the partial trace under the condition that the reservoir is in the thermal state. Fourth-order and even-order higher terms of the Dyson expansion have contributions, which are truncated. To obtain a differential equation, we take $\mathrm{d}/\mathrm{d}t$ of Eq. (7.19). We continue with

$$\dot{\rho}_{S+R}(t) \;=\; -\int_0^t \mathrm{d}t_2 \left[H^{[I]}(t), \left[H^{[I]}(t_2), \rho_{S+R}(t_2)\right]\right] . \tag{7.20}$$

The folded commutator is not very convenient for proceeding the calculation. We know the fact that the Hamiltonian and the density matrix are Hermitian and use $[H_1, [H_2, \rho]] = H_1H_2\rho - H_1\rho H_2 - H_2\rho H_1 + \rho H_2 H_1 = H_1H_2\rho - H_2\rho H_1 + h.c. = [H_1, H_2\rho] + h.c.$ to simplify Eq. (7.20) as follows

$$\dot{\rho}_{S+R}(t) \;=\; -\int_0^t \mathrm{d}t_2 \left[H^{[I]}(t), H^{[I]}(t_2)\rho_{S+R}(t_2)\right] . \tag{7.21}$$

The next step consists of taking the partial trace over the reservoir. The left-hand side of Eq. (7.21) is equal to the density matrix of the system $\rho \equiv \rho_S$; we discard to subscript S indicating the system. On the right-hand side, we keep the partial trace as Tr_R and look how to approximate it next.

$$\dot{\rho}_{S+R}(t) \;=\; -\int_0^t \mathrm{d}t_2 \mathrm{Tr}_R \left[\left[H^{[I]}(t), H^{[I]}(t_2)\rho_{S+R}(t_2)\right]\right] . \tag{7.22}$$

The following assumptions allow one to obtain the Lindblad master equation. First, we assume that system and reservoir are in a product state at all times

$$\rho_{S+R}(t_2) \approx \rho(t_2) \otimes \rho_R(t_2)\,, \tag{7.23}$$

This step is a good approximation if the correlations are small and can be written as $\rho_{S+R}(t_2) = (1-\epsilon)\rho(t_2) \otimes \rho_R(t_2) + \epsilon\rho'(t_2) \otimes \rho'_R(t_2)$ in the next order and $\epsilon \ll 1$. The interpretation is that the correlations decay due to the large reservoir much faster than the system can react. One example would be the spontaneous emission of a two-level system coupled to the vacuum; it is unlikely that the emitted photon returns to the two-level system. The picture changes completely when we would consider a two-level system in an optical cavity, and above assumption breaks down. The second step is to approximate the state of $\rho_R(t_2)$. The assumption is that the reservoir is large in comparison to our system and the perturbation due to the interaction are minimal. Thus, the reservoir stays in its thermal state

$$\rho_R(t_2) \approx \rho_{R\mathrm{th}}\,. \tag{7.24}$$

These two approximations in Eqs. (7.23) and (7.23) are the *Born approximation* for the Lindblad equation. These approximations help us indeed to advance with Eq. (7.22):

$$\dot{\rho}_{S+R}(t) = -\int_0^t \mathrm{d}t_2 \mathrm{Tr}_R\left[\left[H^{[I]}(t), H^{[I]}(t_2)\rho(t_2) \otimes \rho_{R\mathrm{th}}\right]\right]\,. \tag{7.25}$$

The *Markov approximation* is more subtle than the Born approximation. We resolve the two different time dependencies of the density matrix for the system, i.e., $\rho(t)$ on the left-hand side and $\rho(t_2)$ on the right-hand side, with the approximation

$$\rho(t_2) \approx \rho(t)\,. \tag{7.26}$$

The justification is that the time scale of the system's evolution is much longer than the integration time considered. In other words, the system does not adapt fast enough that the density matrix changes in between t and t_2. Systems which would reach their thermal

or equilibrium state very fast would break this assumption. We end up with the following equation after the Born-Markov approximation

$$\dot{\rho}_{S+R}(t) \;=\; -\int_0^t \mathrm{d}t_2 \mathrm{Tr}_R \left[\left[H^{[I]}(t), H^{[I]}(t_2)\rho(t)\otimes\rho_{R\mathrm{th}}\right]\right] . \tag{7.27}$$

The summary of the timescales requires that the correlation time in the reservoir is much shorter than the integration time, and the integration time itself is much shorter than the timescale of the system.

7.5 Partial trace over the reservoir

The main goal of the Lindblad equation is to trace over the reservoir degrees of freedom to simplify the time evolution of our system. After the Born-Markov approximation, we can now calculate the partial trace starting from Eq. (7.27). The interaction Hamiltonian and its corresponding indices will inflate notations quickly and we consider the partial trace term by term. We recall the relations for a contribution when tracing over the thermal state presented in Eq. (7.17); furthermore, we know $b_q b_q^\dagger = b_q^\dagger b_q + 1 = n_q + 1$. The first term is simplified to

$$\begin{aligned}
&\mathrm{Tr}_R\left[H^{[I]}(t)H^{[I]}(t_2)\left(\rho(t)\otimes\rho_{R\mathrm{th}}\right)\right] \\
&= \mathrm{Tr}_R\Bigg[\left(\sum_{k'=1}^{L}\sum_{abq}\left(g_{k'q}\mathrm{e}^{\mathrm{i}(\omega_{ab}-\omega_q)t}S_{k'}(\omega_{ab})b_q + g^*_{k'q}\mathrm{e}^{\mathrm{i}(\omega_{ab}+\omega_q)t}S_{k'}(\omega_{ab})b_q^\dagger\right)\right) \\
&\quad\times\left(\sum_{k''=1}^{L}\sum_{cdq''}\left(g_{k''q''}\mathrm{e}^{\mathrm{i}(\omega_{cd}-\omega_{q''})t_2}S_{k''}(\omega_{cd})b_{q''} + g^*_{k''q''}\mathrm{e}^{\mathrm{i}(\omega_{cd}+\omega_{q''})t_2}S_{k''}(\omega_{cd})b_{q''}^\dagger\right)\right) \\
&\quad\times\left(\rho(t)\otimes\rho_{R\mathrm{th}}\right)\Bigg] \\
&= \sum_{k'k''=1}^{L}\sum_{abcdqq''}\Bigg(\mathrm{e}^{\mathrm{i}(\omega_{ab}t+\omega_{cd}t_2)}S_{k'}(\omega_{ab})S_{k''}(\omega_{cd})\rho(t)g_{k'q}g^*_{k''q''}\mathrm{e}^{-\mathrm{i}(\omega_q t-\omega_{q''}t_2)}\mathrm{Tr}\left[b_q b_{q''}^\dagger\rho_{R\mathrm{th}}\right] \\
&\quad+\mathrm{e}^{\mathrm{i}(\omega_{ab}t+\omega_{cd}t_2)}S_{k'}(\omega_{ab})S_{k''}(\omega_{cd})\rho(t)g^*_{k'q}g_{k''q''}\mathrm{e}^{\mathrm{i}(\omega_q t-\omega_{q''}t_2)}\mathrm{Tr}\left[b_{q''}^\dagger b_q\rho_{R\mathrm{th}}\right]\Bigg)
\end{aligned}$$

$$= \sum_{k'k''=1}^{L} \sum_{abcdq} \Big(\mathrm{e}^{\mathrm{i}(\omega_{ab}t+\omega_{cd}t_2)} S_{k'}(\omega_{ab}) S_{k''}(\omega_{cd}) \rho(t) \\ \times \left(g_{k'q} g^*_{k''q} \mathrm{e}^{-\mathrm{i}\omega_q(t-t_2)} \langle n_q \rangle_R + g^*_{k'q} g_{k''q} \mathrm{e}^{\mathrm{i}(\omega_q(t-t_2)} \left(\langle n_q \rangle_R + 1 \right) \right) \Big) \tag{7.28}$$

Several changes happened in the last three steps. Each Hamiltonian $H^{[I]}(t)$ and $H^{[I]}(t_2)$ needs its own set of indices. The Hamiltonian $H^{[I]}(t)$ keeps the indices from Eq. (7.12). We do the following replacements for $H^{[I]}(t_2)$ with regards to Eq. (7.12): site index $k' \to k''$, the index for the harmonic oscillator $q \to q''$, and indices for the eigenstates of the system Hamiltonian $a \to c$ and $b \to d$. We separate the terms acting on the system and the reservoir, which allows us to transfer the partial trace into a trace over the degrees of freedom of the reservoir. We obtain a Kronecker delta $\delta_{q,q''}$ while tracing out and denote the expectation value of the number operator as $\langle n_q \rangle_R$ and drop the subscript and brackets in the following, i.e., n_q. We need to simplify this notation an introduce the coupling

$$C_{k'k''}(q, t-t_2) = g_{k'q} g^*_{k''q} \mathrm{e}^{-\mathrm{i}\omega_q(t-t_2)} n_q + g^*_{k'q} g_{k''q} \mathrm{e}^{\mathrm{i}(\omega_q(t-t_2)} \left(n_q + 1 \right) . \tag{7.29}$$

The detailed derivation of the second term is left to the reader as the necessary steps are already presented; we obtain

$$\mathrm{Tr}_R \left[H^{[I]}(t_2) \left(\rho(t) \otimes \rho_{R\mathrm{th}} \right) H^{[I]}(t) \right] = C_{k'k''}(q, t-t_2) \mathrm{e}^{\mathrm{i}(\omega_{ab}t+\omega_{cd}t_2)} \\ \times S_{k'}(\omega_{ab}) S_{k''}(\omega_{cd}) \rho(t) . \tag{7.30}$$

Overall, we have now the following differential equation, which only contains the density matrix of the system

$$\dot{\rho}(t) = -\int_0^t \mathrm{d}t_2 \sum_{k'k''=1}^{L} \sum_{abcdq} C_{k'k''}(q, t-t_2) \mathrm{e}^{\mathrm{i}(\omega_{ab}t+\omega_{cd}t_2)} \\ \times \left[S_{k'}(\omega_{ab}), S_{k''}(\omega_{cd}) \rho(t) \right] + h.c. \tag{7.31}$$

7.6 The secular approximation

We need a few more steps starting at Eq. (7.31) to reach the secular approximation. We start with a change of variables introducing $\tau = t - t_2$ leading to

$$\begin{aligned}\dot{\rho}(t) &= -\int_0^t \mathrm{d}\tau \sum_{k'k''=1}^{L} \sum_{abcdq} C_{k'k''}(q,\tau)\mathrm{e}^{\mathrm{i}(\omega_{ab}t+\omega_{cd}(t-\tau))} \\ &\quad \times [S_{k'}(\omega_{ab}), S_{k''}(\omega_{cd})\rho(t)] + h.c. \end{aligned} \tag{7.32}$$

In addition, we transform $\omega_{ab} \to -\omega_{ab}$ and at the same time $S_{k'}(\omega_{ab}) \to S^{\dagger}_{k'}(\omega_{ab})$, which is justified because we are summing over all transitions $a \to b$ and the corresponding transition $b \to a$ must also be in the summation. Thus, we have

$$\begin{aligned}\dot{\rho}(t) &= -\int_0^t \mathrm{d}\tau \sum_{k'k''=1}^{L} \sum_{abcdq} C_{k'k''}(q,\tau)\mathrm{e}^{\mathrm{i}(\omega_{cd}-\omega_{ab})t}\mathrm{e}^{-\mathrm{i}\omega_{cd}\tau} \\ &\quad \times \left[S^{\dagger}_{k'}(\omega_{ab}), S_{k''}(\omega_{cd})\rho(t)\right] + h.c. \end{aligned} \tag{7.33}$$

Moreover, we switch the terms in the commutator in exchange for the minus sign in front of the integral

$$\begin{aligned}\dot{\rho}(t) &= \int_0^t \mathrm{d}\tau \sum_{k'k''=1}^{L} \sum_{abcdq} C_{k'k''}(q,\tau)\mathrm{e}^{\mathrm{i}(\omega_{cd}-\omega_{ab})t}\mathrm{e}^{-\mathrm{i}\omega_{cd}\tau} \\ &\quad \times \left[S_{k''}(\omega_{cd})\rho(t), S^{\dagger}_{k'}(\omega_{ab})\right] + h.c. \end{aligned} \tag{7.34}$$

The interesting term is $\exp(\mathrm{i}(\omega_{cd}-\omega_{ab})t)$. For large difference $\omega_{cd}-\omega_{ab}$, the term underlying sine and cosine term oscillate within a very short period. Similar, fast rotating terms are truncated in the rotating wave approximation. The *secular approximation* approximates this difference by accounting only terms which have zero difference

$$\mathrm{e}^{\mathrm{i}(\omega_{cd}-\omega_{ab})t)} \approx \delta(\omega_{cd}-\omega_{ab})\,. \tag{7.35}$$

This approximation implies that t is huge in comparison to justify this assumption; To ensure this condition, we send the integration boundary $t \to \infty$ and obtain after the secular approximation the following equation describing the dynamics of the density matrix

$$\begin{aligned} \dot{\rho}(t) &= \int_0^\infty \mathrm{d}\tau \sum_{k'k''=1}^{L} \sum_{abcdq} C_{k'k''}(q,\tau)\delta(\omega_{cd}-\omega_{ab})\mathrm{e}^{-\mathrm{i}\omega_{cd}\tau} \\ &\quad \times \left[S_{k''}(\omega_{cd})\rho(t), S^\dagger_{k'}(\omega_{ab})\right] + h.c. \end{aligned} \tag{7.36}$$

The secular approximation is violated for almost degenerate transition frequencies with a vanishing $\omega_{cd}-\omega_{ab} \to 0$. This situation occurs for almost degenerate energy levels, but is not restricted to such a case. An ideal Hamiltonian for fulfilling the secular approximation is a harmonic oscillator as the system with equal level spacing and, thus, no almost degeneracies. We remark that the terms in the commutator do not depend on τ. Therefore, we can define a new variable, which contains the dependency on the integral over τ

$$\Gamma = \Gamma_{abcdqk'k''} = \int_0^\infty \mathrm{d}\tau C_{k'k''}(q,\tau)\delta(\omega_{cd}-\omega_{ab})\mathrm{e}^{-\mathrm{i}\omega_{cd}\tau}\,, \tag{7.37}$$

The resulting equation is almost in Lindblad form

$$\dot{\rho}(t) = \sum_{k'k''=1}^{L} \sum_{abcdq} \Gamma_{abcdqk'k''} \left[S_{k''}(\omega_{cd})\rho(t), S^\dagger_{k'}(\omega_{ab})\right] + h.c. \tag{7.38}$$

7.7 The Lindblad form in the interaction picture

The coupling Γ is complex so far. To transform Eq. (7.38) into Lindblad form, we separate the real and complex part as follows

$$\gamma = \Re(\Gamma)\,, \qquad \eta = \Im(\Gamma)\,, \tag{7.39}$$

where the following relations hold for switching the indices of the sites k' and k''

$$\gamma_{abcdqk'k''} = \gamma_{abcdqk''k'}\,, \qquad \eta_{abcdqk'k''} = -\eta_{abcdqk''k'}\,. \tag{7.40}$$

Using this definition in terms of the real and imaginary part, we obtain in a first step

$$\dot{\rho}(t) = \sum_{k'k''=1}^{L} \sum_{abcdq} (\gamma_{abcdqk'k''} + \mathrm{i}\eta_{abcdqk'k''}) \left[S_{k''}(\omega_{cd})\rho(t), S^{\dagger}_{k'}(\omega_{ab}) \right] + h.c. \tag{7.41}$$

Now, we consider the real part of this equation. We have the following terms

$$\begin{aligned} \Re(\dot{\rho}(t)) = \sum_{k'k''=1}^{L} \sum_{abcdq} \gamma_{abcdqk'k''} \Big(& S_{k''}(\omega_{cd})\rho(t)S^{\dagger}_{k'}(\omega_{ab}) + S_{k'}(\omega_{ab})\rho(t)S^{\dagger}_{k''}(\omega_{cd}) \\ & - S^{\dagger}_{k'}(\omega_{ab})S_{k''}(\omega_{cd})\rho(t) - \rho(t)S^{\dagger}_{k''}(\omega_{cd})S_{k'}(\omega_{ab}) \Big) . \end{aligned} \tag{7.42}$$

We use Eq. (7.40) to switch the site indices of the second and fourth term; we change $\omega_{ab} \leftrightarrow \omega_{cd}$ which is possible due to the fact that the summation over ab and cd loop over the same set of eigenvectors. These two steps turn the real part into Lindblad form

$$\begin{aligned} \Re(\dot{\rho}(t)) &= \sum_{k'k''=1}^{L} \sum_{abcdq} \gamma_{abcdqk'k''} \Big(S_{k''}(\omega_{cd})\rho(t)S^{\dagger}_{k'}(\omega_{ab}) + S_{k''}(\omega_{ab})\rho(t)S^{\dagger}_{k'}(\omega_{cd}) \\ &\qquad - S^{\dagger}_{k'}(\omega_{ab})S_{k''}(\omega_{cd})\rho(t) - \rho(t)S^{\dagger}_{k'}(\omega_{cd})S_{k''}(\omega_{ab}) \Big) \\ &= \sum_{k'k''=1}^{L} \sum_{abcdq} \gamma_{abcdqk'k''} \Big(S_{k''}(\omega_{cd})\rho(t)S^{\dagger}_{k'}(\omega_{ab}) + S_{k''}(\omega_{cd})\rho(t)S^{\dagger}_{k'}(\omega_{ab}) \\ &\qquad - S^{\dagger}_{k'}(\omega_{ab})S_{k''}(\omega_{cd})\rho(t) - \rho(t)S^{\dagger}_{k'}(\omega_{ab})S_{k''}(\omega_{cd}) \Big) \\ &= \sum_{k'k''=1}^{L} \sum_{abcdq} \gamma_{abcdqk'k''} \Big(2S_{k''}(\omega_{cd})\rho(t)S^{\dagger}_{k'}(\omega_{ab}) - \left\{ S^{\dagger}_{k'}(\omega_{ab})S_{k''}(\omega_{cd}), \rho(t) \right\} \Big) , \end{aligned} \tag{7.43}$$

which is the Lindblad form for the dissipative part of the evolution. We still have to consider the imaginary part with the couplings η. The same approach leads to

$$
\begin{aligned}
\Im(\dot{\rho}(t)) &= \sum_{k'k''=1}^{L} \sum_{abcdq} \mathrm{i}\eta_{abcdqk'k''} \Big(S_{k''}(\omega_{cd})\rho(t)S^{\dagger}_{k'}(\omega_{ab}) + S_{k'}(\omega_{ab})\rho(t)S^{\dagger}_{k''}(\omega_{cd}) \\
&\qquad -S^{\dagger}_{k'}(\omega_{ab})S_{k''}(\omega_{cd})\rho(t) - \rho(t)S^{\dagger}_{k''}(\omega_{cd})S_{k'}(\omega_{ab}) \Big) \\
&= \sum_{k'k''=1}^{L} \sum_{abcdq} \mathrm{i}\eta_{abcdqk'k''} \Big(S_{k''}(\omega_{cd})\rho(t)S^{\dagger}_{k'}(\omega_{ab}) - S_{k''}(\omega_{ab})\rho(t)S^{\dagger}_{k'}(\omega_{cd}) \\
&\qquad -S^{\dagger}_{k'}(\omega_{ab})S_{k''}(\omega_{cd})\rho(t) + \rho(t)S^{\dagger}_{k'}(\omega_{cd})S_{k''}(\omega_{ab}) \Big) \\
&= \sum_{k'k''=1}^{L} \sum_{abcdq} \mathrm{i}\eta_{abcdqk'k''} \Big(S_{k''}(\omega_{cd})\rho(t)S^{\dagger}_{k'}(\omega_{ab}) - S_{k''}(\omega_{cd})\rho(t)S^{\dagger}_{k'}(\omega_{ab}) \\
&\qquad -S^{\dagger}_{k'}(\omega_{ab})S_{k''}(\omega_{cd})\rho(t) + \rho(t)S^{\dagger}_{k'}(\omega_{ab})S_{k''}(\omega_{cd}) \Big) \\
&= \sum_{k'k''=1}^{L} \sum_{abcdq} -\mathrm{i}\eta_{abcdqk'k''} \left[S^{\dagger}_{k'}(\omega_{ab})S_{k''}(\omega_{cd}), \rho(t) \right] . \qquad (7.44)
\end{aligned}
$$

Thus, the imaginary part is not contributing to the dissipative part of the dynamics, but represents a correction term to the Hamiltonian reflected in the von-Neumann equation for the time evolution of density matrix, i.e., $\dot{\rho} = -\mathrm{i}\,[H, \rho]$. The complete Lindblad equation in the interaction picture with real and complex contributions from the coupling Γ is

$$
\begin{aligned}
\dot{\rho}(t) &= \sum_{k'k''=1}^{L} \sum_{abcdq} -\mathrm{i}\eta_{abcdqk'k''} \left[S^{\dagger}_{k'}(\omega_{ab})S_{k''}(\omega_{cd}), \rho(t) \right] \qquad (7.45) \\
&\quad + \sum_{k'k''=1}^{L} \sum_{abcdq} \gamma_{abcdqk'k''} \Big(2S_{k''}(\omega_{cd})\rho(t)S^{\dagger}_{k'}(\omega_{ab}) - \Big\{ S^{\dagger}_{k'}(\omega_{ab})S_{k''}(\omega_{cd}), \rho(t) \Big\} \Big) .
\end{aligned}
$$

7.8 The Lindblad form in the Schrödinger picture

The last major step is a representation of the Lindblad master equation in the Schrödinger picture. The transformation of the left-hand side of Eq. (7.45) with $\rho(t) = \mathrm{e}^{\mathrm{i}H_S(t-t_0)}\rho^{[S]}(t)\,\mathrm{e}^{-\mathrm{i}H_S(t-t_0)}$ yields

$$
\dot{\rho}(t) = \mathrm{e}^{\mathrm{i}H_S(t-t_0)} \left(\dot{\rho}^{[S]}(t) + \mathrm{i}\left[H_S, \rho^{[S]}(t) \right] \right) \mathrm{e}^{-\mathrm{i}H_S(t-t_0)} , \qquad (7.46)
$$

where the superscript S in brackets indicates that the density matrix is in the Schrödinger picture. Thus, we have to multiply our terms on the right-hand side in Eq. (7.45) with $\mathrm{e}^{-\mathrm{i}H_S(t-t_0)}$ from the left and $\mathrm{e}^{\mathrm{i}H_S(t-t_0)}$ from the right. We proceed term by term while transforming the density in these terms from the interaction picture to the Schrödinger picture. Moreover, we insert identities when convenient.

$$\begin{aligned}
&\mathrm{e}^{-\mathrm{i}H_S(t-t_0)} S^\dagger_{k'}(\omega_{ab}) S_{k''}(\omega_{cd}) \left(\mathrm{e}^{\mathrm{i}H_S(t-t_0)} \rho^{[S]}(t) \mathrm{e}^{-\mathrm{i}H_S(t-t_0)}\right) \mathrm{e}^{\mathrm{i}H_S(t-t_0)} \\
&= \mathrm{e}^{-\mathrm{i}H_S(t-t_0)} S^\dagger_{k'}(\omega_{ab}) \mathrm{e}^{\mathrm{i}H_S(t-t_0)} \mathrm{e}^{-\mathrm{i}H_S(t-t_0)} S_{k''}(\omega_{cd}) \mathrm{e}^{\mathrm{i}H_S(t-t_0)} \rho^{[S]}(t)
\end{aligned} \tag{7.47}$$

We now act with the eigenstates used in the definition of the operators $S^\dagger_{k'}(\omega_{ab})$ and $S_{k''}(\omega_{cd})$ on the corresponding exponentials turning the Hamiltonian into a phase

$$\begin{aligned}
\ldots &= \mathrm{e}^{-\mathrm{i}b(t-t_0)} S^\dagger_{k'}(\omega_{ab}) \mathrm{e}^{\mathrm{i}a(t-t_0)} \mathrm{e}^{-\mathrm{i}c(t-t_0)} S_{k''}(\omega_{cd}) \mathrm{e}^{\mathrm{i}d(t-t_0)} \rho^{[S]}(t) \\
&= \mathrm{e}^{((a-b)-(c-d))(t-t_0)} S^\dagger_{k'}(\omega_{ab}) S_{k''}(\omega_{cd}) \rho^{[S]}(t) = S^\dagger_{k'}(\omega_{ab}) S_{k''}(\omega_{cd}) \rho^{[S]}(t)\,.
\end{aligned} \tag{7.48}$$

The phase term vanishes due to the delta function $\delta(\omega_{ab} - \omega_{cd})$. The second term can be simplified with an analog approach

$$\begin{aligned}
&\mathrm{e}^{-\mathrm{i}H_S(t-t_0)} \left(\mathrm{e}^{\mathrm{i}H_S(t-t_0)} \rho^{[S]}(t) \mathrm{e}^{-\mathrm{i}H_S(t-t_0)}\right) S^\dagger_{k'}(\omega_{ab}) S_{k''}(\omega_{cd}) \mathrm{e}^{\mathrm{i}H_S(t-t_0)} \\
&= \rho^{[S]}(t) \mathrm{e}^{-\mathrm{i}H_S(t-t_0)} S^\dagger_{k'}(\omega_{ab}) \mathrm{e}^{\mathrm{i}H_S(t-t_0)} \mathrm{e}^{-\mathrm{i}H_S(t-t_0)} S_{k''}(\omega_{cd}) \mathrm{e}^{\mathrm{i}H_S(t-t_0)} \\
&= \rho^{[S]}(t) \mathrm{e}^{-\mathrm{i}b(t-t_0)} S^\dagger_{k'}(\omega_{ab}) \mathrm{e}^{\mathrm{i}a(t-t_0)} \mathrm{e}^{-\mathrm{i}c(t-t_0)} S_{k''}(\omega_{cd}) \mathrm{e}^{\mathrm{i}d(t-t_0)} \\
&= \rho^{[S]}(t) \mathrm{e}^{\mathrm{i}((a-b)-(c-d))(t-t_0)} S^\dagger_{k'}(\omega_{ab}) S_{k''}(\omega_{cd}) = S^\dagger_{k'}(\omega_{ab}) S_{k''}(\omega_{cd})\,,
\end{aligned} \tag{7.49}$$

and the last term is

$$\begin{aligned}
&\mathrm{e}^{-\mathrm{i}H_S(t-t_0)} S^\dagger_{k'}(\omega_{ab}) \left(\mathrm{e}^{\mathrm{i}H_S(t-t_0)} \rho^{[S]}(t) \mathrm{e}^{-\mathrm{i}H_S(t-t_0)}\right) S_{k''}(\omega_{cd}) \mathrm{e}^{\mathrm{i}H_S(t-t_0)} \\
&= \mathrm{e}^{-\mathrm{i}b(t-t_0)} S^\dagger_{k'}(\omega_{ab}) \mathrm{e}^{\mathrm{i}a(t-t_0)} \rho^{[S]}(t) \mathrm{e}^{-\mathrm{i}c(t-t_0)} S_{k''}(\omega_{cd}) \mathrm{e}^{\mathrm{i}d(t-t_0)} \\
&= \mathrm{e}^{\mathrm{i}((a-b)-(c-d))(t-t_0)} S^\dagger_{k'}(\omega_{ab}) \rho^{[S]}(t) \mathrm{e}^{-\mathrm{i}c(t-t_0)} S_{k''}(\omega_{cd}) = S^\dagger_{k'}(\omega_{ab}) \rho^{[S]}(t) \mathrm{e}^{-\mathrm{i}c(t-t_0)} S_{k''}(\omega_{cd})\,,
\end{aligned} \tag{7.50}$$

The Lindblad equation in the Schrödinger picture is then defined as

$$\dot{\rho}^{[S]}(t) = -\mathrm{i}\left[H_S + \sum_{k'k''=1}^{L}\sum_{abcdq}\eta_{abcdqk'k''}S^{\dagger}_{k'}(\omega_{ab})S_{k''}(\omega_{cd}), \rho^{[S]}(t)\right] \tag{7.51}$$
$$+ \sum_{k'k''=1}^{L}\sum_{abcdq}\gamma_{abcdqk'k''}\Big(2S_{k''}(\omega_{cd})\rho^{[S]}(t)S^{\dagger}_{k'}(\omega_{ab}) - \Big\{S^{\dagger}_{k'}(\omega_{ab})S_{k''}(\omega_{cd}), \rho(t)\Big\}\Big).$$

7.9 Notes on the coupling of the Lindblad operators

We have excluded the coupling constant Γ and variables hidden within so far from the discussion. We catch up with this discussion now. The coupling contains the integration over the time and the frequencies q of the harmonic oscillator. The most common approach is the replace the sum over q with and integration, i.e., $\sum_q \to \int \mathrm{d}q$. This step is justified as the reservoir must be large to fulfill the Born-Markov approximation and a sufficient number of modes is present. Depending on the geometry of the environment, the integration over $\mathrm{d}q$ can be in one, two, or three dimensions. Moreover, the different types of reservoir enter over the dispersion relation, which is defined via $g_{k'k''}$. The dependence on temperature also enters via Γ, as the coupling depends on $\langle n_q\rangle_R$ varying with the temperature of the reservoir. We do not go into details as various configurations can be explored from the outline we have given.

CHAPTER 8

EXACT DIAGONALIZATION AND OTHER ENTANGLEMENT-ACCURATE METHODS REVISITED IN QUANTUM SYSTEMS

Submitted to *Journal of Physics A: Mathematical and Theoretical*[1]

D. Jaschke[2] and L. D. Carr[3]

Abstract

Tensor network methods as presented in our open source Matrix Product States library have opened up the possibility to study many-body quantum physics in one and quasi-one-dimensional systems in an easily accessible package similar to density functional theory codes but for strongly correlated dynamics. Here, we address methods which allow one to capture the full entanglement without truncation of the Hilbert space. Such methods are suitable for validation of and comparisons to tensor network algorithms, but especially useful in the case of new kinds of quantum states with high entanglement violating the truncation in tensor networks. Quantum cellular automata are one example for such a system, characterized by tunable complexity, entanglement, and a large spread over the Hilbert space. Beyond the evolution of pure states as a closed system, we adapt the techniques for open quantum systems simulated via the Lindblad master equation. We present three algorithms for solving closed-system many-body time evolution without truncation of the Hilbert space. Exact diagonalization methods have the advantage that they not only keep the full entanglement but also require no approximations to the propagator. Seeking the limits of a maximal number of qubits on a single core, we use Trotter decompositions or Krylov approximation to the exponential of the Hamiltonian. All three methods are also implemented for open systems

[1] "Open source Matrix Product States: Exact diagonalization and other entanglement-accurate methods revisited in quantum systems", D. Jaschke and L. D. Carr (2018). `http://arxiv.org/abs/1802.10052`. Use in agreement with arXiv license [55].

[2] primary researcher and author responsible for the manuscript.

[3] principal investigator and advisor at Colorado School of Mines.

represented via the Lindblad master equation built from local channels. We show their convergence parameters and focus on efficient schemes for their implementations including Abelian symmetries, e.g., $\mathcal{U}(1)$ symmetry used for number conservation in the Bose-Hubbard model or discrete $\mathbb{Z}_2$ symmetries in the quantum Ising model.

8.1 Introduction

Recently, exact diagonalization (ED) methods have seemed less important due to many available simulation methods for many-body quantum systems including the Density Matrix Renormalization Group (DMRG) [72], Quantum Monte Carlo methods [203, 204], dynamical mean field theory [205], and the truncated Wigner approach [149, 206]. The tensor network methods themselves contain a variety of tailored approaches such as Matrix Product States (MPS) [75, 76], Multi-scale Entanglement Renormalization Ansatz (MERA) [83], Tree Tensor Networks (TTN) [79], and Projected Entangled Pair States (PEPS) [84]. But with growing computing resources today, quantum states of larger and larger systems can be simulated without entanglement truncation. The first limitation of the simulation is the calculation of the propagator in the full Hilbert space. This propagator can be approximated. The second limitation is the initial state, which cannot be chosen as the ground state when systems are too large for exact diagonalization methods. Quantum computing and quantum information theory provide us with well-characterized states beyond the class of product or Fock states. With these techniques, system sizes can be pushed to 27 qubits with easily available computational resources, i.e., a single core on a computer. The boundaries of such simulations have recently been pushed to 45 qubits in the context of quantum supremacy [51]. Simulations, using also quantum circuits, have achieved simulations for 49 and 56 qubits [207] shortly after, then 64 qubits [208]. On the other hand, such methods become a valuable comparison for benchmarking tensor network methods when exploring highly entangled states as recently studied with Quantum Elementary Cellular Automata (QECA) [209] based on the original proposition in [210], the Quantum Game of Life [211, 212], and for open quantum systems [49] among other physically important contexts. We foresee fruitful

applications to the developing field of quantum simulators. These systems exist on a variety of platforms and form one significant part in the development of quantum technologies as proposed in the quantum manifesto in Europe [1, 213]. With exact diagonalization methods, quantum simulators with large entanglement have the possibility at hand to simulate systems up to a modest many-body system equivalent to 27 qubits. Furthermore, the area law for entanglement [78] can be violated for long-range interactions [129], and tensor network methods are likely to lose accuracy when the area law does not bound entanglement. Other possible applications are the emerging field of synthetic quantum matter.

The inclusion of open system methods allows us to approach thermalization of few-body quantum systems from different aspects, e.g., exploring whether or not a subsystem follows a thermal state after taking the partial trace of a pure state. A recent study considers the case of six ^{87}Rb atoms [201] and is well within the scope of exact diagonalization. Research on quantum computing and quantum information can profit from such simulations provided through our library, too. For example, one can study mutual information matrices as done in a similar study with the MPS library [214]. Moreover, exact diagonalization methods are more accessible to new researchers in the field as they require less knowledge of the methods and how to tune them with the set of convergence parameters, e.g., associated with our MPS methods [121, 215]. Returning to exact diagonalization methods with the background of the many-body simulations in tensor networks advances them with regards to various aspects. For example, the usage of predefined rules to represent the Hamiltonian not only simplifies the problem but allows one to multiply the Hamiltonian with a state vector when the matrix of the Hamiltonian itself cannot be represented due to memory limitations. The Krylov method employs precisely this feature and overcomes limitations which are present in the Trotter decomposition with the primary purpose of evolving models with nearest-neighbor interactions. Starting with a certain number of predefined rules for the Hamiltonian, sophisticated models can be represented as well as with hand-built ED codes, but at a much lower cost, avoiding development overhead. A preliminary version of

this library was used for the momentum-space study of the Bose-Hubbard model in [216]. We envision that open systems will profit from this approach enormously in the future to provide a variety of different Lindblad channels.

With these motivations in mind, we present three kinds of algorithms retaining the complete Hilbert space and their efficient implementations for closed systems. The first approach calculates the exponential for the propagator exactly. Second, we choose the Trotter decomposition for nearest-neighbor Hamiltonians allowing for larger systems due to the local propagators. In the third algorithm, we approximate the propagated state in the Krylov subspace allowing for the inclusion of long-range terms in the Hamiltonian. The interfaces work seamlessly with our package Open Source Matrix Product States (OSMPS) [52, 215] and therefore support both $\mathcal{U}(1)$ and $\mathbb{Z}_2$ symmetries in the system. The measurements are adapted from tensor network methods and have a many-body focus: For example, we include the bond entropy, a value typically calculated for tensor networks obtained from the Schmidt decomposition for two bipartitions of the system. Local observables and two-site correlators are measured via the reduced density matrices, which are a more efficient approach in comparison to representing the observables on the complete Hilbert space. Beyond closed systems, we include methods for the Lindblad master equation [47, 49], which describes the dynamics of an open quantum system weakly coupled to its environment. Methods such as the matrix exponential, Trotter decomposition, or Krylov approximation can be adapted to density matrices. Quantum trajectories (QT) [217, 218] are another approach to simulate the Lindblad master equation. Quantum trajectories sample over a variety of pure state systems and therefore all of our three time evolution methods can be used for this approach.

In this Article, we discuss our versatile implementation of methods without entanglement truncation and show their convergence. The scaling of computational resources is compared for all three time evolution methods, where each method has its advantage: matrix exponentials avoid errors in the propagator; Trotter decompositions are ideal for nearest-neighbor interactions; and Krylov overcomes the limitation of the matrix exponential on the complete

space without being limited to nearest-neighbor Hamiltonians. These approaches are applicable to various systems. Exact diagonalization can simulate a significant fraction of the number of ions of recent cold ions quantum simulator experiments, i.e., around one-tenth of [26]. This fraction is much closer than, e.g., in systems with ultracold atoms in optical lattices, where thousands to millions of atoms [112] are used in quantum simulators; the gap between ED methods and the experimental number of particles is then much larger. Looking at individual control of trapped ions, the state-of-the-art experiments are simulating 53 ions [25] and ED methods are even more relevant. Moreover, the development of new platforms for a universal quantum computer is likely to be tested on small scales first, and the corresponding numerical methods can contribute to a better understanding of those platforms. Thus, we envision multiple applications of our exact diagonalization codes beyond pure quantum computation and quantum information research. We introduce the construction of the system Hamiltonian in Sec. 8.2. In Sec. 8.3, we discuss the three different time evolution schemes before turning to the implementation of measurements in Sec. 8.4. We give an overview of the convergence of these methods in Sec. 8.5 and discuss the necessary modification with regards to open quantum system according to the Lindblad master equation in Sec. 8.6. After a benchmarking study in Sec. 8.7 of our package versus another standard package, i.e., QuTip, we conclude in Sec. 8.8.

8.2 Construction of Hamiltonians and Statics

We first introduce the definition of systems in OSMPS and explain the exact diagonalization statics. The focus in this section is on closed quantum systems governed by the Schrödinger equation

$$\frac{\partial}{\partial t} |\psi(t)\rangle = -\frac{\mathrm{i}}{\hbar} H |\psi(t)\rangle , \tag{8.1}$$

where $|\psi\rangle$ is the wave function depending on the time t. H represents the Hamiltonian of the system. We consider in the following a generic Hamiltonian with different terms defined

as

$$H = \underbrace{\sum_{\zeta=1}^{n_S}\sum_{k=1}^{L} c_k O_k^{[\zeta]}}_{\text{Local term}} + \underbrace{\sum_{\zeta=1}^{n_B}\sum_{k=1}^{L-1} c'_k O_k^{[B,\zeta]} O_{k+1}^{'[B,\zeta]}}_{\text{Nearest-neighbor term}} + \underbrace{\sum_{\zeta=1}^{n_i}\sum_{k=1}^{L-1}\sum_{k'=k+1}^{L} c_{k',k} O_k^{[I,\zeta]} O_{k'}^{'[I,\zeta]}}_{\text{Long-range term}}, \quad (8.2)$$

where L is the size of the one-dimensional system. We take a look at the different terms one-by-one. The first term represents a local Hamiltonian term acting on a single particle or site in a system. The first sum over ζ allows us to have n_S different local terms. The second sum runs over the different sites in the system, and each local term might have a spatially dependent coupling with the constants c_k. $O_k^{[\zeta]}$ is the corresponding operator acting on site k; actually, identities are padded on the sites $k' \neq k$ via the outer product, or Kronecker product, to represent the operator acting on the full Hilbert space. This term is necessary for many different systems. It represents the interaction with an external field in the quantum Ising model, and encodes the on-site interaction and chemical potential in the Bose-Hubbard model, just to name two examples. In detail, we take a look at the Bose-Hubbard model with the Hamiltonian

$$H_{\text{BH}} = -J\sum_{k=1}^{L-1}\left(b_k b_{k+1}^\dagger + h.c.\right) + \frac{U}{2}\sum_{k=1}^{L} n_k(n_k - \mathbb{I}) - \mu\sum_{k=1}^{L} n_k\,, \quad (8.3)$$

where b and $b^\dagger$ are the bosonic annihilation and creation operators and the number operator n is defined as $n = b^\dagger b$. J is the tunneling energy, and $U > 0$ is the repulsive interaction energy on each site. Thus, the sum over the local terms runs over $\zeta \in \{1, 2\}$. The first operators $O_k^{[\zeta=1]} = n_k(n_k - \mathbb{I})$ is a compound operator combining the number operators and the identity, all acting on site k. The chemical potential is the second local term, i.e., $O_k^{[\zeta=2]} = n_k$. The next term is nearest-neighbor interactions, where the operator $O_k^{[B,\zeta]}$ acting on site k and $O_{k+1}^{'[B,\zeta]}$ on site $k+1$ can be different operators; hermiticity has to be fulfilled for all terms together. Looking at the example of the Bose-Hubbard in Eq. (8.3), the tunneling term is a nearest-neighbor term. Specifically, we have $\zeta \in \{1, 2\}$ for the bond term with $O_k^{[B,\zeta=1]} = b_k$,

$O_{k+1}^{[B,\zeta=1]} = b_{k+1}^\dagger$, $O_k^{[B,\zeta=2]} = b_k^\dagger$, and $O_{k+1}^{[B,\zeta=2]} = b_{k+1}$. The last term is a two-site interaction at arbitrary distance governed by a coupling $c_{k',k} = c(k'-k)$ depending only on the distance between the sites. This term extends many models where the nearest-neighbor interaction is an approximation, and a more accurate Hamiltonian includes further terms. The extended Bose-Hubbard model with long-range tunneling is one example. In the following, we refer to the three terms as site rules, bond rules, and infinite function rules. Appendix 8.10 contains a complete description of more possible terms in a Hamiltonian. We need to build the Hamiltonian on the complete Hilbert space to determine the statics. The same applies to the dynamics if using the complete matrix for taking the exponential or for the Krylov method. For systems without symmetry, this construction can be done purely using the Kronecker product. Using Python for our implementation, this Kronecker product is either done with `numpy.kron` when building a dense Hamiltonian or with `scipy.sparse.kron` aiming for a sparse Hamiltonian. Dense methods allow one to calculate the complete set of eigenvalues and vectors while sparse methods calculate only the eigenvalues and eigenvectors close to the ground state for the static case. Considering the entries in the final matrix in case of a site rule presented in Eq. (8.2), the computational scaling $\mathcal{F}$ is then

$$\mathcal{F}_{\text{site,dense}} = \mathcal{O}(d^{2L}), \qquad \mathcal{F}_{\text{site,sparse}} = \mathcal{O}(d^{L+1}), \tag{8.4}$$

where $\mathcal{F}$ is the number of floating point operations. We introduced d as the local dimension of the Hilbert space of a single site, e.g., for the Ising model $d = 2$. The scaling in Eq. (8.4) includes the number of multiplications, but not any overhead keeping track of the sparse matrices. Similar calculations hold for the remaining rules defined in Eq. (8.2).

The picture gets more complicated when introducing symmetries. We support $\mathcal{U}(1)$ and $\mathbb{Z}_2$ symmetries defined by their diagonal generator defined on the local Hilbert space. For example, the Bose-Hubbard model conserves the number of particles – a $\mathcal{U}(1)$ symmetry – and the simulation can be executed in the symmetry sector with N bosons. The eigenstates of the basis in the symmetry sector can either be passed as an argument, or the algorithm

iterates once over all $D = d^L$ states checking if the state obeys the symmetry, which is possibly slow. Either way, we have a reduced basis of D_S basis states

$$|i\rangle = |i_1, i_2, \ldots, i_L\rangle\,, \qquad i \in \{1, \ldots, D_s\}\,, \tag{8.5}$$

where i_k are the corresponding indices in the local Hilbert space. The complete wave function is written as $|\,\psi\rangle = \sum_i C_i\,|\,i\rangle$ with coefficients C_i fulfilling the normalization constraint of the wave function. Neither can the local basis $|i_k\rangle$ be deduced easily from $|i\rangle$ nor $|i\rangle$ from a set of $|i_k\rangle$, because the complete Hilbert space is not a tensor product of the local Hilbert spaces. Therefore, a Python class `SymmetrySector` provides two key functions:

- A dictionary returns the index $|i\rangle$ providing the tuple of all local dimensions as key. Since dictionaries in Python have an underlying hash table, the lookup is fast. Henceforward we use the class method `__getitem__` for getting dictionary entries in Python, e.g., `SymmSec[(0, 0, 1)]`.

- `SymmetrySector` provides the local indices for the state $|i\rangle$. This implementation is achieved with a simple matrix $\mathcal{B}$. The i^{th} row contains the local indices for state $|i\rangle$. The vector of indices is obtained via the `__call__` attribute as `SymmSec(i)`.

Knowing the basic structure for the symmetries, we continue with the construction of the Hamiltonian in the example of a site rule. To set the matrix elements for the local operator O on site k, we iterate over the D_S basis states in the Hamiltonian. We choose to iterate over the rows $|i\rangle$ and obtain the corresponding local basis states $|i_1, i_2, \ldots, i_L\rangle$ via the dictionary. We need the index for the columns identified via $|i'\rangle$ and the local indices $|i'_1, i'_2, \ldots, i'_L\rangle$. Considering the structure $\mathbb{I} \otimes O_k \otimes \mathbb{I}$, we know that all indices except k stay equal: $i'_{k'} = i_{k'}, \forall k' \neq k$. The index i'_k can be determined by finding the columns with non-zero entries of row i_k of O_k. Therefore, we loop next over the local dimension i'_k of site k where $|i_1, i_2, \ldots, i'_k, \ldots, i_L\rangle$ corresponds to the entry in the column. We depict this procedure in Figure 8.1. The computational time for building a site rule in the complete Hamiltonian

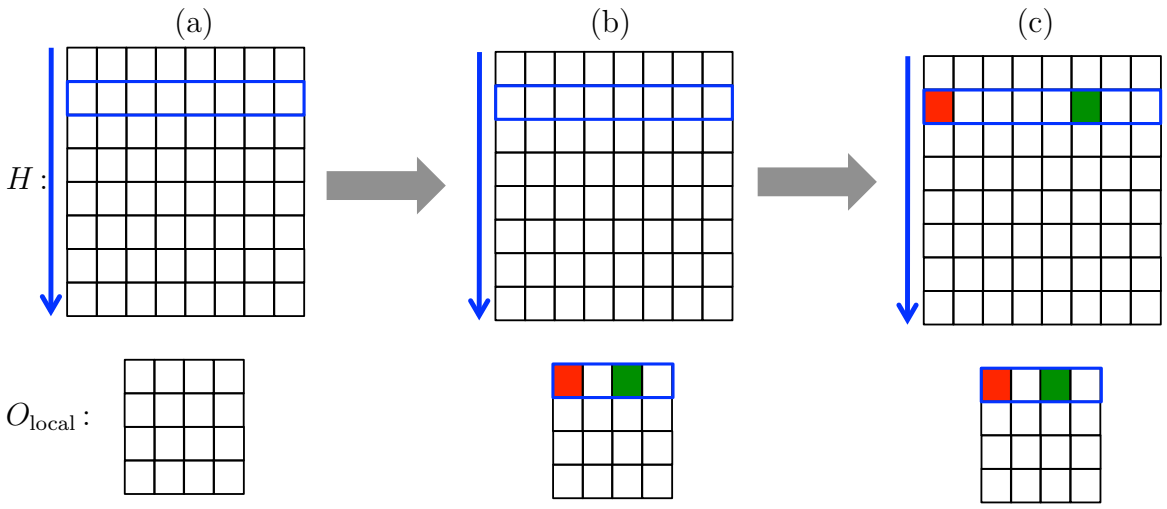

Figure 8.1: *Building the Hamiltonian with Symmetries.* The process of obtaining the Hamiltonian H with symmetry for a site rule can be split into three steps. (a) To build the Hamiltonian, we loop over the rows of H. (b) For each row, we find the corresponding row in the local matrix O_{local} defining the term in the rule set. We mark the non-zero entries in this row. (c) Starting from the non-zero entries marked in step (b), we find the corresponding columns in H and update the matrix element.

H then scales as

$$\mathcal{F}_{\text{Build } H,\text{site}} \quad = \quad \mathcal{O}(LD_S d)\,. \tag{8.6}$$

This scaling can be further improved when iterating only over non-zero elements in the columns of the local operator O_k instead of all the local dimension d. The fact of building a sparse or a dense Hamiltonian does not influence the algorithm apart from setting the matrix elements in a sparse or dense matrix. The interface for addressing a matrix entry in Python is equivalent for both approaches.

The ground and low-lying excited states can now be calculated via the corresponding numpy and scipy functions. For dense matrices, we obtain the full spectrum via `numpy.linalg.eigh` containing all eigenvalues, while in the sparse case only the lowest-lying eigenvalues and corresponding eigenvectors are calculated in `scipy.sparse.linalg.eigsh`. The ground state serves as the default initial state for the dynamics if no other state is specified. At

present, the ground state is calculated from the complete Hamiltonian and therefore large systems are limited through the memory when representing the corresponding matrix.

8.3 Methods for Time Evolution of Closed Systems

Having explained the general setup of the system and how to obtain the ground state, we consider the more important question of time evolution. The first approach for the time evolution of a quantum state is (1) to calculate the propagator as a matrix exponential of the Hamiltonian on the complete Hilbert space. This method requires few modifications with regards to the ground state where we already have functions to construct the Hamiltonian. For time-dependent Hamiltonians, the procedure is especially expensive since the Hamiltonian and its propagator have to be calculated for every time step. Also, the Hilbert space grows exponentially for increasing system size L. Therefore, we consider two additional approximations: (2) the Suzuki-Trotter decomposition applies local propagators to the quantum state, and (3) the Krylov subspace approximates the state directly after applying the propagator. After a brief overview of two test models and their computational scaling in Sec. 8.3.1, we proceed to describe the three time evolution methods in Sec. 8.3.2 to 8.3.4.

8.3.1 Computational Scaling in the Quantum Ising and Bose-Hubbard Model

We introduce the first two models which we use to study the scaling of CPU time T_{CPU} for the different time evolution methods. First, we consider the 1D quantum Ising model [123, 137] defined as

$$H_{\mathrm{QI}} \;=\; -\sum_{k=1}^{L-1} \sigma_k^z \sigma_{k+1}^z - h \sum_{k=1}^{L} \sigma_k^x \,, \tag{8.7}$$

which obeys $\mathbb{Z}_2$ symmetry. The operators σ_k^x and σ_k^z are the Pauli matrices acting on site k. The interaction energy is normalized to 1, and the value of the external field is h. L is the number of sites in the system. Second, we study the Bose-Hubbard Hamiltonian introduced in Eq. (8.3), where the chemical potential μ can be disregarded when we use the

$\mathcal{U}(1)$ symmetry leading to a fixed number of bosons $N = \sum_{k=1}^{L} n_k$.

We present the scaling of the CPU time with increasing system size L for the quantum Ising model in Figure 8.2 (a). We see that the matrix exponential (ME) is limited first, where we simulated up to twelve qubits. Within the different algorithms using the matrix exponential on the complete Hilbert space, the choice of using dense matrices and $\mathbb{Z}_2$ symmetry is optimal. Sparse methods are labeled with *sp*. The symmetry reduces the size of the matrix to be exponentiated in the case of the quantum Ising model by a factor of 2 and therefore reduces the time significantly. The different memory requirements themselves are not the restricting limit. Other simulations have higher memory needs. For the Suzuki-Trotter or Krylov subspace method the use of symmetries is slower in case of the Ising model due to matrix-vector operations, which are needed to decode the basis. In the Krylov method with $\mathbb{Z}_2$ symmetry, we observe the step when switching to a memory-optimized but slower Krylov method for the 10^{th} qubit. This memory-optimized method is necessary for larger systems as the set of Krylov vectors has to be stored, where each Krylov vector is of the same size as the state vector. The slow down for the memory-optimized version originates in reading and writing vectors to and from the hard disk. The Bose-Hubbard model with a local dimension of $d = 5$, corresponding to maximally four bosons per site, is shown in Figure 8.2 (b). Simulations with $\mathcal{U}(1)$ are at unit filling. Due to the large local dimension simulations are limited to smaller system sizes. The benefits of using the symmetry become relevant for the Krylov and Trotter method when going to large system sizes. The details on the implementation leading to those results for each method are described in the following three subsections.

8.3.2 Time Evolution Method 1: The Propagator as a Matrix Exponential

The approach for the time evolution without making any approximations apart from the time-dependence of the Hamiltonian $H(t)$ and the base numerical resolution inherent in any floating point computational scheme is to calculate the propagator as

$$U(t \to t + dt) = \exp\left(-\mathrm{i}H\left(t + dt/2\right) dt\right) . \tag{8.8}$$

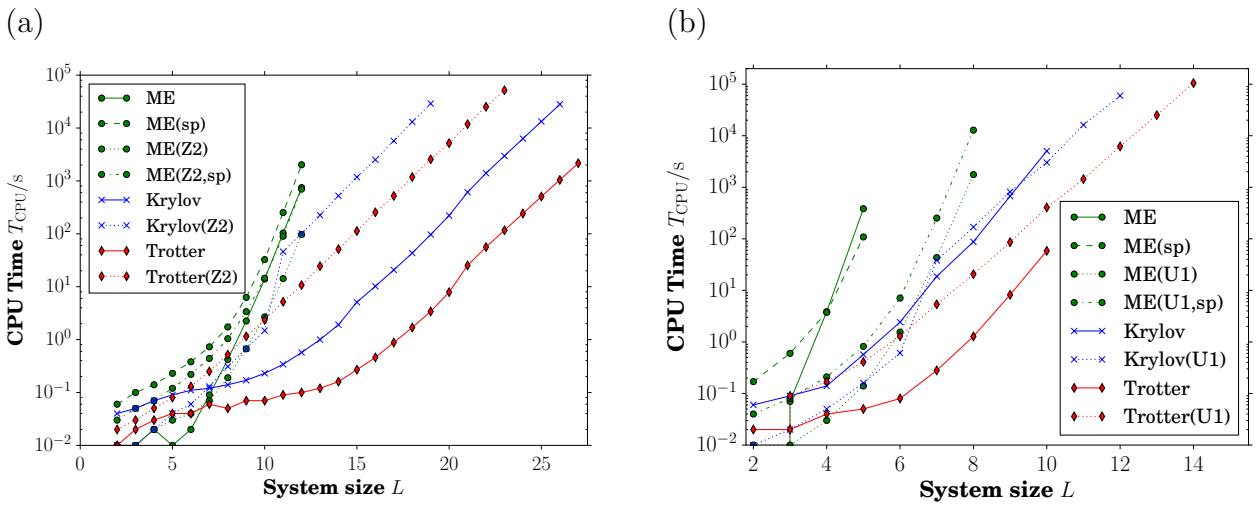

Figure 8.2: *Scaling for Time Evolution Methods.* We profile five time steps for different system sizes L comparing the matrix exponential (ME) with sparse matrices (sp) and with dense matrices to the Trotter decomposition and to the default Krylov method. The computation time in seconds is plotted on a lin-log-scale and all times are taken on a *2x(Intel e5-2680 V4) 28 Cores 2.40 GHz*. (a) The nearest neighbor quantum Ising model has a $\mathbb{Z}_2$ symmetry, which we use in comparison to the methods without symmetry. The main conclusion is that the $\mathbb{Z}_2$ does not accelerate simulations except for the matrix exponential where the size of the Hamiltonian to be exponentiated is crucial, which is reduced by a factor of 2. For the Krylov or Trotter method, it is faster to use no symmetries. (b) The Bose-Hubbard model is considered with a local dimension of $d = 5$, and the $\mathcal{U}(1)$ symmetry is used with unit filling in the simulations marked with $U1$. In contrast to the quantum Ising model, use of the $\mathcal{U}(1)$ symmetry leads to a much smaller fraction of the total Hilbert space and can accelerate simulations and allow for larger system sizes.

We take the corresponding functions `scipy.sparse.linalg.expm` in the sparse case and `scipy.linalg.expm` in the dense case. The construction of H is identical to the static case except that time-dependent coupling may be introduced via the OSMPS interfaces. We point out that the coupling constants are estimated for all methods at mid-time step $t + \frac{dt}{2}$, which corresponds to a time-ordering of $\mathcal{O}(dt^2)$. Finally, the state is propagated with a matrix-vector multiplication. The main problem is that taking the matrix exponential on the complete Hilbert space is expensive in memory and time. The scaling in memory is quadratic in D; the calculation time of the matrix exponential scales cubically with D. Therefore, computation time limits the system size before memory problems. We recall the dimension of the full Hilbert space D scales exponentially with the number of sites L. In the

following two subsections we explain how to simplify this exhaustive computational problem with approximate methods.

8.3.3 Time Evolution Method 2: Trotter Decomposition for Nearest-Neighbor Models

The main bottleneck so far is taking the exponential of a matrix due to CPU time, which grows exponentially with system size. In its original version, the Trotter decomposition allows us to approximate the exponential of the Hamiltonian on the complete Hilbert space with local exponentials on two sites. We present in the following an efficient scheme for applying these two-site propagators to the state, starting without symmetry. We point out that the method in this form is only applicable to Hamiltonians built of site and bond rules [121]. The Suzuki-Trotter decomposition [85] in the first order separates the Hamiltonian into

$$\begin{aligned} \exp(-\mathrm{i}Hdt) &\approx \exp\left(-\mathrm{i}dt\sum_k H_{2k-1,2k}\right)\exp\left(-\mathrm{i}dt\sum_k H_{2k,2k+1}\right) \\ &= \exp(-\mathrm{i}dtH_o)\exp(-\mathrm{i}dtH_e)\,. \end{aligned} \tag{8.9}$$

H_o contains terms acting on odd sites and their right nearest neighbors, and likewise in H_e, except for even sites, with $H = H_o + H_e$. We leave the upper limit for the summation intentionally open since it depends on open versus closed boundary conditions and even vs. odd system sizes L. This decomposition in Eq. (8.9) neglects the second order terms of $\mathcal{O}(dt^2)$ according to the Baker-Campbell-Hausdorff equation [85]. We use higher-order Trotter approximations, see [75], in the implementations defined as

$$\exp(-\mathrm{i}dtH) \approx \exp\left(-\mathrm{i}\frac{dt}{2}H_e\right)\exp(-\mathrm{i}dtH_o)\exp\left(-\mathrm{i}\frac{dt}{2}H_e\right)\,, \tag{8.10}$$

for the second order, and

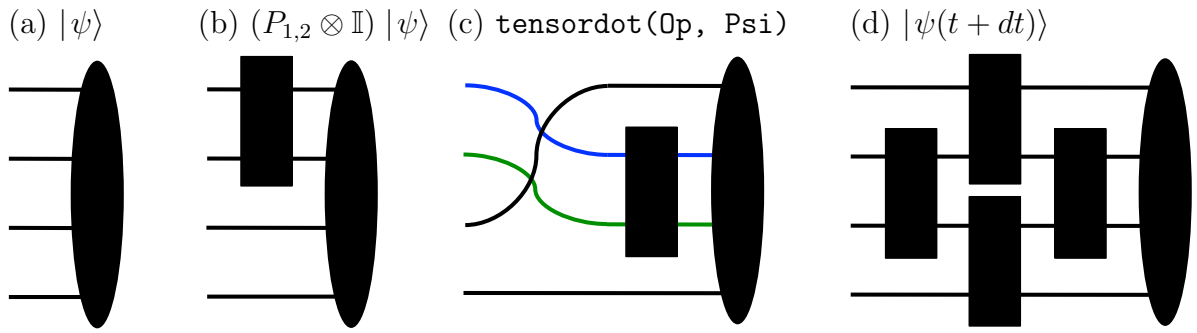

Figure 8.3: *Tensor Operations on a State Vector without Symmetries.* (a) The Hilbert space is a tensor product of local Hilbert spaces, and therefore we can transform our state vector $|\psi\rangle$ into a rank-L tensor. (b) The application of a two-site propagator is reduced to a contraction with the two corresponding indices at a cost of $\mathcal{F} = \mathcal{O}(d^{L+2})$. (c) The implementation of the `tensordot` in numpy permutes the indices which we have to take into account in the algorithm. (d) One step of the second order Trotter decomposition for four sites contains the contraction of the propagators, depicted as rectangles.

$$\begin{aligned}
\exp(-\mathrm{i}dtH) \;\approx\; & \exp(-\mathrm{i}\tau_3 dtH_e)\exp(-\mathrm{i}\tau_4 dtH_o)\exp(-\mathrm{i}\tau_4 dtH_e)\exp(-\mathrm{i}\tau_4 dtH_o) \\
& \times \exp(-\mathrm{i}\tau_2 dtH_e)\exp(-\mathrm{i}\tau_1 dtH_o)\exp(-\mathrm{i}\tau_2 dtH_e) \\
& \times \exp(-\mathrm{i}\tau_4 dtH_o)\exp(-\mathrm{i}\tau_4 dtH_e)\exp(-\mathrm{i}\tau_4 dtH_o)\exp(-\mathrm{i}\tau_3 dtH_e) \quad (8.11) \\
\tau_3 \;=\; & \frac{1}{2(4-4^{\frac{1}{3}})}\,, \tau_1 = 1-8\tau_3\,, \tau_2 = \frac{1}{2}(1-6\tau_3)\,, \tau_4 = 2\tau_3\,, \quad (8.12)
\end{aligned}$$

for the fourth order, respectively. Other formulations of the fourth order approximation exist. We remark that the two-site terms either in H_e or H_o act on different sites and therefore commute. Their exponentials can thus be taken separately. Building the local exponentials, we then distribute the site rules into H_o and H_e, where we choose to weight them with $1/2$ in each layer. This weighting applies to periodic boundary conditions, while in systems with open boundary conditions the first and last site receive a weight of 1.

Now we search for an efficient application scheme of these local propagators for systems without symmetries. A transformation of the state vector into a rank-L tensor allows one to contract the rank-4 tensor of the local propagator with the corresponding sites. This approach avoids building up the propagator on the complete Hilbert space. The function `numpy.tensordot`, depicted in Figure 8.3 (b) and (c), has a computational scaling

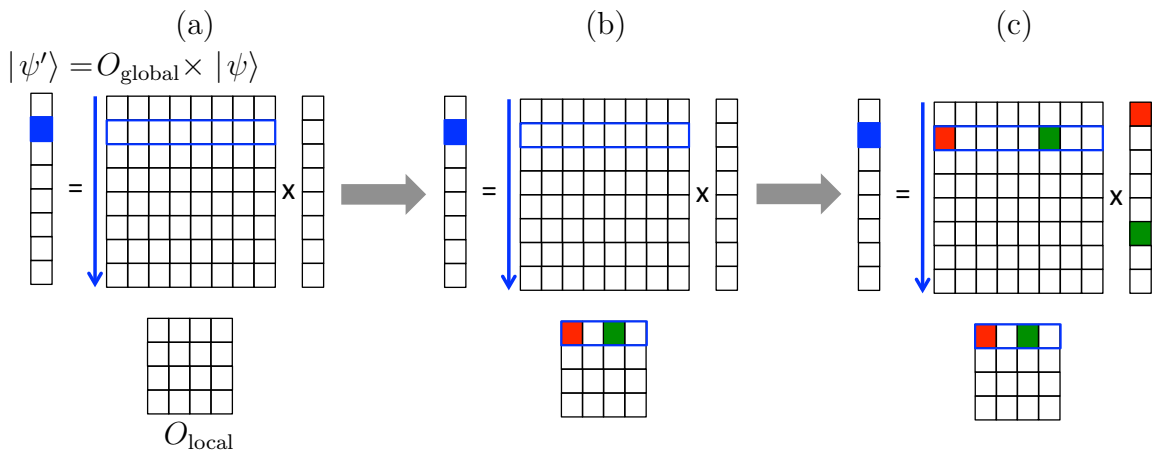

Figure 8.4: *Multiplying the Wave Function by a Local Matrix.* The multiplication $|\psi'\rangle = O_{\text{global}}\,|\psi\rangle$ is carried out in multiple steps, where O_{global} is defined on local Hilbert spaces as operator O_{local} and padded with identities on all other sites. (a) We loop over the rows of the matrix O_{global} and final state $|\psi'\rangle$ and select the corresponding row marking the selected row in blue. (b) In the next step, we find the corresponding row in the matrix O_{local} defined on the local Hilbert space and mark the non-zero elements (red, green) in this row. (c) In the final, third step we find the corresponding column index for each non-zero element in O_{global}, which is identical to the row-index of the wave function $|\psi\rangle$ to be multiplied. Therefore, we can update the blue entry in the new vector $|\psi'\rangle$.

$$\mathcal{F}_{\text{contract 2-site operator}} \;=\; \mathcal{O}(d^{L+2})\,. \tag{8.13}$$

In addition, we have to permute the indices of the state vector back into their original position, which is done once in case of the pure state at the end of one layer. The sketch for the second order decomposition can be found in Figure 8.3 (d), where the different steps described previously are shown. Considering the second order decomposition, the number of terms can be approximated by $3L/2$ leading to an overall scaling of the method for one time step as

$$\mathcal{F}_{\text{Trotter-2 step}} \;=\; \frac{3L}{2}\mathcal{O}(d^{L+2})\,, \qquad \mathcal{F}_{\text{Trotter-4 step}} = \frac{11L}{2}\mathcal{O}(d^{L+2})\,. \tag{8.14}$$

A similar result counting the number of layers is shown for the 4^{th} order. Equation (8.11) shows that we have eleven layers in comparison to three layers in the second order represented

in Eq. (8.10). In comparison, systems with symmetries scale as

$$\mathcal{F}_{\text{contract 2-site operator symm}} = \mathcal{O}(D_S d^2)\,, \quad \mathcal{F}_{\text{Trotter-2 step symm}} = \frac{3L}{2}\mathcal{O}(D_S d^2)\,. \tag{8.15}$$

The trick of rewriting the wave function as a rank-L tensor does not work with symmetries since the basis is not a tensor product of local Hilbert spaces. Here, we take the same approach as when building the Hamiltonian and show a visualization of the algorithm in Figure 8.4. First, we obtain the two-site Hamiltonian and build the subblocks, which conserve the symmetry. This reduction to subblocks is a minor improvement on the performance, taking exponentials on a smaller space and searching for non-zero elements only for the subblocks forming the propagator. In the matrix-vector multiplication, we loop first over the rows of the matrix consisting of the D_S basis states. The local propagator $U_{k,k+1}$ is padded with identity matrices to the left and right, which do not modify the local basis in $|i'\rangle = |i'_1, i'_2, \ldots, i'_L\rangle$ on any site $k' \notin \{k, k+1\}$. Looping over the non-zero entries in the columns of the propagator $U_{k,k+1}$ yields the corresponding local indices for i_k, i_{k+1}. Then the basis state $|i\rangle$ corresponding to the column in the full propagator can be easily obtained. The value is multiplied by the coefficient of C_i of $|\,\psi(t)\rangle$ and added to $C_{i'}$ of the new wave function $|\,\psi'\rangle = |\,\psi(t+dt)\rangle$. Therefore, we have two copies of a wave function $|\,\psi\rangle$ in memory at the same time.

8.3.4 Time Evolution Method 3: Krylov Approximation

The approach via the Trotter decomposition in Sec. 8.3.3 allows one to avoid the matrix exponential of the complete Hilbert space as long as there are no long-range interactions. As mentioned before in the introduction in Sec. 8.1, this is not the case for the exponential rule, infinite function rule, and the MBString rule. An alternative is to approximate the exponential of the complete Hilbert space on a subspace, where the Krylov subspace approach [219] seems to be convenient for this purpose. In detail, it does not approximate the exponential, but instead directly the propagated state

$$|\psi(t+dt)\rangle \approx \exp(-\mathrm{i}H dt)|\psi(t)\rangle\,. \tag{8.16}$$

The new state is written in terms of the basis vectors v_i of the Krylov subspace

$$|\psi(t+dt)\rangle \approx \sum_{i=1}^{m} \xi_i v_i\,, \tag{8.17}$$

where v_i is $H^{i-1}v_i$ orthogonalized against all previous eigenvectors $v_j, j < i$, and ξ_i is the matrix entry $U_{i,1}^{[\mathrm{Krylov}]}$ in the exponential transformed to the Krylov basis. This approach only saves computational effort when the number of Krylov vectors m is much smaller than the dimension of the Hilbert space. The algorithm can be controlled through convergence parameters. We provide four different modes: (0) the built-in scipy method based on the complete Hamiltonian is used for `edlibmode=0`. (1-3) These modes use the Krylov method of OSMPS, which can be tuned by the following convergence parameters. On the one hand, we can set a maximal number of Krylov vectors m building the basis. On the other hand, the algorithm can check a tolerance `lanczos_tol`, which stops the iterations before reaching m. The modes are distinguished as follows:

(0) Built-in scipy method based on the complete Hamiltonian. The complete Hamiltonian is built from the rule sets.

(1) The Hamiltonian is built as a matrix and multiplied with the state vector to construct the Krylov method. Being similar to the scipy method, it cannot achieve the same performance as the scipy implementation in (0).

(2) The Krylov vectors are constructed from a multiplication of the rule set with the state vector and therefore does not need to allocate the memory to represent the matrix H.

(3) The Krylov vectors are constructed from a multiplication of the rule set with the state vector. Instead of keeping all Krylov vectors in memory, this mode saves them temporarily on the hard disk to save memory and reads them on demand.

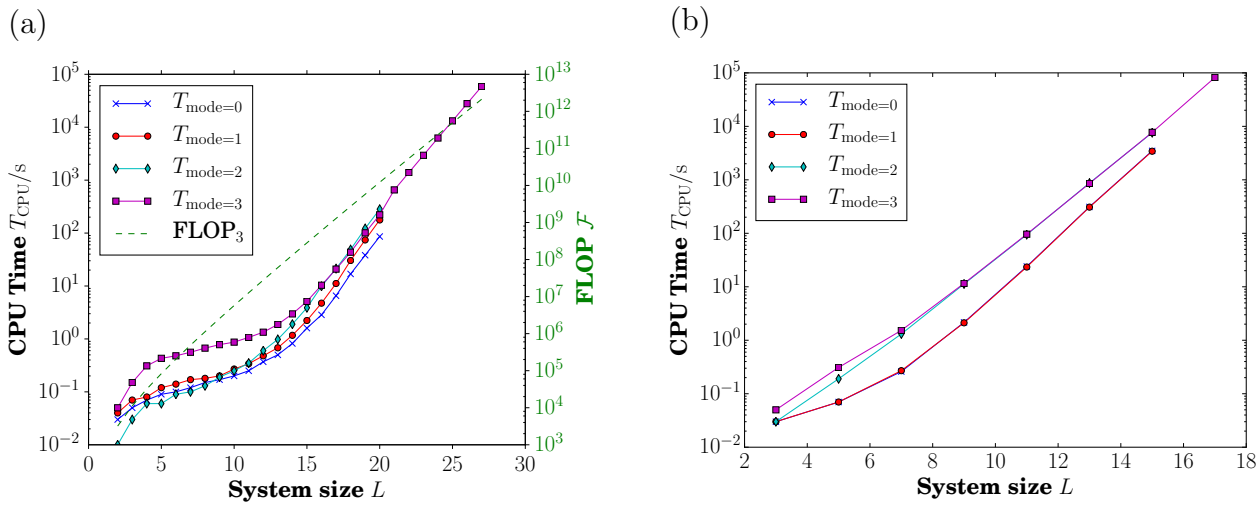

Figure 8.5: *Scaling of the different Krylov Modes.* (a) The Ising model without using its $\mathbb{Z}_2$ symmetry shows that the built-in scipy method with `edlibmode=0` and $T_{\mathrm{mode=0}}$ is fastest except for small systems. Large systems are only considered for mode `edlibmode=3` and we show the corresponding scaling of the floating point operations for this mode in comparison. Times are determined on a *2x(Intel Xeon E5-2680 Dodeca-core) 24 Cores 2.50GHz*. (b) The Bose-Hubbard model for the double-well problem employs the $\mathcal{U}(1)$ symmetry, and we choose a local dimension $d = 5$ and a filling of $N = (L-1)/2$ bosons. The implementations using the rule set for the matrix-vector multiplication (modes 2 and 3) are slower than building the Hamiltonian and calculating the matrix-vector multiplication (modes 0 and 1). Times are determined on a *2x(Intel e5-2680 V4) 28 Cores 2.40 GHz*.

Figure 8.5 shows the CPU times for the different modes for five time-steps, where we introduce the double-well problem based on the Bose-Hubbard Hamiltonian introduced in Eq. (8.3). The potential at the center site splits the system into the two wells,

$$H_{\mathrm{DW}} \quad = \quad H_{\mathrm{BH}} + V \cdot n_{(L-1)/2}\,, \tag{8.18}$$

which is always considered at a filling with $N = (L-1)/2$ particles, L odd. The fraction of Hilbert space needed in comparison to unit filling is smaller and allows us to simulate more sites than with unit filling. Mode 2 is preferable over 0, 1 and 3 for small systems from the viewpoint of CPU times in the case of the quantum Ising Hamiltonian H_{QI} from Eq. (8.7) shown in Figure 8.5(a). For larger systems, the single matrix-vector multiplication in mode 0 may have a favorable scaling over the multiple contractions involved for the rule

set in mode 2. For the Bose-Hubbard double-well problem shown in (b), mode 0 is always preferable. Mode 3 is intended for large systems and can be scaled up to 27 qubits without encountering memory limitations, derived below in Eq. (8.19).

Apart from the implementation of the Krylov algorithm, we need an efficient multiplication $H|\psi\rangle$. Seeking limits beyond twenty qubits, building the Hamiltonian in the Hilbert space is not appropriate. Therefore, we implement directly the matrix-vector product of a rule set with a vector. In the case without symmetries, we transform $|\psi\rangle$ into a rank-L tensor and then use `np.tensordot` in addition to a permutation to obtain the results similar to the procedure in the Trotter decomposition, which requires nested loops over every rule and site. The same applies to the case with symmetries: instead of multiplying the propagator with the state, we apply the multiplication with the matrices of the Hamiltonian rule sets looping over all rules sets and sites. Considering the case with n_s site rules and n_b bond rules without using symmetries, the scaling for $H\,|\psi\rangle$ is equal to

$$\mathcal{F}_{\text{Rule set}\times|\psi\rangle} \;=\; Ln_s\mathcal{O}(d^{L+1}) + 2(L-1)n_b\mathcal{O}(d^{L+1}) \approx L(2n_b+n_s)\mathcal{O}(d^{L+1})\,. \quad (8.19)$$

For one time step, we have to build m Krylov vectors. The leading term in the computational scaling should be the matrix-vector multiplication; therefore, we have

$$\mathcal{F}_{\text{Krylov step}} \;=\; mL(2n_b+n_s)\mathcal{O}(d^{L+1})\,. \quad (8.20)$$

We introduce the number of infinite function rules as n_i. Replacing the $(L-1)$ interactions of a bond rule with the $L(L-1)/2$ interactions of an infinite function rule ($n_i = n_b$), the scaling for one time steps turns into

$$\mathcal{F}'_{\text{Krylov step}} \;=\; mL\,[n_s + (L-1)n_i]\,\mathcal{O}(d^{L+1})\,, \quad (8.21)$$

assuming the phase term is the identity and not contracted as done in the implementation. For fermionic systems with phase operators, the number of floating point operations would

further increase.

If we compare the Krylov method to the 4^{th} order Trotter decomposition for the nearest neighbor case of the quantum Ising model, we estimate that the Krylov takes longer than the Trotter decomposition by a factor of

$$\frac{\mathcal{F}_{\text{Krylov}}}{\mathcal{F}_{\text{Trotter}}} = \frac{2d}{11} m \left(2n_b + n_s\right) \mathcal{O}(m n_b) \,. \tag{8.22}$$

Plugging in the actual numbers with $n_b = n_s = 1$ and $d = 2$, we obtain finally a factor of $3m/11$. We can take the calculation times of Figure 8.2 without $\mathbb{Z}_2$ symmetry and obtain a factor of approximately 30 between the two methods for large systems. That would yield $m \approx 110$, which is above the maximal number specified in the convergence parameters as 100.

In conclusion, these scaling considerations can only serve as estimates. But we point out why long-range simulations are so expensive, according to Eq. (8.22). If we assume that we replace the nearest-neighbor interactions in the quantum Ising model with long-range interactions, i.e., we replace the bond rule by one infinite function rule without phase operators, the resulting long-range model has the following factor in comparison to the nearest-neighbor Trotter decomposition:

$$\frac{\mathcal{F}^{\text{exp}}_{\text{Krylov}}}{\mathcal{F}^{\text{NN}}_{\text{Trotter}-4}} = \frac{2m}{11d} \left[n_s + (L-1)n_i\right] \approx \frac{2m}{11d}(L-1)n_i \,, \tag{8.23}$$

where the approximation in the last steps assumes that the site rule does not contribute the major part to the total computation. The quantum Ising model has one non-local rule $n_i = 1$ and a local dimension $d = 2$, which leads to $m(L-1)/11$. Taking, for example, $L = 18$ and $m = 50$ for the long-range Ising model, one could calculate in the same compute time the nearest-neighbor Ising model with a Trotter decomposition for $L = 24$, since $m(L-1)/11 \approx 77.3 \approx 2^6$.

8.4 Efficient Measurements of Pure States

As our focus is on many-body systems, we draw our attention to the corresponding measurement procedures. In addition to local observables and correlation measurements, we are especially interested in the entanglement between two subsystems known in MPS methods as *bond entropy*. For the local measurement, we use the reduced density matrix ρ_k for site k, tracing out all other sites. This operation scales as $\mathcal{O}(d^{L+1})$. The actual measurement $\mathrm{Tr}(O_k\rho_k)$ is negligible with $\mathcal{O}(d^3)$. The first alternative method is to use the approach of the Trotter decomposition, i.e., contracting a local operator with the state vector leading to $|\,\psi'\rangle = (O_k, |\psi\rangle)$. Then, we calculate the measurement outcome $\langle\psi|\psi'\rangle$ at a cost of $\mathcal{O}(d^{L+1}) = \mathcal{O}(d^L)$. Using the observable O_k padded with identities in the complete Hilbert space has a leading scaling of $\mathcal{O}(d^{2L})$ for the measurement $\langle\psi|O_k|\psi\rangle$, let alone the tensor products to obtain O_k. These considerations are valid for non-symmetry conserving systems. To summarize, local and two-site density matrices are an efficient approach to measurements. In addition, we need the bond entropies. The scaling with system size L for the complete sets of single-site, two-site density matrices, the energy, and bond entropies are shown in Figure 8.6. The CPU times show that the symmetry-adapted algorithms are slower for all four different measurements in the case of the quantum Ising model and its $\mathbb{Z}_2$ symmetry. The Bose-Hubbard model shows a more diverse picture. In the following, we explain the details of the algorithms.

The simplest way to build the single-site density matrix is to use the function `np.tensordot` to contract $|\,\psi\rangle$ and $\langle\psi\,|$ over all indices not appearing in the reduced density matrix after transforming the vectors into rank-L tensors. This function is helpful for systems without symmetries, but we lay out another path to lead to the calculation of reduced density matrices for systems with conserved quantities. Assuming we calculate the density matrix of the first site in Python starting from a state vector $|\psi\rangle$, we have the following order in the row-major

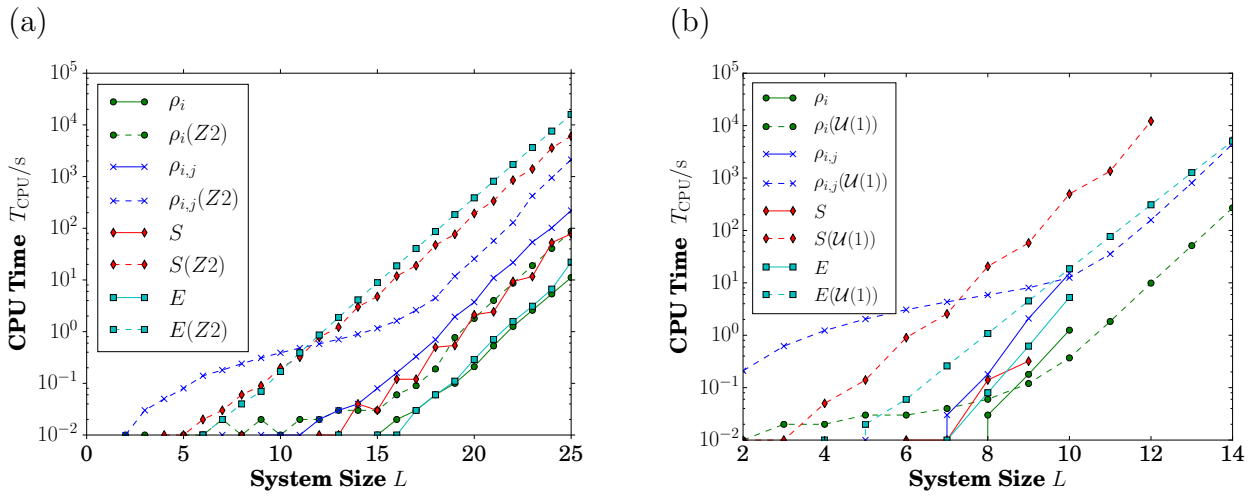

Figure 8.6: *Scaling for Measurements.* We show CPU times for the construction of local and two-site density matrices ρ_k and $\rho_{k,j}$, the bond entropy S, and the energy measurement E. All times are determined on a *2x(Intel Xeon E5-2680 Dodeca-core) 24 Cores 2.50GHz*. (a) We observe from the scaling for the quantum Ising model with and without $\mathbb{Z}_2$ symmetry that the measurements with symmetry are slowed down. The jagged behavior for every second data point in the bond entropy originates in the fact that every even system size and the next bigger odd system size have their eigenvalue decomposition on a matrix of the same dimension, although the odd system size has two of them. But the dimension increases again for the next even system size. (b) For the Bose-Hubbard model, we show the scaling without symmetry and with $\mathcal{U}(1)$ symmetry at unit filling. Due to the local dimension of $d = 5$, system sizes are especially limited if the $\mathcal{U}(1)$ symmetry is not used.

memory[4]

$$|\psi\rangle = [|0\rangle_1 \otimes |\ldots\rangle_{2,\ldots,L}][|1\rangle_1 \otimes |\ldots\rangle_{2,\ldots,L}] = [A][B]\,, \tag{8.24}$$

where we focus on qubits in this example and refer to the blocks as $[A][B]$. The reduced density matrix of the first site is then

$$\rho_1 = \begin{pmatrix} \sum AA^* & \sum AB^* \\ \sum BA^* & \sum BB^* \end{pmatrix}. \tag{8.25}$$

[4] The memory in a computer is linear, but matrices have two dimensions. Row-major memory stores matrices row-by-row. Column-major memory stores matrices column-by-column. Each memory order is generalized to higher rank tensors. Python uses row-major memory order; therefore, we use this order for our example.

The * takes the complex conjugate of the elements. Each of the entries in ρ_1 can be calculated efficiently using the `numpy.sum` and the element-wise multiplication. In fact, it is sufficient to calculate the upper (lower) triangular part of ρ and use the property $\rho = \rho^\dagger$ to fill the lower (upper) triangular part of ρ. Reusing the previous method for k with $k \neq 1$ we choose the following path to avoid writing specific summations for different sites k:

1. Reshape the vector $|\psi\rangle$ into a rank-L tensor with the local dimension (`numpy.reshape`).

2. Permute the index or indices, which are not traced out, to the front (`numpy.transpose`).

3. The reduced density matrix can now be calculated as explained for the first site. We point out that BLAS subroutines `scipy.blas.dsyrk` and `scipy.blas.zherk` allow us to calculate symmetric matrices as well. These functions only build the upper or lower triangular matrix; they are not used right now, but may enhance the computation time for systems without symmetry.

The previous method does not work directly for the reduced density matrices of states in a specific symmetry sector. The first possibility is to map the state vector from the Hilbert space with symmetries back to the complete Hilbert space without symmetries. This method has the disadvantage that the memory needs might increase drastically in addition to the fact of multiplying a lot of zeros. For systems where only a small fraction of the complete Hilbert space is needed, this increase in memory imposes a problem. For example, the Bose-Hubbard model at unit filling for a local dimension of $d = 5$ and fourteen sites corresponds to approximately 23.67 qubits. The complete Hilbert space has a dimension of 5^{14}, which corresponds to approximately 32.51 qubits. We can overcome this problem in two ways. We may use booleans to index the complete Hilbert space into indices being part of the symmetric Hilbert space (True) and not belonging to the symmetry sector specified (False). Thus, we use less memory: a factor of 16 (8) in comparison to complex-valued (real-valued) states knowing that numpy stores each boolean in a byte, not a bit. Assuming this approach is not always enough gain, we use a sparse structure. There are no sparse structures for

tensors or vectors in *scipy*, so we save the state vector in a sparse matrix. Therefore, the permutation has to be accounted for while writing the sparse structure. We propose, again in the simple example of qubits and a single-site density matrix for site k, the following steps focusing solely on the method with the sparse matrix:

1. For each basis state $|\, i\rangle$ we need the index in the Hilbert space only considering the traced out or retained sites. For the new Hilbert space of the retained sites, we create the vector

$$v_{\text{retain}} \;=\; (0, \ldots, 2^0, \ldots, 0)\,, \tag{8.26}$$

   where the entry 2^0 is at the position k. Retaining more than one index, the entries for the l retained sites would be $2^{l-1}, \ldots, 2^0$. In contrast, the vector for the traced out part of the Hilbert space is

$$v_{\text{trace}} \;=\; (2^{L-2}, 2^{L-3}, \ldots, 2^{L-k}, 0, 2^{L-k-1}, \ldots, 2^0)\,, \tag{8.27}$$

   where the entry 0 is at the position k. The indices in the corresponding complete subspace disregarding the symmetry can be obtained with the matrix $\mathcal{B}$, which contains the basis, via a matrix-vector multiplication:

$$i_1 = \mathcal{B} \cdot v_{\text{retain}}\,, \qquad i_2 = \mathcal{B} \cdot v_{\text{trace}}\,. \tag{8.28}$$

   i_1 and i_2 are vectors. Building the vectors is cheap and scales linearly with the number of sites. The expensive part is the two matrix-vector multiplications at $\mathcal{O}(D_S L)$.

2. Looping over all basis states i in the reduced density matrix, we create for each state i a sparse vector. The indices in the present (symmetry-adapted) Hilbert space i_{match} are identified via the comparison $i_1 = i$. The sparse vector contains the entries of $\psi_{i_{\text{match}}}$ at the corresponding indices in the traced out Hilbert space $i_2(i_{\text{match}})$. If we retain l

sites, they approximately have a scaling of $\mathcal{O}(d^l D_S)$, where d^l is due to the loop over the basis states and D_S corresponds to the comparisons $i_1 = k$.

3. Looping over all upper triangular entries $\rho_{i,i'}$ of the density matrix, each entry is calculated via the dot product of the sparse vectors with indices i and i', where we have to take the complex conjugated vector for i'. Although we loop only over the upper triangular part, the leading scaling for the loops is still $\mathcal{O}(d^{2l})$. For the vector-vector multiplication, we can only give an upper limit of $\mathcal{O}(D_S)$ valid for the limit $l = 0$ leading overall to $\mathcal{O}(d^{2l} D_S)$.

So the overall scaling is $\mathcal{O}(D_S L) + \mathcal{O}(d^{2l} D_S)$. The sparse structure in scipy is limited to a dimension of $2^{31} - 1$, which becomes an issue if the complete Hilbert space of the sites traced over exceeds this value. The example above with fourteen sites with a local dimension of $d = 5$ exceeds this limit. Instead of using the indices of the complete Hilbert space, we build a symmetry-adapted basis for the reduced density matrix and use its indices, which can never exceed the number of basis states of the original quantum state. A similar algorithm can be formulated if the resulting density matrix should keep the symmetry-adapted space to the extent possible.

For the calculation of the bond entropy we employ the following algorithm; we do not use the characteristic $\rho = \rho^\dagger$ so far. Starting in the middle of the system we create the density matrix for the left bipartition $1, \ldots, l$ as matrix-matrix multiplication

$$\rho_l = M M^\dagger \,, \tag{8.29}$$

where M is the vector $|\psi\rangle$ reshaped into the dimension d^l, d^{L-l}. In the case of symmetries present, we create M as a sparse matrix. An eigenvalue decomposition yields the bond entropy. The next reduced density matrix is obtained via a partial trace

$$\mathrm{Tr}_{l+1} \rho_{l+1} = \rho_l \,. \tag{8.30}$$

This approach should have a favorable scaling with d^{2l+1} additions in addition to a permutation to form blocks of the memory along `np.transpose((0, 2, 1, 3))`) in regard to calculating the reduced density matrix for every site with a matrix multiplication scaling with d^{L+l}. The summation for each of the d^{2l} entries runs only over the d diagonal entries of the memory block. In the case with symmetries, the scaling for the matrix multiplication does not hold. The second step takes care of the right half of the system building an initial, reduced density matrix for $l+2, \ldots, L$, that is,

$$\rho_{l'} = M^\dagger M \,. \tag{8.31}$$

In the following we trace out the first site in the reduced density matrix instead of the last. The permutation with `np.transpose((1, 3, 0, 2))` delivers the entries to be summed over in blocks of the memory, although we recall that only the diagonal elements are summed over. Overall the bond entropy can be obtained equally well with singular value decomposition of the matrix M build for each splitting. In the tensor network section of OSMPS, eigendecompositions are preferred over SVD, so we use them in this case as well.

8.5 Convergence of Time Evolution Methods

Finally, we are interested in the convergence of those methods, especially in the error of the Trotter decomposition and Krylov evolution in comparison to the matrix exponential on the complete Hilbert space (ME). For the convergence studies we consider the following four kinds of errors taking into account local measurement, correlation measurements between operators on two sites, the energy E and the entanglement specified through the bond entropy or Schmidt entropy S. These error measurements are defined as:

$$\begin{aligned}
\epsilon_{\text{local}} &= \max_k \mathcal{D}(\rho_k, \rho_k^{\text{ME}}), k = 1, \ldots L && (8.32)\\
\epsilon_{\text{corr}} &= \max_{(k,j)} \mathcal{D}(\rho_{k,j}, \rho_{k,j}^{\text{ME}}), k, j = 1, \ldots L, k < j && (8.33)\\
\epsilon_{\text{E}} &= |E - E^{\text{ME}}| && (8.34)\\
\epsilon_{\text{S}} &= |S(L/2) - S^{\text{ME}}(L/2)| \,, && (8.35)
\end{aligned}$$

where the superscript ME specifies that the matrix exponential was used as reference method. The trace distance $\mathcal{D}$ and the bond entropy S are defined as

$$\mathcal{D} = \frac{1}{2}|\rho - \rho'|, \quad |\mathcal{A}| = \sqrt{\mathcal{A}^\dagger \mathcal{A}} \tag{8.36}$$

$$S(l) = -\sum_j \Lambda_j(l) \log(\Lambda_j(l)) \,. \tag{8.37}$$

$\mathcal{A}$ is a matrix used to define the norm and is replaced in this case with the difference of the two density matrices $\rho - \rho'$. $\Lambda_j(l)$ are the eigenvalues of the reduced density matrix of the subsystem reaching from site 1 to l. An alternative distance measure would be the infidelity $\mathcal{I} = 1 - \mathrm{Tr}\sqrt{\sqrt{\rho_A}\rho_B\sqrt{\rho_A}}$, but seems to introduce an additional instability taking the square root of a matrix twice. For the convergence rates, we use

$$r = \frac{1}{\ln(\alpha)} \ln\left(\frac{\epsilon(\alpha dt)}{\epsilon(dt)}\right) , \tag{8.38}$$

where α is the proportion between the size of the time steps for the two evolutions carried out with time steps dt and $\alpha \cdot dt$. ϵ is the error, e.g., one of the measures introduced in Eqs. (8.32) to (8.35). We consider the error with regards to the simulations with the matrix exponential and the smallest time step. We consider two different models and two scenarios for the dynamics. We recall that we introduced the definitions of the Ising Hamiltonian H_{QI} in Eq. (8.7) and the Bose-Hubbard model with H_{BH} in Eq. (8.3). The two scenarios considered are as follows.

1. A linear quench in the paramagnetic (Mott insulator) phase for the Ising (Bose-Hubbard) model starting at $h = 5.0$ ($U = 10$) and reaching after 0.5 time units $h = 4.5$ ($U = 8$). The time is in units of the interaction $\sigma^z\sigma^z$ (tunneling strength J).

2. A sudden quench in the paramagnetic (Mott insulator) phase evolving the ground state of the Ising (Bose-Hubbard) model $h = 5.0$ ($U = 10$) with a value of $h = 4.5$ ($U = 8$) for 0.5 time units.

The results for the scenario *(1)* in case of the Bose-Hubbard model can be found in Figure 8.7. We point out that the Krylov method has a similar error to taking the complete matrix exponential. Greater errors in the Trotter decomposition are due to non-commutating terms in the decomposition originating from Eq. (8.10). For the example in Figure 8.7, we obtain a convergence rate of dt^2 for the second order Trotter decomposition (2.15, 2.0), the fourth order Trotter decomposition (4.21, 2.05), and the Krylov methods (2.73, 2.0), where we consider the pairs $(dt = 0.01, dt' = 0.1)$ and $(dt = 0.001, dt' = 0.01)$ to evaluate the rate of convergence according the distance of the single site density matrices. The limitation to the second order convergence rate for all methods can be explained since the time-ordering is correct up to second order for the time-dependent Hamiltonian. Figure 8.11 in the appendix shows that the convergence rates differ for a time-independent Hamiltonian. The Krylov method is then exact independent of the time step, and the fourth-order Trotter convergence rate is 4.59 for $(dt = 0.01, dt' = 0.1)$ before reaching machine precision. Additional plots for the Ising model and other scenarios can be found in App. 8.14.

8.6 Open Systems in Untruncated Space

The methods so far described are applicable for closed systems described by pure states. These methods ignore the fact that any quantum system is coupled to some extent to its environment. The Lindblad master equation is one way to describe an open quantum system through the evolution of its density matrix ρ. The assumptions are that the system is never entangled with its environment, the correlation time of the environment is small in comparison to the evolution time, and the evolution time itself is small in comparison to the equilibration time of the system. These approximations apply if the environment is large and has no memory. They are referred to as Born-Markov approximation and secular approximation. In addition to Hamiltonian dynamics described via the von Neumann equation, the evolution is described via η Lindblad channels acting on different sites k:

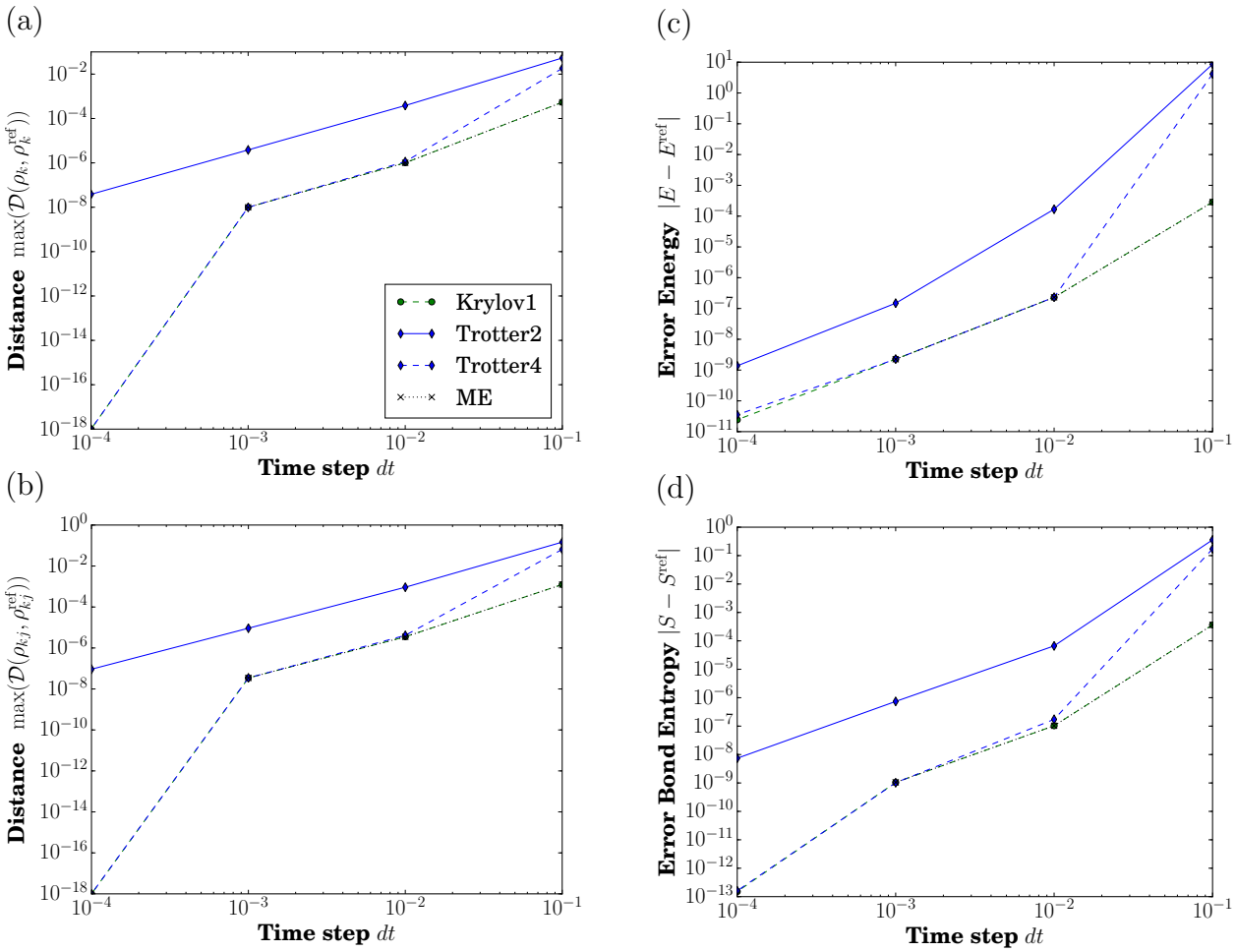

Figure 8.7: *Convergence of Methods for the Bose-Hubbard Model.* We compare the 2nd and 4th order Trotter time evolution and the Krylov method with mode 1 against the reference (ref) takes as the matrix exponential (ME) with $dt = 0.0001$ for various measures. We consider the Bose-Hubbard model in a linear quench from on-site interaction strength $U(t = 0) = 10.0$ to $U(t = 0.5) = 8.0$ for a system size of $L = 6$ and unit filling. The minimal error is set to 10^{-18} indicating machine precision. The measures are (a) the minimal distance over all single-site reduced density matrices, (b) the minimal distance over all two-site density matrices, (c) the error in energy, and (d) the error in the bond entropy for the splitting in the middle of the system.

$$\dot{\rho} \;=\; -\frac{\mathrm{i}}{\hbar}\left[H,\rho\right] + \sum_{\eta,k} L_{\eta,k}\rho L_{\eta,k}^{\dagger} - \frac{1}{2}\left\{L_{\eta,k}^{\dagger}L_{\eta,k},\rho\right\} = -\frac{\mathrm{i}}{\hbar}\left[H,\rho\right] + \sum_{\nu} L_{\nu}\rho L_{\nu}^{\dagger} - \frac{1}{2}\left\{L_{\nu}^{\dagger}L_{\nu},\rho\right\}\,, \tag{8.39}$$

where the indices η and k can be combined in another index $\nu = (\eta, k)$. One of our additional rule sets for the open system is a local Lindblad operator

$$\text{Lind1 rule} \;:\; \sum_{k=1}^{L} w \cdot c_i \cdot L_i\,, \tag{8.40}$$

which would correspond to one channel η. We can always choose zero Lindblad channels and have an evolution of a possibly initially mixed system under the von Neumann equation

$$\dot{\rho} \;=\; -\frac{\mathrm{i}}{\hbar}\left[H,\rho\right]\,. \tag{8.41}$$

In the following, we describe two approaches to simulate the Lindblad master equation. On the one hand, we can simulate the whole density matrix ρ as represented in Eq. (8.39). Therefore, ρ is represented as superket vector $|\rho\rangle\!\rangle$ in the Liouville space obtaining a Schrödinger-like equation. The superket vector is the density matrix written as a vector. A $D \times D$ density matrix turns into a vector with D^2 entries. But first, we lay out the quantum trajectories, which average over many simulations. Each simulation describes a single realization of what possibly could happen in an experiment.

8.6.1 Quantum Trajectories

The method of quantum trajectories has been proposed to avoid simulation of the complete density matrix at the cost of sampling over many realizations of a simulation with pure states. The algorithm used can be described by the following steps [61, 217, 218]:

1. Throw a random number r and evolve under the effective Hamiltonian H_{eff} until the norm drops below r,

$$H_{\text{eff}} \;=\; H - \frac{1}{2}\sum_{\nu} L_\nu^\dagger L_\nu \,. \tag{8.42}$$

2. Throw another random number r_κ and calculate the probabilities p_ν to apply any possible Lindblad operator and the cumulative probability P_ν,

$$p_\nu \;=\; \langle\psi|\, L_\nu^\dagger L_\nu \,|\psi\rangle\,, \qquad P_\nu = \frac{\sum_{j=1}^{\nu} p_j}{\sum_{j=1}^{\nu_{\max}} p_j}\,. \tag{8.43}$$

3. Apply Lindblad operator κ with $P_{\kappa-1} < r_\kappa \leq P_\kappa$ and renormalize $|\,\psi'\rangle = L_\kappa \,|\,\psi\rangle$. Restart with step *(1)*.

This approach can be used with the matrix exponential on the complete Hilbert space, the Trotter and Krylov evolution.

8.6.2 Liouville Space

The Liouville space is a mapping from the Hilbert space defined over

$$O'\rho\, O \to O' \otimes O^T \,|\rho\rangle\!\rangle\,, \tag{8.44}$$

where the original density matrix ρ is now represented as a vector, the super-ket $|\rho\rangle\!\rangle$. The superscript ^{T} is the transpose of the matrix. A quick derivation of the transformation is given in App. 8.15. The corresponding equation governing the evolution of the density matrix is Schrödinger-like,

$$\frac{\partial}{\partial t}\,|\rho\rangle\!\rangle \;=\; \left[-\frac{\mathrm{i}}{\hbar}\left(H\otimes\mathbb{I} - 1\otimes H^T\right) + \sum L_k \otimes L_k^* - \frac{1}{2}\left(L_k L_k^\dagger \otimes \mathbb{I} + \mathbb{I}\otimes L_k^* L_k^T\right)\right]|\rho\rangle\!\rangle \tag{8.45}$$

The short-hand notation is $\partial/\partial t\,|\rho\rangle\!\rangle = \mathcal{L}\,|\rho\rangle\!\rangle$, where $\mathcal{L}$ represents Hamiltonian part and dissipative part of the time evolution in Liouville space. Thanks to the structure we can reuse two of the previous methods with small modifications. In the first method presented, we obtain the propagator via the matrix exponential. Calling appropriate methods for non-

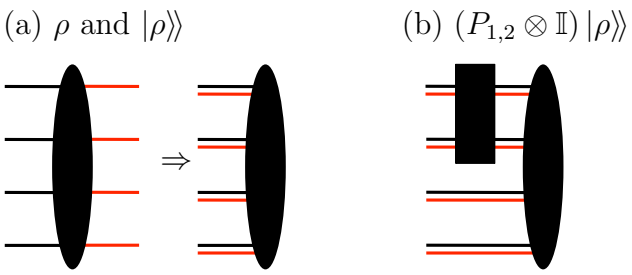

Figure 8.8: *Tensor Operations for the Density Matrix without Symmetries.* (a) The density matrix is rewritten as a rank-$(2L)$ tensor where the first L indices represent the rows of the density matrix (black lines) and the second L indices run over the columns of the density matrix (red) for both ρ and $|\rho\rangle\!\rangle$. (b) The application of a two-site operator to the density matrix corresponds to the contraction over the four indices of the two sites k and $k+1$. This operation comes at a cost of $\mathcal{O}(d^{2L+4})$.

hermitian matrices – the matrix in Eq. (8.45) is not necessarily hermitian due to the term $L_\nu \otimes L_\nu^*$ – we can reuse the method. For the Trotter decomposition, the same strategy is necessary for the local two-site propagators. The matrix exponential for the two site propagator is now of dimension $d^4 \times d^4$ instead of $d^2 \times d^2$ for state vectors. Figure 8.8 shows how to apply the two-site operators acting on the density matrix formatted as a rank-$(2L)$ tensor. Based on the contraction over four indices for two sites, the application scheme for the Trotter decomposition can be adapted. In contrast to the pure system, we permute the tensor after every contraction back to its original order. The Krylov method used previously has to be modified for non-hermitian matrices since the exponential of the matrix in the Krylov subspace is no longer tridiagonal, but of upper Hessenberg form.

8.6.3 Error Analysis in Case Study 1: Coupled Cavities

To check the convergence of the code, we analyze two coupled cavities, or photon Josephson junctions (PJJ), described through the Jaynes-Cummings model with loss [220]. The Hamiltonian of the system without a loss is defined as

$$\begin{aligned} H_{\mathrm{PJJ}} &= (\omega_q n_1 + \omega_c n_2 + \omega_c n_3 + \omega_q n_4) + g\left(\sigma_1^+ a_2 + \sigma_1^- a_2^\dagger + a_3^\dagger \sigma_4^- + a_3 \sigma_4^+\right) \\ &\quad - J\left(a_2^\dagger a_3 + a_2 a_3^\dagger\right), \end{aligned} \tag{8.46}$$

where $\omega_q = 1.0$ ($\omega_c = 1.0$) is the frequency of the qubit (cavity) and n_k are the number operators for the excitations on the corresponding site k. $g = 0.48$ is the coupling constant between cavity and qubit; the cavities are coupled to each other at a strength J representing the tunneling of photons. The transition from the ground (excited) state to the excited (ground) state for the qubits is described with the operator σ^+ (σ^-). The creation (annihilation) operator for the photons in the cavity is $a^\dagger$ (a). We recall that $n_{1,4} \in \mathbb{R}^{2\times 2}$ while the dimension of $n_{2,3}$ varies with the number of photons allowed in the cavity. We add a spontaneous emission from the excited state to the ground state for the qubits. The second type of system-environment interaction is the loss of photons. Both processes assume that the environment is the vacuum and only absorbs excitations, but cannot provide them to the system. We can describe this system with the following Lindblad master equation:

$$\dot{\rho} \;=\; -\mathrm{i}\,[H_{\mathrm{PJJ}}, \rho] + \sum_{k\in\{1,4\}} \gamma_k \sigma_k^-\ \rho\ \sigma_k^+ - \frac{\gamma_k}{2}\left\{\sigma_k^+\sigma_k^-, \rho\right\} + \sum_{k\in\{2,3\}} \gamma_k a_k\ \rho\ a_k^\dagger - \frac{\gamma_k}{2}\left\{a_k^\dagger a_k, \rho\right\}. \tag{8.47}$$

Defining the total number of excitations as $N(t) = \sum_{k=1}^{4} n_k$ and choosing a constant $\gamma = \gamma_k$ for the coupling of the system to the environment via the Lindblad operator, one can show that the following relation holds:

$$N(t) \;=\; N(t=0)\exp(-\gamma t)\,. \tag{8.48}$$

We turn to the error analysis. First, we choose to simulate the case $\gamma = 0$ with the open system code, which is, in fact, the evolution according to the von Neumann equation for density matrices defined in Eq. (8.41). This simulation should reproduce the results for pure state $|\psi\rangle$ and corresponding code. We characterize the error again in terms of the maximal distance between all single site density matrices and two site density matrices, the energy, and bond entropy as defined in Eqs. (8.32) to (8.35). Table 8.1 lists the corresponding errors for our default settings with a total time $T = 10$ with a time step of $dt = 0.01$. The errors

are for the final measurement at $T = 10$. We start with one photon in the right cavity and all other sites in the ground state. Therefore, we can cut off the Hilbert space to a local dimension $d = 2$. We remark that the evolution of the density matrix does not provide the bond entropy and therefore cannot be compared to the result of the pure state. Furthermore, zero error is to be interpreted as numerical zero. Table 8.2 shows the errors for the evolution of the open system with $\gamma = 0.05$, where we introduce also the error in the total number of excitations following Eq. (8.48) as

$$\epsilon_{N(t)} \quad = \quad |N_{\mathrm{EDLib}}(T) - N(t=0)\exp(-\gamma T)| \ . \tag{8.49}$$

We recognize the larger error for quantum trajectories in Table 8.2. This error is due to the finite number of different trajectories. The standard deviation scales with $1/\sqrt{N_{\mathrm{QT}}}$ according to the law of large numbers. Errors related to the algorithm are at a much lower magnitude for proper parameters and would only become visible for very large N_{QT}. We may illustrate this behavior with the following example: We assume there is one particle and we pick the point in time where this particle decayed with probability 0.5 leading to a coin-toss scenario. The normalized standard deviation for the binomial distribution is then $(\sqrt{4N})^{-1}$. For 500 trajectories, we have 0.022. The standard deviation in Table 8.2 is within this order of magnitude. Errors here are for $T = 10$; therefore, the statistics are slightly different.

8.6.4 Error Analysis in Case Study 2: Double-Well

In the second case study, we check the error for simulations with symmetries, where we choose a Bose-Hubbard model with $\mathcal{U}(1)$ symmetry for the number conservation. We introduced the double-well problem before in Eq. (8.18) with its Hamiltonian H_{DW}. For the comparison of the evolution of the von Neumann equation of the density matrix, see Eq. (8.41), to the pure state evolution we choose a system size of $L = 7$ with three bosons over a time of $T = 20$ and a time step of $dt = 0.01$. The height of the potential is $V = 1$. The initial state for the time evolution is the ground state when applying a potential to the

Table 8.1: *Error Analysis for the Density Matrix in the von Neumann Equation.* We simulate the closed system with the open system code of the library using the von Neumann equation in the Liouville space (Liou). As a reference, we use the closed system evolved with the matrix exponential (ME) to obtain errors for the maximal distances of one and two site density matrices, energy, and bond entropy. Zeros in the errors are to be interpreted as numerical zeros. Bond entropies are not calculated for density matrices. All of the methods listed demonstrate the correctness of the code, where, e.g., the error of the Trotter decomposition originates in the Trotter error and is decreased for the fourth order method. The Krylov method runs with the first mode, and the quantum trajectories (QT) have a single trajectory sufficient for a closed system. Additional data for further methods is presented in the Appendix in Table 8.4.

Model	Error	Liou (ME)	Liou (Trotter-2)	Liou (Krylov-1)	QT1 (ME)
H_{PJJ}	$\epsilon_{\mathrm{local}}$	0.0	$1.54 \cdot 10^{-10}$	$2.74 \cdot 10^{-13}$	0.0
	ϵ_{corr}	0.0	$1.83 \cdot 10^{-10}$	$7.37 \cdot 10^{-13}$	0.0
	ϵ_{E}	$6.28 \cdot 10^{-14}$	$6.71 \cdot 10^{-07}$	$5.58 \cdot 10^{-13}$	$5.55 \cdot 10^{-15}$
	ϵ_{S}	–	–	–	$1.78 \cdot 10^{-15}$
H_{DW}	$\epsilon_{\mathrm{local}}$	0.0	$5.34 \cdot 10^{-10}$	$8.54 \cdot 10^{-14}$	$9.03 \cdot 10^{-14}$
	ϵ_{corr}	0.0	$7.67 \cdot 10^{-10}$	$8.8 \cdot 10^{-14}$	$2.7 \cdot 10^{-13}$
	ϵ_{E}	$1.82 \cdot 10^{-12}$	$7.16 \cdot 10^{-06}$	$8.07 \cdot 10^{-13}$	$7.51 \cdot 10^{-13}$
	ϵ_{S}	–	–	–	$4.35 \cdot 10^{-14}$

right well of amplitude 1 in addition to the potential of the barrier localizing the particles in the left well. Upon releasing the barrier for the right well at $t = 0$, the particles start to oscillate between the two wells, i.e., the system is in the Josephson regime. The errors are shown in Table 8.1. The open system is introduced as in [221]

$$\dot{\rho} \;=\; -\mathrm{i}\,[H,\rho] + \sum_{k=1}^{L} \gamma_k n_k \rho\, n_k - \frac{\gamma_k}{2}\left\{n_k^2, \rho\right\}\,, \tag{8.50}$$

and we choose a space-independent coupling $\gamma = \gamma_k = 0.05$ in the following. Table 8.2 contains then the open system case and compares the matrix exponential to the other methods. The setup of this model is discussed in detail as an example in the Appendix A.1.

Table 8.2: *Error Analysis for the Lindblad Master Equation.* We simulate the Lindblad master equation for different time evolution methods and take as reference the implementation using the matrix exponential. In addition, the simulations with H_{PJJ} are compared to the exponential decay of the number of excitations. Quantum trajectories run with 500 different trajectories. Zeros in the errors are to be interpreted as numerical zeros. Bond entropies are not calculated for density matrices and excluded for this reason from the table of errors. Data for additional methods can be found in the Appendix in Table 8.5.

Model	Error	Liou (ME)	Liou (Trotter-2)	Liou (Krylov-1)	QT500 (ME)
H_{PJJ}	$\epsilon_{N(t)}$	$8.88 \cdot 10^{-16}$	$3.22 \cdot 10^{-07}$	$3.7 \cdot 10^{-13}$	$1.15 \cdot 10^{-02}$
	$\epsilon_{\mathrm{local}}$	–	$7.5 \cdot 10^{-11}$	$2.27 \cdot 10^{-13}$	$1.49 \cdot 10^{-05}$
	ϵ_{corr}	–	$8.13 \cdot 10^{-11}$	$1.25 \cdot 10^{-13}$	$4.48 \cdot 10^{-05}$
	ϵ_{E}	–	$1.32 \cdot 10^{-07}$	$3.71 \cdot 10^{-13}$	$1.15 \cdot 10^{-02}$
H_{DW}	$\epsilon_{\mathrm{local}}$	–	$1.32 \cdot 10^{-11}$	0.0	$2.04 \cdot 10^{-03}$
	ϵ_{corr}	–	$2.52 \cdot 10^{-11}$	0.0	$6.44 \cdot 10^{-03}$
	ϵ_{E}	–	$2.53 \cdot 10^{-06}$	$1.16 \cdot 10^{-12}$	$3.75 \cdot 10^{-02}$

8.7 Comparison to QuTip Package for Benchmarking

We compare single features of the ED package of OSMPS with comparable features of the QuTip library [222, 223] under version 4.0.2. The QuTip library provides a far more general framework to simulate closed and open quantum systems. We focus on the benchmark of the following tasks:

- Task (1): Partial trace over a pure state $|\psi\rangle$ retaining the reduced density matrix for the first site ρ_1. We point out that this case does not need a permutation in OSMPS. With regards to the implementation in QuTip, the many-body case does not seem to be the focus, and the density matrix of the complete pure state is built first and then traced out over ρ, which leads to some overhead.

- Task (2): Partial trace over a density matrix ρ retaining the reduced density matrix for the first site ρ_1. Since both libraries start from the density matrix, this comparison is more valuable than tracing over pure states in (1).

- Task (3): Time evolution of the quantum Ising model with a time-independent Hamiltonian. The QuTip library uses an ODE solver to evolve a given initial state in time, which we compare to the Krylov and fourth-order Trotter method from OSMPS. For QuTip we set up a single measurement of the identity matrix. OSMPS takes the default measurements including the measurement of the energy (Hamiltonian) and the overlap to the initial state, where the first one contains the major part of the measurement time in OSMPS. For OSMPS we consider the two approximate methods with the fourth order Trotter (3a) and the Krylov (3b). We do not use the $\mathbb{Z}_2$ symmetry of the system here.

We run the benchmark simulations on an *Intel(R) Core(TM) i7-3610QM CPU @ 2.30GHz, 8 GB RAM* and present the CPU times measured with Python's `time.clock` package in Table 8.3. The run times of the trace over a density matrix are comparable and show that our implementation scales as well as QuTip. The time evolutions are more difficult to compare with regards to the order of the method etc., but the time of the Trotter decomposition for large systems shows that we can offer a valid alternative. The Krylov evolution, as expected from the previous scaling analysis, e.g., in Figure 8.2, takes longer.

8.8 Conclusions

In this paper, we have shown the approaches for exact diagonalization methods including the use of symmetries and other evolution techniques without truncating entanglement, including the Trotter decomposition and the Krylov subspace method. The methods can be extended from closed to open systems.

We have described efficient methods for time evolutions and measurements without symmetries when the Hilbert space is built from a tensor product of local Hilbert spaces. Therefore, the state vector representing the wave function can be rewritten as a rank-L tensor. The methods include especially approaches for the Trotter time evolution, matrix-vector multiplication necessary for the Krylov time evolution, and measurements via reduced density

Table 8.3: *Benchmarking QuTip and OSMPS.* The comparison of run times includes (1) the partial trace of a pure state and (2) a density matrix, both tracing over the sites 2 to L where L is the system size. Furthermore, (3) contains the time evolution for the quantum Ising model for a time-independent Hamiltonian. For OSMPS we distinguish between the 4^{th} Trotter decomposition, i.e., (3a), and the Krylov method labeled as (3b). QuTip uses the default ODE solver. All CPU times $T_{\text{CPU}}(L)$ are given in seconds as a function of the system size L. The times are calculated cumulatively for 100 iterations of the corresponding task.

Task	$T_{\text{CPU}}(4)$	$T_{\text{CPU}}(6)$	$T_{\text{CPU}}(8)$	$T_{\text{CPU}}(10)$	$T_{\text{CPU}}(12)$	$T_{\text{CPU}}(14)$	$T_{\text{CPU}}(26)$
(1), QuTip	0.15	0.16	0.20	0.42	2.76	–	–
(1), OSMPS	0.01	0.01	0.01	0.01	0.01	0.01	22.00
(2), QuTip	0.12	0.14	0.18	0.39	2.71	–	–
(2), OSMPS	0.01	0.01	0.02	0.16	2.61	–	–
(3), QuTip	3.19	4.50	7.16	17.00	57.05	248.60	–
(3a), OSMPS	9.72	14.71	20.86	33.20	72.54	232.75	–
(3b), OSMPS	16.84	20.20	25.60	132.69	314.91	973.38	–

matrices. For symmetry-adapted methods, the key is the mapping into the basis. However, methods for Trotter decomposition or matrix-vector multiplication cannot avoid looping over entries and cannot use faster matrix algebra. Reduced density matrices, in particular, suffer from this limitation and we have presented a feasible approach here, scaling with $\mathcal{O}(D_S L) + \mathcal{O}(d^{2l} D_S)$.

Open system methods according to the Lindblad master equation follow two known approaches via the quantum trajectories and the Liouville space mapping the density matrix to a vector. The evolution of the vector representing the density matrix follows a Schrödinger-like equation. While quantum trajectories can use system sizes and methods equivalent to pure states sampling over many realizations, the methods for Liouville space have to be adapted slightly for the use with density matrices. This adaption refers to the matrix exponential or its approximation. While the Hamiltonian was hermitian, the Liouville operator is not necessarily hermitian. For any propagation of the whole density matrix, we can use the rule of thumb that about half the number of sites of the pure system can be simulated. The disadvantage of quantum trajectories is the error, which was of the order 10^{-2} for the

total number of excitations in the photon Josephson junctions for 500 trajectories. We point out that the number of trajectories needed might differ for various Hamiltonians.

The exact diagonalization methods presented help to develop new methods and can serve as a convergence test and benchmark. One application is the exploration of highly entangled states, which cannot be simulated with tensor network methods. Other Hamiltonians exploring only a small part of the Hilbert space might be scalable in size to more than the 25 qubits of the Ising model, where we show the scaling of Trotter decomposition up to 27 qubits. Models like the Bose-Hubbard model in k-space have long-range interactions and a large bond dimension in the Matrix Product Operators of the Hamiltonian when using tensor network methods such as MPS, and thus find in exact diagonalization methods an attractive alternative. The rule sets allow for the flexible construction of the Hamiltonians without the restriction of the MPO representation with tensor network methods, e.g., any infinite function does not have to be fitted to exponential rules. This argument might apply as well to systems with randomized interactions such as spin glasses [116, 141]. Finally, open quantum systems are another attractive field for exact diagonalization libraries despite the limitations to fewer sites due to the Liouville space. Any formulation of a master equation for ρ could be explored with the easy to program tools within our exact diagonalization codes, e.g., if Lindblad operators are non-local and/or long-range including a coupling through the environment. Especially if the full spectrum of the Hamiltonian is necessary for the Lindblad master equation, exact diagonalization is an ideal test case for any approximation truncating the number of states in the spectrum.

Therefore, these methods are not only useful as problems set in classes, but are worth being improved and optimized for exploring new frontiers in research.

8.9 Acknowledgments

We gratefully appreciate contributions from and discussions with L. Hillberry, S. Montangero, H. North, G. Shchedrin, and M. L. Wall. The calculations were carried out using the high performance computing resources provided by the Golden Energy Computing Organi-

zation at the Colorado School of Mines. This work has been supported by the NSF under the grants PHY-1520915, and OAC-1740130, and the AFOSR under grant FA9550-14-1-0287.

8.10 Rule sets for exact diagonalization

As OSMPS is a many-body library, Hamiltonians are not built by the user, but through *rule sets*. The following rule sets are currently enabled in our open source diagonalization libraries:

$$\text{Site rule} \quad : \quad \sum_{k=1}^{L} w \cdot c_k \cdot O_k \tag{8.51}$$

$$\text{Bond rule} \quad : \quad \sum_{k=1}^{L-1} w \cdot c_k \cdot O_k \otimes O'_{k+1} \tag{8.52}$$

$$\text{Exp rule} \quad : \quad \sum_{k<j}^{L} \frac{w \cdot c_k}{d_p^{(j-k-1)}} O_k \otimes \left(\bigotimes_{q=k+1}^{j-1} Q_q \right) \otimes O'_j \tag{8.53}$$

$$\text{InfiniteFunc} \quad : \quad \sum_{k<j}^{L} w \cdot c_k \cdot f(|j-k|) O_k \otimes \left(\bigotimes_{q=k+1}^{j-1} Q_q \right) \otimes O'_j \tag{8.54}$$

$$\text{MBString} \quad : \quad \sum_{k=1}^{L-j} w \cdot c_k \bigotimes_{j=1}^{W_{\text{MB}}} O_j^{[k+j-1]}, \tag{8.55}$$

where L is the number of sites in the one-dimensional chain, w is a general coupling, and c_k is a possibly space-dependent coupling. O_k, O'_k, and Q_k are operators acting on the local Hilbert space. Q_k targets fermionic systems, which have a phase operator due to the Jordan-Wigner transformation [137, 138] mapping fermions onto the lattice. The Jordan-Wigner transformation is a mapping between spins and fermions where the transformation ensures that the corresponding commutation relations hold. The exponential rule includes a decay parameter $d_p \leq 1$. The function $f(\cdot)$ describes the coupling of the two operators at an arbitrary distance for the InfiniteFunc rule. The Many-Body String (MBString) term has a width of W_{MB} sites and uses the tensor product $\otimes$ to indicate the construction on the composite Hilbert space. Synonyms for the tensor product are "outer product" or "Kronecker product".

8.11 Scaling of memory resources

We have discussed in Figure 8.2 the scaling of the computation time for the different time evolution methods. In this appendix, we discuss the corresponding scaling of the memory resources, shown in Figure 8.9. We use the python package `resource` to track the maximal memory usage over the complete calculation.

The matrix exponential has the highest demands on memory as the complete Hamiltonian has to be stored, see Figure 8.9(a). The two different set of curves distinguish the matrix exponential with and without $\mathbb{Z}_2$ symmetry. The symmetry has a smaller Hilbert space by a factor of 2 and thus lower memory requirements. The difference between dense and sparse methods is minimal within the quantum Ising model.

In contrast, both the Krylov and the Trotter method show higher memory requirements for the symmetry-conserving. We explain this trend with the fact that the mapping for the symmetry must be stored, overcoming the trend that the state vector itself is smaller for systems with $\mathbb{Z}_2$ symmetry. The lower memory for the Trotter without symmetry is due to the Krylov methods storing a set of the Krylov vectors. Figure 8.9(b) shows the same trend for the Bose-Hubbard model, where we recall that the $\mathcal{U}(1)$ symmetry takes a much smaller fraction of the Hilbert space in comparison to the quantum Ising model with and without symmetry.

We have the memory-optimized algorithms for the Krylov algorithm in our library replacing the scipy implementation. Therefore, we take a look at the memory consumption of the different Krylov modes; Figure 8.9(c) considers the quantum Ising model without using the $\mathbb{Z}_2$ symmetry. For example, the memory requirements for 24 qubits with mode 3 are below the memory used for 20 qubits in the other modes. This increased number of qubits is a clear improvement. The Bose-Hubbard double-well problem, see Figure 8.9(d), is the only simulation pushing the limits past laptop and desktop computers. Peaking at around 91GB, such simulations are limited to HPC environments. This high memory demand is related to the measurements. Therefore, we concentrate on simulations without the measurement of

the site and bond entropy to distinguish the different Krylov modes. We conclude that the third mode a priori saves memory for systems without symmetry.

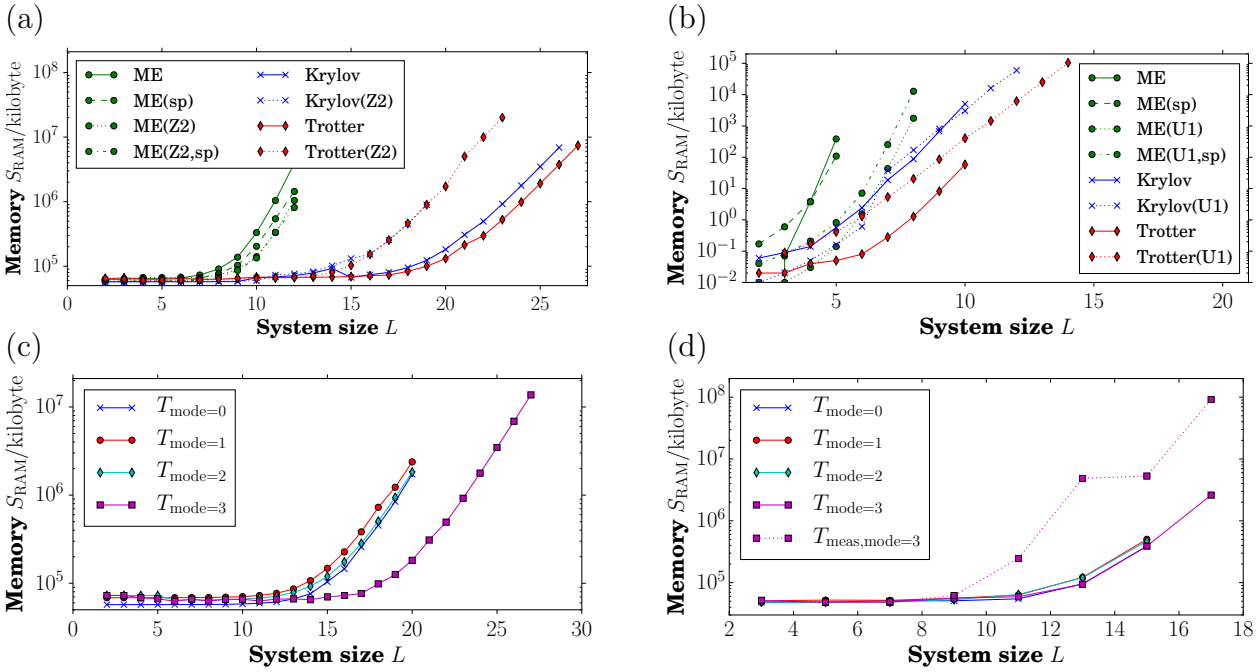

Figure 8.9: *Scaling of the Memory for Time Evolution Methods.* We profile five time steps for different system sizes L comparing the matrix exponential (ME) with sparse matrices (sp) and with dense matrices to the Trotter decomposition and to the default Krylov method. The maximal memory of the process in kilobytes is plotted on a lin-log-scale. (a) The nearest neighbor quantum Ising model has a $\mathbb{Z}_2$ symmetry, which we use in comparison to the methods without symmetry. (b) The Bose-Hubbard model is considered with a local dimension of $d = 5$, and the $\mathcal{U}(1)$ symmetry is used with unit filling in the simulations marked with $U1$. (c) The scaling of the RAM for the different Krylov modes in the quantum Ising model without using its $\mathbb{Z}_2$ symmetry. The memory-optimized mode 3 clearly saves resources for large systems. (d) The memory requirements for the Bose-Hubbard model in a double-well at filling $N = (L-1)/2$ with N odd are dominated by the measurement of the site and bond entropy. Without measurements, the Krylov modes show different RAM requirements.

8.12 Quantum Cellular Automata and Quantum Gates

The algorithms described so far evolve the quantum state or density matrix according to the differential equation presented in Eqs. (8.1), (8.39), or (8.41). The methods using the full matrix exponential and the Trotter decomposition calculate the propagator, which we apply

to the quantum state. But some problems in quantum physics are directly formulated in terms of propagators, i.e., quantum cellular automata [209, 210] and quantum gates. Quantum gates are especially common in quantum information theory: most researchers know the quantum Fourier transformation defined by their gates [85], but not the corresponding Hamiltonian.

As the major steps are already implemented with the application of the propagator to a state, we also provide the tools to formulate dynamics solely in terms of quantum gates defined on quasi-local gates. The time evolution is then formulated as one quantum circuit consisting of multiple sub-circuits. We measure after each sub-circuit, which can be different. Each sub-circuit is a series of gates G_1 to G_K:

$$|\,\psi'\rangle = G_K G_{K-1} \cdots G_2 G_1 \,|\,\psi\rangle\,, \tag{8.56}$$

where $|\,\psi'\rangle$ is the wave-function after the sub-circuit. We set up a QECA rule, i.e., the SWP-rule 6 for $L = 21$ sites [209]. The initial state is a single spin down in the middle of the system. Figure 8.10 describes the evolution according to the rule. We waive a detailed study of the scaling for the quantum circuits or gates. On the one hand, such an evolution without symmetries can be easily estimated by the contraction of the gates to the state. On the other hand, even gates obeying a symmetry and acting on two sites have an upper bound of the Trotter time evolution up to some factor for the number of applications.

In conclusion, this evolution tool comes at almost no additional cost for the implementation. Although we have at present only gates in the OSMPS library, it can be generalized to Kraus operators [85] as the next step, and QECA evolutions with Kraus operators have already been suggested in [224].

8.13 Lindblad Master Equation and the Full Spectrum

The derivation of the Lindblad master equation for a given Hamiltonian is subtle in the many-body scenario. One possibility is the inclusion of the energy eigenstates of the system.

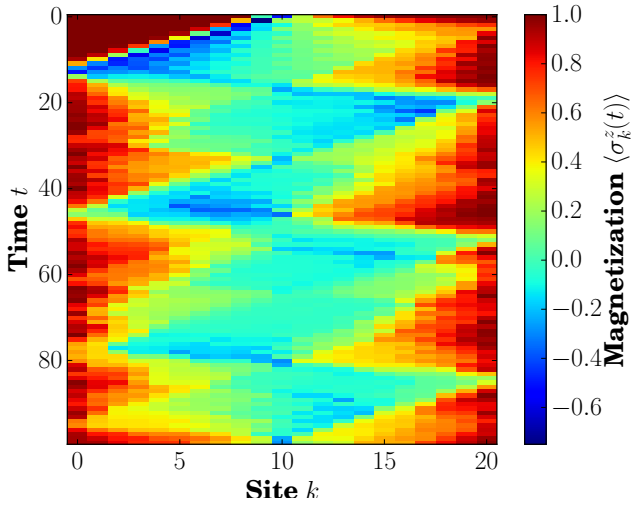

Figure 8.10: *Quantum Cellular Automata example for Quantum Circuits.* Asymmetric SWP Quantum Cellular Automata rule for $L = 21$ sites is one example for the application of quantum circuits.

This approach elegantly handles the secular approximation, but is obviously restricted to many-body systems with approximately six or fewer qubits, or the size of the Hilbert space equal to six qubits. The restriction to six qubits stems from the exponential taken in Liouville space for the Lindblad master equation, defined in Eq. (8.39). Krylov methods or the Trotter approximation are not suitable for this huge number of non-local Lindblad operators. Despite these strict limitations, the full spectrum is worth being included in a library as it allows for the study of thermalization via a reservoir.

In addition to the problem of using the full set of eigenstates, the couplings for the system-reservoir interaction have to be derived or integrated numerically. Both paths are a challenging question. We provide the structure to simulate Lindblad master equations for a system-reservoir Hamiltonian

$$H_{S+R} = H_S + \sum_{k,q} S_k \left(b_{R,q} + b_{R,q}^\dagger \right) + \sum_q \omega_q n_{R,q} \tag{8.57}$$

according to

$$\dot{\rho} = -\frac{\mathrm{i}}{\hbar}\left[H'_S, \rho\right] + \sum_{abcd} \mathcal{C}_{abcd}\left(L_{ab}\rho L^{\dagger}_{cd} - \frac{1}{2}\left\{L^{\dagger}_{cd}L_{ab}, \rho\right\}\right) . \tag{8.58}$$

The Lindblad operators $L_{ab} = |\, a\rangle\langle b\,|$ are transitions between eigenstates $|\, a\rangle$ and $|\, b\rangle$. The coupling $\mathcal{C}_{abcd}$ carries the dependence on the type of reservoir, the interaction strength between system and reservoir, the operator S in terms of the overlap $\langle a|\ S\ |b\rangle$, the temperature of the reservoir, and possible long-range couplings induced by a common reservoir shared by multiple sites. The Hamiltonian H'_S can have corrections with regards to the system Hamiltonian H_S. The reservoir is modeled via a set of harmonic oscillators with frequencies q. We have used this approach to study the thermalization of the quantum Ising model coupled to an electromagnetic field [225].

8.14 Details of Convergence Studies

In this appendix, we extend the convergence studies of the main body of this article, i.e., Sec. 8.5. We showed the dependence of the error on the method and the time step in Figure 8.7 for a time-dependent Hamiltonian in the Bose-Hubbard model. Figure 8.11 shows the same kind of study for the time-independent Hamiltonian corresponding to a sudden quench within the Mott insulator as described in the second scenario in Sec. 8.5. The error from the second order time ordering vanishes and only the Trotter decompositions remain with an error depending on the time step dt. In addition, we present the first scenario with a time-dependent Ising Hamiltonian in Figure 8.12. We calculate again the rate of convergence according to Eq. (8.38) and the maximal distance between the single site density matrices. Those rates are 2.07, 2.0 for the second order Trotter decomposition, 2.93, 1.97 for the fourth order Trotter decomposition, 2.08, 2.0 for the Krylov in mode 1, and the matrix exponential has rates of convergence of 2.08, 2.02. The first value corresponds to the pair $(dt = 0.01, dt' = 0.1)$ and the second value $(dt = 0.001, dt' = 0.01)$. We confirm that the convergence rate of dt^2 is reproduced in the Ising model due to the error in time-ordering.

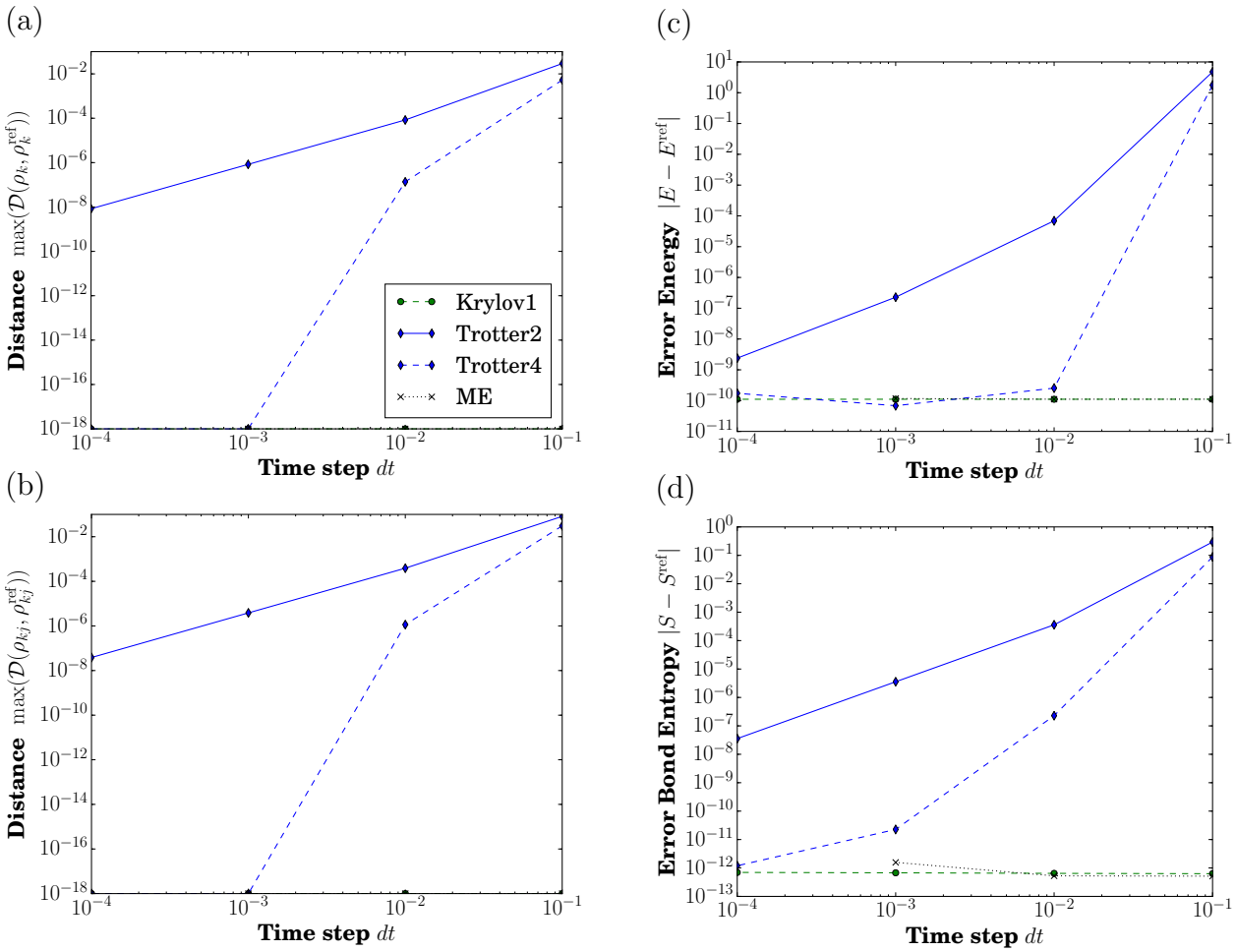

Figure 8.11: *Convergence of Methods for the time-independent Bose-Hubbard Model.* We compare the 2nd and 4th order Trotter time evolution and the Krylov method with mode 1 against the reference (ref) takes as the matrix exponential (ME) with $dt = 0.0001$ for various measures. We consider the Bose-Hubbard model in a linear quench from on-site interaction strength $U(t = 0) = 10.0$ to $U(t = 0.5) = 8.0$ for a system size of $L = 6$ and unit filling. The reference value is the matrix exponential for the smallest time step $dt = 0.0001$. The minimal error is set to 10^{-18} indicating machine precision. The measures are (a) the minimal distance over all single-site reduced density matrices, (b) the minimal distance over all two-site density matrices, (c) the error in energy, and (d) the error in the bond entropy for the splitting in the middle of the system.

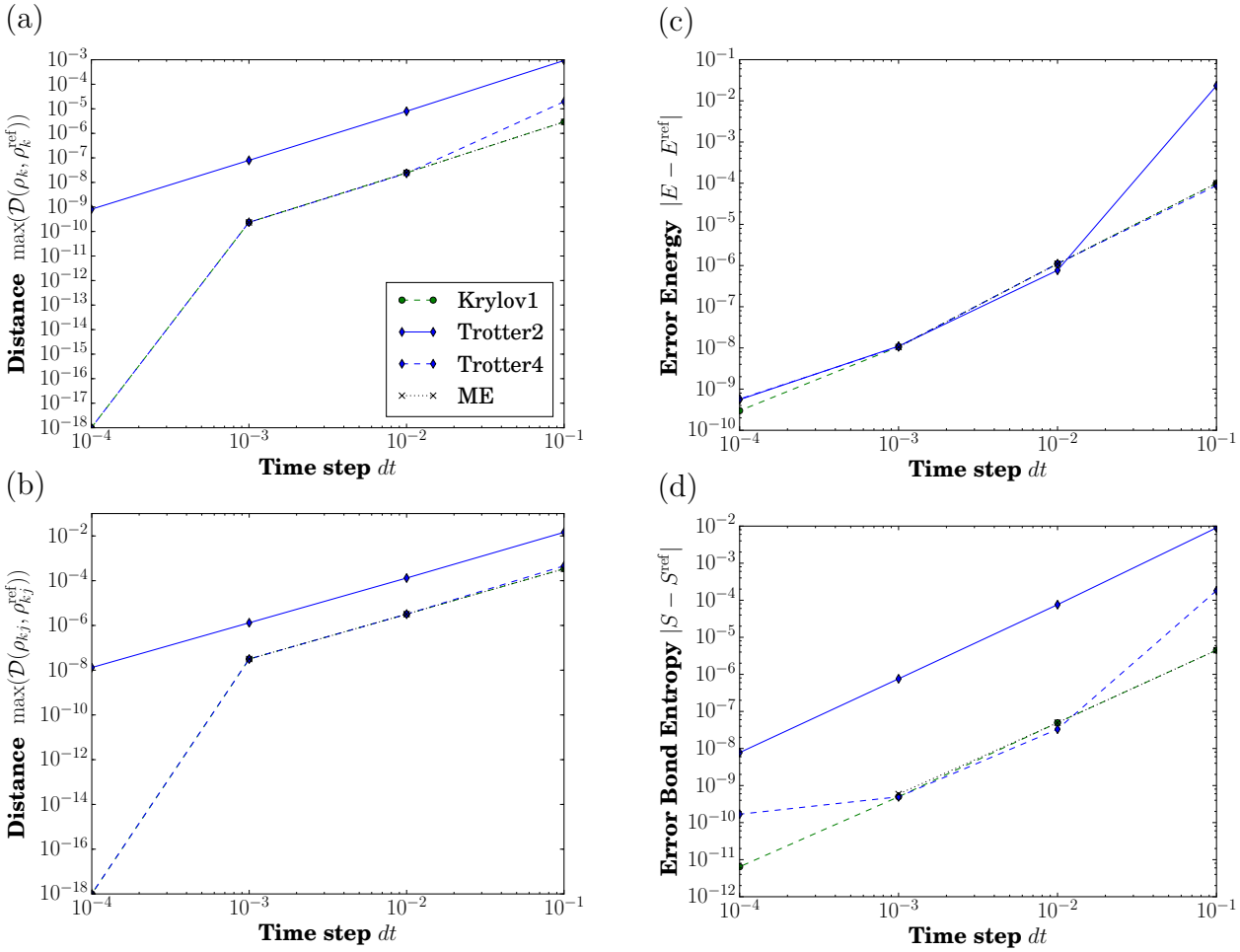

Figure 8.12: *Convergence of Methods for the Quantum Ising Model.* We compare the 2$^{\text{nd}}$ and 4$^{\text{th}}$ order Trotter time evolution and the Krylov method in mode 1 and the matrix exponential (ME). The reference (ref) is the matrix exponential with $dt = 0.001$ for all four measures. We consider the quantum Ising model using its $\mathbb{Z}_2$ symmetry in a linear quench from external field $h(t = 0) = 5.0$ to $h(t = 0.5) = 4.5$ for a system size of $L = 10$. The measures are (a) the minimal distance over all single-site reduced density matrices, (b) the minimal distance over all two-site density matrices, (c) the error in energy, and (d) the error in the bond entropy for the splitting in the middle of the system.

For the open system analysis, we studied the error of the evolution of the von Neumann equation for the density matrix in a closed system and the Lindblad master equation for selected time evolution schemes in Table 8.1 and Table 8.2. Table 8.4 and Table 8.5 show the errors of different settings. We conclude that the 4^{th} order Trotter evolution reduces the error to almost machine precision. The built-in scipy Krylov method delivers a better slightly better result than the Krylov methods from the EDLib of OSMPS, e.g., the error in energy is about two orders (one order) of magnitude smaller for the photon Josephson junctions in the von Neumann (Lindblad master) equation, defined in Eq. (8.47). In Table 8.5 we point out that the errors for the quantum trajectories do not depend on the method. We explain this by the fact that the seed of the pseudo-random number generator is fed with the ID of the trajectory and therefore the trajectories for each method are equal. Also, the error from the quantum trajectory approach is bigger than the error from the time evolution method and, therefore, the latter error is not visible in the table.

8.15 Add-ons for Open Quantum Systems

In the following, we derive the transformation into the Liouville space given via the equation and already introduced in Eq. (8.44)

$$O'\rho O \to O' \otimes O^T \left|\rho\right\rangle\!\right\rangle \,, \tag{8.59}$$

which we used to build the Liouville operator $\mathcal{L}$ for the time evolution of an open system. First, we rewrite the equation in terms of indices[5] where the elements can be permuted:

$$O'\rho O \;\; = \;\; O'_{ij}\rho_{jk}O_{kl} = O'_{ij}O_{kl}\rho_{jk} = O'_{ij}O^T_{lk}\rho_{jk} \,. \tag{8.60}$$

ρ can be transformed into a vector with a combined index (jk). From the two matrices the combination of indices can be achieved using the tensor product:

$$O'\rho O \;\; = \;\; O'_{ij}O^T_{lk} \left|\rho\right\rangle\!\right\rangle_{(jk)} = (O' \otimes O^T)_{(il),(jk)} \left|\rho\right\rangle\!\right\rangle_{(jk)} \,. \tag{8.61}$$

[5]The indices are not related to the same symbols introduced previously.

Table 8.4: *Additional Error Analysis for the Density Matrix in the von Neumann Equation.* We show additional methods extending Table 8.1 for simulations of the closed system with the open system code of the library and the reference result is the closed system solving the Schrödinger equation.

Model: H_{PJJ} Error	$\epsilon_{\mathrm{local}}$	ϵ_{corr}	ϵ_{E}	ϵ_{S}
Liou (Trotter-4)	0.0	0.0	$2.71 \cdot 10^{-13}$	–
Liou (Krylov-0)	0.0	0.0	$7.33 \cdot 10^{-15}$	–
Liou (Krylov-2)	$2.71 \cdot 10^{-13}$	$7.34 \cdot 10^{-13}$	$5.52 \cdot 10^{-13}$	–
Liou (Krylov-3)	$2.71 \cdot 10^{-13}$	$7.34 \cdot 10^{-13}$	$5.52 \cdot 10^{-13}$	–
QT1 (Trotter-4)	0.0	0.0	$1.16 \cdot 10^{-13}$	$2.45 \cdot 10^{-12}$
QT1 (Krylov-0)	0.0	0.0	$4.0 \cdot 10^{-15}$	$8.88 \cdot 10^{-16}$
Model: H_{DW} Error	$\epsilon_{\mathrm{local}}$	ϵ_{corr}	ϵ_{E}	ϵ_{S}
Liou (Trotter-4)	$6.34 \cdot 10^{-13}$	0.0	$3.53 \cdot 10^{-11}$	–
Liou (Krylov-0)	$8.87 \cdot 10^{-14}$	$2.21 \cdot 10^{-13}$	$7.81 \cdot 10^{-13}$	–
Liou (Krylov-2)	$8.56 \cdot 10^{-14}$	$7.95 \cdot 10^{-14}$	$8.04 \cdot 10^{-13}$	–
Liou (Krylov-3)	$8.54 \cdot 10^{-14}$	$1.11 \cdot 10^{-13}$	$8.13 \cdot 10^{-13}$	–
QT1 (Trotter-4)	$9.0 \cdot 10^{-14}$	$9.46 \cdot 10^{-14}$	$3.48 \cdot 10^{-11}$	$2.12 \cdot 10^{-10}$
QT1 (Krylov-0)	$8.99 \cdot 10^{-14}$	$3.91 \cdot 10^{-13}$	$7.74 \cdot 10^{-13}$	$2.38 \cdot 10^{-14}$

Table 8.5: *Additional Error Analysis for the Density Matrix in the Lindblad Master Equation.* We show additional methods extending Table 8.2 for simulations of the open quantum system and the reference result is the open system using the matrix exponential.

Model: H_{PJJ} Error	$\epsilon_{N(t)}$	$\epsilon_{\mathrm{local}}$	ϵ_{corr}	ϵ_{E}
Liou (Trotter-4)	$1.32 \cdot 10^{-13}$	$4.88 \cdot 10^{-15}$	$8.99 \cdot 10^{-15}$	$2.09 \cdot 10^{-14}$
Liou (Krylov-0)	$1.78 \cdot 10^{-14}$	$0.0 \cdot 10^{+00}$	$0.0 \cdot 10^{+00}$	$1.71 \cdot 10^{-14}$
Liou (Krylov-2)	$3.76 \cdot 10^{-13}$	$2.31 \cdot 10^{-13}$	$5.21 \cdot 10^{-13}$	$3.77 \cdot 10^{-13}$
Liou (Krylov-3)	$3.76 \cdot 10^{-13}$	$2.31 \cdot 10^{-13}$	$5.21 \cdot 10^{-13}$	$3.77 \cdot 10^{-13}$
QT500 (Trotter-4)	$1.15 \cdot 10^{-02}$	$1.49 \cdot 10^{-05}$	$4.48 \cdot 10^{-05}$	$1.15 \cdot 10^{-02}$
QT500 (Krylov-0)	$1.15 \cdot 10^{-02}$	$1.49 \cdot 10^{-05}$	$4.48 \cdot 10^{-05}$	$1.15 \cdot 10^{-02}$

Model: H_{BH} Error	$\epsilon_{\mathrm{local}}$	ϵ_{corr}	ϵ_{E}
Liou (Trotter-4)	$4.85 \cdot 10^{-14}$	$4.87 \cdot 10^{-14}$	$1.15 \cdot 10^{-10}$
Liou (Krylov-0)	0.0	0.0	$4.09 \cdot 10^{-13}$
Liou (Krylov-2)	0.0	0.0	$1.17 \cdot 10^{-12}$
Liou (Krylov-3)	0.0	0.0	$1.16 \cdot 10^{-12}$
QT500 (Trotter-4)	$2.04 \cdot 10^{-03}$	$6.44 \cdot 10^{-03}$	$3.75 \cdot 10^{-02}$
QT500 (Krylov-0)	$2.04 \cdot 10^{-03}$	$6.44 \cdot 10^{-03}$	$3.75 \cdot 10^{-02}$

To have the index k of O in the columns of the result of the tensor product, we had transposed O before. We point out that this definition works independently of row- or column-major order of the memory.

CHAPTER 9

OPENING WAYS TO SIMULATE ENTANGLED MANY-BODY QUANTUM SYSTEMS IN ONE DIMENSION

Published previously in *Computer Physics Communications*[1]

D. Jaschke,[2] M. L. Wall,[3] and L. D. Carr[4]

Abstract

Numerical simulations are a powerful tool to study quantum systems beyond exactly solvable systems lacking an analytic expression. For one-dimensional entangled quantum systems, tensor network methods, amongst them Matrix Product States (MPSs), have attracted interest from different fields of quantum physics ranging from solid state systems to quantum simulators and quantum computing. Our open source MPS code provides the community with a toolset to analyze the statics and dynamics of one-dimensional quantum systems. Here, we present our open source library, Open Source Matrix Product States (OSMPS), of MPS methods implemented in Python and Fortran2003. The library includes tools for ground state calculation and excited states via the variational ansatz. We also support ground states for infinite systems with translational invariance. Dynamics are simulated with different algorithms, including three algorithms with support for long-range interactions. Convenient features include built-in support for fermionic systems and number conservation with rotational $\mathcal{U}(1)$ and discrete $\mathbb{Z}_2$ symmetries for finite systems, as well as data parallelism with MPI. We explain the principles and techniques used in this library

[1] "Open source Matrix Product States: Opening ways to simulate entangled many-body quantum systems in one dimension", D. Jaschke, M. L. Wall, and L. D. Carr, CPC 225, 59 (2018). `https://doi.org/10.1016/j.cpc.2017.12.015`. Use in agreement with CC-BY-NC-ND license [56].

[2] primary researcher and author responsible for the manuscript.

[3] author of first release of OSMPS underlying the second release discussed in this publication; contribution of the fortran modules for the time evolution methods to the code base for the second release; detailed feedback and suggestions on the draft; currently at Johns Hopkins University, Applied Physics Laboratory.

[4] principal investigator and advisor.

along with examples of how to efficiently use the general interfaces to analyze the Ising and Bose-Hubbard models. This description includes the preparation of simulations as well as dispatching and post-processing of them.

PROGRAM SUMMARY

Program title: Open Source Matrix Product States (OSMPS), v2.0

Licensing provisions: GNU GPL v3

Programming language: Python, Fortran2003, MPI for parallel computing

Compilers (Fortran): gfortran, ifort, g95

Dependencies: The minimal requirements in addition to the Fortran compiler are BLAS, LAPACK, ARPACK, python, numpy, scipy. Additional packages for plotting include matplotlib, dvipng, and LaTeX packages. The Expokit package, available at the homepage `http://www.maths.uq.edu.au/expokit/`, is required to use the Local Runge-Kutta time evolution.

Operating system: Linux, Mac OS X, Windows

Supplementary material: We provide programs to reproduce selected figures in the Appendices.

Nature of the problem: Solving the ground state and dynamics of a many-body entangled quantum system is a challenging problem; the Hilbert space grows exponentially with system size. Complete diagonalization of the Hilbert space to floating point precision is limited to less than forty qubits.

Solution method: Matrix Product States in one spatial dimension overcome the exponentially growing Hilbert space by truncating the least important parts of it. The error can be well controlled. Local neighboring sites are variationally optimized in order to minimize the energy of the complete system. We can target the ground state and low lying excited states. Moreover, we offer various methods to solve the time evolution following the many-body Schrödinger equation. These methods include e.g. the Suzuki-Trotter decompositions using local propagators or the Krylov method, both approximating the propagator on the complete Hilbert space.

9.1 Introduction

Numerical methods have been widely used to study physical systems in quantum mechanics that are not exactly solvable. In many-body systems we encounter with the exponentially growing Hilbert space a challenge to develop methods which can still simulate quantum systems on a classical computer. Starting with the Density Matrix Renormalization Group (DMRG) [72, 73], a wide range of tensor network methods have been developed. Especially in one dimension, where numerical scaling and conditioning are best, such methods offer strong alternatives to other methods such as Quantum Monte Carlo [203, 204] and the Truncated Wigner approximation [149, 206]. Applications include solid state systems, ultracold atoms and molecules, Rydberg atoms, quantum information and quantum computing, and Josephson junction-based superconducting electro-mechanical nano devices. Matrix Product States (MPSs) [75–77, 226] define the tensor network at the foundation of the DMRG method. MPSs themselves represent a pure quantum state constructed on local Hilbert spaces of lattice sites or discretized systems. They handle the exponentially growing Hilbert space by limiting the entanglement between any two parts of the system. Numerical methods using MPSs support static results such as ground states and time evolution of pure states. In principle, highly entangled states can be represented as MPSs, but due to the upper bound of entanglement set as a parameter, they are only accurate as long as the entanglement does not exceed this bound guaranteeing feasible computation times. This point is addressed in the main part of this paper in detail. Moreover, MPSs can exploit intrinsic characteristics of the systems such as symmetries [227, 228]. Beyond MPSs, tensor network methods are extended for multiple purposes such as 2D systems via Projected Entangled Pair States (PEPS) [84], tree tensor networks (TTNs) [79], open systems with quantum trajectories (QT) [217, 218] or Matrix Product Density Operators (MPDOs) [80, 81]. Although there have been many developments in many-body quantum simulation over the last ten to twenty years [50], from multi-scale entanglement renormalization ansatz (MERA) [83] to minimally entangled typical thermal states (METTS) [177] to dynamical mean-field theory

[205] to time-dependent density functional theory (TDDFT) [229, 230], MPS methods are the most often used and well-established for strongly correlated quantum systems and appropriate for large-scale open source development. The impact of these methods is represented by the large number of open source packages for MPS and DMRG [88–102], not counting proprietary efforts of multiple other groups.

We present in this paper our open source Matrix Product State (OSMPS) library, which is available on SourceForge [52]. We have over 2300 downloads since its initial release in January 2014. The library or a derivative of the library has been used in various publications [44, 121, 176, 214, 231–242]. Our implementations cover features such as variational ground and excited state searches and real time evolution for finite systems as well as ground states of infinite systems [119]. We provide built-in features such as support for symmetries, e.g. rotational $\mathcal{U}(1)$ symmetry used for number conservation in the Bose-Hubbard model and discrete $\mathbb{Z}_2$ symmetry occurring in the quantum Ising model, and present them in the case studies of this article. These symmetries lead to a speedup in terms of computation time and allow us to address specific states. Our libraries also support data parallel execution via Message Passing Interface (MPI) to utilize modern high performance computing resources efficiently. We illustrate the algorithms in our library together with examples of models.

One motivation for the development of OSMPS is our focus on ultracold molecules and other quantum simulator architectures incorporating long-range interacting synthetic quantum matter. Where some MPS-based algorithms are limited to nearest neighbor terms in one-dimensional systems, molecules and many other systems have long-range interactions, e.g. due to dipolar effects. In order to treat such systems, many of the algorithms in OSMPS, including dynamics algorithms, feature support for long-range interactions.

This paper is intended for two audiences: First, tensor network methods and our interfaces are introduced for researchers not familiar with such methods, but in need of numerical simulations of correlations, entanglement, and dynamics in many-body systems. On the other hand, experienced researchers within the tensor networks community should have a

clear way to understand the concrete and useful details of our implementations. The paper is organized as follows. In Sec. 9.2, we introduce the general idea of tensor networks, and provide in addition appropriate references for further reading. We continue with the example of the Ising model in Sec. 9.3 to demonstrate the variational ground state search including the general setup of systems and then highlight the other algorithms in the following sections. Section 9.4 describes the variational search for excited states and the infinite MPS (iMPS) for the thermodynamic limit. The time evolution methods including Krylov, Time-Evolving Block Decimation (TEBD), Time-Dependent Variational Principle (TDVP), and local Runge-Kutta follow in Sec. 9.5. We describe future developments ahead of the conclusion in Sec. 9.7. The appendices cover topics such as convenient features in App. 9.9, convergence studies in App. 9.10, and scaling of resources in App. 9.11. Appendix 9.12 provides a detailed derivation of error bounds for the static simulations. Details on the bound of measurements with the trace distance in App. 9.13, an explanation for Krylov method in App. 9.14, and further auxiliary calculations in App. 9.15 complete the content of the appendices. Appendix B.1 explains the supplemental material.

9.2 Basic concepts in tensor network techniques

In this section, we briefly review the concepts of tensor network techniques. Readers familiar with MPS algorithms can continue on to Sec. 9.3 discussing the design of simulations specifically for OSMPS. The MPS algorithms rely heavily on the Schmidt decomposition of a quantum system, which can be explained best in the case of two subsystems 1 and 2 and their wave function $|\,\psi_{1,2}\rangle$. Each subsystem is defined on a local Hilbert space $\mathcal{H}_k$ of dimension d_k, and is spanned by an orthonormal basis of states $\{|i_k\rangle\}$. The joint Hilbert space of subsystems 1 and 2 is formed via the tensor product $\mathcal{H} = \mathcal{H}_{1,2} = \mathcal{H}_1 \otimes \mathcal{H}_2$ and has a dimension $d_1 \times d_2$. The Schmidt decomposition is then based on a set of local wave functions $|\,\psi_\alpha^{[1]}\rangle$ and $|\,\psi_\alpha^{[2]}\rangle$

$$|\psi_{1,2}\rangle = \sum_{\alpha=1}^{\chi_{\max}} \lambda_\alpha |\psi_\alpha^{[1]}\rangle |\psi_\alpha^{[2]}\rangle \,. \tag{9.1}$$

The Schmidt decomposition corresponds to a singular value decomposition (SVD) where the singular values are the λ_α. The number of non-zero singular values serves as a coarse measure of entanglement between the systems 1 and 2, known as the Schmidt number or Schmidt rank. We dub the maximal number of singular values as $\chi_{\max}$. Tracing out over either of the subsystems, we obtain the reduced density matrix of the other subsystem. This demonstrates that the eigenvalues of the reduced density matrices $\rho_1 = \mathrm{Tr}_2 |\psi_{1,2}\rangle\langle\psi_{1,2}|$ and $\rho_2 = \mathrm{Tr}_1 |\psi_{1,2}\rangle\langle\psi_{1,2}|$ are $\{\lambda_\alpha^2\}$ [85].

The Schmidt decomposition is unique up to rotations within subspaces of degenerate singular values for a chosen basis. Local unitary transformations such as basis transformations affecting each half of the bipartition separately are possible in general, because they do not change the entanglement, i.e., the number and value of non-zero singular values. MPSs generalize the Schmidt decomposition by allowing for rotations within the Schmidt bases $|\psi_\alpha^{[k]}\rangle$ that keep the amount of bipartite entanglement between the two subsystems fixed:

$$|\psi_{1,2}\rangle = \sum_{\alpha=1}^{\chi_{\max}} \sum_{i_1=1}^{d_1} \sum_{i_2=1}^{d_2} A_\alpha^{[1]i_1} A_\alpha^{[2]i_2} \, |\, i_1\rangle \, |\, i_2\rangle \,. \tag{9.2}$$

In addition, while the Schmidt decomposition is only defined for a bipartite system, the MPS form can be extended to any number of degrees of freedom.

We take the example of a two-site system to illustrate the connection between the Schmidt and MPS decompositions. Subsystem 1 is the site with $k = 1$ and subsystem two corresponds to the site with $k = 2$. The MPS decomposition of such a system is described in Eq. (9.2). We rewrite any state $|\,\psi_\alpha\rangle$ in Eq. (9.1) as a matrix of complex numbers $c_{i_1 i_2}$ and its corresponding basis states, that is $\sum_{i_1 i_2} c_{i_1 i_2} |i_1\rangle |i_2\rangle$. In Eq. (9.1), each dimension k is spanned by $\chi_{\max}$ orthonormal vectors. We can rewrite the sets of these vectors as matrices (rank-two tensors), where each column of the matrix represents a vector in the case of site 1, and each row is

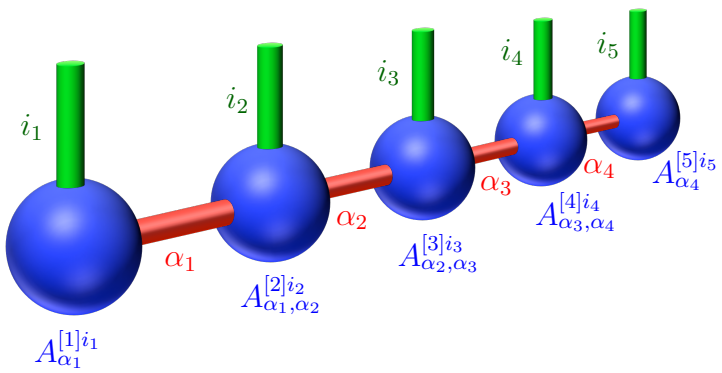

Figure 9.1: *Tensor network representation of an MPS* of five sites for open boundary conditions. The state is decomposed into local tensors representing each site. These tensors are connected to their nearest neighbors via the Schmidt decomposition where singular values are truncated to maintain feasible run times for larger systems. The indices for the local Hilbert space i_k are connected for measurements, e.g. for the norm $\langle\psi|\psi\rangle$, with their complex conjugated counterpart.

filled with one vector for site 2. Then, the matrix $A^{[k]}$ in Eq. (9.2) represents a rank-2 tensor for site k and the singular values are contained in either $A^{[k]}$. A single element of the matrix $A^{[k]}$ can be written as $A^{[k]j_k}_{\alpha} = \left\langle j_k \middle| \psi^{[k]}_{\alpha} \right\rangle$ in the two-site case above. Thus, the indices of the tensors $A^{[k]}$ correspond to the local Hilbert space i_k and the singular values of the Schmidt decomposition α. Throughout the paper we note the site index of a tensor in brackets, i.e., the k in $A^{[k]}$.

In order to generalize this decomposition for a system with L sites, successive SVDs lead to one tensor per site where the tensors are now rank-2 at the boundaries and rank-3 in the bulk of the system, as shown in the representation as a tensor network in Figure 9.1:

$$|\psi_{1,\ldots,L}\rangle = \sum_{\alpha_1\cdots\alpha_{L-1}} \sum_{i_1\cdots i_L} A^{[1]i_1}_{\alpha_1} A^{[2]i_2}_{\alpha_1,\alpha_2} \cdots A^{[L-1]i_{L-1}}_{\alpha_{L-2},\alpha_{L-1}} A^{[L]i_L}_{\alpha_{L-1}} \, |\, i_1\rangle \cdots |\, i_L\rangle \,. \tag{9.3}$$

If we allow the indices α_j to run over exponentially large values $\sim d^{L/2}$ ($d = d_k$ the local dimension, assumed uniform for simplicity), such a representation is exact, but manipulating this exact representation also scales exponentially with the system size and we do not gain anything over exact diagonalization methods.

We now introduce the key approximation in the MPS algorithm, that is the truncation of the Hilbert space according to the singular values from the Schmidt decomposition. The essential idea here is to replace the number of singular values $\chi_{\max}$ with a reduced number χ: for instance, if there are singular values less than 10^{-16} there is no reason to count them towards the amount of entanglement between the two subsystems. Thus χ becomes the *reduced Schmidt rank*, the major convergence parameter of the whole MPS algorithm, as we will show. We obtain these singular values for any splitting in two connected subsystems, and the truncation is encoded in the maximum range of the auxiliary indices α_i. Considering an approximated state $|\psi'\rangle$ truncated to the first χ singular values at some particular bond of the normalized state $|\psi\rangle$ with $\chi_{\max}$ singular values at that bond, the overlap between the two states is

$$\langle\psi'|\psi\rangle \;=\; \frac{\sum_{i=1}^{\chi}\lambda_i^2}{\sqrt{\sum_{i=1}^{\chi}\lambda_i^2}} = \sqrt{\sum_{i=1}^{\chi}\lambda_i^2}\,. \tag{9.4}$$

We prefer the overlap instead of the 2-norm of the overlap since it allows us to relate our result to the quantum fidelity in our case of pure states with real overlaps as $\mathcal{F} = \langle\psi\,|\,\psi'\rangle$. We define the truncation error made in this step as $\epsilon_{\text{local}} = 1 - \langle\psi\,|\,\psi'\rangle$ and obtain

$$\epsilon_{\text{local}} \;=\; 1 - \sqrt{\sum_{i=1}^{\chi}\lambda_i^2} \leq \sum_{i=\chi+1}^{\chi_{\max}}\lambda_i^2\,. \tag{9.5}$$

This upper bound is useful since it relates directly to the truncated singular values. Such a truncation corresponds to a truncation of entanglement through two entanglement measures: the Schmidt rank χ and the von Neumann entropy S. The former is simply the number of non-zero singular values, and is an entanglement monotone. The von Neumann entropy, or bond entropy, S is given as

$$S = -\sum_{i=1}^{\chi}\lambda_i^2\log(\lambda_i^2)\,. \tag{9.6}$$

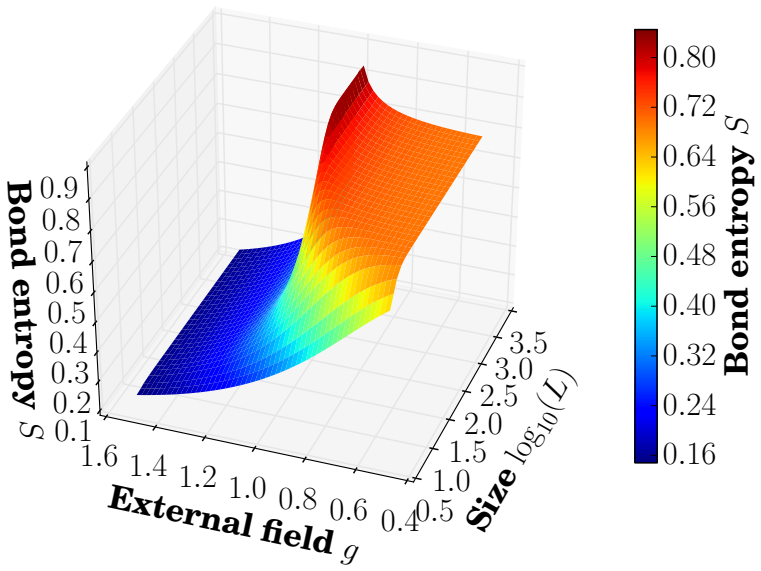

Figure 9.2: *The compression of the quantum state in the MPS* acts on the singular values of the Schmidt decomposition in Eq. (9.1). The bond entropy or von Neumann entropy at the center bond for the nearest-neighbor quantum Ising model $H = -J\sum \sigma_k^z \sigma_{k+1}^z - Jg\sum \sigma_k^x$, defined later in Eq. (9.15), peaks around the critical point for increasing system sizes.

In Figure 9.2 we show the bond entropy for the bipartition at the center bond for the quantum Ising model with transverse field as a function of the system size and external field. Errors in the MPS approach originate in high entanglement; therefore, simulations for increasing system sizes and around the quantum critical point are more vulnerable to smaller cutoffs χ. The quantum critical point for the Ising model is $h_c = 1.0$ and becomes visible as a red ridge in Figure 9.2 for large system sizes. The ground state of the ferromagnetic phase in the limit of zero external field, also called the Greenberger-Horne-Zeilinger (GHZ) state, is the superposition of all spins up and all spins down, i.e. $\left(|\uparrow\cdots\uparrow\rangle + |\downarrow\cdots\downarrow\rangle\right)/\sqrt{2}$. We expect an entropy of $S = -\log(0.5) \approx 0.69$, which agrees well with the results in the Figure 9.2. For gapped 1D systems with short-range interactions, the so-called area law for entanglement [78] states that the entanglement at any bipartition is independent of the length of the subsystems (and hence of the system size L). Since the bond entropy is an entanglement measure, this upper bound can be used as the gap opens away from the critical point. At the critical point, the entanglement grows logarithmically with the subsystem size.

We introduce a list of basic operations that can be performed on tensor networks, and explain the orthogonality center, an isometrization or gauge, used in the OSMPS algorithms. For these linear algebra operations on tensors, we suppress the basis kets of the quantum states for simplicity throughout the paper. One key feature of every MPS with open boundary conditions is that introducing an orthogonality center leads to faster local measurements and error reduction in the truncation [243]. We introduce the left and right canonical form of tensors according to

$$\begin{aligned} A^{[k]i_k}_{\alpha_{k-1},\alpha_k} = L^{[k]i_k}_{\alpha_{k-1},\alpha_k} \text{ if } \begin{cases} A^{[j]} = L^{[j]} \; \forall \; j < k \\ \text{and } \sum_{\alpha_{k-1},i_k} A^{[k]i_k}_{\alpha_{k-1},\alpha_k} (A^{[k]i_k}_{\alpha_{k-1},\alpha'_k})^* = \mathbb{I}_{\alpha_k,\alpha'_k} \, , \end{cases} \\ A^{[k]i_k}_{\alpha_{k-1},\alpha_k} = R^{[k]i_k}_{\alpha_{k-1},\alpha_k} \text{ if } \begin{cases} A^{[j]} = R^{[j]} \; \forall \; j > k \\ \text{and } \sum_{\alpha_k,i_k} A^{[k]i_k}_{\alpha_{k-1},\alpha_k} (A^{[k]i_k}_{\alpha'_{k-1},\alpha_k})^* = \mathbb{I}_{\alpha_{k-1},\alpha'_{k-1}} \, . \end{cases} \end{aligned} \tag{9.7}$$

The left (right) canonical forms $L^{[k]}$ $\left(R^{[k]}\right)$ are unitary matrices, e.g. from the SVD obtained from the Schmidt decomposition in Eq. (9.1). These conditions apply if the singular values have not been multiplied into the tensor. We define the orthogonality center as the site which has only left orthogonal tensors on the left side and right orthogonal tensor on the right side. This feature becomes beneficial for measurements as the contractions in the condition of Eq. (9.7) do not have to be calculated knowing that the result is the identity $\mathbb{I}$. Stated equivalently, the tensor of the orthogonality center $A^{[k]i_k}_{\alpha\beta}$ consists of the coefficients of the wave function in the orthonormal basis spanned by the local states $|i_k\rangle$ and the left and right Schmidt vectors given by products of the other MPS tensors. With these definitions, we can derive the overlap from Eq. (9.4). We assume that we truncate singular values at the bond of the sites k and $k+1$ and the sites up to and including site k are of the form $L^{[j\leq k]}$ and the tensors beginning on site $k+1$ are of type $R^{[j\geq k+1]}$. The truncation does not affect any of the tensors $L^{[j\leq k]}$ or $R^{[j\geq k+1]}$. Contracting these tensors for the overlap with their complex conjugated counterparts, we obtain identities on all sites and $\langle\psi''|\psi\rangle$ simplifies to

$$\langle\psi'|\psi\rangle \;\; = \;\; \sum_{\alpha_{k-1},\alpha_k} \lambda_{\alpha_{k-1},\alpha_k} \lambda'_{\alpha_{k-1},\alpha_k} \, , \tag{9.8}$$

where $|\,\psi''\rangle$ is the unnormalized truncated state and $|\,\psi'\rangle$ the truncated normalized state. The diagonal structure of the matrices λ containing the singular values leads to $\langle\psi'|\psi\rangle = \sum_\alpha \lambda_\alpha \lambda'_\alpha$. Since the smallest singular values in λ' are set to zero, the result is the sum of the squared singular values in λ'. The additional term in the denominator in Eq. (9.4) originates in the normalization of $|\,\psi''\rangle$. We emphasize that this procedure only works if the sites are completely in the form of $L^{[j\leq k]}$ and $R^{[j\geq k+1]}$ since otherwise, the contraction with the complex conjugated tensor does not lead to an identity.

Moreover, we introduce the following actions on tensors in our MPS library:

- **Contractions** over two tensors are defined as the summation over one (or more) common indices, and hence generalize matrix-matrix multiplication to higher-rank tensors. A commonly used example would be to contract two neighboring tensors of an MPS, $A^{[k]i_k}_{\alpha_{k-1},\alpha_k}$ and $A^{[k+1]i_{k+1}}_{\alpha_k,\alpha_{k+1}}$, to one tensor representing the sites k and $k+1$. The summation is in this case over the index α_k and we obtain a tensor $\Theta^{[k,k+1]i_k,i_{k+1}}_{\alpha_{k-1},\alpha_{k+1}}$.

- **Splitting** of a tensor is the reverse action of a contraction. The indices of the tensor form two subgroups where the splitting is enacted between those two groups. Taking the two site tensor $\Theta^{[k,k+1]i_k,i_{k+1}}_{\alpha_{k-1},\alpha_{k+1}}$ as an example, we group α_{k-1}, i_k together and i_{k+1}, α_{k+1} in order to obtain two single site tensors, up to a possible truncation. The splitting can be achieved via three possibilities:

  - An SVD splits the tensor directly into two unitary tensors and the singular values, described by

$$\Theta^{[k,k+1]i_k,i_{k+1}}_{\alpha_{k-1},\alpha_{k+1}} \;=\; L^{[k]i_k}_{\alpha_{k-1},\alpha_k} \lambda_{\alpha_k} R^{[k+1]i_{k+1}}_{\alpha_k,\alpha_{k+1}}\,, \tag{9.9}$$

    where the singular values λ_{α_k} allow us to truncate the state to a certain χ. The maximal bond dimension is defined as $\min(\chi_{k-1}d_k, d_{k+1}\chi_{k+1})$.

  - The eigenvalue decomposition is related to the singular value decomposition, which is the reason the eigenvalue decomposition can replace the SVD. If the

SVD decomposes A into $U\lambda V$, the eigendecomposition $\mathcal{E}(\,\cdot\,)$ is set up as follows:

$$\mathcal{E}(AA^\dagger) = \mathcal{E}\left(U\lambda VV^\dagger\lambda U^\dagger\right) = \mathcal{E}\left(U\lambda^2U^\dagger\right) = U\lambda^2U^\dagger\,. \tag{9.10}$$

The eigendecomposition of $AA^\dagger$, which is built from a matrix-matrix multiplication, returns a unitary matrix and the singular values squared. To obtain the right matrix, we multiply $U^\dagger$ with the original matrix A leading to

$$U^\dagger A = U^\dagger U\lambda V = \lambda V\,, \tag{9.11}$$

which already contains the singular values. After completing the series of steps, we obtain

$$\Theta^{[k,k+1]i_k,i_{k+1}}_{\alpha_{k-1},\alpha_{k+1}} = L^{[k]i_k}_{\alpha_{k-1},\alpha_k}A^{[k+1]i_{k+1}}_{\alpha_k,\alpha_{k+1}}\,, \tag{9.12}$$

where the truncation is possible due to the knowledge of λ^2 in the intermediate step of Eq. (9.10), although the singular values do not appear in the previous equation (9.12). As in the case of the SVD, the maximal bond dimension is $\min(\chi_{k-1}d_k, d_{k+1}\chi_{k+1})$. The unitary matrix can be obtained for the right side starting with $A^\dagger A$. This procedure is generally faster than the SVD.

- The QR decomposition decomposes a matrix into a unitary matrix and an upper triangular matrix T. If the unitary matrix is on the right side, it may be referred to as RQ decomposition. It does not allow for truncation as the singular values are not calculated. The example for the QR is

$$\Theta^{[k,k+1]i_k,i_{k+1}}_{\alpha_{k-1},\alpha_{k+1}} = L^{[k]i_k}_{\alpha_{k-1},\alpha_k}T^{[k+1]i_{k+1}}_{\alpha_k,\alpha_{k+1}}\,. \tag{9.13}$$

Therefore, the new bond dimension is the maximal one, $\chi = \chi_{\max} = \min(\chi_{k-1}d_k,$ $d_{k+1}\chi_{k+1})$. The fact that the QR scenario is not rank revealing is the reason for not using it in the splitting of two sites in the library, but it is used for shifting

as explained in the following.

The different options for splitting a tensor are summarized in Figure 9.3. We choose the SVD to obtain the singular values and two unitary matrices. In contrast, the eigenvalue decomposition yields a unitary matrix and the singular values. The QR decomposition differs from the first two methods as it does not reveal the singular values and returns only one unitary matrix. Therefore, the QR is computationally less expensive than the approach with the eigenvalue decomposition. The SVD is computationally more costly than both other algorithms.

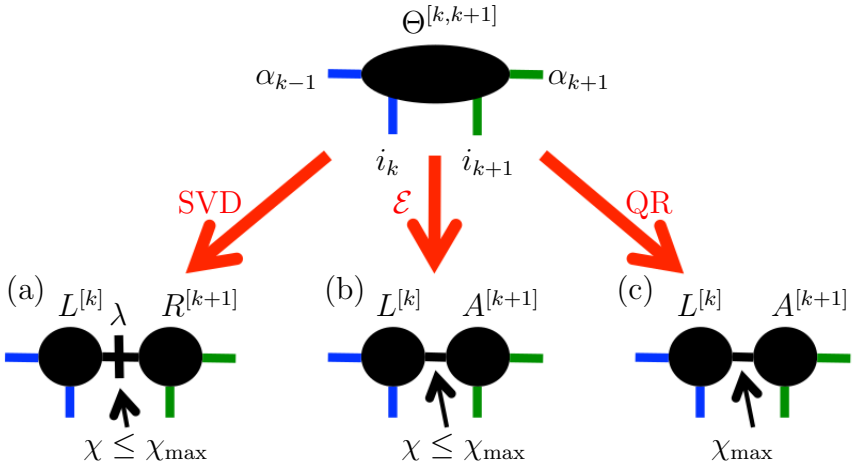

Figure 9.3: *Methods for splitting a two site tensor* into two one site tensors include (a) an SVD decomposition, (b) an eigenvalue decomposition $\mathcal{E}$ in combination with matrix multiplications, and (c) a QR decomposition.

- **Shifting** the orthogonality center can be done with local operations, meaning that the operations act only at one site at a time and do not use any two site tensors. Running an SVD or QR (RQ) decomposition for site k on a single rank-3 tensor with dimensions χ_{k-1}, d, and χ_k, we reshape the tensor as a $\chi_l d \times \chi_r$ ($\chi_l \times d\chi_r$) matrix and obtain a left-canonical (right-canonical) unitary tensor for site k and an additional matrix. The additional matrix consists of the singular values contracted into a unitary matrix when choosing an SVD. For the QR (RQ) decomposition we obtain a left (right) canonical unitary and an additional upper triangular matrix. This additional matrix can be

contracted to the corresponding neighboring site $k \pm 1$, resulting in that site becoming the new orthogonality center. We note in this case that the QR and RQ decomposition does not change the ranks of the matrices, and is roughly a factor of two faster than the SVD.

With the knowledge of the basic features of an MPS, we introduce in the next chapter how a model is defined in the OSMPS library and how we obtain results as in Figure 9.2.

9.3 Defining systems and variational ground state search

We now outline the definition of systems in OSMPS. As an example we consider finding the ground state of the finite size quantum Ising model. The 1D long-range transverse field Ising Hamiltonian is [123, 127]

$$H = -J \sum_{i<j\leq L} \frac{\sigma_i^z \sigma_j^z}{(j-i)^\alpha} - Jg \sum_{i=1}^{L} \sigma_i^x \,, \tag{9.14}$$

where the operators are defined over the Pauli matrices $\{\sigma_i^x, \sigma_i^y, \sigma_i^z\}$ acting on a site i in the system. The interactions between the spins at different sites decay following a power-law introduced in the first term of the Hamiltonian governed by α, the distance $|j-i|$, and the overall energy scale J. The external field is governed by the dimensionless g appearing in the second term of the Hamiltonian. The number of sites is L. We focus in this section on the nearest neighbor case H_{NN} obtained for the limit $\alpha \to \infty$, commonly called the transverse quantum Ising model,

$$H_{\mathrm{NN}} = -J \sum_{i=1}^{L-1} \sigma_i^z \sigma_{i+1}^z - Jg \sum_{i=1}^{L} \sigma_i^x \,. \tag{9.15}$$

The overall approach to OSMPS is a user-friendly Python environment calling a Fortran core for the actual calculations. This scheme is depicted in Figure 9.4. Thus, we guide the reader through the simulation with a corresponding summary of the Python files; the complete files are contained in supplemental material, see Appendix B.1.

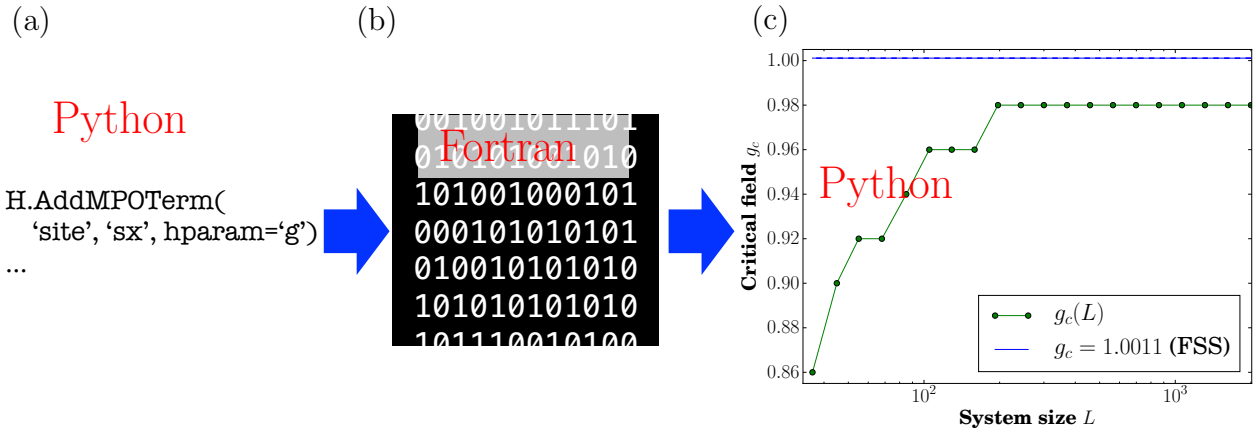

Figure 9.4: *OSMPS flow chart for a simulation.* The OSMPS library combines a user-friendly interface in Python with a computationally powerful core written in Fortran. (a) The simulation setup is done in Python. (b) A write function provides the files for Fortran and a corresponding read function imports the results from Fortran to Python (blue arrows). (c) The Python front end then takes care of the evaluation of the data. The plot in the flow charts shows the critical value of the external field in the Ising model as a function of the system size L evaluated via the maximum of the bond entropy. Finite size scaling (FSS) delivers the critical field in the thermodynamic limit for $L \to \infty$.

From a quantum mechanical point of view the following steps are necessary to describe a system. First, we have to generate the operators which are acting on the local Hilbert space, described in Sec. 9.3.1. Once we have the operators, we build the Hamiltonian out of rule sets in Sec. 9.3.2. Then, we set up the measurements to be carried out in Sec. 9.3.3. This procedure completes the definition of the quantum system, but we have two more tasks with regards to the numerics. In the fourth step we define the convergence parameters of the algorithm, where Sec. 9.3.4 describes this step for the variational ground state search. Finally, the simulation is set up and executed in Sec. 9.3.5.

One general comment remains before starting with a detailed description of the simulation setup. Every simulation in OSMPS is represented by a Python dictionary, which contains observables and convergence parameters as well as general parameters such as the system size.

9.3.1 Operators

OSMPS comes with predefined sets of operators for three different physical systems to facilitate the setup of simulations. These predefined sets of operators are returned by the corresponding functions for bosonic systems such as the Bose-Hubbard model, fermionic systems including their phase operators originating from the Jordan-Wigner transformation, or spin operators. We use the last set in the example for the quantum Ising model. The corresponding function `BuildSpinOperators` returns the set of operators $\{\sigma^+, \sigma^-, S^z, \mathbb{I}\}$. In order to obtain the Pauli operators σ^x and σ^z from the spin lowering and raising operators $\sigma^\pm$ and the spin operator S_z, we suggest following the prescription in Source Code 9.1.

Source Code 9.1: Defining the operators of the quantum Ising model overwriting S^Z with σ^Z.

```
9.38    # These are rotated Pauli operators to obtain a
9.39    # diagonal generator for Z2
9.40    Operators = mps.BuildSpinOperators(spin=0.5)
9.41    Operators['sx'] = 2 * Operators['sz']
9.42    Operators['sz'] = - (Operators['splus']
9.43                         + Operators['sminus'])
9.44    Operators['gen'] = np.array([[0, 0], [0, 1.]])
```

9.3.2 Hamiltonians

Through these operators, stored in a dictionary-like Python class, we define the Hamiltonian and later on the observables. The Hamiltonian is described as a matrix product operator (MPO), which is effectively an MPS with rank-four tensors instead of rank-three tensors:

$$H = \sum_{i_1,\ldots,i_L} \sum_{i'_1,\ldots,i'_L} \sum_{\alpha_1,\ldots,\alpha L-1} M^{[1]i'_1,i_1}_{\alpha_1} M^{[2]i'_2,i_2}_{\alpha_1,\alpha_2} \cdots M^{[L]i'_L,i_L}_{\alpha_{L-1}} \, |\, i'_1\rangle\langle i_1 \,| \cdots |\, i'_L\rangle\langle i_L \,| \ . \tag{9.16}$$

A key property is that an MPO acting on an MPS can be written as another MPS, generally with a larger bond dimension. The physical indices i_k act on the physical indices of an MPS and take them to new physical indices i'_k. The auxiliary indices α of the MPO are fused with the corresponding auxiliary indices in the MPS. For most physical operators, this structure of rank-4 tensors is sparse and therefore we rather seek for an efficient implementation in terms of MPO-matrices $M^{[k]}$ than in rank-4 tensors. The MPO matrix $M^{[k]}$ including the iteration over all indices for one site representing the rule sets [121, 244] for local terms, bond terms for the interaction of nearest neighbors, and exponential rules for long-range interactions between two sites takes the form

$$M^{[k]} = \begin{pmatrix} A^{[k]}_{\alpha_{k-1}=1,\alpha_k=1} & 0 & 0 & 0 \\ A^{[k]}_{\alpha_{k-1}=2,\alpha_k=1} & A^{[k]}_{\alpha_{k-1}=2,\alpha_k=2} & 0 & 0 \\ A^{[k]}_{\alpha_{k-1}=3,\alpha_k=1} & 0 & A^{[k]}_{\alpha_{k-1}=3,\alpha_k=3} & 0 \\ A^{[k]}_{\alpha_{k-1}=4,\alpha_k=1} & A^{[k]}_{\alpha_{k-1}=4,\alpha_k=2} & A^{[k]}_{\alpha_{k-1}=4,\alpha_k=3} & A^{[k]}_{\alpha_{k-1}=4,\alpha_k=4} \end{pmatrix} , \tag{9.17}$$

where $k = 2, 3, \ldots, L-1$. The matrix structure in Eq. (9.17) corresponds to the auxiliary indices. Each element within this structure $A_{\alpha_{k-1},\alpha_k}$ is a matrix acting on the local Hilbert space of site k, e.g. the Pauli matrix σ^z_k. Thus the auxiliary indices α of the rank-4 tensor encode the row and column of $M^{[k]}$, while the indices i_k and i'_k are related to the local Hilbert space located in the rows and columns of the matrices $A_{\alpha_{k-1},\alpha_k}$. We now illustrate the meaning of the matrices depending on their position in $M^{[k]}$. In order to build the MPO for the Hamiltonian for the long-range Ising model, we only need the first column, last row, and the diagonal of $M^{[k]}$ and store it as a sparse structure. Matrices in the first column (last row) of $M^{[k]}$ are multiplied with identity operators on the right (left) side of site k, i.e., they do not interact with any sites right (left) of themselves. Diagonal elements propagate operators through the system and are completed by other operators to the left and right of

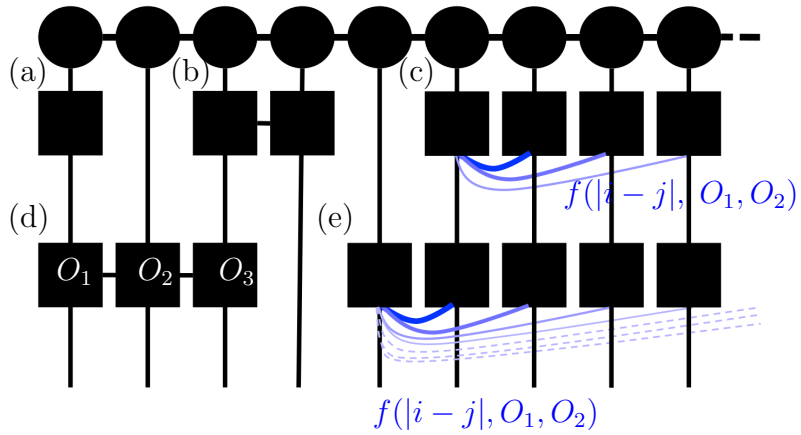

Figure 9.5: *Rules for building a Hamiltonian.* (a) Local terms; (b) bond terms acting on two neighboring sites; (c) finite range terms of two operators O_1, O_2 and a coupling depending on the distance. The coupling function $f(x)$ is a finite sum of a limited number of neighboring sites. (d) String of arbitrary operators, e.g., a three-body term built from O_1, O_2, and O_3 and (e) infinite terms of two operators O_1 and O_2 with a distance depending on decaying coupling either as a general function $f(|j-i|)$ (InfiniteFunction) or as an exponential (Exponential). Any infinite function is expressed as a sum of exponentials within OSMPS. The coupling function $f(x)$ is extended to all sites.

site k, and hence represent long-range interactions. For the first and last site we define the MPO-matrix as vectors

$$M^{[1]} = \begin{pmatrix} A^{[1]}_{1,1} & A^{[1]}_{1,2} & A^{[1]}_{1,3} & A^{[1]}_{1,4} \end{pmatrix}, \quad M^{[L]} = \begin{pmatrix} A^{[L]}_{1,1} \\ A^{[L]}_{2,1} \\ A^{[L]}_{3,1} \\ A^{[L]}_{4,1} \end{pmatrix}, \tag{9.18}$$

corresponding to the auxiliary rank-one structure for the MPO matrices at the boundary in Eq. (9.16). Note that the first MPO matrix is a row vector and the last is a column vector, resulting in the contracted MPO object Eq. (9.16) being a 1×1 matrix in the auxiliary indices.

We now build the nearest neighbor Hamiltonian H_{NN} from Eq. (9.15) for the quantum Ising model to continue with our example. Figure 9.5 shows the possible rule sets provided through OSMPS. We need the local site term depicted in Figure 9.5(a) and the bond term from Figure 9.5(b). In general these operators are filled with identities on all other sites and

act on each possible site. The corresponding MPO-matrices depending on the site index k are then

$$\begin{aligned} M^{[1]} &= \begin{pmatrix} -Jg\sigma_1^x & -J\sigma_1^z & \mathbb{I} \end{pmatrix}, \; M^{[k]} = \begin{pmatrix} \mathbb{I} & 0 & 0 \\ \sigma_k^z & 0 & 0 \\ -Jg\sigma_k^x & -J\sigma_k^z & \mathbb{I} \end{pmatrix}, \\ M^{[L]} &= \begin{pmatrix} \mathbb{I} \\ \sigma_L^z \\ -Jg\sigma_L^x \end{pmatrix}, \end{aligned} \tag{9.19}$$

where $k = 2, 3, \ldots, L-1$. To see how this MPO structure results in the proper many-body operator, we will explicitly build the Hamiltonian for three sites, i.e., $H = M^{[1]} \times M^{[2]} \times M^{[3]}$, where $\times$ is understood to be ordinary matrix multiplication in the auxiliary indices together with tensor products on the physical indices. We start by multiplying the row vector for the first site with the matrix for the second site leading to the first line of the following equation. The multiplication of this result with the column vector for the last and the third site results then in the Hamiltonian

$$\begin{aligned} M^{[1]} \times M^{[2]} \times M^{[3]} &= \begin{pmatrix} (-Jg\sigma_1^x - J\sigma_1^z\sigma_2^z - Jg\sigma_2^x) & -J\sigma_2^z & \mathbb{I} \end{pmatrix} \times \begin{pmatrix} \mathbb{I} \\ \sigma_3^z \\ -Jg\sigma_3^x \end{pmatrix} \\ &= -Jg\sigma_1^x - J\sigma_1^z\sigma_2^z - Jg\sigma_2^x - J\sigma_2^z\sigma_3^z - Jg\sigma_3^x \,. \end{aligned} \tag{9.20}$$

The MPO matrices have more entries for models beyond nearest neighbor interactions. The local terms remain in the last row of the first column as the identities stay in their places. The diagonal is set in the case of long-range interactions with an identity times a decay factor. The larger the distance between two sites becomes, the higher the contribution of the decay multiplied at each site in between. Elements in the lower triangular part of the matrix besides the first column and last row are used e.g. in the FiniteTerm rule set.

Independent of the system, we first initialize an instance of the `MPO` class. The different types of terms are specified via a string argument in the class function `AddObservable`. Keyword arguments to any MPO terms are the weight and Hamiltonian parameters `hparam`.

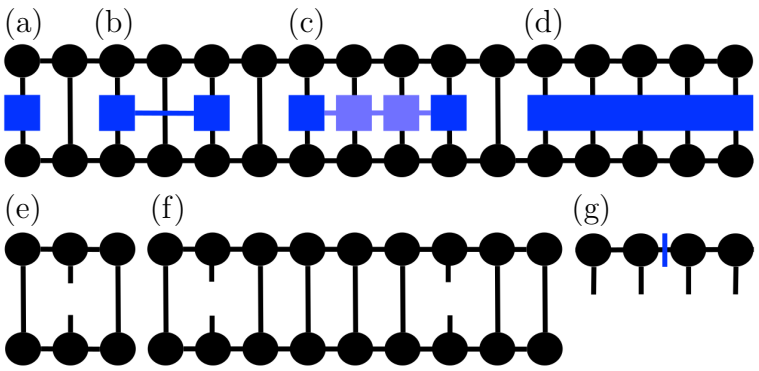

Figure 9.6: *OSMPS measurements* can be selected from the following options: (a) Local terms. (b) Two-site correlators including correlations for fermionic systems. (c) String operators of type $\langle O_A O_B O_B \dots O_B O_B O_C \rangle$. (d) MPO as used in the default measurement of the energy (Hamiltonian). (e) Single site density matrices tracing over the remaining system. (f) Two-site density matrices tracing out everything but two sites as defined in Eq. (9.21). (g) Singular values between left and right part of the MPS.

Further arguments specific for the rule can be found in the documentation, e.g. the infinite function can take the function as an additional keyword argument.

Source Code 9.2: Defining the Hamiltonian of the quantum Ising model.

```
9.49    H = mps.MPO(Operators)
9.50    H.AddMPOTerm('bond', ['sz','sz'], hparam='J',
9.51                 weight=-1.0)
9.52    H.AddMPOTerm('site', 'sx', hparam='g',
9.53                 weight=-1.0)
```

In the code we have given a string variable name for the coupling of the bond and site terms. The energy scale (`J=1`) and the different values for h are specified later in the Python setup script inside the dictionary representing the simulation allowing for flexibility.

9.3.3 Observables

In order to evaluate the behavior of the system, we have to define the observables. Figure 9.6 shows the possible measurements: local site terms including site and bond entropy, correlations, MPOs, string operators and one or two-site reduced density matrices where the reduced density matrices ρ_i and $\rho_{i,j}$ are defined as

$$\rho_i = \mathrm{Tr}_{k \neq i} (\rho) \ , \qquad \rho_{i,j} = \mathrm{Tr}_{k \neq i,j} (\rho) \ , \tag{9.21}$$

where the density matrix on the complete system is defined as $\rho = |\psi\rangle\langle\psi|$. The energy as an MPO measurement of the Hamiltonian, the bond dimension, the variance within variational algorithms, or the overlap between the initial state and the time evolved state (Loschmidt echo) are measured by default. For the Ising example, we measure $\langle\sigma_i^z\rangle$ and $\langle\sigma_i^z\sigma_j^z\rangle$. Due to the local observable we gain as well the bond entropy shown in Figure 9.2. Source Code 9.3 shows the necessary code for measuring these observables.

Source Code 9.3: Defining the observables of the quantum Ising model.

```
9.71    # Initialize instance of observable class and
9.72    # add local observable
9.73    myObservables = mps.Observables(Operators)
9.74    myObservables.AddObservable('site', 'sz', 'z')
9.75
9.76    # add correlation functions
9.77    myObservables.AddObservable('corr', ['sz','sz'],
9.78                                'zz')
```

9.3.4 Fundamentals of the library: Variational ground state search

The previous steps completed the setup of the physical system, and we continue with the specification of the convergence parameters. Therefore, we explain the variational algorithm

used to find the ground state which serves as input for the algorithms for excited state search and real time evolution.

From exact diagonalization, we know how to find the ground state via solving the eigenequation, which is optimally done with sparse methods such as the Lanczos algorithm [245]. The same procedure cannot be used in the same way beyond a few tens of particles due to the exponentially growing Hilbert space in the many-body system, but the variational ground state search adapts the eigenvalue problem to an effective eigenvalue problem for a few neighboring sites. In principle, the eigenequation $H|\psi\rangle = E|\psi\rangle$ can be solved for the ground state on the complete Hilbert space using imaginary time evolution, e.g. with the Krylov method presented for the dynamics later, using the equation $\mathrm{e}^{-\beta H}$ with $\beta \to \infty$. The thermodynamic beta approaches infinity as the system approaches the ground state at zero temperature. Instead of searching for the global minimum, we seek for local minima transferring the problem to an effective eigenequation for n neighboring sites in the OSMPS algorithm. The other $L - n$ sites are kept fixed while finding the effective ground state of the n sites. This effective eigenproblem does not grow exponentially with the system size, but depends on the local dimension and the bond dimension of the constant parts of the system, i.e. $d^n\chi^2$. The number of these effective eigenvalue problems grows linearly with the system size. In the following for simplicity we set $n = 2$, which corresponds to the value used in OSMPS:

$$\varepsilon[|\psi\rangle] = \langle\psi|H|\psi\rangle - E\langle\psi|\psi\rangle \quad \underset{\text{global}}{\overset{\text{local}}{\rightleftharpoons}} \quad H_{\text{eff}} A^{[k,k+1]} = E A^{[k,k+1]} \,. \tag{9.22}$$

The local minimization over n neighboring sites is done iteratively moving through the neighboring pairs of sites until convergence is reached (see details in Appendix 9.10). We point out the role of the effective Hamiltonian in more detail with regards to the Lanczos algorithm. The Lanczos algorithm finds the eigenvalues and vector of a problem using only matrix vector multiplications, in our case $H \mid v\rangle$ for some vector $\mid v\rangle$. Because we restrict ourselves to the sites $k, k+1$, the tensors of the other sites remain constant and we can

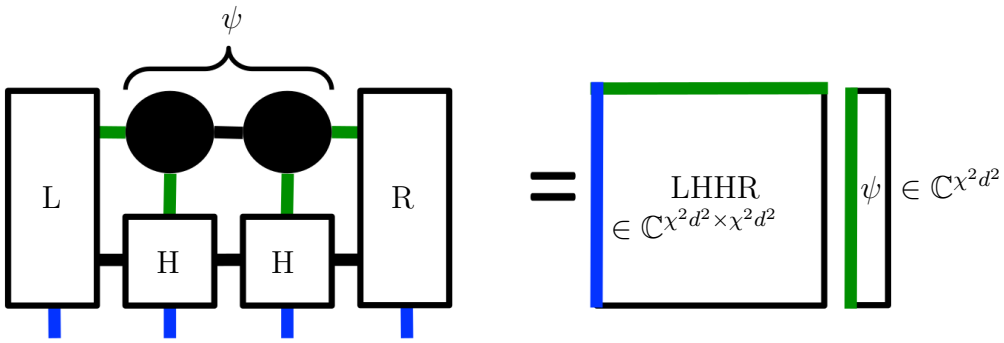

Figure 9.7: *Effective Hamiltonian for the Lanczos algorithm* is built via the contractions of all MPO matrices with tensors for the sites $k' \neq k, k+1$.

contract them with their MPO matrices. These fixed sites form an environment which acts as part of the total matrix vector multiplication. The contraction can be continued until we only have one tensor L to the left and one tensor R to the right representing those contractions.[5] Together with the MPO matrices $M^{[k]}$ and $M^{[k+1]}$, the tensors L and R build the effective Hamiltonian. We now find the minimum in energy for this effective Hamiltonian with regards to sites k and $k+1$. This effective Hamiltonian is resumed in Figure 9.7. In the case of matrices, the Lanczos algorithm is ideal for sparse problems and calculating only a few eigenvectors. In the tensor network scenario it provides a considerable speedup in contrast to dense methods due to the tensor network structure: contracting the tensors L, R, and the MPO matrices $M^{[k],}$ and $M^{[k+1],}$ step-by-step to $|v\rangle$ is more efficient than building H_{eff} of dimension $\chi^2 d^2 \times \chi^2 d^2$ and multiplying it with $|v\rangle$ or solving the eigenvalue problem, i.e. $\mathcal{O}(\chi^3)$ versus $\mathcal{O}(\chi^6)$ [121]. The two-site eigenvalue problem corresponds to finding the stationary point of the energy functional through the equation

$$\frac{\partial}{\partial \left(A^{[k,k+1]}\right)} \left(\langle\psi|H|\psi\rangle - E\langle\psi|\psi\rangle\right) = 0\,. \tag{9.23}$$

where E, the energy eigenvalue, is a Lagrange multiplier enforcing normalization, and the derivative with respect to a tensor is defined to be a tensor of the same shape whose elements

[5] In this context the symbol L represents the left tensor and not the system size.

are the derivatives with respect to the individual tensor elements.

Source Code 9.4: Defining the two sets of convergence parameters for the quantum Ising simulation.

```
9.84    conv = mps.MPSConvParam(max_bond_dimension=40,
9.85                            variance_tol=1e-10,
9.86                            local_tol=1e-10,
9.87                            max_num_sweeps=4)
9.88    modparam = ['max_bond_dimension', 'max_num_sweeps']
9.89    conv.AddModifiedConvergenceParameters(0, modparam,
9.90                                          [80, 4])
```

The key to obtaining meaningful results are the convergence parameters of the variational algorithm. The convergence parameters are stored in a corresponding Python object which is shown in Source Code 9.4 and the different parameters are defined in the following. For example, the variance $V_\psi = \langle H^2 - \langle H \rangle^2 \rangle$ indicates the distance from an eigenstate. Table 9.1 presents out of the analysis in Appendix 9.10 the parameters to obtain ground states with a variance tolerance $\varepsilon_\mathrm{V} = 10^{-12}$, effectively $L \times 10^{-12}$ for the whole system, for different models. Here, we concentrate on the values of the Lanczos tolerance ε_l and bond dimension where other parameters are kept constant. Those are especially interesting because the bond dimension defines the fraction of the Hilbert space which can be captured. On the other hand, the Lanczos tolerance determines the accuracy of the eigenvector solved in Eq. (9.23). The parameters kept constant are the number of Lanczos iterations. If the number of Lanczos iterations is sufficiently high the accuracy of the Lanczos tolerance is met, otherwise not. The local tolerance $\varepsilon_\mathrm{local}$, defining the cutoff of the singular values in the Schmidt decomposition of Eq. (9.1), guarantees that we do not use the full bond dimension if the sum of the singular values squared are below the local tolerance. It relates to the variance tolerance and defaults

to

$$\varepsilon_{\text{local}} = \frac{\varepsilon_{\text{V}}}{4L} \,. \tag{9.24}$$

The motivation to choose this value is that the local error made during one sweep consists of the approximately $2L$ splittings, where the additional factor of two is a safety factor to ensure good convergence. The number of sweeps through the system, optimizing each pair of two sites twice, is specified with the number of inner sweeps N_{i}, which is bounded between `min_num_sweeps` and `max_num_ sweeps`, and N_{o}, the parameter for the outer sweeps `max_outer_sweeps`. The maximal number of overall sweeps N_{sweep} is then

$$N_{\text{sweep}} = N_{\text{i}} \cdot N_{\text{o}} \,. \tag{9.25}$$

Convergence is checked after every inner sweep. One outer sweep is completed after the set of N_{i} inner sweeps followed by an adjustment of the local tolerances. The new local tolerance $\varepsilon'_{\text{local}}$ is decreased according to

$$\varepsilon'_{\text{local}} = \varepsilon_{\text{local}} \frac{\varepsilon_{\text{V}}}{V_\psi} \,, \tag{9.26}$$

where V_ψ is the actual variance on the current MPS. Equation (9.26) assumes a linear connection between the local tolerance and the variance fulfilled for small local tolerances [246]. Moreover, we have two more parameters to grow the system up to L sites with the same algorithm later explained in Sec. 9.4.2 for the infinite system. The local tolerance (`warmup_tol`) and the maximal bond dimension (`warmup_bond_dimension`) during that warmup phase can be tuned individually. These values provided in Table 9.1 provide a first overview of how models behave within OSMPS. We choose points with high entanglement within each model. The parameters are either close to a critical point or in a phase which has high entanglement such as the superfluid phase of the Bose-Hubbard model.

Table 9.1: *Empirically Determined Convergence Parameters.* The convergence parameters for the bond dimension χ and Lanczos tolerance ε_l for four different models achieve a variance tolerance 10^{-12} using a state with high entropy. The quantum Ising model (QI) and quantum long-range Ising model (LRQI) are evolved close to the critical point. The Bose-Hubbard model (Bose) is considered in the superfluid phase and a spinless Fermi model (Fermi) with nearest neighbor repulsive interaction W and nearest neighbor tunneling J is again in a region with high entanglement with $J = 1.04$. Details on the study are in Appendix 9.10.

Parameter	QI	LRQI	Bose	Fermi
χ	46	100	261	177
ε_l	$2.6 \cdot 10^{-9}$	$2.15 \cdot 10^{-8}$	$1.1 \cdot 10^{-10}$	$5.1 \cdot 10^{-7}$
Number of inner sweeps	2	2	2	4
Number of outer sweeps	1	1	1	1
System size L	128	128	32	65
Lanczos iterations	500	500	500	500

Finally, we present arguments as to why the variance tolerance is a convenient convergence criterion. In Appendix 9.12 we derive the bounds of multiple variables, we provide a short summary of those bounds here. The variance of the ground state V_ψ determines a bound on ϵ, where ϵ is the contribution for $|\psi_\perp\rangle$ of all states orthogonal to the true ground state $|\psi_0\rangle$ in the result $|\psi\rangle$ returned from OSMPS:

$$|\psi\rangle = f\,|\psi_0\rangle + \epsilon\,|\psi_\perp\rangle\,, \quad |\epsilon| \leq \frac{\sqrt{V_\psi}}{\Delta_{0,1}}\,. \tag{9.27}$$

The value of $\Delta_{0,1}$ is the energy gap between the ground state and the first excited state. Starting from there, we derive in Appendix 9.12 bound on an observable O acting on $|\psi\rangle$ as well as the bond entropy S:

$$|\langle\psi_0|\,O\,|\psi_0\rangle - \langle\psi|\,O\,|\psi\rangle| \;\leq\; 3\epsilon\mathcal{M}\,, \quad \mathcal{M} = \max_{|\phi\rangle,|\phi'\rangle} |\langle\phi|\,O\,|\phi'\rangle\,, \tag{9.28}$$

$$\epsilon_\mathrm{S} = |S(\rho_0) - S(\rho)| \;\leq\; \frac{\sqrt{2V_\psi}}{\Delta_{0,1}}\log(D) - \frac{\sqrt{2V_\psi}}{\Delta_{0,1}}\log\left(\frac{\sqrt{2V_\psi}}{\Delta_{0,1}}\right)\,. \tag{9.29}$$

In Eq. (9.29) the dimension of the density matrix, D, appears in addition to the variance and the gap. We pick as an example for the error bounds the nearest neighbor quantum

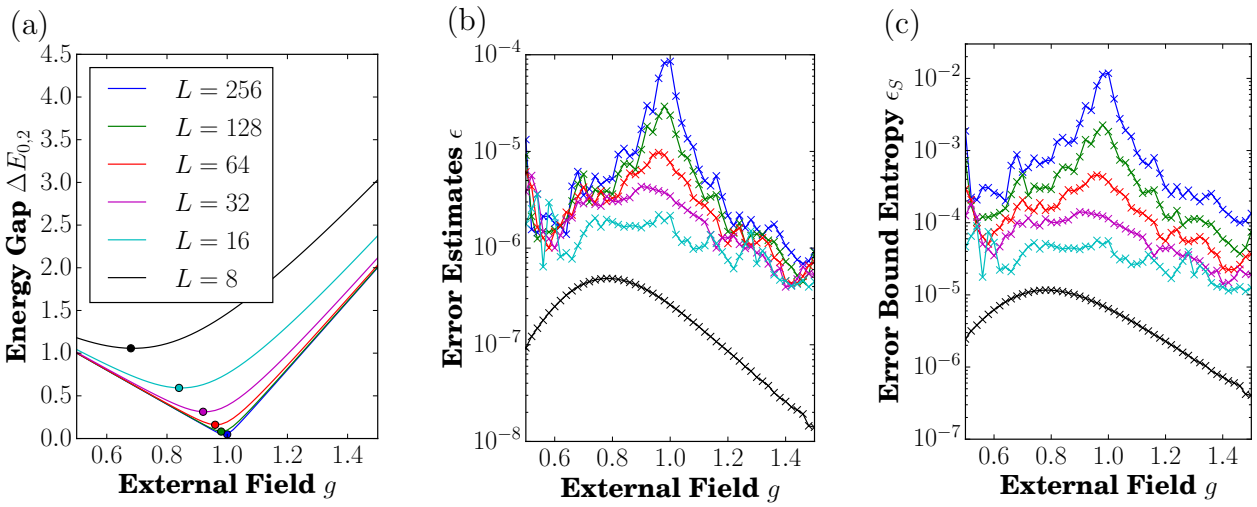

Figure 9.8: *Error bounds applied to the quantum Ising model.* We consider the Ising model with $\mathbb{Z}_2$ symmetry for the demonstration of error bounds. (a) The energy gap $\Delta E_{0,2}$ between the ground state and the second excited is shown, as the error depends on the inverse of the gap. The gap decreases towards the critical points and in the thermodynamic limit $L \to \infty$. The first excited state is located in the odd symmetry sector and therefore not relevant for this calculation. (b) The error bound for ϵ, where ϵ is the contribution orthogonal to the ground state. Observables such as the spin measurements, e.g. σ^x with a maximum of 1, are bounded by 3ϵ. (c) The bound for the error in the bond entropy ϵ_S depends furthermore on the dimension of bipartition, which increases the bound especially for larger systems.

Ising model with $\mathbb{Z}_2$ symmetry. Due to the symmetry, the first excited states lies, in contrast to the ground state, in the odd sector. Therefore, the relevant gap is the energy difference between the ground state and second excited state. The value of the gap for different systems sizes and the upper error bound for ϵ and ϵ_S are shown in Figure 9.8.

9.3.5 Running the simulations

Finally, we discuss how to set up simulations and execute them on the computer. Each simulation is contained in a dictionary and we can create a list of dictionaries to run multiple simulations at the same time. While certain parameters such as the measurement setup stay the same for a set of simulations, other parameters may be varied. In this example we create an empty list `params` and add the dictionaries to the list looping over the system size L and the external field h. The dictionary is shown in Source Code 9.5.

Source Code 9.5: Appending different simulations looping over L and g.

```
9.102             params.append({
9.103                     'simtype' : 'Finite',
9.104                     # Filenames and directories
9.105                     'job_ID' : 'sim_01_ising_z2_',
9.106                     'unique_ID' : '_L%04d'%ll \
9.107                                   + '_g%3.6F'%gg,
9.108                     'Write_Directory' : 'TMP_01_ISING/',
9.109                     'Output_Directory' : '
                             OUTPUTS_01_ISING/',
9.110                     # System size and Hamiltonian
9.111                     # parameters
9.112                     'L' : ll,
9.113                     'J' : J,
9.114                     'g' : gg,
9.115                     # Other parameters
9.116                     'MPSConvergenceParameters' : conv,
9.117                     'MPSObservables' : myObservables,
9.118                     # For error calculation (gap)
9.119                     'n_excited_states' : 1,
9.120                     'eMPSConvergenceParameters' : conv,
9.121                     'logfile' : True,
9.122                     'verbose' : 1,
9.123                     # Z2 symmetry
9.124                     'Discrete_generators' : ['gen'],
9.125                     'Discrete_quantum_numbers' : [0]
9.126                 })
```

In the following we generate a submit script for our simulations by writing the files for Fortran with a call to

```
MainFiles = mps.WriteMPSParallelFiles(params, Operators, H, hpcsetting,
PostProcess=False)
```

and the simulations are executed when submitted to the computing cluster. The fourth argument `hpcsetting` is a dictionary with various settings such as the number of nodes requested on the cluster. As an alternative, the user may call the parallel executable on a local machine and can find the corresponding call inside the submit script. We do not cover the post-processing itself here, but the sample scripts presented in the supplemental materials in Appendix B.1 provide guidance on how to read the results with the corresponding OSMPS functions and access the measurements inside the dictionaries.

9.4 Highlights of static algorithms

In the previous section we presented static simulations for the ground state, which builds a basis for other algorithms within OSMPS. The next algorithm searches for the excited state obtained through variational means. It can find sequentially ascending excited states above the ground state. In addition, we highlight our infinite size statics as a method to calculate properties for the ground state in the thermodynamic limit with an example.

9.4.1 Excited state search

The search for excited states, eMPS, is implemented in a successive fashion after the ground state has been obtained. The algorithm is based on the variational procedure now introducing additional Lagrange multipliers to Eq. (9.23) to enforce orthogonality with previously obtained eigenstates. If the ground state is now labeled as $|\,\psi_0\rangle$ and the i^{th} excited state as $|\psi_i\rangle$, we then need i additional Lagrange multipliers μ_i corresponding to the number of states with lower energy. These Lagrange multipliers enforce orthogonality between the eigenstates, $\langle\psi_i|\psi_j\rangle = \delta_{i,j}$:

$$\varepsilon[|\psi_i\rangle] = \langle\psi_i|H|\psi_i\rangle - E\langle\psi_i|\psi_i\rangle - \sum_{j=0}^{i-1} \mu_j \langle\psi_i|\psi_j\rangle \,. \tag{9.30}$$

We base our example for the excited state search on the previous study of the quantum Ising model. We introduce long-range interactions following a power law decay in this example. The corresponding Hamiltonian of the long-range Ising model was presented in Eq. (9.14), and we recall that it was defined as

$$H \;=\; -J \sum_{i<j\leq L} \frac{\sigma_i^z \sigma_j^z}{(j-i)^\alpha} - Jg \sum_{i=1}^{L} \sigma_i^x \,.$$

The update to the Hamiltonian due to the long-range interaction is reflected in Source Code 9.6. Since we loop over different α, we generate the Hamiltonian as well inside the loop over the different parameters and generate a list of them; in the previous example we could use a single MPO because only the couplings changed, but not the function describing the coupling. For the complete file see the supplemental material, Appendix B.1.

Source Code 9.6: Adapting the MPO for the long-range Ising model.

```
9.94        H = mps.MPO(Operators, PostProcess=PostProcess)
9.95        invalpha = lambda x: 1/(x**alpha)
9.96        H.AddMPOTerm('InfiniteFunction', ['sz','sz'],
9.97                     hparam='J', weight=-1.0,
9.98                     func=invalpha, L=ll, tol=1e-10)
9.99        H.AddMPOTerm('site', 'sx', hparam='g',
9.100                    weight=-1.0)
```

In order to calculate the excited states, we add the information showed in Source Code 9.7 to the simulation dictionary. In general it is possible to define different observables or convergence parameters for the ground state and the excited state, although it is not possible

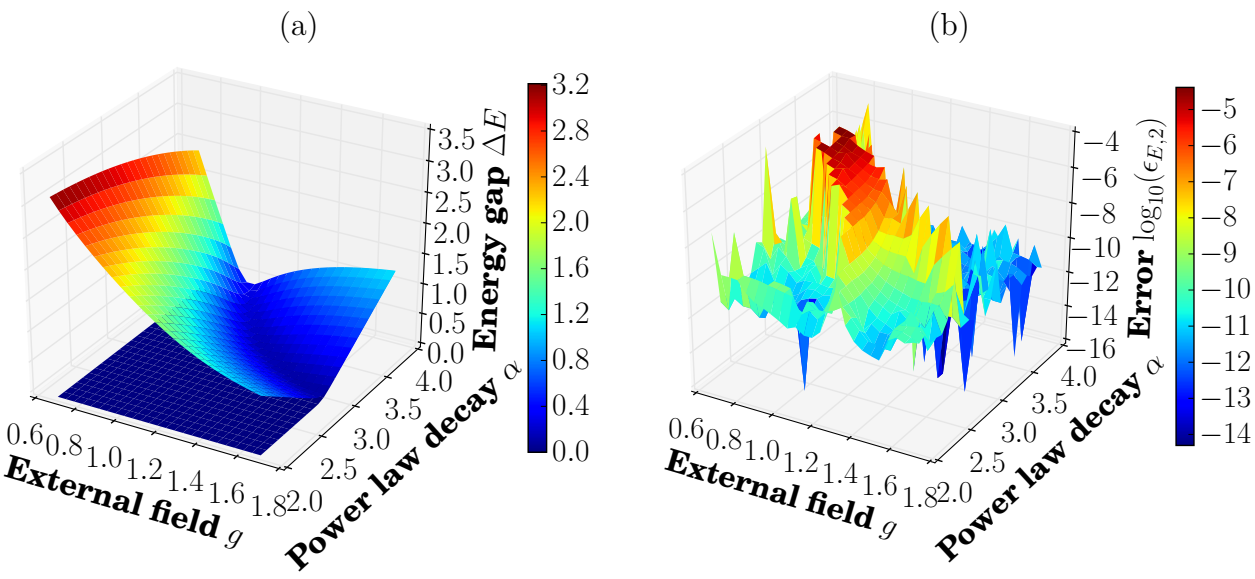

Figure 9.9: *Energy gap for the long-range quantum Ising model* as a function of the interaction strength α and the external field g. (a) The energy gap between the ground state and the first excited state is close to degeneracy in the ferromagnetic phase of the long-range quantum Ising model. The gap between ground and second excited states closes toward the quantum critical point, e.g. for $\alpha = 4$ around $g \approx 1$. The eigenenergies for the second excited state are compared to the eigenenergies of the ground state and the second excited state of the combined odd and even symmetry sector in (b) to estimate the error. (Same labels apply to color bar and z-axis.)

to have different settings for each excited state. We present the results of the excited states of the long-range Ising model in Figure 9.9. The excited states can reveal physical phenomena or support theory, e.g. we deduct from Figure 9.9 the close to degenerate ground and first excited state in the ferromagnetic phase. Both the ground and second excited state in the ferromagnetic phase belong to the even sector of the $\mathbb{Z}_2$ symmetry, and their closing gap indicates the position of the quantum critical point. This closing gap can be seen as valley starting around $\alpha = 4$ and $g = 1.0$. We use the symmetry conserving simulation to calculate the ground state and first excited state and show the errors in energy in Figure 9.9(b) and (c). In the latter one we see as well the growing error around the critical point. Because the variational state can only guarantee to find an eigenstate, but might end up in a minimum corresponding to a higher excited state, it is useful to resort the energies and converge results

with more excited states than actually desired.

Source Code 9.7: Specify the number of excited states to be calculated and the settings for convergence and measurements.

```
9.124                    # eMPS
9.125                    'n_excited_states' : ne,
9.126                    'eMPSConvergenceParameters' : conv,
9.127                    'eMPSObservables' : myObservables
```

9.4.2 Infinite systems in the thermodynamic limit

The OSMPS library possesses another tool to obtain information about the ground state of a quantum system, which is applicable in the thermodynamic limit. The iMPS algorithm searches for the ground state of a translationally invariant Hamiltonian [119]. The core idea of the algorithm is based on a unit cell of L sites. The Hamiltonian is translationally invariant in the sense that we consider an infinite sequence of these unit cells with the same Hamiltonian. Within the L sites, the Hamiltonian can depend on the site, creating a sublattice or similar features.

The final state is obtained when the state of the unit cell is converged by parameters discussed in the following. Starting with the first unit cell the ground state of the system is obtained. The system size is increased by inserting another unit cell in the middle of the system and summarizing the previous result in an environment. The new ground state of the unit cell is computed under the action of the environment. Subsequent steps of inserting cells while growing the environment lead to the result. The class `iMPSConvParam` comes with the convergence parameters for the bond dimension χ, and the local tolerance and the settings for the Lanczos algorithm keep their meaning in regard to previous algorithms. We introduce the maximal number of iMPS iterations determining how often a new unit cell is introduced into the iMPS state before stopping the algorithm. To break out of the algorithm before reaching the maximal number of iMPS iterations we consider the orthogonality fidelity $\mathcal{F}$

(`variance_tol`). In order to define this orthogonality fidelity $\mathcal{F}$, we introduce the density matrices ρ_{n-1}, i.e., the density matrix of the previous step, and ρ_n^R as the density matrix of the present step without the new unit cell introduced in step n. The overlap or fidelity serves then as a convergence criterion:

$$\mathcal{F}(\rho_{n-1}, \rho_n^R) \;=\; \sqrt{\sqrt{\rho_n^R}\rho_{n-1}\sqrt{\rho_n^R}}\,. \tag{9.31}$$

We can use the algorithm to compare the results of the first study of the nearest neighbor limit with those of iMPS. In Figure 9.10 we show the bond entropy of the iMPS which peaks at the critical point. We point out that of all simulations, three fail being the second, fifth data point and the bond entropy at the critical point. In comparison we show the largest finite size system with $L = 2000$ with and without using the $\mathbb{Z}_2$ symmetry. Both lines show good agreement. Possible disagreement in the bond entropy may arise from the actual ground state, i.e. $\left(|\uparrow\cdots\uparrow\rangle + |\downarrow\cdots\downarrow\rangle\right)/\sqrt{2}$. But any other superposition of all spins up plus all spins down fulfills the minimization of the energy as well. Furthermore, the output of the infinite system is partly different from the finite size algorithm, e.g. the maximal distance for the correlation is specified. More of those differences are described in detail in the manual.

9.5 Time evolution methods

The only missing piece to complete the library at this point is the time evolution of quantum states. In total we provide four different algorithms: Krylov time evolution [247] by default, the Time-Dependent Variational Principle algorithm (TDVP) [120], a local Runge-Kutta method (LRK) [122], and a Sornborger-Stewart decomposition [85, 248]. The Sornborger-Stewart decomposition is an alternate decomposition to the Trotter decomposition and is used to implement the Time-Evolving Block Decimation (TEBD) [76]. The first three methods support long-range interactions, and align with our motivation to support such systems.

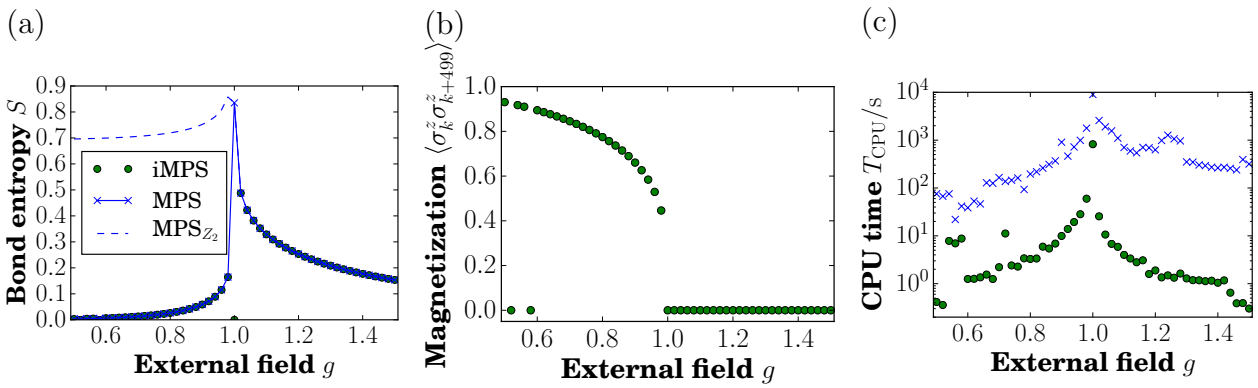

Figure 9.10: *The quantum Ising model in the infinite MPS simulations.* (a) The bond entropy of the iMPS peaks at the critical point $g_c = 1.0$ which reproduces the results of the finite size MPS simulation for $L = 2000$ without $\mathbb{Z}_2$ symmetry. In general, the bond entropy of the iMPS in the ferromagnetic phase can lie in between the results with and without the $\mathbb{Z}_2$ symmetry. (b) The magnetization based on the correlation $\langle\sigma_i^z\sigma_{i+499}^z\rangle$ dies away at $g = 1.0$. (c) The compute times of the iMPS simulations in comparison with the finite size algorithm at $L = 2000$. iMPS can give a quick estimate of the behavior in the thermodynamic limit.

9.5.1 Computational error and convergence

We first provide an overview of each method's behavior in terms of convergence in Figure 9.11. The figure compares the OSMPS algorithms to analogous exact diagonalization time propagation schemes, focusing on four key measures:

1. *The maximum trace distance of all local reduced density matrices*,

$$\begin{aligned} \epsilon_{\text{local}} &= \max_{i\in\{1,\ldots L\}} \mathcal{D}(\rho_i, \rho_i^{\text{ED}}), \quad \mathcal{D}(\rho_A, \rho_B) \equiv \frac{1}{2}|\rho_A - \rho_B|\,, \\ |A| &\equiv \sqrt{A^\dagger A}\,. \end{aligned} \tag{9.32}$$

   The superscript *ED* refers to the results of exact diagonalization methods. Equation (9.32) can be used to bound any local observable, as explained in Appendix 9.13.

2. The error of *correlation measurements.* We consider the maximal trace distance ϵ_{corr}, here on all two-site density matrices, to bound the error for the correlation measurements:

$$\epsilon_{\text{corr}} \quad = \quad \max_{(i,j)} \mathcal{D}(\rho_{i,j}, \rho_{i,j}^{\text{ED}}), \quad i,j \in \{1, \ldots L \mid |i < j\} \; . \tag{9.33}$$

3. The *energy* of the system:

$$\epsilon_{\text{E}} \quad = \quad |E - E^{\text{ED}}| \, . \tag{9.34}$$

4. As the maximal bond dimension is one of the key parameters in MPS algorithms, we finally compare the *bond entropy* defined over the von Neumann entropy S of singular values squared obtained by cutting the system in half:

$$\epsilon_{\text{S}} \quad = \quad |S(L/2) - S^{\text{ED}}(L/2)| \, . \tag{9.35}$$

   The maximal bond dimension necessary in small systems which can still be studied in exact diagonalization is unfortunately limited. Therefore, we cannot study the effects of truncation in comparison to exact diagonalization.

We compare the OSMPS results with the data from exact diagonalization. Therefore, we take the simulation with the smallest time step corresponding to the most accurate result. In addition, we display the error from the static simulation as a lower bound for the error. The static simulation serves as an input state for the dynamics and sets the lower bound for the error. Figure 9.11 shows the error at the end of the time evolution for a quench in the Ising model. The quench starts at $g(t = 0) = 5.0$ and ends at $g(t = 0.5) = 4.5$ for a system size of $L = 10$. The time is in units of $\hbar/J$. The exact diagonalization method, which is always at time-ordering $\mathcal{O}(dt^2)$, takes the whole Hamiltonian to the exponent evaluating the coupling at $t + 0.5\mathrm{d}t$ resulting in $\mid \psi(T)\rangle \; = \; \exp(-\mathrm{i}H(0.5dt)dt) \exp(-\mathrm{i}H(1.5dt)dt) \cdots \exp(-\mathrm{i}H(T - 0.5dt)dt) \mid \psi(0)\rangle$. In contrast, the MPS time evolution methods support higher order time ordering, which is not used for the studies within this work. We briefly point out the trends within this Figure 9.11. We defined the first error as the maximal trace distance over all

single site density matrices ϵ_{local}, which is shown in Figure 9.11(a). We see two major trends for ϵ_{local}. First, there is a clear difference between the second and fourth order methods in the case of TEBD and LRK algorithms, labeled as TEBD2 and TEBD4 as well as LRK2 and LRK4, respectively. The fourth order algorithms and the TDVP and Krylov algorithms nearly match the result of exact diagonalization for $dt \geq 10^{-3}$ in comparison to the ED result with $dt = 10^{-4}$. Figure 9.11(b) analyzes the second error, i.e., the error in the reduced two site density matrices ϵ_{corr}. This error is much larger, which is already present in the ground and therefore initial state with an order of magnitude of 10^{-7}. The third kind of error, the error in energy ϵ_{E}, is shown in Figure 9.11(c). ϵ_{E} decreases for all the methods with the same overall trend. We recall that the Hamiltonian in this case contains single site terms and nearest neighbor terms, so large errors in two site reduced density matrices with sites far apart would not contribute to the error in the energy. The error in the bond entropy ϵ_{S}, the fourth value considered for the estimate of the error, follows the behavior of the previous measures, see Figure 9.11(d). All methods except TEBD2 and LRK2 do not improve from $dt = 10^{-3}$ to $dt = 10^{-4}$ as the entropy is already close to the static result. In general, we seek for the method which consumes the least resources to achieve a certain error for a given problem. Figure 9.11(e) answers this question. We take the error ϵ_{local} as example and plot it as a function of the CPU time. This allows us for example to compare the second order methods versus their fourth order algorithm. Both the TEBD and LRK fourth order methods use less resources at a bigger dt to achieve the same error in comparison to their second order equivalent. The error reported back from OSMPS is analyzed in Figure 9.11(f). We consider the Krylov method first: the reported error is bigger for a smaller time step despite the results clearly getting better in the previous plots. The reported Krylov error contains errors from state fitting and cutting the bond dimension. Although it is not necessary to cut the bond dimension, there still remains the possibility for truncation due to the local tolerance criteria. Since the reported error is accumulated during the evolution, the small contributions add up due to the multiple time steps. Considering the error for $dt = 0.0001$ of

the order 10^{-9} with 5000 time steps, each time step adds about 10^{-13} to the total error. The other time evolutions report purely the error from truncation of singular values restricted to the local tolerance in this evolution. Increasing errors for decreasing time steps follow the same arguments as for the Krylov time evolution. In Appendix 9.10 we discuss in detail the sudden quench and the following evolution under a time-independent Hamiltonian.

The conclusion drawn from this first study is that the total error is bounded by

$$\epsilon \leq \epsilon_{dt} + \epsilon_{\text{method}} + \epsilon_{\chi} \,, \tag{9.36}$$

where ϵ_{dt} is due to evaluating a time-dependent Hamiltonian at discrete points in time. The second error originates from the specific method used to evolve the quantum system in time; an example for ϵ_{method} would be the approximation in the Sornborger-Stewart decomposition. Finally, all methods have in common that they truncate singular values to remain with a certain χ leading to ϵ_{χ}. This source of error will dominate the error even for well-chosen settings, since the entanglement grows over time and therefore saturates the bond dimension for long enough evolution time. Figure 9.17 in the appendix is one example for this behavior. Equation (9.36) is an upper bound for the error. A detailed analysis of the error goes beyond the scope of this work. We emphasize that all three kind of error sources manifest in the four different error measures defined in Eqs. (9.32) to (9.35). The scaling of the first error source ϵ_{dt} can be obtained through exact diagonalization since there is neither an error depending on the method nor a truncation of the Hilbert space. ϵ_{dt} appears in the same way for all MPS methods using the same time-ordering as done in this error study. We remain with the estimate of the errors due to the method ϵ_{method} and the truncation in the bond dimension ϵ_{χ}. The Hilbert space for the MPS simulations with $L = 10$ is small enough to capture all singular values and ϵ_{χ} is not present. Therefore, ϵ_{method} can be seen in Figure 9.11 if at the same order of magnitude as ϵ_{dt}. For example, the TEBD2 method has an additional error introduced through the Sornborger-Stewart decomposition making it less accurate than the exact diagonalization result with the same time step. We discuss a time-independent

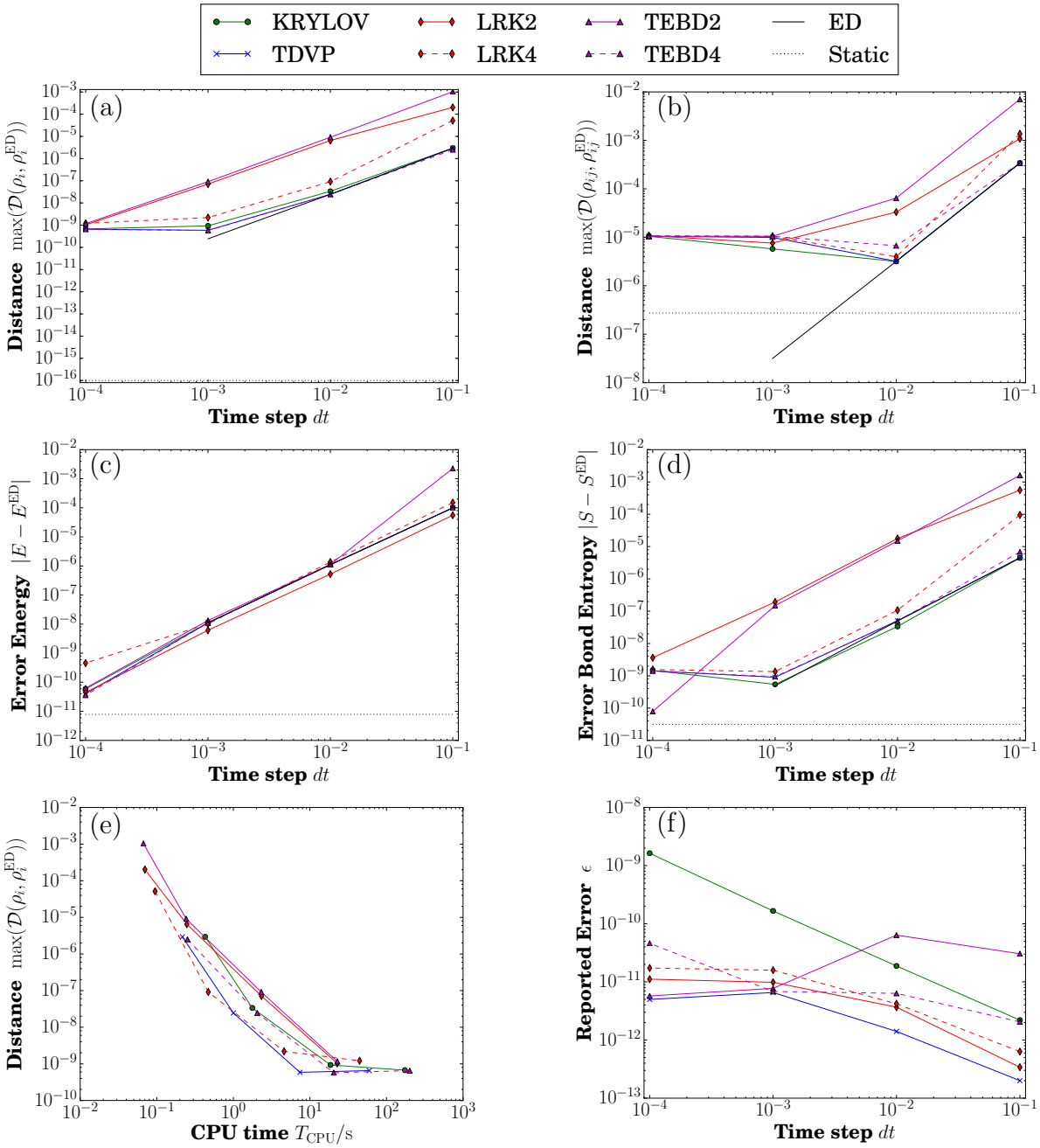

Figure 9.11: *Scaling of the error in time evolution methods* decreases as expected with the size of the time step. This example shows a quench of the Ising model in the paramagnetic phase. The error decreases as $\mathcal{O}(dt^2)$, the leading order of the error due to time-slicing the time-dependent Hamiltonian $H(t)$ with a CFME. The error for the exact diagonalization method is not plotted for $dt = 10^{-4}$, because this is the result used as a reference and naturally leads to zero error. The time step dt is in units of $\hbar/J$. Curves are a guide to the eye; points represent actual data.

Hamiltonian in Appendix 9.10 with $\epsilon_{dt} = 0$. Therefore, ϵ_{method} can be estimated independent of the other errors in this case.

Before we discuss particular time-propagation methods, we first discuss how OSMPS accounts for time-ordering of propagators for time-dependent Hamiltonians. When considering time-ordering in MPS algorithms, we want to apply as few operators as possible to avoid increasing the bond dimension, and would like all operators to be easily and efficiently constructed from the MPO form of the Hamiltonian. Therefore, OSMPS uses Commutator-free Magnus expansions (CFMEs) [121, 249]. CFMEs are advantageous over other expressions such as the Dyson series or the original formulation of the Magnus series due to explicit unitarity and the avoidance of nested integrals and/or commutators. OSMPS implements a few different CFMEs with orders of error N, defined such that the propagator is accurate to $\mathcal{O}\left(\delta t^{N+1}\right)$, and numbers of exponentials s. The default settings are $N = 2$ and $s = 1$, where the CFME amounts to evaluating the Hamiltonian in $[t, t + \delta t]$ using the midpoint rule for integration. Having introduced the general convergence of the methods, we now look at each method individually and discuss their principles.

9.5.2 Krylov time evolution

The Krylov method [121, 250, 251] is the default option for real time evolution in the OSMPS code. The main point of using this technique is the support of long-range interactions. The Krylov method applies the exponential of an operator expressed as an MPO to an MPS

$$|\,\psi(t + dt)\rangle \approx \exp(-\mathrm{i}H dt)\,|\,\psi(t)\rangle\,, \tag{9.37}$$

using the method of Krylov subspace approximations [247, 252]. In the time-independent case H is the Hamiltonian, while in the time-dependent case it is an operator constructed by the particular CFME used.

The Krylov algorithm is not limited to the MPS algorithm, but it is commonly used to obtain the new vector of a matrix exponential acting on a vector. The idea [219] is to change into a truncated basis (the Krylov subspace) $V' = [v_1, v_2', \ldots, v_n']$ in order to calculate the propagated state $|\,\psi(t+dt)\rangle = \exp(-\mathrm{i}A dt)\,|\,\psi(t)\rangle$. The vectors v_j' are chosen as $A^{j-1}\,|\,\psi\rangle$ and are orthonormalized to the basis $V = [v_1, v_2, \ldots, v_n]$. In particular, the first Krylov vector is $v_1 = |\,\psi\rangle = V\,|\,e_1\rangle$ with $|\,e_1\rangle = (1,0,0,0,\ldots,0)^T$. Approximating the dot product between the exponential and the state vector leads to

$$\begin{aligned} \exp(-\mathrm{i}A dt)\,|\,v_1\rangle &\approx VV^\dagger \exp(-\mathrm{i}A dt)\,|\,v_1\rangle = VV^\dagger \exp(-\mathrm{i}A dt)V\,|\,e_1\rangle \\ &= V\exp(-\mathrm{i}V^\dagger A V dt)\,|\,e_1\rangle\,. \end{aligned} \tag{9.38}$$

Calculating the exponential M of the matrix $V^\dagger A V \in \mathbb{R}^{n\times n}$ is a numerically feasible task as long as the number of basis vectors n is much smaller than the dimension of the Hilbert space D. Furthermore, the relation simplifies to a real tridiagonal matrix for Hermitian matrices, which is satisfied by the Hamiltonian. This leads to

$$\exp(-\mathrm{i}A dt)\,|\,v_1\rangle \approx VM\,|\,e_1\rangle = \sum_{i=1}^{n} M_{1,i}\,|\,v_i\rangle\,. \tag{9.39}$$

While in many applications where the state is represented as a vector this is enough to obtain the approximation of $|\,\psi(t+dt)\rangle$, the problem in the case of the MPS is that the summation over $|\,v_i\rangle$ cannot be exactly carried out, as the set of MPSs with fixed bond dimension do not form a vector space. Based on the previous approaches using variational algorithms, we instead find $|\,\psi(t+dt)\rangle$ by variationally optimizing the overlap

$$|\,\psi(t+dt)\rangle = \sum_{i=1}^{n} m_{1,i}\,|\,v_i\rangle \quad \Leftrightarrow \quad 1 = \langle\psi(t+dt)|\left(\sum_{i=1}^{n} m_{1,i}\,|\,v_i\rangle\right). \tag{9.40}$$

This procedure is done optimizing local tensors as in the ground state search. However, instead of solving an eigenvalue problem at each iteration, this optimization takes the form of a linear system of equations as shown on the left part of Eq. (9.40). By exploiting

the isometrization of MPSs (see Eq. (9.7)), this linear system of equations is transformed into an inequality keeping the distance between the new state $|\,\psi(t+dt)\rangle$ and its Krylov representation $\sum m_{1,i}\,|\,v_i\rangle$ below a specified tolerance. The interested reader can find further details on this algorithm in Refs. [75, 121].

9.5.3 Sornborger-Stewart decomposition

This implementation inside the OSMPS library is suitable for nearest-neighbor Hamiltonians. The Sornborger-Stewart decomposition [248] used in the OSMPS algorithms sweeps through the system acting on every site, instead of every second pair of sites as in a more common alternative Suzuki-Trotter decomposition [85]. The second order expansion takes the form

$$\exp\left(-\mathrm{i}\mathrm{d}t\sum_{i=1}^{L-1}H_{i,i+1}\right)=\prod_{i=1}^{L-1}\exp\left(-\mathrm{i}\frac{\mathrm{d}t}{2}H_{i,i+1}\right)\prod_{i=1}^{L-1}\exp\left(-\mathrm{i}\frac{\mathrm{d}t}{2}H_{L-i,L-i+1}\right)\,. \tag{9.41}$$

We again follow the Krylov approach to propagate the quantum state under the given MPO taking the exponential in the Krylov subspace. The essential difference is the local characteristics of the Hamiltonian in the Sornborger-Stewart decomposition. With the orthogonality center at one of the sites i and $j=i+1$ being acted on, the overlap from the left and right is the identity operator. If we denote the two sites acted on with $|\,C\rangle$ and the parts to the left of i and right of j with $|\,L_i\rangle$ and $|\,R_j\rangle$, the actual state vector $|\,\psi\rangle$ can be derived from Eq. (9.39),

$$|\,\psi\rangle \;=\; \sum_{i,j}|\,L_i\rangle\,|\,C_{i,j}\rangle\,|\,R_j\rangle\,. \tag{9.42}$$

Within the construction of the Krylov basis $[v_1,\ldots,v_n]$ the states $|\,L_i\rangle$ and $|\,R_j\rangle$ remain unchanged as shown in Appendix 9.14. The same applies to the sum of the propagated state

$$|\,\psi(t+dt)\rangle = \sum_k c_k v_k\,, \tag{9.43}$$

leading to the following construction of the state in the MPS picture:

$$|\,\psi(t+dt)\rangle = \sum_{i,j} |\,A_i\rangle \left(\sum_k c_k\, |\,C_{i,j}(v_k)\rangle \right) |\,B_j\rangle\,. \tag{9.44}$$

That means that we can sum locally over the two site tensors, as they form a vector space, in contrast to the long-range case where we had to variationally find the MPS closest to the summation.

In order to specify the error due to the method, we have to consider the decomposition of the exponential. By separating non-commuting terms in matrix exponential, we get an error of order dt^2 in the first order approximation for a single time step:

$$\exp\left[(A+B)dt\right] = \exp(Adt)\exp(Bdt) + \mathcal{O}(dt^2)\,. \tag{9.45}$$

Having implemented the second and fourth order approximations we obtain methodical errors ϵ_{method} for the whole time evolution as follows. ϵ_{method} is defined as part of the total error in Eq. (9.36).

$$\epsilon_{\text{TEBD2}} = \mathcal{O}(dt^2)\,, \qquad \epsilon_{\text{TEBD4}} = \mathcal{O}(dt^4)\,. \tag{9.46}$$

In addition to the error of the Sornborger-Stewart decomposition, we have as well an error from the Krylov subspace approximation to the exponential for the local two-site propagators. The error bound for a single step is derived in [252].

The convergence parameters necessary to set up time evolution with TEBD methods reflect the simplicity of the approach. The parameter `psi_local_tol` determines the local truncation on the singular values, while the pair (`lanczos_ tol`, `max_num_lanczos_iter`) provides the tolerance for the Krylov approximation and the maximal number of Krylov

vectors. In addition, the maximum bond dimension χ can be defined.

With regards to the convergence study for the quench in the Ising model in Figure 9.11 we make two observations. The fourth order Sornborger-Stewart method is better than second order implementation of Sornborger-Stewart, as expected due to the smaller error at each time step. The rate of convergence as a function of the time step dt, that is, the slope of the line, is equal for both implementations. The error ϵ_{dt} from the time-ordering of the time-dependent Hamiltonian governs both implementations with $\mathcal{O}(dt^2)$ and the better convergence of the fourth order Sornborger-Stewart cannot be observed. In contrast, if the Hamiltonian is time-independent, there is no error from the time-ordering. Figure 9.16 in Appendix 9.10 indicates that TEBD4 has a higher rate of convergence in this case. The total error has to be considered in comparison to the Krylov time evolution in Sec. 9.5.2 or the TDVP discussed in Sec. 9.5.4. We remark that the fourth order TEBD method has a comparable error to the Krylov and TDVP method within one order of magnitude for the smallest time step $dt = 10^{-4}$. Larger time steps and the second order method TEBD2 introduce errors which are sometimes two orders of magnitude larger than the errors introduced through Krylov or TDVP, especially for large time steps.

9.5.4 Time-dependent variational principle

As a third option for the time evolution of a quantum system, we provide the time-dependent variational principle (TDVP) [120]. This is another method supporting long-range interactions. In brief, all other previous methods apply the propagator, which is an entangling many-body operator, to a state represented as an MPS, and produces a new state obtained as an MPS. The updated MPS has a larger bond dimension in general, so then we must variationally project this new MPS onto the set of states with reduced computational resources. The approach of the TDVP method is instead to project the time-dependent Schrödinger equation onto the manifold of MPSs with fixed bond dimension, and then integrate this equation directly within this manifold. OSMPS has implemented the two-site version of this algorithm [120], in which the bond dimension is still allowed to grow over

the course of time evolution, but the propagator is determined from a projection of the full many-body operator onto a more local subspace. We remark that TDVP performs well on the convergence study against exact diagonalization methods in the example of Figure 9.11. All four estimates for the error defined in Eqs. (9.32) to (9.35) and shown in the four upper panels of Figure 9.11 are close to exact diagonalization result with the same time step used as reference. The maximal distance of all reduced two-site density matrices does not reach the reference due to initial errors in the static results for the ground state.

9.5.5 Local Runge-Kutta propagation

Another option for time evolution with long-range interactions available in OSMPS is the local Runge-Kutta method proposed in [122]. The basic idea can be summarized as using the Runge-Kutta method on the local MPO matrices instead of the whole propagator. The new MPO representing the propagator U_{LRK} has a compact representation, i.e., it does not increase in bond dimension beyond that of the Hamiltonian MPO. Since the method is defined on the MPO, it is the third method supporting long-range interactions.

A detailed overview on how to build the MPO for the propagator, U_{LRK}, as a second order approximation is beyond the scope of this description; we suggest [122] to the interested reader. But we do provide here a short description of how the application of the MPO to the MPS is implemented in OSMPS. We fit the product of the MPO and the MPS to a new MPS, where the new MPS represents the propagated state,

$$\min_{|\psi(t+dt)\rangle} \| \, |\psi(t+dt)\rangle - U_{\mathrm{LRK}} \, |\psi(t)\rangle \| \, . \, . \tag{9.47}$$

This fit employs the same method used to fit the next Krylov vector $|\, v_{i+1}\rangle = H \, |\, v_i\rangle$ in the Krylov method. The four upper panels of Figure 9.11 show a similar behavior with regards to the convergence of the LRK method as for the TEBD method. The higher order variant of the LRK method reduces the error, but the rate of convergence is not better due to the time-dependent Hamiltonian and the particular choice of CFME. Within the implementation

of this time evolution method we use the EXPOKIT package [253, 254] to calculate matrix exponentials.

9.5.6 Time evolution case study: Bose-Hubbard model in a rotating saddle point potential

We consider bosons in an optical lattice confined in a rotating potential as an example of the setup of a time evolution in OSMPS. We consider the potential V_{xy} with a saddle point at $x = y = 0$ and a weight c,

$$V_{xy} = c\left(x^2 - y^2\right) . \tag{9.48}$$

Figure 9.12(a) shows this potential for a two dimensional lattice. We consider a one-dimensional optical lattice in this potential marked by the red sites and start to rotate V_{xy}; the one-dimensional system sees the following potential V_S depending on the angle of rotation ϕ and the distance r from the center of the potential and integrate it into the Bose-Hubbard Hamiltonian:

$$V_S = c\left(r\cos(\phi(t))\right)^2 - c\left(r\sin(\phi(t))\right)^2 , \tag{9.49}$$

$$H = -J\sum_{i=1}^{L-1} b_i b_{i+1} + h.c. + \frac{U}{2}\sum_{i=1}^{L} n_i(n_i - \mathbb{I}) + \sum_{i=1}^{L} V_S(t,i)n_i . \tag{9.50}$$

We slowly ramp up the frequency of the rotations with an acceleration α starting with a flat potential

$$\phi(t) = \frac{\pi}{4} + \frac{1}{2}\alpha t^2 . \tag{9.51}$$

In order to estimate the stability of the system, we first calculate the standard deviation of the number operator with regards to spatial dimension x for every measurement in time, denoted by $\sigma_x(n)$ [6]. We calculate $\sigma_t(\sigma_x(n, \tau = 5))$, that is the standard deviation of $\sigma_x(n)$ for time intervals $t - \tau$ to t for $\tau = 5$, in a second step. For fast enough frequencies the rotating

[6] We emphasize that this is not the Pauli operator, but the standard derivation using in contrast to the Pauli operators the subscript

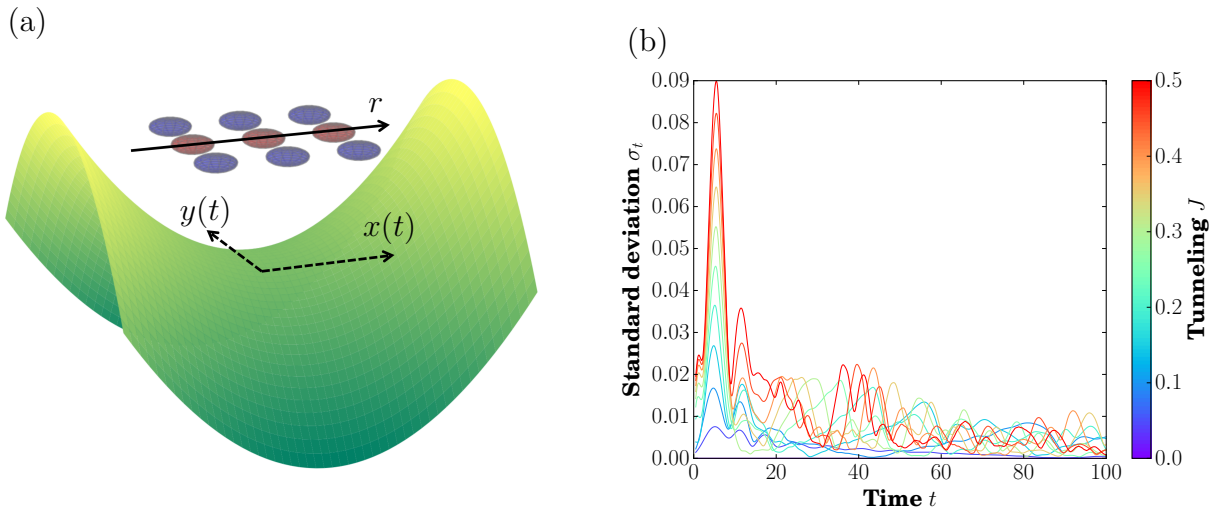

Figure 9.12: *Bose-Hubbard model in a rotating saddle-point potential.* The system shows an increasing stability for faster frequencies. (a) In order to simulate a one dimensional system from the two dimensional optical lattice, we consider one slice of sites marked in red with its coordinate system r. The saddle point potential in green and yellow rotates under the system characterized by the coordinates $x(t), y(t)$. (b) The standard deviation over time intervals of $\tau = 5$ is measured for the spreading in x, i.e. the standard deviation of the number operator. This observable can be expressed as $\sigma_t(\sigma_x(n), \tau = 5)$. The time t is in units of $\hbar/U$ and the tunneling J is in units of the on-site interaction U.

potential stabilizes the system, which can be seen in Figure 9.12(b). The other trend is that towards the superfluid regime, with higher tunneling, the stability decreases. The first peak shows this trend.

The setup of the dynamics has many common steps with the statics. The definition of the operators, the MPO representing the Hamiltonian, and the observable class do not change. In regard to the time-dependent potential V_S in Eq. (9.49), we define the weight c, the acceleration α (`alpha`), the system size L, and the function returning the corresponding potential at a point in time t. The latter step is shown in Source Code 9.8.

Source Code 9.8: Define a time-dependent function for the rotating saddle potential.

```
9.76    def Vt(t, c=c, alpha=alpha, L=L):
9.77        # Grid with particles symmetric around 0
```

Source Code 9.8 Continued

```
9.78            # at unit distance
9.79            grid = np.linspace(-L / 2 + 0.5,
9.80                               L / 2 - 0.5, L)
9.81
9.82            phit = np.pi / 4 + 0.5 * alpha * t**2
9.83
9.84            return c * ((grid * np.cos(phit))**2
9.85                        - (grid * np.sin(phit))**2)
```

Next, we build the time evolution. As before with MPOs, observables, and convergence parameters, the dynamics are contained in an instance of a Python class: `QuenchList`. Once created, we can add multiple quenches which are executed sequentially. We only add one quench in our example in Source Code 9.9. Different convergence parameters are supported for each quench you add.

Source Code 9.9: Creating the class object containing one or more quenches.

```
9.87    tconv = mps.TEBDConvParam(max_bond_dimension=60)
9.88    Quench = mps.QuenchList(H)
9.89    Quench.AddQuench(['Vt'], 100.0, 0.01, [Vt],
9.90                     stepsforoutput=10,
9.91                     ConvergenceParameters=tconv)
```

As a last step we have to specify the dynamics in the dictionary for the simulation, including the quenches and the observables to be measured during the dynamics. The additional lines are shown in Source Code 9.10. The initial state of the time evolution is the ground state if not specified otherwise.

Source Code 9.10: Additional dictionary entries for the time evolution.

```
9.114             'Quenches' : Quench,
9.115             'DynamicsObservables' : myObs,
```

The post processing works similar to the statics. A listed list contains the dictionaries with the results of the simulation. The outer list contains the different simulations, and the inner list contains the measurements for each time. The complete Python code may be found in the supplemental material described in Appendix B.1.

9.6 Future developments

The present OSMPS library has a wide field of possible applications including two-component mixtures [232], topological phases [237], and complexity in the quantum mutual information [214]. Still, we are planing to enhance the code to solve other sets of problems. The need for enhancements is driven by our research in atomic, molecular, and optical physics, macroscopic quantum phenomena, and complexity, but we are open to suggestions from the community for extensions to the OSMPS library. For instance, the feature to provide the singular values of a bipartition in addition to its bond entropy began as suggestions made on our developer's site [255]. We already have a broad suite of tools for the current MPS algorithms for finite systems; therefore, we are focusing on implementing additional measurements or new MPO rule sets to target Hamiltonians which are impossible or difficult to build with present rule sets. For the measurements, observables such as unequal time correlations are a possible add-on. A user-friendly support for ladder systems or rectangular systems with $L_x \gg L_y$ could be one focus for new types of Hamiltonians, either as new rule sets or with convenient interfaces in Python. In contrast, other tensor network structures such as PEPS are not being considered as an extension to the library at this point. Periodic boundary conditions are on the agenda for selected MPO rule sets.

On the other hand, we intend to extend OSMPS for a new set of problems in the future, namely open quantum systems. We anticipate them to be key component to establish a more realistic picture of simulations with regards to experiments, for example, future quantum computers will suffer effects such as decoherence from the coupling to the environment; including those effects in simulations fosters the understanding and addresses problems induced by open systems. The standard approach is the Lindblad master equation describing a system coupled weakly to a Markovian environment. Several approaches have been proposed to implement the Lindblad master equation, i.e. quantum trajectories, MPDOs, and Locally Purified Tensor Networks (LPTNs) [82]. We are developing as well techniques to evolve open quantum systems with a non-Markovian environment within the tensor network algorithms.

Finally, small features are on the list of future developments, e.g. providing optional support for results in HDF5 file format for more convenient data post processing, improving the speedup when using shared-memory parallelization with openMP, and a TEBD algorithm which is not based on the Krylov approximation.

9.7 Conclusions

In this paper we have presented a description of the MPS library OSMPS containing a set of powerful tools to study static and dynamic properties of entangled one-dimensional many body quantum systems, where the initial focus is on a broad set of methods for quantum simulators based on atomic, molecular and optical physics architectures. These algorithms and interfaces are widely generalizable to other fields of quantum physics, e.g. condensed matter and materials modeling. The usefulness of our methods is underscored by the rapid community adaption and subsequent publications in various areas of quantum physics making use of the OSMPS library or a derivative based on OSMPS [44, 121, 176, 214, 231–242]. OSMPS has been downloaded more than 2300 times from over 55 countries since its initial release on SourceForge in January 2014.

We combine a Fortran core with an easy to use Python front end. By introducing the Python interface we hide the complex structures of the core algorithms from the end user. Moreover, Python is a simpler programming language lowering the barrier to start simulations for non-specialists and students. OSMPS provides fast and easy-to-access numerical predictions for 1D quantum many-body systems. We facilitate this learning process by the recent integration of a small exact diagonalization package inside OSMPS written purely in Python [189]. On the other hand, we also support sophisticated enough features to provide helpful tools for quantum many-body theorists and specialists in quantum computational physics. We presented these tools throughout the paper describing the features of the library, which include ground states of infinite systems and ground states plus low lying excited states in finite size systems. For the dynamics of finite size systems, we provided four different tools starting from a nearest-neighbor Sornborger-Stewart decomposition, a modified Trotter approach, to methods supporting long-range interactions such as Krylov subspaces, local Runge-Kutta, and the time dependent variational principle. We gave a detailed description of the nuanced convergence properties of these methods.

We anticipate that many unexplored problems in quantum simulators, materials modeling, and other areas are suitable for OSMPS, starting with long-range quantum physics and its still unexplored corners reaching to less studied models, e.g. facets of the XYZ model, and the vast variety of untouched far from equilibrium dynamics. The development of new features in OSMPS, as described in Sec. 9.6, follows new emerging fields in quantum physics which come naturally with explorations and requests by the community of both end users and developers.

Providing the library as an open source package including a dedicated forum fosters continued community development and research in many-body entangled quantum physics with a transparent tool, much as density function theory (DFT) was instrumental to the materials genome initiative. Especially the aspect of modifying the core code to integrate tailored tools on top or integrate modules into other open source packages strengthens the

idea of cooperative research. The version 2.0 of our library described in this paper and updates to it are available under the *GNU General Public License* (GPL3) [256] and the Expokit license on our homepage `http://sourceforge.net/projects/openmps/`.

9.8 Acknowledgments

We gratefully appreciate contributions from and discussions with A. Dhar, B. Gardas, A. Glick, W. Han, D. M. Larue, and D. Vargas during the development of OSMPS. We are equally thankful to the ALPS collaboration [88, 257] and to C. W. Clark, I. Danshita, R. Mishmash, B. I. Schneider, and J. E. Williams who contributed heavily to the predecessor of OSMPS, OpenTEBD [97]. The calculations were carried out using the high performance computing resources provided by the Golden Energy Computing Organization at the Colorado School of Mines. This work has been supported by the NSF under the grants PHY-120881, PHY-1520915, and OAC-1740130, and the AFOSR under grant FA9550-14-1-0287.

9.9 Convenient features

OSMPS contains several features which exploit physical considerations to increase the power and reach of the algorithms or are not intrinsically based on physics but simplify the handling of simulations for the user. These convenient features are covered in this part of the appendix.

- **Symmetry conservation:** OSMPS supports an arbitrary number of $\mathcal{U}(1)$ symmetries. In order to employ symmetries, the user has to provide the symmetry generator for each $\mathcal{U}(1)$ symmetry in a diagonal form. For the convergence study on the Bose-Hubbard model in Appendix 9.10, the symmetry generator is the number operator n (which is diagonal). Therefore, simulations can be easily adapted to number conservation if possible. The advantage of the $\mathcal{U}(1)$ symmetries is the ensuing numerical speedup. It is comparable to the use of block-diagonal matrices versus the full matrix with the block diagonal structure. Decompositions are carried out on smaller sub-

spaces. Taking advantage of the block diagonal structure leads to a speedup of more than an order of magnitude for the example simulation treated in Table 9.2.

Consider the one-dimensional Bose Hubbard model

$$H = -J \sum_{i=1}^{L-1} b_i b_{i+1}^\dagger + h.c. + \frac{1}{2} U \sum_{i=1}^{L} n_i (n_i - \mathbb{I}) - \mu \sum_{i=1}^{L} n_i \,, \tag{9.52}$$

where the chemical potential μ regulates the average number of particles $\bar{n} = \frac{1}{L} \sum_{i=1}^{L} \langle n_i \rangle$ in the non-number conserving case. We scan for unit filling with $\bar{n}(\mu = -0.22) \approx 1$ and use this chemical potential for the comparison together with $U = 1.0$ and $J = 0.5$. The compute times are determined from a *2x(Intel Xeon E5-2680 Dodeca-core) 24 Cores 2.50GHz* node. The Fortran library is compiled with *ifort* and optimization flag `O3` and using *mkl*. We see that the unit filling case can improve the simulation by an order of magnitude or more.

Table 9.2: Comparison of the CPU time T_{CPU} in seconds for number conserving and non-number conserving MPS algorithm in the case of the Bose Hubbard model with local dimension $d = 6$ and $L = 32$ for different convergence parameters.

Settings	T_{CPU}/s (no $\mathcal{U}(1)$)	T_{CPU}/s with $\mathcal{U}(1)$
$\chi = 10, \varepsilon_{\text{V}} = 10^{-4}, \varepsilon_{\text{l}} = 10^{-4}$	42	22
$\chi = 60, \varepsilon_{\text{V}} = 10^{-7}, \varepsilon_{\text{l}} = 10^{-6}$	654	21
$\chi = 320, \varepsilon_{\text{V}} = 10^{-12}, \varepsilon_{\text{l}} = 10^{-10}$	19838	150

In addition, we study the Ising model defined in Eq. (9.15) where we can make use of the $\mathbb{Z}_2$ symmetry, which reduces the dimension of the Hilbert space by half. In the block diagonal structure, we never have more than two blocks and we expect that using a symmetry-conserving MPS does not lead to the same speedup as in the Bose-Hubbard model. In Table 9.3 we find that for small bond dimension the overhead due to symmetry conservation is larger than the actual gain. This is in agreement with previous results in [228]. Starting with $\chi = 320$ in this table, the simulation with $\mathbb{Z}_2$

is faster than the one without symmetry. The simulations were run with the same setting as the Bose-Hubbard model simulations on a *2x(Intel Xeon E5-2680 Dodeca-core) 24 Cores 2.50GHz* node. The times include the ground state calculation, one local measurement, and one correlation measurement where the value of the external field $g = 0.98$ is close to the critical point.

Table 9.3: Comparison of the CPU time T_{CPU} in seconds for MPS ground states with and without conservation of $\mathbb{Z}_2$ symmetry in the quantum Ising model. The system size is $L = 128$, the interaction $J = 1$, the external field $g = 0.98$, and default convergence parameters are used if not specified in the table.

Settings	T_{CPU}/s (no $\mathbb{Z}_2$)	T_{CPU}/s with $\mathbb{Z}_2$
$\chi = 10, \varepsilon_{\mathrm{V}} = 10^{-4}, \varepsilon_{\mathrm{l}} = 10^{-4}$	0.15	0.79
$\chi = 60, \varepsilon_{\mathrm{V}} = 10^{-7}, \varepsilon_{\mathrm{l}} = 10^{-6}$	0.57	1.94
$\chi = 320, \varepsilon_{\mathrm{V}} = 10^{-12}, \varepsilon_{\mathrm{l}} = 10^{-10}$	6.31	5.81

- **Support for fermionic systems:** Fermionic systems obey nonlocal anticommutation relations different from the local commutation relations of bosons. In order to represent fermionic operators in OSMPS, we use a Jordan-Wigner transformation [137, 138] which uses locally anticommuting operators together with strings of phase operators $(-1)^n$, with n the number operator. The routines within MPS, for example, the measurement of correlation functions and construction of Hamiltonian terms, have a flag `Phase` for whether a string of phase operators is needed to enforce proper fermionic anticommutation relations.

  Such fermions can be described via the Fermi-Hubbard model [258]. We consider in the following an example of spinless fermions using the Hamiltonian from [259] in a one-dimensional system

$$H_F = W \sum_{i=1}^{L-1} \left(n_i - \frac{1}{2} \right) \left(n_{i+1} - \frac{1}{2} \right) - J \sum_{i=1}^{L-1} \left(c_i^\dagger c_{i+1} + h.c. \right) . \tag{9.53}$$

We briefly introduce the phase terms for fermionic systems and show that it affects the system. Instead of comparing a single correlation measurement or the single particle density matrix built from the correlations $\langle c_i^\dagger c_j \rangle$, we use the quantum depletion ξ from the eigenvalues Ξ_i of the single particle density matrix, yielding a single value. Furthermore, the quantum depletion ξ is constant for spinless fermions and errors can be detected more easily. If Ξ_i are the eigenvalues of the single particle density matrix, the depletion is defined as

$$\xi = 1 - \frac{\max_i \Xi_i}{\sum_i \Xi_i} \,. \tag{9.54}$$

Figure 9.13 shows multiple aspects of the model with a system size of $L = 65$ and approximately half-filling with 33 fermions in the system. The deviation from the average filling at each site

$$\delta \;\; = \;\; \frac{1}{65} \sum_{i=1}^{65} \left| n_i - \frac{33}{65} \right| \,, \tag{9.55}$$

and the bond entropy indicate the phase transition from a charge density wave to a superfluid phase dominated by the tunneling term in the Hamiltonian. Those values are plotted in Figure 9.13(a). In Figure 9.13(b) we show the quantum depletion in three different scenarios including calculating it correctly from the correlation with the phase terms, and incorrectly from the correlation without phase terms and the reduced density matrices. We emphasize that the reduced density matrices never contain phase terms and cannot be used to calculate correlation in fermionic systems which need a phase term.

- **MPI:** Message Passing Interface (MPI) is the standard for distributed memory parallel high performance computing. OSMPS supports the setup of data parallelism via MPI. Although data parallelism is the most basic implementation of a parallel algorithm,

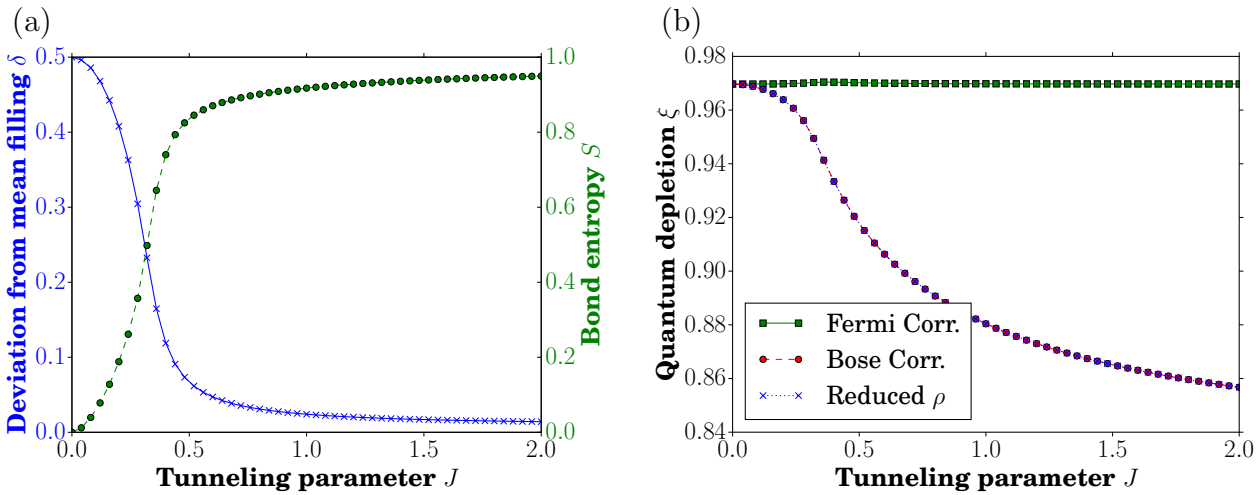

Figure 9.13: *Spinless Fermions at half-filling.* (a) The deviation from the mean-filling δ (blue x's) shows the two different phases. For small tunneling $J < 1$ there is an alternating order of empty-occupied sites dominating. In contrast, the tunneling term with $J > 1$ leads to a superfluid-like phase. The bond entropy S shows the same phase transition with a peak around $J = 1.0$. We point out that the simulation for $J = 0$ fails because there are no fluctuations to feed the variational minimization in the ground state search. The tunneling parameter J is in units of the nearest-neighbor interaction W. The first point uses a small perturbation of $J = 10^{-4}$. (b) The quantum depletion ξ is calculated from the correlation matrix $\langle c_i^\dagger c_j \rangle$. The result from the boson-type correlation without a phase term and the reduced density matrices are identical, corresponding to the lower curve. Both results do not match the correct curve when accounting for the phase terms of the Jordan-Wigner transformation.

it represents the most efficient approach when iterating over a set of parameters. For a large fraction of problems, we can assume that iterations over a set of parameters are necessary as in the case of phase diagrams, finite-size scalings, to analyze Kibble-Zurek scalings, or to scan over a variety of initial conditions. We provide a Fortran implementation with one master and $(p-1)$ workers where p is the total number of cores. Furthermore, a Python implementation is available with p workers where one of them is distributing jobs.

As an example for the scaling of the MPI implementation, we take a look at the Fortran implementation and the simulations necessary to generate the data for Figure 9.2. We run the simulation on one or two nodes of the type *2x(Intel Xeon E5-2680 Dodeca-core)*

24 Cores 2.50GHz with 12, 24, 36, and 48 cores. The duration of the jobs can be found in Table 9.4. We recall that the set of simulations iterates over 30 data points for the system size L and 51 data points for the external field g, i.e., 1530 data points in total. In the case of 48 cores, the average workload is approximately 32 data points. Since the master distributes the jobs to the workers one by one, each worker might handle less (more) jobs if their jobs take more (less) than the average time of one data point. In the setup of the simulation, we avoid getting stuck in long simulations at the end having other cores running idle, because we address the large system sizes first. The longest single data point takes about 4.5 hours. This setup leads to a good scaling of the simulation time when increasing the number of cores. In fact, when increasing the number of cores from 12 by a factor of n, the speedup is greater than n. This is related to the fact that the master distributing the jobs has less weight for more cores. The parallel efficiency E_P is calculated with the cumulative CPU time of all simulations T_Σ and the actual run time of the job T_N on N cores. We assume that the cumulative CPU time corresponds to the time of the serial job:

$$E_P \;=\; \frac{T_\Sigma}{N \cdot T_N}\,. \tag{9.56}$$

The initial increase of E_P seen in Table 9.4 is again explained with the master running almost idle.

Table 9.4: *MPI scaling for OSMPS.* As example for the MPI scaling of the duration time T_{Job} in hours and minutes of all simulations, we execute the simulations for Figure 9.2 on different numbers of cores. In order to evaluate the scaling the number of workers excluding the master job distributing the jobs has to be considered.

Cores (Workers)	12 (11)	24 (23)	36 (35)	48 (47)	72 (71)	96 (95)
T_{Job} (hh:mm)	68:03	32:47	21:17	15:52	10:40	7:50
Efficiency E_P	91.7%	95.9%	97.3%	97.9%	97.1%	97.5%

- **Templates:** The OSMPS library supports calculations with real and complex numbers as well as standard MPS or symmetry conserving MPS algorithms inside the Fortran modules. The different data types lead to many redundant subroutines which we overcome by using templates. Subroutines are written for a generic type, e.g. `MPS_TYPE`. When generating the module the necessary types are plugged in, e.g. `MPS`, `MPSc`, `qMPS`, and `qMPSc`. The corresponding call to such a subroutine is covered under an interface (containing all the subroutines for the different types). These templates reduce errors copying from type to type and keep modules shorter.

9.10 Convergence studies

OSMPS can be tuned via multiple parameters modifying simulations with regards to the convergence. Therefore, we provide some guidelines for the convergence parameters along with examples. We divide this appendix in one part looking at the details of the finite size statics followed by additional studies of the time evolution methods.

9.10.1 Finite size variational algorithms

Due to the variational search we have several convergence parameters. We can divide them into three categories:

- *Lanczos*: Lanczos tolerance, maximal number of Lanczos iterations
- *Chi/bond dimension*: maximal bond dimension, local tolerance, variance tolerance
- *Iteration*: min/max num sweeps, max outer sweeps

Due to the number of convergence parameters, we present a simplified picture of convergence issues with a single set of convergence parameters. We support multiple subsequently executed sets of convergence parameters, which allow users to refine their target state in multiple steps when increasing the bond dimension, Lanczos iterations and number of sweeps while decreasing the Lanczos tolerance, local tolerance, and variance tolerance. In general,

the control of convergence over the soft cutoffs defined via tolerances should be preferred over the hard cutoff specified as the bond dimension or number of Lanczos iterations.

For the convergence study presented in Table 9.1 we concentrate on the Lanczos tolerance ε_l, the variance tolerance ε_V and the bond dimension χ. The maximal number of Lanczos iterations is set to a sufficiently high value to ensure convergence (500, default is 100). The number of inner sweeps is set to exactly 2, i.e. a minimum and maximum of 2, except for the spinless fermions with 4. We consider exactly one outer sweep. Since every additional outer sweep lowers the local tolerance $\varepsilon_\mathrm{local}$ for the cut-off of singular values, we prevent different $\varepsilon_\mathrm{local}$ depending on the number of outer sweeps carried out. The warmup phase to grow the system up to L sites has a warmup tolerance 100 times bigger than the variance tolerance and the warmup bond dimension is half of the bond dimension. The local tolerance is then connected with the variance tolerance as specified in the default settings:

$$\varepsilon_\mathrm{local} = \frac{\varepsilon_\mathrm{V}}{4L}\,. \tag{9.57}$$

For the remaining three parameters ε_l, ε_V and χ the variance tolerance determines if a simulation is converged according to the criterion

$$\langle H^2 - \langle H\rangle^2\rangle < \varepsilon_\mathrm{V} L\,. \tag{9.58}$$

The actual behavior may vary for different models. We study the convergence behavior of the Ising model, the Bose Hubbard model, and a spinless Fermi-Hubbard model. Future possibilities for similar studies include spinful Fermi-Hubbard or Bose-Hubbard models, XYZ models, quantum rotors, and disordered systems. Starting with the Ising model, we show in Figure 9.14 (a) the boundary between converging and non-converging simulations over a grid of ε_l and χ. In Figure 9.14 (b) the energy difference to the smallest value can be found. The point is close to the quantum critical point ($g = 0.98$ with $g_c = 1.0$) so the settings also serve as an upper bound for points further away from the critical point.

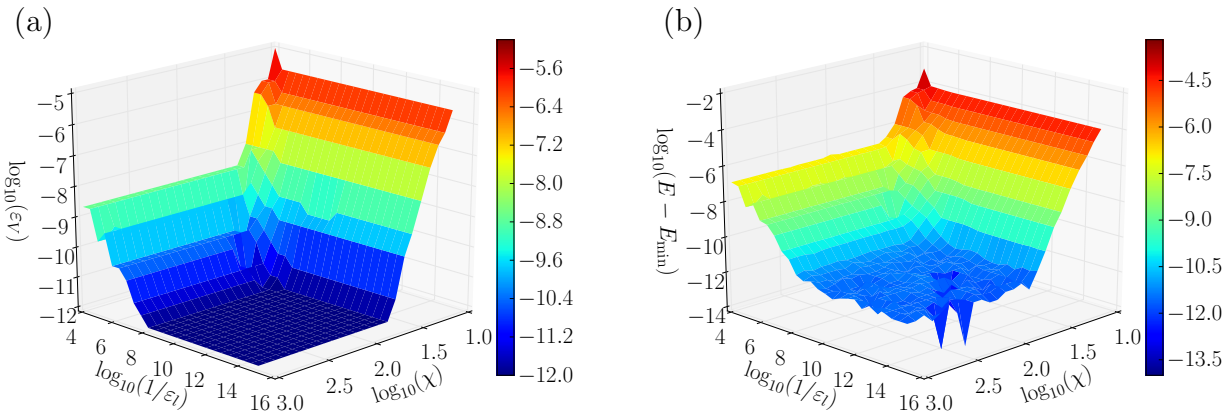

Figure 9.14: *Convergence study for the quantum Ising model.* (a) The boundary between converged and non-converged simulations as a function of the bond dimension and Lanczos tolerance. The surface shows the first converged simulations fulfilling the variance tolerance criteria. Smaller variance tolerances will lead to non-convergence for fixed parameters. With this plot, we can estimate the maximal variance tolerance that can be achieved using a given bond dimension and Lanczos tolerance. (b) The energy difference as a function of bond dimension and Lanczos tolerance for the first converged simulation in regard to the variance tolerance (see (a)) reproduces the expectation that the energy difference decreases as the convergence criteria defined over the variance decreasing tolerance is met. Same labels apply to color bar and z-axis.

In the next example we turn to the long-range quantum Ising model with the Hamiltonian presented in Eq. (9.14). We evaluate the convergence behavior again close to the critical point. For a power-law decay with $\alpha = 3.0$ and a system size of $L = 128$ we have a critical field of $g_c \approx 1.35$ [176]. We leave the remaining parameter fixed in comparison to the nearest neighbor quantum Ising model. Figure 9.15 (a) shows again the boundary between converging and non-converging simulations based on the variance tolerance ε_V iterating over the bond dimension χ and the Lanczos tolerance ε_l. We see that we need a much higher bond dimension in comparison to the nearest-neighbor Ising model.

For the Bose Hubbard model introduced in Eq. (9.52) the same type of plot is shown in Figure 9.15(b). The algorithm includes number conservation at unit filling and the system size is $L = 32$. We choose the point with $U = 0.5$, $t = 0.5$ and $\mu = 0$ in the superfluid regime

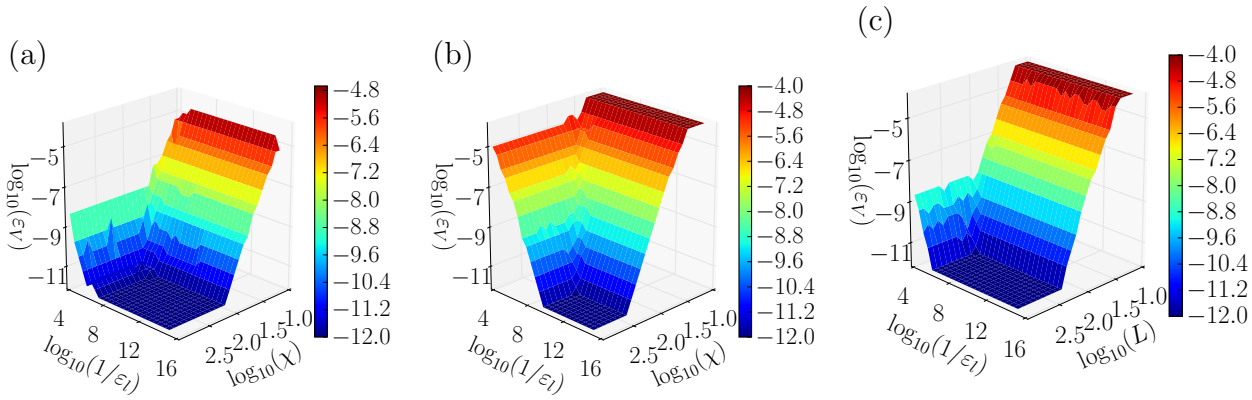

Figure 9.15: *Convergence study.* We study the variance tolerance achieved as a function of the bond dimension and the Lanczos tolerance for (a) the long-range Ising model, (b) the Bose-Hubbard model, and (c) a spinless Fermi-Hubbard model. (Same labels apply to color bar and z-axis.)

exhibiting long-range correlations. In contrast, the Mott insulator has less entanglement and therefore the superfluid parameters can serve as upper bound. In the Figure 9.14 and Figure 9.15 we observe that the Bose-Hubbard model needs, in comparison to the Ising model, stricter convergence parameters to arrive at an equal variance tolerance.

Finally, we consider the spinless fermions introduced in Eq. (9.53) and present the result on the convergence in Figure 9.15 (c). As with the Ising model, we choose a point in the region with high entanglement judged by the bond entropy evaluated in Figure 9.13, that is a tunneling energy of $J = 1.04$. Furthermore, we take $L = 65$, and the system is filled with 33 fermions. In contrast to the other simulations we increase the minimum and maximum number of inner sweeps to 4. Comparing the Fermi-Hubbard model to the quantum Ising model since both have a local dimension of $d = 2$ and are nearest-neighbor, we see that the fermionic system needs a larger bond dimension χ in comparison.

9.10.2 Time evolution methods for finite size systems

In this part of the appendix we expand the convergence study of the time evolution methods with additional examples to demonstrate some key points. Figure 9.11 in Sec. 9.5.1

shows aspects of a quench in the paramagnetic phase of the Ising model for $L = 10$. Due to the time-dependence of the Hamiltonian, we already make an error due to the evaluation of the Hamiltonian at discrete points in time. Now, we study the convergence of the different algorithms under the evolution of a time-independent Hamiltonian. Therefore, we use the same ground state of the Ising model at an external field $g = 5.0$ and evolve it under the Hamiltonian with an external field of $g = 4.5$, which corresponds to a sudden quench. The results are shown in Figure 9.16.

We start the discussion with the maximal distance of the single site reduced density matrices. For the Krylov and TDVP algorithms, the decrease of the time step dt does not improve the result, but seems to make it worse. Since there is no error in the method or from the time slicing of the Hamiltonian depending on dt, the number of applications is the critical variable to estimate the error. In contrast, TEBD and LRK have an error depending on dt in ϵ_{method}. Therefore the second order methods are worse than the fourth order and smaller time steps improve the result if it did not yet reach the lower bound. We recall that the lower bound is considered to be error between the ground state results of MPS and exact diagonalization. The two-site reduced density matrices, the energy, and the bond entropy support this trend. Further the errors in energy give an indication to judge on the rate of convergence for LRK and TEBD. If we consider the data points for $dt = 0.1$ and $dt = 0.01$, the slope for the TEBD4 curve is bigger than the one for TEBD2 indicating a better rate of convergence. Then TEBD4 reaches the lower bound induced by the error of the initial state or is at the level of the error of the TDVP and Krylov method. The LRK methods have the same rate of convergence following this argumentation. The look at the CPU times yields then a counterintuitive result. The most precise simulation with TDVP has the biggest time step and one of the shortest run times. The reported error from OSMPS follows the arguments from the time-dependent Hamiltonian. Without any truncation besides the local tolerance, more time steps add up to more error contributions.

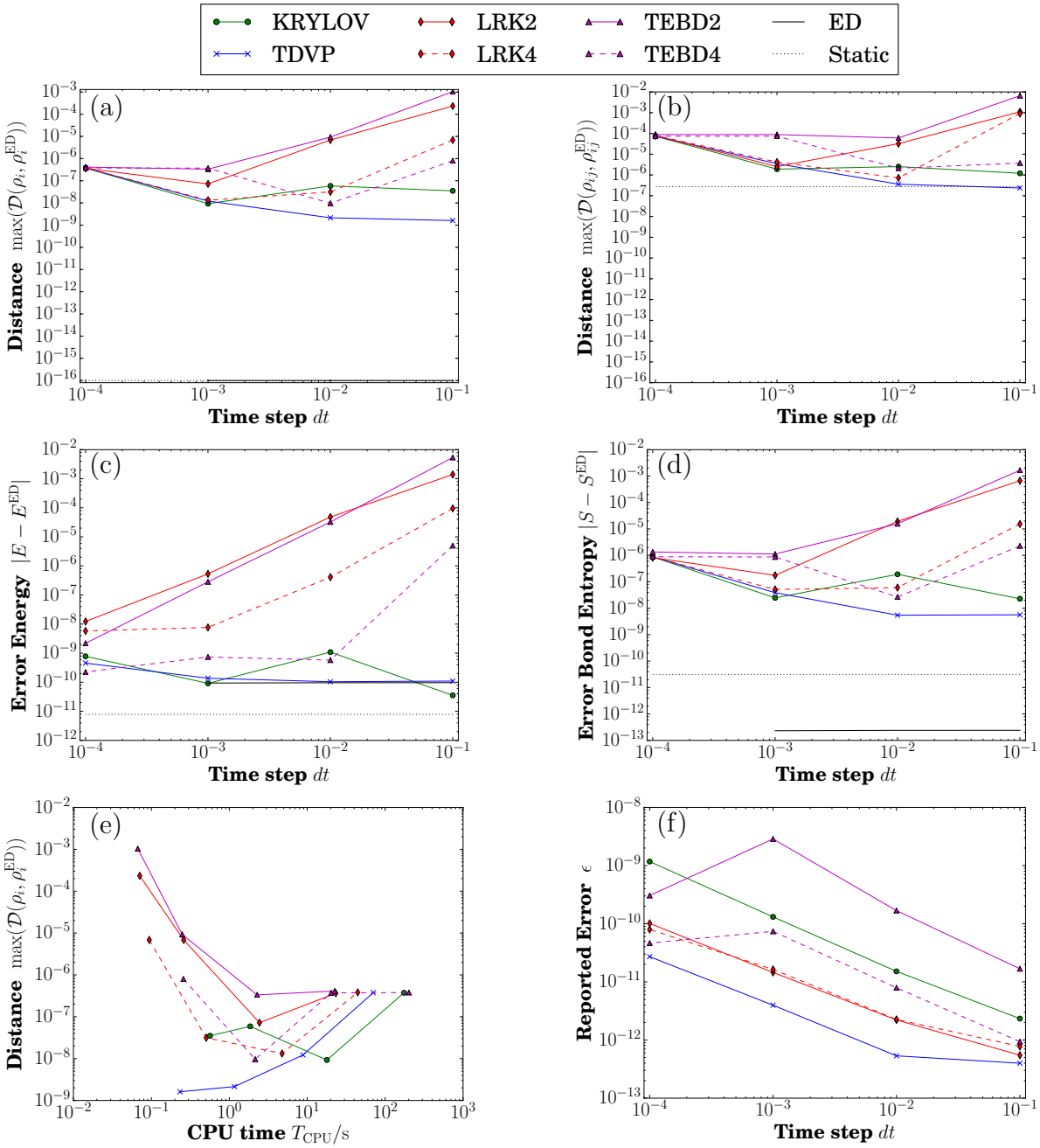

Figure 9.16: *Scaling of the error in time evolution methods* decreases as expected with the size of the time step for methods where the error depends on the time step. This is the example of a sudden quench of the Ising model in the paramagnetic phase evolving the ground state of an external field $g = 5.0$ at constant $g = 4.5$ for $L = 10$. The time step dt is in units of $\hbar/J$. Curves are a guide to the eye; points represent actual data.

A second approach to estimate the error for time evolution is the forth-back scheme [260]. The unitary time evolution under the Hamiltonian H for a time τ followed by the evolution

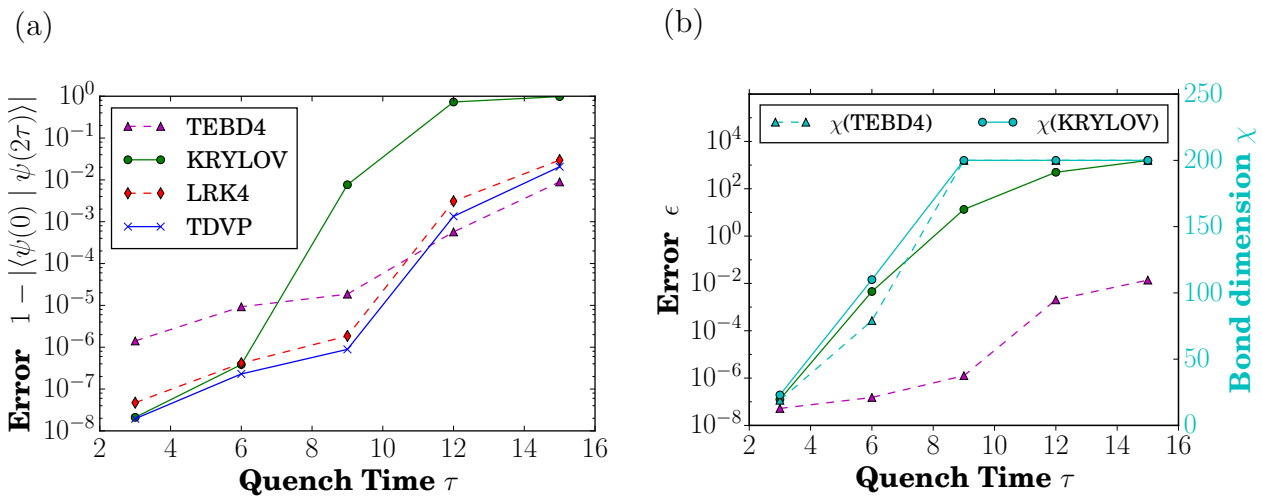

Figure 9.17: *Error with forth-back time evolution.* Unitary time evolution is reversible and can help to estimate the error of time evolution schemes. We quench for times τ with the Hamiltonian H followed by the inverse direction, i.e., $-H$, again for τ. H is the Hamiltonian of the nearest neighbor Ising model. (a) The error defined over the Loschmidt echo shows that the precision of the final state declines for longer evolution times τ. τ is in units of the interaction $\hbar/J$. (b) The reason for this trend is the entanglement generated, which cannot be captured with $\chi_{\max} = 200$, and thus the cumulative error ϵ grows. ϵ includes truncation errors and, in the case of the Krylov method, errors from fitting states and $H\,|\psi\rangle$. (Legend for TEBD2 and KRYLOV from (a) applies for the errors ϵ.)

under $-H$ for another τ should return to the initial state. We analyze this error for the nearest neighbor Ising model with $L = 30$ and quench times from $\tau = 3$ to $\tau = 15$ in units of $\hbar/J$. We choose the default settings for the time evolution, except $\chi_{\max} = 200$. The initial state is a product state with all spins pointing in x-direction, except the spin on site 16 pointing opposite to the x-direction: $|\,\psi(0)\rangle = |{\mapsto_1} \cdots {\to_{15}} {\leftarrow_{16}} {\to_{17}} \cdots {\to_{30}}\rangle$. The time step is $dt = 0.01$. We observe the error grows with the quench time τ in Figure 9.17 (a), which is an effect of the growing entanglement during the time evolution. One minus the absolute value of the Loschmidt echo corresponds to the infidelity and is therefore a good error measure. This reasoning is supported by part (b) of Figure 9.17: the maximal bond dimension is exhausted for the larger τ and the cumulative error grows. The error includes the truncation for the TEBD, and additional contribution from the fitting of wave function in the Krylov method. Obviously, one can generalize this approach to any model and study

this error previous to simulating new or different Hamiltonians and initial conditions.

9.11 Scaling of computational resources

We consider the scaling of computational resources, especially computation time and memory, as a function of common parameters of simulations. These include the system size L and the maximal bond dimension χ. While the default parallelization is data parallelism using the MPI interface to OSMPS with a straightforward scaling explained in Appendix 9.9, we consider as well the openMP (Open Multi Processing) algorithms used by the underlying libraries, namely LAPACK and BLAS.

First, we consider the scaling with the maximal bond dimension χ. We consider in this scenario the quantum Ising model for a system size of $L = 1063$, which corresponds to one data point from Figure 9.2. The value of the external field is the critical value for the thermodynamic limit, i.e., $g = 1.0$. The simulations were run on a *2x(Intel Xeon E5-2680 Dodeca-core) 24 Cores 2.50GHz* node and the corresponding data is shown in Figure 9.18. In order to have a better understanding of the data we plot in each case the bond dimension. For the memory in Figure 9.18(a) we see that the file size saturates once the bond dimension saturates. The file contains the complete information about the state in binary format and gives a good estimate of the memory needs for each simulation. For linear algebra operations within LAPACK, the additional memory allocated as workspace is on the order of the matrix size. The size of the matrices handled is bounded by the local dimension and the maximal bond dimension leading to a maximum size of $d\chi_{\max} \times d\chi_{\max}$. Figure 9.18(b) shows the CPU time for each simulation. It naturally saturates with the bond dimension. Before the saturation point it grows linearly with the bond dimension actually used.

For the scaling of the resources with the system size L we consider the set of simulations generating Figure 9.2 and pick the external field $g = 1.0$. The data is for *Penguin Relion 2x(Intel X5675) 12 cores 3.06GHz* nodes. As previously, we show the bond dimension utilized in addition to the file size or computation time. If the bond dimension saturates starting at $L > 500$, the file size grows linearly with the system size L as shown in Figure 9.18(c). In

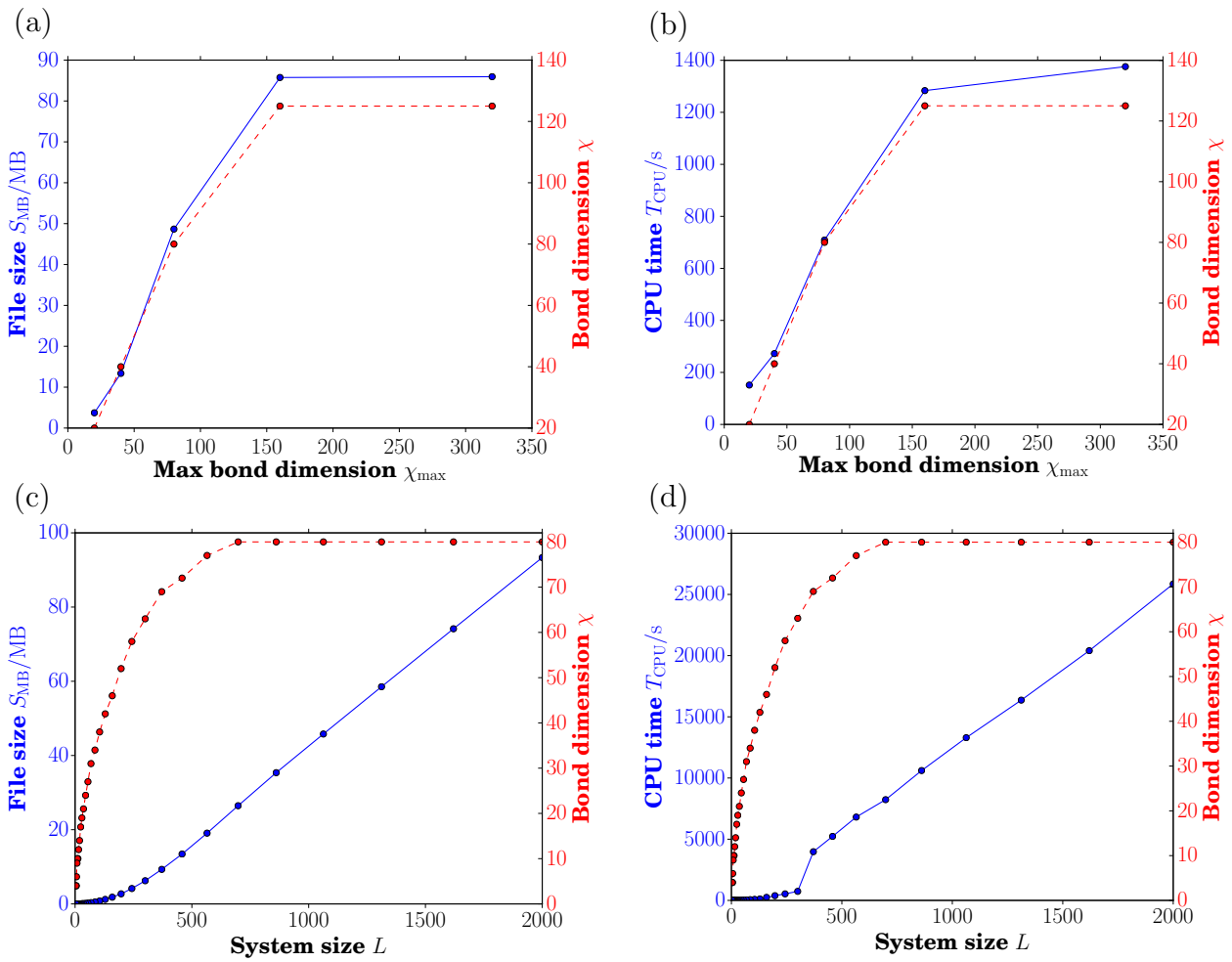

Figure 9.18: *Scaling of computational resources.* We consider the Ising model and vary the bond dimension and the system size. (a) The file size of the ground state indicates the memory resources necessary for the simulation. The parameters are $L = 1063$ and $g = 1.0$ for different maximal bond dimensions χ_{max}. (b) The scaling of the CPU time as a function of χ_{max}. Parameters equal to (a). (c) The file size of the ground state for $\chi_{\mathrm{max}} = 80$ at $g = 1.0$ for a set of different system sizes from the data of Figure 9.2. (d) The scaling of the CPU time for different system sizes. Parameters equal to (c).

contrast, in the growth for $L < 500$ the file size increases faster than linear. In addition to the growing system size, the fact that a larger system can have more entanglement leads to the increase in file size. Figure 9.18(d) shows the CPU times for the equivalent setup with a similar result as for the file size. The scaling is linear as soon as the bond dimension actually used saturates. Before the growth appears nonlinear with a jump.

We examine the use of openMP as the last part of the analysis of resources. OpenMP allows for parallel computing with shared memory on one compute node. In contrast, the tasks of MPI jobs never have access to the same memory and have to send any data. In our type of implementation data is sent between the master node and the workers. On current clusters this allows one to use parallelization with up to 24 cores. We study the efficiency of openMP and what speedup can be gained. OSMPS does not have implementations for openMP itself, but the LAPACK and BLAS or respectively mkl libraries can support openMP on the level of the linear algebra operations within OSMPS. We find that openMP, implemented in this form, does not increase the speed of the simulation, as described in Table 9.5. The simulation time shown is the duration of the job and not the CPU time on a *2x(Intel Xeon E5-2680 Dodeca-core) 24 Cores 2.50GHz* node.

Table 9.5: *OpenMP scaling for OSMPS.* As an example for the scaling we simulate the ground state of the Ising model for $L = 1063$ at an external field of $g = 1.0$ for different numbers of threads and different bond dimensions and list the duration of the simulation T_{Job} in seconds. This case corresponds to a data point of Figure 9.2. We see that openMP does not come with any real speedup. The maximal bond dimension used is 124, which affects the last two rows.

Cores	1	2	4	8	16	24
$T_{\text{Job}}(\chi_{\max} = 20)/\text{s}$	150	154	154	155	154	168
$T_{\text{Job}}(\chi_{\max} = 40)/\text{s}$	270	273	271	274	275	302
$T_{\text{Job}}(\chi_{\max} = 80)/\text{s}$	699	780	789	734	749	739
$T_{\text{Job}}(\chi_{\max} = 160)/\text{s}$	1293	1273	1232	1188	1161	1396
$T_{\text{Job}}(\chi_{\max} = 3200)/\text{s}$	1368	1372	1259	1241	1237	1278

9.12 Error bounds for static simulations

Ideally, numerical simulations yield a corresponding bound for the error of their results. For DMRG there are calculations available discussing the behavior of the error. Local observables in a two-dimensional Heisenberg models are discussed in terms of the truncation error in [74, 75, 261]. The error in variational MPS methods is mentioned in [246, 262] and relates the variance to the squared norm of the difference between the exact and the

approximate quantum state. We present an alternate approach using the variance as well to derive error expressions for multiple observables.

In static MPS simulations the variance of the Hamiltonian, which bounds the error of the energy, is returned as an error estimate for the result. Therefore, it remains for us to show how other observables or measures are bounded by the variance of the state, where we take the ground state as an example. The basic idea is to assume we have a final state $|\psi\rangle$ as an MPS

$$|\psi\rangle = f|\psi_0\rangle + \epsilon|\psi_\perp\rangle\,, \tag{9.59}$$

with $f = \langle\psi|\psi_0\rangle$, $|\epsilon|^2 = 1 - |f|^2$, and $|\psi_0\rangle$ the true ground state, while $|\psi_\perp\rangle$ is orthogonal to the ground state and contains all errors. In this appendix we keep the notation that $|\,\psi\rangle$ is the state from the OSMPS simulation with a variance V_ψ, $|\,\psi_0\rangle$ is the true ground state and $|\,\psi_\perp\rangle$ contains all contributions orthogonal to the true ground state.

9.12.1 Bounding ϵ with the variance delivered by open source Matrix Product States

The first step is to bound ϵ from the information gathered in OSMPS, that is the variance of H. Furthermore, in addition to the above orthogonality relation $\langle\psi_\perp|\psi_0\rangle$, any power H^n is subject to the relation $\langle\psi_\perp|\,H^n\,|\psi_0\rangle = 0$, since $|\,\psi_0\rangle$ is an eigenstate of H. We recall that the Hamiltonian is represented without errors except if an `InfiniteFunction` rule is fitted through a series of `Exponential` rules. The error due to the fitting procedure is not covered in this Appendix. Writing the variance in terms of this decomposition we obtain

$$\begin{aligned}
&V_\psi = \langle\psi|\,H^2\,|\psi\rangle - \left(\langle\psi|\,H\,|\psi\rangle\right)^2 \\
&= |f|^2\,\langle\psi_0|\,H^2\,|\psi_0\rangle + f^*\epsilon\,\langle\psi_0|\,H^2\,|\psi_\perp\rangle + f\epsilon^*\,\langle\psi_\perp|\,H^2\,|\psi_0\rangle + |\epsilon|^2\,\langle\psi_\perp|\,H^2\,|\psi_\perp\rangle \\
&- \left(|f|^2\,\langle\psi_0|\,H\,|\psi_0\rangle + f^*\epsilon\,\langle\psi_0|\,H\,|\psi_\perp\rangle + f\epsilon^*\,\langle\psi_\perp|\,H\,|\psi_0\rangle + |\epsilon|^2\,\langle\psi_\perp|\,H\,|\psi_\perp\rangle\right)^2 \\
&= |f|^2\,\langle\psi_0|\,H^2\,|\psi_0\rangle + |\epsilon|^2\,\langle\psi_\perp|\,H^2\,|\psi_\perp\rangle - |f|^4\,\langle\psi_0|\,H\,|\psi_0\rangle^2 \\
&-2|f|^2|\epsilon|^2\,\langle\psi_0|\,H\,|\psi_0\rangle\,\langle\psi_\perp|\,H\,|\psi_\perp\rangle - |\epsilon|^4\,\langle\psi_\perp|\,H\,|\psi_\perp\rangle^2\,.
\end{aligned} \tag{9.60}$$

We introduce the eigenenergy $E_0 = \langle\psi_0| H |\psi_0\rangle$ of our true ground state and the energy $E_\perp = \langle\psi_\perp| H |\psi_\perp\rangle$, which is not an eigenenergy of the system because $|\psi_\perp\rangle$ can be a linear combination of eigenstates. Next, we use the relation $|f|^2 = 1 - |\epsilon|^2$ and we add a zero in terms of $\pm(|\epsilon|^2 - |\epsilon|^4)E_\perp^2$ to simplify the expression:

$$\begin{aligned} V_\psi &= (1-|\epsilon|^2)\langle\psi_0| H^2 |\psi_0\rangle + |\epsilon|^2 \langle\psi_\perp| H^2 |\psi_\perp\rangle \\ &\quad -(1-2|\epsilon|^2+|\epsilon|^4)E_0^2 - 2(|\epsilon|^2-|\epsilon|^4)E_0E_\perp - |\epsilon|^4E_\perp^2 \\ &\quad +(|\epsilon|^2-|\epsilon|^4)E_\perp^2 - (|\epsilon|^2-|\epsilon|^4)E_\perp^2 \\ &= (1-|\epsilon|^2)V_0 + |\epsilon|^2V_\perp + (|\epsilon|^2-|\epsilon|^4)(E_\perp - E_0)^2 \,. \end{aligned} \tag{9.61}$$

We abbreviate the energy difference as $\Delta = E_\perp - E_0$, define the variance of $|\psi_\perp\rangle$ as $V_\perp$, and the variance of $|\psi_0\rangle$ as $V_0 = 0$. We introduce $\tilde{\epsilon} = |\epsilon|^2$ leading to the following quadratic equation:

$$\Delta^2\tilde{\epsilon}^2 - (V_\perp + \Delta^2)\tilde{\epsilon} + V_\psi = 0\,. \tag{9.62}$$

We remark that the variance of an eigenstate of H is zero, applied to $V_0 = 0$. The equation has two solutions returning the values for $|\epsilon|^2$:

$$|\epsilon_1|^2 = \frac{1}{2}\left(1 + \frac{V_\perp}{\Delta^2} - \sqrt{\left(1+\frac{V_\perp}{\Delta^2}\right)^2 - 4\frac{V_\psi}{\Delta^2}}\right) \tag{9.63}$$

$$|\epsilon_2|^2 = \frac{1}{2}\left(1 + \frac{V_\perp}{\Delta^2} + \sqrt{\left(1+\frac{V_\perp}{\Delta^2}\right)^2 - 4\frac{V_\psi}{\Delta^2}}\right)\,. \tag{9.64}$$

Plugging $|\epsilon|^2 = 1 - |f|^2$ into Eq. (9.62), we get another quadratic equation and two solutions for $|f|^2$:

$$\Delta^2|f|^4 - (\Delta^2 - V_\perp)|f|^2 + (V_\psi - V_\perp) = 0\,, \tag{9.65}$$

$$|f_1|^2 = \frac{1}{2}\left(1 - \frac{V_\perp}{\Delta^2} + \sqrt{\left(1 + \frac{V_\perp}{\Delta^2}\right)^2 - \frac{4V_\psi}{\Delta^2}}\right)\,, \tag{9.66}$$

$$|f_2|^2 = \frac{1}{2}\left(1 - \frac{V_\perp}{\Delta^2} - \sqrt{\left(1 + \frac{V_\perp}{\Delta^2}\right)^2 - \frac{4V_\psi}{\Delta^2}}\right)\,. \tag{9.67}$$

According to the normalization condition we recognize that f_1 and ϵ_1 build one solution, as well as f_2 and ϵ_2:

$$|f_i|^2 + |\epsilon_i|^2 = 1\,,\; i \in \{1, 2\}\,. \tag{9.68}$$

Under the assumption that the major part of our state is in the ground state, we choose the smaller ϵ_1. This is the first assumption in the calculation and we proceed to bound ϵ^2 using the fact that $0 \leq V_\perp \leq V_\psi$ and then implementing a Taylor expansion in V_ψ/Δ, which is small if the variance of the ground state has sufficiently converged targeting in the default setup a value of $L \times 10^{-10}$ and we have an energy gap in the system. We point out the role of the gap Δ in the following steps in detail:

$$\begin{aligned}
|\epsilon|^2 &\leq \frac{1}{2}\left(1 + \frac{V_\psi}{\Delta^2} - \sqrt{1 - 4\frac{V_\psi}{\Delta^2}}\right) \\
&\approx \frac{1}{2}\left(1 + \frac{V_\psi}{\Delta^2} - \left(1 - 2\frac{V_\psi}{\Delta^2} - \mathcal{O}\left(\frac{V_\psi^2}{\Delta^4}\right)\right)\right) \\
&= \frac{1}{2}\left(\frac{3V_\psi}{2\Delta^2} + \mathcal{O}\left(\frac{V_\psi^2}{\Delta^4}\right)\right)\,.
\end{aligned} \tag{9.69}$$

Finally, we use the minimal gap between the ground state and the first excited state $\Delta_{0,1} = E_1 - E_0$ to approximate Δ. The inverse energy difference between the ground state and a superposition of all excited states can be bound with the smallest gap:

$$|\epsilon|^2 \leq \frac{3V_\psi}{4\Delta_{0,1}^2} + \mathcal{O}\left(\frac{V_\psi^2}{\Delta_{0,1}^4}\right) \quad \Longrightarrow \quad |\epsilon| \leq \frac{\sqrt{V_\psi}}{\Delta_{0,1}} + \mathcal{O}\left(\frac{V_\psi}{\Delta_{0,1}^2}\right)\,. \tag{9.70}$$

This bound shows that the variance can be a good approximation for the error as long as the gap to the next eigenstate is finite. This gap refers to the next accessible eigenstate in case symmetries are used. For simulations around the critical point with a closing gap the bound becomes less precise due to the closing gap. But for finite systems considered in this calculation, the gap remains.

In addition, we list the implicit and explicit assumptions during the derivation of the bound

- We converged mainly to the ground state. The solutions in Eqs. (9.63) and (9.65) and in Eqs. (9.64) and (9.67) are in general true for any eigenstate of H.
- By taking the solution represented by the pair of Eqs. (9.63) and (9.65) we assume that the main part of the solution is in the eigenstate.
- The energy gap to the first state above the ground state used in the Taylor expansion is assumed not to be small. This approximation may fail around quantum critical points with a closing energy gap.
- $V_\perp \leq V_\psi$: the variance of the subset of states is smaller if the minimal energy is canceled from the set of states. This is true because one end of the distribution is cut.

9.12.2 Bounding observables

The ϵ derived above is only useful if bounds for other measures can be obtained. For a local Hermitian observable O with a maximal absolute value $\mathcal{M}$ defined as

$$\mathcal{M} = \max_{|\phi\rangle,|\phi'\rangle} |\langle\phi| O |\phi'\rangle| \tag{9.71}$$

we obtain the following bound between the measurement on the true ground state $|\psi_0\rangle$ and the state $|\psi\rangle$ resulting from the OSMPS simulation:

$$
\begin{aligned}
&|\langle\psi_0|\,O\,|\psi_0\rangle - \langle\psi|\,O\,|\psi\rangle| \\
&= \big|(1-|f|^2)\langle\psi_0|\,O\,|\psi_0\rangle - \epsilon f^*\langle\psi_0|\,O\,|\psi_\perp\rangle - \epsilon^* f\langle\psi_\perp|\,O\,|\psi_0\rangle \\
&-|\epsilon|^2\langle\psi_\perp|\,O\,|\psi_\perp\rangle\big| \\
&\leq (1-|f|^2)\,|\langle\psi_0|\,O\,|\psi_0\rangle| + 2|\epsilon f|\,|\langle\psi_0|\,O\,|\psi_\perp\rangle| + |\epsilon|^2\,|\langle\psi_\perp|\,O\,|\psi_\perp\rangle| \\
&\leq 2|\epsilon|(|f|+|\epsilon|)\mathcal{M} \leq 2\sqrt{2}|\epsilon|\mathcal{M} \leq 3|\epsilon|\mathcal{M}\,. \qquad (9.72)
\end{aligned}
$$

Here in, $|f|+|\epsilon|$ is always smaller than $\sqrt{2}$, which originates in the normalization of the state and can be derived from maximizing the constraint problem $\mathcal{L}(f,\epsilon,\gamma) = |f| + |\epsilon| + \gamma(|f|^2 + |\epsilon|^2 - 1)$, where γ is a Lagrange multiplier for the normalization constraint. So in general it is possible to bound values of an observable.

9.12.3 Density matrices and their bounds

In the following, we derive an expression for the complete density matrix, any reduced density matrix of the system, and a bound for the trace distance between the MPS result and the (reduced) density matrix of the ground state. We start by expressing the mixed contribution of the form $|\psi_0\rangle\langle\psi_\perp|$ in a more convenient way.

Lemma 1 (Mixed contributions $|\psi_0\rangle\langle\psi_\perp|$) *A mixed contribution of the form* $\mathrm{e}^{-\mathrm{i}\phi}\,|\psi_0\rangle\langle\psi_\perp| + \mathrm{e}^{\mathrm{i}\phi}\,|\psi_\perp\rangle\langle\psi_0|$ *with an arbitrary phase* ϕ *can be decomposed into positive matrices* $\sigma_\pm$ *with one non-zero eigenvalue of value* 1 *as*

$$
|\psi_0\rangle\langle\psi_\perp| + |\psi_\perp\rangle\langle\psi_0| = \sigma_+ - \sigma_-\,, \qquad (9.73)
$$

where $\sigma_\pm$ *fulfill all characteristics of a density matrix (and are not the spin lowering/raising operators).*

Proof. We take the pure states $|\psi_\pm\rangle = (|\psi_0\rangle \pm \mathrm{e}^{\mathrm{i}\phi}\,|\psi_\perp\rangle)/\sqrt{2}$, where ϕ is an arbitrary phase. These pure states define the density matrices $\sigma_\pm$:

$$
\begin{aligned}
\sigma_\pm &= |\psi_\pm\rangle\langle\psi_\pm| \\
&= \frac{1}{2}\,|\psi_0\rangle\langle\psi_0| + \frac{1}{2}\,|\psi_\perp\rangle\langle\psi_\perp| \pm \frac{1}{2}\left(\mathrm{e}^{-\mathrm{i}\phi}\,|\psi_0\rangle\langle\psi_\perp| + \mathrm{e}^{\mathrm{i}\phi}\,|\psi_\perp\rangle\langle\psi_0|\right)\,. \qquad (9.74)
\end{aligned}
$$

Therefore, the difference $\sigma_+ - \sigma_-$ leads to the term we need while canceling out the contributions from $|\psi_\perp\rangle\langle\psi_\perp|$ and $|\psi_0\rangle\langle\psi_0|$:

$$\sigma_+ - \sigma_- = \mathrm{e}^{-\mathrm{i}\phi}\,|\psi_0\rangle\langle\psi_\perp| + \mathrm{e}^{\mathrm{i}\phi}\,|\psi_\perp\rangle\langle\psi_0|\ . \tag{9.75}$$

Lemma 2 (Error bound on density matrix) *Knowing ϵ in $|\psi\rangle = f\,|\psi_0\rangle + \epsilon\,|\psi_\perp\rangle$, we can express the (reduced) density matrix ρ representing the OSMPS result as*

$$\rho = |f|^2\rho_0 + \tilde{\epsilon}_+\rho_+ - \tilde{\epsilon}_-\rho_-\,, \quad \tilde{\epsilon}_\pm < 2|\epsilon|\,, \tag{9.76}$$

where ρ_0 is the density matrix of the exact ground state and $\rho_\pm$ are density matrices containing the error.

Proof. We build the density matrix ρ on the complete Hilbert space as

$$\begin{aligned}\rho &= |\psi\rangle\langle\psi| = |f|^2\,|\psi_0\rangle\langle\psi_0| + f\epsilon^*\,|\psi_0\rangle\langle\psi_\perp| + f^*\epsilon\,|\psi_\perp\rangle\langle\psi_0| + |\epsilon|^2\,|\psi_\perp\rangle\langle\psi_\perp| \\ &= |f|^2\,|\psi_0\rangle\langle\psi_0| + |f\epsilon|\left(\mathrm{e}^{-\mathrm{i}\phi}\,|\psi_0\rangle\langle\psi_\perp| + \mathrm{e}^{\mathrm{i}\phi}\,|\psi_\perp\rangle\langle\psi_0|\right) + |\epsilon|^2\,|\psi_\perp\rangle\langle\psi_\perp|\,,\end{aligned} \tag{9.77}$$

where we have chosen the phase ϕ such that $f\epsilon^* = |f\epsilon|\mathrm{e}^{-\mathrm{i}\phi}$. From Lemma 1 we obtain

$$\begin{aligned}\rho &= |f|^2\rho_0 + |\epsilon f|(\sigma_+ - \sigma_-) + |\epsilon|^2\rho_\perp = |f|^2\rho_0 + |\epsilon|\left((|f|\sigma_+ + |\epsilon|\rho_\perp) - |f|\sigma_-\right) \\ &= |f|^2\rho_0 + |\epsilon|\left((|f| + |\epsilon|)\frac{|f|\sigma_+ + |\epsilon|\rho_\perp}{|f| + |\epsilon|} - |f|\sigma_-\right)\,.\end{aligned} \tag{9.78}$$

Defining the density matrices with positive and negative signs, we obtain

$$\begin{aligned}\rho &= |f|^2\rho_0 + \tilde{\epsilon}_+\rho_+ - \tilde{\epsilon}_-\rho_-\,, \quad \tilde{\epsilon}_+ = |\epsilon|(|f| + |\epsilon|) \le 2|\epsilon|\,, \quad \tilde{\epsilon}_- = |\epsilon f| \le |\epsilon|\,, \\ \rho_+ &= \frac{|f|\sigma_+ + |\epsilon|\rho_\perp}{|f| + |\epsilon|}\,, \quad \rho_- = \sigma_-\,,\end{aligned} \tag{9.79}$$

where all matrices $\rho_{0,\pm}$ are density matrices with trace 1 and fulfilling positivity.

Lemma 3 (Bound on reduced density matrices) *The bound on the reduced density matrices ρ_A of the OSMPS result is equal to the bound on the complete density matrix, which*

is

$$\rho_A \;=\; \mathrm{Tr_B}\rho = |f|^2\rho_{0,A} + \tilde{\epsilon}_+\rho_{+,A} - \tilde{\epsilon}_-\rho_{-,A}\,, \tag{9.80}$$

where we consider an arbitrary bipartition of our system in parts A and B, tracing out over the bipartition B.

Proof. In order to obtain a reduced density matrix, we define subsystem A and B and take the partial trace over subsystem B:

$$\rho_A \;=\; \mathrm{Tr_B}\rho = \mathrm{Tr_B}\left(|f|^2\rho_0 + \tilde{\epsilon}_+\rho_+ - \tilde{\epsilon}_-\rho_-\right)\,. \tag{9.81}$$

As a linear operation the previous expression can be rewritten as

$$\begin{aligned}\rho_A &= |f|^2\mathrm{Tr_B}\rho_0 + \tilde{\epsilon}_+\mathrm{Tr_B}\rho_+ - \tilde{\epsilon}_-\mathrm{Tr_B}\rho_- \\ &= |f|^2\rho_{0,A} + \tilde{\epsilon}_+\rho_{+,A} - \tilde{\epsilon}_-\rho_{-,A}\,.\end{aligned} \tag{9.82}$$

9.12.4 Bound for the trace distance

Now that we are able to bound the density matrices with regards to the density matrix of the exact ground state, we can continue to prove a bound expressed in the trace distance $\mathcal{D}$.

Lemma 4 (Bound on the trace distance) *The trace distance between the density matrix ρ from OSMPS and the density matrix of the true ground state ρ_0 can be bounded with*

$$\mathcal{D}(\rho,\rho_0) \leq \frac{\sqrt{2V_\psi}}{\Delta_{0,1}}\,. \tag{9.83}$$

Proof. We continue with a bound on the trace distance defined as

$$\mathcal{D}(\rho,\rho_0) \;=\; \frac{1}{2}\mathrm{Tr}\sqrt{(\rho-\rho_0)^\dagger(\rho-\rho_0)} = \frac{1}{2}\left|\rho-\rho_0\right|\,, \tag{9.84}$$

where the simplification can be made due to the Hermitian property of the density matrices. We first concentrate on expressing the difference between the density matrices in a convenient way using the expressions for $\tilde{\epsilon}_\pm$ in Eq. (9.79):

$$\begin{aligned} \rho - \rho_0 &= |f|^2\rho_0 + \tilde{\epsilon}_+\rho_+ - \tilde{\epsilon}_-\rho_- - \rho_0 = \tilde{\epsilon}_+\rho_+ - \tilde{\epsilon}_-\rho_- - |\epsilon|^2\rho_0 \\ &= \tilde{\epsilon}_+\rho_+ - |\epsilon|\left(|f|\rho_- + |\epsilon|\rho_0\right) = \tilde{\epsilon}_+(P - M)\,, \\ P &\equiv \rho_+\,, \quad M \equiv \frac{|f|\rho_- + |\epsilon|\rho_0}{|f| + |\epsilon|}\,. \end{aligned} \tag{9.85}$$

The new matrices P and M are again defined so that they fulfill the requirements for a density matrix (Hermitian, positive, trace equal to 1). In the next step we make use of the triangular inequality of the trace norm:

$$\begin{aligned} \mathcal{D}(\rho, \rho_0) &= \frac{1}{2}\mathrm{Tr}\,|\rho - \rho_0| = \frac{|\epsilon|(|f| + |\epsilon|)}{2}\mathrm{Tr}\,|P - M| \\ &\leq \frac{|\epsilon|(|f| + |\epsilon|)}{2}\left(\mathrm{Tr}|P| + \mathrm{Tr}|M|\right) = |\epsilon|(|f| + |\epsilon|) \\ &\leq \sqrt{2}|\epsilon| \leq \frac{\sqrt{2V_\psi}}{\Delta_{0,1}}\,. \end{aligned} \tag{9.86}$$

9.12.5 Bound on the bond entropy

In order to get the bound on the bond entropy, we use Fannes' inequality [85] stating that the difference of the entropy S of two density matrices of dimension $D \times D$ is bounded by the trace distance $\mathcal{D}$ between those two density matrices:

$$|S(\rho) - S(\sigma)| \leq \mathcal{D}\log_a(D) - \mathcal{D}\log_a(\mathcal{D})\,, \quad \forall \mathcal{D} \leq \frac{1}{e} \approx 0.36\,, \tag{9.87}$$

with the logarithm for the von Neumann entropy base a and D the dimension of the Hilbert space for the density matrices ρ and σ. The inequality was derived for logarithm base two, $a = 2$, but holds for any basis. Therefore, the bound for the bond entropy is

$$\epsilon_\mathrm{S} \equiv |S(\rho_0) - S(\rho)| \leq \frac{\sqrt{2V_\psi}}{\Delta_{0,1}}\log(D) - \frac{\sqrt{2V_\psi}}{\Delta_{0,1}}\log\left(\frac{\sqrt{2V_\psi}}{\Delta_{0,1}}\right)\,. \tag{9.88}$$

9.13 Bounding measurement with the trace distance

We have used the trace distance of reduced density matrices to judge the convergence of our results. We now show that the trace distance bounds from above any observable defined on the reduced density matrix. As a preliminary result we need that the absolute value of the eigenvalues of a Hermitian matrix correspond to the singular values of the matrix. Therefore, we use the fact that the matrix can be decomposed via an eigenvalue decomposition $A = U\Lambda U^\dagger$ and a singular value decomposition $A = \tilde{U}\lambda\tilde{V}^\dagger$. Both decompositions are unique up to a permutation of the orthonormal basis vectors and basis transformations within degenerate sets of eigenvalues and singular values, respectively. Calculating $AA^\dagger$, which is by definition positive semi-definite even for a general A, with both expressions leads to

$$AA^\dagger = U\Lambda^2 U^\dagger = \tilde{U}\lambda^2\tilde{U}^\dagger\,, \tag{9.89}$$

which shows that the absolute values of the eigenvalues Λ are equal to the singular values λ. In the case where the observable is positive semi-definite and the ordering of the eigenvalues and singular values is equal, e.g. descending, the decompositions are equal, except for rotations within degenerate subsets. In contrast, for observables with at least one negative eigenvalue and sorting in descending order by the absolute value, the decompositions are not equal as negative signs are contained in the unitary matrices of the singular value decomposition. We use the fact that the absolute values of the eigenvalues of a Hermitian matrix are the singular values in the following when estimating the difference between the measurement of an observable Q for two different density matrices ρ and σ defined as

$$\epsilon(\rho,\sigma,Q) \;=\; |\mathrm{Tr}(Q\rho) - \mathrm{Tr}(Q\sigma)| = |\mathrm{Tr}\left(Q(\rho-\sigma)\right)|\,. \tag{9.90}$$

In order to bound this with the trace distance of ρ and σ we use the von Neumann trace inequality [263] on the matrices Q and $(\rho - \sigma)$ leading to

$$\epsilon(\rho,\sigma,Q) \;\leq\; \sum_{i}^{D} \kappa_i |\Lambda_i| \,, \tag{9.91}$$

where κ_i are the singular values of Q sorted in descending order with $\kappa_i > \kappa_{i+1}$. The Λ_i are the eigenvalues of $(\rho-\sigma)$ sorted in descending order with $|\Lambda_i| > |\Lambda_{i+1}|$. D is the dimension of the density matrix and the corresponding Hilbert space. We derived the relation Eq. (9.89) for this purpose. We approximate Eq. (9.91) by choosing the maximal singular values $\kappa_{\max}$ from all κ_i:

$$\epsilon(\rho,\sigma,Q) \;\leq\; \kappa_{\max} \sum_{i} |\Lambda_i| = \kappa_{\max} \mathrm{Tr}\, |\Lambda_i| = \kappa_{\max} 2\mathcal{D}(\rho,\sigma) \,. \tag{9.92}$$

For further convenience we estimate $\kappa_{\max}$ as a function of the observable Q. In the case of a Hermitian observable $Q = Q^\dagger$ we use again the connection between eigenvalues and singular values from Eq. (9.89). The eigenvalues of a square matrix can be estimated with Geršgorin circles [245, 264, 265]. Each Geršgorin circle has its origin in the diagonal element of the matrix; the radius is the sum of the absolute values of the non-diagonal of the corresponding row (or column). In this case we are only interested in the absolute values and the expression for $\kappa_{\max}$ in terms of the Geršgorin circles simplifies to

$$\kappa_{\max} \leq \max_i \left(\sum_j |Q_{i,j}| \right) \,. \tag{9.93}$$

In the case of a non-Hermitian Q, i.e., the correlation measurement $\langle b_i b_j^\dagger \rangle$, we can obtain an estimate using the fact that the singular values are connected to the eigenvalues of $QQ^\dagger$. If Q has the singular value decomposition $Q = USV^\dagger$, then $QQ^\dagger$ has the eigenvalue decomposition $QQ^\dagger = US^2U^\dagger$. Therefore, the square root of the non-negative eigenvalues of $QQ^\dagger$ are the singular values of Q. For the non-Hermitian Q we can estimate $\kappa_{\max}$ with the Geršgorin circles over $QQ^\dagger$ as

$$\kappa_{\max} \leq \max_i \sqrt{\left(\sum_j \left| [QQ^\dagger]_{i,j} \right| \right)}. \tag{9.94}$$

In conclusion, these bounds show that the trace distance is a meaningful quantity to bound the error on any other observable.

9.14 Details of the Krylov method

For the real-time TEBD algorithm we used the Krylov approximation to the propagated state for a local propagator on two sites. In this appendix, we clarify why sums throughout the algorithm can be done locally without involving the other parts of the subsystem. As an example we take the first step of the Gram-Schmidt orthogonalization procedure which can be generalized to sums. We denote the two local sites i and $j = i + 1$ acted on with $|\, C\rangle$ and the other parts of the system to left and right with $|\, L_i\rangle$ and $|\, R_j\rangle$. Moreover, the orthogonality center is in $|\, C\rangle$ which could be either site i or j. Using the Schmidt decomposition within the MPS, $|\psi\rangle$ can be written as

$$|\, v_1\rangle \;\; = \;\; |\psi\rangle = \sum_{i,j} |\, L_i\rangle \, |\, C_{i,j}\rangle \, |\, R_j\rangle \tag{9.95}$$

where the indices i and j run to the corresponding bond dimension at the splitting. In order to find the second basis vector $|\, v_2\rangle$ we calculate

$$|\, v_2\rangle \propto H_C \, |\, v_1\rangle - \langle v_1 |\, H_C^\dagger \, |\, v_1\rangle \, |\, v_1\rangle \,, \tag{9.96}$$

with H_C the local Hamiltonian acting on the two sites of $|\, C\rangle$. Using Eq. (9.95) to expand the second basis vector, we obtain the local summation:

$$
\begin{aligned}
|\,v_2\rangle \;\; &\propto \;\; H_C \sum_{i,j} |\,L_i\rangle\,|\,C_{i,j}\rangle\,|\,R_j\rangle \\
&\quad - \left[\sum_{i,i',j,j'} \langle L_{i'}|\,\langle C_{i',j'}|\,\langle R_{j'}|\,H_C^\dagger\,|\,L_i\rangle\,|\,C_{i,j}\rangle\,|\,R_j\rangle\right] \sum_{i,j} \left(|\,L_i\rangle\,|\,C_{i,j}\rangle\,|\,R_j\rangle\right) .
\end{aligned}
\tag{9.97}
$$

The expression in brackets in Eq. (9.97) is simplified due to the canonical form of the MPS. We obtain Kronecker deltas for $\langle L_{i'}|L_i\rangle = \delta_{i,i'}$ and $\langle R_{j'}|R_j\rangle = \delta_{j,j'}$. We point out that the expression $H_C\,|\,L_i\rangle\,|\,C_{i,j}\rangle\,|\,R_j\rangle$ is a short hand notation for $(\mathbb{I}_L \otimes H_C \otimes \mathbb{I}_R)\,|\,L_i\rangle\otimes|\,C_{i,j}\rangle\otimes|\,R_j\rangle = \mathbb{I}_L\,|\,L_i\rangle \otimes H_C\,|\,C_{i,j}\rangle \otimes \mathbb{I}_R\,|\,R_j\rangle$. These steps lead us to:

$$
\begin{aligned}
|\,v_2\rangle \;\; &= \;\; \sum_{i,j} |\,L_i\rangle\,(H_C\,|\,C_{i,j}\rangle)\,|\,R_j\rangle - \sum_{i,j} \left(|\,L_i\rangle\,|\,C_{i,j}\rangle\,|\,R_j\rangle\right) \sum_{i,j} \langle C_{i,j}|\,H_C\,|\,C_{i,j}\rangle \\
&= \;\; \sum_{i,j} |\,L_i\rangle\,(H_C\,|\,C_{i,j}\rangle)\,|\,R_j\rangle - \sum_{i,j} h_{1,1}\,|\,L_i\rangle\,|\,C_{i,j}\rangle\,|\,R_j\rangle\,,
\end{aligned}
\tag{9.98}
$$

where we introduced the overlap $h_{1,1} \equiv \sum_{i,j}\langle C_{i,j}\,|\,H_C\,|\,C_{i,j}\rangle$ representing a scaling of the MPS. For readers familiar with the Krylov method, we point out that $h_{1,1}$ is the corresponding entry in the upper Hessenberg matrix used to build the exponential in the Krylov subspace. In order to scale the MPS with a scalar the orthogonality center is modified. The identity operator is acting $|\,L_i\rangle$ and $|\,R_j\rangle$ leaving them unchanged. Knowing that the orthogonalization procedure does not change any $|\,L_i\rangle$ and $|\,R_j\rangle$, similar arguments apply to show that we can sum locally over the scaled Krylov basis $|\,v_k\rangle$.

We consider now the scaling of TEBD-Krylov in comparison to a usual TEBD taking the matrix exponential. In the usual TEBD implementation we can consider four steps: *1)* Build two-site tensor, *2)* calculate local propagator with Hamiltonian, *3)* contract propagator to two site tensor, and *4)* split two site tensor. Without considering speedup due to symmetries, a basic computational complexity analysis yields

$$
\mathcal{O}_{\text{TEBD}} \;\; = \;\; \mathcal{O}(\chi^3 d^2) + \mathcal{O}(d^6) + \mathcal{O}(\chi^2 d^4) + \mathcal{O}(\chi^3 d^3)\,,
\tag{9.99}
$$

where we assume cubic scaling for the matrix exponential and the splitting. In case of the Krylov-TEBD (KTEBD) we have the following steps: *1)* contract the single site tensors to a two site tensor, *2)* build n Krylov vectors, *3)* m' calculations of overlap to previous vectors and m'' subtraction for orthogonalization ($m = m' + m''$), *4)* taking the matrix exponential in the Krylov basis, *5)* adding the weighted Krylov vectors to the solution, and *6)* finally splitting the two site tensor. All the scalings are chronological, resulting in

$$\begin{aligned} \mathcal{O}_{\text{KTEBD}} &= \mathcal{O}(\chi^3 d^2) + \mathcal{O}(n\chi^2 d^4) + \mathcal{O}(m\chi^2 d^2) \\ &\quad + \mathcal{O}(n^3) + \mathcal{O}(n\chi^2 d^2) + \mathcal{O}(\chi^3 d^3)\,. \end{aligned} \tag{9.100}$$

We again assumed cubic scaling for matrix exponential and splitting, which is an upper bound in the case of the matrix exponential being tridiagonal and symmetric. The overall scaling seems to be dominated by the splitting with $\mathcal{O}(\chi^3 d^3)$, but we calculate the difference to see which algorithm is favorable in which cases:

$$\begin{aligned} \mathcal{O}_{\text{KTEBD}} - \mathcal{O}_{\text{TEBD}} &= \mathcal{O}(n^3) - \mathcal{O}(d^6) + \mathcal{O}((n-1)\chi^2 d^4) \\ &\quad + \mathcal{O}((m+n)\chi^2 d^2)\,, \end{aligned} \tag{9.101}$$

where TEBD is faster when the expression is greater than zero. If we assume in favor of KTEBD $d = \chi$ and $n = 2$, the second and the third term cancel each other. Thus, the remaining terms show that TEBD is always faster than KTEBD according to this scaling. These equations do not include quantum numbers. A careful study is contemplated to prove or disprove the scaling equations once both methods are implemented as pointed out in the future developments in Sec. 9.6.

9.15 Auxiliary calculations

The overlap between the truncated state $|\psi'\rangle$ and the untruncated normalized state $|\psi\rangle$ is defined over the singular values λ'_i of the truncated state and the singular values λ_i of the untruncated state. In the following χ is the number of singular values in $|\psi'\rangle$ and $\chi_{\max}$ is the untruncated number of singular values. The singular values for the truncated state are

calculated via a normalization

$$\lambda_i' = \frac{\lambda_i}{\sqrt{\sum_{j=1}^{\chi} \lambda_j^2}}. \tag{9.102}$$

This expression leads us directly to the overlap between the two states

$$\langle \psi' | \psi \rangle = \sum_{i=1}^{\chi_{\max}} \lambda_i' \lambda_i = \sum_{i=1}^{\chi} \lambda_i' \lambda_i = \frac{1}{\sqrt{\sum_{i=1}^{\chi} \lambda_i^2}} \sum_{i=1}^{\chi} \lambda_i^2 = \sqrt{\sum_{i=1}^{\chi} \lambda_i^2}. \tag{9.103}$$

For the error we calculate $1 - \langle \psi' | \psi \rangle$ and abbreviate with $x \equiv \langle \psi' | \psi \rangle$:

$$\begin{aligned} 1 - \langle \psi' | \psi \rangle &= 1 - x \\ &= \frac{1}{2}\left(1 - 2x + x^2\right) + \frac{1}{2}\left(1 - x^2\right) = \frac{1}{2}\left(1 - x\right)^2 + \frac{1}{2}\left(1 - x^2\right) \\ &\leq (1 - x^2) \end{aligned} \tag{9.104}$$

where the inequality is based on $x \leq 1$. By definition via Eq. (9.103), x is real and bounded as $0 \leq x \leq 1$. This is based on the normalization constraint and knowing that the singular values λ_i are positive. The following inequality is only valid for $x \leq 1$: Equation (9.104) is further simplified to the sum over the truncated singular values using the fact that the original state with $\chi_{\max}$ singular values was normalized:

$$1 - \langle \psi' | \psi \rangle \leq 1 - \sum_{i=1}^{\chi} \lambda_i^2 = 1 - \left(1 - \sum_{i=\chi+1}^{\chi_{\max}} \lambda_i^2\right) = \sum_{i=\chi+1}^{\chi_{\max}} \lambda_i^2. \tag{9.105}$$

CHAPTER 10

OPEN SOURCE MATRIX PRODUCT STATES: MANY-BODY ENTANGLED OPEN QUANTUM SYSTEMS

Submitted to *Quantum Science and Technology*[1]

D. Jaschke,[2] S. Montangero,[3] and L. D. Carr[4]

Abstract

We present an open source code to simulate entangled dynamics of open quantum systems governed by the Lindblad master equation with tensor network methods. Tensor network methods using matrix product states have been proven very useful to simulate many-body quantum systems and have driven many innovations in research. Since the matrix product state design is tailored for closed one-dimensional systems governed by the Schrödinger equation, the next step for many-body quantum dynamics is the simulation of one-dimensional open quantum systems. We review the three dominant approaches to the simulation of open quantum systems via the Lindblad master equation: quantum trajectories, matrix product density operators, and locally purified tensor networks. The package *Open Source Matrix Product States* combines these three major methods to simulate one-dimensional open quantum systems with the Lindblad master equation. We access the same underlying tensor network algorithms for all techniques, e.g., the tensor contractions optimized in the same way, allowing us to have a meaningful comparison between the different approaches based on selected examples. These examples include the finite temperature states of the transverse quantum Ising model, the dynamics of an exciton traveling under the influence of spontaneous emission and dephasing, and a double-well potential simulated with the Bose-Hubbard

[1] "OSMPS: Many-body entangled open quantum systems", D. Jaschke, S. Montangero, and L. D. Carr (2018). `https://arxiv.org/abs/1804.09796`. Use in agreement with arXiv license [55].

[2] primary researcher and author responsible for the manuscript.

[3] feedback on the final versions of the draft with his expertise in tensor network methods; currently professor at Università degli Studi di Padova.

[4] principal investigator and advisor at Colorado School of Mines.

model including dephasing. We analyze which approach is favorable leading to the conclusion that a complete set of all three methods is most beneficial, pushing the limits of different scenarios. The convergence studies using analytical results for macroscopic variables and exact diagonalization methods as comparison, show, for example, that matrix product density operators are favorable for the exciton problem in our study.

10.1 Introduction

The study of the combination of many-body quantum systems and open systems is one of the critical pieces *needed* to develop powerful quantum simulators and quantum computers. While the many-body part is strictly necessary to scale these systems to sizes useful for applications, open quantum systems help one to understand the effects of decoherence and, therefore, the lifetime of the actual system. Further questions are the analysis of steady states and the transient dynamics approaching them. Reservoir engineering has the purpose of preparing the system in a defined state; this state is equal to the steady state and, therefore, protected from decoherence. The process of thermalization is another example for open quantum system research. The open system implementations in our *Open Source Matrix Product States* (OSMPS) package combine two popular approaches: tensor networks for many-body simulations and the Lindblad master equation as a default approach for Markovian open quantum systems.

The Lindblad master equation [46–48] is one common approach to open quantum systems, although its limitations are well-known. The benefit of this approach is the conservation of the properties of the density matrix, i.e., norm and positivity. The assumptions during the derivation, e.g., the Born-Markov and secular approximation, limit the use of the Lindblad master equation to quantum systems weakly coupled to large reservoirs. Other approaches to open quantum systems are for example hierarchical equations of motions [266, 267] or various techniques for non-Markovian open quantum systems [65], but a versatile implementation of the Lindblad equation is the first step towards the implementation of a tensor network suite to study open quantum systems.

The history of tensor networks for quantum mechanics reaches back to the density matrix renormalization group (DMRG) [72], then recasted into thematrix product state (MPS) language [75, 76]; recent papers highlight the equivalence between the two approaches [77]. Based on the original MPS idea, many different tensor networks have been derived ranging from tree-tensor networks (TTN) [79] over the multi-scale entanglement renormalization ansatz (MERA) [83] to projected entangled pair states [84], where the latter is designed for two-dimesional systems; TTN and MERA can solve both one-dimensional systems and generalizations to higher dimension. We focus in this work on one-dimensional systems in an MPS-like chain structure. Tensor networks are very-well suited for this kind of low-dimensional many-body system, where the area law describing the scaling of the entanglement is the most favorable [78]. We concentrate on tensor networks for open systems and a background in MPS techniques is assumed. The point of this paper is the side-by-side discussion of three different approaches relating the technical implementation and their implications for the convergence of actual simulations. The first of the three approaches are quantum trajectories (QT) [217, 218] providing a statistical approach to the Lindblad master equation. In contrast, both matrix product density operators (MPDOs) [80, 81] and locally purified tensor networks (LPTNs) [82] simulate the complete density matrix. The latter two approaches can also simulate thermal states, which are otherwise only accessible through METTS [177] or after building a sufficient number of eigenstates. Both MPDO and LPTN representations have their limitations as discussed in References [268–270]. Very briefly, the arguments against each approach are that MPDOs do not conserve positivity and the corresponding check is an NP-hard problem. In contrast, there are states which have a representation in terms of MPDOs and maintain translational invariance, while LPTNs leak a similar representation for this set of states. We point out that there are previous comparisons between two of the methods [221].

The outline of the paper is as follows. Section 10.2 is a very brief review of methods used to simulate open quantum systems with tensor network methods. We present an overview of

possible applications of the methods in the quickly developing fields of quantum simulators in Sec. 10.3. Section 10.4 provides the actual details of the implementation in the OSMPS package. We follow the structure of earlier work [215] connecting the different time evolution methods to the open system. The setup of the simulations and their convergence is discussed in Sec. 10.5. We conclude our results in Sec. 10.6.

10.2 Theoretical Approaches to the Simulation of Open Quantum Systems

Before going into details of the numerical setup for the simulation of the Lindblad master equation, it is worthwhile to keep in mind the existing alternative approaches for the simulation of open quantum systems. Amongst all the different techniques which have been outlined for open quantum systems are stochastic methods [271], Redfield master equations [49], or solving the full system. Some of these methods are within the reach of tensor network methods, e.g., the Redfield master equation. Others, i.e., the simulation of the full system, can already be achieved with MPS methods as long as system plus environment together are not too big. The Lindblad master equation is the first choice among above list as it conserves norm, Hermiticity, and positivity of the state. OSMPS uses the Lindblad equation

$$\dot{\rho} \;=\; \tfrac{1}{\hbar}[\rho, H] + \sum_{\nu} L_\nu \rho L_\nu^\dagger - \frac{1}{2}\{L_\nu^\dagger L_\nu, \rho\}\,, \tag{10.1}$$

which describes the evolution of the density matrix ρ under the Hamiltonian H and a set of Lindblad operators L_ν. Thereafter, $\hbar$ is set to one. As we are treating many-body systems, the index ν can be a combined index running itself over the different Lindblad operators μ and different sites k in the system, i.e., $\nu = (\mu, k)$. The Lindblad equation includes the approximations explained as follows. Ideally, given unlimited resources, we would simulate the Schrödinger equation for the system S of interest and its environment E

$$\frac{\partial}{\partial t}\,|\psi_{S+E}\rangle = -\tfrac{1}{\hbar} H_{S+E}(t)\,|\psi_{S+E}\rangle\,. \tag{10.2}$$

Considering that the environment can be enormous and the Hilbert space grows exponentially with system size, we apply the following three approximations to Eq. (10.2) to obtain the Lindblad equation. (i) System and environment are in a product state at $t = 0$ and stay in a product state over the time evolution, i.e., $\rho_{S+R}(t) = \rho_S(t) \otimes \rho_E$. Correlations decay fast if the reservoir is large and the reservoir remains unperturbed by the interaction with the system. This assumption settles the timescales between the environment τ_E and the system τ_S: $\tau_E \ll \tau_S$. (ii) Furthermore, the timescale of the system holds $\tau_S \ll \tau_{S,\mathrm{eq}}$; the equilibration time of the system $\tau_{S,\mathrm{eq}}$ is longer than the time step. (iii) We truncate fast oscillating terms similar to the rotating wave approximation when considering transitions of different frequencies in the system, where their difference sets the timescale. These approximations are formally described in terms of the Born-Markov approximation, i.e., (i) and (ii), and the secular approximation, see (iii).

In order to simulate a system according to the Lindblad master equation, we distinguish two paths. QTs evolve pure states sampling over a variety of trajectories. This approach is motivated by the fact that in an experimental setup every measurement projects the density matrix into a pure state; we assume that the measurement outcomes are non-degenerate for each state for simplicity. The QT approach models the probability for the projection into a specific state. Therefore, a single simulation only reflects one possible outcome of an experiment. To obtain the outcome for Eq. (10.1), sampling over different trajectories is necessary. One advantage of this method is that we use pure states and there is no significant increase in the computational scaling with respect to an MPS simulation for each trajectory. The local dimension of the MPS used in each QT is the same as for the MPS in a closed system. Furthermore, any MPS can be used as initial state without increasing the bond dimension prior to the time evolution. During the time evolution, we rely on the capabilities of the MPS compression scheme to reduce entanglement, which is obsolete after a quantum jump. The additional steps for choosing the Lindblad operator to be applied to the MPS are not significant. The computational scaling of the open quantum system is reflected in the

number of trajectories. The different trajectories can be easily parallelized across different cores with MPI (Message Passing Interface).

On the other hand, ρ can be directly simulated, e.g, mapping the density matrix ρ to a superket vector $|\rho\rangle\rangle$ [80, 81] resulting in a Schrödinger-like equation. The superket $|\rho\rangle\rangle$ is constructed by building a vector out of all entries in the density matrix ρ. The governing equation is then

$$\frac{\partial}{\partial t}|\rho\rangle\rangle = \mathcal{L}(t)|\rho\rangle\rangle\,, \tag{10.3}$$

where the non-Hermitian Liouville operator $\mathcal{L}(t)$ corresponds to the Hamiltonian and is defined as:

$$\begin{aligned}\mathcal{L}(t) &= -\frac{1}{\hbar}H(t)\otimes\mathbb{I} + \frac{1}{\hbar}\mathbb{I}\otimes H^T(t) \\ &+ \sum_\nu L_\nu\otimes(L_\nu^\dagger)^T - \frac{1}{2}\left(L_\nu^\dagger L_\nu\otimes\mathbb{I} + \mathbb{I}\otimes\left(L_\nu^\dagger L_\nu\right)^T\right).\end{aligned} \tag{10.4}$$

Overall, this approach allows us to simulate systems replacing the Hamiltonian with $\mathcal{L}$ at the cost of increased local dimension. If the total dimension of the closed system is D, the dimension of the problem in Liouville space is D^2.

Finally, we can evolve the purification of ρ denoted with X [82]. Since the density matrix is by definition positive, we can decompose it into

$$\rho = XX^\dagger\,. \tag{10.5}$$

For example, a pure state $|\psi\rangle$ is equal to its purification $X = |\psi\rangle$. To preserve the structure of the complex conjugate pair, we use instead of Eq. (10.1) the more general Kraus operators representing a completely positive trace preserving map (CPT map):

$$\rho(t+dt) = \sum_{\nu'} K_{\nu'}\rho(t)K_{\nu'}^\dagger \tag{10.6}$$

$K_{\nu'}$ are called Kraus operators. There is a connection to derive the Kraus operators via Choi's theorem from the Lindblad equation [272], or we approximate the Kraus operators in first order in dt and truncating higher order terms of dt when expanding $\rho(t+dt) \approx \rho(t) + dt\dot{\rho}(t)$ with $\dot{\rho}(t)$ as defined in the Lindblad master equation (10.1) [273].

The MPS algorithms profit from considerable speed-ups when symmetries are present in the system and encoded to the tensor network. We distinguish between Abelian symmetries, considered in the following, and non-Abelian symmetries. Abelian groups are preferable from the perspective of an implementation as operations commute and keeping track of quantum numbers reduces to a simple group operations; in contrast, non-Abelian groups have to use the Clebsch-Gordan coefficients. We can use symmetries in the Schrödinger equation when the commutation of some operator G commutes with the Hamiltonian, $[H, G] = 0$, and has a definition in terms of the local Hilbert spaces. For example, the Bose-Hubbard model conserves the number of particles and $N = \sum_k n_k$ commutes with the Bose-Hubbard Hamiltonian, see later on in Eq. (10.35). We can also use the Abelian symmetry in the Liouville equation if the Lindblad operators do not violate the symmetry,

$$\left[\mathcal{L}, G \otimes \mathbb{I} + \mathbb{I} \otimes G^T\right] = 0\,. \tag{10.7}$$

Thus, we cannot add loss of particles with an annihilation operator as a Lindblad operator in a number-conserving simulations: the Lindblad operator violates the symmetry.

This brief overview enables us to take a closer look at the different evolution methods in Sec. 10.4.

10.3 Quantum simulators and open quantum systems

Quantum simulators are a primary focus of current research for multiple intriguing reasons, amongst them their possibility to explore fundamental physical phenomena, mimic new materials, and the development of new quantum technology, e.g., towards quantum computers. The quantum simulators are also in the focus of a recent research program, i.e.,

the European quantum technologies flagship program [1–3], the Chinese effort aiming for the same goals, and the proposed US national quantum initiative. It is worthwhile to take a closer look at the different architectures and their connection to open quantum systems. Quantum simulators represent an important fraction of possible applications of any tensor network algorithm simulating Lindblad master equations and, in future, beyond.

Rydberg systems are one promising platform for quantum simulators, and reference [274] outlines their possible applications within the framework of the Lindblad master equation. The Lindblad operators described therein are quasi-local, meaning acting on a neighborhood of sites.

The treatment of superconducting qubits coupled to phonon modes is another architecture [186], allowing one to couple the superconducting qubit to other degrees of freedom in the systems. The Lindblad equation was used in this context to simulate the lifetime of the phonon modes [275].

Trapped ions system are considered to be quantum simulators for open systems themselves as pointed out in references [276, 277]. Although the primary focus is on simulating open quantum systems according to Kraus operators, the application of numerical simulations to this scenario seems very fruitful to us. We mentioned the close connection between the Lindblad master equation in Eq. (10.1) and the Kraus maps in Eq. (10.6). The review in [278] highlights the quantum simulator applications of Rydberg systems and trapped ions. Moreover, it lists examples for ultracold atoms systems in an open system context. The atomic, molecular, and optical (AMO) platforms provide another set of problems to be studied. Atomic bosons can heat due to the interaction with the optical lattice [279], and molecules have even more degrees of freedom [20] to be used within open quantum systems. The different internal degrees of freedom, i.e., rovibrational and motional degrees of freedom, can be used for encoding individual reservoirs for each molecule; one degree of freedom acts as a system, while another degree of freedom acts as a reservoir for the first [280].

In summary, this incomplete list shows the possible application of open quantum systems in the quantum simulator context. We argue that the consideration of system-environment effects will be an even more intensive focus of future research as decoherence times of experiments increase and errors decrease. We have picked four examples toward this goal of describing quantum simulators. We look at finite temperature states in Sec. 10.5.1, where the quantum Ising model is one possibility to describe many two-level quantum systems. Section 10.5.2 turns to the transport of an exciton, which travels under the influence of the interaction with an environment. The last two examples are dedicated to the Bose-Hubbard model, which is key to many bosonic atomic and molecular systems. We consider the double-well potential with a wave function initially trapped in one well in Sec. 10.5.3, where the oscillations between left and right well are damped out in the open quantum system. Then, we move to the dissipative state preparation in Appendix 10.8.

10.4 Tensor Networks Simulations of the Lindblad Master Equation

This section covers the technical aspects of all three approaches to open quantum systems. We start with the simulation of the Lindblad master equation in terms of MPDOs[80, 81] and describe in detail the issues raised by a non-Hermitian operator. The quantum trajectories [217, 218] share the non-Hermitian operator with the MPDOs, and we explain quantum trajectories in the following section. Finally, we discuss the third approach using LPTNs [82]. Once we have covered these aspects, we turn to the convergence of the different approaches. Readers aware of the technical details or solely interested in the practical application of the methods may, therefore, skip this section and to straight to Sec. 10.5.

10.4.1 Matrix Product Density Operators

The formulation of MPDOs heavily relies on the Liouville operator and superket notation in Eq. (10.4) and the similarity to the Schrödinger equation. The first steps into the MPDOs implementation inside OSMPS describe the notations of the superket $|\rho\rangle\rangle$ and we first introduce the static aspect of MPDOs, i.e., their ability to calculate thermal states. Then,

we move toward matrix product operators (MPOs) [121] of the Liouville operator. Knowing these two principal objects, i.e., the superket and the MPO, we move forward to the time-evolution methods using the MPO, i.e., Krylov, local Runge-Kutta (LRK) [122], and the time-dependent variational principle (TDVP) [120]. Finally, we fill in the description of the Krylov time-evolving block decimation (KTEBD) and the well-established time-evolving block decimation (TEBD) [76] algorithm and its modifications for the evolution of the Lindblad master equation. In fact, the time evolution methods for the quantum trajectories revisit many issues already discussed here as both methods deal with a non-Hermitian propagator.

10.4.1.1 Construction of Matrix Product Density Operator states

We limit ourselves to the construction of two classes of initial states for the time evolution. On the one hand, we convert MPS states to MPDOs. Suitable MPS states include product states, ground states, low-lying excited states, and pure states obtained via unitary time evolution. On the other hand, we would like to have finite temperature states via an imaginary time evolution of MPDOs. Therefore, the infinite temperature state has to be given as an initial state for the imaginary time evolution as it serves as a starting point for cooling. This procedure is explained in Sec. 10.4.1.2. With the knowledge of the infinite temperature state which is a mixed product state, the construction for product states of any other type can be derived.

Figure 10.1 describes the transformation of an MPS into an MPDO. If the tensor $A^{[k]}_{\alpha,i,\beta}$ represents the site k in the MPS, we add an auxiliary link of dimension one and obtain $A^{[k]}_{\alpha,i,\kappa,\beta}$. We contract this tensor with its complex conjugate tensor $\left(A^{[k]}_{\alpha',i',\kappa,\beta'}\right)^*$ over κ leading to the MPDO representation $B_{(\alpha,\alpha'),(i,i'),(\beta,\beta')}$. The contraction over the auxiliary index corresponds to the outer product $|\,\psi\rangle\langle\psi\,|$, taken locally on site k. Thus, the usage of an outer product is an alternative to the auxiliary index. The indices in parentheses represent fused indices; therefore, the new tensor is again of rank 3. The fusion of two indices produces a new index using a Cartesian product to map the elements, e.g., $\alpha, \alpha' \to (\alpha, \alpha') = \alpha''$. The dimension of the new index α'' is the product of the dimension of the two original indices α and α'. We

notice the increase in the dimension of links: for a tensor with bond dimensions (χ, d, χ) in the MPS, the new bond dimensions in the MPDO are (χ^2, d^2, χ^2). The number of sub-tensors for a symmetric tensor network also increases. If we have n sub-tensors in an MPS site, the MPDO representation of the site has n^2 sub-tensors.

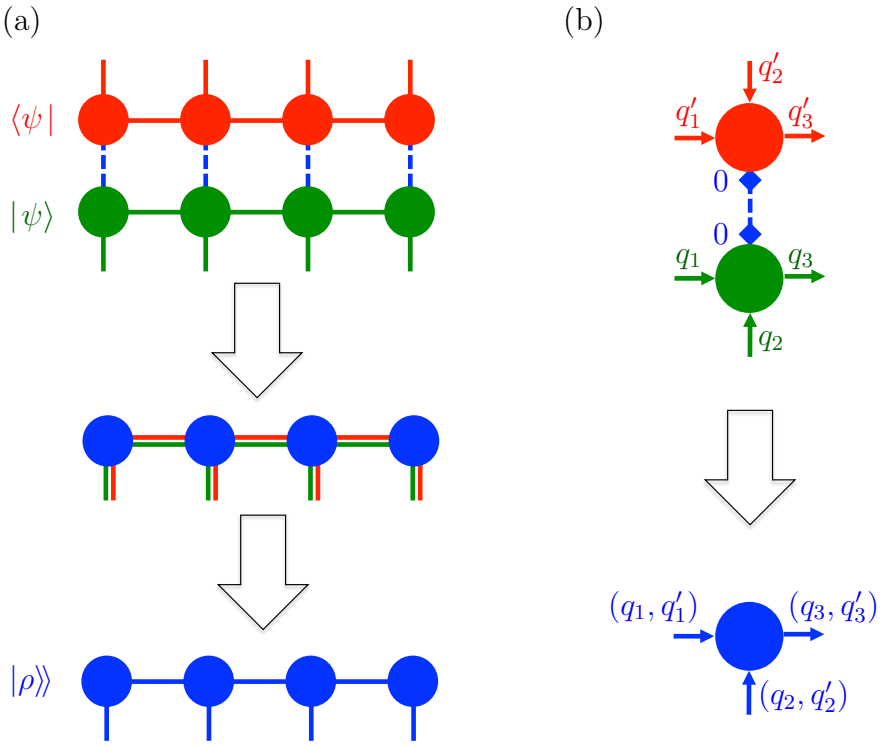

Figure 10.1: *MPDO from MPS state.* (a) In an MPS without symmetries, each site tensor is contracted over a one-dimensional auxiliary link with its complex conjugated counterpart. The corresponding links are fused. (b) The auxiliary tensor contracted over in an MPS with symmetries is labeled with a dummy quantum number 0. We get all combination of sub-tensors. In addition to merging the links of the sub-tensors, the quantum numbers are combined.

The infinite temperature state ρ_∞ is straightforward to implement in an MPDO without symmetries but has some subtleties when symmetries are used. The density matrix ρ_∞ is the identity matrix normalized to trace one. If we do not have symmetries, the global identity is a product of local identities $\rho_\infty \propto \bigotimes_{k=1}^{L} 1_k$. Thus, the bond dimension between sites in the MPDO is $\chi = 1$, and the tensors are $B_{\alpha,(i,i'),\beta} = \delta_{ii'}$. In contrast, the product of local identity for a symmetric MPDO contains states in all possible symmetry sectors and does

not lead to ρ_∞ for a specific sector. Instead, we construct the state ρ_∞ representing the Gibbs distribution at infinite temperature from symmetric sub-tensors on each site k filled with

$$B^{[k]}_{\alpha,(i,i'),\beta}((q_1,q_1'),(q_2,q_2'),(q_3,q_3')) = \delta_{ii'}\delta_{q_1q_1'}\delta_{q_2q_2'}\,. \tag{10.8}$$

The incoming quantum number from the left must be chosen in such a way that is possible to obtain it with the local Hilbert spaces on the left. The outgoing quantum number $q_3 = q_1 + q_2$ must allow us to have the sector specified: $q_3^{[k=L]}$ on the last site must match the global sector exactly. We illustrate these choices with the Bose-Hubbard model with a maximum filling of 3, i.e., local dimension $d = 4$. Further, we specify the system size $L = 5$ and unit filling. $q_1^{[k=2]} \in \{0,1,2,3\}$ for the second site $k = 2$, $q_1^{[l=2]} = 4$ cannot be achieved from a single site on the left. Similar, for the fourth site $k = 4$, $q_3^{[k=4]} \in \{2,3,4,5\}$. Any lower filling cannot reach unit filling with a single site on the right. Higher $q_3^{[k=4]}$ are already above unit filling and do not match the symmetry sector. In conclusion, the symmetric ρ_∞ has already a bond dimension $\chi > 1$ from the beginning and can contain a large number of sub-tensors. For example, the bond dimension of the Bose-Hubbard model on L sites with maximal filling $d-1$ for each site has an upper bound for the bond dimension of $d(N-d+2)$ distributed on the block-diagonal structure. We present a detailed calculation in Appendix 10.9. A generalization to more complicated symmetries is possible, but a generalized equation for the maximal bond dimension of any model and symmetry is difficult to obtain.

10.4.1.2 Imaginary time evolution for finite-T states

The finite temperature (finite-T) states are based on the Gibbs distribution defined as $\rho(T) = \exp(-H/(k_BT))/\mathcal{N}$ with $\mathcal{N} = \mathrm{Tr}\left[\exp(-H/(k_BT))\right]$ and $k_B = 1$ the Boltzmann constant and have been pointed out as a feature of MPDOs from their definition on [80, 81]. From the Gibbs distribution, we rewrite the unnormalized state as

$$
\begin{aligned}
\mathrm{e}^{-H/(k_B T)} &= \mathrm{e}^{-H/(2k_B T)} \mathbb{I} \mathrm{e}^{-H/(2k_B T)} \\
&\propto \mathrm{e}^{-H/(2k_B T)} \rho_\infty \mathrm{e}^{-H/(2k_B T)} \\
&= \mathrm{e}^{\frac{1}{2k_B T}\left(-H\otimes\mathbb{I}-\mathbb{I}\otimes H^T\right)} \left|\rho_\infty\right\rangle\!\right\rangle \,, \qquad (10.9)
\end{aligned}
$$

which corresponds to an imaginary time evolution similar to the ground state algorithm of an MPS. The operator in Liouville space is Hermitian. In detail, we enable the TEBD algorithms for imaginary time evolution. The definition of the initial state $|\rho_\infty\rangle\!\rangle$ was discussed in the previous Sec. 10.4.1.1 as an example of how to construct initial states represented as an MPDO.

10.4.1.3 Matrix Product Operators in Liouville space

For the simulation of the Lindblad master equation with matrix MPO techniques, we transform Eq. (10.1) into the Liouville space. This transformation allows us to represent the density matrix as vector $|\rho\rangle\!\rangle$ and use MPS techniques developed for pure states on an enlarged local space. The local dimension d for pure states $|\,\psi\rangle$ translates into a local dimension $d_{\mathcal{L}} = d^2$ for the simulation of $|\rho\rangle\!\rangle$. In recent work [215], we presented the evolution techniques in the OSMPS package for pure states based on formulating the Hamiltonian H of the system as an MPO. We can reuse all evolution techniques for MPDOs once we can formulate $\mathcal{L}$ as an MPO. We restrict the Hamiltonian to local terms and bond terms, i.e., nearest neighbor interactions, to explain the procedure. But the methods are generalized to any rule set present in OSMPS for the Liouville space. For the MPS evolution, we know that the bond dimension of the MPO for n_{site} local terms and n_{bond} nearest neighbor terms is $\chi_{\mathrm{MPO}} = 2 + n_{\mathrm{bond}}$. We explain how to build the MPO matrices along the quantum Ising model with the Hamiltonian

$$
H_{\mathrm{QI}} = -J \sum_{j=1}^{L-1} \sigma_j^z \sigma_{j+1}^z - g \sum_{j=1}^{L} \sigma_j^x \,, \qquad (10.10)
$$

where σ_j^x and σ_j^z are the Pauli matrices acting on site j. The interaction strength between neighboring spins is J, the coupling to the external field is g, and the system size is L. The MPO operator-valued matrix in the bulk of the system for the Hamiltonian H_{QI} is

$$M_H = \begin{pmatrix} \mathbb{I} & 0 & 0 \\ \sigma^z & 0 & 0 \\ -g\sigma^x & -J\sigma^z & \mathbb{I} \end{pmatrix}, \tag{10.11}$$

where the two of the four dimensions of the rank 4 MPO tensor are encoded into the row and columns of this matrix. These two indices are contracted with left and right neighboring MPO-matrices and the number of rows/columns is the bond dimension of the MPO. The first (last) MPO is an operator-valued row (column) vector. The remaining two dimensions are the dimensions of the matrix for each entry. In this notation, 0 is to be understood as a $d \times d$ matrix of zeros. A convenient implementation uses operator-valued sparse matrices instead of building the full rank 4 tensor with a large fraction of zeros [121]. We transform this MPO to the Liouville space according to Eq. (10.3); the relevant terms are the Hamiltonian terms $H \otimes \mathbb{I} - \mathbb{I} \otimes H^T$. We reorder the subspaces such that the terms for each site are collected. The two links for the Hilbert space of each site have been fused previously. Thus, the new operator-valued entries have a dimension of $d^2 \times d^2$. This transformation increases the MPO bond dimension to $\chi_{\mathrm{MPO},\mathcal{L}} = 2 + 2n_{\mathrm{bond}}$:

$$M_{\mathcal{L}} = \begin{pmatrix} \mathbb{I} & 0 & 0 & 0 \\ \sigma^z \otimes \mathbb{I} & 0 & 0 & 0 \\ \mathbb{I} \otimes (\sigma^z)^T & 0 & 0 & 0 \\ -g\sigma^x \otimes \mathbb{I} - \mathbb{I} \otimes -g(\sigma^x)^T & -J\sigma^z \otimes 1 & -(\mathbb{I} \otimes -J(\sigma^z)^T) & \mathbb{I} \end{pmatrix}. \tag{10.12}$$

Here in the construction of $M_{\mathcal{L}}$, we assume that the $\mathcal{L}$ is multiplied with the usual $(-\imath \mathrm{d}t)$ in the evolution. The different signs in front of $H \otimes \mathbb{I}$ and $\mathbb{I} \otimes H^T$ are considered together with the coupling constant of the Hamiltonian term and are not double-counted. So far, this step allows us to evolve a closed initially pure or mixed system. To include local Lindblad operators L_μ acting on each site as part of the dissipative part of the evolution, we add the

following matrix based on Eq. (10.3) to the previous result in Eq. (10.12), which contains the Hamiltonian part of the evolution in Liouville space:

$$M_{\mathcal{L}} \;=\; \begin{pmatrix} & & 0 & 0 & 0 \\ & & 0 & 0 & 0 \\ & & 0 & 0 & 0 \\ \imath\gamma\left(L_\mu \otimes L_\mu^* - \frac{1}{2} L_\mu^\dagger L_\mu \otimes \mathbb{I} - \frac{1}{2}\mathbb{I} \otimes L_\mu^T L_\mu^*\right) & & 0 & 0 & 0 \end{pmatrix} . \tag{10.13}$$

The imaginary unit takes into account the multiplication of $(-\imath \mathrm{d}t)$ leaving only $\mathrm{d}t$ after the construction of the argument for the exponential. Thus, the local Lindblad operators do not increase the bond dimension of the MPO. We implement another type of Lindblad operator similar to a Hamiltonian many-body string term, i.e., the many-body string Lindblad operator

$$L_k(r) = L_k \otimes L_{k+1} \otimes \cdots \otimes L_{k+r-1} \,. \tag{10.14}$$

The MPO bond dimension for a many-body string Hamiltonian term is $r-1$ for the Hamiltonian, and $2(r-1)$ for the Liouville operator. The many-body string Lindblad term has a bond dimension of $3(r-1)$. In detail, we implement three terms with bond dimension $(r-1)$, which are the three different terms in the dissipative part

$$L_k \otimes \cdots \otimes L_{k+r-1}\, \rho\, L_k^\dagger \otimes \cdots \otimes L_{k+r-1}^\dagger \,, \tag{10.15a}$$

$$-\frac{1}{2} L_k^\dagger L_k \otimes \cdots \otimes L_{k+r-1}^\dagger L_{k+r-1}\, \rho \,, \tag{10.15b}$$

$$-\frac{1}{2} \rho\, L_k^\dagger L_k \otimes \cdots \otimes L_{k+r-1}^\dagger L_{k+r-1} \,. \tag{10.15c}$$

The tripling of the bond dimension for a multi-site Lindblad rule equivalent to a Hamiltonian rule holds in general. Equation (10.15a) represents $L\rho L^\dagger$ in the Lindblad equation, see Eq. (10.1). The other two terms, i.e., Eqs. (10.15b) and (10.15c), build the anti-commutator. The setup of $\mathcal{L}$ as an MPO is the primary step to use the evolution methods. Nonetheless, the MPS methods cannot be used blindly since $\mathcal{L}$ does not necessarily maintain Hermiticity

in contrast to the Hamiltonian, i.e., $\mathcal{L}^\dagger \neq \mathcal{L}$. The Hamiltonian contributions in Eq. (10.3) are still Hermitian, factoring out the imaginary unit ı. $L_\nu^\dagger L_\nu \otimes \mathbb{I}$ and $\mathbb{I} \otimes (L_\nu^\dagger L_\nu)^T$ are Hermitian themselves, but not with the additional $-$ı factored out from the Hamiltonian. $L_v \otimes (L_\nu^\dagger)^T$ is not necessarily Hermitian in itself or with an additional $-$ı. In the following, we briefly discuss the adaptions for each method with regards to the closed system MPS implementation.

10.4.1.4 Krylov-Arnoldi subspace method

The Krylov approximation [121, 219] directly builds the new state after the time step dt evaluating the product $\exp(\mathcal{L}\mathrm{d}t) \mid \psi\rangle$. The exponential taken within the Krylov subspace is much smaller than the dimension of the Hilbert space or Liouville space scaling with d^L and d^{2L}, respectively. The exponential in the Krylov subspace is used to approximate the new state after the time step; thus, the exponential does not represent a propagator. We recall that in case of a Hamiltonian, which is by definition Hermitian, the matrix to be exponentiated in Krylov subspace is tridiagonal. We label it Krylov-Lanczos in analogy to the Lanczos eigenvalue algorithm for Hermitian matrices. In contrast, the Liouville operator may violate Hermiticity, and we use the Krylov-Arnoldi algorithm. We use the name Krylov-Arnoldi due to the similarity with the Arnoldi algorithm solving for eigenvalues of a non-Hermitian matrix. The Krylov-Arnoldi algorithm results in an upper Hessenberg matrix within the Krylov subspace. In theory, we can use the Krylov-Lanczos algorithm as a fallback for Hamiltonian mixed state evolutions.

This change from Krylov-Lanczos to Krylov-Arnoldi is the major change from Hamiltonian dynamics to Lindblad master equation. The Krylov-Lanczos algorithm, in detail described in [121], relies furthermore on fitting MPO to states, orthogonalizing states, and fitting a state to a sum of states. As our state is formulated as a superket and the MPO represented in Liouville space, these methods can be used without further modification, keeping an implementation cheap.

10.4.1.5 Local Runge-Kutta

The local Runge-Kutta (LRK) method is another method allowing us to evolve Hamiltonians with long-range interactions [122]. The version for the Schrödinger equation takes the MPO of the Hamiltonian and calculates an MPO representation of the propagator for the corresponding time step. The propagator MPO has a smaller bond dimension, by one, and is an efficient representation. It can either be contracted to obtain the new state or fitted. The steps to obtain the MPO of the propagator involve an intermediate mapping to hard-core bosons. A generalization to the non-Hermitian Liouville operator including non-local Lindblad operators is beyond this work here. But we can use the specific structure of the MPO for the propagator to generalize it at least to local Lindblad operators and their representation in Liouville space.

Therefore, we look at the operator-valued MPO matrix of the propagator W^{II} consisting of operator-valued four sub-matrices with subscript A, B, C, and D:

$$W^{II} = \begin{pmatrix} W_D^{II} & W_C^{II} \\ W_B^{II} & W_A^{II} \end{pmatrix}, \tag{10.16}$$

Every term expect W_D^{II} involves the mapping to hard-core bosons; therefore, we do not describe W_A^{II}, W_B^{II}, and W_C^{II} as their definition does not change for local Lindblads and details can be found in [122]. W_D^{II} contains all local site terms and is simply the exponential of these local terms, i.e., the propagator of a system truncating all interactions. For example, this local site term is the coupling to the transverse field in the quantum Ising model with a Pauli matrix or the number operator n_k acting on site k and the on-site interaction $n_k(n_k - 1)$ for the Bose-Hubbard model with appropriate weight for both cases. In the implementation of the Schrödinger equation, D is the sum over all site rules for site k and therefore Hermitian. The corresponding exponential uses this fact. If the Lindblad operators are local, the Lindblad operators can be included entirely in this term D in the MPDO approach. The exponential has then to be calculated for a general matrix because the Lindblad terms

$L_\nu \otimes L_\nu^*$ do not necessarily enforce Hermiticity. Since the other terms are not affected by the local terms, they can stay in place as they are.

Evidently, this approach only works for local Lindblad operators. To what extent non-local Lindblad operators are covered by the method remains a subject of future research. Moreover, the current implementation makes the symmetric tensor to the full space and back to calculate the representation for the LRK-propagators. For that reason, the symmetry implementation only needs to consider a correct mapping.

10.4.1.6 Time-Dependent Variational Principle

The TDVP [120] is the third evolution method based on the MPO. The propagation is based on one or two MPO sites including overlap of the MPO with the other sites in the MPS. To calculate the propagator in the closed system case, the Krylov-Lanczos method with the tridiagonal matrix is used. In the Liouville case, the algorithm is again adapted for the Hessenberg matrix yielded by the Krylov-Arnoldi algorithm, and it is implemented in OSMPS.

10.4.1.7 Time-Evolving Block Decimation

The first and second release of OSMPS use a Krylov subspace method for TEBD [76], which was argued to be slow [215] in comparison to the direct matrix exponential of the Hamiltonian in closed systems. We now have both methods implemented, with KTEBD and TEBD taking the matrix exponential of the Hamiltonian or Liouville operator, respectively. KTEBD follows closely the restriction of the Krylov method. Moving from Hermitian operators to non-Hermitian operators, the matrix in the Krylov subspace turns from symmetric tridiagonal to an upper Hessenberg form. We have to adapt the matrix exponential. Evidently, for taking the exponential of the Liouville operator, we also have to choose a matrix exponential for non-Hermitian matrices; we rely on LAPACK's `ZGEEV`. The symmetric MPDO profits from taking the exponentials of the block-diagonal structure. When building the block-diagonal structure, we ensure that every possible block is present by adding a $0 \cdot \mathbb{I}$,

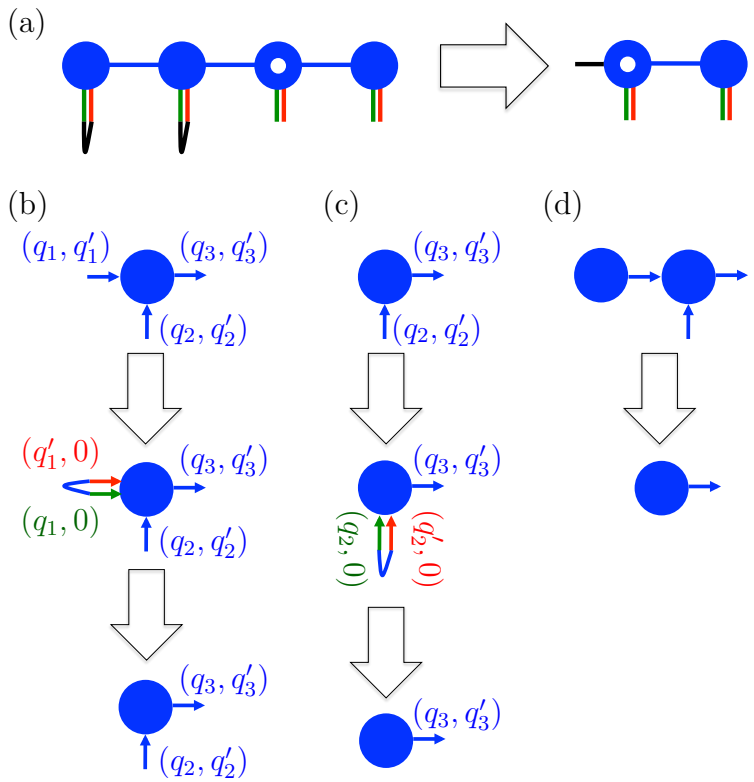

Figure 10.2: *Left transfer tensor for an MPDO.* The left transfer tensor for the k^{th} site is built by taking a partial trace of the sites $1, \ldots, k-1$. (a) We first split and then contract the local Hilbert spaces on the sites 1 and 2 corresponding to a partial trace, see black curves. The results left transfer tensor of rank 1 is also shown in black on the right. the first site is built with the following steps. (b) Contract incoming link to the left by splitting the link into its original underlying links. Then, (c) Contract the local Hilbert space after splitting it. The transfer tensors for sites $k \geq 2$ can be built with subsequent steps (c) Contract the transfer tensor from the site $k-1$ and (d) again.

where $\mathbb{I}$ is the identity operator of the corresponding subspace. An identity scaled with zeros adds the information about all present diagonal blocks without altering the matrix itself.

10.4.1.8 Measurements with overlaps

Measurements of the MPS representation profit immensely from the gauge installed, which reduces local measurements to operations on a single tensor. Similarly, correlations are only affected by the sites measured and all sites in between [75]. Unfortunately, MPDOs do not have such a benefit, and the complete tensor network has to be contracted to find the measurement outcome. Therefore, we define a few operations to allow us to obtain

those measures. These operations are similar to the left-right overlaps and transfer matrices between two states in our MPS algorithms. In detail, we build the tensors $L_{\alpha}^{[k-1]}$ and $R_{\beta}^{[k+1]}$ such that the local measurements on site k of the operator $O^{[k]}$ reduce to the contraction

$$\mathrm{Tr}\left(\rho O^{[k]}\right) \;=\; \sum_{\alpha,i,i',\beta} L_{\alpha}^{[k-1]} B^{[k]}_{\alpha,(i,i'),\beta} O^{[k]}_{(i,i')} R_{\beta}^{[k+1]} \,. \tag{10.17}$$

The critical step is the initialization on the left and right end, respectively. We implement the concept which allows us to use general states, e.g., partially traced out MPS.[5] The three major steps are sketched in Figure 10.2 for the left side of the tensor network. Figure 10.2 is an overview of the objective tracing out over site one and two and obtain a rank 1 tensor to be contracted with the rest of the system. First, we split the link to the left of the MPDO. This step is defined under the assumption that the link was created as a combined link. The correct decomposition can be stored; this link cannot change during any MPDO algorithm. If quantum numbers are present as in Figure 10.2(b), we store the conserved quantities in the first half and fill the second half with zeros. This trick is necessary since the number of conserved quantities is an attribute of the tensor, not to a specific link. We contract over the local Hilbert space of the site in the next step, i.e., Figure 10.2(c). The dimensions and quantum numbers of the original Hilbert space can be obtained from the identity operator. Transfer tensors for matrices in the bulk of the system are obtained via a contraction of the transfer tensor on the left, see Figure 10.2(d), followed by the contraction of the local Hilbert space. We build the right overlap in an analog approach from the other side. This scheme corresponds in other words to the partial trace of selected sites in the density matrix.

10.4.2 Quantum Trajectories

Quantum trajectories follow the idea that any mixed quantum state can be sampled and written via an ensemble of pure states

[5] Such an approach is beneficial for the following example: (i) Obtain MPS via ground state or time evolution. (ii) Trace out over a subsystem followed by (iii) a conversion to an MPDO.

$$\rho = \sum_i |\,\phi_i\rangle\langle\phi_i\,| \ . \tag{10.18}$$

The essential points of the implementation are the effective, non-Hermitian Hamiltonian and the sampling over the different trajectories. The latter are well covered with the data parallelism via MPI present in the package; from the point where the number of trajectories is specified, they are spread across all possible cores as any other set of simulations in OSMPS, e.g., ground state searches for different system sizes. The non-Hermiticity of the effective Hamiltonian can be addressed analogously to the MPDO cases but on the level of the Hilbert space and pure quantum states. The effective Hamiltonian H_{eff} derived from Eq. (10.1) is

$$H_{\text{eff}} \;\; = \;\; H - \frac{\imath\hbar}{2} \sum_\nu L_\nu^\dagger L_\nu \, . \tag{10.19}$$

This effective Hamiltonian H_{eff} violates Hermiticity and conservation of norm when used in the Schrödinger equation. The latter has its use on the decision on when to apply the Lindblad operators to the system. The non-Hermiticity leads to changes in the time evolution methods as discussed in the previous section for the MPDO. The Krylov method, TDVP, and KTEBD switch from Krylov-Lanczos to Krylov-Arnoldi approximation of the new state. TEBD uses a function for non-Hermitian matrices to exponentiate H_{eff}. The LRK method has to use a non-Hermitian matrix exponential for the local terms but has one additional problem. LRK itself does not conserve norm which enhances or prevents the loss of norm due to H_{eff}.

It remains to present the actual algorithm for the trajectories, which is described in many places [221], but reviewed here briefly for completeness. While looping over the time steps of the evolution, we execute the following steps: (i) Draw a random number $r_{\mathcal{N}} \in \mathcal{U}(0,1)$ and ensure the state $|\,\psi(t=0)\rangle$ is normalized at the beginning. The uniform distribution between 0 and 1 is written as $\mathcal{U}(0,1)$. This normalization is necessary as the decreasing norm of $|\,\psi(t)\rangle$ is used in the following steps. (ii) Calculate time steps under H_{eff} without

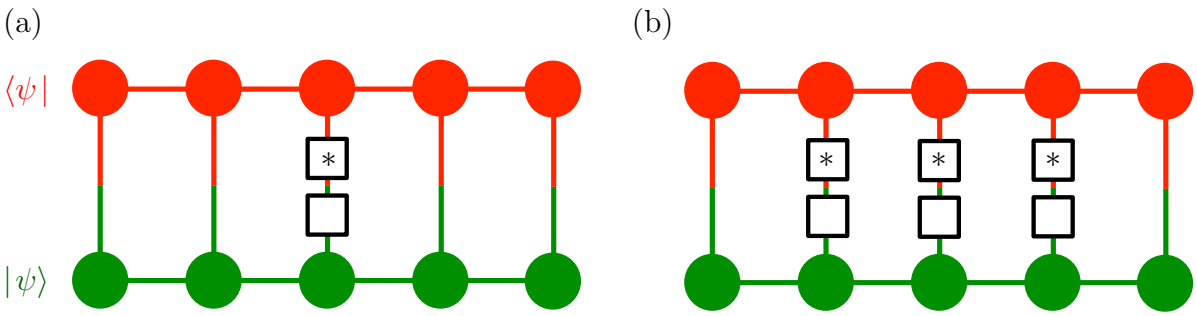

Figure 10.3: *Contraction for unweighted probabilities in quantum trajectories.* (a) Local Lindblad operators obtain their weight by a measurement of norm after contracting it to the current quantum state. This step can be reduced to a single site operation. (b) The many-body string Lindblad terms, here shown for three sites, need to contract the local operators with the state for each site before measuring the norm, i.e., the unweighted probability.

renormalizing the state. (iii) Measure the norm $\mathcal{N}$ of the state. If $\mathcal{N} < r_{\mathcal{N}}$, then we apply a quantum jump according to the steps (a) through (c) described below. Otherwise, we continue to the next step in the time evolution, i.e. (i). The steps to select a random quantum jump are the following. (a) Calculate unweighted probabilities for each Lindblad operator L_ν as $p_\nu = \langle\psi\,|\,L_\nu^\dagger L_\nu\,|\,\psi\rangle$. Figure 10.3 shows the contractions to obtain the p_ν's for the two types of Lindblad operators implemented in the package. (b) We normalize p_ν to $P_\nu = p_\nu / \sum_\nu p_\nu$. (c) We draw a random number $r_\kappa \in \mathcal{U}(0,1)$. We apply to the state the Lindblad operator L_κ such that $P_{\kappa-1} < r_\kappa \leq P_\kappa$ holds. The state is renormalized after application of the Lindblad operator L_κ and we continue the time evolution with step (i).

It is worthwhile to take a look at the measurement procedure for QTs. Local measurements or correlations can be averaged over all trajectories with equal weight. For example, a local observable $\langle O_k\rangle$ is calculated for QTs as

$$\langle O_k\rangle \;=\; \frac{1}{N_{\mathrm{QT}}}\sum_{j=1}^{N_{\mathrm{QT}}}\langle O_k\rangle_j\,, \tag{10.20}$$

where N_{QT} is the number of trajectories and $\langle O_k\rangle_j$ is the observable of the j^{th} trajectory. Here, we use the concept that the density matrix is a statistic ensemble of pure states $\rho = \sum_j p_j\,|\psi_j\rangle\langle\psi_j|$ with equal probabilities $p_j = 1/N_{\mathrm{QT}}$. Obviously, this approach does not

work for all observables; the purity $\mathcal{P}$ of each $|\,\psi_j\rangle$ is equal to one, but the purity of the density matrix is not necessary the average, i.e., one. We can calculate the purity as

$$\mathcal{P} \;=\; \mathrm{Tr}\left[\rho^2\right] = \sum_{j,j'=1}^{N_{\mathrm{QT}}} \frac{1}{N_{\mathrm{QT}}^2} \mathrm{Tr}\left[|\,\psi_j\rangle\langle\psi_j\,||\,\psi_{j'}\rangle\langle\psi_{j'}\,|\right] , \tag{10.21}$$

where each of the N_{QT}^2 traces can be represented as contraction across a tensor network. But this measurement goes beyond simple MPI parallelization as the measurement needs all states at the time of the measurement and a posteriori averaging is not possible. We can extend this argument to any term with power differing from first order in ρ. Therefore, non-linear measures need all trajectories for measuring, which can either be achieved with saving each state or while waiting until all trajectories have reached the measurement.

10.4.3 Locally Purified Tensor Networks

LPTN time evolution relies on the Trotter decomposition and Kraus operators applied to the purification of the density, as previously outlined in Reference [82]. Therefore, we restrict the description to the technical implementations used within OSMPS. We start with a brief description of the construction and continue with open system decomposition. We conclude with the setup for finite temperature. The current implementation is restricted to nearest-neighbor interaction in the Hamiltonian and local Lindblad operators. Furthermore, no symmetries are present.

10.4.3.1 Construction of Locally Purified Tensor Networks

We focus on the conversion of MPS to LPTN and the definition of the infinite temperature density matrix ρ_∞. The conversion from an MPS tensor $A^{[k]}_{\alpha,i,\beta}$ representing site k to an LPTN tensor is as simple as inserting an additional link of dimension 1, i.e., $B^{[k]}_{\alpha,i,\kappa,\beta}$. The local tensors for the definition of ρ_∞ have the link dimension $(1, d, d, 1)$ and are diagonal in the entries

$$B^{[k]}_{\alpha,i,\kappa,\beta} \;=\; \delta_{i,\kappa}\,. \tag{10.22}$$

10.4.3.2 Trotter decomposition for open systems

The evolution of an LTPN separates the Hamiltonian part of the Liouville operator $\mathcal{L}$ from the dissipative part $\mathcal{D} = \sum_\nu L_\nu \rho L_\nu^\dagger - \frac{1}{2}\{L_\nu^\dagger L_\nu, \rho\}$ in a second order Trotter decomposition. The exponential of the time evolution is approximated with

$$\mathrm{e}^{\mathcal{L}dt} \approx \mathrm{e}^{-\frac{1}{\hbar}[H,\rho]\frac{dt}{2}}\mathrm{e}^{\mathcal{D}dt}\mathrm{e}^{-\frac{1}{\hbar}[H,\rho]\frac{dt}{2}}\,. \tag{10.23}$$

The Hamiltonian contribution evolves each part of the purification $\rho = XX^\dagger$, where it is sufficient to propagate X. The Hamiltonian itself is approximated with two-site propagators in a Sornborger decomposition [248]. We remain with the dissipative part, which we express as Kraus operators:

$$\mathrm{e}^{\mathcal{D}dt}\,|\rho\rangle\!\rangle \;=\; \sum_{\nu'} K_{\nu'} X X^\dagger K_{\nu'}^\dagger = \sum_{\nu'} (K_{\nu'} X)(K_{\nu'} X)^\dagger\,. \tag{10.24}$$

We recall that the local Kraus operators keep the locally purified tensor network in its form. We generate the Kraus operators from the first order approximation [273]

$$\mathrm{e}^{\mathcal{D}dt}\,|\rho\rangle\!\rangle \;=\; \sum_{\nu'=0}^{N} K_{\nu'}\rho K_{\nu'}^\dagger + \mathcal{O}(dt)\,, \tag{10.25}$$

$$K_{\nu'=0} \;=\; \mathbb{I} - \frac{dt}{2}\sum_{\nu=1}^{N} L_\nu^\dagger L_\nu\,, \tag{10.26}$$

$$K_\nu \;=\; \sqrt{dt}L_\nu\,, \nu = 1,\ldots,N\,. \tag{10.27}$$

Alternatively, we can decompose the exponential of the Liouville operator into Kraus operators. The contraction of the Kraus operators increases the auxiliary dimension κ to a larger $\kappa' = \kappa(N+1)$. The dimension is reduced in a truncation similar to the truncation when

splitting nearest neighbor sites.

10.4.3.3 Imaginary time evolution for finite-T states

The finite temperature states according to the Gibbs distribution are generated in an imaginary time evolution starting from the infinite temperature state ρ_∞ as explained in Sec. 10.4.1.2. As evolution is purely Hamiltonian and does not contain any dissipative part $\mathcal{D}$, we can reuse the decompositions for MPS/MPDO methods. Both second and fourth order Sornborger approximations are available.

10.5 Simulation Setup and Convergence

We describe the convergence of the different scenarios in the next three subsections. We start with the analysis of the finite-T states in Sec. 10.5.1; we use the quantum Ising model as example. Then, we move to the Lindblad master equation and consider simulations without and with symmetry. Section 10.5.2 considers the dissipative dynamics of an exciton for the convergence study of a system without conserved symmetry. The transient dynamics of the Bose-Hubbard model with number conservation are described in Sec. 10.5.3.

10.5.1 Finite-T states in the Ising model (MPDO and LPTN)

We now turn to finite temperature states according to the Gibbs distribution and their convergence. We compare LPTNs and MPDOs; quantum trajectories cannot simulate finite temperature states. We take the quantum Ising model defined in Eq. (10.10) as an example. The comparison is restricted to the TEBD2 time evolution methods and the overall Hilbert space without addressing a specific sector in the $\mathbb{Z}_2$ symmetry.

Figure 10.4 answers two important questions: which method needs less CPU time to run the simulations and which network type uses its bond dimension more efficiently? The first answer is important to use computational resources in the best possible way whenever both tensor networks can be applied to the problem. The second question can deliver a partial answer as to which is the most favorable network to store entanglement for any state similar

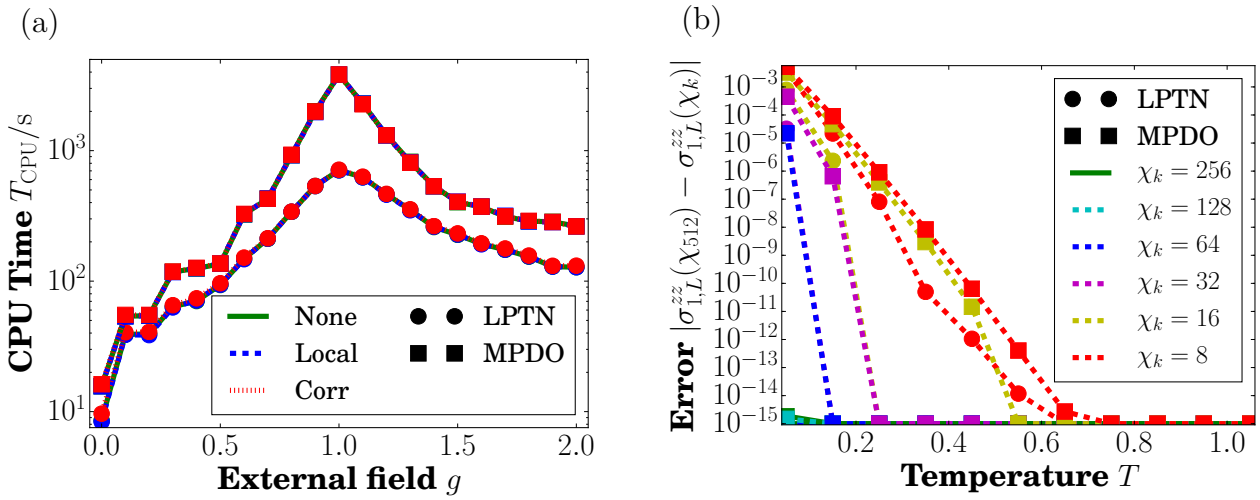

Figure 10.4: *Performance of finite-T simulations.* We consider the quantum Ising model without $\mathbb{Z}_2$ symmetry to study basic convergence of the finite-T states represented by LPTNs and MPDOs. The system size for the simulations is $L = 100$. (a) The CPU times T_{CPU} for different measuremts indicate that LPTNs are favorable for this model. The bond dimension is $\chi = 512$. The measurements are not the major cost and all three curves for "None", "Local", and "Corr" overlap. (b) We compare the error of the zz-correlation measurement between the first and last site to the most accurate result with $\chi = 512$. We conclude from the lower errors for the same bond dimension that LPTNs use their bond dimension more efficiently in this example.

to those finite-T states. We consider the finite-T evolution with the first measurements at $T = 1.05$ and the last measurement at $T = 0.05$ in steps of $\Delta T = 0.1$. We use a time step $dt = 0.01$, and additional steps $dt' < dt$ to reach the measurements at the corresponding temperatures. The temperatures are in units of the interaction J, and we have a unitless $k_B = 1$.

We first discuss Figure 10.4(a) and the computational effort for the imaginary evolution and the measurements. We choose a system size of $L = 100$, a maximal bond dimension $\chi = 512$, and three type of measurements: (i) only default measurements as the energy; and (ii) default measurements and two local observables, i.e., σ^x_j and σ^z_j. (iii) The last type of simulations computes the default measurements, the local measurements presented previously, and the correlations of the Pauli matrices in the x- and z-direction. All simulations are carried out on a *Penguin Relion 1752DDR/QSFP 2x(Intel X5675) 12 cores 3.06 GHz*. The peak of

the CPU time T_{CPU} is located around the critical point; the entanglement is maximal at the critical point of the Ising model, i.e., $g = 1.0$. We see a clear difference between the LPTN and MPDO times for no measurements, which is related in aspects to the computational scaling of the underlying operations. LPTNs build the two-site Hamiltonian on a $d^2 \times d^2$ matrix, where the local dimension d is equal to two in the qubit example. In contrast, the Hamiltonian represented in Liouville space is of dimension $d^4 \times d^4$. The contraction of a single two-site propagator with a two-site tensor then scales as $\chi^2 d^6$ for the LPTN and $\chi^2 d^8$ for the MPDO. We remark that our MPDO implementation could be further optimized using the fact that the commutator $\left[H \otimes \mathbb{I}, \mathbb{I} \otimes H^T\right] = 0$. Thus, we can simplify the action of the two site propagator in Liouville space to $\exp\left(H \otimes \mathbb{I} + \mathbb{I} \otimes H^T\right) = \left(\exp(H) \otimes \mathbb{I}\right)\left(\mathbb{I} \otimes \exp\left(H^T\right)\right)$. Each exponential can be applied separately in two steps with a scaling of $\chi^2 d^6$ for each contraction. However, this approach would in our eyes defeat the purpose of an MPDO, which is representing the density matrix as an MPS; but here, the link of the local dimension has to remain split throughout the complete evolution. Synergy effects between the MPDO and MPS implementation would be decreasing. The measurements, executed in addition to the imaginary time evolution, increase computation time where they are beyond fluctuations. LPTNs tend to have less cost for measurements as local and quasi-local measurements do not have to contract the complete tensor network. But overall, the selected measurements are not the significant costs in these simulations.

Figure 10.4(b) describes the error for different bond dimensions in comparison to the most accurate bond dimension. We choose this most accurate bond dimension as $\chi_{\max} = 512$. The system size is $L = 100$, and we set the transverse field to $g = 1.0$ maximizing the possible entanglement in the quantum Ising model. The correlation is among the observables most affected by a limited bond dimension; therefore we consider

$$\epsilon_{zz} \quad = \quad \left|\langle \sigma_1^z \sigma_L^z \rangle_{\chi_{\max}} - \langle \sigma_1^z \sigma_L^z \rangle_{\chi}\right|, \tag{10.28}$$

where $\chi < \chi_{\max}$. We see a decreasing error ϵ_{zz} as the bond dimension χ approaches $\chi_{\max}$ for both LPTN and MPDO. This behavior is expected. But we also observe that each curve representing the LPTN has a smaller error than the corresponding MPDO curve. Assuming that the simulations with the highest bond dimension are both converged and yield the correct results, LPTNs use the bond dimension more efficiently than MPDOs. This statement is supported by the error in the energies for the the final temperature. The LPTN has a maximal absolute error of $2.09 \cdot 10^{-5}$ for $L = 100$, $\chi = 512$, $g = 1.0$, while the error for the MPDO yields $6.21 \cdot 10^{-4}$. Thermal energies for low enough temperatures can be calculated via the eigenvalues of Majorana Hamiltonian after the Jordan-Wigner transformation; energies of excited states E' are truncated if $\exp(-(E' - E_0)/T) < 10^{-16}$ and avoids iterating over all 2^L eigenenergies. This effect might also contribute to the CPU times observed. Lower bond dimension leads to the use of less computational resources. Unlike a variational or imaginary time ground state search, we cannot stop the algorithm at a defined precision and compare the CPU times.

One may ask where the speed-up of the LPTN in comparison to the MPDO occurs and how it scales with system size. This question is in relation with the known growth of entanglement associated with quantum critical phenomena [281, 282]. We consider the system sizes $L \in \{100, 150, 200\}$ at the critical point $g = 1.0$ for the scenario with local measurements at bond dimension $\chi = 512$. We compare the the ratio r of MPDO over LTPN from measurement 1 to 10 and 10 to 11 according to the time stamp of the results files. We obtain the ratios $r(L) = \{4.17, 4.38, 4.36\}$ for ascending system sizes, and $r(L) = \{5.52, 6.00, 6.13\}$ are the ratios between the measurements 10 and 11. We observe the trend that the speed-up has a larger contribution at the end of the time-evolution and increases with system size. We point out that the major part of the time evolution takes place for the last data points due to the inverse relation of temperature to evolution time. In conclusion for the finite-T simulations, LPTNs scale better in the scenario of the quantum Ising model. The maximal difference in CPU time is around the critical point and suggests that LPTNs

support entanglement better for imaginary time evolutions.

10.5.2 Local Lindblad operators without symmetry (QT, MPDO, and LTPN)

Lindblad equations without conserved quantities and local channels have a variety of applications reaching from the quantum Ising model with local spin flips over XXZ model transport problems using local channels at both end of the chains [168] to lossy photon cavities. We choose to simulate the transport of an exciton with the initial condition and Hamiltonian based on reference [283, 284]. Examples of the Lindblad operators for transport problems can be motivated from [285], which describes energy loss and dephasing noise in molecular structures. We consider the Hamiltonian

$$H = J\sum_{k=1}^{L-1} b_k b_{k+1}^\dagger + h.c. + \Delta\sum_{k=1}^{L} n_k - \mu\left(b_k^\dagger + b_k\right), \tag{10.29}$$

and J is the tunneling strength, Δ an on-site potential, and μ the driving due to the electromagnetic field. The latter is turned off on all sites for all simulations, i.e., $\mu = 0$. The corresponding Lindblad master equation with loss of a strength γ and dephasing, coupled with γ_d, is defined as

$$\frac{\partial}{\partial t}\rho = -\frac{\imath}{\hbar}\left[H,\rho\right] + \sum_{k=1}\gamma\left(b_k\rho b_k^\dagger - \frac{1}{2}\left\{b_k^\dagger b_k,\rho\right\}\right) + \sum_{k=1}\gamma_d\left(n_k\rho n_k - \frac{1}{2}\left\{n_k n_k,\rho\right\}\right). \tag{10.30}$$

We define the initial state $|\,\psi(t=0)\rangle$ as a product state on three subsystems A, B, and C, i.e., $|\,\psi(t=0)\rangle = |\,\psi(t=0)\rangle_A \otimes |\,\psi(t=0)\rangle_B \otimes |\,\psi(t=0)\rangle_C$. The subsystems A and C are in the vacuum state $|\,\psi(t=0)\rangle_A = |\,0\cdots 0\rangle$ and $|\,\psi(t=0)\rangle_C = |\,0\cdots 0\rangle$, respectively. Subsystem A contains L_A sites; subsystem C spans L_C sites. The initial exciton is defined via the relation from [284] on the subsystem B with a size of L_B sites:

$$|\,\psi(t=0)\rangle_B \propto \sum_{k=L_A+1}^{L_A+L_B} \mathrm{e}^{\imath k_0 k a}\mathrm{e}^{-a^2(k-k_0)^2/(2\sigma^2)} b_k^\dagger\,|\,0\cdots 0\rangle\,. \tag{10.31}$$

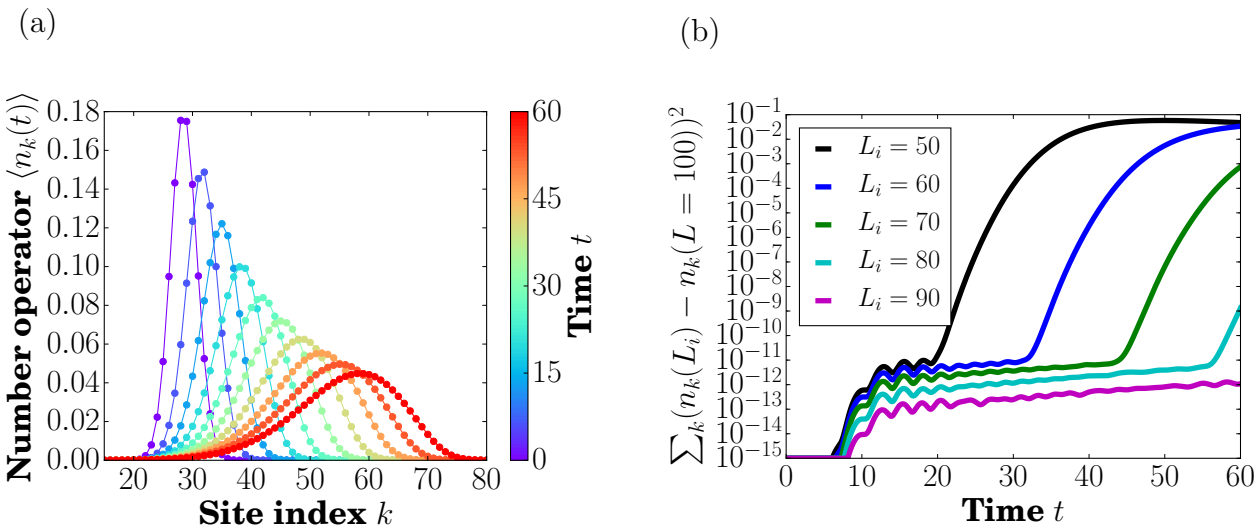

Figure 10.5: *Exciton dynamics with open boundary conditions.* (a) The dynamics of the largest system with $L = 100$. The initial wave package loses height while spreading out. (b) We consider different system sizes L to estimate when the reflection of the exciton returns from the boundary at site $k = L$. The exciton is initially in the sites $k = 11, \ldots, 40$ and moving right. System sizes of $L = 60$ ($L = 90$) are sufficient to simulate the closed system for a time of $t = 30$ ($t = 60$). Times are in the unit of the local term Δ.

Thus, the total system has a system size of $L = L_A + L_B + L_C$ sites. The exciton on subsystem B is not a product state and has entanglement. It can be constructed on the completed Hilbert space and decomposed via SVDs to an MPS. This approach is limited to about 24 sites and supported by the OSMPS Python interface. On the other hand, we can write the state as a sum of MPSs, where each state in the sum of Eq. (10.31) has a bond dimension of 1. We compress this MPS yielded by the summation, which scales better with larger L_B. Figure 10.5(a) pictures the exciton at different points in time and we observe a loss of height while spreading out in the closed system. We are well aware that this setup of the problem has problems from the back reflection of the exciton at the boundary $k = L$. Therefore, Figure 10.5(b) shows the deviation of the exciton's mean position for different system sizes for the closed system over time in comparison to $L = 100$. We see small errors at the order of 10^{-12} and do not concentrate on these errors as 10^{-12} is at the order of truncated singular values. We conclude that a system size of $L = 90$ is sufficient for an evolution time

$\tau = 60$ without considering reflections from the boundary. To estimate the error, we look at the number operator $N(t) = sum_{k=1}^{L} n_k(t)$ as

$$\epsilon_{N(t)} = |N(t) - N(0)\exp(-\gamma t)| \ , \tag{10.32}$$

where the relation $dN(t)/dt = -\gamma N(t)$ can be easily derived when considering the commutation relation between b_k, $b_{k'}^{\dagger}$ and $n_{k''}$ as well as $d/dtN(t) = d/dt\mathrm{Tr}\left[N\rho(t)\right] = d/dt\mathrm{Tr}\left[Nd/dt\rho(t)\right]$. This property is one result which can be checked besides convergence regarding the bond dimension or other convergence parameters. We start with an analysis of the momentum of the exciton; the position of the maximum of the exciton, the mean, the standard deviation, and the skewness give a good impression of the dynamics, see Figure 10.6(a). We observe that for a coupling $\lambda = \lambda_d = 0.05$ the position of the maximum remains almost equal to the closed system case. The mean, i.e., "center of mass", propagates at a slower speed in the open system in comparison to the closed system. This trend is reflected in the increased standard deviation and skewness of the exciton. These measures can be used for a more detailed analysis of the open system dynamics of the exciton, but we turn to the evaluation of the different tensor networks and algorithms.

Figure 10.6(b) shows the error in the number of excitations, which decays exponentially according to Eq. (10.32). TDVP has the lowest error; TEBD has a local minimum of the error around $t \approx 10$ switching between under- and overestimating the number of excitations in the system and recovers the envelope otherwise in our understanding. The LRK has an error similar to TEBD. In the long time limit, all of these three algorithms using MPDOs have a similar error. The Krylov method has an error about an order of magnitude bigger at the beginning and recovers the error of the other algorithms in the long-time limit; it is not considered an option in our opinion. If we consider the second tensor network, LTPN, the error is the largest in the long-time limit. If we consider in addition the CPU times in Figure 10.6(d) for each simulation as a function of the maximal bond dimension, we can get a much better picture as to what method is best suited to the problem. Two things become

evident. (i) The Krylov method for MPDOs is two orders of magnitude slower than the next slowest algorithm for MPDOs. The other algorithms reach a saturation of the CPU time, and we conclude that they do not exceed the maximal bond dimension. Otherwise, TEBD is preferable when applicable. For long-range interactions in the Hamiltonian, LRK is preferable over TDVP from a resource viewpoint. (ii) The LPTN algorithm requires much higher resources in comparison to MPDO methods. We remind the reader that a maximal bond dimension $\chi_{\max} = \kappa = 32$ leads to a bond dimension of 32^2 in many tensor operations due to the auxiliary link in the local tensors of the same dimension. This approach is fair when comparing the splitting of a two-site tensor when $\chi_{\max,\mathrm{MPS}} = \chi_{\max,\mathrm{MPDO}}\kappa_{\max}$; in both cases, we split a matrix of $\chi_{\max,\mathrm{MPS}}d \times \chi_{\max,\mathrm{MPS}}d$. Thus, we can compare the LPTN data for $\chi = 16$ with the MPDOs of $\chi = 256$. The error does not outweigh the higher CPU time. It remains the question if novel methods for LPTNs can overcome the problem [286], which also consider the optimal ratio between χ and κ for LPTNs.

Finally, Figure 10.6(c) answers in parts how efficiently the different algorithms use their bond dimension. We compare the values of the number operator for MPDOs with $\chi_{\max} = 1024$ and LTPNs with $\chi_{\max} = \kappa = 32$ to simulation with lower bond dimension and get a more detailed picture of convergence. MPDOs profit from using a very low bond dimension for TDVP and TEBD. We remark that this model including this initial condition has very low requirements with regards to the bond dimension with MPS and MPDO methods. In fact, simulations with $\chi_{\max}/64 = 16$ are already not distinguishable from simulations with $\chi_{\max}$. In contrast, the LRK method shows, despite the same error in the total number of excitations, an error between bond dimensions 512 and 1024, i.e., they must exceed bond dimensions up to and beyond 512. The Krylov method does not use the full bond dimension according to this data, but is less efficient in using the bond dimension in comparison to TEBD and TDVP. The LTPN algorithm has the highest error for this comparison, although the bond dimension for both links is with 32 much lower. Saturating both links leads to the larger CPU times and the higher error if values are truncated throughout the simulation. The

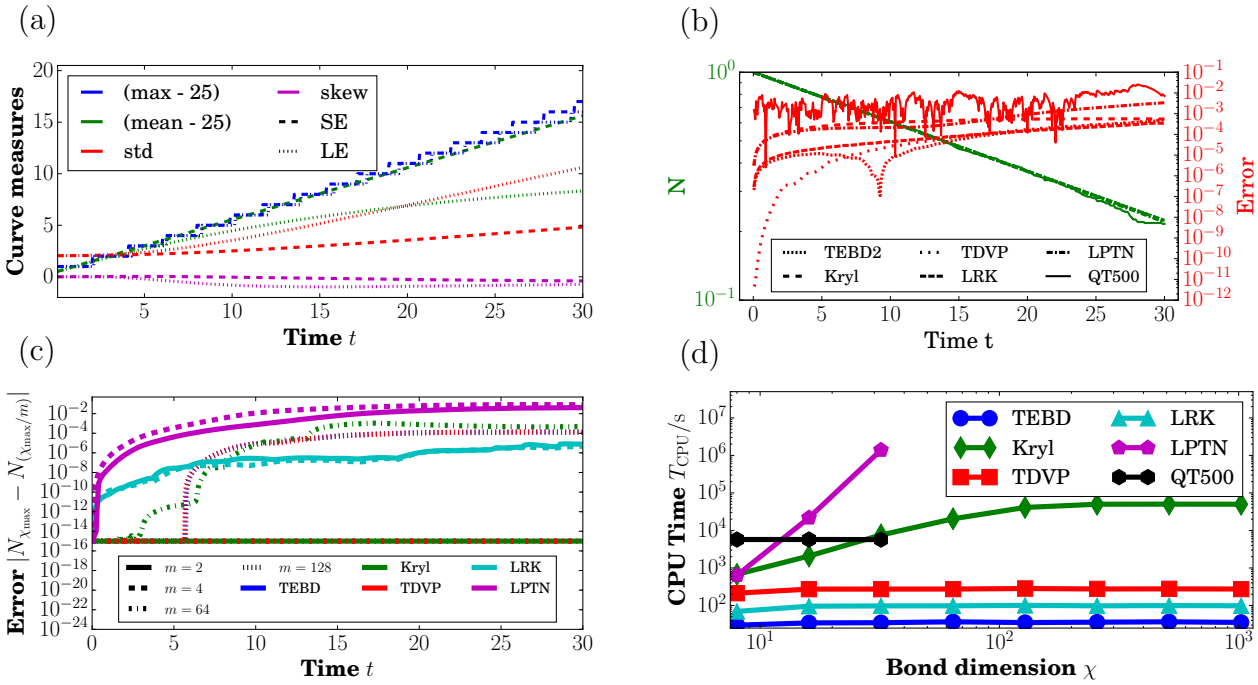

Figure 10.6: *Convergence of open quantum system exciton dynamics.* (a) The different momenta of the exciton capture best the effects of the dephasing. Although the maximum (max) of the exciton almost stays constant, the mean (mean), standard deviation (std), and skewness (skew) capture the dynamics of the Lindblad equation (LE) with coupling $\lambda = \lambda_d = 0.05$ very well, shown side-by-side with the Schrödinger equation (SE). (b) The coupling to the decay Lindblad operator induces an exponential decay of the total number of particles in the excited state. All time evolution methods reproduce this exponential decay (green); thus, we show the corresponding error (red). The TDVP for MPDO works best. (Linestyles in the legend are used for green and red curves.) (c) We show how efficiently the bond dimension is used by comparing the convergence of $N(t)$ for the different bond dimension to the maximal bond dimension, i.e., $\chi_{\max}^{\mathrm{MPDO}} = 1024$ and $\chi_{\max}^{\mathrm{LPTN}} = \kappa_{\max} = 32$. MPDO simulations with TEBD and TDVP use the bond dimension very efficiently for this problem and already show no error for $\chi = 16$ in comparison to $\chi_{\max}$. (d) From a pure resource perspective, TEBD is favorable over LRK over TDVP and over Krylov when using MPDOs. LPTN-TEBD also scales unfavorable, but the additional link for each site with $\chi = \kappa$ induces matrices with dimension χ^2 rather than χ affecting the scaling of operations.

inefficient use of the bond dimension in the LPTN is related to the loopy network structure when looking at a the complete network representing ρ instead of its purification. Recent efforts to overcome this problem via intermediate steps have not been considered for this implementation [286].

The quantum trajectories run with $N_{\mathrm{QT}} = 500$ and yield an error above the MPDO and LTPN result, see again Figure 10.6(b). While the error in MPDO and LTPN is solely due to truncation and the error induced by the Trotter decomposition, the QTs could further improve by taking more trajectories. The error follows the law of large numbers. If we consider the CPU times for each method obtained on a *2x(Intel Xeon E5-2680 Dodeca-core) 24 Cores 2.50GHz* node compiled with *ifort*, the QTs exceed with $N_{\mathrm{QT}} = 500$ already the resources for the MPDO. Here, QTs run with TEBD and, thus, the fastest method. Therefore, more trajectories are not considered as they would increase the difference in CPU time further. This CPU time is the cumulative time for all simulations, and large-scale parallelization can make them favorable for getting a quick picture of the physics. We point out once again the very low bond dimension used in the MPDOs, which makes them favorable, and models with higher entanglement might profit more from QTs. This statement is supported by the next example, i.e., Sec. 10.5.3. We recall that converting an MPS to an MPDO increases the bond dimension from χ to χ^2 and any decomposition, such as an SVD, scales cubically with the matrix dimension.

10.5.3 Local Lindblad operators with symmetry (QT and MPDO)

The last convergence study treats a Lindblad master equation with a conserved quantity. This symmetry restricts us to the usage of QTs and MPDOs. We choose as our Hamiltonian the Bose-Hubbard model

$$H = -J \sum_{k=1}^{L-1} \left(b_k^\dagger b_{k+1} + h.c. \right) + \frac{U}{2} \sum_{k=1}^{L} n_k (n_k - 1) + \sum_{k=1}^{L} V(k) n_k \,. \tag{10.33}$$

J sets the tunneling strength and the repulsive on-site interaction is U. b_k ($b_k^\dagger$) is the bosonic annihilation (creation) operator acting on site k. The Hamiltonian conserves the number of bosons, i.e., the commutator $[H, N] = 0$ with $N = \sum_{k=1}^{L} n_k$. The chemical potential, i.e., $\mu \sum_{k=1}^{L} n_k$ can be discarded in simulations with number conservation; it represents an energy shift without influence on the simulation. But we include a potential $V(x)$ to capture the potential of the double well. We choose a dephasing operator as the Lindblad operator, i.e., $L_k = n_k$ acting on each site k.

We consider a double-well scenario with two wells of L_W sites, separated by a one-site barrier with $V(L_W + 1) \neq 0$. The total size of the system is $L = 2L_W + 1$ and we choose a filling of $N = L_W$. The initial state for the time evolution is the ground state of the particles trapped in the left well with $V(x) = 1$ ($V(x) = 0.5$) for $L = 5$ ($L = 21$) for all $x > L_W$. At $t = 0$, the wave function starts to oscillate between the two wells in a Josephson-like regime. The coupling to the open system damps out the oscillations; we show this effect in Figure 10.7(a) with the center of mass, or mean, as a function of time, i.e.,

$$x_{\text{mean}}(t) \quad = \quad \frac{1}{N} \sum_{k=1}^{L} k n_k(t) \,. \tag{10.34}$$

Two of the curves show the simulation for closed system time evolution with MPS and MPDO and validate that the MPDO tensor network can simulate the closed system correctly until entanglement generation introduces significant errors to the MPDO. The effects of the dephasing lead to a damping of the oscillation as shown in the two additional curves with $\gamma = 0.05$ and $\gamma = 0.1$. The system size is $L = 21$, and we choose an initial bond dimension of the ground state of $\chi = 5$. We assume that the ground state has initial errors, but as we compare time evolution methods, all time evolution methods start with the same ground state. As the initial bond dimension of the MPDO is $\chi^2 = 25$, that allows us to run with medium bond dimensions and judge on the error due to truncation. The data shown in Figure 10.7(a) is for bond dimension $\chi = 256$ for the MPS and MPDO during the time evolution.

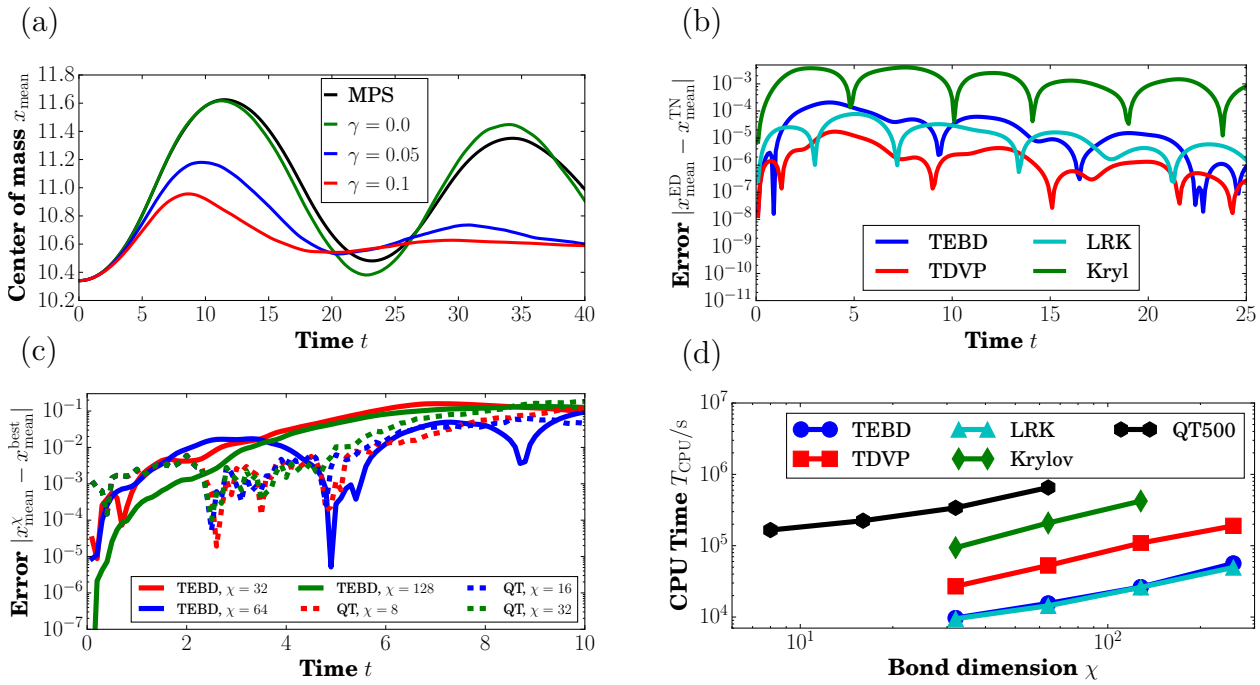

Figure 10.7: *Convergence of open quantum system Bose-Hubbard dynamics.* (a) The center of mass starts oscillating after we release the potential on the right well at time $t = 0$ and keep only a one-site potential in the middle to separate wells. We observe that the simulations for MPS and MPDO of a closed system mismatch after about ten time units. The coupling of the system to a dephasing damps the oscillations. (b) We compare the error of tensor network (TN) methods against exact diagonalization for a small system of $L = 5$. (c) We compare the errors of QTs with TEBD and $N_{\mathrm{QT}} = 500$ and simulations with MPDOs and TEBD to the TEBD simulations with the highest bond dimension, i.e., $\chi = 256$. Errors grow fast and show the numerical challenges associated with this problem setup. (d) We compare the computational resources for MPDO and QT algorithms. The coupling to the environment is $\gamma = 0.05$. TEBD and LRK use the least resources, then comes TDVP. The quantum trajectories with N_{QT} and TEBD are located above MPDOs with TEBD. Due to the limitation in bond dimension in this example and the possibility of parallelizing, they are an attractive option.

We presented the error for the exciton dynamics based on the exponential decay; we are not aware that we have an equally suited result to compare the dynamics of the double well and Bose-Hubbard model. Thus, we start with a comparison between the tensor network algorithms and exact diagonalization. The OSMPS package includes exact diagonalization methods implemented in Python [189], and one of their purposes is exactly the accessibility for validating other techniques with an independent method. We simulate with $L = 5$ sites and set the local dimension to $d = 3$, i.e., states with more than two bosons per site are truncated. The error of the center of mass for the simulation with TDVP is minimal through most of the simulation and bounded by 10^{-5} according to Figure 10.7. The next best methods are LRK and TEBD, while Krylov has the largest error bounded by 10^{-3}. The choice of the position of the center of mass a as macroscopic observable comes with a couple of local minima of the error; the position of the center of mass can align in two states, although the states are different and the envelope is more meaningful and conclusive.

We now analyze how the convergence scales with bond dimension. The trends are similar for the different time evolution methods, where the reason is the exhausted bond dimension and truncation of singular values. Figure 10.7(c) shows the error in the center of mass of TEBD simulations with bond dimension $\chi = 32, 64, 128$ to the most accurate simulation with $\chi = 256$. The significant difference between the simulations reveals the need for high bond dimensions in this problem and we cut the error plots at ten time units. We conclude that the bond dimension is used completely after very short times for MPDOs; only simulations with $\chi = 128$ can keep the error below 10^{-5} for the first couple of time steps. The QTs averaged over 500 runs are compared to the most accurate MPDO simulation, both run with TEBD. We have three regimes. (i) The MPDO simulations are more accurate at the very beginning of the time evolution as the QTs suffer from statistical averaging. This regime ends at $t \approx 2$ (ii) The error of the QTs drops below the MPDO simulations with small bond dimension. The error due to truncation in the MPDO is worse than the error from the average of the trajectories. (iii) For times $t > 5$, the difference between the QTs and the

MPDO with $\chi = 256$ grows. Without involving more details, the difference can be due to either method.

Finally, we turn to the actual resources used in Figure 10.7(d). We observe that both TEBD and LRK use the same amount of resources. TDVP is less than an order of magnitude above these two methods. The Krylov method takes much longer than TDVP, which is in the end about an order of magnitude difference to the fastest method, i.e., LRK. We run the QTs with a much lower bond dimension; the actual bond dimensions 8 (16) are comparable after squaring it in the transformation from MPS to an MPDO of bond dimension 64 (256). The resources are more than a magnitude higher; we recall that they can be easily parallelized in contrast to an MPDO simulation. The large error at low bond dimension for MPDOs makes QTs much more attractive than in the previous case of the exciton transport.

10.6 Conclusions

In this work, we have presented three different evolution techniques for one-dimensional quantum systems under the Lindblad master equation with tensor network methods. Therefore, the *Open Source Matrix Product States* (OSMPS) package allows the quantum community to explore the advantages of each method. Open quantum system dynamics provide access to more advanced simulations of quantum simulators including the effects of the interaction with the environment as simulated with the Lindblad master equation throughout this work.

We described the bond dimension of the Liouville operator represented as a matrix product operator (MPO); this MPO is used to evolve matrix product density operators beyond nearest-neighbor interactions and the time-evolving block decimation (TEBD), i.e., the time-dependent variational principle, the local Runge-Kutta time evolution, and the Krylov time evolution. Section 10.4.1 provides insights into the scaling of methods due to the bond dimension of the MPO. For example, non-local rules with a bond dimension $\chi_{\mathrm{H-MPO}}$ to represent the Hamiltonian H have a bond dimension of $\chi_{\mathcal{L}-\mathrm{MPO}} = 2\chi_{\mathrm{H-MPO}}$ to depict the Liouville operator. If we define Lindblad terms analog to Hamiltonian terms, e.g., we replace

a nearest-neighbor interaction of a Hamiltonian with a Lindblad operator acting on nearest-neighbor sites, they have a bond dimension three times as big as $\chi_{\mathrm{H-MPO}}$. We found that different approaches are favorable in different situations. Locally purified tensor networks (LPTNs) had the best scaling in the example of the finite temperature states of the quantum Ising model. For the dissipative dynamics of an exciton, we found MPDOs as the optimal solution due to the low entanglement throughout the simulation. When the entanglement generated during the time evolution exhausts the maximal bond dimension as observed in the Bose-Hubbard double well, quantum trajectories (QTs) became a good alternative to MPDOs.

The examples also show the problem sizes one can treat with the OSMPS package. The finite temperature states via imaginary time evolution and TEBD can treat almost as many sites as imaginary time evolution with MPS can, i.e., finding the ground state. In detail, we compared the thermal states for $L = 100$ sites. Changing the local dimension or the final temperature can increase the computational scaling away from the MPS case; the number of time steps necessary scales inversely with the final temperature at a fixed time step in the evolution. CPU times on the order of 1000 seconds on a cluster did not reach the limits of the method.

The exciton dynamics represents an example which does not generate much entanglement during the evolution, and the simulation stays below 100 seconds on an HPC cluster, given the best choice of the method being TEBD with MPDOs. This system is evolved for 30 time units of the local potential with 600 time steps and 80 sites. Bond dimension is not exhausted in the example, where the maximum is set to 512. Admittedly, this system can be scaled up more for research, which was prevented in our case due to the exploration of the methods not scaling favorably.

In contrast, the double well simulation shows the effect of entanglement generated during the time evolution and preventing more precise simulations of larger systems. We have 21 sites with 10 bosons and a local dimension of 4. The MPDO simulations produce visible

errors beginning at time 10 in the units of the tunneling at a bond dimension of $\chi = 256$. The dissipative Bose-Hubbard model with two-site Lindblad operators using TEBD-MPDO follows the same direction with limited system sizes and further restriction with regards to quantum trajectories and the construction of MPOs.

However, we strongly emphasize that each of the examples presented handles system sizes which are well beyond the means of exact diagonalization and, therefore, tensor networks are a very fruitful possibility to numerically explore these systems in the open quantum dynamics context.

These studies underline the necessity to explore different methods for the simulation of density matrices with tensor networks and choose the most suitable method for pushing the limits in each case. We have presented useful case studies with the quantum Ising model at finite temperature, dissipative exciton dynamics, and the open quantum system Bose-Hubbard modeling a double well with dephasing. Each of them could be a starting point for more extensive studies or serve as a blueprint to study other models, e.g., finite temperature diagrams of other spin models of the XYZ class.

Evidently, tensor network methods have to evolve past the Markovian case of the Lindblad master equation. The development of methods within the tensor network algorithms to capture such non-Markovian effects is one future direction in the design of new methods.

10.7 Acknowledgments

We gratefully appreciate contributions from and discussions with D. Alcala, I. de Vega, M. T. Lusk, G. Shchedrin, and M. L. Wall. This work has been supported by the AFOSR under grant FA9550-14-1-0287, and the NSF under the grants PHY-1520915 and OAC-1740130. We acknowledge support of the U.K. Engineering and Physical Sciences Research Council (EPSRC) through the "Quantum Science with Ultracold Molecules" Programme (Grant No. EP/P01058X/1). The calculations were carried out using the high performance computing resources provided by the Golden Energy Computing Organization at the Colorado School of Mines. S.M. gratefully acknowledges the support of the DFG via a Heisenberg fellowship

and the TWITTER project.

10.8 Non-Local Lindblad operators with symmetry (MPDO)

We discuss the case of a non-local Lindblad operator acting on two neighboring sites and explain the challenges such equations face. The Lindblad operators conserve the number of bosons. We choose as a Hamiltonian the Bose-Hubbard model, but in contrast to Eq. (10.35) we do not have an on-site potential,

$$H = -J\sum_{k=1}^{L-1}\left(b_k^\dagger b_{k+1} + h.c.\right) + \frac{U}{2}\sum_{k=1}^{L} n_k(n_k-1)\,. \tag{10.35}$$

J sets the tunneling strength and the repulsive on-site interaction is U. b_k ($b_k^\dagger$) is the bosonic annihilation (creation) operator acting on site k. The Hamiltonian conserves the number of bosons, i.e., the commutator $[H, N] = 0$ with $N = \sum_{k=1}^{L} n_k$. The chemical potential, i.e., $\mu\sum_{k=1}^{L} n_k$ can be discarded in simulations with number conservation; it represents an energy shift without influence on the simulation. The dissipative state preparation for the Bose-Hubbard model is the focus of the references [287, 288] and further discussed in [278, 289]. We use the Lindblad operators from these approaches, i.e.,

$$L_k = \left(b_k^\dagger + b_{k+1}^\dagger\right)(b_k - b_{k+1})\,, \quad k \in \{1,\ldots,(L-1)\}\,. \tag{10.36}$$

This formulation is not directly suitable for any of our Lindblad rule sets. In fact, the two-site operator is not a product term and is therefore challenging. We recall that a Lindblad operator of the type $L = A + B$ cannot be split into two Lindblad operators $L_A = A$ and $L_B = B$; a look at the corresponding terms of $L\rho L^\dagger$ reveals the missing cross-terms. Thus, we create a new type of rule set which is similar to the many-body string Lindblad operators, but allows us to define different operators for the operators on the left and right:

$$L_{A,k\cdots k'}\rho L^\dagger_{B,k\cdots k'} - \frac{1}{2}\left\{L^\dagger_{B,k\cdots k'}L_{A,k\cdots k'},\rho\right\}, \tag{10.37}$$

$$L_{A,k\cdots k'} = L_{A,k}\otimes L_{A,k+1}\otimes\cdots\otimes L_{A,k'}, \tag{10.38}$$

$$L_{B,k\cdots k'} = L_{B,k}\otimes L_{B,k+1}\otimes\cdots\otimes L_{B,k'}. \tag{10.39}$$

Now, we can define the following set of Lindblad operators L_μ

$$\begin{aligned}
L_{\mu=1,k} &= n_k\,; \quad L_{\mu=2,A,k} = n_k\,, L_{\mu=2,B,k} = -b^\dagger_k b_{k+1}\,;\\
L_{\mu=3,A,k} &= n_k\,, L_{\mu=3,B,k} = b_k b^\dagger_{k+1}\,; \quad L_{\mu=4,A,k} = n_k\,, L_{\mu=4,B,k} = -n_{k+1}\,;\\
L_{\mu=5,A,k} &= -b^\dagger_k b_{k+1}\,, L_{\mu=5,B,k} = n_k\,; \quad L_{\mu=6,A,k} = -b^\dagger_k b_{k+1}\,, L_{\mu=6,B,k} = -b^\dagger_k b_{k+1}\,;\\
L_{\mu=7,A,k} &= -b^\dagger_k b_{k+1}\,, L_{\mu=7,B,k} = b_k b^\dagger_{k+1}\,; \quad L_{\mu=8,A,k} = -b^\dagger_k b_{k+1}\,, L_{\mu=8,B,k} = -n_{k+1}\,;\\
L_{\mu=9,A,k} &= b_k b^\dagger_{k+1}\,, L_{\mu=9,B,k} = n_k\,; \quad L_{\mu=10,A,k} = b_k b^\dagger_{k+1}\,, L_{\mu=10,B,k} = -b^\dagger_k b_{k+1}\,;\\
L_{\mu=11,A,k} &= b_k b^\dagger_{k+1}\,, L_{\mu=11,B,k} = b_k b^\dagger_{k+1}\,; \quad L_{\mu=12,A,k} = b_k b^\dagger_{k+1}\,, L_{\mu=12,B,k} = -n_{k+1}\,;\\
L_{\mu=13,A,k} &= n_{k+1}\,, L_{\mu=13,B,k} = n_k\,; \quad L_{\mu=14,A,k} = n_{k+1}\,, L_{\mu=14,B,k} = -b^\dagger_k b_{k+1}\,;\\
L_{\mu=15,A,k} &= n_{k+1}\,, L_{\mu=15,B,k} = b_k b^\dagger_{k+1}\,; \quad L_{\mu=16,k} = n_{k+1}\,.
\end{aligned} \tag{10.40}$$

The representation of this set of Lindblad operators together with the Hamiltonian in an MPO is not recommended. We have a bond dimension of 48 (2 for local terms, 4 for tunneling in the Hamiltonian, 3×14 for the nearest-neighbor Lindblad terms). From the perspective of this bond dimension, only TEBD remains as a valid option for time evolution with MPDOs. QTs have problems due to the different terms $L_{A,k\cdots k'}$ and $L_{B,k\cdots k'}$. Therefore, extension of the QTs to Lindblad operators with no convenient representation in terms of rule sets, such as the example in Eq. (10.36), are convenient and considered for the future.

The coupling of the single-site Lindblad operator n_k is a function of the lattice site; the two boundary sites have only half the coupling of the bulk. We point out that each of the terms conserves the number of bosons in the system and thus the Liouville operator commutes with the global number operator N, i.e., $\left[\mathcal{L}, N\otimes\mathbb{I} + 1\otimes N^T\right] = 0$. We defined this condition in Eq. (10.7).

For the simulation, we start in the ground state of the Bose-Hubbard model in the Mott insulating phase at unit filling. The BKT transition is around $J/U \approx 0.305$ [290] in the

thermodynamic limit. We choose $J = 0.1$ and $U = 1.0$ is the energy scale. At $t = 0$, we couple the system to the reservoir with the Lindblad operators defined in Eq. (10.37). We define the depletion as $\xi = 1 - \max_i(\Xi_i) / \sum_i \Xi_i$ with Ξ_i being the eigenvalues of the single-particle density matrix $\langle b_k^\dagger b_{k'} \rangle$. The depletion decreases for the superfluid as compared to the Mott insulator when dealing with ground states.

Figure 10.8(a) describes the evolution of the depletion towards the steady state. We choose a system size of $L = 20$ and consider states up to two bosons; we have a local dimension of $d = 3$. The data is for a bond dimension of $\chi = 256$. The steady state differs for the coupling strengths $\gamma = 0.01, 0.05, 0.1$ and has a lower depletion for stronger coupling to the reservoir. We now look at the convergence of the different methods; unfortunately, we are not aware of a good observable to check as we had with the exponential decay in the exciton example. Thus, we compare between the exact diagonalization implementation and the tensor network algorithms in Figure 10.8(b). We consider a system size of $L = 5$ due to the restriction of simulation a system in Liouville space with exact diagonalization methods. We obtain that the value of the depletion is converged at the order of 10^{-3} where the value of the depletion is on the order of one. The bond dimension for the MPDO simulation is $\chi = 100$.

We conclude that the simulation of Lindblad operators acting on multiple sites is possible. For such operators which cannot be represented as product term, the simulation can get expensive to infeasible when MPOs and the corresponding time evolution method are used. The TEBD algorithm, as shown in this example, is the most convenenient alternative for such system dealing only with nearest-neighbor interactions. We recall that TEBD is restricted to nearest-neighbor terms in OSMPS.

10.9 Bond dimension infinite-T Bose-Hubbard state

We derive an upper bound for the bond dimension of the Bose-Hubbard model in an MPDO for the infinite temperature states. We assume that we have a local dimension d and a filling of N particles. We pick L sufficiently large such that $d \ll L$ and $N \approx L$. We pick a

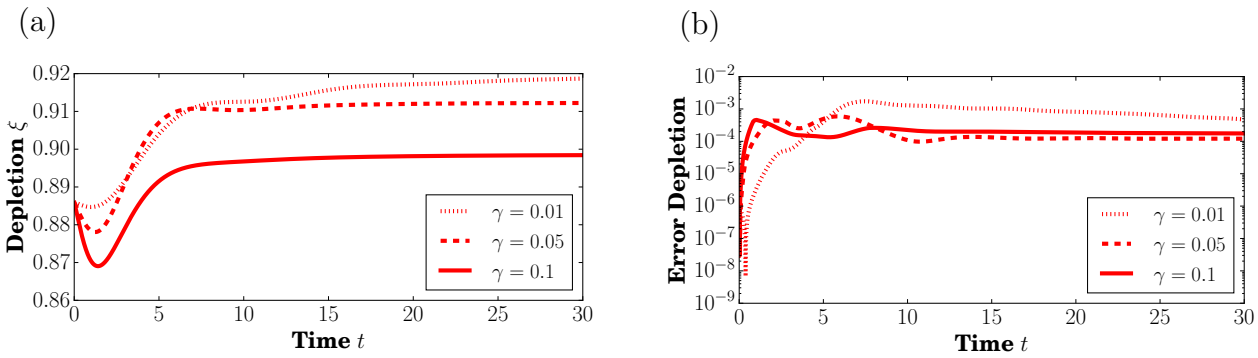

Figure 10.8: *Non-local Lindblads with the Bose-Hubbard model.* (a) The dynamics of the depletion converging to the steady-state value with a two-site nearest-neighbor Lindblad operator. (b) We calculate the dynamics for a small system $L = 5$ with exact diagonalization and TEBD and show the error of the TEBD as compared to exact diagonalization for the depletion with three different coupling strenghts γ.

site in the middle of the system and obtain $N+1$ blocks in the block-diagonal structure. The first d blocks have bond dimensions $1, 2, \ldots, d$ and the last d blocks have bond dimensions $d, d-1, \ldots, 2, 1$. The remaining fillings have a bond dimension of d. Thus, we have a total number of subtensors

$$n \quad = \quad d(N - 2d + 1) + d(d + 1) = d(N - d + 2)\,, \tag{10.41}$$

where the number of subtensors can serve as an upper bound to estimate the bond dimension χ, i.e., $\chi \leq n$.

CHAPTER 11

SOFTWARE CONSIDERATIONS

This chapter highlights the changes in the second and third release of the *Open Source Matrix Product States* simulation package and explain how they support physics and good coding practice. Moreover, we point out future directions for the package through a science gateway, which will be especially amenable to the large community of quantum simulation experimentalists as well as students, and other newcomers to the field. Projects as described in [291] show that such projects can be made accessible to cititize scientists.

The first release of OSMPS was developed by Michael L. Wall during his Ph.D. thesis and development continued thereafter [292], see also reference [121]. Several methods included in the second release are also based on his efforts and therefore not included in the list of the developments in the next Section 11.1. These developments include the time evolution methods with the time-dependent variational principle, the Krylov time-evolving block decimation, and the local Runge-Kutta time evolution method for closed systems, which were added in the second release. The implementations described in the following sections are based on the first release.

11.1 Second release of openMPS

The checkpoints added in the second release provide an essential feature for the time-evolution of quantum systems. The length of jobs on many computer clusters is limited. To converge simulations in system size or bond dimension, it is very useful to run simulations beyond this time limit. The checkpoints in the second release save the state of the MPS at every measurement during the time evolution. They also write the last measurement reached to a file. This information can be used to pick up simulations at the same point later. Except from setting a flag in python to allow OSMPS to use this feature, checkpoints

are completely handled in Fortran. Therefore, we have to iterate through all couplings of the MPO before picking up the time evolution at the last measurement.

The first release had the possibility to use the $\mathcal{U}(1)$ symmetry, which is present in many models, e.g., in the Bose-Hubbard model or the bilinear biquadratic spin-one model. Models such as the quantum Ising model profit from a $\mathbb{Z}_2$ symmetry, which we added in the second release. As both symmetries are Abelian, the $\mathbb{Z}_2$ can reuse some subroutines from the $\mathcal{U}(1)$ symmetry. The actual group operations are changed. Although the computational benefit is much smaller as the number of symmetry sectors is only two, this symmetry helps to capture physics better. The best example is the quantum Ising model where the ground state is now well defined in the ferromagnetic phase and is not a linear combination of the two almost degenerate states. The access to excited states is improved as well, as we can distinguish the excited states according to their symmetry sector. For example, the characterization of the gap in the quantum Ising model without symmetry needs to calculate the ground state and two excited states. With symmetry, the ground state and the first excited state are sufficient.

Furthermore, the second release has access to complex operators in the Hamiltonian. The implementation of complex operators is mainly a question of providing the additional interfaces and taking daggered operators instead of transposed operators whenever necessary. Complex operators are of interest in Bose-Hubbard type models with a phase in the hopping term or spin models with an external field coupling in the y-direction. As a side note, interaction terms of the type $\sigma_k^y \sigma_{k+1}^y$ can be mapped to real operators and do not necessarily require complex operators.

The calling structure to contractions and decompositions was improved from the first to the second release. Although matrix-matrix multiplication and matrix decompositions are defined on matrices, the underlying LAPACK libraries do require one to pass a rank-2 object. Such subroutines operate purely based on the knowledge of the leading dimension, the number of rows, and the number of columns. The first release did not profit from

this freedom in many cases and copied rank-3 or rank-4 tensors to matrices before calling LAPACK routines. Avoiding these steps of reshaping tensors and copying them helps to optimize run times.

We take a look at the run times of the second release of OSMPS in comparison to the first release to underline the effect of some of the improvements. The results are shown in Table 11.1. We limit ourselves to the time for the ground state, the correlations, and one time evolution. For the ground state search we state an approximate speedup of 1.15 in v2. The measurement $\mathcal{C}$ has as well improved, which becomes especially visible for larger system sizes, e.g. with a speedup of 3.84 for $L = 40$ and $\chi = 30$ due to small improvements in the algorithm. The Krylov time propagation seems to get slower, but for largest systems and bond dimension considered, we have a speedup in comparison to v1 of OSMPS. We remark that some bugs from v1 have been fixed by us in order to be able to run these comparison.[1]

Table 11.1: *Comparison between OSMPS v1 and v2* for the statics, measurements, and dynamics of the Bose-Hubbard model with number conservation. Three different system sizes and two bond dimensions show the trends that v2 improved. v1 was developed in the Ph.D. thesis of Michael. L. Wall [121, 292]. The improvements for v2 discussed in this table are based on work for this thesis.

Version / Size	$\psi_0(\chi_{30})$	$\mathcal{C}(\chi_{30})$	$\psi(T)(\chi_{30})$	$\psi_0(\chi_{60})$	$\mathcal{C}(\chi_{60})$	$\psi(T)(\chi_{60})$
v1, $L = 10$	4.3	$1.1 \cdot 10^{-2}$	3535	4.0	$1.1 \cdot 10^{-2}$	7301
v2, $L = 10$	3.8	$1.0 \cdot 10^{-2}$	4429	3.5	$1.0 \cdot 10^{-2}$	8491
v1, $L = 20$	14	$6.8 \cdot 10^{-2}$	11926	13	$7.6 \cdot 10^{-2}$	37770
v2, $L = 20$	12	$3.5 \cdot 10^{-2}$	19186	11	$3.8 \cdot 10^{-2}$	49510
v1, $L = 40$	34	0.5	27385	30	0.58	145036
v2, $L = 40$	29	0.13	57413	25	0.15	125710

11.2 Third release of openMPS

The third release comes with a re-design of the structure of OSMPS. These improvements allow us to develop new functionality faster and implement extensions easier. In the

[1] MPOOps_include.f90, line 74, initialize `H%ti = .true.`, qTensors_include.f90, line 184, `tmphash(1:V%N)=V%hash(:V%n)`, and TimeEvolutionOps_include.f90, line 255, `if(j > nkrylov) j = nkrylov`

following, we describe the different features improved for the third release, i.e., templating, error tracking, tensor handling, and documentation from source code.

The templates have been a very convenient feature from the first release on. They allow developers to generate functions for different data types at a low cost. For example, the multiplication of a real scalar with a real or complex matrix is basically the same. One template takes care of both implementations. The corresponding interfaces in fortran are used to call the subroutine independent of the actual data type; fortran will select the right implementation for the corresponding data type. The major issue with the approach taken for release one is that the rules for replacing the data type were applied to complete files; replacements for construction interfaces are constructed for a complete module. We have often been confronted with the implementation of such subroutines just to comply with the replacement defined in a global rule. Thus, the approach in the third release is the definition of the replacement rules ahead of each function. The interfaces can be defined immediately after the function. This step allows us to have direct access to change the function in one file without modifying global rules. All implementations of subroutines and functions can now go into one file; previously, we had one file for contractions of ordinary tensors and one file for contractions of tensors with symmetries.

This approach reduces the templates files to `MODULE_templates.f90`, `MODULE_types_templates.f90`, and `MODULE_include.f90`. The first contains the general structure of any Fortran module, the second the definition of types, the last all functions and subroutines. We profit from this simplified structure to add more functionality to the templating in the forms of `MODULE_tests.f90`, `MODULE_mpi.f90`, and `MODULE_omp.f90`. These additions are not required to run OSMPS, but contain additional features such as MPI implementation of functions, openMP implementations, or tests for subroutines. The final goal is to switch these options on and off depending on the compiler flags passed to OSMPS. The current MPI data parallelism implementation can be seen as a prototype toward parallelization of single simulations in the future development of OSMPS as a release v4.

Another issue with fortran in general, and amplified due to the template structure in OSMPS, is error tracking. (a) It is difficult to raise errors and propagate errors in Fortran. (b) If we get the line number of an error during compiling or run-time, the line number refers to the module built from the template, and not the template itself. We suggest the use of an optional argument `errstat` containing the current error status of the program. Using the new functions `raise_error` and `propagate_error`, we can track errors up to main function during execution of the program. Using above templates with the functionality to replace keys, both functions accept the key `LINE_ID`, which will be replaced with the name of the template file and the line number. Thus, errors can be directly tracked back to the template file. This approach cannot be used for line numbers generated for errors raised by the compiler. For such errors, we use python dictionaries to find the corresponding line in the template file. This replacement is done automatically when calling `python BuildOSMPS.py`. The error tracking can be turned off if performance is considered an issue.

The definitions of tensors in the first and second release depends on the rank of the tensor, and is limited to rank four. This approach is halfway efficient thanks to the templates, but the third release takes a new approach to have a more versatile toolbox for tensor network algorithms in the future: we define an arbitrary rank tensor. Some experience for this approach is based on previous work [87]. The price for this step is the mapping from the linear memory, before the dimensions could be addressed directly, back and forth. Thus, we mainly updated permutation of indices, reading, writing, and specific contractions. The contractions follow this new approach. We can replace endless specific cases of contractions with basically one subroutine handling the contraction, which is much easier to optimize. The prefered scheme is now a possible permutation to arange indices followed by a call to LAPACK for the actual contraction. Contractions which still have an overhead can be optimized in addition, as the contraction of a small rank-2 tensor to an interior index of a large tensor. Similarly, decompositions are now defined for an arbitrary tensor and a bipartition of the links.

The contractions for tensors with symmetries also have a slightly modified implementation. Up through the second release, the matching sub-tensors were contracted once a matching hash from the symmetries appears. We have replaced this approach with a two-step process. First, we find all matching sub-tensors. Then, we contract them. The second step can now be done in parallel with openMP or MPI, although not currently used.

Moreover, we have continued an effort to generate the documentation for subroutines and functions in Fortran and Python from source code wherever possible. The corresponding result compiled into an html page can be found for the second release on [293].

Some features found their way into the new release such as the imaginary time evolution for an MPS, which comes almost for free once the MPDO can be evolved in imaginary time evolution. At present, the implementation for excited states is untested. The infinite Matrix Product States (iMPS) are not available due to multiple issues with the modified interfaces. The full transition of lost features from v2 such as the excited state search and iMPS presents a subject toward a release v4 in the future.

11.3 Building a sustainable science gateway for openMPS

The effort of building a science gateway, i.e., a web interface to the Open Source Matrix Product States, is the next step to provide a convenient set of numerical tools for the community of quantum simulator experiments and theorists. Science gateways help as a cloud resource to move software packages away from the aura of computational experts to tools accessible and usable for everyone. Specific features can foster the sharing of research data among a research group and the whole community. Imagine you have a "dropbox" to share your complete quantum simulations, including the data, online. In the following paragraphs, we describe basic business considerations for a sustainable science gateway to the OSMPS simulation software as released in v3; these considerations help to estimate how such a science gateway can eventually continue to operate independent of NSF funding. The selection of topics and the majority of ideas go back to the *Incubator Bootcamp* organized by the *Science Gateways Community Institute*.

11.3.1 Sustainabilty is entangled with relevance

The projects in the Carr Theoretical Physics Research Group have received multiple grants to develop the numerical software from the openTEBD project over the openMPS project to the new science gateway encapsulating the openMPS package in a more accessible way. In an evolving science landscape, it is in the interest of the NSF to fund novel research and help existing projects to get independent financial resources as well as in the interest of each project to acquire additional financial sources to diversify their funding. In order to make these steps to alternative funding sources requires even more than an NSF proposal to carve out the relevance for the user and other stakeholders to make the project essential and valuable those groups. Sustainability will target all stakeholders to secure the resources necessary for maintaining or moving forward the project. Within the next chapters, we highlight multiple aspects of achieving sustainability with basic business techniques. These discussions include the identification of the user base and stakeholders and continue with developing the market landscape of existing and possible future competitors. We evaluate different revenues models in the following, relating them to successful models used in the past for science gateways. Based on the revenue models, we can develop a budget targeting our openMPS gateway. Finally, we visit important issues such as usability, the technology landscape, and marketing.

11.3.2 User base

Knowing the potential user base for our science gateway lays the foundation for most of the subsequent steps in our analysis. We split the users into two main groups. First, we identify users targeted in the near future. Then, we outline a future user base. For each of these users, we develop a value proposition, which we use later on as reminder to develop the other topics. Furthermore, we outline here key attributes of these user groups such as their size, possible ways of addressing them.

"*The openMPS science gateway will help experimental quantum physicists to simulate their quantum simulator numerically by accessing a tunable web application with platform specific pre-settings.*"

Our first user group is the actual physicists running the quantum simulator experiments. A very conservative lower bound on the number of experiments is about 200 based on the Toronto list [294] of quantum simulator experiments across a variety of AMO (atomic molecular optical) platforms. This list does not include other types of architectures such as superconducting qubits, and we estime that 300 research groups working on all different platforms is a reaonable guess. With the current programs launched for quantum technologies in Eurore, China, and the US, this number is expected to grow further. Assuming approximately five researchers per experiment, we have a potential number of 1,500 customers. We expect these users to be staff researchers, post-doctoral researchers, graduate students, and possibly undergraduate students. The best way to reach them are tutorials at large conferences.

"*The openMPS science gateway will help PIs of quantum simulator experiments to provide their groups a transparent, state-of-the-art tool via a web application actively supporting sharing results within collaborations.*"

The group of PIs is closely linked to the previous group. As a group PI, this group is unlikely to use the actual software to simulate many-body quantum systems. For us they serve as excellent multipliers to spread the word around their research groups, as well as potential sources of funding, see Section 11.3.5 below. Due to their small number, i.e., approximately 300, personal contact or email would be a manageable effort.

"*The openMPS science gateway will help theoretical quantum physicists to verify their analytical or numerical results by providing an open source numerical simulation package plus an accessible web interface, both closely linked.*"

The group of theoretical physicists is partly already covered with the actual open source package. If they want a validation of analytical results or a benchmarking of their own numerical results, the openMPS science gateway can comply with this goal. The close

connection to the underlying openMPS simulation package encourages and allows users to learn, verify, and adapt the underlying algorithms. Therefore, they represent for us not only potential users, but also potential contributors to the code base. We can target these researchers with actual publications on the algorithms or our simulation package or more technical talks at conferences.

"*The openMPS science gateway will help students to learn and simulate many-body quantum systems present in recent research by providing an online platform supplementary to their quantum mechanics course and at a user-selected speed.*"

The group of students is huge in comparison to the previous user groups. According to data from the American Physical Society (APS), there are around 8,000 undergraduate students in their last year in 2015 in the US alone [295]. Assuming that the material is accessible for undergraduate students in the last two years of their degree, we have 16,000 US undergraduate students. Assuming, that 25% continue as graduate students in physics and look in their first year into our science gateway, we have an additional 2,000 potential users. In the US, the undergraduate and graduate students add up to 20,000. As an educated guess, we assume that the US has around one third of the physics students; world-wide 60,000 potential students could use our science gateway. The best way to address them seems to be online tutorials and course-like online material. Our benefit is that they represent potential future users doing theory or experiments and are then already familiarized with our fashion of approaching many-body quantum systems.

"*The openMPS science gateway will help physics faculty to integrate many-body quantum physics into their coursework by providing resources and material independent from the HPC resources available at their campus and without the requirement to set up these systems.*"

The faculty teaching quantum mechanics at a university is the counterpart of the previous group. The faculty acts another time as a multiplier: if they are using our science gateway for course work, their students are already familiar with our approach and more likely to reuse it in case they continue to do research. According to the APS [296], there are about 760

institutions in the US granting any kind of physics degree. Assuming at least one course of quantum mechanics is offered and the US amounts to one third of the institutions worldwide, we have approximately 2,000 faculty each year. The challenge for this group is to provide material through the science gateway which can be integrated seamlessly into their course work.

So far, we have outlined the users involved with quantum physics. Looking further into the future, we can list more groups: (i) Closely related to the question of open quantum systems, electronic transport problems could build another user group labeled by nano-electronic applications. (ii) Bio-physics is another possible long-term goal for our science gateway. Biological, and within here mostly molecular, processes which take place at very small length scale might be affected by quantum mechanical effects, e.g., as pointed out for photosynthesis. Including explicit features to address these problems can broaden the user base of the openMPS gateway.

11.3.3 Stakeholders

Another important aspect of any science gateway is to emphasize the value of the project to any stakeholder. In the following, we provide a list of stakeholders involved in our projects. (i) The National Science Foundation (NSF) is providing the initial funding to develop the science gateway and might be a partial funding source to add new features after this. (ii) The Science Gateway Community Institute supports the project through their services offered. (iii) The Colorado School of Mines (CSM), and especially the physics department, offer their administrative infrastructure and financial support. In return, they expect the project to impact the perception of the school and department in a positive way. (iv) The high-performance computing (HPC) group and Computing, Communications, and Information Technologies (CCIT) department at CSM are two additional stakeholders within the institution. The interaction with the stakeholders could be intensified by initiating an advisory board representing each group and involving them actively into major decisions for the gateway.

11.3.4 Market landscape

The evaluation of the market landscape has a two-fold purpose. On the one hand, we identify all possible solutions, which can replace our science gateway. On the other hand, we take the same perspective for the underlying numerical algorithms. Then, we continue to list the market drivers important to the potential users. This step finally leads to the market landscape and the identification of our position within it.

11.3.5 Revenue models

We collect different revenue models and outline their basic idea in the context of the openMPS science gateway. We choose a set of the most promising approaches and plug in numbers in order to estimate their actual revenue. Throughout the process, we can generate ideas from sustainability models successfully followed by other science gateways, identified by the Science Gateways Community Institute.

(1) The first group of possible income is to charge the user directly. This model can be implemented either through a subscription for all features or a free account with basic features, where more advanced features are only available to subscribed users. Many users might consider the subscription model in contrast to the open source model we run for the underlying model. The acceptance for a complete subscription might therefore be low. A basic and premium account imposes the question, which additional services are worth a subscription fee. We consider here additional CPU time to run larger simulations or collaboration features to share simulations across users.

(2) Another approach is to target universities or research groups for the charge. For example, a university cluster could be added to the possible list of clusters for a list of users. This approach would allow these users to run on their resources independent from CPU time limits given in our gateway. As this approach requires some initial setup, a one-time installation fee and a yearly subscription fee are justified. In case the subscription is not renewed, the clusters can be removed from the list for these users. Also, model (1) could

be designed towards research groups where additional resources can be bought for a set of users instead of single users. The two approaches cover together users with their own HPC infrastructure and users who do not have access to their own HPC facilities.

(3) Licensing fees are another possible source of income. As the underlying openMPS package is released as open source, the licensing is restricted to the actual science gateway. A license would allow a university or research group to install the gateway on their own infrastructure with their own computational resources. While the maintenance of the complete server infrastructure might be an obstacle for many possible customers, tracking the licenses and ensuring that they are not used after the licensing period ended are a major headache to us. From this perspective, the previous solution to add private resources seems preferable.

(4) We can offer consulting services, i.e., workshops running over a few days to introduce to the gateway, its methods, and the underlying features to simulate many-body quantum systems. This would be an event specific fee excluding travel cost.

(5) A donation model is not very likely to work in a market environment with a rather small user base. The endowment model, as practiced for Stanford Encyclopedia of Philosophy, requires some large set of stakeholders benefitting from the investment in one fashion or another. Replacing the many donors by a few or single donors to build up the endowment is difficult to plan, but would most likely rely on private industry having an interest in the further development of our platform. As quantum simulators and quantum computing spreads from academia into industry with major companies such as Google, Microsoft, and IBM investing in these technologies, we consider this option as possible in the near-term future.

(6) The advertisement based income streams have a limited potential. The number of site visitors is negligible for the integration of GoogleAds or similar services. A cooperation with an industry partner could be more valuable, although the investment might depend more on the interest of the partner in the project than on the value of generating new customers.

At present, we consider models (2) and (4) as the most promising approaches, with (5) as another promising option to diversify our income model depending on the upcoming development in the quantum industry. For the access to a personal cluster we estimate a one-time charge of $1K for the initial setup and a subscription fee of $100 per year. Assuming that we have generated already a sufficiently large user base out of the 170 quantum experiment groups during the first three years supported by NSF, we estimate that four groups will add one of their clusters each year as an additional resource. Then, this model generates $4.4K income in the first year. If we offer in addition packages of additional node hours for research groups, we have to consider these, too. One node costs approximately $10K and can be used 8.700h per year. If we want to get back the investment within a year at 100% usage, we have to charge around $1.15/node-hour. This very coarse estimate does not include power consumption, which is $0.05 for one node hour according to our HPC group, and not a major factor. Comparing it to commercial offers at $0.08/CPU-hour (penguincomputing), this estimate is in a good range, where new nodes have 28 CPU cores or more. If we offer packages of 500 node hours at $575 and sell four of them during the first year, we generate another $2.3K income. If we look at approach (4), we have to estimate on the one hand how many days per year we offer training. Five days per year seems to be a conservative estimate, e.g., one two-day and one three-day workshop. On the other hand, we need the charge per seminar-day. We assume $1.1K is a reasonable amount. To simplify the approach, that does not include potential travel or housing costs, which have to be covered in addition to the $1.1K per day. Therefore, the consulting adds up to $5.5K per year. In summary, we generate $12.3K income from three different models.

11.3.6 Budgeting

The question of budgeting is an essential question for the sustainability. The overall focus should be what is necessary to keep the gateway running, known as an action-based budget. We first outline the action necessary for the gateway, followed by putting together the actual items.

The minimum effort for the quantum simulator should keep the gateway up and running without any additional effort to implement new features and extend the user base. These minimal efforts can be considered as (i) one month of the PI to work on the administration and advertisement of the gateway. We can extract the approximate cost for this item from the current NSF proposal for the initial setup of the gateway. This estimate is about \$20K. (ii) 0.5 FTE of a graduate student, where the other half of the funding for the student could be from another funding source or as teaching assistant. We take the same approach and the cost is around \$25K based on the recent NSF proposal, including stipend, tuition, and fees. This item takes care of the maintenance of the gateway dealing with user requests, fixing bugs, and installing additional resources for the gateway as needed. The interaction with potential developers volunteering is included here. (iii) The third part is the technical equipment to host the gateway, which we include with \$2K. All three costs do not include the university overhead, which is approximately 50% for grants and 10% for other income. (iv) Support from the HPC department at Mines can be estimated with 100h/per year, which comes at present as service from the university. If we calculate 40\$/h, this support adds up to \$4K per year. (v) We want to foster the development effort in the community to integrate new features. Obtaining 100h of volunteer developing each year results in another \$4K of indirect support. Thus, the bare minimum is \$47K per year, where we profit according to the items above from services not charged of about \$8K.

Based on this minimal budget, we extend it with further issues allowing us extending the gateway. (vi) 0.5FTE of a graduate student to develop new features for the gateway. These features can be new models for novel experimental platforms or extending new aspects to the existing models. (vii) Costs for traveling to conferences such as national meetings on supercomputing taken from the NSF proposal to be \$4K. The ideal budget to maintain, improve, and grow our science gateway is \$76K per year and additional services not charged of the value of \$8K. We perceive the challenge associated with a sustainable model and take this conclusion as a motivation to investigate further sources of income in the future.

11.3.7 Usability

Studies of the usability are difficult at the current stage of the project. Therefore, we describe how to provide the best possible experience to users. Partially, we profit from our interactions with users of the OSMPS package. Reviewing their requests over the past years might give some guidance to common misconceptions we have when trying to understand our users. On the other hand, the pool of undergraduate and graduate students in the group not involved in the development of OSMPS or the science gateway can serve as advanced testers for an alpha version; they are all experienced with numerical tools. But the usability studies should be emphasized once the alpha version is available.

11.3.8 Technology landscape and security

The technology landscape is at present the vision of what we intend to implement. Major building blocks are the cluster we are using in addition to choosing the underlying software platforms. We recall that the initial cluster for our science gateway is *Mio*, which is maintained and managed by the HPC group of the Colorado School of Mines. This choice is due to the strong support from Mines to get dedicated nodes for the gateway on *Mio*. The access to this cluster is restricted to users on campus; in contrast, the science gateway must be accessible for all users on and off campus. Thus, we have one first characteristic of the landscape, which is the server hosting the gateway outside the Mines firewall, and on the other side of the firewall to *Mio*. The necessary libraries, programming languages, and compilers to run the simulations are available on this cluster, i.e., Python, Fortran, and LAPACK. The interface to our gateway is the only piece to be added.

We plan to use a combination of the Apache Airavata together with the airavata-django portal for the server side. The front end emphasizes the browser applications and we do not anticipate a desktop application in the near future. The advantage of this choice is from our perspective that django and OSMPS both are based on Python and interfaces between the science gateway and the underlying library might simplify. Moreover, large result files could

be stored in HDF5 file format in the future and Python provides support to access this file format.

The cybersecurity aspects can then be summarized so far. (i) We have to process user input, e.g., for user-defined functions for potentials or system size. Such functions have to be called in the following. This user input could be used for buffer overflow attacks or using function calls for the attack. (ii) Sensitive information on the server are access information to the computer clusters used for computation, such as *Mio*. This sensitive information also includes the user IDs including email addresses and hashed passwords. (iii) Less sensitive data are the code base of the science gateway itself and possible statistics generated while running the gateway. The same sensitivity includes results from simulations stored on the server or the associated files for generating the simulations.

11.3.9 Marketing

The marketing will be the final step after finishing the development of the gateway. We will focus on scientific users for the initial version of the gateway. Here, we can build on the strong background with two open source packages maintained in the Carr Theoretical Physics Research Group, i.e., openTEBD [97] and OSMPS [52] and various publications on numerical methods for these simulation packages and associated libraries [121, 189, 215] not including research using these methods. This reputation will allow the group to offer introductory courses at the APS March Meeting or the APS DAMOP Meeting, amongst other venues; each of them are attended by thousands of physicists. The other opportunity where we plan to offer an introduction to our science gateway is the workshop *Open Quantum System Dynamics: Quantum Simulators and Simulations Far From Equilibrium* organized by the Kavli Institute for Theoretical Physics and hosted in Spring 2019. These events are the opportunity to have direct interactions with users and improve future marketing based on this experience and the needs we learn about during these events.

11.3.10 Conclusions on the science gateway plan

We conclude this section on the science gateway with a short analysis of the strengths and weaknesses of the our science gateways as far as we can judge them at this preliminary stage. Weaknesses might be getting adequte growing resources in terms of CPU capacity on the local cluster. Therefore, we have to possibly plan to include further clusters into our gateway. Furthermore, the hosting of a server structure is not a key competence of a physics department and finding new physics students covering the range of skills from research to web development can be challenging.

Advantages of this layout of the science gateway are that the core functionality running the simulations has been available as a stand-alone package for the past nine years in one form or another. The strong ties and support from the host institution, i.e., the Colorado School of Mines, in terms of the dedicated nodes for the science gateway and the support from the HPC group at Mines is another key strength.

CHAPTER 12

CONCLUSIONS AND DISCUSSIONS

Finally, we conclude on the results of this thesis in Sec. 12.1 and summarize open research questions in Sec. 12.2. The first put the results of this work in context; the latter is a list of open questions.

12.1 Conclusions

This work contains state-of-the-art methods for numerical simulations of closed and open entangled quantum systems on a classical computer. These algorithms using tensor network methods are integrated into the existing simulation platform Open Source Matrix Product States, which represents a long-term effort to provide open source software to the community for the simulation of entangled many-body quantum systems. This package had over 2,000 downloads during the period of this thesis. The inclusion of the exact diagonalization methods as a playground for testing new methods and enabling advanced simulations not yet covered by tensor network methods was one milestone in the development cycle. The second milestone is the set of the three major tensor network algorithms to simulate the Lindblad master equation in one-dimensional systems and now available via our simulation platform.

Beyond multiple case-studies, e.g., exciton transport and the Bose-Hubbard double well, in the context of the numerical work, we exploit our software to analysis the Kibble-Zurek hypothesis in a quantum Ising chain with long-range interactions. The generation of defects during such a quench is closely related to adiabatic quantum computing quenching from a known initial state to the solution of an optimization problem. Systems with strong long-range interactions have an increased defect density in comparison to weaker long-range interactions in the case of the ferromagnetic quantum Ising model. The study of thermalization of a quantum system in contact with a thermal reservoir governed by the Lindblad

equation reveals thermalization timescales. These results can be used to protect from decoherence or enforce thermalization of the quantum Ising chain. The analysis emphasizes the need to explore scenarios beyond the single-site single-channel Lindblad operators, i.e., neighborhood single-channel and global multi-channel Lindblad operators. The concrete results of each chapter are listed in the following.

In detail, we showed in a thorough analysis the effects from long-range interactions in the static phase diagram as well as in the quenches through the quantum critical points, for both the ferromagnetic model and the antiferromagnetic model. The ferromagnetic and antiferromagnetic model show distinguishing features in the static phase diagram. Stronger long-range interactions support the ferromagnetic order and the necessary external field to break this order and transition to the paramagnetic phase becomes larger. In fact, the phase diagram predicts that there is no external field large enough to break the ferromagnetic order when the interactions reach $\alpha = 1$ or $1/r^\alpha = 1/r$ in the thermodynamic limit. The antiferromagnetic model is vastly different. The system is frustrated for the completely interacting limit $\alpha = 0$ as all spins try to anti-align with all other spins − an impossible task. Thus, very small external fields bring the system into a paramagnetic order. Then, we turn to the simulation of the dynamics of the finite size system quenching from the paramagnetic phase to the ferromagnetic and antiferromagnetic limit, respectively. The quenches evaluate the generation of defects and depend on the velocity of the quench. From there, we calculate the power-law exponents describing the density of defects. We observe a decreasing exponent for the ferromagnetic model with stronger long-range interactions. This trend means that more defects are generated for stronger long-range interactions. If we consider this finding with regards to adiabatic quantum computing, we suggest that experiments should stay close to the nearest-neighbor limit in the case of a choice. In contrast, the antiferromagnetic model shows a constant power law exponent for all α within the error bars. Overall, we observe the finite-size effects which lead to a deviation from the value predicted in the thermodynamic limit. For example, the power-law exponent describing the generation of defects for the

ferromagnetic model differs by ten percent from 1/2 for a system size $L = 128$.

The open system problem set in Chapter 5 gives first insights to open quantum systems and the necessary methods to understand them. The form of a problem set is an ideal choice and this chapter also represents the pedagogical part of this thesis. The study of the thermalization of a quantum Ising chain with a few qubits explores several aspects of thermalization and their description within open quantum systems, in detail with the Lindblad master equation. The understanding of the Lindblad equations and conditions for thermalization of a single multi-level system are feasible, but the transfer to many-body systems beyond the scope of calculating all eigenstates is non-trivial and an open research question. One question is therefore if we can find a consistent technique using, as we call them, neighborhood single-channel Lindblad operators. The answer to that question is that we thermalize the system with such operators in the two limits. The paramagnetic limit corresponds to a non-interacting model of isolated qubits and, thus, the question is reduced to thermalization of a single qubit. The neighborhood single-channel Lindblad operators spanning three sites are sufficient to thermalize the system in the ferromagnetic limit. Even a linear combination of these two solutions does not lead to thermalization between the two limits in the phase diagram. Nonetheless, or now even more, such neighborhood single-channel Lindblad operators remain a tempting goal. This fact becomes apparent when looking at the global multi-channel approach using all eigenstates of the system Hamiltonian, where the number of eigenstates grows exponentially with the number of particles in many-body systems. But the global multi-channel approach allows us to explore the process of thermalization within the Lindblad master equation. We observe different phenomena when choosing the operator in the interaction Hamiltonian such as a spin-flip. The thermalization becomes very slow towards the paramagnetic limit; in fact, the eigenstates and the spin-flip operator share a common basis of eigenstates, and the spin-flip operator cannot induce any change to the system. Apart from the paramagnetic limit, we find favorable system-reservoir configurations in the ferromagnetic regime of the quantum Ising model. The configuration

of a common reservoir shared by all spins and allowing for reservoir-mediated long-range interactions has infinitely long timescales for system size $L = 5$ due to a closing gap of the Liouville operator. This feature tells us that at least certain states are protected from decoherence. In contrast, spins each coupled to their independent local reservoir thermalize faster and keep the gap of the Liouville operator open. Thus, this configuration is favorable for preparing a state in the thermal state. Chapter 7 contains the details on the derivation of the Lindblad master equation used in Chapter 6. Although the derivation is a textbook example, its specific use adapted to the quantum Ising chain is important to present a complete picture with multi-channel Lindblad operators.

The different techniques presented in the exact diagonalization methods show how to push limits on a single core to a maximal number of qubits. The methods provide algorithms between a simple exact diagonalization code without any advanced features and the most recent highly specialized codes running for quantum circuits on distributed machines. One feature for Hamiltonian dynamics governed by the Schrödinger equation is the use of rule sets inspired by our many-body methods. These rule sets are the next level beyond sparse matrices for these problems. For a small system, we may store the complete Hamiltonian with all zeros; we can save a significant amount of memory when storing only non-zero elements and their indices for growing system size. Finally, we use just the rule for how to build the Hamiltonian on demand instead of ever building the actual matrix. For example, this information is sufficient to multiply the Hamiltonian with the state vector and use Krylov subspace methods. Such methods allow us to use Hamiltonians with long-range interactions. Each of the methods for the Schrödinger equation is translated into the case for the Lindblad master equation. The upper limit of particles which we can simulate with the Lindblad equation is half of the maximal number of particles of the Schrödinger equation. This part of the OSMPS simulation platform has served its purposes very well. These motivations are as follows. (i) The implementation of novel approaches served us to simulate quantum systems, e.g., the global multi-channel Lindblad operators in the thermalization study of

the quantum Ising spin chain. This possibility is very useful to explore new methods before moving them to the many-body scenario. (ii) We have an easy accessible verification for tensor network methods as both parts of the package are based on the same syntax to set up the system. We used the ED part of our package to evaluate the errors of open system evolution of MPDOs in the corresponding 10. (iii) The ED algorithms can serve as a learning platform for advanced undergraduate and graduate students familiarizing with the field. This approach is reflected in the usage of the package in the open quantum system problem set or during senior design projects to simulate transport in a quantum wire with the Lindblad master equation.

The principal novel results from the paper on the second release of the open source Matrix Product States are the error bounds obtained for the ground states of any system. These error bounds allow us to have a much better understanding of the accuracy of the algorithms for various observables knowing a few key values, i.e., the energy gap to the first excited state, the variance of the energy, and the system size. The error of the bond entropy, an entanglement measure, for the quantum Ising model is below 10^{-2} for 256 sites and clearly below 10^{-3} for 64 sites. These numbers show the influence of the system size and the closing energy gap for a larger system. Otherwise, the paper is directed at users searching for a description between the manual and more technical papers discussing the different tensor network methods. Thus, we show the parallel efficiency using the Message Passing Interface of above 91% for twelve or more cores while scanning a phase diagram and different system sizes, i.e., 1530 data points in total.

The tensor network algorithms for many-body open quantum systems yield different types of results. The tensor network theory gains additional insight into the advantage of different options to simulate mixed states via density matrices. Matrix product density operators, locally purified tensor networks, and quantum trajectories are for the first time united in one software package to our knowledge. A comparison is not biased because all methods rely on the same underlying modules for tensor operations. Although each

model and Hamiltonian might have different preferences, we can state the following trends. Locally purified tensor networks are preferable to generate thermal states via imaginary time evolution. Our example considered the quantum Ising model. Systems with low generation of entanglement during time evolution are very suitable for matrix product density operators; locally purified tensor networks are not preferable due to their loopy network structure. Quantum trajectories are an option if a large number of cores is available to distribute the trajectories. An example of such a system is the transport of excitons. Quantum trajectories are favorable for systems such as the Bose-Hubbard model when generating a high level of entanglement during the time evolution, where matrix product density operators suffer from a squared bond dimension when generating them from a matrix product state. Researchers interested in the simulation of many-body open quantum systems have a cookbook with three examples including the scaling for such simulations. We recall the case of the Lindblad operator $L = (b_k^\dagger + b_{k+1}^\dagger)(b_k - b_{k+1})$ which has an enormous bond dimension of 48 when representing the Liouville operator in comparison with a bond dimension of less than ten in the other examples. Such explanations help to develop an understanding of the numerical aspects for users without deep numerical expertise. The additional considerations with regards to our simulation platform in Chapter 11 complete the numerical aspects of this thesis. In detail, we discuss good coding practices and the efforts to build a science gateway for entangled quantum many-body systems.

In conclusion, this thesis provides an overview of a variety of methods to simulate quantum systems, which is essential for quantum simulators architectures. On the one hand, the numerical simulation on a classical computer may help to test different models, e.g., Hamiltonians and models for open quantum systems, and help with the optimization of these tools. On the other hand, there has been a huge effort to prove or disprove quantum advantage simulating systems of more than fifty qubits with quantum circuits. Although our tools are not equivalent to this intriguing question, they provide useful methods to compare with. Thus, we provide with our open source software relevant algorithms and simulations for to-

day's research questions and point out future directions in Sec. 12.2. We have investigated questions such as the Kibble-Zurek hypothesis under the influence of long-range interactions or the thermalization of a quantum system in various extensions of the standard Lindblad picture with these tools ourselves.

12.2 Outlook

The research discussed in this thesis raises many questions in physics which are beyond the scope of this work. Nonetheless, they are worthy of being pointed out and we motivate their investigation with a brief discussion.

Within closed quantum systems, many other models could be considered with long-range interaction as we did for the quantum Ising model. The nearest-neighbor interaction was a necessary approximation to use many-body simulations with time-evolving block decimation in the past, but adding effects from long range interaction might be necessary to keep up with experiments as they become more precise. The necessary time evolution methods for long-range interactions in tensor networks are well-established by now. The large community of researchers working on long-range physics, e.g., as present in ultracold molecules, appreciates such methods. The possible models to be studied include the extended Bose-Hubbard model, other spin-$\frac{1}{2}$ models of the XYZ family, and higher spin models such as the spin-one bilinear biquadratic model. Moreover, one may extend our studies to Fermi-Hubbard models.

There are multiple research questions accessible due to the extension of tensor networks to density matrices and open systems. We have briefly introduced the transport of excitons as an example to test the many-body open quantum system. This topic is an exciting question which could be explored further, either in more advanced Hamiltonians representing the exciton or looking at specific physical problems such as the interference of excitons or the loss of information in an exciton after traveling through a region with decoherence.

The quenches through the quantum critical studies in the long-range Ising chain can be repeated for an open system. The closed system is perfectly adiabatic for infinite quench times; thus, the final state of the quench is the ground state. If we couple the system to a

reservoir, infinitely slow quenches suffer from decoherence. Therefore, the investigation of the quench time minimizing the total number of defects from decoherence and non-adiabatic quenches is a necessary next step. The relevance of this research can be seen directly in context with adiabatic quantum computing. The finite temperature states via imaginary time evolution can be used to derive experimentally relevant phase diagrams, e.g., for the Bose-Hubbard model. These phase diagrams, although they cannot have a quantum phase transition in the strict $T = 0$ definition, may help to understand when a phase transition can be observed at finite temperature in an experiment. Furthermore, these finite-temperature states can be used as the initial state to study dynamics, e.g., the BKT transition of the Bose-Hubbard model. In addition, the understanding of the Kibble-Zurek hypothesis in a finite-temperature setting has unanswered questions itself. The dilemma in the finite temperature can be seen in the different energy spectrum at both sides of the quantum critical point; thus, an infinitely slow adiabatic quench will not produce the thermal state on the other side of the quantum critical point. On the other hand, quenching in a "forth-back" scheme allows us to recover the thermal state for a perfect adiabatic quench, but the forth quench introduces defects which affect the back quench.

The few qubit Ising chain has demonstrated how to thermalize a quantum system coupled to a reservoir in the limit of the Lindblad master equation. We may take this consideration as a starting point for many more research questions to be explored. These problems include the thermalization with other types of reservoirs than a three-dimensional electromagnetic field, and methods to include non-Markovian effects truncated in the Lindblad master equation. To extend these few qubit problems to many-body systems, we are still in search of local or quasi-local Lindblad operators leading to a thermalization of a general Hamiltonian. Such operators are more accessible to be used in matrix product operators than the current eigenstates of the Hamiltonian. Once these questions concerning the thermalization of a quantum system are resolved, research can move to systems with multiple degrees of freedom; each degree of freedom might be coupled to a reservoir at a different tempera-

ture. Examples for such systems are trapped ions including the motional and spin degrees of freedom and ultracold molecules with a huge set of rovibrational states. The latter can be cooled conveniently, but translational degrees of freedom of the molecules in the optical lattice remain at higher temperatures and cannot yet be cooled to the temperature of the rovibrational states.

If we consider the purely technical aspects of our work, further investigations on the optimal compression of a density matrix can be pursued in our current simulation software. There is an open question if matrix product density operators or locally purified tensor networks are the advantageous approach to represent density matrices of a quantum system. We have shown examples where either approach is favorable, so a further understanding, if there is an underlying theory, would be appreciated.

The development side of the OSMPS package contains many optional extensions which improve specific aspects of the code. These changes may target storage of results with the HDF5 file system and further parallelization schemes. With the new features implemented in the third release, we can work on openMP solutions, MPI parallelization for a single simulation instead of data parallelism, and an MPI/openMP hybrid solution. OpenMP is especially beneficial for simulations with symmetries as the block diagonal structure can be easily spread across cores. The possibility to accelerate tensor network simulations with GPUs is another option to be explored, for instance using openACC. While the parallelization of exact diagonalization can rely on standard implementations such as ScaLAPACK and we can profit from constructing all Lindblad operators in the multi-channel approach in parallel, tensor network methods have a higher barrier to overcome. We think here of the gauge essential to one-dimensional tensor networks such as matrix product states. Reinstalling this gauge requires a serial step iterating along the chain, which limits the serial efficiency in the limit of many cores. In the best scenario, we can use two cores for this procedure approaching the center site from the two ends. Parallel schemes are nonetheless available for time-evolving block decimation, which we have also explored for locally purified tensor

networks in a side project and the variational ground state search [297].

The inclusion of many default models for the science gateway is necessary to keep the online platform up to date with the most recent research. We suggest adding default models for modeling the most important types of quantum simulators, i.e., ultracold atoms, ultracold molecules, trapped ions, color vacancy centers, superconducting qubits, Rydberg systems, and integrated quantum optics.

REFERENCES CITED

[1] Elizabeth Gibney. Billion-euro boost for quantum tech. *Nature*, 523:426, Apr 2016. doi: 10.1038/nature.2016.19796.

[2] A. Acín, I. Bloch, H. Buhrman, T. Calarco, C. Eichler, J. Eisert, D. Esteve, N. Gisin, S. J. Glaser, F. Jelezko, S. Kuhr, M. Lewenstein, M. F. Riedel, P. O. Schmidt, R. Thew, A. Wallraff, I. Walmsley, and F. K. Wilhelm. The European Quantum Technologies Roadmap. *ArXiv e-prints 1712.03773*, Dec 2017. URL `https://arxiv.org/abs/1712.03773`.

[3] Max F. Riedel, Daniele Binosi, Rob Thew, and Tommaso Calarco. The european quantum technologies flagship programme. *Quantum Science and Technology*, 2(3):030501, 2017. doi: 10.1088/2058-9565/aa6aca. URL `http://stacks.iop.org/2058-9565/2/i=3/a=030501`.

[4] Stephen Chen. China building world's biggest quantum research facility, Sep 2017. URL `http://www.scmp.com/news/china/society/article/2110563/china-building-worlds-biggest-quantum-research-facility`. last visited April 14 2018.

[5] Elsa B. Kania. Is china seeking quantum surprise?, March 2018. URL `https://thebulletin.org/china-seeking-%E2%80%9Cquantum-surprise%E2%80%9D11552`. last visited April 14 2018.

[6] ID Quantique. URL `http://www.idquantique.com/`. last visited April 17 2017.

[7] Juan Yin, Yuan Cao, Yu-Huai Li, Sheng-Kai Liao, Liang Zhang, Ji-Gang Ren, Wen-Qi Cai, Wei-Yue Liu, Bo Li, Hui Dai, Guang-Bing Li, Qi-Ming Lu, Yun-Hong Gong, Yu Xu, Shuang-Lin Li, Feng-Zhi Li, Ya-Yun Yin, Zi-Qing Jiang, Ming Li, Jian-Jun Jia, Ge Ren, Dong He, Yi-Lin Zhou, Xiao-Xiang Zhang, Na Wang, Xiang Chang, Zhen-Cai Zhu, Nai-Le Liu, Yu-Ao Chen, Chao-Yang Lu, Rong Shu, Cheng-Zhi Peng, Jian-Yu Wang, and Jian-Wei Pan. Satellite-based entanglement distribution over 1200 kilometers. *Science*, 356(6343):1140–1144, 2017. ISSN 0036-8075. doi: 10.1126/science.aan3211. URL `http://science.sciencemag.org/content/356/6343/1140`.

[8] B. Hensen, H. Bernien, A. E. Dréau, A. Reiserer, N. Kalb, M. S. Blok, J. Ruitenberg, R. F. L. Vermeulen, R. N. Schouten, C. Abellán, W. Amaya, V. Pruneri, M. W. Mitchell, M. Markham, D. J. Twitchen, D. Elkouss, S. Wehner, T. H. Taminiau, and R. Hanson. Loophole-free Bell inequality violation using electron spins separated by 1.3 kilometres. *Nature*, 526:682, 10 2015. doi: 10.1038/nature15759. URL http://dx.doi.org/10.1038/nature15759.

[9] Peter W. Shor. Polynomial-Time Algorithms for Prime Factorization and Discrete Logarithms on a Quantum Computer. *SIAM Review*, 41(2):303–332, 1999. doi: 10.1137/S0036144598347011. URL http://dx.doi.org/10.1137/S0036144598347011.

[10] Lov K. Grover. A Fast Quantum Mechanical Algorithm for Database Search. In *Proceedings of the Twenty-eighth Annual ACM Symposium on Theory of Computing*, STOC '96, pages 212–219, New York, NY, USA, 1996. ACM. ISBN 0-89791-785-5. doi: 10.1145/237814.237866. URL http://doi.acm.org/10.1145/237814.237866.

[11] Thomas N. Theis and H.-S. Philip Wong. The end of Moore's Law: A new beginning for information technology. *Computing in Science & Engineering*, 19(2):41–50, 2017. doi: 10.1109/MCSE.2017.29.

[12] M. H. Anderson, J. R. Ensher, M. R. Matthews, C. E. Wieman, and E. A. Cornell. Observation of Bose-Einstein Condensation in a Dilute Atomic Vapor. *Science*, 269 (5221):198–201, 1995. ISSN 0036-8075. doi: 10.1126/science.269.5221.198. URL http://science.sciencemag.org/content/269/5221/198.

[13] Immanuel Bloch, Jean Dalibard, and Wilhelm Zwerger. Many-body physics with ultracold gases. *Rev. Mod. Phys.*, 80:885–964, Jul 2008. doi: 10.1103/RevModPhys.80.885. URL https://link.aps.org/doi/10.1103/RevModPhys.80.885.

[14] Markus Greiner, Olaf Mandel, Tilman Esslinger, Theodor W. Hänsch, and Immanuel Bloch. Quantum phase transition from a superfluid to a Mott insulator in a gas of ultracold atoms. *Nature*, 415:39, 01 2002. doi: 10.1038/415039a. URL http://dx.doi.org/10.1038/415039a.

[15] Jacob F. Sherson, Christof Weitenberg, Manuel Endres, Marc Cheneau, Immanuel Bloch, and Stefan Kuhr. Single-atom-resolved fluorescence imaging of an atomic Mott insulator. *Nature*, 467:68–72, 08 2010. doi: 10.1038/nature09378. URL http://dx.doi.org/10.1038/nature09378.

[16] Christian Gross and Immanuel Bloch. Quantum simulations with ultracold atoms in optical lattices. *Science*, 357(6355):995–1001, 2017. ISSN 0036-8075. doi: 10.1126/science.aal3837. URL http://science.sciencemag.org/content/357/6355/995.

[17] Jiazhong Hu, Alban Urvoy, Zachary Vendeiro, Valentin Crépel, Wenlan Chen, and Vladan Vuletić. Creation of a Bose-condensed gas of ^{87}Rb by laser cooling. *Science*, 358(6366):1078–1080, 2017. ISSN 0036-8075. doi: 10.1126/science.aan5614. URL http://science.sciencemag.org/content/358/6366/1078.

[18] V. S. Letokhov, M. A. Ol'shanii, and Yu B. Ovchinnikov. Laser cooling of atoms: a review. *Quantum and Semiclassical Optics: Journal of the European Optical Society Part B*, 7(1):5, 1995. doi: 10.1088/1355-5111/7/1/002. URL http://stacks.iop.org/1355-5111/7/i=1/a=002.

[19] Wolfgang Ketterle and N.J. Van Druten. Evaporative Cooling of Trapped Atoms. volume 37 of *Advances In Atomic, Molecular, and Optical Physics*, pages 181 – 236. Academic Press, 1996. doi: 10.1016/S1049-250X(08)60101-9. URL http://www.sciencedirect.com/science/article/pii/S1049250X08601019.

[20] Lincoln D. Carr, David DeMille, Roman V. Krems, and Jun Ye. Cold and ultracold molecules: science, technology and applications. *New Journal of Physics*, 11(5):055049, 2009. URL http://stacks.iop.org/1367-2630/11/i=5/a=055049.

[21] Jee Woo Park, Zoe Z. Yan, Huanqian Loh, Sebastian A. Will, and Martin W. Zwierlein. Second-scale nuclear spin coherence time of ultracold ^{23}Na^{40}K molecules. *Science*, 357 (6349):372–375, 2017. ISSN 0036-8075. doi: 10.1126/science.aal5066. URL http://science.sciencemag.org/content/357/6349/372.

[22] Cheng Chin, Rudolf Grimm, Paul Julienne, and Eite Tiesinga. Feshbach resonances in ultracold gases. *Rev. Mod. Phys.*, 82:1225–1286, Apr 2010. doi: 10.1103/RevModPhys.82.1225. URL https://link.aps.org/doi/10.1103/RevModPhys.82.1225.

[23] Nikolay V. Vitanov, Andon A. Rangelov, Bruce W. Shore, and Klaas Bergmann. Stimulated raman adiabatic passage in physics, chemistry, and beyond. *Rev. Mod. Phys.*, 89:015006, Mar 2017. doi: 10.1103/RevModPhys.89.015006. URL https://link.aps.org/doi/10.1103/RevModPhys.89.015006.

[24] J. I. Cirac and P. Zoller. Quantum Computations with Cold Trapped Ions. *Phys. Rev. Lett.*, 74:4091–4094, May 1995. doi: 10.1103/PhysRevLett.74.4091. URL https://link.aps.org/doi/10.1103/PhysRevLett.74.4091.

[25] J. Zhang, G. Pagano, P. W. Hess, A. Kyprianidis, P. Becker, H. Kaplan, A. V. Gorshkov, Z. X. Gong, and C. Monroe. Observation of a many-body dynamical phase transition with a 53-qubit quantum simulator. *Nature*, 551:601–604, 11 2017. doi: 10.1038/nature24654. URL http://dx.doi.org/10.1038/nature24654.

[26] J. G. Bohnet, B. C. Sawyer, J. W. Britton, M. L. Wall, A. M. Rey, M. Foss-Feig, and J. J. Bollinger. Quantum spin dynamics and entanglement generation with hundreds of trapped ions. *Science*, 352:1297–1301, Jun 2016. doi: 10.1126/science.aad9958.

[27] Rainer Blatt and David Wineland. Entangled states of trapped atomic ions. *Nature*, 453:1008 – 1015, 06 2008. doi: 10.1038/nature07125. URL `http://dx.doi.org/10.1038/nature07125`.

[28] Marcus W. Doherty, Neil B. Manson, Paul Delaney, Fedor Jelezko, Jörg Wrachtrup, and Lloyd C.L. Hollenberg. The nitrogen-vacancy colour centre in diamond. *Physics Reports*, 528(1):1 – 45, 2013. ISSN 0370-1573. doi: 10.1016/j.physrep.2013.02.001. URL `http://www.sciencedirect.com/science/article/pii/S0370157313000562`.

[29] F. Jelezko and J. Wrachtrup. Single defect centres in diamond: A review. *physica status solidi (a)*, 203(13):3207–3225, 2006. ISSN 1862-6319. doi: 10.1002/pssa.200671403. URL `http://dx.doi.org/10.1002/pssa.200671403`.

[30] D. D. Sukachev, A. Sipahigil, C. T. Nguyen, M. K. Bhaskar, R. E. Evans, F. Jelezko, and M. D. Lukin. Silicon-vacancy spin qubit in diamond: A quantum memory exceeding 10 ms with single-shot state readout. *Phys. Rev. Lett.*, 119:223602, Nov 2017. doi: 10.1103/PhysRevLett.119.223602. URL `https://link.aps.org/doi/10.1103/PhysRevLett.119.223602`.

[31] P. C. Maurer, G. Kucsko, C. Latta, L. Jiang, N. Y. Yao, S. D. Bennett, F. Pastawski, D. Hunger, N. Chisholm, M. Markham, D. J. Twitchen, J. I. Cirac, and M. D. Lukin. Room-Temperature Quantum Bit Memory Exceeding One Second. *Science*, 336(6086):1283–1286, 2012. ISSN 0036-8075. doi: 10.1126/science.1220513. URL `http://science.sciencemag.org/content/336/6086/1283`.

[32] I. Gross, W. Akhtar, V. Garcia, L. J. Martínez, S. Chouaieb, K. Garcia, C. Carrétéro, A. Barthélémy, P. Appel, P. Maletinsky, J. V. Kim, J. Y. Chauleau, N. Jaouen, M. Viret, M. Bibes, S. Fusil, and V. Jacques. Real-space imaging of non-collinear antiferromagnetic order with a single-spin magnetometer. *Nature*, 549:252, 09 2017. doi: 10.1038/nature23656. URL `http://dx.doi.org/10.1038/nature23656`.

[33] Jean-Philippe Tetienne, Nikolai Dontschuk, David A. Broadway, Alastair Stacey, David A. Simpson, and Lloyd C. L. Hollenberg. Quantum imaging of current flow in graphene. *Science Advances*, 3(4), 2017. doi: 10.1126/sciadv.1602429. URL `http://advances.sciencemag.org/content/3/4/e1602429`.

[34] F. Jelezko, T. Gaebel, I. Popa, M. Domhan, A. Gruber, and J. Wrachtrup. Observation of Coherent Oscillation of a Single Nuclear Spin and Realization of a Two-Qubit Conditional Quantum Gate. *Phys. Rev. Lett.*, 93:130501, Sep 2004. doi: 10.1103/PhysRevLett.93.130501. URL https://link.aps.org/doi/10.1103/PhysRevLett.93.130501.

[35] J. R. Maze, J. M. Taylor, and M. D. Lukin. Electron spin decoherence of single nitrogen-vacancy defects in diamond. *Phys. Rev. B*, 78:094303, Sep 2008. doi: 10.1103/PhysRevB.78.094303. URL https://link.aps.org/doi/10.1103/PhysRevB.78.094303.

[36] Peng-Bo Li, Shao-Yan Gao, Hong-Rong Li, Sheng-Li Ma, and Fu-Li Li. Dissipative preparation of entangled states between two spatially separated nitrogen-vacancy centers. *Phys. Rev. A*, 85:042306, Apr 2012. doi: 10.1103/PhysRevA.85.042306. URL https://link.aps.org/doi/10.1103/PhysRevA.85.042306.

[37] Matthias Steffen, Shwetank Kumar, David P. DiVincenzo, J. R. Rozen, George A. Keefe, Mary Beth Rothwell, and Mark B. Ketchen. High-Coherence Hybrid Superconducting Qubit. *Phys. Rev. Lett.*, 105:100502, Sep 2010. doi: 10.1103/PhysRevLett.105.100502. URL https://link.aps.org/doi/10.1103/PhysRevLett.105.100502.

[38] M. H. Devoret, A. Wallraff, and J. M. Martinis. Superconducting Qubits: A Short Review. *arXiv 0411174*, Nov 2004. URL https://arxiv.org/abs/cond-mat/0411174.

[39] Hannes Bernien, Sylvain Schwartz, Alexander Keesling, Harry Levine, Ahmed Omran, Hannes Pichler, Soonwon Choi, Alexander S. Zibrov, Manuel Endres, Markus Greiner, Vladan Vuletić, and Mikhail D. Lukin. Probing many-body dynamics on a 51-atom quantum simulator. *Nature*, 551:579–584, 11 2017. doi: 10.1038/nature24622. URL http://dx.doi.org/10.1038/nature24622.

[40] Peter Schauß, Marc Cheneau, Manuel Endres, Takeshi Fukuhara, Sebastian Hild, Ahmed Omran, Thomas Pohl, Christian Gross, Stefan Kuhr, and Immanuel Bloch. Observation of spatially ordered structures in a two-dimensional Rydberg gas. *Nature*, 491:87 – 91, 10 2012. doi: 10.1038/nature11596. URL http://dx.doi.org/10.1038/nature11596.

[41] Qi-Yu Liang, Aditya V. Venkatramani, Sergio H. Cantu, Travis L. Nicholson, Michael J. Gullans, Alexey V. Gorshkov, Jeff D. Thompson, Cheng Chin, Mikhail D. Lukin, and Vladan Vuletić. Observation of three-photon bound states in a quantum nonlinear medium. *Science*, 359(6377):783–786, 2018. ISSN 0036-8075. doi: 10.1126/science.aao7293. URL http://science.sciencemag.org/content/359/6377/783.

[42] A. Piñeiro Orioli, A. Signoles, H. Wildhagen, G. Günter, J. Berges, S. Whitlock, and M. Weidemüller. Relaxation of an isolated dipolar-interacting rydberg quantum spin system. *Phys. Rev. Lett.*, 120:063601, Feb 2018. doi: 10.1103/PhysRevLett.120.063601. URL https://link.aps.org/doi/10.1103/PhysRevLett.120.063601.

[43] J. R. Rydberg. La consitution des spectres d'émission des éléments chimiques. *Den Kungliga Svenska Vetenskapsakademiens Handlingar*, 1890. Bandet 23, No. 11.

[44] M. L. Wall, Erman Bekaroglu, and Lincoln D. Carr. Molecular Hubbard Hamiltonian: Field regimes and molecular species. *Phys. Rev. A*, 88:023605, Aug 2013. doi: 10.1103/PhysRevA.88.023605. URL http://link.aps.org/doi/10.1103/PhysRevA.88.023605.

[45] W. Kohn. Analytic Properties of Bloch Waves and Wannier Functions. *Phys. Rev.*, 115:809–821, Aug 1959. doi: 10.1103/PhysRev.115.809. URL https://link.aps.org/doi/10.1103/PhysRev.115.809.

[46] A. Kossakowski. On quantum statistical mechanics of non-Hamiltonian systems. *Reports on Mathematical Physics*, 3(4):247 – 274, 1972. ISSN 0034-4877. doi: 10.1016/0034-4877(72)90010-9. URL http://www.sciencedirect.com/science/article/pii/0034487772900109.

[47] G. Lindblad. On the generators of quantum dynamical semigroups. *Communications in Mathematical Physics*, 48(2):119–130, 1976. ISSN 1432-0916. doi: 10.1007/BF01608499. URL http://dx.doi.org/10.1007/BF01608499.

[48] Vittorio Gorini, Andrzej Kossakowski, and E. C. G. Sudarshan. Completely positive dynamical semigroups of N-level systems. *Journal of Mathematical Physics*, 17(5):821–825, 1976. doi: 10.1063/1.522979. URL http://aip.scitation.org/doi/abs/10.1063/1.522979.

[49] Heinz-Peter Breuer and Francesco Petruccione. *The Theory of Open Quantum Systems*. Clarendon Press, Oxford, 1. publ. in paperback, [reprint] edition, 2009. ISBN 978-0-19-921390-0. URL https://global.oup.com/academic/product/the-theory-of-open-quantum-systems-9780199213900.

[50] L. D. Carr. *Understanding Quantum Phase Transitions*. Condensed Matter Physics. CRC Press, Boca Raton, FL, 2010. ISBN 9781439802618. doi: 10.1080/00107514.2012.672462. URL http://www.crcpress.com/Understanding-Quantum-Phase-Transitions/Carr/p/book/9781439802519.

[51] Thomas Häner and Damian S. Steiger. 0.5 Petabyte Simulation of a 45-qubit Quantum Circuit. In *Proceedings of the International Conference for High Performance Computing, Networking, Storage and Analysis*, SC '17, pages 33:1–33:10, New York, NY, USA, 2017. ACM. ISBN 978-1-4503-5114-0. doi: 10.1145/3126908.3126947. URL http://doi.acm.org/10.1145/3126908.3126947.

[52] Open Source Matrix Product States (OpenMPS), . URL http://sourceforge.net/projects/openmps/. sourceforge.net/projects/openmps/.

[53] Attribution 3.0 unported (cc by 3.0), . URL https://creativecommons.org/licenses/by/3.0/. last visited March 10, 2018.

[54] New journal of physics copyright. URL http://iopscience.iop.org/journal/1367-2630/page/NJPcopyrightstatement. last visited March 10 2018.

[55] arxiv.org - non-exclusive license to distribute. URL http://arxiv.org/licenses/nonexclusive-distrib/1.0/. last visited March 10, 2018.

[56] Attribution-noncommercial-noderivatives 4.0 international (cc by-nc-nd 4.0), . URL http://creativecommons.org/licenses/by-nc-nd/4.0/. last visited March 10, 2018.

[57] Elsevier copyright. URL http://www.elsevier.com/about/our-business/policies/copyright. last visited March 10 2018.

[58] Luca D'Alessio, Yariv Kafri, Anatoli Polkovnikov, and Marcos Rigol. From quantum chaos and eigenstate thermalization to statistical mechanics and thermodynamics. *Advances in Physics*, 65(3):239–362, 2016. doi: 10.1080/00018732.2016.1198134. URL https://doi.org/10.1080/00018732.2016.1198134.

[59] Marcos Rigol, Vanja Dunjko, and Maxim Olshanii. Thermalization and its mechanism for generic isolated quantum systems. *Nature*, 452:854, Apr 2008. doi: 10.1038/nature06838. URL http://dx.doi.org/10.1038/nature06838.

[60] Anatoli Polkovnikov, Krishnendu Sengupta, Alessandro Silva, and Mukund Vengalattore. *Colloquium* : Nonequilibrium dynamics of closed interacting quantum systems. *Rev. Mod. Phys.*, 83:863–883, Aug 2011. doi: 10.1103/RevModPhys.83.863. URL http://link.aps.org/doi/10.1103/RevModPhys.83.863.

[61] Andrew J. Daley. Quantum trajectories and open many-body quantum systems. *Advances in Physics*, 63(2):77–149, 2014. doi: 10.1080/00018732.2014.933502. URL https://doi.org/10.1080/00018732.2014.933502.

[62] V. Weisskopf and E. Wigner. Berechnung der natürlichen Linienbreite auf Grund der Diracschen Lichttheorie. *Zeitschrift für Physik*, 63(1):54–73, Jan 1930. ISSN 0044-3328. doi: 10.1007/BF01336768. URL https://doi.org/10.1007/BF01336768.

[63] A. J. van Wonderen and L. G. Suttorp. Kraus map for non-Markovian quantum dynamics driven by a thermal reservoir. *EPL (Europhysics Letters)*, 102(6):60001, 2013. URL http://stacks.iop.org/0295-5075/102/i=6/a=60001.

[64] L. Ferialdi. Exact non-Markovian master equation for the spin-boson and Jaynes-Cummings models. *Phys. Rev. A*, 95:020101, Feb 2017. doi: 10.1103/PhysRevA.95.020101. URL http://link.aps.org/doi/10.1103/PhysRevA.95.020101.

[65] Inés de Vega and Daniel Alonso. Dynamics of non-markovian open quantum systems. *Rev. Mod. Phys.*, 89:015001, Jan 2017. doi: 10.1103/RevModPhys.89.015001. URL http://link.aps.org/doi/10.1103/RevModPhys.89.015001.

[66] Michael Fleischhauer, Atac Imamoglu, and Jonathan P. Marangos. Electromagnetically induced transparency: Optics in coherent media. *Rev. Mod. Phys.*, 77:633–673, Jul 2005. doi: 10.1103/RevModPhys.77.633. URL https://link.aps.org/doi/10.1103/RevModPhys.77.633.

[67] K. Stannigel, P. Rabl, and P. Zoller. Driven-dissipative preparation of entangled states in cascaded quantum-optical networks. *New Journal of Physics*, 14(6):063014, 2012. doi: 10.1088/1367-2630/14/6/063014. URL http://stacks.iop.org/1367-2630/14/i=6/a=063014.

[68] M. Abdi, P. Degenfeld-Schonburg, M. Sameti, C. Navarrete-Benlloch, and M. J. Hartmann. Dissipative Optomechanical Preparation of Macroscopic Quantum Superposition States. *Phys. Rev. Lett.*, 116:233604, Jun 2016. doi: 10.1103/PhysRevLett.116.233604. URL https://link.aps.org/doi/10.1103/PhysRevLett.116.233604.

[69] Beatriz Olmos, Igor Lesanovsky, and Juan P. Garrahan. Out-of-equilibrium evolution of kinetically constrained many-body quantum systems under purely dissipative dynamics. *Phys. Rev. E*, 90:042147, Oct 2014. doi: 10.1103/PhysRevE.90.042147. URL https://link.aps.org/doi/10.1103/PhysRevE.90.042147.

[70] Christoph W. Groth, Michael Wimmer, Anton R. Akhmerov, and Xavier Waintal. Kwant: a software package for quantum transport. *New Journal of Physics*, 16(6):063065, 2014. doi: 10.1088/1367-2630/16/6/063065. URL http://stacks.iop.org/1367-2630/16/i=6/a=063065.

[71] Lincoln D. Carr and Mark T. Lusk. Quantum physics: Strongly correlated transport. *Nature*, 491(7426):681–682, Nov 2012. ISSN 0028-0836. doi: 10.1038/491681a. URL http://dx.doi.org/10.1038/491681a.

[72] Steven R. White. Density matrix formulation for quantum renormalization groups. *Phys. Rev. Lett.*, 69:2863–2866, Nov 1992. doi: 10.1103/PhysRevLett.69.2863.

[73] Steven R. White. Density-matrix algorithms for quantum renormalization groups. *Phys. Rev. B*, 48:10345–10356, Oct 1993. doi: 10.1103/PhysRevB.48.10345. URL http://link.aps.org/doi/10.1103/PhysRevB.48.10345.

[74] U. Schollwöck. The density-matrix renormalization group. *Rev. Mod. Phys.*, 77:259–315, Apr 2005. doi: 10.1103/RevModPhys.77.259. URL http://link.aps.org/doi/10.1103/RevModPhys.77.259.

[75] U. Schollwöck. The density-matrix renormalization group in the age of matrix product states. *Annals of Physics*, page 118, Aug 2011. doi: 10.1016/j.aop.2010.09.012.

[76] Guifré Vidal. Efficient Classical Simulation of Slightly Entangled Quantum Computations. *Phys. Rev. Lett.*, 91:147902, Oct 2003. doi: 10.1103/PhysRevLett.91.147902. URL http://link.aps.org/doi/10.1103/PhysRevLett.91.147902.

[77] G. Kin-Lic Chan, A. Keselman, N. Nakatani, Z. Li, and S. R. White. Matrix Product Operators, Matrix Product States, and ab initio Density Matrix Renormalization Group algorithms. *ArXiv e-prints 1605.02611*, May 2016. URL http://arxiv.org/abs/1605.02611.

[78] J. Eisert, M. Cramer, and M. B. Plenio. *Colloquium* : Area laws for the entanglement entropy. *Rev. Mod. Phys.*, 82:277–306, Feb 2010. doi: 10.1103/RevModPhys.82.277. URL http://link.aps.org/doi/10.1103/RevModPhys.82.277.

[79] Y.-Y. Shi, L.-M. Duan, and G. Vidal. Classical simulation of quantum many-body systems with a tree tensor network. *Phys. Rev. A*, 74:022320, Aug 2006. doi: 10.1103/PhysRevA.74.022320. URL http://link.aps.org/doi/10.1103/PhysRevA.74.022320.

[80] F. Verstraete, J. García-Ripoll, and J. Cirac. Matrix Product Density Operators: Simulation of Finite-Temperature and Dissipative Systems. *Phys. Rev. Lett.*, 93:207204, Nov 2004. doi: 10.1103/PhysRevLett.93.207204. URL http://link.aps.org/doi/10.1103/PhysRevLett.93.207204.

[81] Michael Zwolak and Guifré Vidal. Mixed-State Dynamics in One-Dimensional Quantum Lattice Systems: A Time-Dependent Superoperator Renormalization Algorithm. *Phys. Rev. Lett.*, 93:207205, Nov 2004. doi: 10.1103/PhysRevLett.93.207205. URL http://link.aps.org/doi/10.1103/PhysRevLett.93.207205.

[82] A. H. Werner, D. Jaschke, P. Silvi, M. Kliesch, T. Calarco, J. Eisert, and S. Montangero. Positive Tensor Network Approach for Simulating Open Quantum Many-Body Systems. *Phys. Rev. Lett.*, 116:237201, Jun 2016. doi: 10.1103/PhysRevLett.116.237201. URL http://link.aps.org/doi/10.1103/PhysRevLett.116.237201.

[83] G. Vidal. Class of Quantum Many-Body States That Can Be Efficiently Simulated. *Phys. Rev. Lett.*, 101:110501, Sep 2008. doi: 10.1103/PhysRevLett.101.110501. URL http://link.aps.org/doi/10.1103/PhysRevLett.101.110501.

[84] Verstraete F., Murg V., and Cirac J. I. Matrix product states, projected entangled pair states, and variational renormalization group methods for quantum spin systems. *Advances in Physics*, 57(2):143–224, 2008. doi: 10.1080/14789940801912366. URL http://dx.doi.org/10.1080/14789940801912366.

[85] Michael A. Nielsen and Isaac L. Chuang. *Quantum Computation and Quantum Information*. Cambridge Univ. Press, Cambridge, United Kingdom, 9. print. edition, 2007. doi: 10.1080/00107514.2011.587535. URL http://www.cambridge.org/catalogue/catalogue.asp?isbn=9780521635035.

[86] Original photography by D. Jaschke.

[87] P. Silvi, F. Tschirsich, M. Gerster, J. Jünemann, D. Jaschke, M. Rizzi, and S. Montangero. The Tensor Networks Anthology: Simulation techniques for many-body quantum lattice systems. *ArXiv e-prints 1710.03733*, Oct 2017. URL https://arxiv.org/abs/1710.03733.

[88] Algorithms and Libraries for Physics Simulations (ALPS). URL http://alps.comp-phys.org. http://alps.comp-phys.org, last visited Feb 27, 2017.

[89] BLOCK – DMRG for quantum chemistry. URL http://sanshar.github.io/Block/. http://sanshar.github.io/Block/, last visited Feb 27, 2017.

[90] Sebastian Wouters, Ward Poelmans, Paul W. Ayers, and Dimitri Van Neck. CheMPS2: A free open-source spin-adapted implementation of the density matrix renormalization group for ab initio quantum chemistry. *Computer Physics Communications*, 185(6): 1501 – 1514, 2014. ISSN 0010-4655. doi: 10.1016/j.cpc.2014.01.019. URL http://www.sciencedirect.com/science/article/pii/S0010465514000496.

[91] DMRG++. URL https://web.ornl.gov/~gz1/dmrgPlusPlus/index.html. https://web.ornl.gov/ gz1/dmrgPlusPlus/index.html, last visited Feb 27, 2017.

[92] J. García-Ripoll. Matrix product states. URL http://github.com/juanjosegarciaripoll/mps. http://github.com/juanjosegarciaripoll/mps, last visited Feb 27, 2017.

[93] ITensor – Intelligent Tensor. URL http://itensor.org/. http://itensor.org/, last visited Feb 27, 2017.

[94] Piet Dargel and Thomas Köhler. MPS-DMRG Applet. URL http://www.theorie.physik.uni-goettingen.de/~thomas.koehler/doku.php?id=en:start. http://www.theorie.physik.uni-goettingen.de/ thomas.koehler/doku.php?id=en:start, last visited Feb 27, 2017.

[95] Ashley Milsted. evoMPS. URL http://github.com/amilsted/evoMPS. http://github.com/amilsted/evoMPS, last visited Feb 27, 2017.

[96] MPS Toolkit, . URL http://people.smp.uq.edu.au/IanMcCulloch/mptoolkit/. http://people.smp.uq.edu.au/IanMcCulloch/mptoolkit/, last visited Mar 7, 2017.

[97] OpenTEBD: Open Source Time-Evolving Block Decimation, . URL http://sourceforge.net/projects/opentebd/. http://sourceforge.net/projects/opentebd/, last visited Feb 27, 2017.

[98] James R. Garrison and Ryan V. Mishmash. Simple DMRG. URL http://github.com/simple-dmrg/simple-dmrg/. http://github.com/simple-dmrg/simple-dmrg/, last visited Feb 27, 2017.

[99] Snake DMRG. URL http://github.com/entron/snake-dmrg. http://github.com/entron/snake-dmrg, last visited Feb 27, 2017.

[100] Gabriele De Chiara, Matteo Rizzi, Davide Rossini, and Simone Montangero. Density Matrix Renormalization Group for Dummies. *Journal of Computational and Theoretical Nanoscience*, 5(7):1277–1288, July 2008. doi: 10.1166/jctn.2008.2564.

[101] Miroslav Urbanek and Pavel Soldán. Parallel implementation of the time-evolving block decimation algorithm for the Bose-Hubbard model. *Computer Physics Communications*, 199:170 – 177, 2016. ISSN 0010-4655. doi: 10.1016/j.cpc.2015.10.016. URL http://www.sciencedirect.com/science/article/pii/S0010465515003963.

[102] Uni10 – Universal Tensor Network Library. URL http://yingjerkao.github.io/uni10/. http://yingjerkao.github.io/uni10/, last visited Feb 27, 2017.

[103] David DeMille. Diatomic molecules, a window onto fundamental physics. *Physics Today*, 68(12):34–40, 2015. doi: http://dx.doi.org/10.1063/PT.3.3020. URL http://scitation.aip.org/content/aip/magazine/physicstoday/article/68/12/10.1063/PT.3.3020.

[104] R. Blatt and C. F. Roos. Quantum simulations with trapped ions. *Nat Phys*, 8(4): 277–284, Apr 2012. ISSN 1745-2473. doi: 10.1038/nphys2252. URL http://dx.doi.org/10.1038/nphys2252.

[105] B. Neyenhuis, B. Yan, S. A. Moses, J. P. Covey, A. Chotia, A. Petrov, S. Kotochigova, J. Ye, and D. S. Jin. Anisotropic Polarizability of Ultracold Polar ^{40}K^{87}Rb Molecules. *Phys. Rev. Lett.*, 109:230403, Dec 2012. doi: 10.1103/PhysRevLett.109.230403. URL http://link.aps.org/doi/10.1103/PhysRevLett.109.230403.

[106] Peter K. Molony, Philip D. Gregory, Zhonghua Ji, Bo Lu, Michael P. Köppinger, C. Ruth Le Sueur, Caroline L. Blackley, Jeremy M. Hutson, and Simon L. Cornish. Creation of Ultracold ^{87}Rb^{133}Cs Molecules in the Rovibrational Ground State. *Phys. Rev. Lett.*, 113:255301, Dec 2014. doi: 10.1103/PhysRevLett.113.255301. URL http://link.aps.org/doi/10.1103/PhysRevLett.113.255301.

[107] Johannes Zeiher, Peter Schauß, Sebastian Hild, Tommaso Macrì, Immanuel Bloch, and Christian Gross. Microscopic Characterization of Scalable Coherent Rydberg Superatoms. *Phys. Rev. X*, 5:031015, Aug 2015. doi: 10.1103/PhysRevX.5.031015. URL http://link.aps.org/doi/10.1103/PhysRevX.5.031015.

[108] H. Labuhn, D. Barredo, S. Ravets, S. de Léséleuc, T. Macrì, T. Lahaye, and A. Browaeys. Tunable two-dimensional arrays of single Rydberg atoms for realizing quantum Ising models. *Nature*, 534(7609):667–670, Jun 2016. ISSN 0028-0836. URL http://dx.doi.org/10.1038/nature18274. Letter.

[109] D. M. Silevitch, G. Aeppli, and T. F. Rosenbaum. Switchable hardening of a ferromagnet at fixed temperature. *Proc Natl Acad Sci USA*, 107:2797, 2010.

[110] B. Naylor, M. Brewczyk, M. Gajda, O. Gorceix, E. Maréchal, L. Vernac, and B. Laburthe-Tolra. Competition between Bose-Einstein Condensation and Spin Dynamics. *Phys. Rev. Lett.*, 117:185302, Oct 2016. doi: 10.1103/PhysRevLett.117.185302. URL http://link.aps.org/doi/10.1103/PhysRevLett.117.185302.

[111] L. Chomaz, S. Baier, D. Petter, M. J. Mark, F. Wächtler, L. Santos, and F. Ferlaino. Quantum-Fluctuation-Driven Crossover from a Dilute Bose-Einstein Condensate to a Macrodroplet in a Dipolar Quantum Fluid. *Phys. Rev. X*, 6:041039, Nov 2016. doi: 10.1103/PhysRevX.6.041039. URL http://link.aps.org/doi/10.1103/PhysRevX.6.041039.

[112] Yijun Tang, Nathaniel Q. Burdick, Kristian Baumann, and Benjamin L. Lev. Bose-Einstein condensation of ^{162}Dy and ^{160}Dy. *New Journal of Physics*, 17(4):045006, 2015. URL http://stacks.iop.org/1367-2630/17/i=4/a=045006.

[113] N. Dogra, F. Brennecke, S. D. Huber, and T. Donner. Phase transitions in a Bose-Hubbard model with cavity-mediated global-range interactions. *Phys. Rev. A*, 94: 023632, Aug 2016. doi: 10.1103/PhysRevA.94.023632. URL http://link.aps.org/doi/10.1103/PhysRevA.94.023632.

[114] Bo-Bo Wei, Christian Burk, Jörg Wrachtrup, and Ren-Bao Liu. Magnetic ordering of nitrogen-vacancy centers in diamond via resonator-mediated coupling. *EPJ Quantum Technology*, 2:18, 2015.

[115] Andrew Lucas. Ising formulations of many NP problems. *Frontiers in Physics*, 2: 5, 2014. ISSN 2296-424X. doi: 10.3389/fphy.2014.00005. URL http://journal.frontiersin.org/article/10.3389/fphy.2014.00005.

[116] Wenhao Wu, B. Ellman, T. F. Rosenbaum, G. Aeppli, and D. H. Reich. From classical to quantum glass. *Phys. Rev. Lett.*, 67:2076–2079, Oct 1991. doi: 10.1103/PhysRevLett.67.2076. URL http://link.aps.org/doi/10.1103/PhysRevLett.67.2076.

[117] Renate Landig, Lorenz Hruby, Nishant Dogra, Manuele Landini, Rafael Mottl, Tobias Donner, and Tilman Esslinger. Quantum phases from competing short- and long-range interactions in an optical lattice. *Nature*, 532(7600):476–479, Apr 2016. ISSN 0028-0836. URL http://dx.doi.org/10.1038/nature17409. Letter.

[118] Lea F. Santos, Fausto Borgonovi, and Giuseppe Luca Celardo. Cooperative Shielding in Many-Body Systems with Long-Range Interaction. *Phys. Rev. Lett.*, 116:250402, Jun 2016. doi: 10.1103/PhysRevLett.116.250402. URL http://link.aps.org/doi/10.1103/PhysRevLett.116.250402.

[119] I. P. McCulloch. Infinite size density matrix renormalization group, revisited. *ArXiv e-prints 0804.2509*, Apr 2008. URL https://arxiv.org/abs/0804.2509.

[120] Jutho Haegeman, Christian Lubich, Ivan Oseledets, Bart Vandereycken, and Frank Verstraete. Unifying time evolution and optimization with matrix product states. *Phys. Rev. B*, 94:165116, Oct 2016. doi: 10.1103/PhysRevB.94.165116. URL http://link.aps.org/doi/10.1103/PhysRevB.94.165116.

[121] M. L. Wall and Lincoln D. Carr. Out-of-equilibrium dynamics with matrix product states. *New Journal of Physics*, 14(12):125015, 2012. URL http://stacks.iop.org/1367-2630/14/i=12/a=125015.

[122] Michael P. Zaletel, Roger S. K. Mong, Christoph Karrasch, Joel E. Moore, and Frank Pollmann. Time-evolving a matrix product state with long-ranged interactions. *Phys. Rev. B*, 91:165112, Apr 2015. doi: 10.1103/PhysRevB.91.165112. URL http://link.aps.org/doi/10.1103/PhysRevB.91.165112.

[123] Ernst Ising. Beitrag zur Theorie des Ferromagnetismus. *Zeitschrift für Physik*, 31(1): 253–258, 1925. ISSN 0044-3328. doi: 10.1007/BF02980577. URL http://dx.doi.org/10.1007/BF02980577.

[124] Wojciech H. Zurek, Uwe Dorner, and Peter Zoller. Dynamics of a Quantum Phase Transition. *Phys. Rev. Lett.*, 95:105701, Sep 2005. doi: 10.1103/PhysRevLett.95.105701. URL http://link.aps.org/doi/10.1103/PhysRevLett.95.105701.

[125] Lukasz Cincio, Jacek Dziarmaga, Marek M. Rams, and Wojciech H. Zurek. Entropy of entanglement and correlations induced by a quench: Dynamics of a quantum phase transition in the quantum Ising model. *Phys. Rev. A*, 75:052321, May 2007. doi: 10.1103/PhysRevA.75.052321. URL http://link.aps.org/doi/10.1103/PhysRevA.75.052321.

[126] Adolfo del Campo, Marek M. Rams, and Wojciech H. Zurek. Assisted Finite-Rate Adiabatic Passage Across a Quantum Critical Point: Exact Solution for the Quantum Ising Model. *Phys. Rev. Lett.*, 109:115703, Sep 2012. doi: 10.1103/PhysRevLett.109.115703. URL http://link.aps.org/doi/10.1103/PhysRevLett.109.115703.

[127] Amit Dutta and J. K. Bhattacharjee. Phase transitions in the quantum Ising and rotor models with a long-range interaction. *Phys. Rev. B*, 64:184106, Oct 2001. doi: 10.1103/PhysRevB.64.184106. URL http://link.aps.org/doi/10.1103/PhysRevB.64.184106.

[128] Thomas Koffel, M. Lewenstein, and Luca Tagliacozzo. Entanglement Entropy for the Long-Range Ising Chain in a Transverse Field. *Phys. Rev. Lett.*, 109:267203, Dec 2012. doi: 10.1103/PhysRevLett.109.267203. URL http://link.aps.org/doi/10.1103/PhysRevLett.109.267203.

[129] Davide Vodola, Luca Lepori, Elisa Ercolessi, and Guido Pupillo. Long-range Ising and Kitaev models: phases, correlations and edge modes. *New Journal of Physics*, 18(1): 015001, 2016. URL http://stacks.iop.org/1367-2630/18/i=1/a=015001.

[130] Sebastian Fey and Kai Phillip Schmidt. Critical behavior of quantum magnets with long-range interactions in the thermodynamic limit. *Phys. Rev. B*, 94:075156, Aug 2016. doi: 10.1103/PhysRevB.94.075156. URL http://link.aps.org/doi/10.1103/PhysRevB.94.075156.

[131] J. Schachenmayer, B. P. Lanyon, C. F. Roos, and A. J. Daley. Entanglement Growth in Quench Dynamics with Variable Range Interactions. *Phys. Rev. X*, 3:031015, Sep 2013. doi: 10.1103/PhysRevX.3.031015. URL http://link.aps.org/doi/10.1103/PhysRevX.3.031015.

[132] Jens Eisert, Mauritz van den Worm, Salvatore R. Manmana, and Michael Kastner. Breakdown of Quasilocality in Long-Range Quantum Lattice Models. *Phys. Rev. Lett.*, 111:260401, Dec 2013. doi: 10.1103/PhysRevLett.111.260401. URL http://link.aps.org/doi/10.1103/PhysRevLett.111.260401.

[133] Philip Richerme, Zhe-Xuan Gong, Aaron Lee, Crystal Senko, Jacob Smith, Michael Foss-Feig, Spyridon Michalakis, Alexey V. Gorshkov, and Christopher Monroe. Non-local propagation of correlations in quantum systems with long-range interactions. *Nature*, 511(7508):198–201, Jul 2014. ISSN 0028-0836. URL http://dx.doi.org/10.1038/nature13450. Letter.

[134] P. Hauke and L. Tagliacozzo. Spread of Correlations in Long-Range Interacting Quantum Systems. *Phys. Rev. Lett.*, 111:207202, Nov 2013. doi: 10.1103/PhysRevLett.111.207202. URL http://link.aps.org/doi/10.1103/PhysRevLett.111.207202.

[135] Mohammad F. Maghrebi, Zhe-Xuan Gong, Michael Foss-Feig, and Alexey V. Gorshkov. Causality and quantum criticality in long-range lattice models. *Phys. Rev. B*, 93:125128, Mar 2016. doi: 10.1103/PhysRevB.93.125128. URL http://link.aps.org/doi/10.1103/PhysRevB.93.125128.

[136] Michael Kastner. Diverging Equilibration Times in Long-Range Quantum Spin Models. *Phys. Rev. Lett.*, 106:130601, Mar 2011. doi: 10.1103/PhysRevLett.106.130601. URL http://link.aps.org/doi/10.1103/PhysRevLett.106.130601.

[137] Subir Sachdev. *Quantum Phase Transitions*. Cambridge University Press, Cambridge, United Kingdom, 2nd edition, 2011. doi: 10.1017/CBO9780511973765.

[138] P. Jordan and E. Wigner. Über das Paulische Äquivalenzverbot. *Zeitschrift für Physik*, 47(9):631–651, 1928. ISSN 0044-3328. doi: 10.1007/BF01331938. URL http://dx.doi.org/10.1007/BF01331938.

[139] Davide Vodola, Luca Lepori, Elisa Ercolessi, Alexey V. Gorshkov, and Guido Pupillo. Kitaev Chains with Long-Range Pairing. *Phys. Rev. Lett.*, 113:156402, Oct 2014. doi: 10.1103/PhysRevLett.113.156402. URL http://link.aps.org/doi/10.1103/PhysRevLett.113.156402.

[140] A. Yu Kitaev. Unpaired Majorana fermions in quantum wires. *Physics-Uspekhi*, 44 (10S):131, 2001. URL http://stacks.iop.org/1063-7869/44/i=10S/a=S29.

[141] David Sherrington and Scott Kirkpatrick. Solvable Model of a Spin-Glass. *Phys. Rev. Lett.*, 35:1792–1796, Dec 1975. doi: 10.1103/PhysRevLett.35.1792. URL http://link.aps.org/doi/10.1103/PhysRevLett.35.1792.

[142] H.J. Lipkin, N. Meshkov, and A.J. Glick. Validity of many-body approximation methods for a solvable model: (I). Exact solutions and perturbation theory. *Nuclear Physics*, 62(2):188 – 198, 1965. ISSN 0029-5582. doi: 10.1016/0029-5582(65)90862-X. URL http://www.sciencedirect.com/science/article/pii/002955826590862X.

[143] A. Dutta, G. Aeppli, B. K. Chakrabarti, U. Divakaran, T. F. Rosenbaum, and D. Sen. Quantum phase transitions in transverse field spin models: from statistical physics to quantum information. *ArXiv e-prints 1012.0653*, Dec 2010. URL https://arxiv.org/abs/1012.0653.

[144] T. Boothby, A. D. King, and A. Roy. Fast clique minor generation in Chimera qubit connectivity graphs. *Quantum Information Processing*, 15:495–508, Jan 2016. doi: 10.1007/s11128-015-1150-6.

[145] Immanuel Bloch, Jean Dalibard, and Sylvain Nascimbene. Quantum simulations with ultracold quantum gases. *Nat Phys*, 8(4):267–276, Apr 2012. ISSN 1745-2473. doi: 10.1038/nphys2259. URL http://dx.doi.org/10.1038/nphys2259.

[146] Jacek Dziarmaga. Dynamics of a quantum phase transition and relaxation to a steady state. *Advances in Physics*, 59(6):1063–1189, 2010. doi: 10.1080/00018732.2010.514702. URL http://dx.doi.org/10.1080/00018732.2010.514702.

[147] Anatoli Polkovnikov and Vladimir Gritsev. Universal Dynamics Near Quantum Critical Points. In Lincoln D. Carr, editor, *Understanding Quantum Phase Transitions*, chapter 3, pages 59–90. CRC Press, Taylor & Francis Group, Boca Raton, 2011.

[148] C. De Grandi, V. Gritsev, and A. Polkovnikov. Quench dynamics near a quantum critical point. *Phys. Rev. B*, 81:012303, Jan 2010. doi: 10.1103/PhysRevB.81.012303. URL http://link.aps.org/doi/10.1103/PhysRevB.81.012303.

[149] J. Schachenmayer, A. Pikovski, and A. M. Rey. Many-Body Quantum Spin Dynamics with Monte Carlo Trajectories on a Discrete Phase Space. *Phys. Rev. X*, 5:011022, Feb 2015. doi: 10.1103/PhysRevX.5.011022. URL http://link.aps.org/doi/10.1103/PhysRevX.5.011022.

[150] C. W. von Keyserlingk and S. L. Sondhi. Phase structure of one-dimensional interacting Floquet systems. I. Abelian symmetry-protected topological phases. *Phys. Rev. B*, 93:245145, Jun 2016. doi: 10.1103/PhysRevB.93.245145. URL http://link.aps.org/doi/10.1103/PhysRevB.93.245145.

[151] Jad C. Halimeh and Valentin Zauner-Stauber. Dynamical phase diagram of quantum spin chains with long-range interactions. *Phys. Rev. B*, 96:134427, Oct 2017. doi: 10.1103/PhysRevB.96.134427. URL https://link.aps.org/doi/10.1103/PhysRevB.96.134427.

[152] Daniel Barredo, Henning Labuhn, Sylvain Ravets, Thierry Lahaye, Antoine Browaeys, and Charles S. Adams. Coherent Excitation Transfer in a Spin Chain of Three Rydberg Atoms. *Phys. Rev. Lett.*, 114:113002, Mar 2015. doi: 10.1103/PhysRevLett.114.113002. URL http://link.aps.org/doi/10.1103/PhysRevLett.114.113002.

[153] M. L. Wall, K. Maeda, and Lincoln D. Carr. Realizing unconventional quantum magnetism with symmetric top molecules. *New Journal of Physics*, 17(2):025001, 2015. doi: 10.1088/1367-2630/17/2/025001. URL http://iopscience.iop.org/article/10.1088/1367-2630/17/2/025001/meta.

[154] Diego A. Alcala, Joseph A. Glick, and Lincoln D. Carr. Entangled Dynamics in Macroscopic Quantum Tunneling of Bose-Einstein Condensates. *Phys. Rev. Lett.*, 118:210403, May 2017. doi: 10.1103/PhysRevLett.118.210403. URL https://link.aps.org/doi/10.1103/PhysRevLett.118.210403.

[155] Salvatore R. Manmana, Andreas M. Läuchli, Fabian H. L. Essler, and Frédéric Mila. Phase diagram and continuous pair-unbinding transition of the bilinear-biquadratic $s = 1$ Heisenberg chain in a magnetic field. *Phys. Rev. B*, 83:184433, May 2011. doi: 10.1103/PhysRevB.83.184433. URL http://link.aps.org/doi/10.1103/PhysRevB.83.184433.

[156] F. Verstraete and J. I. Cirac. Renormalization algorithms for Quantum-Many Body Systems in two and higher dimensions. *eprint arXiv:cond-mat/0407066*, July 2004.

[157] M.B. Plenio and S. Virmani. An introduction to entanglement measures. *Quant. Inf. Comput.*, 7:001, Jan 2007. URL http://www.rintonpress.com/xqic7/qic-7-12/001-051.pdf.

[158] John Cardy. *Scaling and Renormalization in Statistical Physics*. Cambridge University Press, 2003.

[159] Eric Jones, Travis Oliphant, Pearu Peterson, et al. scipy.optimize.curve_fit from SciPy: Open source scientific tools for Python, 2001–. URL http://www.scipy.org/. [Online; accessed 2016-03-14].

[160] T. W. B. Kibble. Topology of cosmic domains and strings. *Journal of Physics A: Mathematical and General*, 9(8):1387, 1976. URL http://stacks.iop.org/0305-4470/9/i=8/a=029.

[161] W. H. Zurek. Cosmological experiments in superfluid helium? *Nature*, 317(6037):505–508, Oct 1985. doi: 10.1038/317505a0. URL http://dx.doi.org/10.1038/317505a0.

[162] Jacek Dziarmaga. Dynamics of a Quantum Phase Transition: Exact Solution of the Quantum Ising Model. *Phys. Rev. Lett.*, 95:245701, Dec 2005. doi: 10.1103/PhysRevLett.95.245701. URL http://link.aps.org/doi/10.1103/PhysRevLett.95.245701.

[163] T. Baumgratz, M. Cramer, and M. B. Plenio. Quantifying Coherence. *Phys. Rev. Lett.*, 113:140401, Sep 2014. doi: 10.1103/PhysRevLett.113.140401.

[164] Heng-Na Xiong, Ping-Yuan Lo, Wei-Min Zhang, Da Hsuan Feng, and Franco Nori. Non-markovian complexity in the quantum-to-classical transition. *Scientific Reports*, 5:13353, Aug 2015. doi: 10.1038/srep13353. URL http://dx.doi.org/10.1038/srep13353.

[165] Magdalena Stobińska, Falk Töppel, Pavel Sekatski, and Adam Buraczewski. Towards loophole-free Bell inequality test with preselected unsymmetrical singlet states of light. *Phys. Rev. A*, 89:022119, Feb 2014. doi: 10.1103/PhysRevA.89.022119. URL https://link.aps.org/doi/10.1103/PhysRevA.89.022119.

[166] Angel Rivas and Susana F. Huelga. *Open Quantum Systems*. Springer, Heidelberg Dordrecht London New York, 2012. doi: 10.1007/978-3-642-23354-8. URL http://dx.doi.org/10.1007/978-3-642-23354-8.

[167] Tomaz Prosen. Third quantization: a general method to solve master equations for quadratic open Fermi systems. *New Journal of Physics*, 10(4):043026, 2008. doi: 10.1088/1367-2630/10/4/043026. URL http://stacks.iop.org/1367-2630/10/i=4/a=043026.

[168] T. Prosen. Exact Nonequilibrium Steady State of a Strongly Driven Open XXZ Chain. *Phys. Rev. Lett.*, 107:137201, Sep 2011. doi: 10.1103/PhysRevLett.107.137201. URL https://link.aps.org/doi/10.1103/PhysRevLett.107.137201.

[169] Zi Cai and Thomas Barthel. Algebraic versus exponential decoherence in dissipative many-particle systems. *Phys. Rev. Lett.*, 111:150403, Oct 2013. doi: 10.1103/PhysRevLett.111.150403. URL https://link.aps.org/doi/10.1103/PhysRevLett.111.150403.

[170] R. Rota, F. Storme, N. Bartolo, R. Fazio, and C. Ciuti. Critical behavior of dissipative two-dimensional spin lattices. *Phys. Rev. B*, 95:134431, Apr 2017. doi: 10.1103/PhysRevB.95.134431. URL https://link.aps.org/doi/10.1103/PhysRevB.95.134431.

[171] Jean-Sébastien Bernier, Ryan Tan, Lars Bonnes, Chu Guo, Dario Poletti, and Corinna Kollath. Light-cone and diffusive propagation of correlations in a many-body dissipative system. *Phys. Rev. Lett.*, 120:020401, Jan 2018. doi: 10.1103/PhysRevLett.120.020401. URL https://link.aps.org/doi/10.1103/PhysRevLett.120.020401.

[172] Patrick P Hofer, Martí Perarnau-Llobet, L David M Miranda, Géraldine Haack, Ralph Silva, Jonatan Bohr Brask, and Nicolas Brunner. Markovian master equations for quantum thermal machines: local versus global approach. *New Journal of Physics*, 19 (12):123037, 2017. doi: 10.1088/1367-2630/aa964f. URL http://stacks.iop.org/1367-2630/19/i=12/a=123037.

[173] G. Smith, J. A. Smolin, X. Yuan, Q. Zhao, D. Girolami, and X. Ma. Quantifying Coherence and Entanglement via Simple Measurements. *ArXiv e-prints 1707.09928*, Jul 2017. URL https://arxiv.org/abs/1707.09928.

[174] J. Onam González, Luis A. Correa, Giorgio Nocerino, José P. Palao, Daniel Alonso, and Gerardo Adesso. Testing the Validity of the 'Local' and 'Global' GKLS Master Equations on an Exactly Solvable Model. *Open Systems & Information Dynamics*, 24(04):1740010, 2017. doi: 10.1142/S1230161217400108. URL http://www.worldscientific.com/doi/abs/10.1142/S1230161217400108.

[175] Sina Hamedani Raja, Massimo Borrelli, Rebecca Schmidt, Jukka P. Pekola, and Sabrina Maniscalco. Thermodynamic fingerprints of non-Markovianity in a system of coupled superconducting qubits. *Phys. Rev. A*, 97:032133, Mar 2018. doi: 10.1103/PhysRevA.97.032133. URL https://link.aps.org/doi/10.1103/PhysRevA.97.032133.

[176] Daniel Jaschke, Kenji Maeda, Joseph D. Whalen, Michael L. Wall, and Lincoln D. Carr. Critical phenomena and Kibble-Zurek scaling in the long-range quantum Ising chain. *New Journal of Physics*, 19(3):033032, 2017. doi: 10.1088/1367-2630/aa65bc. URL http://stacks.iop.org/1367-2630/19/i=3/a=033032.

[177] E. M. Stoudenmire and Steven R. White. Minimally entangled typical thermal state algorithms. *New Journal of Physics*, 12(5):055026, 2010. URL http://stacks.iop.org/1367-2630/12/i=5/a=055026.

[178] R. Schmied, T. Roscilde, V. Murg, D. Porras, and J. I. Cirac. Quantum phases of trapped ions in an optical lattice. *New Journal of Physics*, 10(4):045017, 2008. doi: 10.1088/1367-2630/10/4/045017. URL http://stacks.iop.org/1367-2630/10/i=4/a=045017.

[179] M. Everitt, J. Dunningham, and B. T. Varcoe. Quantum Computing with Rydberg Atoms in Cavities. In *Frontiers in Optics 2009/Laser Science XXV/Fall 2009 OSA Optics & Photonics Technical Digest*, page FThU3. Optical Society of America, 2009. doi: 10.1364/FIO.2009.FThU3. URL http://www.osapublishing.org/abstract.cfm?URI=FiO-2009-FThU3.

[180] Hashem Zoubi and Helmut Ritsch. Chapter 3 - excitons and cavity polaritons for optical lattice ultracold atoms. In Ennio Arimondo, Paul R. Berman, and Chun C. Lin, editors, *Advances in Atomic, Molecular, and Optical Physics*, volume 62 of *Advances In Atomic, Molecular, and Optical Physics*, pages 171 – 229. Academic Press, 2013. doi: 10.1016/B978-0-12-408090-4.00003-7. URL http://www.sciencedirect.com/science/article/pii/B9780124080904000037.

[181] C. F. R. Mateus, M. C. Y. Huang, Yunfei Deng, A. R. Neureuther, and C. J. Chang-Hasnain. Ultrabroadband mirror using low-index cladded subwavelength grating. *IEEE Photonics Technology Letters*, 16(2):518–520, Feb 2004. ISSN 1041-1135. doi: 10.1109/LPT.2003.821258.

[182] A. Recati, P. O. Fedichev, W. Zwerger, J. von Delft, and P. Zoller. Atomic Quantum Dots Coupled to a Reservoir of a Superfluid Bose-Einstein Condensate. *Phys. Rev. Lett.*, 94:040404, Feb 2005. doi: 10.1103/PhysRevLett.94.040404. URL https://link.aps.org/doi/10.1103/PhysRevLett.94.040404.

[183] Peter P. Orth, Ivan Stanic, and Karyn Le Hur. Dissipative quantum Ising model in a cold-atom spin-boson mixture. *Phys. Rev. A*, 77:051601, May 2008. doi: 10.1103/PhysRevA.77.051601. URL https://link.aps.org/doi/10.1103/PhysRevA.77.051601.

[184] Inés de Vega, Diego Porras, and J. Ignacio Cirac. Matter-wave emission in optical lattices: Single particle and collective effects. *Phys. Rev. Lett.*, 101:260404, Dec 2008. doi: 10.1103/PhysRevLett.101.260404. URL https://link.aps.org/doi/10.1103/PhysRevLett.101.260404.

[185] Michael Stewart, Ludwig Krinner, Arturo Pazmiño, and Dominik Schneble. Analysis of non-Markovian coupling of a lattice-trapped atom to free space. *Phys. Rev. A*, 95:013626, Jan 2017. doi: 10.1103/PhysRevA.95.013626. URL https://link.aps.org/doi/10.1103/PhysRevA.95.013626.

[186] Yiwen Chu, Prashanta Kharel, William H. Renninger, Luke D. Burkhart, Luigi Frunzio, Peter T. Rakich, and Robert J. Schoelkopf. Quantum acoustics with superconducting qubits. *Science*, 358(6360):199–202, 2017. ISSN 0036-8075. doi: 10.1126/science.aao1511. URL http://science.sciencemag.org/content/358/6360/199.

[187] Jamir Marino, Alessio Recati, and Iacopo Carusotto. Casimir Forces and Quantum Friction from Ginzburg Radiation in Atomic Bose-Einstein Condensates. *Phys. Rev. Lett.*, 118:045301, Jan 2017. doi: 10.1103/PhysRevLett.118.045301. URL https://link.aps.org/doi/10.1103/PhysRevLett.118.045301.

[188] Malte Vogl, Gernot Schaller, and Tobias Brandes. Criticality in Transport through the Quantum Ising Chain. *Phys. Rev. Lett.*, 109:240402, Dec 2012. doi: 10.1103/PhysRevLett.109.240402. URL https://link.aps.org/doi/10.1103/PhysRevLett.109.240402.

[189] D. Jaschke and L. D. Carr. Open source Matrix Product States: Exact diagonalization and other entanglement-accurate methods revisited in quantum systems. *ArXiv e-prints 1802.10052*, Feb 2018. URL https://arxiv.org/abs/1802.10052.

[190] Berislav Buca and Tomaz Prosen. A note on symmetry reductions of the Lindblad equation: transport in constrained open spin chains. *New Journal of Physics*, 14(7): 073007, 2012. doi: 10.1088/1367-2630/14/7/073007. URL http://stacks.iop.org/1367-2630/14/i=7/a=073007.

[191] R. H. Lehmberg. Radiation from an N-Atom System. I. General Formalism. *Phys. Rev. A*, 2:883–888, Sep 1970. doi: 10.1103/PhysRevA.2.883. URL https://link.aps.org/doi/10.1103/PhysRevA.2.883.

[192] Massimo Ostilli and Carlo Presilla. Thermalization of noninteracting quantum systems coupled to blackbody radiation: A Lindblad-based analysis. *Phys. Rev. A*, 95:062112, Jun 2017. doi: 10.1103/PhysRevA.95.062112. URL https://link.aps.org/doi/10.1103/PhysRevA.95.062112.

[193] M. S. Sarandy and D. A. Lidar. Adiabatic approximation in open quantum systems. *Phys. Rev. A*, 71:012331, Jan 2005. doi: 10.1103/PhysRevA.71.012331. URL https://link.aps.org/doi/10.1103/PhysRevA.71.012331.

[194] Victor V. Albert and Liang Jiang. Symmetries and conserved quantities in Lindblad master equations. *Phys. Rev. A*, 89:022118, Feb 2014. doi: 10.1103/PhysRevA.89.022118. URL https://link.aps.org/doi/10.1103/PhysRevA.89.022118.

[195] Birger Horstmann, J. Ignacio Cirac, and Géza Giedke. Noise-driven dynamics and phase transitions in fermionic systems. *Phys. Rev. A*, 87:012108, Jan 2013. doi: 10.1103/PhysRevA.87.012108. URL https://link.aps.org/doi/10.1103/PhysRevA.87.012108.

[196] Ángel Rivas, Susana F. Huelga, and Martin B. Plenio. Quantum non-Markovianity: characterization, quantification and detection. *Reports on Progress in Physics*, 77(9): 094001, 2014. doi: 10.1088/0034-4885/77/9/094001. URL http://stacks.iop.org/0034-4885/77/i=9/a=094001.

[197] Heinz-Peter Breuer, Elsi-Mari Laine, Jyrki Piilo, and Bassano Vacchini. Colloquium: Non-Markovian dynamics in open quantum systems. *Rev. Mod. Phys.*, 88:021002, Apr 2016. doi: 10.1103/RevModPhys.88.021002. URL https://link.aps.org/doi/10.1103/RevModPhys.88.021002.

[198] Jongseok Lim, Matthew D. Frye, Jeremy M. Hutson, and M. R. Tarbutt. Modeling sympathetic cooling of molecules by ultracold atoms. *Phys. Rev. A*, 92:053419, Nov 2015. doi: 10.1103/PhysRevA.92.053419. URL https://link.aps.org/doi/10.1103/PhysRevA.92.053419.

[199] C. J. Hemming and R. V. Krems. Collisional decoherence of internal-state superpositions in a trapped ultracold gas. *Phys. Rev. A*, 81:052701, May 2010. doi: 10.1103/PhysRevA.81.052701. URL https://link.aps.org/doi/10.1103/PhysRevA.81.052701.

[200] Eric Braaten, H.-W. Hammer, and G. Peter Lepage. Lindblad equation for the inelastic loss of ultracold atoms. *Phys. Rev. A*, 95:012708, Jan 2017. doi: 10.1103/PhysRevA.95.012708. URL https://link.aps.org/doi/10.1103/PhysRevA.95.012708.

[201] Adam M. Kaufman, M. Eric Tai, Alexander Lukin, Matthew Rispoli, Robert Schittko, Philipp M. Preiss, and Markus Greiner. Quantum thermalization through entanglement in an isolated many-body system. *Science*, 353(6301):794–800, 2016. ISSN 0036-8075. doi: 10.1126/science.aaf6725. URL http://science.sciencemag.org/content/353/6301/794.

[202] Benjamin Smeltzer, Lilian Childress, and Adam Gali. ^{13}C hyperfine interactions in the nitrogen-vacancy centre in diamond. *New Journal of Physics*, 13(2):025021, 2011. doi: 10.1088/1367-2630/13/2/025021. URL http://stacks.iop.org/1367-2630/13/i=2/a=025021.

[203] Anders W. Sandvik and Juhani Kurkijärvi. Quantum Monte Carlo simulation method for spin systems. *Phys. Rev. B*, 43:5950–5961, Mar 1991. doi: 10.1103/PhysRevB.43.5950. URL http://link.aps.org/doi/10.1103/PhysRevB.43.5950.

[204] N. V. Prokof'ev, B. V. Svistunov, and I. S. Tupitsyn. Exact, complete, and universal continuous-time worldline Monte Carlo approach to the statistics of discrete quantum systems. *Journal of Experimental and Theoretical Physics*, 87(2):310–321, 1998. doi: 10.1134/1.558661.

[205] Antoine Georges, Gabriel Kotliar, Werner Krauth, and Marcelo J. Rozenberg. Dynamical mean-field theory of strongly correlated fermion systems and the limit of infinite dimensions. *Rev. Mod. Phys.*, 68:13–125, Jan 1996. doi: 10.1103/RevModPhys.68.13.

[206] Anatoli Polkovnikov. Phase space representation of quantum dynamics. *Annals of Physics*, 325(8):1790–1852, 2010. doi: 10.1016/j.aop.2010.02.006.

[207] E. Pednault, J. A. Gunnels, G. Nannicini, L. Horesh, T. Magerlein, E. Solomonik, and R. Wisnieff. Breaking the 49-Qubit Barrier in the Simulation of Quantum Circuits. *ArXiv e-prints 1710.05867*, Oct 2017. URL `https://arxiv.org/abs/1710.05867`.

[208] Z. Chen, Q. Zhou, C. Xue, X. Yang, G. Guo, and G. Guo. 64-Qubit Quantum Circuit Simulation. *ArXiv e-prints 1802.06952*, Feb 2018. URL `https://arxiv.org/abs/1802.06952`.

[209] Logan E. Hillberry. Entanglement and complexity in quantum elementary cellular automata. Master's thesis, Colorado School of Mines, 2016. URL `http://inside.mines.edu/~lcarr/theses/hillberry_thesis_2016.pdf`. http://inside.mines.edu/∼lcarr/theses/hillberry_thesis_2016.pdf.

[210] J. Watrous. On one-dimensional quantum cellular automata. In *Proceedings of IEEE 36th Annual Foundations of Computer Science*, pages 528–537, Oct 1995. doi: 10.1109/SFCS.1995.492583.

[211] D. Bleh, T. Calarco, and S. Montangero. Quantum Game of Life. *EPL (Europhysics Letters)*, 97(2):20012, 2012. URL `http://stacks.iop.org/0295-5075/97/i=2/a=20012`.

[212] David L. Vargas. Quantum complexity: Quantum mutual information, complex networks, and emergent phenomena in quantum cellular automata. Master's thesis, Colorado School of Mines, 2016. URL `http://inside.mines.edu/~lcarr/theses/vargas_thesis_2016.pdf`. http://inside.mines.edu/∼lcarr/theses/vargas_thesis_2016.pdf.

[213] Aymard de Touzalin, Charles Marcus, Freeke Heijman, Ignacio Cirac, Richard Murray, and Tommaso Calarco. Quantum Manifesto for Quantum Technologies, 2016. URL `http://qurope.eu/system/files/u7/93056_QuantumManifesto_WEB.pdf`. https://ec.europa.eu/futurium/en/content/quantum-manifesto-quantum-technologies, last visited 01/03/2018.

[214] Marc Andrew Valdez, Daniel Jaschke, David L. Vargas, and Lincoln D. Carr. Quantifying Complexity in Quantum Phase Transitions via Mutual Information Complex Networks. *Phys. Rev. Lett.*, 119:225301, Nov 2017. doi: 10.1103/PhysRevLett.119.225301. URL `https://link.aps.org/doi/10.1103/PhysRevLett.119.225301`.

[215] Daniel Jaschke, Michael L. Wall, and Lincoln D. Carr. Open source Matrix Product States: Opening ways to simulate entangled many-body quantum systems in one dimension. *Computer Physics Communications*, 225C:59–91, 2018. ISSN 0010-4655. doi: 10.1016/j.cpc.2017.12.015. URL http://www.sciencedirect.com/science/article/pii/S0010465517304204.

[216] M. A. Valdez, G. Shchedrin, M. Heimsoth, C. E. Creffield, F. Sols, and L. D. Carr. Many-body Quantum Chaos and Entanglement in a Quantum Ratchet. *ArXiv e-prints 1612.07716*, Dec 2016. URL http://arxiv.org/abs/1612.07716.

[217] Jean Dalibard, Yvan Castin, and Klaus Mølmer. Wave-function approach to dissipative processes in quantum optics. *Phys. Rev. Lett.*, 68:580–583, Feb 1992. doi: 10.1103/PhysRevLett.68.580.

[218] R. Dum, P. Zoller, and H. Ritsch. Monte carlo simulation of the atomic master equation for spontaneous emission. *Phys. Rev. A*, 45:4879–4887, Apr 1992. doi: 10.1103/PhysRevA.45.4879.

[219] Cleve Moler and Charles Van Loan. Nineteen Dubious Ways to Compute the Exponential of a Matrix, Twenty-Five Years Later. *SIAM Review*, 45(1):3–49, 2003. doi: 10.1137/S00361445024180.

[220] S. Schmidt, D. Gerace, A. A. Houck, G. Blatter, and H. E. Türeci. Nonequilibrium delocalization-localization transition of photons in circuit quantum electrodynamics. *Physical Review B*, 82(10):100507, sep 2010. ISSN 1098-0121. doi: 10.1103/PhysRevB.82.100507.

[221] L. Bonnes and A. M. Läuchli. Superoperators vs. Trajectories for Matrix Product State Simulations of Open Quantum System: A Case Study. *ArXiv e-prints 1411.4831*, Nov 2014. URL http://arxiv.org/abs/1411.4831.

[222] J. R. Johansson, P. D. Nation, and Franco Nori. QuTiP 2: A Python framework for the dynamics of open quantum systems. *Computer Physics Communications*, 184 (4):1234 – 1240, 2013. ISSN 0010-4655. doi: 10.1016/j.cpc.2012.11.019. URL http://www.sciencedirect.com/science/article/pii/S0010465512003955.

[223] QuTip: Quantum Toolbox in Python. URL http://qutip.org. http://qutip.org.

[224] Gavin K. Brennen and Jamie E. Williams. Entanglement dynamics in one-dimensional quantum cellular automata. *Phys. Rev. A*, 68:042311, Oct 2003. doi: 10.1103/PhysRevA.68.042311. URL https://link.aps.org/doi/10.1103/PhysRevA.68.042311.

[225] Daniel Jaschke, Lincoln D. Carr, and Inés de Vega. in prep., 2018.

[226] Román Orús. A practical introduction to tensor networks: Matrix product states and projected entangled pair states. *Annals of Physics*, 349:117 – 158, 2014. ISSN 0003-4916. doi: 10.1016/j.aop.2014.06.013. URL http://www.sciencedirect.com/science/article/pii/S0003491614001596.

[227] Sukhwinder Singh, Robert N. C. Pfeifer, and Guifré Vidal. Tensor network decompositions in the presence of a global symmetry. *Phys. Rev. A*, 82:050301, Nov 2010. doi: 10.1103/PhysRevA.82.050301. URL http://link.aps.org/doi/10.1103/PhysRevA.82.050301.

[228] Sukhwinder Singh, Robert N. C. Pfeifer, and Guifre Vidal. Tensor network states and algorithms in the presence of a global U(1) symmetry. *Phys. Rev. B*, 83:115125, Mar 2011. doi: 10.1103/PhysRevB.83.115125. URL http://link.aps.org/doi/10.1103/PhysRevB.83.115125.

[229] Erich Runge and E. K. U. Gross. Density-Functional Theory for Time-Dependent Systems. *Phys. Rev. Lett.*, 52:997–1000, Mar 1984. doi: 10.1103/PhysRevLett.52.997. URL http://link.aps.org/doi/10.1103/PhysRevLett.52.997.

[230] This algorithm is not appropriate for capturing entanglement dynamics and strong correlations.

[231] E. Anisimovas, M. Račiūnas, C. Sträter, A. Eckardt, I. B. Spielman, and G. Juzeliūnas. Semisynthetic zigzag optical lattice for ultracold bosons. *Phys. Rev. A*, 94:063632, Dec 2016. doi: 10.1103/PhysRevA.94.063632.

[232] Filipe F. Bellotti, Amin S. Dehkharghani, and Nikolaj T. Zinner. Comparing numerical and analytical approaches to strongly interacting two-component mixtures in one dimensional traps. *The European Physical Journal D*, 71(2):37, 2017. ISSN 1434-6079. doi: 10.1140/epjd/e2017-70650-8.

[233] A. Dhar, J. J. Kinnunen, and P. Törmä. Population imbalance in the extended Fermi-Hubbard model. *Phys. Rev. B*, 94:075116, Aug 2016. doi: 10.1103/PhysRevB.94.075116.

[234] Michele Dolfi, Bela Bauer, Sebastian Keller, Alexandr Kosenkov, Timothée Ewart, Adrian Kantian, Thierry Giamarchi, and Matthias Troyer. Matrix product state applications for the ALPS project. *Computer Physics Communications*, 185(12): 3430 – 3440, 2014. ISSN 0010-4655. doi: 10.1016/j.cpc.2014.08.019. URL http://www.sciencedirect.com/science/article/pii/S0010465514003002.

[235] Bartłomiej Gardas, Jacek Dziarmaga, and Wojciech H. Zurek. Dynamics of the quantum phase transition in the one-dimensional Bose-Hubbard model: Excitations and correlations induced by a quench. *Phys. Rev. B*, 95:104306, Mar 2017. doi: 10.1103/PhysRevB.95.104306. URL https://link.aps.org/doi/10.1103/PhysRevB.95.104306.

[236] Z.-X. Gong, M. F. Maghrebi, A. Hu, M. Foss-Feig, P. Richerme, C. Monroe, and A. V. Gorshkov. Kaleidoscope of quantum phases in a long-range interacting spin-1 chain. *Phys. Rev. B*, 93:205115, May 2016. doi: 10.1103/PhysRevB.93.205115.

[237] Z.-X. Gong, M. F. Maghrebi, A. Hu, M. L. Wall, M. Foss-Feig, and A. V. Gorshkov. Topological phases with long-range interactions. *Phys. Rev. B*, 93:041102, Jan 2016. doi: 10.1103/PhysRevB.93.041102.

[238] Andrew P. Koller, Michael L. Wall, Josh Mundinger, and Ana Maria Rey. Dynamics of Interacting Fermions in Spin-Dependent Potentials. *Phys. Rev. Lett.*, 117:195302, Nov 2016. doi: 10.1103/PhysRevLett.117.195302. URL http://link.aps.org/doi/10.1103/PhysRevLett.117.195302.

[239] Mohammad F. Maghrebi, Zhe-Xuan Gong, and Alexey V. Gorshkov. Continuous Symmetry Breaking in 1D Long-Range Interacting Quantum Systems. *Phys. Rev. Lett.*, 119:023001, Jul 2017. doi: 10.1103/PhysRevLett.119.023001. URL https://link.aps.org/doi/10.1103/PhysRevLett.119.023001.

[240] Angelo Russomanno and Emanuele G. Dalla Torre. Kibble-Zurek scaling in periodically driven quantum systems. *Europhysics Letters*, 115(3):30006, 2016. URL http://stacks.iop.org/0295-5075/115/i=3/a=30006.

[241] M. L. Wall and L. D. Carr. Dipole-dipole interactions in optical lattices do not follow an inverse cube power law. *New Journal of Physics*, 15(12):123005, 2013. URL http://stacks.iop.org/1367-2630/15/i=12/a=123005.

[242] Hendrik Weimer. String order in dipole-blockaded quantum liquids. *New Journal of Physics*, 16(9):093040, 2014. URL http://stacks.iop.org/1367-2630/16/i=9/a=093040.

[243] F. Verstraete, D. Porras, and J. I. Cirac. Density Matrix Renormalization Group and Periodic Boundary Conditions: A Quantum Information Perspective. *Phys. Rev. Lett.*, 93:227205, Nov 2004. doi: 10.1103/PhysRevLett.93.227205. URL http://link.aps.org/doi/10.1103/PhysRevLett.93.227205.

[244] Gregory M. Crosswhite and Dave Bacon. Finite automata for caching in matrix product algorithms. *Phys. Rev. A*, 78:012356, Jul 2008. doi: 10.1103/PhysRevA.78.012356.

[245] G. H. Golub and C. F. Van Loan. *Matrix Computations*. Johns Hopkins Studies in Mathematical Sciences. The Johns Hopkins University Press, Baltimore, MD, 3rd edition, 1996. URL https://jhupbooks.press.jhu.edu/content/matrix-computations.

[246] Ian P. McCulloch. From density-matrix renormalization group to matrix product states. *Journal of Statistical Mechanics: Theory and Experiment*, 2007(10):P10014, 2007. URL http://stacks.iop.org/1742-5468/2007/i=10/a=P10014.

[247] Y. Saad. Analysis of Some Krylov Subspace Approximations to the Matrix Exponential Operator. *SIAM Journal on Numerical Analysis*, 29(1):209–228, 1992. doi: 10.1137/0729014.

[248] A. T. Sornborger and E. D. Stewart. Higher-order methods for simulations on quantum computers. *Phys. Rev. A*, 60:1956–1965, Sep 1999. doi: 10.1103/PhysRevA.60.1956. URL http://link.aps.org/doi/10.1103/PhysRevA.60.1956.

[249] A. Alvermann and H. Fehske. High-order commutator-free exponential time-propagation of driven quantum systems. *Journal of Computational Physics*, 230(15):5930 – 5956, 2011. ISSN 0021-9991. doi: 10.1016/j.jcp.2011.04.006.

[250] Salvatore R. Manmana, Alejandro Muramatsu, and Reinhard M. Noack. Time evolution of one-dimensional Quantum Many Body Systems. *AIP Conference Proceedings*, 789(1):269–278, 2005. doi: 10.1063/1.2080353.

[251] Juan José García-Ripoll. Time evolution of Matrix Product States. *New Journal of Physics*, 8(12):305, 2006. URL http://stacks.iop.org/1367-2630/8/i=12/a=305.

[252] E. Gallopoulos and Y. Saad. Efficient Solution of Parabolic Equations by Krylov Approximation Methods. *SIAM Journal on Scientific and Statistical Computing*, 13(5):1236–1264, 1992. doi: 10.1137/0913071.

[253] Expokit. URL http://www.maths.uq.edu.au/expokit/. http://www.maths.uq.edu.au/expokit/, last visited Feb 27, 2017.

[254] R. B. Sidje. Expokit. A Software Package for Computing Matrix Exponentials. *ACM Trans. Math. Softw.*, 24(1):130–156, 1998. doi: 10.1145/285861.285868.

[255] The request were made in the questions on fermionic systems and MPS simulations.

[256] GNU General Public License. URL http://www.gnu.org/licenses/gpl-3.0.en.html. http://www.gnu.org/licenses/gpl-3.0.en.html, last visited Feb 27, 2017.

[257] B. Bauer, L. D. Carr, H. G. Evertz, A. Feiguin, J. Freire, S. Fuchs, L. L Gamper, J. Gukelberger, E. Gull, S. Guertler, A. Hehn, R. Igarashi, S. V. Isakov, D. Koop, P. N. Ma, P. Mates, H. Matsuo, O. Parcollet, G. Pawłowski, J. D. Picon, L. Pollet, E. Santos, V. M. Scarola, U. Schollwöck, C. Silva, B. Surer, S. Todo, S. Trebst, M. Troyer, M. L. Wall, P. Werner, and S. Wessel. The ALPS project release 2.0: open source software for strongly correlated systems. *Journal of Statistical Mechanics: Theory and Experiment*, 2011(05):P05001, 2011. URL `http://stacks.iop.org/1742-5468/2011/i=05/a=P05001`.

[258] J. Hubbard. Electron Correlations in Narrow Energy Bands. *Proceedings of the Royal Society of London A: Mathematical, Physical and Engineering Sciences*, 276(1365): 238–257, 1963. doi: 10.1098/rspa.1963.0204.

[259] Lei Wang, Philippe Corboz, and Matthias Troyer. Fermionic quantum critical point of spinless fermions on a honeycomb lattice. *New Journal of Physics*, 16(10):103008, 2014. doi: 10.1088/1367-2630/16/10/103008. URL `http://stacks.iop.org/1367-2630/16/i=10/a=103008`.

[260] Dominique Gobert, Corinna Kollath, Ulrich Schollwöck, and Gunter Schütz. Real-time dynamics in spin-$\frac{1}{2}$ chains with adaptive time-dependent density matrix renormalization group. *Phys. Rev. E*, 71:036102, Mar 2005. doi: 10.1103/PhysRevE.71.036102. URL `https://link.aps.org/doi/10.1103/PhysRevE.71.036102`.

[261] Steven R. White and A. L. Chernyshev. Neél Order in Square and Triangular Lattice Heisenberg Models. *Phys. Rev. Lett.*, 99:127004, Sep 2007. doi: 10.1103/PhysRevLett.99.127004. URL `http://link.aps.org/doi/10.1103/PhysRevLett.99.127004`.

[262] L. Michel and I. P. McCulloch. Schur Forms of Matrix Product Operators in the Infinite Limit. *ArXiv e-prints 1008.4667*, Aug 2010. URL `http://arxiv.org/abs/1008.4667`.

[263] L. Mirsky. A trace inequality of John von Neumann. *Monatshefte für Mathematik*, 79 (4):303–306, 1975. ISSN 1436-5081. doi: 10.1007/BF01647331. URL `http://dx.doi.org/10.1007/BF01647331`.

[264] S. Geršgorin. Über die Abgrenzung der Eigenwerte einer Matrix. *Bulletin de l'Académie des Sciences de l'URSS. Classe des sciences mathématiques et naturelles*, pages 749–754, 1931.

[265] Liqun Qi. Some simple estimates for singular values of a matrix. *Linear Algebra and its Applications*, 56:105 – 119, 1984. ISSN 0024-3795. doi: 10.1016/0024-3795(84)90117-4. URL `http://www.sciencedirect.com/science/article/pii/0024379584901174`.

[266] Yoshitaka Tanimura and Ryogo Kubo. Time Evolution of a Quantum System in Contact with a Nearly Gaussian-Markoffian Noise Bath. *Journal of the Physical Society of Japan*, 58(1):101–114, 1989. doi: 10.1143/JPSJ.58.101.

[267] Yoshitaka Tanimura. Nonperturbative expansion method for a quantum system coupled to a harmonic-oscillator bath. *Phys. Rev. A*, 41:6676–6687, Jun 1990. doi: 10.1103/PhysRevA.41.6676.

[268] Gemma De las Cuevas, Norbert Schuch, David Pérez-García, and J. Ignacio Cirac. Purifications of multipartite states: limitations and constructive methods. *New Journal of Physics*, 15(12):123021, 2013. doi: 10.1088/1367-2630/15/12/123021.

[269] M. Kliesch, D. Gross, and J. Eisert. Matrix-Product Operators and States: NP-Hardness and Undecidability. *Phys. Rev. Lett.*, 113:160503, Oct 2014. doi: 10.1103/PhysRevLett.113.160503.

[270] Gemma De las Cuevas, T. S. Cubitt, J. I. Cirac, M. M. Wolf, and David Pérez-García. Fundamental limitations in the purifications of tensor networks. *Journal of Mathematical Physics*, 57(7):071902, 2016. doi: 10.1063/1.4954983.

[271] R. Biele and R. D'Agosta. A stochastic approach to open quantum systems. *Journal of Physics: Condensed Matter*, 24(27):273201, 2012. doi: 10.1088/0953-8984/24/27/273201. URL `http://stacks.iop.org/0953-8984/24/i=27/a=273201`.

[272] Man-Duen Choi. Completely positive linear maps on complex matrices. *Linear Algebra and its Applications*, 10(3):285 – 290, 1975. ISSN 0024-3795. doi: 10.1016/0024-3795(75)90075-0.

[273] Paola Cappellaro. Lecture notes "22.51 Quantum Theory of Radiation Interactions, Fall 2012", 2012. URL `https://ocw.mit.edu`.

[274] Hendrik Weimer, Markus Müller, Igor Lesanovsky, Peter Zoller, and Hans Peter Büchler. A Rydberg quantum simulator. *Nature Physics*, 6:382, Mar 2010. doi: 10.1038/nphys1614. URL `http://dx.doi.org/10.1038/nphys1614`.

[275] Yiwen Chu, Prashanta Kharel, William H. Renninger, Luke D. Burkhart, Luigi Frunzio, Peter T. Rakich, and Robert J. Schoelkopf. Supplemental material of [186].

[276] Julio T. Barreiro, Markus Müller, Philipp Schindler, Daniel Nigg, Thomas Monz, Michael Chwalla, Markus Hennrich, Christian F. Roos, Peter Zoller, and Rainer Blatt. An open-system quantum simulator with trapped ions. *Nature*, 470:486 – 491, Feb 2011. doi: 10.1038/nature09801. URL `http://dx.doi.org/10.1038/nature09801`.

[277] P. Schindler, M. Müller, D. Nigg, J. T. Barreiro, E. A. Martinez, M. Hennrich, T. Monz, S. Diehl, P. Zoller, and R. Blatt. Quantum simulation of dynamical maps with trapped ions. *Nature Physics*, 9:361 EP –, May 2013. doi: 10.1038/nphys2630. URL `http://dx.doi.org/10.1038/nphys2630`. Article.

[278] Markus Müller, Sebastian Diehl, Guido Pupillo, and Peter Zoller. Engineered Open Systems and Quantum Simulations with Atoms and Ions. In Paul Berman, Ennio Arimondo, and Chun Lin, editors, *Advances in Atomic, Molecular, and Optical Physics*, volume 61, Supplement C of *Advances In Atomic, Molecular, and Optical Physics*, pages 1 – 80. Academic Press, 2012. doi: 10.1016/B978-0-12-396482-3.00001-6. URL `http://www.sciencedirect.com/science/article/pii/B9780123964823000016`.

[279] Hannes Pichler, Johannes Schachenmayer, Andrew J. Daley, and Peter Zoller. Heating dynamics of bosonic atoms in a noisy optical lattice. *Phys. Rev. A*, 87:033606, Mar 2013. doi: 10.1103/PhysRevA.87.033606. URL `https://link.aps.org/doi/10.1103/PhysRevA.87.033606`.

[280] Matthijs P. Branderhorst, Pablo Londero, Piotr Wasylczyk, Ian Walmsley, Constantin Brif, Herschel Rabitz, and Robert Kosut. Coherent Control of Decoherence in Diatomic Molecules. In *Conference on Lasers and Electro-Optics/Quantum Electronics and Laser Science Conference and Photonic Applications Systems Technologies*, page JTuB2. Optical Society of America, 2006. URL `http://www.osapublishing.org/abstract.cfm?URI=QELS-2006-JTuB2`.

[281] A. Osterloh, Luigi Amico, G. Falci, and Rosario Fazio. Scaling of entanglement close to a quantum phase transition. *Nature*, 416:608, Apr 2002. URL `http://dx.doi.org/10.1038/416608a`.

[282] G. Vidal, J. I. Latorre, E. Rico, and A. Kitaev. Entanglement in quantum critical phenomena. *Phys. Rev. Lett.*, 90:227902, Jun 2003. doi: 10.1103/PhysRevLett.90.227902.

[283] Mark T. Lusk, Charles A. Stafford, Jeramy D. Zimmerman, and Lincoln D. Carr. Control of exciton transport using quantum interference. *Phys. Rev. B*, 92:241112, Dec 2015. doi: 10.1103/PhysRevB.92.241112. URL `https://link.aps.org/doi/10.1103/PhysRevB.92.241112`.

[284] Xiaoning Zang, Simone Montangero, Lincoln D. Carr, and Mark T. Lusk. Engineering and manipulating exciton wave packets. *Phys. Rev. B*, 95:195423, May 2017. doi: 10.1103/PhysRevB.95.195423. URL `https://link.aps.org/doi/10.1103/PhysRevB.95.195423`.

[285] M. B. Plenio and S. F. Huelga. Dephasing-assisted transport: quantum networks and biomolecules. *New Journal of Physics*, 10(11):113019, 2008. doi: 10.1088/1367-2630/10/11/113019. URL http://stacks.iop.org/1367-2630/10/i=11/a=113019.

[286] Hannes Wegener and Simone Montangero. in prep.

[287] S. Diehl, A. Micheli, A. Kantian, B. Kraus, H. P. Büchler, and P. Zoller. Quantum states and phases in driven open quantum systems with cold atoms. *Nature Physics*, 4:878 – 883, Sep 2008. doi: 10.1038/nphys1073. URL http://dx.doi.org/10.1038/nphys1073.

[288] B. Kraus, H. P. Büchler, S. Diehl, A. Kantian, A. Micheli, and P. Zoller. Preparation of entangled states by quantum Markov processes. *Phys. Rev. A*, 78:042307, Oct 2008. doi: 10.1103/PhysRevA.78.042307. URL https://link.aps.org/doi/10.1103/PhysRevA.78.042307.

[289] G. Kordas, D. Witthaut, P. Buonsante, A. Vezzani, R. Burioni, A. I. Karanikas, and S. Wimberger. The dissipative Bose-Hubbard model. *The European Physical Journal Special Topics*, 224(11):2127–2171, Nov 2015. ISSN 1951-6401. doi: 10.1140/epjst/e2015-02528-2. URL https://doi.org/10.1140/epjst/e2015-02528-2.

[290] S. Ejima, H. Fehske, and F. Gebhard. Dynamic properties of the one-dimensional Bose-Hubbard model. *EPL (Europhysics Letters)*, 93(3):30002, 2011. doi: 10.1209/0295-5075/93/30002. URL http://stacks.iop.org/0295-5075/93/i=3/a=30002.

[291] R. Heck, O. Vuculescu, J. J. Sørensen, J. Zoller, M. G. Andreasen, M. G. Bason, P. Ejlertsen, O. Elíasson, P. Haikka, J. S. Laustsen, L. L. Nielsen, A. Mao, R. Müller, M. Napolitano, M. K. Pedersen, A. R. Thorsen, C. Bergenholtz, T. Calarco, S. Montangero, and J. F. Sherson. Remote optimization of an ultra-cold atoms experiment by experts and citizen scientists. *ArXiv e-prints 1709.02230*, Sep 2017. URL https://arxiv.org/abs/1709.02230.

[292] Michael L. Wall. *Quantum Many Body Physics of Ultracold Molecules in Optical Lattices: Models and Simulation Methods*. PhD thesis, Colorado School of Mines, 2012. URL http://inside.mines.edu/~lcarr/theses/wall_thesis_2012.pdf. http://inside.mines.edu/∼lcarr/theses/wall_thesis_2012.pdf.

[293] Osmps documentation, . URL https://openmps.sourceforge.io. for release 2, last visited April 23 2018.

[294] Research groups. URL https://ucan.physics.utoronto.ca/research-groups/. last visited April 17 2018.

[295] Bachelor's in physics, . URL https://www.aps.org/programs/education/statistics/bachelors.cfm. last visisted April 17 2018.

[296] Physics bachelor's and phds continue to trend upward, . URL https://www.aps.org/publications/apsnews/200811/degrees.cfm. last visisted April 17 2018.

[297] E. M. Stoudenmire and Steven R. White. Real-space parallel density matrix renormalization group. *Phys. Rev. B*, 87:155137, Apr 2013. doi: 10.1103/PhysRevB.87.155137. URL https://link.aps.org/doi/10.1103/PhysRevB.87.155137.

[298] Supplemental Material for this manuscript via SourceForge forum. URL https://sourceforge.net/p/openmps/discussion/admin/thread/30452693/. https://sourceforge.net/p/openmps/discussion/admin/thread/30452693/, last visited Aug 14, 2017.

[299] E. Hoover. Unofficial CSM Thesis Template. URL http://www.compholio.com/csm/csm-thesis/. LaTeXtemplate used to for this thesis, last visited April 19 2018.

APPENDIX A

BEST PRACTICE: APPENDIX PUBLISHED WITH "EXACT DIAGONALIZATION AND OTHER ENTANGLEMENT-ACCURATE METHODS REVISITED IN QUANTUM SYSTEMS"

A.1 Best-Practice Example

In this appendix, we concentrate on the setup of an actual simulation for the exact diagonalization library within OSMPS. We choose the double-well problem using the Bose-Hubbard model with the Hamiltonian introduced in Eq. (8.18) and compare the behavior of the closed system versus the open system. Figure A.1 represents a sketch of the problem. The first step of any Python program is importing the necessary packages. We need the Python packages for MPS, the EDLib, numpy, a function for copying classes, the interface to the system parameters, and the plotting library. We show the corresponding code snippet always in the following Source Code. Source Code A.1 shows the importing of the packages.

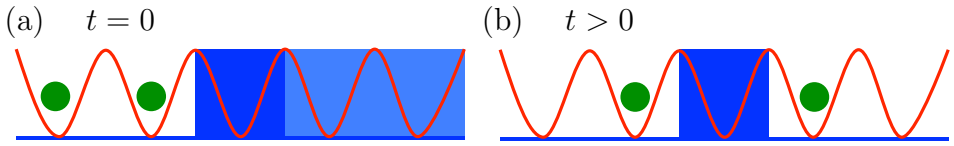

Figure A.1: *Bose-Hubbard Double-Well Problem.* Two bosons occupy five sites. The first two sites represent the left well, the center site represents the barrier, and the two last sites are the right well. (a) The initial state at time $t = 0$ is the ground state of the system with a potential on the middle site (3rd site, dark blue) and the right well (4th and 5th site, light blue). (b) For times $t > 0$, we switch of the potential on the right well and the bosons oscillate between the left and right well.

Source Code A.1: Import the packages.

```
A.1 import MPSPyLib as mps
A.2 import MPSPyLib.EDLib as ed
```

Source Code A.1 Continued

```
A.3 import numpy as np
A.4 from copy import deepcopy
A.5 import sys
A.6 import matplotlib.pyplot as plt
```

The next parts of the code are in the main function. First, we generate the operators for the Bose-Hubbard model. In addition to the set of bosonic operators, OSMPS can provide fermionic operators and spin operators. We choose a maximum of four bosons per site leading to a local dimension of $d = 5$. Furthermore, we have to construct the interaction operator $n(n - \mathbb{I})$. Matrices within `Operators` are accessed via string keys following the dictionary structure of Python. Similar new operators are defined as a new entry in the dictionary.

Source Code A.2: Generate the operators for the Bose-Hubbard model.

```
A.18     # Generate bosonic operators
A.19     Operators = mps.BuildBoseOperators(4)
A.20     Operators['interaction'] = 0.5 * (np.dot(Operators['
            nbtotal'],
A.21                                                 Operators['
                                                        nbtotal'])
A.22                                              - Operators['nbtotal
                                                     '])
```

In the next step, we build the Hamiltonian consisting of the tunneling term $b_k b_{k+1}^\dagger + h.c.$, the interaction $n(n - \mathbb{I})$, and a site-dependent potential to model the double-well and its action through the number operator n. The argument `hparam` is the coupling for each term in the Hamiltonian defined as a string. The actual value is specified later on for each simulation allowing for flexibility, which is then shown in Source Code A.6. We define all values, which are constant for all simulations directly as variables. We make a copy of the

MPO for the open system and add the Lindblad term.

Source Code A.3: Create the Hamiltonian via rule sets.

```
A.24    # Define Hamiltonian MPO for closed systems (Hc) and
           open system (Ho)
A.25    Hc = mps.MPO(Operators)
A.26    Hc.AddMPOTerm('bond', ['bdagger', 'b'], hparam='J',
           weight=-1.0)
A.27    Hc.AddMPOTerm('site', 'interaction', hparam='U',
           weight=1.0)
A.28    Hc.AddMPOTerm('site', 'nbtotal', hparam='Vx', weight
           =1.0)
A.29
A.30    Ho = deepcopy(Hc)
A.31    Ho.AddMPOTerm('lind1', 'nbtotal', hparam='gamma',
           weight=1.0)
A.32
A.33    L = 5
A.34    J = 1.0
A.35    U = 1.0
A.36    fill = 2
A.37    Vx0 = np.array([0.0, 0.0, 1.0, 1.0, 1.0])
```

As a next step, the measurements are defined. We restrict ourselves to the local number operator, which allows us to show the oscillations between the two wells. The arguments in `AddObservable` specify the type of measurement, if applicable, the operators used, and a string identifier to access the results in a dictionary later on.

Source Code A.4: Define the observables.

```
A.39    # Default measures
A.40    Obs = mps.Observables(Operators)
A.41    Obs.AddObservable('site', 'nbtotal', '<n>')
```

We define the dynamics as objects of the `QuenchList` class, one for the closed and one for the open system. We start with the potential with the barrier in the middle of the system and define a function, which returns the time-independent potential. For the time evolution, we use the Krylov method. The time-dependency `timedep` must be set by hand in this case.

Source Code A.5: Define the dynamics via the QuenchList class.

```
A.43    # Define the dynamics
A.44    Vt = np.array([0.0, 0.0, 1.0, 0.0, 0.0])
A.45    def quenchfunc(t, Vt=Vt):
A.46        return Vt
A.47
A.48    T = 100.0
A.49    dt = 0.01
A.50    tConv = mps.KrylovConvParam()
A.51
A.52    CQuenches = mps.QuenchList(Hc)
A.53    CQuenches.AddQuench(['Vx'], T, dt, [quenchfunc],
A.54                        ConvergenceParameters=tConv,
A.55                        stepsforoutput=10, timedep=False)
A.56
A.57    OQuenches = mps.QuenchList(Ho)
```

Source Code A.5 Continued

```
A.58    OQuenches.AddQuench(['Vx'], T, dt, [quenchfunc],
A.59                        ConvergenceParameters=tConv,
A.60                        stepsforoutput=10, timedep=False)
```

The simulations to be carried out are specified in a list of dictionaries. We start with the dictionary for the closed system. The necessary keys can be found in the documentation, but we point out that we now specify the `hparam` used in the definition of the rule sets for the Hamiltonian.

Source Code A.6: Add the closed system to the list of simulations.

```
A.62    # Define the closed system simulation as a dictionary
           inside a list
A.63    params = [{
A.64         'simtype' : 'Finite',
A.65         'job_ID' : 'DoubleWell',
A.66         'unique_ID' : '_SE',
A.67         'Write_Directory' : 'TMP/',
A.68         'Output_Directory' : 'OUTPUTS/',
A.69         # System settings
A.70         'L' : L,
A.71         'J' : J,
A.72         'U' : U,
A.73         'Vx' : Vx0,
A.74         'Abelian_generators' : ['nbtotal'],
A.75         'Abelian_quantum_numbers' : [fill],
A.76         'Quenches' : CQuenches,
A.77         'DynamicsObservables' : Obs,
A.78         'MPSObservables' : Obs
```

Source Code A.6 Continued

```
A.79        }]
```

Since we do not iterate over different system sizes, we can construct the basis states for the $\mathcal{U}(1)$ symmetry once prior to running the simulations. Although EDLib would build the symmetry sector for each simulation automatically, it would use a general method, which is not necessary in this case. The class containing the basis is constructed via the following Source Code A.7.

Source Code A.7: Construct the basis states for a single $\mathcal{U}(1)$ symmetry.

```
A.81        # Construct symmetry sector
A.82        SymmSec = ed.SingleU1Symmetry(Operators, params[0])
A.83        params[0]['SymmSec'] = SymmSec
```

In the next step, we iterate two different coupling for the Lindblad operators. We can append the additional dictionaries to the list.

Source Code A.8: Add open system simulations with two different couplings to the list of simulations.

```
A.85        # Add two different coupling strengths for the open
               system
A.86        for gamma in [0.025, 0.05]:
A.87            params.append({
A.88                'simtype' : 'Finite',
A.89                'job_ID' : 'DoubleWell',
A.90                'unique_ID' : '_ME_gamma%3.6f'%(gamma),
A.91                'Write_Directory' : 'TMP/',
A.92                'Output_Directory' : 'OUTPUTS/',
A.93                # System settings
```

Source Code A.8 Continued

```
A.94                'L' : L,
A.95                'J' : J,
A.96                'U' : U,
A.97                'Vx' : Vx0,
A.98                'gamma' : gamma,
A.99                'Abelian_generators' : ['nbtotal'],
A.100               'Abelian_quantum_numbers' : [fill],
A.101               'Quenches' : CQuenches,
A.102               'DynamicsObservables' : Obs,
A.103               'StaticObservables' : Obs,
A.104               'SymmSec' : SymmSec
A.105           })
```

Since we use different rule sets for the MPO in the simulations, we need a list of MPOs with the same length as the simulation list. Afterwards, we can execute the simulations.

Source Code A.9: Build a list of Hamiltonians and run simulations.

```
A.107       # Different MPO for simulations --> list of MPOs as
               used in params
A.108       Hlist = [Hc, Ho, Ho]
A.109
A.110       if(not PostProcess):
A.111           MainFile = mps.WriteFiles(params, Operators, Hlist
                   , PostProcess)
A.112           ed.runED(params, Operators, Hlist)
A.113           return
```

The post-processing imports the results as dictionaries. For the statics, the list contains the dictionaries directly, for dynamics the first list iterates over the different simulations and the inner list iterates over the dictionaries for each time step.

Source Code A.10: Reading the results and plotting them.

```
A.115   # PostProcess
A.116   # -----------
A.117
A.118   MainFile = mps.WriteFiles(params, Operators, Hlist,
            PostProcess)
A.119
A.120   StatOut = mps.ReadStaticObservables(params)
A.121   DynaOut = mps.ReadDynamicObservables(params)
A.122
A.123   fig = plt.figure()
A.124   plt.rc('text', usetex=True)
A.125   plt.rc('font', family='serif', size=22)
A.126   ax1 = fig.add_subplot(121)
A.127
A.128   # Plot populations ground state (equal for all systems
            )
A.129   ax1.plot(range(1, L + 1), StatOut[0]['<n>'], 'bo:')
A.130   ax1.set_xlabel(r'Site index $i$')
A.131   ax1.set_ylabel(r'Population $\langle n_i \rangle$')
A.132   plt.xticks(list(range(1, L + 1)))
A.133
A.134   # Plot dynamics population left well
A.135   ax2 = fig.add_subplot(122)
```

Source Code A.10 Continued

```
A.136       label = [r'$\gamma = 0.0$', r'$\gamma = 0.025$', r'$\
               gamma = 0.05$']
A.137       ii = -1
A.138
A.139       for DynaOutii in DynaOut:
A.140           ii += 1
A.141           tlist = np.linspace(DynaOutii[0]['time'],
                   DynaOutii[-1]['time'],
A.142                                len(DynaOutii))
A.143           Nleft = np.zeros((len(DynaOutii)))
A.144
A.145           # jj is running over the different time steps
A.146           for jj in range(len(DynaOutii)):
A.147               Nleft[jj] = np.sum(DynaOutii[jj]['<n>'][:2])
A.148
A.149           ax2.plot(tlist, Nleft, label=label[ii])
A.150
A.151       ax2.set_xlabel(r'Time $t$')
A.152       ax2.set_ylabel(r'Population left well $N_{\mathrm{left
               }}$')
A.153       ax2.legend(loc='upper right')
A.154
A.155       plt.show()
A.156       return
```

The plot obtained from this simulation is presented in Figure A.2 and shows that the coupling considered in the Lindblad master equation leads to a damping of the oscillations between the left and right well. The last lines of the code call the main function in case the script is called, which allows us in addition to import the function from another module.

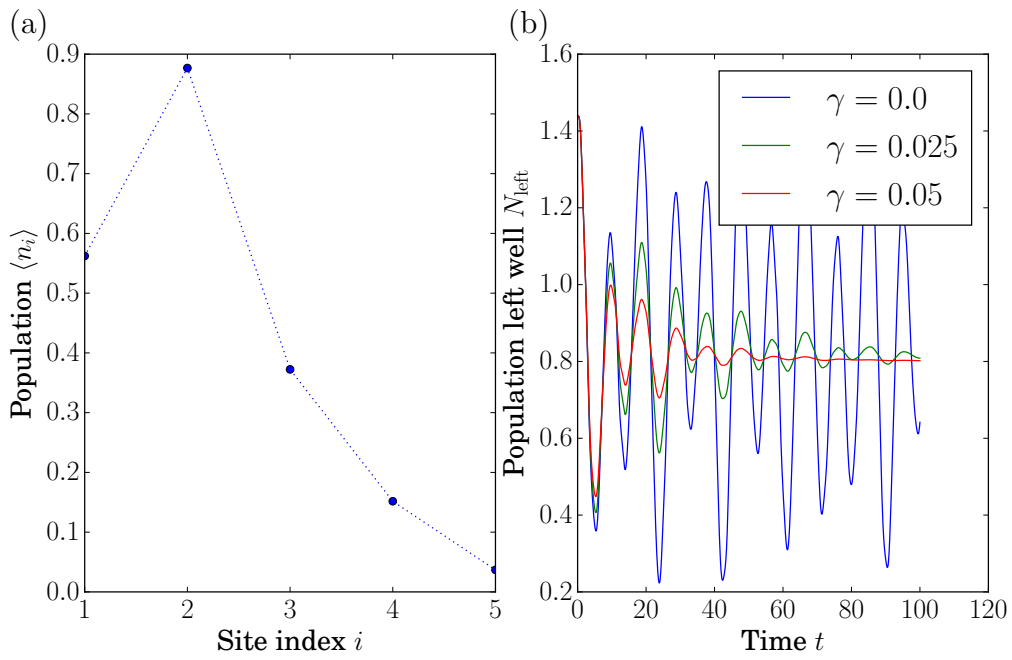

Figure A.2: *Closed and Open System Double-Well Problem.* (a) The initial state is characterized by the population per site on the left. We obtain it via an eigendecomposition of the Hamiltonian, where only the left well has a zero chemical potential. (b) The oscillations between the two wells damp faster for larger coupling γ to the reservoir of the Lindblad master equation. The limit $\gamma = 0$ is the closed system. The time t is in units of the tunneling J.

Source Code A.11: Calling the main function.

```
A.159 if(__name__ == '__main__'):
A.160     PostProcess = False
A.161
A.162     for keyval in sys.argv[1:]:
A.163         key, val = keyval.split('=')
A.164         if(key == '--PostProcess'): PostProcess = (val ==
                  'True') or (val == 'T')
A.165
A.166     main(PostProcess)
```

APPENDIX B

OPEN SOURCE MATRIX PRODUCT STATES: SUPPLEMENTAL MATERIAL PUBLISHED WITH "OPENING WAYS TO SIMULATE ENTANGLED MANY-BODY QUANTUM SYSTEMS IN ONE DIMENSION"

B.1 Supplemental Material

We provide further, supplemental, material in our forum [298] and our package with version 2.1. This material includes:

- Building and installing the open source Matrix Product States library: instructions for minimalists who do not want to read the full manual.
- User support and contributions to the code.
- Code for selected examples to reproduce plots in this paper, i.e., the nearest-neighbor Ising model, the long-range Ising model, and the dynamics of the Bose-Hubbard model.

B.2 Building and installing the open source Matrix Product States library

In order to install OSMPS, one needs to provide at a minimum the following packages covering the Fortran and Python installation and linear algebra tools:

- Python (at least 2.6 or 2.7 recommended, 3.x tested successfully)
- numpy and scipy
- Fortran2003 compiler, e.g. *gfortran* for Linux.
- BLAS and LAPACK
- ARPACK

More packages might be convenient e.g. for plotting with Python, but are not mandatory. The remaining part of the installation is covered by Python. We distinguish between a global and a local installation where the local installation can only be accessed in the same directory or through providing the path. For global installation only one must execute on the command line

```
sudo python setup.py install
```

The Fortran library is compiled then with the command

```
python BuildOSMPS.py --os=unixmpi
```

with prefix `sudo` for the global installation in order to provide the admin privileges. Some default settings are available via command line options as shown for compiling with unix and MPI. Similarly, a local installation can be specified with the option `--local='./'`. More specific settings can be made inside the Python script, which builds the makefile for the Fortran libraries.

B.3 User support and contributing to the code

Being an open source project we welcome anyone willing to help improve OSMPS or share her knowledge with the library. On the project website `http://sourceforge.net/projects/openmps/` on SourceForge we maintain a forum for discussions about OSMPS. These discussions include questions about the installation and use of the algorithms for new users, suggestions for future implementations, and help requests for implementing new features on your own.

The current version of OSMPS is organized via the *svn* version control system via SourceForge. It is possible without a user account to fetch the newest version of the library via *svn*. In order to contribute to OSMPS, a user account on *SourceForge* is necessary so that we can add you to the developers team.

B.4 Files to reproduce plots in this work

We provide the files for the quantum Ising model, the long-range quantum Ising model and the dynamics of the Bose-Hubbard model as examples how Python scripts for OSMPS are designed from the definition of the model to post-processing.

Source Code B.1: Example of nearest neighbor Ising model.

```
B.1  import MPSPyLib as mps
B.2  import numpy as np
B.3  import sys
B.4  import os
B.5  import matplotlib.pyplot as plt
B.6  from mpl_toolkits.mplot3d.axes3d import Axes3D
B.7  from matplotlib import cm
B.8  from scipy.optimize import curve_fit
B.9  from copy import deepcopy
B.10
B.11
B.12 def main(PostProcess):
B.13     """
B.14     Main method running simulation for the following
B.15     plots in the OSMPS paper:
B.16
B.17     1) Bond entropy of the Ising model as function of
B.18        the external field and the system size (see
B.19        Figure 2).
B.20
B.21     2) Finite size scaling to find the critical value
B.22        in the thermodynamic limit (see Figure 4).
```

Source Code B.1 Continued

```
B.23        3) The scaling of resources in Figures 16(c) and
B.24           (d).
B.25
B.26        **Arguments**
B.27
B.28        PostProcess : Boolean (here)
B.29            When PostProcess is ``True``, then data for
B.30            the level is evaluated. Otherwise simulation
B.31            is executed (with MPI). In order to pass
B.32            arguments on the command line use ``T`` for
B.33            ``True`` and ``F`` for ``False``.
B.34        """
B.35        # Build spin operators
B.36        # --------------------
B.37
B.38        # These are rotated Pauli operators to obtain a
B.39        # diagonal generator for Z2
B.40        Operators = mps.BuildSpinOperators(spin=0.5)
B.41        Operators['sx'] = 2 * Operators['sz']
B.42        Operators['sz'] = - (Operators['splus']
B.43                             + Operators['sminus'])
B.44        Operators['gen'] = np.array([[0, 0], [0, 1.]])
B.45
B.46        # Define Hamiltonian / system settings
B.47        # ------------------------------------
B.48
B.49        H = mps.MPO(Operators)
B.50        H.AddMPOTerm('bond', ['sz','sz'], hparam='J',
```

Source Code B.1 Continued

```
B.51                    weight=-1.0)
B.52        H.AddMPOTerm('site', 'sx', hparam='g',
B.53                    weight=-1.0)
B.54
B.55        # overall energy
B.56        J = 1.0
B.57
B.58        # Choose length of the systems for equal spacing
B.59        # in log-plot (reverse order to submit long
B.60        # simulations first)
B.61        nl = 30
B.62        Llist = list(map(int, 10**(np.linspace(0.65, 3.30103,
               nl))))[::-1]
B.63
B.64        # Grid of the external field
B.65        ng = 51
B.66        glist = np.linspace(0.5, 1.5, ng)
B.67
B.68        # Define Observables
B.69        # ------------------
B.70
B.71        # Initialize instance of observable class and
B.72        # add local observable
B.73        myObservables = mps.Observables(Operators)
B.74        myObservables.AddObservable('site', 'sz', 'z')
B.75
B.76        # add correlation functions
B.77        myObservables.AddObservable('corr', ['sz','sz'],
```

Source Code B.1 Continued

```
B.78                                    'zz')
B.79
B.80        # Specify convergence parameters
B.81        # ------------------------------
B.82
B.83        nc = 2
B.84        conv = mps.MPSConvParam(max_bond_dimension=40,
B.85                                variance_tol=1e-10,
B.86                                local_tol=1e-10,
B.87                                max_num_sweeps=4)
B.88        modparam = ['max_bond_dimension', 'max_num_sweeps']
B.89        conv.AddModifiedConvergenceParameters(0, modparam,
B.90                                              [80, 4])
B.91
B.92        # Create list of simulations
B.93        # --------------------------
B.94
B.95        params = []
B.96
B.97        for jj in range(nl):
B.98            ll = Llist[jj]
B.99
B.100           for gg in glist:
B.101
B.102               params.append({
B.103                       'simtype' : 'Finite',
B.104                       # Filenames and directories
B.105                       'job_ID' : 'sim_01_ising_z2_',
```

Source Code B.1 Continued

```
B.106                       'unique_ID' : '_L%04d'%ll \
B.107                                     + '_g%3.6F'%gg,
B.108                       'Write_Directory' : 'TMP_01_ISING/',
B.109                       'Output_Directory' : 'OUTPUTS_01_ISING
                              /',
B.110                       # System size and Hamiltonian
B.111                       # parameters
B.112                       'L' : ll,
B.113                       'J' : J,
B.114                       'g' : gg,
B.115                       # Other parameters
B.116                       'MPSConvergenceParameters' : conv,
B.117                       'MPSObservables' : myObservables,
B.118                       # For error calculation (gap)
B.119                       'n_excited_states' : 1,
B.120                       'eMPSConvergenceParameters' : conv,
B.121                       'logfile' : True,
B.122                       'verbose' : 1,
B.123                       # Z2 symmetry
B.124                       'Discrete_generators' : ['gen'],
B.125                       'Discrete_quantum_numbers' : [0]
B.126                   })
B.127
B.128       if(not PostProcess):
B.129           # Run simulations
B.130           # ---------------
B.131
B.132           hpcdic = {'queueing' : 'slurm',
```

Source Code B.1 Continued

```
                    'partition' : 'lcarr',
                    'time' : '143:59:59',
                    'nodes' : ['062', '063', '064'],
                    'ThisFileName' : '01_Ising.py',
                    'mpi' : 'srun'}

        # Generate sbatch script for CSM cluster
        MainFiles = mps.WriteMPSParallelFiles(
            params, Operators, H, hpcdic,
            PostProcess=PostProcess)

        return

    # Evaluation of the simulations
    # =============================

    base = 'OUTPUTS_01_ISING/'

    if(os.path.isfile(base + "01_Ising_BondEntropy.npy")):
        # Read from previous PostProcess
        bond_entropy = np.load(base + "01
           _Ising_BondEntropy.npy")
        err_bentropy = np.load(base + "01
           _Ising_BondEntropyError.npy")
        converged = np.load(base + "01_Ising_converged.npy
           ")
        variance = np.load(base + "01_Ising_variance.npy")
        runtimes = np.load(base + "01_Ising_runtimes.npy")
```

Source Code B.1 Continued

```
B.158           filesize = np.load(base + "01_Ising_filesize.npy")
B.159           bonddim2 = np.load(base + "01_Ising_bonddim2.npy")
B.160       else:
B.161           # Read from Fortran output
B.162           MainFiles = mps.WriteFiles(params, Operators, H,
B.163                                      PostProcess=True)
B.164           Outputs = mps.ReadStaticObservables(params)
B.165
B.166           # Create array for values of bond entropy
B.167           bond_entropy = np.zeros((nl, ng, nc), dtype=float)
B.168           err_bentropy = np.zeros((nl, ng, nc), dtype=float)
B.169           converged = np.zeros((nl, ng, nc))
B.170           variance = np.zeros((nl, ng, nc))
B.171           runtimes = np.zeros((nl, ng, nc))
B.172           filesize = np.zeros((nl, ng))
B.173           bonddim2 = np.zeros((nl, ng))
B.174
B.175           # Get mapping from simulation to hashes
B.176           hdic = read_hashes(params[0])
B.177
B.178           # index for Outputs-list
B.179           idx = 0
B.180
B.181           # Looping over the results
B.182           for ii in range(nl):
B.183               for jj in range(ng):
B.184                   # idx     : ground state, convergence
                           parameters 0
```

Source Code B.1 Continued

```
B.185                    # idx + 1 : ground state, convergence
                            parameters 1
B.186                    # idx + 2 : excited state, convergence
                            parameters 0
B.187                    # idx + 3 : excited state, convergence
                            parameters 1
B.188
B.189                    for kk in range(nc):
B.190                        Output = Outputs[idx + kk]
B.191                        eOutput = Outputs[idx + kk + 2]
B.192
B.193                        bond_entropy[ii, jj, kk] = Output['
                                BondEntropy'][Llist[ii] // 2]
B.194                        err_bentropy[ii, jj, kk] =
                                error_entropy(Output, eOutput)
B.195                        converged[ii, jj, kk] = int(Output["
                                converged"] == "T")
B.196                        variance[ii, jj, kk] = Output["
                                variance"]
B.197                        runtimes[ii, jj, kk] = mps.get_runtime
                                (Output)
B.198
B.199                    out = Outputs[idx]['Output_Directory']
B.200                    key = out + Outputs[idx]['job_ID'] +
                            Outputs[idx]['unique_ID']
B.201                    thishash = hdic[key]
B.202
```

Source Code B.1 Continued

```
B.203                   filesize[ii, jj] = os.path.getsize(out +
                            thishash + '_002.bin') / 1024.**2
B.204                   bonddim2[ii, jj] = Outputs[idx + 1]['
                            bond_dimension']
B.205
B.206                   idx += 4
B.207
B.208           np.save(base + "01_Ising_BondEntropy.npy",
                    bond_entropy)
B.209           np.save(base + "01_Ising_BondEntropyError.npy",
                    err_bentropy)
B.210           np.save(base + "01_Ising_converged.npy", converged
                    )
B.211           np.save(base + "01_Ising_variance.npy", variance)
B.212           np.save(base + "01_Ising_runtimes.npy", runtimes)
B.213           np.save(base + "01_Ising_filesize.npy", filesize)
B.214           np.save(base + "01_Ising_bonddim2.npy", bonddim2)
B.215
B.216       # Use tex fonts throughout
B.217       plt.rc('text', usetex=True)
B.218       plt.rc('font', family='serif', size=22)
B.219
B.220       # Surface plot for bond entropy
B.221       # ----------------------------
B.222
B.223       # specify which convergence parameter
B.224       ncp = 1
```

Source Code B.1 Continued

```
B.225       surface_plot_bond_entropy(np.array(Llist), glist,
               bond_entropy[:, :, ncp])
B.226
B.227       # Set upper and lower bound for plotting manually
B.228       err_bentropy[np.isnan(err_bentropy)] = 1.0
B.229       err_bentropy[err_bentropy < 1e-7] = 1e-7
B.230       err_bentropy[err_bentropy > 1.0] = 1.0
B.231       #surface_errplot_bond_entropy(np.array(Llist), glist,
               err_bentropy[:, :, ncp])
B.232
B.233       # Plot scaling resources
B.234       # ----------------------
B.235
B.236       plot_scaling_filesize(np.array(Llist), filesize[:,
               25], bonddim2[:, 25])
B.237       plot_scaling_runtimes(np.array(Llist), runtimes[:, 25,
                0], bonddim2[:, 25])
B.238
B.239       # Finite size scaling for bond entropy (exclude very
               small systems)
B.240       # -----------------------------------
B.241
B.242       # Find the maximum for each systems size
B.243       gc = np.zeros((nl), dtype=float)
B.244
B.245       for ii in range(nl):
B.246           pos = np.argmax(bond_entropy[ii, :, ncp])
B.247           gc[ii] = glist[pos]
```

Source Code B.1 Continued

```
B.248
B.249       p0 = [1.0, 1.0]
B.250       [gci, nu], covar = curve_fit(fit_func, Llist[:20], gc
               [:20], p0=p0)
B.251
B.252       fig = plt.figure()
B.253       ax = fig.add_subplot(111)
B.254       ax.plot(Llist[:20], gc[:20], 'go-', label=r'$g_c(L)$')
B.255       ax.plot(Llist[:20], [gci] * len(gc[:20]), 'b-', label=
               r'$g_c = %3.4f$ (FSS)'%(gci))
B.256       ax.plot(Llist[:20], [gci - covar[0,0]] * len(gc[:20]),
               'b--')
B.257       ax.plot(Llist[:20], [gci + covar[0,0]] * len(gc[:20]),
               'b--')
B.258       ax.set_xlabel(r'\textbf{System size} $L$')
B.259       ax.set_ylabel(r'\textbf{Critical field} $g_c$')
B.260       ax.set_xscale('log')
B.261
B.262       plt.legend(loc='lower right')
B.263       plt.savefig("01_Ising_FSS.pdf")
B.264
B.265       return
B.266
B.267
B.268   def fit_func(ll, gc, nu):
B.269       """
B.270       Fitting functions for the finite size scaling.
B.271
```

Source Code B.1 Continued

```
B.272       **Arguments**
B.273
B.274       ll : int
B.275           System size.
B.276
B.277       gc : float
B.278           Value for the critical point to be fitted.
B.279
B.280       nu : float
B.281           Value of the critical exponent to be fitted.
B.282       """
B.283       return gc - ll**(-1 / nu)
B.284
B.285
B.286   def error_entropy(Out0, Out1):
B.287       """
B.288       Calculate the error of the bond entropy of the ground
               state with the
B.289       results of the ground state and first excited state.
B.290
B.291       **Arguments**
B.292
B.293       Out0 : dictionary
B.294           containing the results of the ground state as
                  dictionary.
B.295
B.296       Out1 : dictionary
```

Source Code B.1 Continued

```
B.297           containing the results of the first excited state
                   as dictionary.
B.298       """
B.299       gap = Out1['energy'] - Out0['energy']
B.300       coeff = np.sqrt(2 * Out0['variance']) / gap
B.301       dim = Out0['L'] // 2
B.302
B.303       if(coeff > 1 / np.exp(1)): return np.nan
B.304
B.305       return coeff * (dim * np.log(2) - np.log(coeff))
B.306
B.307
B.308   def surface_plot_bond_entropy(xgrid, ygrid, data):
B.309       """
B.310       A general 3d plot used to plot the bond entropy.
B.311
B.312       **Arguments**
B.313
B.314       xgrid : numpy array (1D)
B.315           Contains the data points for the first axis.
B.316           Log10 is applied to this axis.
B.317
B.318       ygrid : numpy array (1D)
B.319           Contains the data points for the second axis.
B.320
B.321       data : numpy 2d array
B.322           Contains the values of the z-axis.
B.323       """
```

Source Code B.1 Continued

```
B.324       # Meshgrid (logrithmic over system size)
B.325       xm, ym = np.meshgrid(np.log10(xgrid), ygrid)
B.326
B.327       fig = plt.figure()
B.328       ax = fig.add_subplot(111, projection='3d')
B.329       surf = ax.plot_surface(xm, ym, np.transpose(data),
B.330                              rstride=1, cstride=1,
B.331                              cmap=cm.jet,
B.332                              linewidth=0, antialiased=False)
B.333
B.334       ax.set_xlabel(r'\textbf{Size} $\log_{10}(L)$',
               labelpad=20.0)
B.335       ax.set_ylabel(r'\textbf{External field} $g$', labelpad
               =15.0)
B.336       ax.set_zlabel(r'\textbf{Bond entropy} $S$', labelpad
               =10.0)
B.337       ax.view_init(elev=35, azim=-160)
B.338
B.339       cbar = plt.colorbar(surf, shrink=0.8)
B.340       cbar.set_label(r'\textbf{Bond entropy} $S$')
B.341
B.342       plt.tight_layout(pad=1.5)
B.343       plt.savefig('01_Ising_BondEntropy.pdf')
B.344
B.345       return
B.346
B.347
B.348   def surface_errplot_bond_entropy(xgrid, ygrid, data):
```

Source Code B.1 Continued

```
B.349       """
B.350       A general 3d plot used to plot the error of the bond
               entropy.
B.351
B.352       **Arguments**
B.353
B.354       xgrid : numpy array (1D)
B.355           Contains the data points for the first axis.
B.356           Log10 is applied to this axis.
B.357
B.358       ygrid : numpy array (1D)
B.359           Contains the data points for the second axis.
B.360
B.361       data : numpy 2d array
B.362           Contains the values of the z-axis. Log10 is
                  applied
B.363           to these values.
B.364       """
B.365       # Meshgrid (logrithmic over system size)
B.366       xm, ym = np.meshgrid(np.log10(xgrid), ygrid)
B.367
B.368       fig = plt.figure()
B.369       ax = fig.add_subplot(111, projection='3d')
B.370       surf = ax.plot_surface(xm, ym, np.transpose(np.log10(
               data)),
B.371                              rstride=1, cstride=1,
B.372                              cmap=cm.jet,
B.373                              linewidth=0, antialiased=False)
```

Source Code B.1 Continued

```
B.374
B.375       ax.set_xlabel(r'\textbf{System size} $\log_{10}(L)$',
               labelpad=20.0)
B.376       ax.set_ylabel(r'\textbf{External field} $g$', labelpad
               =15.0)
B.377       ax.set_zlabel(r'\textbf{Error bound bond entropy} $\
               log_{10}(\epsilon_{S})$', labelpad=10.0)
B.378
B.379       cbar = plt.colorbar(surf)
B.380       cbar.set_label(r'\textbf{Error bound bond entropy} $\
               log_{10}(\epsilon_{S})$')
B.381
B.382       plt.savefig("01_Ising_ErrBondEntropy.pdf",
               bbobx_inches="tight")
B.383
B.384       return
B.385
B.386
B.387   def plot_scaling_filesize(Ls, filesize, bonddims):
B.388       """
B.389       Plot the filesize of a ground state as a function of
               the
B.390       system size.
B.391
B.392       **Arguments**
B.393
B.394       Ls : list
B.395           Contains the list of different system sizes.
```

Source Code B.1 Continued

```
B.396
B.397       filesize : list
B.398           Contains the corresponding filesize at each
B.399           system size.
B.400
B.401       bonddims : list
B.402           Contains the information about the maximal
B.403           bond dimension used for a simulation.
B.404       """
B.405
B.406       fig = plt.figure()
B.407       ax = fig.add_subplot(111)
B.408       ax.plot(Ls, filesize, 'bo-')
B.409       for elem in ax.get_yticklabels():
B.410           elem.set_color('b')
B.411
B.412       axo = ax.twinx()
B.413       axo.plot(Ls, bonddims, 'ro--')
B.414       for elem in axo.get_yticklabels():
B.415           elem.set_color('r')
B.416       axo.set_ylim([0, 82])
B.417
B.418       ax.set_xlabel(r'\textbf{System size} $L$')
B.419       ax.tick_params(direction='out', pad=2)
B.420
B.421       ax.set_ylabel(r'\textbf{File size} $S_{\mathrm{MB}}$',
                color='b')
```

Source Code B.1 Continued

```
B.422       axo.set_ylabel(r'\textbf{Bond dimension} $\chi$',
                color='r')
B.423
B.424       plt.tight_layout(pad=0.2)
B.425       plt.savefig('C2_ScalingFile.pdf')
B.426
B.427       return
B.428
B.429
B.430   def plot_scaling_runtimes(Ls, runtimes, bonddims):
B.431       """
B.432       Plot the runtimes as a function of the system size.
B.433
B.434       **Arguments**
B.435
B.436       Ls : list
B.437           Contains the list of different system sizes.
B.438
B.439       runtimes : list
B.440           Contains the corresponding runtimes at each
B.441           system size.
B.442
B.443       bonddims : list
B.444           Contains the information about the maximal
B.445           bond dimension used for a simulation.
B.446       """
B.447       fig = plt.figure()
B.448       ax = fig.add_subplot(111)
```

Source Code B.1 Continued

```
B.449       ax.plot(Ls, runtimes, 'bo-')
B.450       for elem in ax.get_yticklabels():
B.451           elem.set_color('b')
B.452
B.453       axo = ax.twinx()
B.454       axo.plot(Ls, bonddims, 'ro--')
B.455       for elem in axo.get_yticklabels():
B.456           elem.set_color('r')
B.457       axo.set_ylim([0, 82])
B.458
B.459       ax.set_xlabel(r'\textbf{System size} $L$')
B.460       ax.tick_params(direction='out', pad=2)
B.461
B.462       ax.set_ylabel(r'\textbf{CPU time} $T_{\mathrm{CPU}} /
               \mathrm{s}$', color='b')
B.463       axo.set_ylabel(r'\textbf{Bond dimension} $\chi$',
               color='r')
B.464
B.465       plt.tight_layout(pad=0.2)
B.466       plt.savefig('C2_ScalingTime.pdf')
B.467
B.468       return
B.469
B.470
B.471   def read_hashes(param):
B.472       """
B.473       Return mapping from names to hash to read file size.
B.474
```

Source Code B.1 Continued

```
B.475       **Arguments**
B.476
B.477       param : dict
B.478           example dictionary to get name of output folder
                    etc.
B.479       """
B.480       out = param['Output_Directory']
B.481       jobid = param['job_ID']
B.482
B.483       fh = open(out + jobid + '_static_mapping.dat', 'r')
B.484       dic = {}
B.485
B.486       for line in fh:
B.487           key, val = line.replace('\n', '').split()
B.488           dic[key] = val
B.489
B.490       return dic
B.491
B.492
B.493   if(__name__ == "__main__"):
B.494       args = {"PostProcess" : "F"}
B.495
B.496       for elem in sys.argv[1:]:
B.497           try:
B.498               key, val = elem.replace("--", "").split("=")
B.499               args[key] = val
B.500           except:
B.501               pass
```

Source Code B.1 Continued

```
B.502
B.503       args["PostProcess"] = ((args["PostProcess"] == "T") or
B.504                              (args["PostProcess"] == "True")
                                      )
B.505       main(args["PostProcess"])
```

Source Code B.2: Example of the long-range Ising model.

```
B.1  import MPSPyLib as mps
B.2  import numpy as np
B.3  import sys
B.4  import os
B.5  import matplotlib.pyplot as plt
B.6  from mpl_toolkits.mplot3d.axes3d import Axes3D
B.7  from matplotlib import cm
B.8  from copy import deepcopy
B.9
B.10
B.11 def main(PostProcess):
B.12     """
B.13     Main method running simulation to find excited
B.14     states for the long range quantum Ising model.
B.15     Either running simulations with MPI or doing
B.16     evaluation on a single core. It produces the
B.17     following plot, but does not contain the
B.18     plots for the error analysis agains the
B.19     simulations with Z2 symmetry.
B.20
```

Source Code B.2 Continued

```
B.21      1) Energy gap for the long-range Ising model, see
B.22         Figure 8(a).
B.23
B.24      **Arguments**
B.25
B.26      PostProcess : Boolean (here)
B.27          When PostProcess is ``True``, then data for
B.28          the level is evaluated. Otherwise simulation
B.29          is executed (with MPI). In order to pass
B.30          arguments on the command line use ``T`` for
B.31          ``True`` and ``F`` for ``False``.
B.32      """
B.33      # overall energy
B.34      J = 1.0
B.35
B.36      # Length of the systems / number of excited states
B.37      ll = 128
B.38      nl = 1
B.39      ne = 4
B.40
B.41      # Grid external field, interaction strength/decay
B.42      ng = 25
B.43      glist = np.linspace(0.7, 1.7, ng)
B.44
B.45      nalpha = 25
B.46      alphalist = np.linspace(2.0, 4.0, nalpha)
B.47
B.48      # Build operators (start with spin operators,
```

Source Code B.2 Continued

```
B.49    # get sigma_{x,z})
B.50    # ---------------
B.51
B.52    Operators = mps.BuildSpinOperators(spin=0.5)
B.53    Operators['sx'] = Operators['splus'] \
B.54                      + Operators['sminus']
B.55    Operators['sz'] *= 2
B.56
B.57    # Define Observables
B.58    # ------------------
B.59
B.60    myObservables = mps.Observables(Operators)
B.61
B.62    # Site terms
B.63    myObservables.AddObservable('site', 'sz', 'z')
B.64
B.65    # correlation functions
B.66    myObservables.AddObservable('corr', ['sz', 'sz'],
B.67                                'zz')
B.68    myObservables.SpecifyCorrelationRange(1000)
B.69
B.70    # Specify convergence parameters
B.71    # ------------------------------
B.72
B.73    nc = 2
B.74    conv = mps.MPSConvParam(max_bond_dimension=40,
B.75                            variance_tol=1e-10,
B.76                            local_tol=1e-10,
```

Source Code B.2 Continued

```
B.77                                max_num_sweeps=4)
B.78        modparam = ['max_bond_dimension', 'max_num_sweeps']
B.79        conv.AddModifiedConvergenceParameters(0, modparam,
B.80                                              [80, 4])
B.81
B.82        # Create list of simulations and Hamitlonians
B.83        # ------------------------------------------
B.84
B.85        params = []
B.86        Hlist = []
B.87
B.88        for jj in range(nalpha):
B.89            alpha = alphalist[jj]
B.90
B.91            # Define the Hamitlonian
B.92            # ----------------------
B.93
B.94            H = mps.MPO(Operators, PostProcess=PostProcess)
B.95            invalpha = lambda x: 1/(x**alpha)
B.96            H.AddMPOTerm('InfiniteFunction', ['sz','sz'],
B.97                         hparam='J', weight=-1.0,
B.98                         func=invalpha, L=ll, tol=1e-10)
B.99            H.AddMPOTerm('site', 'sx', hparam='g',
B.100                        weight=-1.0)
B.101
B.102           for gg in glist:
B.103
B.104               Hlist.append(deepcopy(H))
```

Source Code B.2 Continued

```
B.105
B.106                params.append({
B.107                        'simtype' : 'Finite',
B.108                        # Filenames and directories
B.109                        'job_ID' : 'sim_02_lrising_L%04d'%ll,
B.110                        'unique_ID' : '_alpha%3.6F'%alpha \
B.111                                    + '_g%3.6F'%gg,
B.112
B.113                        'Write_Directory' : 'TMP_02_LRISING/',
B.114                        'Output_Directory' : '
                                OUTPUTS_02_LRISING/',
B.115                        # System size and Hamiltonian
B.116                        # parameters
B.117                        'L' : ll,
B.118                        'J' : J,
B.119                        'g' : gg,
B.120                        'alpha' : alpha,
B.121                        # Other parameters
B.122                        'MPSConvergenceParameters' : conv,
B.123                        'MPSObservables' : myObservables,
B.124                        # eMPS
B.125                        'n_excited_states' : ne,
B.126                        'eMPSConvergenceParameters' : conv,
B.127                        'eMPSObservables' : myObservables
B.128                    })
B.129
B.130        if(not PostProcess):
B.131            # Generate sbatch script for CSM cluster
```

Source Code B.2 Continued

```
B.132           # ------------------------------------
B.133
B.134           hpcdic = {'queueing' : 'slurm',
B.135                     'partition' : 'lcarr',
B.136                     'time' : '143:59:59',
B.137                     'nodes' : ['084', '085', '086'],
B.138                     'ThisFileName' : '02_LRIsing.py',
B.139                     'mpi' : 'srun'},
B.140
B.141           MainFiles = mps.WriteMPSParallelFiles(
B.142               params, Operators, Hlist, hpcdic
B.143               PostProcess=PostProcess)
B.144
B.145           return
B.146
B.147       # Evaluation of the simulations
B.148       # ============================
B.149
B.150       base = 'OUTPUTS_02_LRISING/'
B.151
B.152       if(os.path.isfile(base + "02_LRIsing_Energies.npy")):
B.153           energies = np.load(base + "02_LRIsing_Energies.npy
                   ")
B.154       else:
B.155           MainFiles = mps.WriteFiles(params, Operators,
                   Hlist,
B.156                                      PostProcess=True)
B.157           Outputs = mps.ReadStaticObservables(params)
```

Source Code B.2 Continued

```
B.158
B.159           # Create array for values of bond entropy
B.160           energies = np.zeros((nl, ng, nalpha, ne + 1, nc),
                    dtype=float)
B.161
B.162           def unravel_idx(nl, ng, nalpha, ne, nc):
B.163               idx = -1
B.164               for ii in range(nl):
B.165                   for jj in range(ng):
B.166                       for kk in range(nalpha):
B.167                           for ee in range(ne + 1):
B.168                               for cc in range(nc):
B.169                                   idx += 1
B.170                                   yield idx, ii, jj, \
B.171                                         kk, ee, cc
B.172
B.173           for idx, ii, jj, kk, ee, cc in unravel_idx(nl, ng,
                    nalpha, ne, nc):
B.174               Output = Outputs[idx]
B.175               if(cc == 0):
B.176                   print(Output['energy'], ee,
B.177                         Output['state'],
B.178                         Output['convergence_parameter'])
B.179               energies[ii, jj, kk, ee, cc] = Output['energy'
                        ]
B.180
B.181           np.save(base + "02_LRIsing_Energies.npy", energies
                    )
```

Source Code B.2 Continued

```
B.182
B.183       # Sort energies if flag
B.184       sort = True
B.185       if(sort):
B.186           for ii in range(nl):
B.187               for jj in range(ng):
B.188                   for kk in range(nalpha):
B.189                       for cc in range(nc):
B.190                           idx = energies[ii, jj, kk, :, cc].
                                    argsort()
B.191                           energies[ii, jj, kk, :, cc] =
                                    energies[ii, jj, kk, idx, cc]
B.192
B.193       # Specify plotted convergence parameters
B.194       pnc = nc - 1
B.195
B.196       diff01 = energies[0, :, :, 1, pnc] - energies[0, :, :,
                0, pnc]
B.197       diff02 = energies[0, :, :, 2, pnc] - energies[0, :, :,
                0, pnc]
B.198       diff12 = energies[0, :, :, 2, pnc] - energies[0, :, :,
                1, pnc]
B.199
B.200       # Surface plot for bond entropy
B.201       # ----------------------------
B.202
B.203       # Meshgrid (logrithmic over system size)
B.204       xm, ym = np.meshgrid(glist, alphalist)
```

Source Code B.2 Continued

```
B.205
B.206       # Use tex fonts
B.207       plt.rc('text', usetex=True)
B.208       plt.rc('font', family='serif', size=22)
B.209
B.210       plot_gaps_surface(xm, ym, diff01, diff02)
B.211
B.212       return
B.213
B.214
B.215   def plot_gaps_surface(xm, ym, diff01, diff02):
B.216       fig = plt.figure()
B.217       ax = fig.add_subplot(111, projection='3d')
B.218
B.219       vmin = min(np.min(diff01), np.min(diff02))
B.220       vmax = max(np.max(diff01), np.max(diff02))
B.221
B.222       surf01 = ax.plot_surface(xm, ym, np.transpose(diff01),
B.223                                rstride=1, cstride=1, vmin=
                                        vmin, vmax=vmax,
B.224                                cmap=cm.jet,#coolwarm,
B.225                                linewidth=0, antialiased=
                                        False)
B.226       surf02 = ax.plot_surface(xm, ym, np.transpose(diff02),
B.227                                rstride=1, cstride=1, vmin=
                                        vmin, vmax=vmax,
B.228                                cmap=cm.jet,#coolwarm,
```

Source Code B.2 Continued

```
B.229                                   linewidth=0, antialiased=
                                           False)
B.230
B.231       ax.set_xlabel(r'\textbf{External field} $g$', labelpad
               =15.0)
B.232       ax.set_ylabel(r'\textbf{Power law decay} $\alpha$',
               labelpad=15.0)
B.233       ax.set_zlabel(r'\textbf{Energy gap} $\Delta E$',
               labelpad=10.0)
B.234
B.235       cbar = plt.colorbar(surf01, shrink=0.8, pad=0.07)
B.236
B.237       plt.tight_layout(pad=2.5)
B.238       plt.savefig('02_LRIsing_Gaps.pdf')
B.239
B.240       return
B.241
B.242
B.243   if(__name__ == "__main__"):
B.244       args = {"PostProcess" : "F"}
B.245
B.246       for elem in sys.argv[1:]:
B.247           try:
B.248               key, val = elem.replace("--", "").split("=")
B.249               args[key] = val
B.250           except:
B.251               pass
B.252
```

Source Code B.2 Continued

```
B.253     args["PostProcess"] = ((args["PostProcess"] == "T") or
B.254                            (args["PostProcess"] == "True")
                                    )
B.255     main(args["PostProcess"])
```

Source Code B.3: Example of dynamics in the Bose-Hubbard model.

```
B.1  import MPSPyLib as mps
B.2  import numpy as np
B.3  import sys
B.4  import os.path
B.5  import matplotlib.pyplot as plt
B.6  from matplotlib import cm
B.7
B.8
B.9  def main(PostProcess):
B.10     """
B.11     Main method to simulate the Bose-Hubbard model in
B.12     a rotating saddle point potential. The script
B.13     reproduces Figure 11(b).
B.14
B.15     **Arguments**
B.16
B.17     PostProcess : Boolean (here)
B.18         When PostProcess is ``True``, then data for
B.19         the level is evaluated. Otherwise simulation
B.20         is executed (with MPI). In order to pass
B.21         arguments on the command line use ``T`` for
```

Source Code B.3 Continued

```
B.22            ``True`` and ``F`` for ``False``.
B.23        """
B.24        # Build operators
B.25        # ---------------
B.26
B.27        Operators = mps.BuildBoseOperators(6)
B.28        Operators['interaction'] = \
B.29            0.5 * (np.dot(Operators['nbtotal'],
B.30                          Operators['nbtotal'])
B.31                   - Operators['nbtotal'])
B.32
B.33        # Define Hamiltonian / system settings
B.34        # ------------------------------------
B.35
B.36        # system size and filling
B.37        L = 30
B.38        fill = 20
B.39
B.40        H = mps.MPO(Operators)
B.41        H.AddMPOTerm('bond', ['bdagger', 'b'],
B.42                     hparam='t', weight=-1.0)
B.43        H.AddMPOTerm('site', 'interaction',
B.44                     hparam='U', weight=1.0)
B.45        H.AddMPOTerm('site', 'nbtotal',
B.46                     hparam='Vt', weight=1.0)
B.47
B.48        # accelaration of rotating potential
B.49        # (t=100 39.8 rotations, t=101: 40.6 rotations)
```

Source Code B.3 Continued

```
B.50        alpha = 0.05
B.51
B.52        # and scaling prefactor c * (x**2 - y**2)
B.53        c = 0.01
B.54
B.55        # overall energy scale
B.56        U = 1.0
B.57
B.58        # choose different tunneling strengths
B.59        nt = 11
B.60        ts = np.linspace(0.0, 0.5, nt)
B.61
B.62        # Define observables
B.63        # ------------------
B.64
B.65        myObs = mps.Observables(Operators)
B.66        myObs.AddObservable('site', 'nbtotal', 'n')
B.67        myObs.AddObservable('corr', ['b', 'bdagger'],
B.68                            'spdm')
B.69
B.70        # Specify convergence parameters
B.71        # ------------------------------
B.72
B.73        conv = mps.MPSConvParam(max_bond_dimension=60)
B.74
B.75        # Define quench function
B.76        def Vt(t, c=c, alpha=alpha, L=L):
B.77            # Grid with particles symmetric around 0
```

Source Code B.3 Continued

```
B.78            # at unit distance
B.79            grid = np.linspace(-L / 2 + 0.5,
B.80                               L / 2 - 0.5, L)
B.81
B.82            phit = np.pi / 4 + 0.5 * alpha * t**2
B.83
B.84            return c * ((grid * np.cos(phit))**2
B.85                        - (grid * np.sin(phit))**2)
B.86
B.87        tconv = mps.TEBDConvParam(max_bond_dimension=60)
B.88        Quench = mps.QuenchList(H)
B.89        Quench.AddQuench(['Vt'], 100.0, 0.01, [Vt],
B.90                         stepsforoutput=10,
B.91                         ConvergenceParameters=tconv)
B.92
B.93        params = []
B.94        for ii in range(nt):
B.95            # Get tunneling parameters
B.96            tt = ts[ii]
B.97
B.98            params.append({
B.99                'simtype' : 'Finite',
B.100               # Directories
B.101               'job_ID' : 'BoseHubbard_RotSaddle',
B.102               'unique_ID' : '_tau%3.6f'%(tt),
B.103               'Write_Directory' : 'TMP_03_Hubbard/',
B.104               'Output_Directory' : 'OUTPUTS_03_Hubbard/',
B.105               # System parameters
```

Source Code B.3 Continued

```
B.106                'L' : L,
B.107                'U' : U,
B.108                't' : tt,
B.109                'Vt' : np.zeros((L)),
B.110                'MPSConvergenceParameters' : conv,
B.111                'Abelian_generators' : ['nbtotal'],
B.112                'Abelian_quantum_numbers' : [fill],
B.113                'MPSObservables' : myObs,
B.114                'Quenches' : Quench,
B.115                'DynamicsObservables' : myObs,
B.116                # Other settings
B.117                'logfile' : True
B.118            })
B.119
B.120        if(not PostProcess):
B.121            # Run simulations
B.122            # ---------------
B.123
B.124            hpcdic = {'queueing' : 'slurm',
B.125                      'partition' : 'lcarr',
B.126                      'time' : '143:59:59',
B.127                      'nodes' : ['026', '027'],
B.128                      'ThisFileName' : '05_RotSaddle.py',
B.129                      'mpi' : 'srun'}
B.130
B.131            MainFiles = mps.WriteMPSParallelFiles(
B.132                params, Operators, H, hpcdic,
B.133                PostProcess=PostProcess)
```

Source Code B.3 Continued

```
B.134
B.135           return
B.136
B.137       # Post Process
B.138       # ------------
B.139
B.140       # Number of measurements in time evolution
B.141       nm = 1000
B.142
B.143       if(os.path.isfile("OUTPUTS_03_Hubbard/nstdxt.npy")):
B.144           # Data has been saved in a previous post-
                    processing
B.145           nstdxt = np.load("OUTPUTS_03_Hubbard/nstdxt.npy")
B.146       else:
B.147           # Read data from Fortran output
B.148           MainFiles = mps.WriteFiles(params, Operators, H,
B.149                                      PostProcess=PostProcess
                                               )
B.150           Outputs = mps.ReadDynamicObservables(params)
B.151
B.152           # Array to save standard deviation on particle
                    number over space for each t
B.153           nstdx = np.zeros((nt, nm))
B.154
B.155           for ii in range(nt):
B.156               for tt in range(nm):
B.157                   nstdx[ii, tt] = np.std(Outputs[ii][tt]['n'
                            ])
```

Source Code B.3 Continued

```
B.158
B.159           # Get a std deviation in time for 50 subsequent
                   measurements
B.160           nstdxt = np.zeros((nt, nm - 50))
B.161
B.162           for ii in range(nt):
B.163               for jj in range(50, nm):
B.164                   nstdxt[ii, jj - 50] = np.std(nstdx[ii, jj
                           - 50:jj])
B.165
B.166           np.save("OUTPUTS_03_Hubbard/nstdxt.npy", nstdxt)
B.167
B.168       # Plotting
B.169       # --------
B.170
B.171       plt.rc('text', usetex=True)
B.172       plt.rc('font', family='serif', size=22)
B.173
B.174       color = cm.rainbow(np.linspace(0, 1, ts.shape[0]))
B.175       mi = np.min(np.array(ts))
B.176       ma = np.max(np.array(ts))
B.177       clabel = r'\textbf{Tunneling} $J$'
B.178       cticks = np.linspace(mi, ma, 6)
B.179       cbarinfo = plt.contourf([[0, 0], [0, 0]],
B.180                               np.linspace(mi, ma, 101), cmap
                                       =cm.rainbow)
B.181       plt.clf()
B.182
```

Source Code B.3 Continued

```
B.183       fig = plt.figure()
B.184       ax = fig.add_subplot(111)
B.185
B.186       for ii in range(nt):
B.187           ax.plot(np.linspace(0.5, 100.0, nm - 50), nstdxt[
                    ii], c=color[ii])
B.188
B.189       cbar = plt.colorbar(cbarinfo)
B.190       cbar.set_ticks(cticks)
B.191       cbar.set_label(clabel)
B.192
B.193       ax.set_xlabel(r'\textbf{Time} $t$')
B.194       ax.set_ylabel(r'\textbf{Standard deviation} $\sigma_{t
                }$')
B.195
B.196       plt.tight_layout(pad=0.2)
B.197       plt.savefig('05_RotSaddle_std_txn.pdf')
B.198
B.199       return
B.200
B.201
B.202   if(__name__ == "__main__"):
B.203       args = {"PostProcess" : "F"}
B.204
B.205       for elem in sys.argv[1:]:
B.206           try:
B.207               key, val = elem.replace("--", "").split("=")
B.208               args[key] = val
```

Source Code B.3 Continued

```
B.209            except:
B.210                pass
B.211
B.212        args["PostProcess"] = ((args["PostProcess"] == "T") or
B.213                               (args["PostProcess"] == "True")
                                       )
B.214        main(args["PostProcess"])
```